ADVANCES IN FLUID MECHANICS IX

WIT PRESS

Editors
M. Rahman &
C.A. Brebbia

Advances in Fluid Mechanics IX

WIT PRESS

WIT Press publishes leading books in Science and Technology.
Visit our website for the current list of titles.
www.witpress.com

WIT eLibrary

Home of the Transactions of the Wessex Institute.
Papers presented at Advances in Fluid Mechanics VIII are archived in the WIT eLibrary in volume 74 of WIT Transactions on Engineering Sciences (ISSN 1743-3533). The WIT eLibrary provides the international scientific community with immediate and permanent access to individual papers presented at WIT conferences.
http://library.witpress.com.

NINETH INTERNATIONAL CONFERENCE ON
ADVANCES IN FLUID MECHANICS

Advances in Fluid Mechanics IX

CONFERENCE CHAIRMEN

M. Rahman
Dalhousie University, Canada

C.A. Brebbia
Wessex Institute of Technology, UK

INTERNATIONAL SCIENTIFIC ADVISORY COMMITTEE

R. Bourisli
P. Chu
S. D'Alessio
A. Macpherson
F. Morency
T. Moulden
K. Patra
B. Sarler
S. Sinkunas
L. Skerget
V. Tesar

ORGANISED BY
The Wessex Institute of Technology, UK
University of Split, Croatia

SPONSORED BY
WIT Transactions on Engineering Sciences
International Journal of Computational Methods and Experimental Measurement

WIT Transactions

Transactions Editor

Carlos Brebbia
Wessex Institute of Technology
Ashurst Lodge, Ashurst
Southampton SO40 7AA, UK

Editorial Board

F Rachidi EMC Group, Switzerland

M Rahman Dalhousie University, Canada

K R Rajagopal Texas A & M University, USA

T Rang Tallinn Technical University, Estonia

J Rao Case Western Reserve University, USA

J Ravnik University of Maribor, Slovenia

A M Reinhorn State University of New York at Buffalo, USA

G Reniers Universiteit Antwerpen, Belgium

A D Rey McGill University, Canada

D N Riahi University of Illinois at Urbana-Champaign, USA

B Ribas Spanish National Centre for Environmental Health, Spain

K Richter Graz University of Technology, Austria

S Rinaldi Politecnico di Milano, Italy

F Robuste Universitat Politecnica de Catalunya, Spain

J Roddick Flinders University, Australia

A C Rodrigues Universidade Nova de Lisboa, Portugal

F Rodrigues Poly Institute of Porto, Portugal

C W Roeder University of Washington, USA

J M Roesset Texas A & M University, USA

W Roetzel Universitaet der Bundeswehr Hamburg, Germany

V Roje University of Split, Croatia

R Rosset Laboratoire d'Aerologie, France

J L Rubio Centro de Investigaciones sobre Desertificacion, Spain

T J Rudolphi Iowa State University, USA

S Russenchuck Magnet Group, Switzerland

H Ryssel Fraunhofer Institut Integrierte Schaltungen, Germany

S G Saad American University in Cairo, Egypt

M Saiidi University of Nevada-Reno, USA

R San Jose Technical University of Madrid, Spain

F J Sanchez-Sesma Instituto Mexicano del Petroleo, Mexico

B Sarler Nova Gorica Polytechnic, Slovenia

S A Savidis Technische Universitat Berlin, Germany

A Savini Universita de Pavia, Italy

G Schmid Ruhr-Universitat Bochum, Germany

R Schmidt RWTH Aachen, Germany

B Scholtes Universitaet of Kassel, Germany

W Schreiber University of Alabama, USA

A P S Selvadurai McGill University, Canada

J J Sendra University of Seville, Spain

J J Sharp Memorial University of Newfoundland, Canada

Q Shen Massachusetts Institute of Technology, USA

X Shixiong Fudan University, China

G C Sih Lehigh University, USA

L C Simoes University of Coimbra, Portugal

A C Singhal Arizona State University, USA

P Skerget University of Maribor, Slovenia

J Sladek Slovak Academy of Sciences, Slovakia

V Sladek Slovak Academy of Sciences, Slovakia

A C M Sousa University of New Brunswick, Canada

H Sozer Illinois Institute of Technology, USA

D B Spalding CHAM, UK

P D Spanos Rice University, USA

T Speck Albert-Ludwigs-Universitaet Freiburg, Germany

C C Spyrakos National Technical University of Athens, Greece

I V Stangeeva St Petersburg University, Russia

J Stasiek Technical University of Gdansk, Poland

G E Swaters University of Alberta, Canada

S Syngellakis University of Southampton, UK

J Szmyd University of Mining and Metallurgy, Poland

S T Tadano Hokkaido University, Japan

H Takemiya Okayama University, Japan

I Takewaki Kyoto University, Japan

C-L Tan Carleton University, Canada

E Taniguchi Kyoto University, Japan

S Tanimura Aichi University of Technology, Japan

J L Tassoulas University of Texas at Austin, USA

M A P Taylor University of South Australia, Australia

A Terranova Politecnico di Milano, Italy

A G Tijhuis Technische Universiteit Eindhoven, Netherlands

T Tirabassi Institute FISBAT-CNR, Italy

S Tkachenko Otto-von-Guericke-University, Germany

N Tosaka Nihon University, Japan

Advances in Fluid Mechanics IX

Editors

M. Rahman
Dalhousie University, Canada

C.A. Brebbia
Wessex Institute of Technology, UK

WIT*PRESS* **Southampton, Boston**

Editors:

M. Rahman
Dalhousie University, Canada

C.A. Brebbia
Wessex Institute of Technology, UK

Published by

WIT Press
Ashurst Lodge, Ashurst, Southampton, SO40 7AA, UK
Tel: 44 (0) 238 029 3223; Fax: 44 (0) 238 029 2853
E-Mail: witpress@witpress.com
http://www.witpress.com

For USA, Canada and Mexico

WIT Press
25 Bridge Street, Billerica, MA 01821, USA
Tel: 978 667 5841; Fax: 978 667 7582
E-Mail: infousa@witpress.com
http://www.witpress.com

British Library Cataloguing-in-Publication Data

A Catalogue record for this book is available
from the British Library.

ISBN: 978-1-84564-600-4
eISBN: 978-1-84564-601-1
ISSN: (print) 1746-4471
ISSN: (on-line) 1743-3533

The text of the papers in this volume were set individually by the authors or under their supervision. Only minor corrections to the text may have been carried out by the ublisher.

Printed in Great Britain by Lightning Source, UK.

Preface

The field of fluid mechanics is vast and has numerous and diverse applications in many areas of applied mathematics and engineering sciences. AFM 2012 is the ninth International Conference on Advances in Fluid Mechanics held in Split, Croatia in 2012. The conference is reconvened following the success of all previous meetings. The papers in this book cover a wide range of topics in the area of advances in fluid mechanics. The meeting was organised by the Wessex Institute of Technology, UK and the University of Split, Croatia.

The conference has reconvened every two years since 1996, and originated a very successful book series on the same topics which has resulted over 65 volumes since then. The first conference in this series took place in New Orleans, USA (1996); followed by Udine, Italy (1998); Montreal, Canada (2000); Ghent, Belgium (2002); Lisbon, Portugal (2004); Skiathos, Greece (2006); the New Forest, UK (2008); and the Algarve, Portugal (2010).

The papers in the book are arranged in the following sections: Computational methods; Environmental measurements; Hydrodynamics; Fluid Structure interaction; Multiphase flow; Applications in biology; Electronic components; Environmental fluid mechanics; Heat and mass transfer; and Industrial applications.

This volume is part of the Transactions of Wessex Institute series, published in paper and digital format and distributed throughout the world. In addition, all papers are archived within Wessex Institute electronic library (http://library.witpress.com) where they are permanently and easily available to the world scientific community.

The Editors are indeed indebted to all authors as well as the members of International Scientific Advisory Committee who helped review the papers.

The Editors,
Split, Croatia, 2012

Contents

Section 6: Bubble and drop dynamics

Section 7: Heat and mass transfer

Section 8: Hydrodynamics

Section 9: Applications in biology

This page intentionally left blank

Section 1
Fluid structure interaction

This page intentionally left blank

Nonlinear diffraction of water waves: a classical perturbation method

M. Rahman[1], S. H. Mousavizadegan[2] & D. Bhatta[3]
[1]*Faculty of Computer Science, Dalhousie University, Halifax, Canada*
[2]*Faculty of Marine Technology, Amirkabir University of Technology, Iran*
[3]*The University of Texas Pan-American, Edinburg, USA*

Abstract

This paper deals with the classical theory of the perturbation method to determine the solution of wave forces on a circular cylinder in regular waves. Nonlinear diffraction of water waves is considered here to demonstrate the powerful perturbation technique. The solution obtained by this method is compared with the available experimental data. It is found that the analytical solution agrees with the experimental data quite well. When we talk about wave effects on offshore structures, it is necessary to distinguish between small and large dimensions in relation to the characteristic wavelength and the wave amplitude. It is well known that the Morison equation displayed an empirical relationship in terms of the coefficient of mass, C_M, and of the coefficient of drag, C_D, the two hydrodynamic coefficients used to calculate wave forces on a small submerged cylinder. This relationship involves the inertia force and viscous drag force on the cylinder and assumes that the object is small so as not to disturb the incident wave field. However, as the diameter of the cylinder becomes large compared to the incident wavelength, the Morison equation does not apply and a diffraction theory must be used. In this case, viscous drag forces are assumed to be insignificant for smooth dimension structures (cylinders) and the inertia forces predominate. In this paper we discuss the theoretical formulation of second order wave loads. We have obtained the mathematical expressions for the forces and moments to predict the wave loads on large monolithic offshore structures.
Keywords: Morison equation, inertia force, drag force, nonlinear diffraction, radiation, wave forces, moments, perturbation method, second-order theory, offshore structures, cylinders, diffracted waves, incident waves.

WIT Transactions on Engineering Sciences, Vol 74, © 2012 WIT Press
www.witpress.com, ISSN 1743-3533 (on-line)
doi:10.2495/AFM120011

1 Introduction

The determination of wave forces on offshore structures is essential to study the effects of waves, wind and current on them. The offshore structures should experience minimal movement to provide a stable work station for operations such as drilling and production of oil. The solution to the problem of ocean wave interaction with offshore structures is usually very complex. In many cases, only an approximate solution is sought. Some of the mathematical techniques required for the hydrodynamic problem associated with the design of offshore structures are analytical while many are numerical in nature. While the evolution of computers has made the numerical methods more advantageous over the classical analytical methods, numerical methods alone cannot find absolute success without being complemented by either analytical methods or at least experiments; in this sense analytical methods become a cost efficient and handy technique for designers in most cases.

Morison *et al.* [1] gave an empirical relationship in terms of coefficient of mass, C_M, and of coefficient of drag, C_D, the two hydrodynamic coefficients to calculate wave forces on a small submerged cylinder in regular waves. However, when the size of the structure is large compared to the wavelength, there are considerable scattering and diffraction in the wave pattern and in that situation the Morison equation is not suitable to calculate the wave loads and we must use the diffraction theory. A linear diffraction theory was first formulated by MacCamy and Fuchs [2] to calculate the wave loads on a vertical circular cylinder. The cylinder extends from well above the surface to the bottom of the sea. A number of investigators including Mogridge and Jamieson [3] have used this theory to obtain the wave loads on large submerged cylinders in the sea. In all these investigations, the analyses were restricted to linear theory only, which has very limited applications in a practical field because the character of the ocean waves is very often nonlinear. To improve the correlation between experimental data and theory, it is necessary to include the nonlinear effects in the diffraction theory.

Taking into consideration this motivation, many investigators have directed their attention towards nonlinear theory in water waves. Chakrabarti [4] obtained an expression for wave forces on a cylinder using Stokes's fifth order theory, but the kinematic boundary condition was not satisfied in the vicinity of the cylinder. The results obtained were compared with the second order theory of Yamaguchi and Tsuchiya [5] and he concluded that his theory and experimental showed good agreement with their experimental data. Raman and Venkatanarasaiah [6] obtained a nonlinear solution using a perturbation technique. Unfortunately, their experimental results were obtained using a relatively small diameter cylinder, for which the previous workers had assumed the viscous drag forces to be significant.

This paper deals with the theory of second-order wave load expressions to predict the wave forces and moments on large monolithic offshore structures. The theory is applied to a surface-piercing cylinder in regular waves. Following Stoker [7], we have developed a mathematical model of the nonlinear wave theory to correlate with nature. A perturbation technique has been used to solve the

nonlinear diffraction problem. For the case of fixed offshore structures, closed form solutions for drift forces and moments have been obtained using the second-order theory, and the predictions have been compared with available experimental data.

2 Mathematical formulation

A rigid vertical surface-piercing circular cylinder of radius a and the diameter $D = 2a$ is acted upon by a train of regular surface waves of height H, progressing in the positive $x-$ direction (Figure 1). It is assumed that the fluid is incompressible and the motion irrotational. When the amplitude is large, the small amplitude theory does not hold good. In practice, the finite amplitude wave theory, namely the nonlinear wave theory, is of primary importance. In linear wave, the wave amplitudes to the second and higher orders are considered negligible, whereas in the finite amplitude wave theory these higher order terms are retained so as to give an accurate representation of the wave motion.

Let $\phi(r, \theta, z, t)$ denote the total fluid velocity potential and let $z = \eta(r, \theta, t)$ be the equation of the free surface, where (r, θ, z) are the cylindrical coordinates. Then everywhere in the region of the flow, the fluid motion is governed by Laplace's equation.

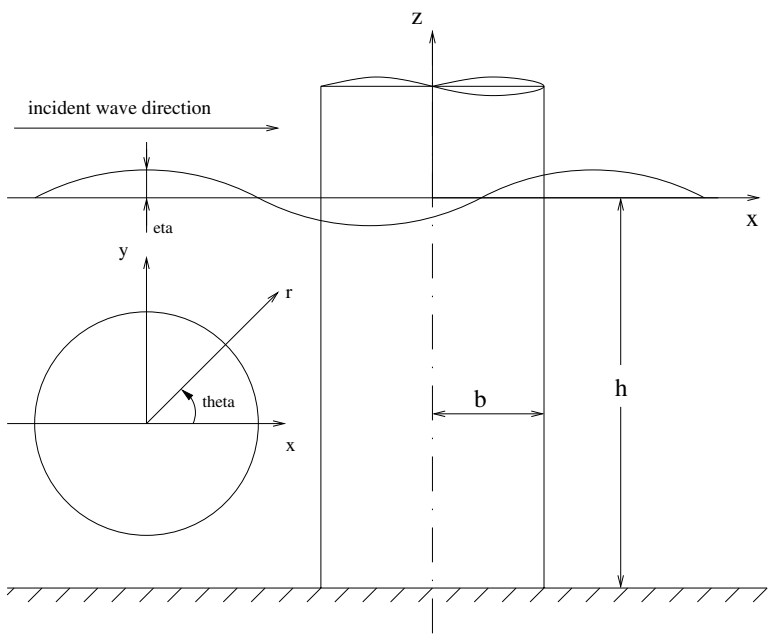

Figure 1: Definition sketch for a surface-piercing circular cylinder in regular waves.

The motion is governed by the equation:

$$\nabla^2\phi = \frac{\partial^2\phi}{\partial r^2} + \frac{1}{r}\frac{\partial\phi}{\partial r} + \frac{1}{r^2}\frac{\partial^2\phi}{\partial\theta^2} + \frac{\partial^2\phi}{\partial z^2} = 0, \tag{1}$$

in the region

$$a \le r < \infty;\ -h \le z < \eta;\ -\pi \le \theta \le \pi.$$

Here ∇ is the Laplacian operator. Equation (1) is Laplace's equation and it is derived from the fluid continuity equation. The boundary conditions associated with the equation (1) are as follows:

Bottom boundary condition:

Assuming the floor of the ocean to be flat, the boundary condition at the ocean bottom states that the vertical component of the velocity is zero at the bottom

$$\frac{\partial\phi}{\partial z} = 0 \quad \text{on} \quad z = -h; \tag{2}$$

Body surface boundary condition:

On the surface of the body the velocity of the fluid must be equal to zero

$$\frac{\partial\phi}{\partial r} = 0 \ \text{ on } \ r = a; \ \ -h \le z \le \eta \tag{3}$$

Dynamic free surface boundary condition:

The dynamic free surface condition is derived from the Bernoulli equation, on the assumption that the atmospheric pressure outside the fluid is constant.

$$\frac{\partial\phi}{\partial t} + g\eta + \frac{1}{2}\left[(\frac{\partial\phi}{\partial r})^2 + (\frac{1}{r}\frac{\partial\phi}{\partial\theta})^2 + (\frac{\partial\phi}{\partial z})^2\right] = 0; \ \ z = \eta, \ \ r \ge a. \tag{4}$$

Kinematic free surface boundary condition:

The kinematic condition states that a particle lying on the free surface will continue to remain on the surface. Mathematically,

$$\frac{\partial\eta}{\partial t} + (\frac{\partial\phi}{\partial r})(\frac{\partial\eta}{\partial r}) + \frac{1}{r^2}(\frac{\partial\phi}{\partial\theta})(\frac{\partial\eta}{\partial\theta}) = \frac{\partial\phi}{\partial z}; \ \text{ on } \ z = \eta, \ \ r \ge a. \tag{5}$$

In addition to the above boundary conditions, there is the Orr-Sommerfeld radiation condition to be satisfied by the scattering potential Φ_s, where $\phi = Re\left\{(\Phi_I + \Phi_s)e^{-i\sigma t}\right\}$ in which Φ_I and Φ_s are defined to be the complex incident and complex scattered potentials respectively. This boundary condition states that the diffracted wave must vanish at infinity and mathematically can be defined by the Orr-Sommerfeld condition

$$\lim_{r\to\infty}\sqrt{r}\left\{\frac{\partial}{\partial r} \pm ik\right\}\Phi_s = 0, \tag{6}$$

where $\sqrt{-1} = i$ and k is the incident wave number. Here Re stands for the real part, σ is the wave frequency.

The velocity components in cylindrical coordinates are $\mathbf{V} = \nabla\phi$, i.e.

$$v_r = \frac{\partial\phi}{\partial r}, \quad v_\theta = \frac{1}{r}\frac{\partial\phi}{\partial\theta}, \quad \text{and} \quad v_z = \frac{\partial\phi}{\partial z},$$

where ϕ is the total velocity potential, η is the height of the free surface, h is the depth of water below the still water level, v_r, v_θ and v_z are the velocity components, g is the acceleration due to gravity, k is the incident wave number ($= 2\pi/L$), x, y, z are rectangular coordinates, r, θ, z are the cylindrical coordinates, t is the time variable and L is the wavelength. The Cartesian form of (1) is

$$\nabla^2\phi = \frac{\partial^2\phi}{\partial x^2} + \frac{\partial^2\phi}{\partial y^2} + \frac{\partial^2\phi}{\partial z^2} = 0 \tag{7}$$

where $x = r\cos\theta$, $y = r\sin\theta$ and $z = z$.

The formulas for the forces $\mathbf{F}$ and moments $\mathbf{M}$ of the fluid on the body S can be written in vector form as follows:

$$\left\{ \begin{array}{c} \mathbf{F} \\ \mathbf{M} \end{array} \right\} = \int\int_S P \left\{ \begin{array}{c} \mathbf{n} \\ \mathbf{r}\times\mathbf{n} \end{array} \right\} dS,$$

where $\mathbf{n}$ is the outward normal vector from the body surface, P is the pressure field which can be obtained from the Bernoulli's equation as illustrated in the next section and $\mathbf{r}$ is the radial distance vector.

3 Perturbation method of solution

The problem is to work with the complete form of the equation to assume that the solution can be represented in terms of a power series expansion of the parameter ε where $\varepsilon = kH/2 = kA$. A is the amplitude of the wave. Thus expanding ϕ, η and P as a series in powers of ε yields

$$\phi = \sum_{n=1}^{\infty} \varepsilon^n \phi_n, \tag{8}$$

$$\eta = \sum_{n=1}^{\infty} \varepsilon^n \eta_n, \tag{9}$$

$$P = \sum_{n=0}^{\infty} \varepsilon^n P_n. \tag{10}$$

The sum of the terms up to index n represents the nth-order theory for any particular quantity, P represents the pressure field, and ϕ, η and P are all functions

of x, y,z and t. At the free surface, $z = \eta(x, y, t)$, and so we have

$$\phi(x, y, z, t) = \phi[x, y, \eta(x, y, t), t]. \tag{11}$$

The modified velocity potential at the free surface is

$$\phi(x, y, \eta, t) = \varepsilon\phi_1(x, y, 0, t) + \varepsilon^2[\phi_2(x, y, 0, t) + \eta_1(\frac{\partial\phi_1}{\partial z})_{z=0}] + O(\varepsilon^3). \tag{12}$$

Substituting the series into the dynamic and kinematic free surface boundary conditions, it is found that the first-order potential ϕ_1 and the second-order potential ϕ_2 satisfy the following equations, respectively:

$$\frac{\partial^2\phi_1}{\partial t^2} + g\frac{\partial\phi_1}{\partial z} = 0 \quad \text{on} \quad z = 0, \tag{13}$$

$$\frac{\partial^2\phi_2}{\partial t^2} + g\frac{\partial\phi_2}{\partial z} = -\eta_1\frac{\partial}{\partial z}\left\{\frac{\partial^2\phi_1}{\partial t^2} + g\frac{\partial\phi_1}{\partial z}\right\} - \frac{\partial}{\partial t}\left\{(\frac{\partial\phi_1}{\partial x})^2 + (\frac{\partial\phi_1}{\partial y})^2 + (\frac{\partial\phi_1}{\partial z})^2\right\}, \quad r \geq a. \tag{14}$$

The pressure $P(r, \theta, z, t)$ may be determined from the Bernoulli's equation and on substitution for ϕ as a series in power of ε, leads to

$$P = -\rho gz - \varepsilon\rho\frac{\partial\phi_1}{\partial t} - \varepsilon^2\rho[\frac{\partial\phi_2}{\partial t} + \frac{1}{2}((\frac{\partial\phi_1}{\partial r})^2 + \frac{\partial\phi_1}{\partial z})^2 + \frac{1}{r^2}\frac{\partial\phi_1}{\partial\theta})^2)] + O(\varepsilon^3). \tag{15}$$

The total horizontal force is

$$F_x = \int_0^{2\pi}\int_{-h}^{\eta} |P|_{r=a}(-a\cos\theta)dzd\theta. \tag{16}$$

Now let us write F_x as a perturbation series up to order ε^2 as follows:

$$F_x = \varepsilon F_{x1} + \varepsilon^2 F_{x2}, \tag{17}$$

where the first order contribution is

$$\varepsilon F_{x1} = a\rho\int_0^{2\pi}\left\{\int_{-h}^{0}(\varepsilon\frac{\partial\phi_1}{\partial t})_{r=a}\right\}\cos\theta d\theta \tag{18}$$

and the second-order contribution is

$$\varepsilon^2 F_{x2} = a\rho\int_0^{2\pi}[\int_0^{\varepsilon\eta}(gz + \varepsilon\frac{\partial\phi_1}{\partial t})_{r=a}dz + \varepsilon^2\int_{-h}^{0}\left\{\frac{\partial\phi_2}{\partial t} + \frac{1}{2}(\frac{\partial\phi_1}{\partial z})^2 + \frac{1}{2a^2}(\frac{\partial\phi_1}{\partial\theta})^2\right\}_{r=a} dz]\cos\theta d\theta. \tag{19}$$

It is to be noted here that in the second-order force evaluation given in (19), the first term on the right can be defined as the *waterline force*, the third term as the *dynamic force* and the second term as the *quadratic force* as stated by Lighthill [8].

The expressions for ϕ_1 and ϕ_2 are given as follows (Rahman [9]):

$$\phi_1 = \frac{\sigma \cosh k(z+h)}{k^2 \sinh kh} e^{-i\sigma t} \sum_{m=0}^{\infty} \delta_m i^m A_m(kr) \cos m\theta,$$

$$\phi_2 = \frac{\sigma e^{-2i\sigma t}}{2k^2} \sum_{m=0}^{\infty} \left\{ \int_0^{\infty} D_m(k_2) A_m(k_2 r) \cosh k_2(z+h) dk_2 \right\} \cos m\theta.$$

with the dispersion relation which is $\sigma^2 = gk \tanh kh$.

4 Forces and moments on the circular cylinder

Using the results presented by Rahman and Heaps [10], the non-dimensional forms of the first-order and second-order components of the total forces may now be written as

$$\frac{F_{x1}}{\rho g D^3} = \frac{\tanh kh}{2(ka)^3} \cdot \frac{\cos(\sigma t - \alpha_1)}{|H_1^{(1)'}(ka)|}, \tag{20}$$

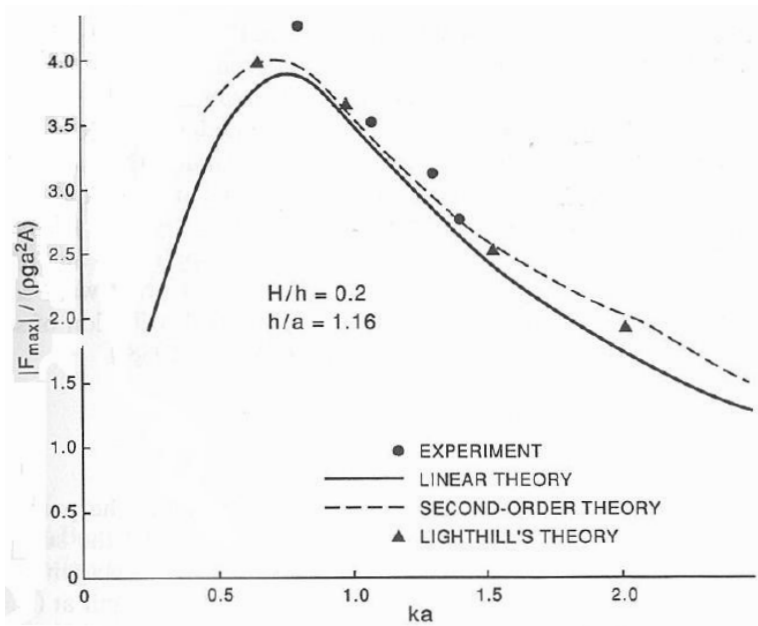

Figure 2: Comparison of linear and second-order wave forces with the experimental data of Chakrabarti [4].

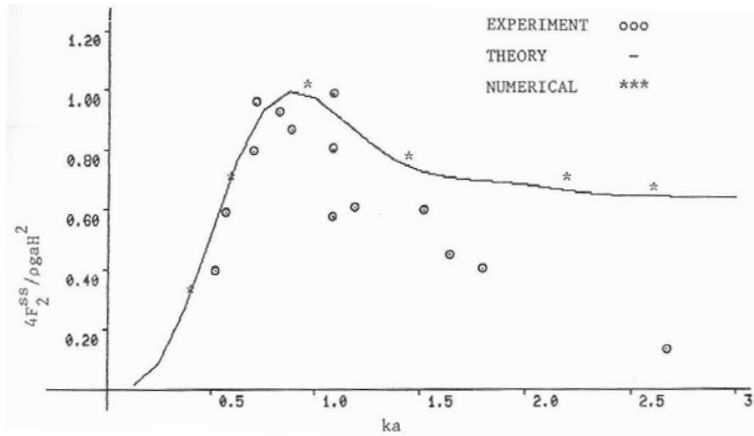

Figure 3: Potential drift force on fixed circular cylinders, $h/a = 1.16$: Comparison with the numerical data of Garrison [11].

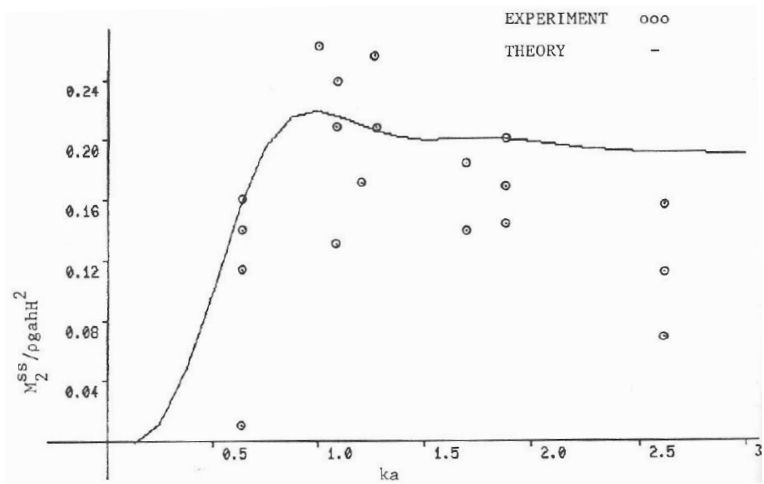

Figure 4: Potential drift moment on fixed circular cylinders, $h/a = 1.16$: Comparison with the numerical data of Garrison [11].

and

$$\frac{F_{x2}}{\rho g D^3} = \left\{ \frac{e^{-2i\sigma t}\tanh kh}{8(ka)} \int_0^\infty G(k_2)dk_2 + c.c. \right\}$$
$$- \frac{1}{4\pi(ka)^4} \sum_{\ell=0}^{\infty} (-1)^\ell [(3 - \frac{2kh}{\sinh 2kh}) + \frac{\ell(\ell+1)}{a^2k^2}$$
$$\times (1 + \frac{2kh}{\sinh 2kh})] \times [C_\ell \cos 2\sigma t - S_\ell \sin 2\sigma t]$$
$$- \frac{1}{4\pi(ka)^4} \sum_{\ell=0}^{\infty} [(1 - \frac{\ell(\ell+1)}{a^2k^2})(1 + \frac{2kh}{\sinh 2kh})E_\ell] \qquad (21)$$

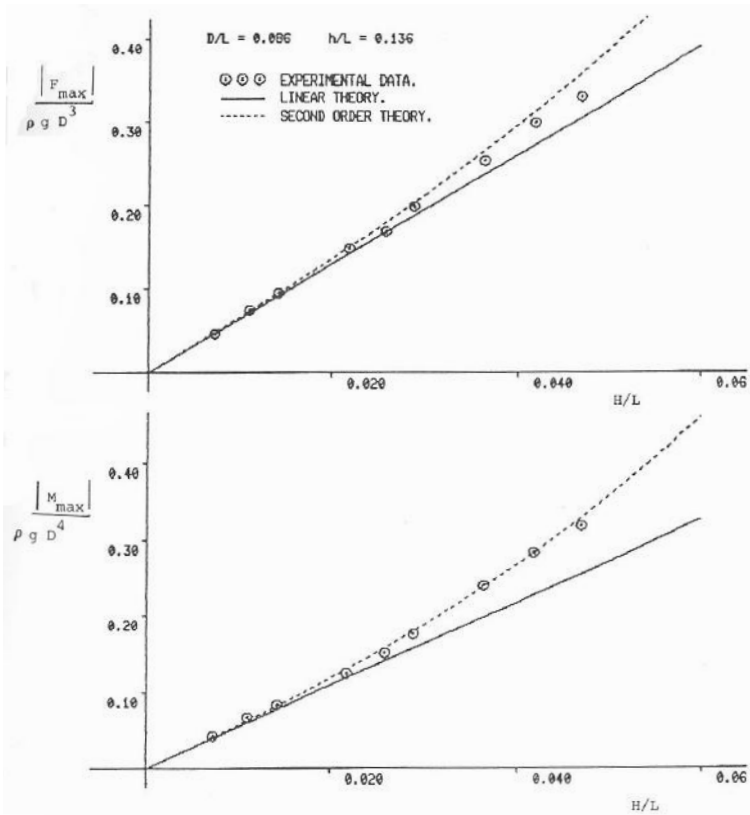

Figure 5: Comparison of predicted and measured forces and moments on circular cylinders (Experimental data of Mogridge and Jamieson [3]).

where

$$G(k_2a) = \frac{\int_{ka}^{\infty} A_1(k_2r)B_1(kr)d(kr)}{(k_2a)\left[(k_2a) - \frac{4ka\tanh kh}{\tanh k_2h}\right] H_1^{(1)'}(k_2a)}. \tag{22}$$

The second-order force (21) contains two parts; one oscillatory and the other steady state. They are defined, respectively, as

$$\frac{F_{x2}}{\rho g D^3} = \frac{F_2^{OS}}{\rho g D^3} + \frac{F_2^{SS}}{\rho g D^3}.$$

Similarly, the non-dimensional forms of the linear and of the second-order moments are given by

$$\frac{\varepsilon M_1}{\rho g D^4} = C_M \frac{(H/L)\pi}{16(D/L)(ka)}[kh\tanh kh + sechkh - 1]\cos(\sigma t - \alpha_1), \tag{23}$$

and

$$\frac{\varepsilon^2 M_2}{\rho g D^4} = \frac{(H/L)^2(h/D)}{4\pi^3(D/L)^4}\sum_{\ell=0}^{\infty}[\frac{\ell(\ell+1)}{k^2a^2}B - C]E_\ell$$
$$+ [\frac{(H/L)^2(h/D)}{8(D/L)^2}\tanh khe^{-2i\sigma t}\int_0^\infty G(k_2a)\lambda(k_2h)d(k_2a) + c.c.]$$
$$- \frac{(H/L)^2(h/D)}{4\pi^3(D/L)^4}\sum_{\ell=0}^{\infty}(-1)^{\ell+1}[A + \frac{\ell(\ell+1)}{k^2a^2}B]$$
$$\times [C_\ell \cos 2\sigma t - S_\ell \sin 2\sigma t]. \tag{24}$$

The second-order moment (24) contains two parts; one oscillatory and the other steady state. They are defined, respectively, as

$$\frac{M_2}{\rho g D^4} = \frac{M_2^{OS}}{\rho g D^4} + \frac{M_2^{SS}}{\rho g D^4}.$$

The graphical representations of these results are displayed with the comparison of the experimental and numerical data. It is worth mentioning here that all the parameters defined here are found in the work of Rahman [9].

5 Results and conclusions

The analytical and numerical and experimental results are displayed and discussed in this section. In Fig. 2, both the first-order and the second-order solutions (see Rahman [9]) are compared with the force measurements of Chakrabarti [4], which are generally seen to be closer to the second-order predictions. The normalized dynamic drift forces and moments are potted against the diffraction parameter ka in Fig. 3 and Fig. 4 using the analytical results. This results are compared with the numerical solutions obtained by Garrison [11] and the present predicted results quite agree with the Garrison's numerical data. Garrison used the Green function method to determine the drift forces and moments. In Fig. 5, analytical solutions are compared with the experimental data of Mogridge and Jamieson [3] for a vertical circular cylindrical structure. These results were computed taking the averages of the positive and negative maximum loads. The theoretical predictions of moments seem to agree very well with the measured values for the given range of parameters.

Acknowledgements

We are grateful to the Natural Sciences and Engineering Research Council of Canada for its financial support leading to this paper. We are also thankful to the Faculty of Computer Science at Dalhousie University for the computer facilities provided to complete this paper.

References

[1] Morison, J. R., O'Brien, M. P., Johnson, J. W. and Schaaf, S. A. (1950). *The forces exerted by surface waves on piles*, J. Petrol. Technology, **186**, 149–154.

[2] MacCamy, R. C. and Fuchs, R. A. (1954). *Wave forces on piles: a diffraction theory*, U. S. Army Beach Erosion Board, Techn. Memo. No. **69**, December, 17 pages.

[3] Mogridge, G. R. and Jamieson, W. W. (1975). *Wave forces on circular caissons: theory and experiment*, Can. J. Civ. Engg., **2**, 540–548.

[4] Chakrabarti, S. K. (1975). *Second-order wave forces on large vertical cylinders*, Proc. ASCE, **101, WW3**, 311–317.

[5] Yamaguchi, M and Tsuchiya, Y. (1974). *Nonlinear effects of wave pressures and wave forces on a large cylindrical pile*, Proc. Civ. Engg. Soc. in Japan, **229**, 41–53 (in Japanese).

[6] Raman, H. and Venkatanarasaiah, P. (1976). *Forces due to nonlinear water waves on vertical cylinders*, Proc. ASCE, **102, WW3**, 301–316.

[7] Stoker, J. J. (1957). *Water waves*, Interscience, New York.

[8] Lighthill, M. J. (1979). *Waves and hydrodynamic loading*, Proc. Second Int. Conf. on The Behaviour of Offshore Structures, BOSS'79, London, **1**, 1–40.

[9] Rahman, M. (1988). *The hydrodynamics of waves and tides with applications*, Topics in Engineering Vol. **4**. Edited by Carlos Brebbia and J. J. Connor, Computational Mechanics Publications, Southampton UK and Boston USA.

[10] Rahman, M. and Heaps, H. S. (1983). *Wave forces on offshore structures: nonlinear wave diffraction by large cylinders*, J. Physical Oceano., **13**, 2225–2235.

[11] Garrison, C. J. (1984). *Wave structure interaction*, Proc. Specialty Conf. Comput. Methods in Offshore Engg., CSCE, Halifax, N.S., Canada, 1–72.

This page intentionally left blank

Design and testing of wind deflectors for roof-mounted solar panels

G. V. Kudav[1], Y. M. Panta[1] & M. Yatsco[2]
[1]*Youngstown State University, Department of Mechanical Engineering, Ohio, USA*
[2]*V&M Star, Youngstown, USA*

Abstract

The amount of solar energy that can be produced in the US and throughout the world has seen an unprecedented potential to fulfill growing energy demand. Solar panels can be installed on the ground or on the roof of a building. Roof mounted solar panels could experience occasional high wind loads especially lift and drag forces. Solar panels are bolted directly onto the roof and are secured using ballasts as counter weights against the wind loads. We propose the use of efficient wind deflectors designed and strategically placed in front of the panels as reported here. The deflectors under study were proven to minimize the wind loads on solar panels, ensuring the safety of civilians and surrounding property.

The present study utilizes wind tunnel testing and computational simulation using the commercial computational fluid dynamics software ANSYS Fluent for a steady, turbulent wind flow (standard k-ε model) over an inclined rooftop-solar panel. The study shows promising results in the prediction of the wind forces for an effectively designed wind management system. As specified earlier, results were compared and validated by both wind tunnel experiments and computational simulations for a meaningful conclusion. Solar panels with various aspect ratios for high incoming wind speeds in the range 40–50 m/s (i.e. 90–110 mph) with several angles of attack were modeled and simulated. We report the analysis of high wind loads on the solar panels leading to the design of an optimized wind deflector to counter such loads. It was concluded that an elliptically profiled wind deflector, with uniformly spaced short fins that were positioned before the tilted panels, was proven to minimize the high wind loads by as much as half, compared to the wind loads without the deflector.
Keywords: rooftop solar panels, solar panel deflectors, wind loads, ballast.

WIT Transactions on Engineering Sciences, Vol 74, © 2012 WIT Press
www.witpress.com, ISSN 1743-3533 (on-line)
doi:10.2495/AFM120021

1 Introduction

Solar power has gained several increasing domestic and commercial applications as a renewable source of energy [1]. The two most common methods of solar panel deployment are on the ground or on the roof. Ground-mounted solar panel racks need open land that can considerably increase initial project investment and also the system installation costs. The more logical and cost saving alternative would be to mount the solar panel racks on the roof of a building without the need to purchase or lease an open lot to install the solar panel system. This also enables the solar panels to be installed even in densely populated locations where space costs are at a premium. Other advantages of installing the racks on the roof are the ease of installation and maintenance in that there is no need to dig holes for the support beams of the solar panel racks as there is for ground-mounted racks.

Earlier research studies indicate that the optimum tilt angles for the solar panels are between 22^o and 48^o which can allow sufficient sunlight in solar panels. Tilt angles close to about 30^o are the best for various regions in the US as indicated by figure 1. One previous study [2] has presented some good strategies for mounting solar panel arrays on roofs. It is important to mention here that these tilt angles are influenced by the latitude of the location and the solar azimuth angle. A recent study [3] reported that wind tunnel experiments can successfully analyze wind uplift on solar panel models. The study also discussed the effect of guide plates for the reduction of lift forces in various experimental configurations of the solar panels. A more recent study revealed the usefulness of wind tunnel experiments and computational fluid dynamics (CFD) analysis for roof-mounted solar photovoltaic arrays in correlating CFD simulation results with the wind tunnel test data [4].

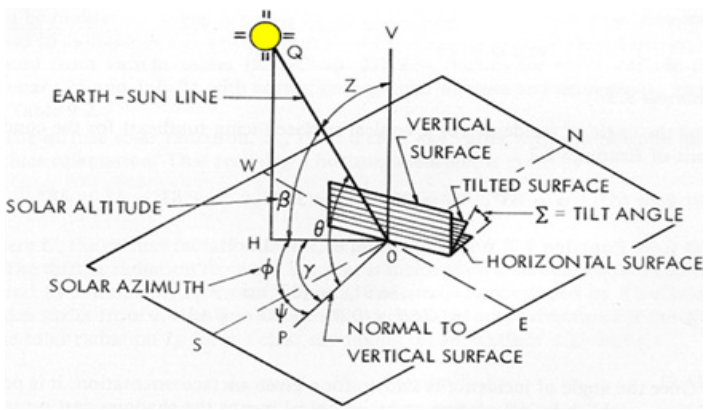

Figure 1: The solar azimuth angle for a photovoltaic array situated in the Northern hemisphere [5].

The solar panel racks can be installed on almost any type of flat roof surface made of tar, gravel, or rubber. Major considerations for the roof-mounted panel racks are wind speed and wind direction resulting in aerodynamics forces or wind loads on the racks. General wind data maps [2] help determine the ranges of wind speeds, their direction, and the angle of attacks in the continental United States throughout the year. Similarly, general wind data maps of other continents and countries can also be used to estimate the ranges of wind speeds and their direction/angle of attacks. Wind loads often necessitate the use of heavy ballast to counter such loads. The ballast weight, however, could exceed the allowable structural load on the roof. Therefore, efficient wind deflecting systems could reduce or ideally eliminate use of ballast.

A recent study revealed the usefulness of wind tunnel experiments and CFD analysis for roof-mounted solar photovoltaic arrays [6]. With the aid of CFD and wind tunnel facilities, the current work presents the design of wind deflectors to minimize the wind loads, especially the drag and lift forces, on the solar panels. The computational analysis comprises the use of CFD software ANSYS Fluent in an iterative mode for one-quarter and full scale models. These results were further validated with wind tunnel tests. Several geometries of wind deflectors were designed and analyzed to minimize wind load reduction and the one that reduced the overall drag and lift forces the most was ultimately chosen and offered to the research sponsor – Northern States Metal, NSM, Youngstown, Ohio, USA [7] – for possible development and marketing.

2 Theory

An algorithm with a set of governing equations including i) the mass/continuity (eqn (1)), ii) the momentum/Navier-Stokes (eqn (2)), iii) the turbulent kinetic energy (eqn (3)), and iv) the dissipation rate equations (eqn (4)) are used for mathematical modeling of the wind flow domain around the solar panel. These governing equations are embedded within ANSYS Fluent to analyze the fluid properties, specifically the lift and drag characteristics on (i) the solar panel and (ii) the solar panel with the deflector placed in front of the panel. Mathematical modeling was carried out in order to analyze the wind forces of the incoming high-speed wind on the given panel model and the deflector. The standard k-ε turbulence model for the turbulent flow was chosen for ANSYS Fluent [8, 9].

Mass – Continuity Equation:

$$\frac{\partial \rho}{\partial t} + \nabla.(\rho \boldsymbol{V}) = \mathbf{0} \tag{1}$$

Momentum – Navier-Stokes Equations:

$$\rho\left[\frac{\partial \boldsymbol{V}}{\partial t} + \boldsymbol{V}\cdot(\nabla \boldsymbol{V})\right] = -\nabla p + \mu \nabla.(\nabla \boldsymbol{V}) + \boldsymbol{f} \tag{2}$$

$$\frac{\partial}{\partial t}(\rho k) + \frac{\partial}{\partial x_i}(\rho k u_i) = \frac{\partial}{\partial x_j}\left[\left(\mu + \frac{\mu_t}{\sigma_k}\right)\frac{\partial k}{\partial x_j}\right] + P_k + P_b - \rho\epsilon - Y_M + S_k \quad (3)$$

$$\frac{\partial}{\partial t}(\rho \epsilon) + \frac{\partial}{\partial x_i}(\rho \epsilon u_i) = \frac{\partial}{\partial x_j}\left[\left(\mu + \frac{\mu_t}{\sigma_\epsilon}\right)\frac{\partial \epsilon}{\partial x_j}\right] + C_{1\epsilon}\frac{\epsilon}{k}(P_k + C_{3\epsilon}P_b) - C_{2\epsilon}\rho\frac{\epsilon^2}{k} + S_\epsilon \quad (4)$$

$$\mu_t = \rho C_\mu \frac{k^2}{\epsilon} \quad (5)$$

where the nomenclature for the symbols has the usual meaning and they are defined below [7]:

$\boldsymbol{V}$ = total velocity vector of the fluid
$u, v, w \equiv$ x-, y-, and z-components of the velocity, respectively
$\boldsymbol{f}$ = body forces
k = turbulent kinetic energy
ε = the rate of dissipation.
$\boldsymbol{\mu_t}$ = the turbulent viscosity
$G_k \equiv$ generation of turbulent kinetic energy due to the mean velocity gradient
$G_b \equiv$ generation of turbulent kinetic energy due to buoyancy
$Y_M \equiv$ contribution of the fluctuating dilatation in compressible turbulence overall dissipation rate
$S_k \equiv$ user defined source term
$S_\varepsilon \equiv$ user defined source term

Other arbitrary constants in Eqns. (3) and (4) are used from the ANSYS Fluent Manual: $C_{1\varepsilon}$ = 1.44, $C_{2\varepsilon}$ = 1.92, C_μ = 0.09, σ_k = 1.00, and σ_ε = 1.3. These values are acceptable for wall-bounded and free shear flows and are appropriate for a CFD study of solar panel racks positioned in a wall-bounded fluid domain [8, 9].

3 Methodology

As ballast for the solar panel to add substantial weight on a roof mounting, a wind deflector was conceptualized as an alternative solution to reduce or replace the use of such ballast. Based on the study, it was recommended that wind deflectors were placed on all sides of the solar panel racks as a complete wind management system to reduce the head-wind and side-wind effects. If all sided wind deflectors are not economically viable, the wind deflector on the front is highly recommended to minimize the head-wind effects. Although the wind deflector itself will add a minimal weight on the roof it is negligible compared to that of ballast. Multiple deflectors of various surface profiles were designed that

included vertical, inclined, parabolic, elliptic and elliptic with fins shapes. Only a sketch of the elliptic deflectors is shown in figure 2.

Wind flows over the physical model with and without a deflector were tested for wind forces using wind tunnel instruments. Similarly, wind flows with and without a deflector were simulated, and analyzed for wind forces using ANSYS Fluent software. Based on the preliminary CFD analysis among the deflector shapes for high winds, an elliptic finned-deflector (figure 2(b)) was chosen for further analysis by CFD simulation and testing in the wind tunnel for its relative superior performance.

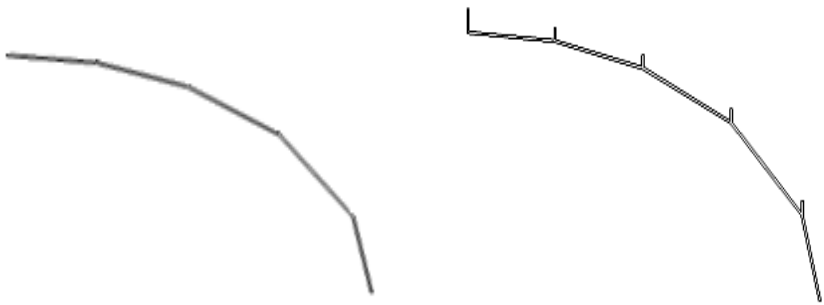

(a) (b)

Figure 2: Side views of the deflector: (a) elliptic, (b) elliptic plus fins.

As mentioned, two methods that included computations using CFD simulations and experiments using wind tunnel testing were employed for wind load analysis. These methodologies are given below.

3.1 Methodology I: computations/simulations

Computational analysis involves solving a problem through the use of an algorithm and mathematical model. ANSYS Fluent software that combines numerical techniques with the intricacies of fluid flow is employed for the modeling of wind flow over the solar panel. The software was built to model and analyze many types of laminar and turbulent fluid flows. The software has different packages and add-ons that allow one to model various geometries with the chosen flow models. The software comes with geometry modeling software, called ANSYS Design Modeler. The remaining add-ons include ANSYS Meshing, ANSYS Fluent, and CFD Post. Details of the ANSYS Fluent, computational models/simulations for the wind flow analysis of the rooftop solar panel racks are discussed in the sections that follow.

3.1.1 CFD software

The procedure to set-up and run a successful simulation in ANSYS Fluent, for a fluid flow problem, consists of a series of steps that are completed sequentially. The procedure is outlined as preprocessing, processing, and post-processing. The

algorithm, descretization technique and the convergence criteria of ANSYS Fluent are summarized below:
1. Construction of the geometrical models using ANSYS Design Modeler.
2. Division of the fluid domain into discrete volumes using ANSYS Meshing.
3. Modeling using ANSYS Fluent (figure 3).
4. Defining the boundary conditions and fluid properties.
5. Solving in Fluent until a converged solution is achieved (eqn. (6)).

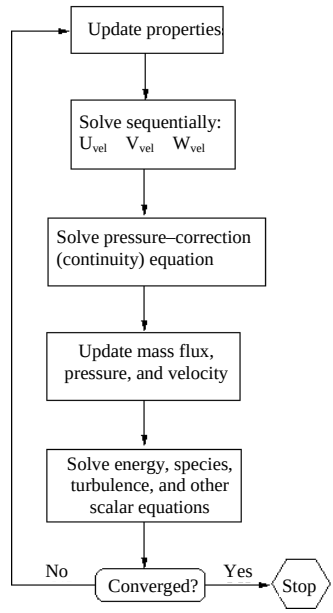

Figure 3: Pressure-based segreagated algorithm used in ANSYS Fluent [9].

3.1.1.1 Pressure-based segregated algorithm The pressure-based solver uses an algorithm to solve for the governing equations in a sequential order with an iterative process as shown in figure 3.

3.1.1.2 Discretization technique ANSYS Fluent utilizes a discretization technique to turn a general scalar equation into an algebraic equation which enables the equations to be solved numerically. The governing equations are integrated about each of the volumes created during the meshing process.

$$\sum_{f}^{Nfaces} \rho_f \vec{v}_f \phi_f \cdot \vec{A}_f = \sum_{f}^{Nfaces} \Gamma_\phi \nabla \phi_f \cdot \vec{A}_f + S_\phi V \tag{6}$$

where

$N_{faces} \equiv$ number of faces enclosing the cell

$\phi_f \equiv$ value of ϕ convected through the face f

$\rho_f \vec{v}_f \cdot \vec{A}_f \equiv$ mass flux through the face f

$\vec{A}_f \equiv$ area of face f

$\nabla \phi_f \equiv$ gradient of ϕ at face f

$V \equiv$ cell volume

3.1.1.3 Convergence criteria The use of a numerical modeling technique requires ways to measure the validity and accuracy of the simulated solution. The convergence criteria in ANSYS Fluent depend on the type of model chosen. These residuals, depending on the type of model selected, involve x- and y-components of the velocities, k and ε that include continuity, momentum, turbulence, and energy.

3.1.2 Computer models and simulations

When modeling the fluid domain surrounding a solar panel using the CFD software, incompressible, steady, Newtonian fluid was assumed of a turbulent nature with no buoyancy effects and no heat considerations. The layout of the flow fields for two computer models that include five solar panels and five solar panels with a deflector at the front are shown in figures 4(a) and 4(b). The reduction in the wind loads on the panel using the wind deflector as predicted by CFD results are discussed in a subsequent section below.

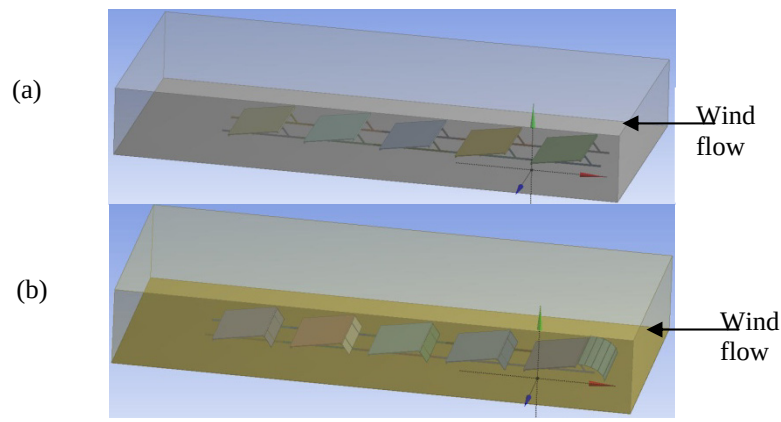

Figure 4: Layout of the flow field for CFD simulation: (a) five solar panels, and (b) five solar panels with a deflector at the front [8].

3.2 Methodology II: experimentations

It is a well-known fact that CFD analysis alone is not an absolute measure of the accuracy in the design of any turbulent flow management system due to inherent uncertainty in the turbulence parameters in the flow field. However, comparisons between results from wind tunnel tests and CFD simulations for a few benchmark models provide the degree of confidence required in the implementation of the design at reduced cost and time. As full scale models were too large to fit into our wind tunnel test section, quarter-scale models were developed and tested in our university's wind tunnel facility. All full-scale solar panel racks that were investigated in this study were at an inclination of 10^o with respect to the horizontal axis for a wind speed of 49 m/s (110 mph).

3.2.1 Wind tunnel instrumentation

The experimental analysis consisted of conducting multiple wind tunnel tests of quarter-scale rooftop solar panel racks and wind deflectors. Figure 5 shows the schematic of the test setup. The fan motor speed was controlled using VFD (PowerFlex-4M, Allen-Bradley) to generate variable input frequencies to the motor that translates into variable wind speeds in the tunnel as inlet wind speed The VFD was actuated via a laptop (Dell E5500) utilizing LABVIEW v8.6 drivers and National Instruments' module NI 9264 by providing voltage in the range of 0~10 Vdc. At each motor rpm, the pitot- static tube that was connected to an electronic pressure sensor (Model 20 INCH D-MV R8B22-58 supplied by All Sensors) measured the pressure difference ($P_0 - P_\infty$), where P_0 is the stagnation pressure and P_∞ is the static pressure in the wind tunnel. The pressure sensor outputs a dc voltage to NI 9219 with a supplied excitation voltage of 2.5 Vdc. Then through a calibration procedure provided by All Sensors, the voltage was converted to a pressure difference in inches of water.

Through Bernoulli's equation, the pressure difference was converted to wind speed in mph. The NI modules interfaced with the NI DAQ module cDAQ-9172 and were controlled by the LABVIEW program. The wind tunnel was calibrated by recording wind speeds at various input frequencies from 0 to 80 Hz in order to interpolate between the wind speed and the corresponding input frequency. The models to be tested were to be mounted on a melamine board. Four load cells (FUTEK's model LCF300:50-lb) were used to record either lift or drag forces. The load cells operate on a full Wheatstone bridge. NI 9237 provided the bridge circuitry. Through a calibration equation provided by FUTEK, the output dc voltage was converted to a force in lbf and then to N through LABVIEW.

3.2.2 Physical models and testing

The load cells were installed with two orientations in order to measure the two major wind forces; namely lift (vertical) and drag (horizontal) forces, for several incoming wind speeds. Following figure 5, figures 6 to 8 below show the wind tunnel and solar panel/load cell setup for wind lift and drag force measurements. The results that were obtained from the wind tunnel analysis were then used to verify the CFD simulations.

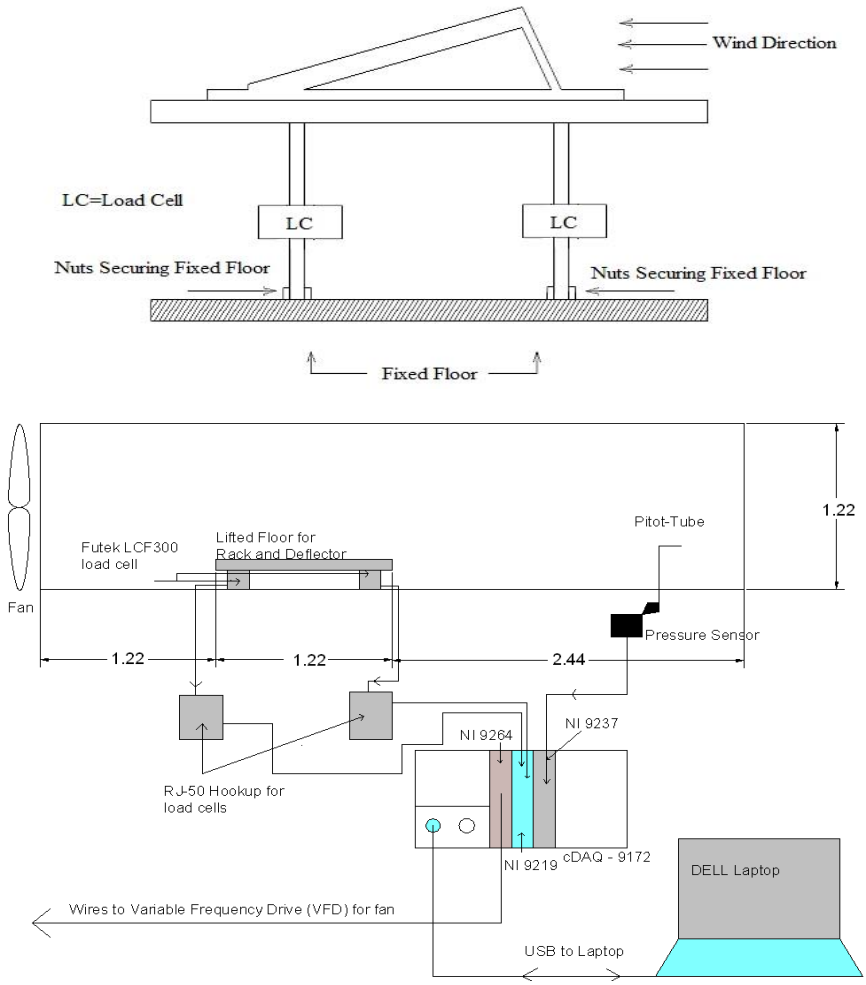

Figure 5: Wind tunnel test setup (all dimensions are in m).

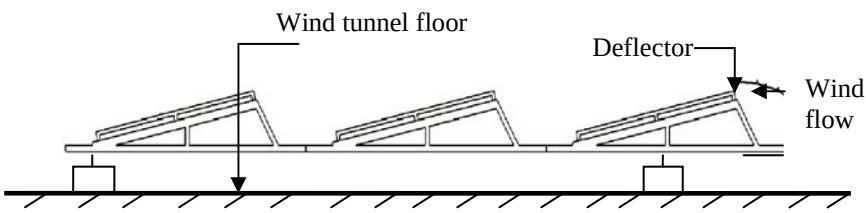

Figure 6: Deflector-panel orientation for a 3-rack system in the wind tunnel.

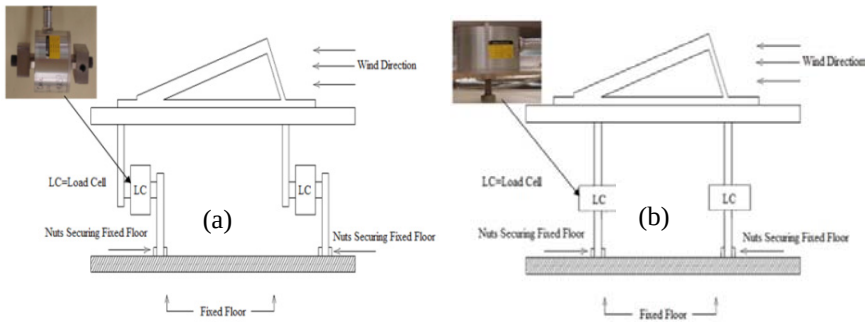

Figure 7: Load cell placement: (a) horizontal for the lift; (b) vertical for the drag force measurement.

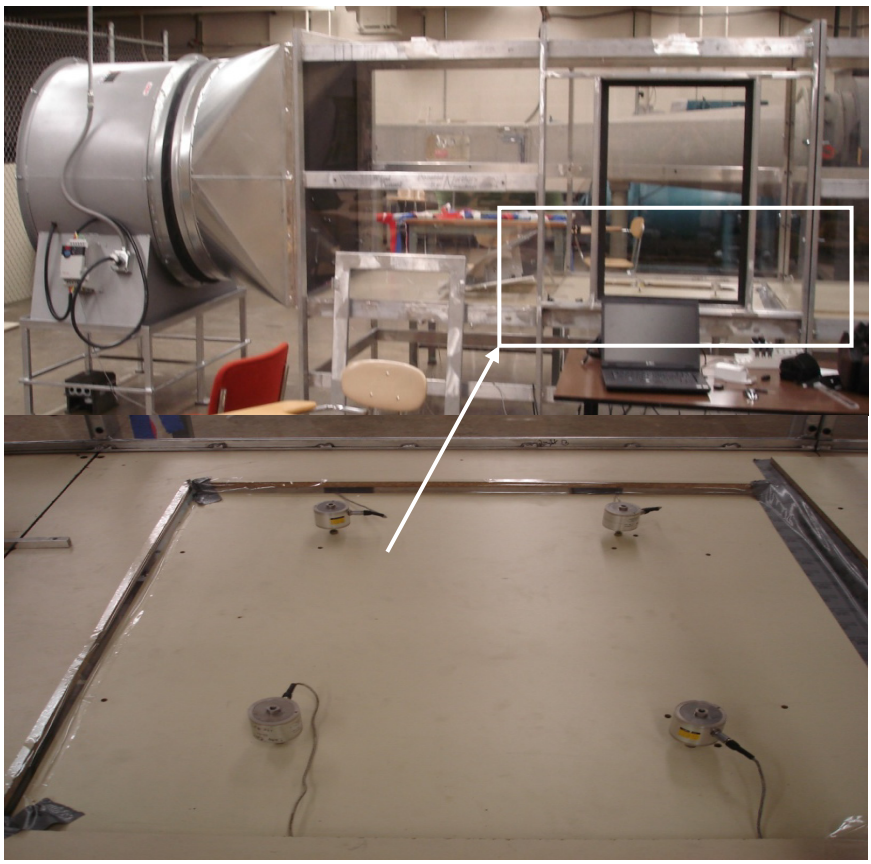

Figure 8: Wind tunnel instrumentation showing load cells on the testing floor (zoomed and shown) for wind uplift force measurement.

4 Results and discussions

The results we report here are presented in the two subsections below. First the wind loads measured for scaled models in the wind tunnel and predicted by CFD analysis are presented followed by the CFD results for the full scale model only.

4.1 Wind tunnel results

Measurements were recorded at four different speeds: 6.7, 9.0, 11.2, and 12.0 m/s (15, 20, 25, and 27 mph). For all the test configurations of the scaled models, the lift and drag forces increased as the wind speed increased from 6.7 m/s (15 mph) to 12 m/s (27 mph) as expected due to the forces being proportional to the square of wind speed. For rack-only arrangement, the minimum and maximum lift forces were 5.34 N and 16.90 N respectively while for the rack-with-deflector system the minimum and maximum lift forces were 2.67 N and 7.56 N respectively. Therefore, it can be concluded solely from the wind tunnel test data that using the deflector reduces the lift forces for the rack-deflector arrangement by approximately 50% for the speeds tested while the drag forces have minimal changes.

4.2 CFD simulation results compared with the wind tunnel test data

As shown in table 1, the use of the deflector reduced wind uplift by 51.29%, but increased the drag force by 28.33%. It should be noted that positive values for the forces represent a reduction and vice versa. The CFD analysis estimated a net reduction of 37.14% and 9.16% for the lift and drag forces, respectively. A similar trend was found in the experimental and computational analysis of the three-rack model with and without deflector.

Table 1: Wind tunnel test data and CFD results for quarter-scale models with input wind velocity=12 m/s – comparison in %.

Quarter-Scale Models for wind speed =12 m/s	Wind Tunnel Vs CFD Difference in %	With Deflector, Reduction in Wind Loads as Measured by			
		Wind Tunnel Tests, %		CFD Simulations, %	
	Lift., FL	Lift., FL	Drag, FD	Lift., FL	Drag, FD
Single Rack Only	27.84	51.29	-28.33	37.14	9.16
Single Rack and Deflector	6.88				
3 Racks Array	28.27	45.61	-26.25	54.09	20.54
3 Racks Array and	8.27				

For a single-rack model, the percentage reduction was 54.29% and 37.14% for experimental and computational results, respectively. The percentage reduction was even closer when the two methods were compared for the three-rack model with deflector: 45.61% for experimental uplift and 54.09% for computational uplift. In terms of drag results, the experimental results resulted in slight additions to the drag force, for both single-rack and three-rack models using the deflector, the addition was around 25%. This addition in wind drag is expected as the addition of the deflector with the rack arrays will somewhat

increase the amount of drag force. When the respective drag and uplift forces are compared for both the scenarios of single-rack only and three-rack array, drag forces were ~70% smaller than the wind uplifts. This comparison explains that the reduction in wind uplifts is more crucial than the wind drag forces for design and installation purposes.

5 Conclusion

We conclude that an elliptic deflector with equally spaced short fins when placed in front of the panel rack greatly reduces uplift on the panels. Wind tunnel experiments showed a slight increase in drag force when a deflector was placed at the front. This is due to the fact that the deflector acts as a bluff body obstruction to the wind flow over the panel. There is a close agreement between computational results and the wind tunnel test data in terms of the calculation of lift forces; however, drag forces were not compared. Lift forces were mainly responsible for the structural stability of solar panels under high winds. It was also noted that a selective grid scheme and refinement in the flow domain have a significant influence and improve CFD results, but lead to much longer simulation run times and convergence. It was concluded that an elliptically profiled wind deflector with uniformly spaced short fins, positioned before the tilted panels, minimizes the high wind loads by as much as 50% compared to the wind loads without its use. Details of the study are currently being reviewed and will also be published in a journal paper.

Acknowledgement

This work was funded in part by Northern States Metal, Inc., Austintown, Ohio, USA.

References

[1] Spratley, W.A., 1998, Solar Rooftops as Distributed Resources, *The Electricity Journal* 11, pp. 40.
[2] Addressing http://www.nafcointernational.com on 02/01/2012 *NAFCO International Inc, 2006-2011, Fond Du Lac, WI, USA.*
[3] Barkaszi, S.F. and Dunlop, J.P., 2001, Discussion of Strategies for Mounting Photovoltaic Arrays on Rooftops, *Proceedings of Solar Forum 2001, Solar Energy: The Power to Choose*, April 21-26, Washington D.C., pp. 6.
[4] Chung, K., Chang, K., Liu Y., 2008, Reduction of wind uplift of a solar collector model *Journal of Wind Engineering and Industrial Aerodynamics*, 96, pp. 1294.
[5] Yatsco, M. 2011, Numerical Analysis and Wind Tunnel Validation of Wind Deflectors for Rooftop Solar Panel Racks. *Master's Thesis, School of Graduate Studies & Research, Youngstown State University, Youngstown, Ohio, USA.*

[6] Meroney, R.N., Neff, D.E., 2010, *Wind effects on roof-mounted solar photovoltaic arrays: CFD and wind-tunnel evaluation,* The Fifth Computational Wind Engineering (CWE2010), Chapel Hill, North Carolina, May 23-27.
[7] Addressing http://www.extrusions.com/ on 02/01/2012 *Northern States Metals, Inc., Youngstown, OH, USA.*
[8] Jiyuan Tu, Guan Heng Yeoh, and Chaoqun Liu, 2008, *Computational Fluid Dynamics: A Practical Approach*, Butterworth-Heinemann.
[9] Addressing http://www.ansys.com/ on 02/01/2012 *ANSYS Customer Portal for Fluent Documentation and User Manuals.*

This page intentionally left blank

PIV measurements of laminar flow around a hemisphere

A. Goharzadeh, L. Khezzar & A. Molki
Department of Mechanical Engineering, The Petroleum Institute, Abu Dhabi, UAE

Abstract

This paper presents an experimental study of laminar flow past a smoothed hemisphere using the Particle Image Velocimetry technique. The experimental setup consists of a rectangular channel, through which water flows over a 30-mm diameter hemisphere mounted on a horizontal surface. From the measured velocity distribution around the hemisphere a physical insight into the flow is presented. Vertical and horizontal 2D velocity distributions are obtained for a constant Reynolds number of Re=800, corresponding to a regime of laminar flow. Measurements revealed the three dimensional structure of the flow including a horseshoe vortex surrounding the hemisphere and arch-shaped vortices in the downstream region. Both instantaneous and average velocity distribution were studied. The location of the reattachment point, the separation line, and the reverse flow are identified and discussed.
Keywords: PIV, horseshoe vortex, hemisphere, dome.

1 Introduction

Hemispherical shapes are widely used in many industrial applications such as domed roofs in civil engineering to cover buildings or above-ground steel tanks to store fluids. Domes were used in hydraulic channels as a mechanism to generate and study the shedding of hairpin vortices in their wake [1]. Predicting the three dimensional structure of flow field around a hemisphere is challenging for engineers due to the complexity added by the curved surface. Therefore, in order to ensure proper design of such engineering structures, detailed knowledge of the flow structure around them is necessary.

WIT Transactions on Engineering Sciences, Vol 74, © 2012 WIT Press
www.witpress.com, ISSN 1743-3533 (on-line)
doi:10.2495/AFM120031

The flow around domes is characterized by large-scale three-dimensional motions with separation and multiple re-attachment points, which at times exhibit a highly unsteady behaviour. Thus, a small recirculating bubble exists around the front stagnation point and a horseshoe vortex starts to develop and envelopes parts of the dome. The wake is characterized by vortex shedding, flow separation, and reattachment. Several parameters affect the flow behaviour around domes: the dome shape, the Reynolds number (based on the approaching free stream velocity and dome diameter), the inflow conditions such as the approaching boundary layer shape, and the upstream-wall and dome surface conditions.

Most of the experimental studies were conducted under turbulent flow conditions. For example, Taniguchi *et al.* [2], Savory and Toy [3] and Cheng and Fu [4] conducted experimental investigations to study the effect of three different approaching boundary layers in addition to the effect of dome surface roughness on the mean pressure distribution and on the critical Reynolds number beyond which the pressure distribution becomes invariable. Tamai *et al.* [5] explored the formation and shedding of vortices from a dome in a water tunnel and determined the frequencies characterizing each phenomenon. As the maximum Reynolds number reached 10^4, the Strouhal number had a value of 0.2. Approaching the front side, successive expanding recirculating zones and the formation of the well-known horseshoe vortices were observed. The number of these structures increases with increasing Reynolds number until a critical value of about 3,000, beyond which only one single recirculation zone persists with a constant size. Behind the dome, arched vortex tubes form and are shed individually or coalesce before shedding depending on a critical Reynolds number of 2,000. Using split-fiber probes and hot-wire anemometers Tavakol *et al.* [6] investigated the turbulent flow around a dome by obtaining axial velocity profiles and its root mean square (RMS) component. In their numerical investigations of laminar flow around a hemisphere, Kim and Choi [7] found that the separation angle is fixed at 90° from the stagnation point at Reynolds numbers below 300 and that the flow loses its symmetry and steadiness with increasing Reynolds number with clear hairpin type vortex shedding. The onset of asymmetry and periodicity occur at a Reynolds number of between 170-180 and 190-200 respectively.

It appears that relatively few experimental studies were performed on laminar flow around hemispherical domes; in other words, the majority being confined to turbulent flows and where only point measurements were obtained. From these measurements, extrapolated but incomplete pictures of the flow structure were proposed. The flow around a dome is complex and three-dimensional and only planar velocity measurements can provide a more complete picture of the flow structure. Hence, the present work aims to fill this gap by reporting on velocity measurements and flow mapping obtained by using Particle Image Velocimetry (PIV) technique. The results are of sufficient accuracy to provide a benchmark for the testing of computational methods of such flows [7].

2 Experimental facility and conditions

2.1 Experimental setup

Experiments were conducted in a water tunnel in a closed circuit arrangement with the flow loop in a vertical configuration. The water tunnel consists of a reservoir, head tower, flow conditioning section, contraction section, square flume, and a downstream tower. The reservoir is of monolithic type, constructed from clear acrylic, and contains the working fluid. Flow is generated using a submersible pump (Grundfos Model KP 250). Flow conditioning is achieved by means of a perforated cylinder which distributes the flow to the head tower, a stainless steel perforated plate, and a series of acrylic screens. The contraction section has a 2.52:1 area ratio with a symmetrical cross section and analytically developed contours. The contraction guides the flow from the head tower to the square flume which acts as the experimental test section.

As shown in figure 1a, a smooth hemispherical dome with a diameter of 30 mm was mounted in the test section and placed 220 mm downstream of the contraction section. The dome was fabricated from acrylic using a conventional lathe machine and painted in black colour to minimize reflection. Flow velocity in the test section is estimated to vary from 15 to 300 mm/s with an uncertainty of +/-2% and is controlled using a ball valve.

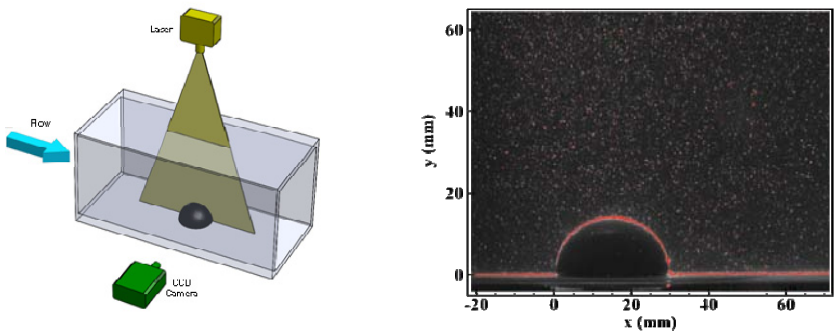

(a) Schematic view

(b) Example of PIV image in *x-y* plane with a large field of view 90x70 mm^2

Figure 1: Flow visualization system.

In the central region of the channel, the flow over the hemisphere is laminar and characterized by a constant fluid-based Reynolds number:

$$R_e = \frac{UD}{\nu} \tag{1}$$

where U=22 mm/s is the bulk stream velocity in the horizontal direction, D=30 mm the dome diameter and ν=0.8 mm^2/s the kinematic viscosity of water at a constant temperature of T=30°C corresponding to the Reynolds number of Re=800.

2.2 Flow conditions and measurement devices

Using PIV, all flow field measurements were taken in two directions: (i) in the central vertical axial plane of the dome arrangement, fig. 1a, and (ii) in the horizontal plane near the bottom wall. To illuminate theses measurement planes, a laser sheet was projected vertically and horizontally, with a charge coupled device CCD camera positioned perpendicular to the plane to record particle motion, as illustrated in figure 1a. The water was seeded with polyamide particles tracers with an average diameter of 22 μm and density of 1.016 g/cm^3 for flow visualization. The PIV flow field measurements were undertaken at two different locations: (i) upstream region, far from the dome location and (ii) around the dome region. An example of a PIV image is shown in figure 1b, which demonstrates the flow around the hemispheric obstacle. The flow was observed with a field of view of 90×70 mm^2. The tracers' density was 15–20 particles per interrogation area. A diode laser was used as the light source for PIV measurements having a maximum power output of 200 W at a wavelength of 532 nm. A cylindrical lens (f=28 mm) was used to generate a light sheet of approximately 1 mm thickness.

The synchronization between laser light pulses and the camera was accomplished by transistor-transistor logic pulses from the synchronizer. The time interval between each pair of images was 200 ms with the pulse separation time adjusted to 10 ms. Full-frame images of 1024×1024 pixels (figure 2b) were acquired and transferred to a computer via a frame grabber. Using the DAVIS FLOWMASTER software provided by the Lavision System (Germany), the 2D PIV image was divided into 32×32 pixels size sub-regions using a multi-grid correlation process with 50% overlap. The average particle velocities were calculated using 100 images coupled with the cross correlation method. The spurious vectors calculated based on the local median filtering were less than 3%. No data smoothing was used for the calculation of the velocity measurements.

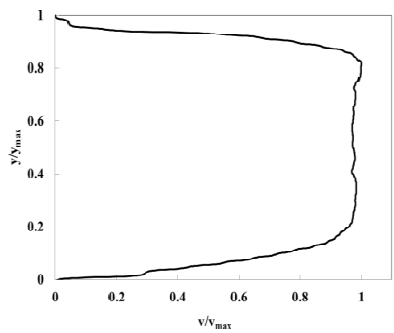

(a) Mean axial velocity at inlet.

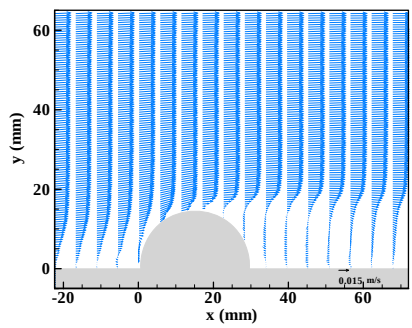

(b) Averaged axial velocity profiles around the dome.

Figure 2: Velocity measurements using PIV.

3 Results and discussions

To verify the upstream flow conditions, a cross stream averaged velocity profile was obtained and is illustrated in figure 2a. The velocity profile reached a maximum velocity between $0.2<y/y_{max}<0.8$. The flow does represent a developing type. The boundary layers are visible at the top and bottom side of the channel.

In figure 2b, the large view of the averaged velocity profile around the dome is presented for the Re=800. It is important to note that the flow is focused near the bottom wall of the channel and therefore the velocity does not reach its minimum value near top wall (0<y<60 mm).

The magnitude of particle velocities is constant far from the hemisphere with an average velocity of 22 mm/s. Naturally and through the action of the pressure field as the fluid particles approach the hemisphere, their velocities decrease.

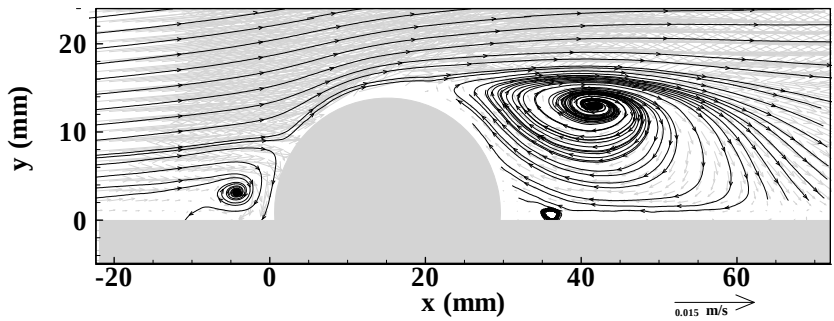

(a) Averaged axial velocity vector plot and its corresponding streamlines in a mid vertical plane for Re=800.

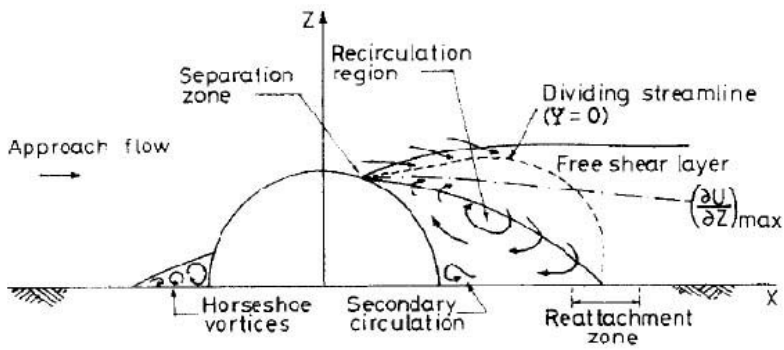

(b) Schematic flow characteristics at $Re=1.4\times10^5$ [3].

Figure 3: Flow characteristics near the hemisphere, side view.

Streamlines of the averaged velocity field, are presented in figure 3a, and compared with previous experimental observations reported by Savory and Toy [3], fig. 3b. In this paper the flow is laminar (Re=800). The averaged velocity profile shows parallel streamlines in the upstream region far from the dome obstacle (figure 3a). As the flow approaches the dome the streamlines are deviated in different directions. In lower layers behind the obstacle, the direction of the velocity changes. An upstream recirculating region similar to the previous observation [3] is denoted with a front stagnation streamline. Both the reattachment zone and the secondary circulation are clearly visible using the streamlines. The separation zone is located between (x=21 mm and y=12 mm). Although similarities are observed between previous experimental results [3] and the present PIV measurements, fundamental differences exist such as the size and position of the recirculating zone. The PIV measurements indicate that the center of the recirculating zone is located both further downstream of the dome and at higher vertical position. This difference is due to the characteristics of the fluid flow (laminar and confined flow in this experiment versus turbulent and open flow in the previous study [3]). The other similarity which can be observed, is at the front side of the dome obstacle. Horseshoe vortices are shown in both cases, figs. 3a and b. However, in the present experiment the dimensions of the horseshoe vortices are larger than in the previous study of [3] and represent almost half of the dome diameter.

The magnitude of the vertical (V_y) and horizontal (V_x) velocities are illustrated in figures 4a and 4b respectively. As shown in figure 4a, the maximum axial velocity appears at x=10 mm and y=15 mm, where the velocity is deviated from its original direction due to the presence of the dome as an obstacle. The negative velocities represented in dark blue color (or dark gray color in black and white print-B/W) correspond to the existence of horseshoe vortices. The negative and positive velocities are characterized by the dark blue (or dark gray in B/W print) and red colors (or medium gray in B/W print) respectively. The horizontal light blue region represents the thin boundary zone where the velocity is zero corresponding to the region where the main and recirculating flows are separated.

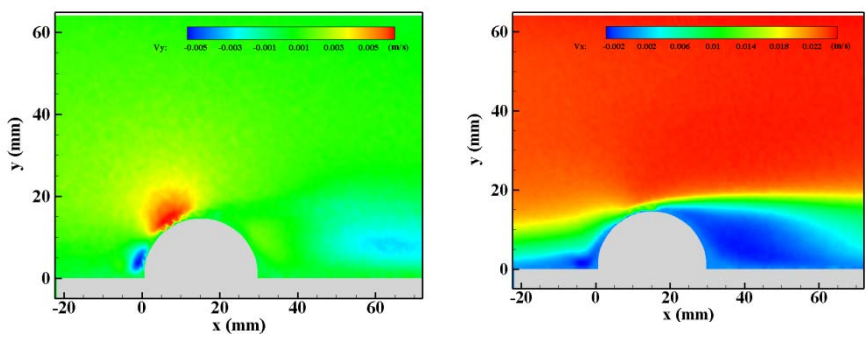

(a) Vertical velocity (V_y). (b) Axial velocity (V_x).

Figure 4: Velocity magnitude near the hemisphere, side view (Re=800).

Figure 5a illustrates the streamlines around the dome in a horizontal plane near the bottom wall. In this case, since the laser is projected horizontally only part of the flow is optically accessible for measurements due to shadowing. The laser illuminates the horizontal flow field at 0.1mm above the bottom wall as a camera records PIV pictures from the top view. Measurements are compared with the flow characteristics obtained by Savory and Toy [3] in which horseshoe vortices are observed around the dome. The reattachment is also clearly shown behind the dome. In particular, the bottom parts of the arch type downstream vortices mentioned above are captured by the PIV measurements. However, the flow field between two figures is slightly different. The horseshoe zone in front and around the dome is larger in the present experiment.

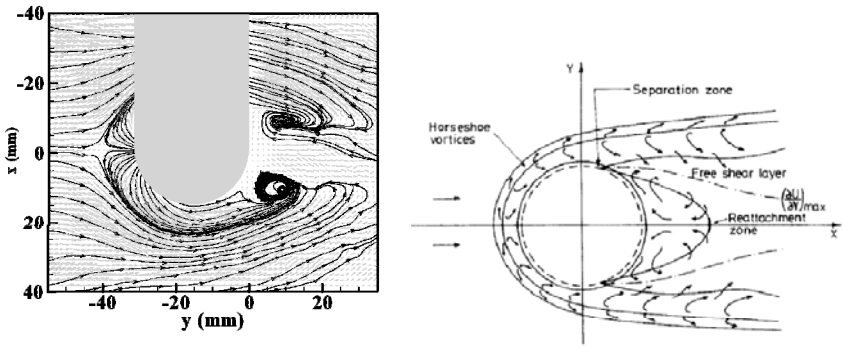

(a) Averaged velocity vector plot in a horizontal plane for Re=800.

(b) Schematic flow characteristics at $Re=1.4\times10^5$ [3].

Figure 5: Flow characteristics in a horizontal plane near the hemisphere bottom wall.

The PIV measurements show that the flow is highly three dimensional around the dome. It was also observed that flow inside the horseshoe vortices and reattachment zone is not stable. The location of the separation zones fluctuate with time between two instantaneous images. However, the averaged velocity shows a structure and a quasi-symmetric flow in the horizontal plane.

4 Conclusions

Laminar flow past a smooth hemisphere was investigated using the Particle Image Velocimetry technique. Vertical and horizontal 2D velocity distributions at Re=800, showed a laminar flow. The averaged velocity distributions around the hemispherical obstacle were obtained and velocity field illustrated the presence of a complex three dimensional flow containing intriguing structures such as a horseshoe vortex enveloping the dome and arch-shaped vortices in the

downstream region. The location of the reattachment point, the separation line, and the reverse flow are also identified and discussed. The characteristics of laminar flow around the dome share several similar features with the case of turbulent flow [3] with significant difference in the size of vortices and their location. The results of this research can be employed to validate further numerical predictions of this complex flow field. Future experiments will focus on the influence of the dome surface roughness and velocity distribution of turbulent flows around the hemispherical obstacle.

References

[1] Acarlar, M.S. and Smith C.R., A study of hairpin vortices in a laminar boundary layer, Part1. Hairpin vortices generated by a hemisphere protuberance. *J. Fluid Mech.*, **175**, pp. 1–41, 1987.
[2] Taniguchi, S., Sakamoto, H., Kiya, M. and Arie, M., Time-averaged aerodynamic forces acting on a hemisphere immersed in a turbulent boundary. *J. Wind Eng. Ind. Aerod*., **9**, pp. 257–273, 1982.
[3] Savory, E. and Toy, N., Hemispheres and hemisphere-cylinders in turbulent boundary layers. *J. Wind Eng. Ind. Aerod.*, **23**, pp. 345–364, 1986.
[4] Cheng, C.M. and Fu, C.L., Characteristic of wind loads on a hemispherical dome in smooth flow and turbulent boundary layer flow. *J. Wind Eng. Ind. Aerod.*, **98**, pp. 328–344, 2010.
[5] Tamai, N., Asaeda, T. and Tanaka, N., Vortex structures around a hemispheric hump. Bound-Lay. *Meteorol.*, **39**, pp. 301–314, 1987.
[6] Tavakol, M.M., Yaghoubi, M. and Masoudi Motlagh, M.M., Air flow aerodynamic on a wall mounted hemisphere for various turbulent boundary layers. *Exp. Thermal and Fluid Sci*., **34**, pp. 538–553, 2010.
[7] Kim, D. and Choi, H., Laminar flow past a hemisphere. *Phy. of Fluids*, **15(8)**, pp. 2457-2460, 2003.

Oil squeezing power losses in gears: a CFD analysis

F. Concli & C. Gorla
Politecnico di Milano, Department of Mechanical Engineering, Milano, Italy

Abstract

Efficiency is becoming more and more of a main concern in the design of power transmissions and the demand for high efficiency gearboxes is continuously increasing; also the euro standards for the reduction of pollutant emissions from light vehicles imposed to improve the efficiency of the engines and gear transmissions are becoming more and more restrictive. For this reason the resources dedicated to this goal are continuously increasing.

The first step to improve efficiency is to have appropriate models to compare different design solutions. Even if the efficiency of transmissions is quite high compared to the efficiency of the engines and appropriate models to predict the power losses due to gear meshing, to bearings and to seals that already exist, in order to have further improvement, some aspects like the power losses related to the oil churning, oil squeezing and windage are still to be investigated. In previous papers, the authors have investigated by means of CFD (computational fluid dynamic) analysis and experimental measurements the churning losses of planetary speed reducers (in which there is a relative motion between the "planets + planet carrier" and the lubricant). This report is focused on the oil squeezing power loss. This kind of loss is associated with the compression-expansion process by the meshing teeth. The contraction of the volume at the gear mesh implies an overpressure that induces a fluid flow primarily in the axial direction and this, for viscous fluids, means additional power losses and a decrease of efficiency.

In this work this phenomenon has been studied by means of some CFD simulations. The influence of some operating conditions, such as the lubricant properties, rotational speed and temperature, have been studied.
Keywords: efficiency, gear, power losses, oil squeezing, lubrication, CFD.

WIT Transactions on Engineering Sciences, Vol 74, © 2012 WIT Press
www.witpress.com, ISSN 1743-3533 (on-line)
doi:10.2495/AFM120041

1 Introduction

As the fuel economy requirements and euro standards for the reduction of pollutant emissions are becoming more and more stringent, efficiency is becoming a main concern also in the design of power transmissions. Reducing fuel consumption and particulate emission levels through increasing efficiency has not only a strong impact on the economy and on the environment, but also on the reliability on the transmissions: a reduction of the power losses means also a reduction of the heat generated and, therefore, of the operating temperature of the transmission. A lower temperature is favorable for the system reliability.

Sources of losses in a gearbox can be classified according to [1] into two main categories: (i) load dependent power losses and (ii) load independent power losses. The load dependent power losses are primarily related to a mechanical power loss due to friction at the gear contact and between the rolling elements and the races of the bearings. The load independent power losses, in turn, are primarily related to viscous effects. These losses can be further subdivided into oil churning and windage losses that are the result of the interaction between the oil/air and the moving/rotating elements like gears and shafts, into pocketing/squeezing losses due to the pumping effect of the mating gears and into other viscous dissipations like those of the bearings.

In order to predict these kinds of losses, literature provides many publications about the load dependent power losses, but only few works about load independent power losses. These works are primarily concerning the churning losses of ordinary gears, the spin power losses and the losses of the bearings. What is still wanted are appropriate studies to predict the oil pumping/squeezing power losses. The works on this topic are few and simplified. Strasser [10] proposed a simplified fluid-dynamic model to predict the oil squeezing power losses in a spur gear pair. This model takes into account the variation of the gap between the teeth but it approximates the geometry. Seetharaman and Kahraman [11] proposed a physic based fluid mechanics model to predict the spin power losses of a gear pair due to oil churning and windage. This model calculate the losses like the sum of the losses associated to the interactions of individual gears and the fluid and the power losses due to pumping of the oil at the gear mesh. To predict the oil pumping losses, Seetharaman and Kahraman developed an analytical model that take into account the variation of the volume of the gap between the teeth without simplifying the geometry like in the model proposed by Strasser. These models are able to give results in a very short time but they give only approximate results. For this reason the authors have investigated this kind of losses by mean of CFD simulations that are able to correctly solve the velocity and the pressure fields without simplifications and, therefore, give more information about the phenomena. In this study the influence on this kind of losses of the oil temperature and of the rotational speed of the gears have been investigated.

2 Problem description

Between two mating gears, the volume of the cavity between the teeth is continuously changing. The sudden contraction of this volume caused by the gears revolution implies an overpressure in the gap. The lubricant is therefore squeezed out primary in the axial directions. After the reaching of the minimum value for the volume, this increase again causing a negative pressure in the gap and, consequently, a fluid flow takes place from the oil bath to the cavity between the teeth.

This process is cyclic and, in general, there are multiple cavities that are squeezed together. Due to the viscous properties of the lubricant, this phenomenon induces power losses.

Figure 1 illustrates the phenomena: the volume (marked in grey) decreases from picture 1a (where a gear pair starts the contact) to picture 1b. Figure 1c shows the moment in which a second gear pair mates and figure 1d the quick growth of the cavity volume.

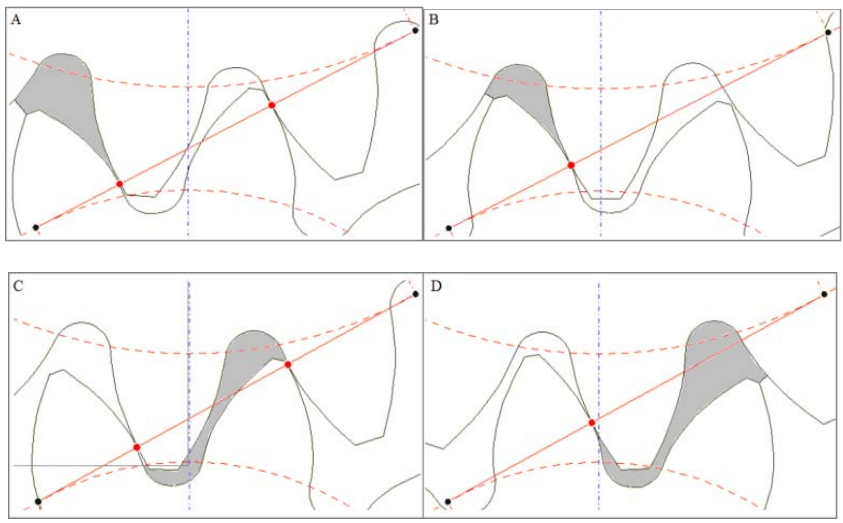

Figure 1: Change of the volume of the cavity during the engaging of the gears.

3 Geometry

In order to study this kind of power losses, a spur gear pair has been used. Pinion and gear have the same dimensions. Table 1 summarized the main parameter of the gears.

For this initial study, a full immersion lubrication has been adopted. This solution has been chosen in order to simplify the model. A partial immersion, in fact, complicates a lot the problem because it involves multiphase flows. The

aim of this initial study was to understand the effect of the mating gears on the axial flows, so the full immersion lubrication was considered appropriate at this point of the research.

Table 1: Geometrical parameters of the gear pair.

helix angle on reference cylinder β_b [rad]	0	Pitch circle r [mm]	14,4
Pressure angle α' [rad]	0,358452	Working pitch circle r' [mm]	14,45
Working pressure angle α [rad]	0,349066	Number of teeth z	36
Centre distance a [mm]	28,8	Base circle r_b [mm]	13,5315
Working centre distance a' [mm]	28,9	Module m [mm]	0,8
Tip radius r_a [mm]	15,175	Face width b [mm]	15,5
Root circle r_i [mm]	13,4375		

4 Geometrical model

In order to reduce the number of cells and thank to the symmetry of the gear pair, only half domain has been modeled. The aim of this work was to study in detail the behavior of the lubricant in the region of meshing. For this reason only five teeth pro gear have been modeled.

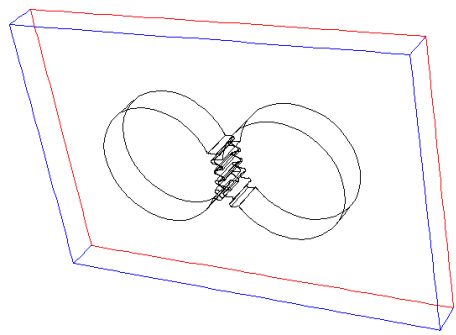

Figure 2: Geometrical model: marked in blue the symmetry plane.

The computational domain for the CFD analysis has been modeled by means of 3D cad software and discretized with a swept mesh. This meshing technique

consists in creating a mesh on one side of the region, known as the source side, and then copying the nodes of that mesh, one element layer at a time, until the end side, known as the target side, is reached.

The whole model has been discretized with triangular prisms. This kind of elements allows a larger aspect ratio compared with the tetrahedral cells in which it will invariably affects the skewness of the cell, which is undesirable as it may affect accuracy and convergence. Some mesh refinements have been performed in order to find the best compromise between the accuracy of the solution and the computational time. The real problem during the meshing operation is that it's necessary to model the thin oil film that rise between the mating teeth. The thickness of this film has a big influence on the results in terms of power losses. For this reason some geometries with different film thickness have been modelled.

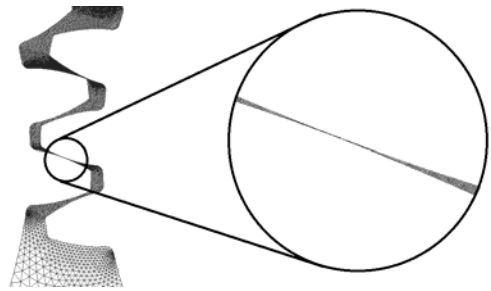

Figure 3: Details of the mesh.

After a convergence study, the final model had a film thickness of about 0.5 μm. That means that the required mesh is extra fine. The smallest element has a length of about 0.2 μm.

Table 2: Mesh statistics.

minimum volume [m³]	3.01E-09
maximum volume [m³]	5.51E-03
total volume [m³]	3.14E+01
minimum face area [m²]	1.60E-06
maximum face area [m²]	6.03E+00
minimum orthogonal quality	0.38633

5 Numerical model

To simulate the problem, a VOF approach has been used. This method is an Eulerian method characterized by a mesh that is (in this case) moving in a certain prescribed manner to accommodate the evolving shape of the interface.

The governing equations are the conservation equations for mass and momentum. The energy equation is not activated in these simulations.

$$\frac{\partial \rho}{\partial t} + \nabla \cdot (\rho \vec{\boldsymbol{v}}) = \quad (1)$$

$$\frac{\partial}{\partial \boldsymbol{t}}(\boldsymbol{\rho}\vec{\boldsymbol{v}}) + \boldsymbol{\nabla} \cdot (\boldsymbol{\rho}\vec{\boldsymbol{v}}\vec{\boldsymbol{v}}) = -\boldsymbol{\nabla p} + \boldsymbol{\nabla} \cdot [\boldsymbol{\mu}(\boldsymbol{\nabla}\vec{\boldsymbol{v}} + \boldsymbol{\nabla}\vec{\boldsymbol{v}}^{\boldsymbol{T}})] + \boldsymbol{\rho}\vec{\boldsymbol{g}} + \vec{\boldsymbol{F}} \quad (2)$$

ρ is the density, t is the time, $\vec{\boldsymbol{v}}$ is the velocity vector, P is the pressure, $\rho\vec{\boldsymbol{g}}$ and $\vec{\boldsymbol{F}}$ are the gravitational body force and external body forces.

For compressible flows, the unknowns are the velocity components and the density while the pressure is evaluated with a constitutive equation. For incompressible flows, the variables are the pressure and the velocity components. The solution of the system of equations for incompressible flows is accomplished by the fact that there are not equations where the pressure is explicity defined. To calcluate it, the continuity equation is substituted with an equation for the pressure; with some manipulation the pressure appears like unknown term in the momentum equation.

For this reasons a SIMPLE (Semi Implicit Method for Pressure-Linked Equations) scheme has been adopted as suggested for flows in closed domains to solve the pressure-velocity-couplig. This algorithm uses a relationship between velocity and pressure corrections to enforce mass conservation and to obtain the pressure field. The idea is that the pressure field must guarantee, at every time, the continuity equations. Is it therefore necessary to obtain a diefferntial equation for the pressure unknown derived from continuity and momentum equations.
In this method the pressure field is calculated as

$$P^{n+1} = P^* + P' \quad (3)$$

where P^* is the estimated pressure guessed or obtained at the previous time step/iteration from the momentum equations and P' is the pressure correction

The velocity field is calculated as

$$\vec{\boldsymbol{v}}^{n+1} = \vec{\boldsymbol{v}}^* + \vec{\boldsymbol{v}} \quad (4)$$

where $\vec{\boldsymbol{v}}^*$ is the estimated velocity calculated from the pressure P^* and $\vec{\boldsymbol{v}}'$ is the velocity correction.

The gear surfaces have been set like no slip walls and the lateral sides of the domain as zero pressure to simulate the steady oil bath and as symmetry respectively.

In order to reproduce the operating conditions, a rigid motion of the boundaries corresponding to the pinion and the gear has been applied by means of User Defined Functions (UDF) written in the c++ language. With this boundary motion it is possible to reproduce the real operating conditions in which gears are mating together. The time step for the transient analysis has been

chosen as dynamic. This means that every step, the new time increment depends on the velocity field.

$$t = \frac{V_{cell,min}^{\frac{1}{3}}}{U} \tag{5}$$

where $V_{cell,min}$ is the volume of the smallest cell in the computational domain and U is the velocity scale of the problem. This allows us to increase the calculations without the risk to lose the convergence.

This boundary motion implies a deformation of the fluid domain. For this reason it is necessary do update the mesh every time step. In order to do that, a dynamic mesh model has been adopted: the spring-based smoothing + remeshing. In this method, the edges between any two mesh nodes are idealized as a network of interconnected springs. The initial spacing of the edges before any boundary motion constitutes the equilibrium state of the mesh. A displacement at a given boundary node will generate a force proportional to the displacement along all the springs connected to the node. With a linear elastic behavior, the force on a mesh node can be written as

$$\vec{\boldsymbol{F}}_i = \sum_j^{n_i} k_{ij}\left(\Delta\vec{\boldsymbol{x}}_j - \Delta\vec{\boldsymbol{x}}_i\right) \tag{6}$$

where $\Delta\vec{\boldsymbol{x}}_j$ and $\Delta\vec{\boldsymbol{x}}_i$ are the displacements of node i and its neighbor j, n_i is the number of the neighboring nodes connected to the node i and k_{ij} is the spring constant between node i and its neighbor j. The spring constant for the edge connecting nodes i and j is defined as

$$k_{ij} = \frac{1}{\sqrt{|\vec{x}_j - \vec{x}_i|}} \tag{7}$$

At equilibrium, the net force on a node due to all the springs connected to the node must be zero. This condition results in an iterative equation such that

$$\Delta\vec{\boldsymbol{x}}_i^{m+1} = \frac{\sum_j^{n_i} k_{ij}\Delta\vec{\boldsymbol{x}}_j^m}{\sum_j^{n_i} k_{ij}} \tag{8}$$

Since displacements are known at the boundaries, Equation (8) is solved using a Jacobi sweep on all interior nodes. At convergence, the positions are updated such that

$$\vec{\boldsymbol{x}}_i^{n+1} = \vec{\boldsymbol{x}}_i^n + \Delta\vec{\boldsymbol{x}}_j^{m,converged} \tag{9}$$

where $n+1$ and n re used to denote the positions at the next time step and the current time step, respectively.

Figure 4 shows the adopted mesh before and after the calculations. It is possible to appreciate the good efficiency of the smoothing-based algorithm for the mesh update. After the iterations, the elements have still a good aspect ratio and approximately the same dimensions that they had at the beginning.

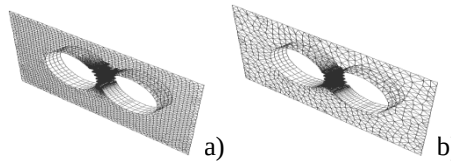

Figure 4: a) Detail of the mesh at the first time step; b) Detail of the mesh after some iterations.

6 Operating conditions

The purpose of the simulations is to calculate the power losses due to oil squeezing under different operating conditions.

In order to do that, the resistant torque on the driving shaft has been monitored. This resistant torque is calculated with a surface integral on the moving walls with respect to the gearbox axis and it is composed of two parts: the first given by the pressure and the second by the viscous effects. Starting from the resistant torque it is possible to calculate the power losses just by multiplying it by the rotational speed. The simulations have been computed with different combinations of operating temperature (which means different density and viscosity) and rotational speed.

Table 3 shows the combinations of parameters for each simulation. $\boldsymbol{T}$ is the operating temperature in °C, $\boldsymbol{\omega}$ the rotational speed of the planet carrier in [rad/s], $\boldsymbol{\rho}$ the density in [Kg/m³] and $\boldsymbol{\eta}$ the dynamic viscosity in [Pa*s].

Table 3: Parameters for each simulation.

Rotational speed ω[rad/s]	Temperature T [°C]	Density ρ [kg/m³]	Dynamic Viscosity η [Pa*s]
52	40	1040.86	0.2289
105	40	1040.86	0.2289
157	40	1040.86	0.2289
52	65	1021.61	0.1481
105	65	1021.61	0.1481
157	65	1021.61	0.1481
52	90	1002.36	0.0702
105	90	1002.36	0.0702
157	90	1002.36	0.0702

A commercial oil whit this characteristics can be, for example, the Klübersynth GH 6-220 Synthetic Gear Oil.

7 Results

Figure 5a shows the pressure field on the symmetry plane. It is possible to appreciate that in the upper cavity the pressure is higher than in the oil bath. That's because this cavity is decreasing his volume.

The lower cavity, in turn, shows a lower pressure depending on the fact that it is increasing his volume.

Figure 5b shows the velocity distribution in the axial direction. It can be appreciate the flux in the axial direction.

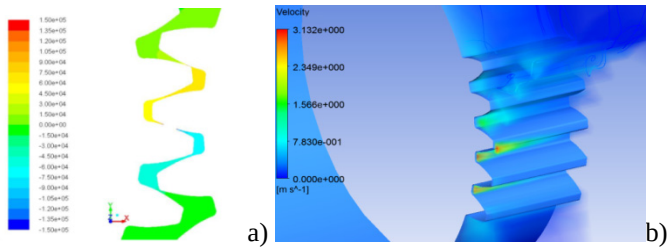

Figure 5: Contour of the pressure [Pa] on the symmetry plane; b) Velocity distribution in the field of action.

Figure 6 to 8 show the results in terms of power losses on the driving wheel for different operating conditions and for 1 cycle. Since gear mesh is, also the resistant torque necessary to squeeze the oil has a periodic trend.

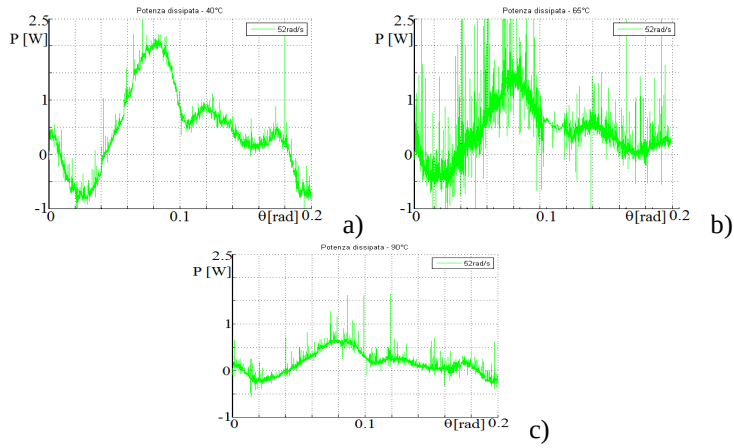

Figure 6: Power losses on the driving shaft; a) 40°C – 52rad/s; b) 65°C – 52rad/s; c) 90°C – 52rad/s.

From the diagrams it can be seen that, as expected, the resistant torque decreases with temperature while it increases with rotational speed. It can be also seen that this kind of losses are low in the case of the highest temperature and the lower speed (figure 6c), in which they are less than 1 W, while in the case of lowest temperature and higher speed (figure 8a) they became significant.

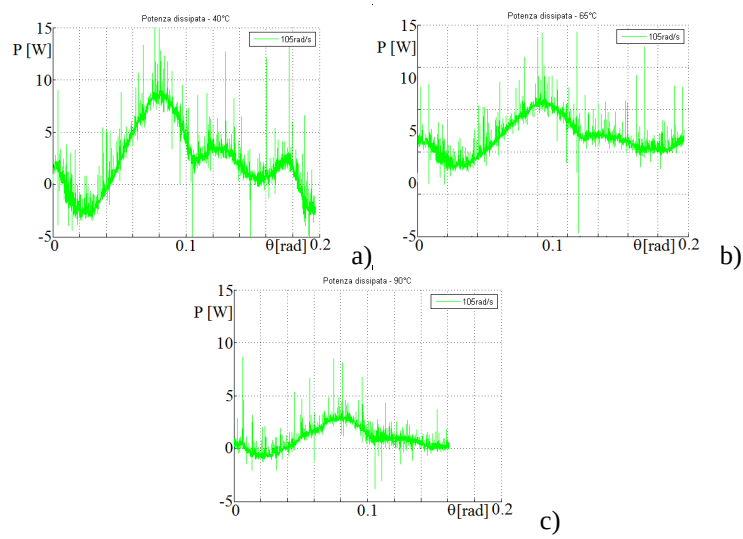

Figure 7: Power losses on the driving shaft; a) 40°C – 105rad/s; b) 65°C – 105rad/s; c) 90°C – 105rad/s.

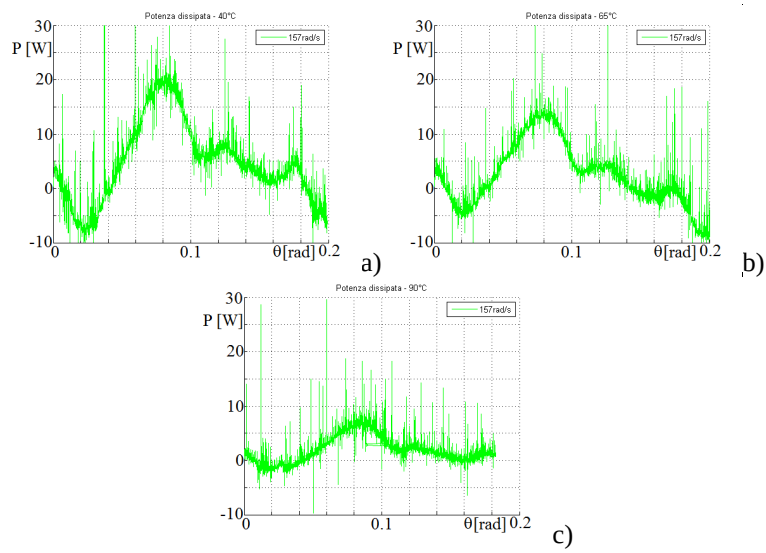

Figure 8: Power losses on the driving shaft; a) 40°C – 157rad/s; b) 65°C – 157rad/s; c) 90°C – 157rad/s.

Figure 9 shows the power losses along the contact path. In the position 1 the first teeth pair (1s+2s), as shown in figure 10a, is already engaged. The second teeth pair (2s+3s) is starting the contact. In the position 2 of figure 8, the first teeth pair ended the contact (figure 10b).

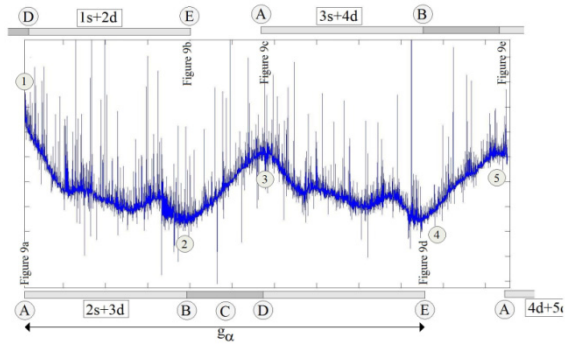

Figure 9: Power losses versus length of contact.

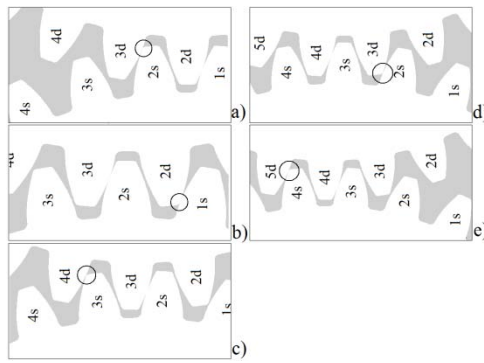

Figure 10: Different engaging steps.

Between 1 and 2, the mating teeth pairs are therefore 2. In the position 3, another teeth pair (3s+4d) starts the contact (figure 10c) while the second teeth pair (2s+3s) is already engaged. Like in position 2, in position 4 a teeth pair (2s+3s) ended the contact (figure 10d).

From this position to position 5, the engaged teeth pair is again only one, like between position 2 and position 3. Finally, in position 5, like in position 3, a teeth pair starts the contact while another teeth pair is already engaged (figure 10e).

8 Conclusions

As reliable models to predict the oil squeezing losses at the gear mating are still not available, a CFD model has been applied in order to predict this important component of losses. The simulations show that this kind of losses increase, as expected, with the rotational speed and decrease with temperature. The results show also that for low regimes and high temperature the kind of losses are particularly low.

Future works will be the study of other geometries and other kinds of lubrications.

References

[1] Niemann, G., Winter, H., Maschinenelemente – Band 2: Getriebe allgemein, Zahnradgetriebe – Grundlagen, Stirnradgetriebe — 2.Auflage – Springer, Berlin 2003.
[2] ISO/TR 14179-2:2001(E) – Gears – Thermal capacity – Part 2: Thermal load-carrying capacity.
[3] Catalogo generale SKF – Edizione scolastica – Gruppo SKF, Dicembre 2006.
[4] Concli, F., Gorla, C., Arigoni, R., Cognigni, E., Musolesi, M.,:" Planetary Speed Reducers: Efficiency, Backlash, Stiffness", International conference on gears, Munich 2010.
[5] Concli, F., Gorla, C., Arigoni, R., Musolesi, M.:" Riduttori di precisione a gioco ridotto ed alta efficienza", Organi di trasmissione – febbraio 2011, Tecniche Nuove, Milano 2011.
[6] Concli, F., Gorla, C.:"Computational and experimental analysis of the churning power losses in an industrial planetary speed reducers", Multiphase flow IV, Wessex Institute of technology, 2011.
[7] Csobàn, A., Kozma, M., Influence of the Oil Churning, the Bearing and the Tooth Friction Losses on the Efficiency of Planetary Gears, Journal of Mechanichal Engineering 56(2010)4, pp. 231-238.
[8] Concli,F, Gorla,C, Churning power losses in planetary speed reducer: computational-experimental analysis, EngineSOFT International Conference 2012 Conference Proceedings, 2011.
[9] Concli,F, Gorla,C, Influence of lubricant temperature, lubricant level and rotational speed on the churning power losses in an industrial planetary speed reducer: computational and experimental study - International Journal of Computational Methods and Experimental Measurements – Wssex Institute of Technology.
[10] D. Strasser, Einfluss des Zahnflanken- und Zahnkopfspieles auf die Leerlaufverlustleistung von Zahnradgetrieben – Dissertation zur Erlangung del Grades Doktor-Ingenieur – Bochum 2005.
[11] Seetharaman, A. Kahraman, Load-Independent Spin Power Losses of a Spur Gear Pair: Model Formulation, Journal of Tribology APRIL 2009, Vol. 131.
[12] Patankar, S.V., Numerical heat transfer and fluid flow, Taylor & Francis, USA 1980.
[13] Versteeg, H.K., Malalasekera, W., An introduction to computational fluid dynamics – The finite volume method, Longman Group, London 1995.
[14] Comini, G., Fondamenti di termofluidodinamica computazionale, SGEditoriali, Padova 2004.

Complete Francis turbine flow simulation at Derbendikan power station

R. A. Saeed[1], V. Popov[2] & A. N. Galybin[2,3]
[1]*University of Sulaimani, Iraq*
[2]*Wessex Institute of Technology, UK*
[3]*Institute of Physics of the Earth, Russia*

Abstract

This paper presents the results of simulations of the complete three-dimensional fluid flow through the Spiral Casing, Stay Vane, Guide Vane, and then through the Francis turbine runner of the Derbendikan power station. To investigate the flow in the Francis turbine and also to identify the loads acting on the turbine blades, a three-dimensional model was prepared according to specifications provided. The results show that the maximum absolute pressure of 4.4×10^5 Pa is reached at the leading edge of the turbine runner and the maximum tangential velocity reaches 33 m/s in the turbine runner.
Keywords: Francis turbine runner, numerical simulation, CFD modelling.

1 Introduction

Generally the flow field in Francis turbines is quite complicated due to its three-dimensional nature and the curvature of the passages between runner blades. The complexity of the problem requires the application of numerical approaches which are capable of producing accurate results for flow velocity field and pressure distributions on the runner. The application of *CFD* is an efficient way for the analysis of fluid flow through hydraulic turbines [1]. Nava *et al.* [2] presented an application of *CFD* to compute the loads caused by water pressure on a blade of the Francis turbine runner. There is a satisfactory agreement between numerical simulations and experimental measurements as reported by Farhat *et al.* [4], who compared the flow simulation results and experimental data for the whole Francis turbine. Three-dimensional steady flow analysis of the flow passages from the entrance runner to the outlet in Francis turbine type has

WIT Transactions on Engineering Sciences, Vol 74, © 2012 WIT Press
www.witpress.com, ISSN 1743-3533 (on-line)
doi:10.2495/AFM120051

been reported by Ikeda *et al*. [5]. This analysis provides the distributed pressure and water velocity within the computational domain.

In this paper, the pressure distribution and flow velocity field were investigated by using Computational Fluid Dynamics (*CFD*) for specific operating condition. Detailed analysis of the fluid flow through the turbine runner is necessary in order to study the fluid flow conditions. For this purpose the Spiral Casing, Stay Vane, Guide Vane, Runner and upper part of the Draft tube have been considered. The corresponding model is shown in Figure 1.

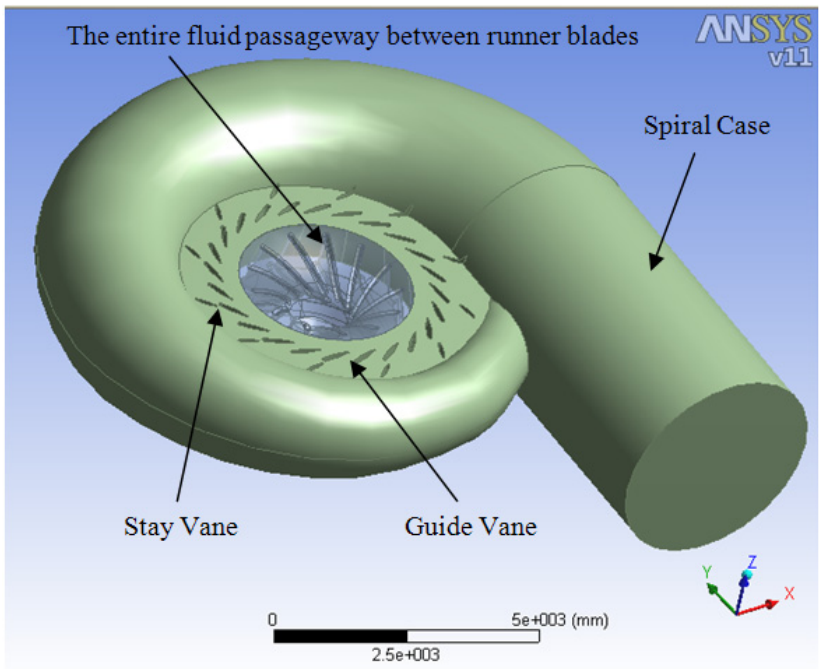

Figure 1: Geometrical model used in the simulation.

This work includes the analysis of the performance of the Francis turbine of Unit 2 in Derbendikan hydropower station; one of the major suppliers of electrical power generation in the north of Iraq- Kurdistan Region. The investigated turbine has the following data [7]: number of runner blades 13, number of guide vanes 24, rated head 80 *m*, power output at rated head 83 *MW*, discharge at rated head 113 m^3/s, rotational speed 187.5 *rpm*.

2 Flow simulations

The flow simulation of the Francis turbine runner is quite complicated and can be calculated only by using numerical methods. *CFD* simulation of the Francis turbine runner was performed to obtain pressure distribution and flow velocity

through the turbine runner. Following previous research [9, 10], for the computational domain, the Spiral Casing, Stay Vane, Guide Vane, Runner and upper part of the Draft tube is considered.

2.1 Geometrical model

The first step of flow simulation is building the geometrical model of the flow domain. According to the provided specifications from Derbendikan hydropower station a three-dimensional geometrical model has been created, as shown in Figures 1 and 2. The geometry of the fluid domain has been created on AutoCAD software and inserted into ANSYS software.

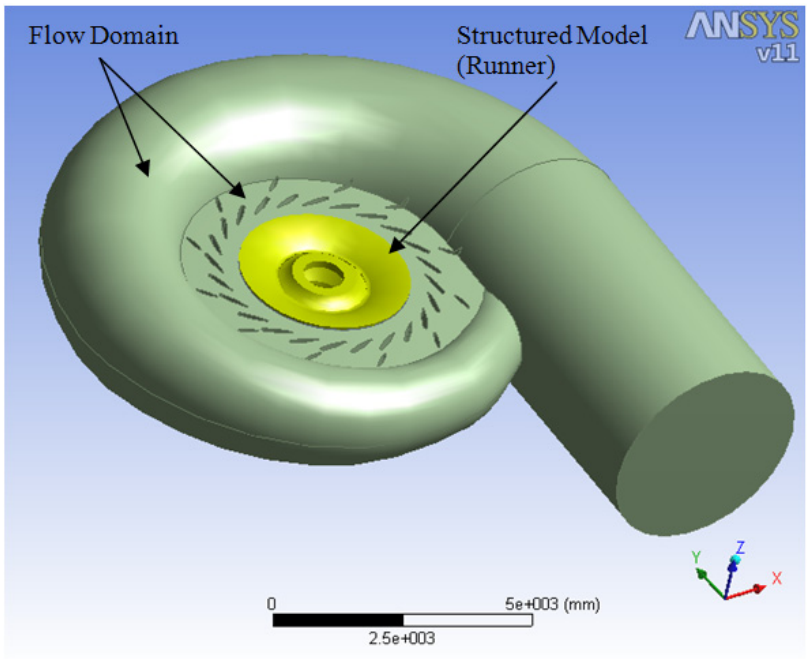

Figure 2: Flow domain and structured model.

As shown in the figure, the entire fluid passageway between the inlet from the Spiral Case side and the outlet from the draft tube side for the turbine is considered.

The flow in the runner was computed in the rotating frame of reference, while the flow in the stationary components was calculated in the stationary frame of reference. Figure 2 shows the detail of the connection between flow domains used for *CFD* simulations and Francis turbine runner model.

2.2 Discretization process

In this study, three-dimensional discretization has been used with the finite volume method (*FVM*) provided by the ANSYS CFX software. For the computational domain, unstructured 3D tetrahedral meshing has been employed, due to its flexibility when solving complex geometries, as shown in Figure 3. The whole computational mesh consists of 3,241,986 volumes and 628,677 nodes.

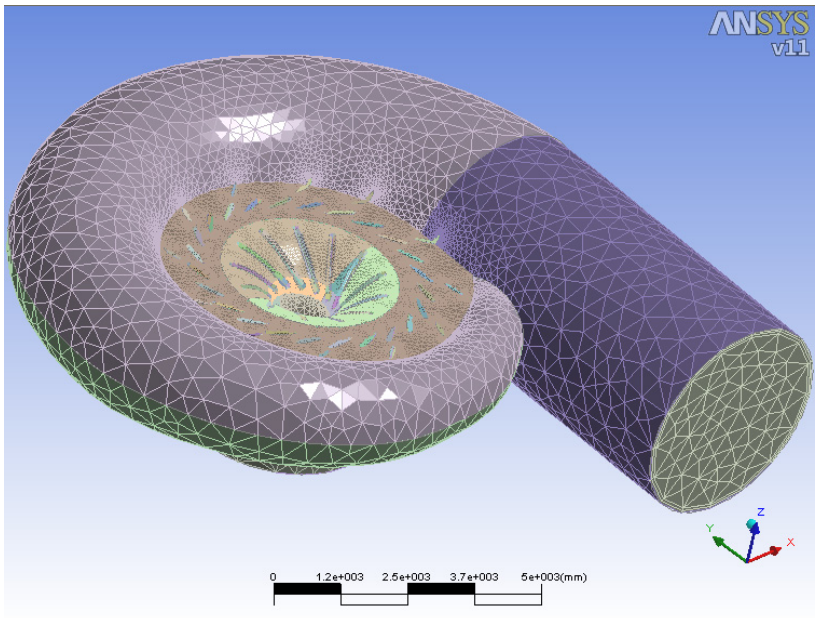

Figure 3: 3D structured grids of the computational domain.

2.3 Numerical modelling of turbulent fluid flow

The flow is considered to be viscous, incompressible and turbulent. The present paper focuses on 3-D Navier-Stokes simulations using the commercial code ANSYS CFX. The continuity equation and Reynolds-averaged Navier-Stokes (*RANS*) equation for incompressible flow have been used as governing equations in the following form [11]:

$$\frac{\partial U_i}{\partial X_i} = 0 \tag{1}$$

$$\frac{\partial U_i}{\partial t} + U_j \frac{\partial U_i}{\partial X_j} + \frac{1}{\rho}\frac{\partial P}{\partial X_i} - \frac{\partial}{\partial X_j}\left(\upsilon\left(\frac{\partial U_i}{\partial X_j} + \frac{\partial U_j}{\partial X_i}\right) - \tau_{ij}\right) = 0 \tag{2}$$

where U, p, υ and ρ are velocity, pressure, kinematic viscosity and density, respectively, and τ_{ij} are the components of the viscous stress tensor, also called the Reynolds Stress Tensor. The turbulent effects on the flow field are taken into account through the Reynolds Stresses τ_{ij} , those are calculated from the k-ε turbulence model, which is frequently used for modelling turbulent flow.

2.4 Boundary conditions

The computations assume steady state incompressible uniform fluid flow in normal direction in the entrance of Spiral Case. Total mass flow in stationary frame was specified at the inlet while static pressure was defined at the outlet boundary. Inlet boundary conditions at given performance point of the hydraulic turbine runner are derived from an operation condition which include discharge Q (82 m^3/s), where the Guide Vanes opening is 80%. Outlet boundary condition is defined to an opening with an average relative pressure to atmospheric pressure.

2.5 Resolution phase

In engineering applications in order to achieve convergence of the solution to an acceptable level, the residual is usually set between four to six orders of magnitude lower than the actual values [12]. Iterative methods are used to solve the corresponding system of algebraic equations, which allows one to characterize the accuracy of the approximation solution by analysing the residual. In this study, the *RMS* residuals settled to a steady state value within 100 iterations. The non-dimensional residual of the momentum and continuity equations was between 10^{-4} to 10^{-6}.

2.6 Results and discussion

Three-dimensional analyses of fluid flow through the Spiral Case, Stay and Guide Vanes and then through the turbine blades channel have been carried out. The distributions of pressure and water velocity within the computational domain are illustrated in the form of contour and streamlines that are generated with the ANSYS CFX postprocessor.

The variation of pressure distributions and tangential velocity in the computational domain obtained from the *CFD* analysis for specific operating conditions are plotted in a plane which is passing through the centre of Spiral Case and across the axis's of rotation as shown in Figure 3(A and B).

The symmetrical inflow to the runner in circumferential direction can be observed, which results in symmetrical distribution pressure from the uniform flow distribution of the runner inlet, as shown in Figure 4B. The tangential velocity increase has been detected at the lower ring, which is due to the smaller area at the distributor region, as evident in Figure 4A.

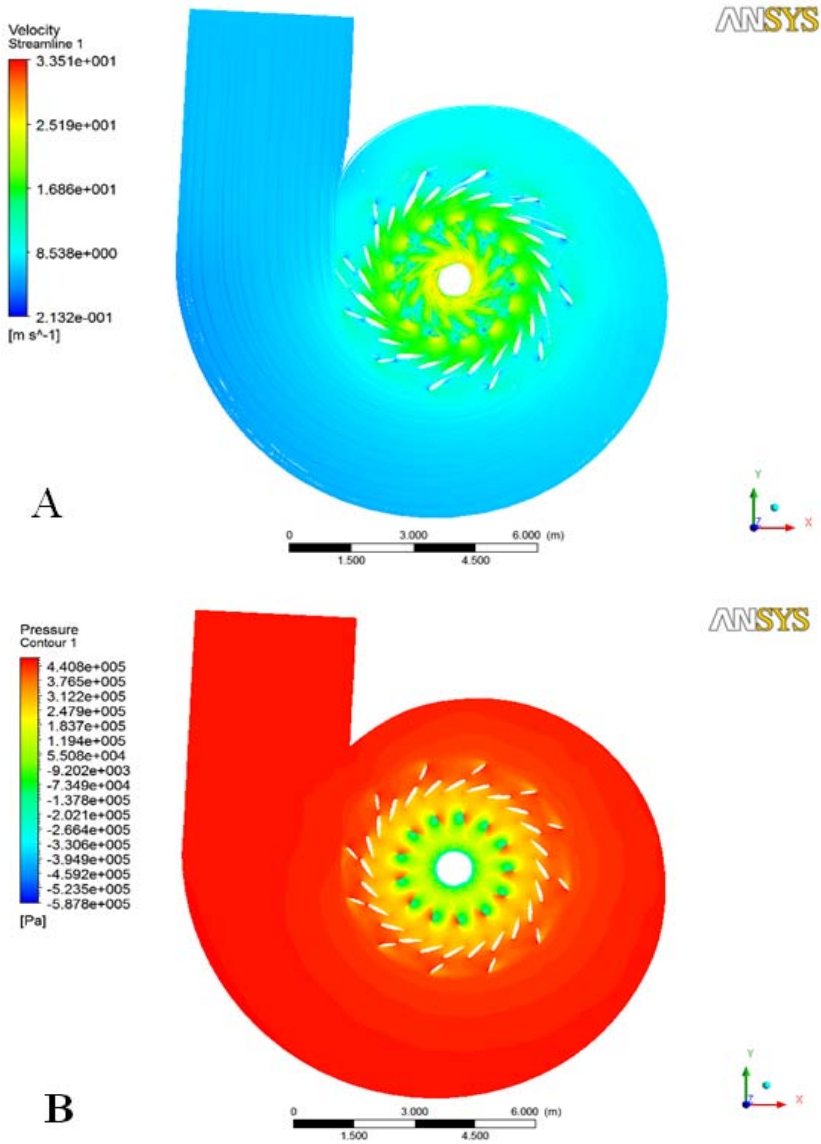

Figure 4: (A) Variation of tangential velocity [ms^{-1}] and (B) pressure distributions [Pa] in the computational domain.

Figure 5(A and B), show the streamlines of the tangential velocity and the runner surface pressure distributions in the plane passing through the centre of Spiral Case and parallel to the axis's of rotation. The tangential velocity component decreases on the blade at the leading edge, which is due to the sharp.bend of the flow in the stagnation regions near the blades, as observed in

Figure 5A. From Figure 5B, reduction from high pressure in the runner inlet to low pressure at the runner outlet is clearly observed. High magnitudes of water pressure are observed at the leading edge of the runner due to stagnation pressure on the blades, which results from the rapid decrease in the magnitude of the tangential velocity close to the bend of the flow.

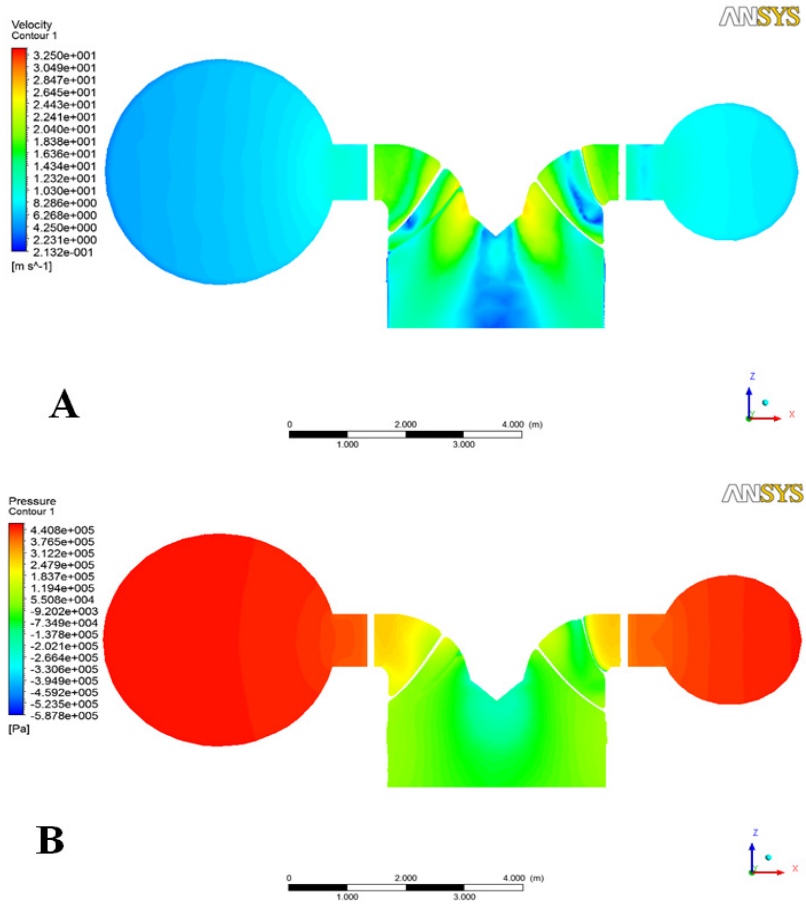

Figure 5: (A) Tangential velocity [ms^{-1}] and (B) the distribution of pressure [Pa] in the turbine.

At the top of the runner the pressure is quite high whereas at the bottom the pressure is low. The increasing pressure on the blades is clearly visible due to stagnation. The reduction of pressure on the runner blade suction side is explained by higher magnitudes of the velocity at the trailing edge. Also, the pressure differences from the pressure and suction side are high and these differences provide the torque on the shaft.

As illustrated in Figure 6, the flow is coming out from the spiral inlet to the upper part of the draft tube at the outlet. The flow is streamlined up to the runner outlet and recirculation is established in the draft tube. This is due to the change in the direction of the flow in the draft tube.

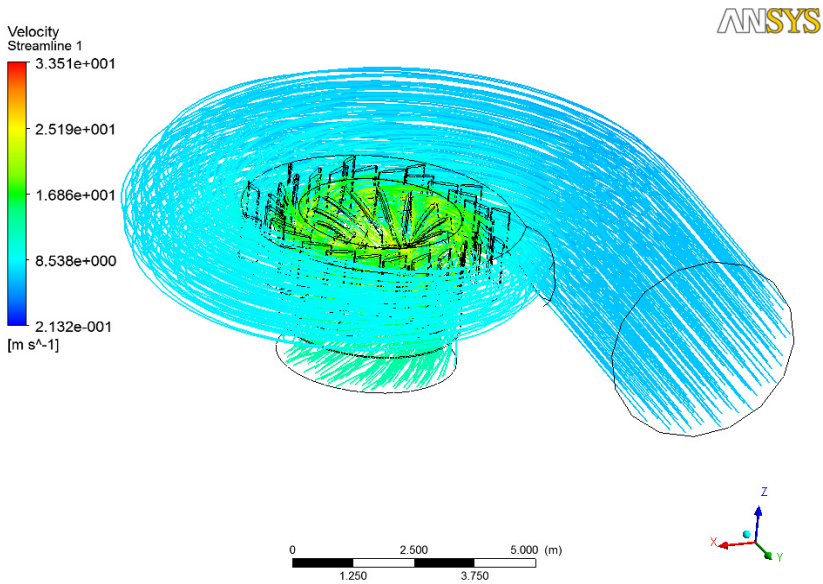

Figure 6: Tangential velocity [ms^{-1}] of the computational domain.

As observed in Figure 6, the flow direction is almost radial at the outlet region of the runner and it is nearly axial at the centre. While the recirculation region varies with the inlet boundary conditions, it increases gradually by decreasing velocity at the inlet. There is a sharp increase in the magnitude of velocity close to the trailing edge of the blade near the ring, due to the reduction of the area between the blade and the ring.

3 Conclusions

The simulation of the 3D steady-state fluid flow with moving reference frame in the entire Francis turbine from spiral case through stay vanes, wicket gates, and runner down to the draft tube is presented. The flow field simulation needs to include the entire flow passage to accurately model the runner surface pressure distributions and the streamlines of tangential velocity. Both these characteristics have been examined for a specific operation condition. Numerical simulation of the entire Francis turbine flow shows clearly the influence of the operation condition on the variation of pressure distributions and tangential velocity in the computational domain. The results show good agreement with the previous studies. The pressure profiles are used further to study stresses in the runner.

References

[1] Avellan, F., Etter, S., Gummer, J. H., Seidel, U., 2000, "Dynamic Pressure Measurements on a Model Turbine Runner and Their Use in Preventing Runner Fatigue Failure", 20th IAHR Symposium, Charlotte, North Carolina, USA.

[2] Nava, J. M. F., Gómez, O. D., Hernández J. A. R. L., Flow induced stresses in a Francis runner using ANSYS, International ANSYS Conference Proceedings, 2006.

[3] Bjorndal, H., Moltubakk, T., Aunemo, H., 2001, "Flow Induced Stresses in a Medium Head Francis Runner - Strain gauge measurements in an operating plant and comparison with Finite Element Analysis", 10th International Meeting of the IAHR Work Group on the Behaviour of Hydraulic Machinery under Steady Oscillatory Conditions, Trondheim, Norway.

[4] Farhat, M., S. Natal, Avellan, F., Paquet, F., Lowys, Py., Couston, M., 2002, "Onboard Measurements of Pressure and Strain Fluctuations in a Model of Low Head Francis Turbine Part 2 : Measurements and Preliminary Analysis Results", Proceedings of the 21st IAHR Symposium on Hydraulic Machinery and Systems, Lausanne, pp. 873-880.

[5] Ikeda, K., Inagaki, M., Niikura, K., Oshima, K., 700-m 400-MW Class Ultrahigh-head Pump Turbine, Hitachi Review Vol. 49, No. 2, pp. 81-87, 2000

[6] Farhat, M., Avellan, F., Seidel, U., 2002, "Pressure Fluctuation Measurements in Hydro Turbine Models", 9th International Symposium on Transport Phenomena and Dynamics of Rotating Machinery, Honolulu, Hawaii, USA.

[7] Fattah, S. S., Khoshnaw, F. M., Saeed, R. A., 2005, "An Investigation about Preventing Cavitation Damage and Fatigue Failure in Derbendikhan Power Station", Fluid Structure Interaction and Moving Boundary Problems, Spain, Vol. 84, pp. 97-106.

[8] Friziger, J. H., 2002. Computational Methods for Fluid Dynamics. Springer, New York, USA.

[9] Čarija Z., Mrša, Z., 2003, "Complete Francis Turbine Flow Simulation for the Whole Range of Discharges", 4th International Congress, of Croatian Society of Mechanics, Bizovac, Croatia, pp. 105-111.

[10] Ruofu, X., Zhengwei, W., Yongyao, L., 2008, "Dynamic Stresses in a Francis Turbine Runner Based on Fluid-Structure Interaction Analysis", Tsinghua Science and Technology, Vol. 13, No. 5, pp. 587-592.

[11] Ruprecht, A., Heitele, M., Helmrich, T., Moser, W., Aschenbrenner, T., 2000, "Numerical simulation of a complete Francis turbine including unsteady rotor/stator interactions", Proceedings of the 20th IAHR.

[12] Hirsch, C., 2007, Numerical Computation of Internal and External Flows, John Wiley and Sons, Ltd, Oxford, Great Britain.

This page intentionally left blank

The characteristics of open cavity flow with a length to depth ratio of 4

Y. Y. Pey[1], L. P. Chua[1] & W. L. Siauw[2]
[1]*Department of Mechanical and Aerospace Engineering, Nanyang Technological University, Singapore*
[2]*DSO National Laboratories, Singapore*

Abstract

The objective of this study is to characterize the flow behavior of an internal cavity of L/D=4, with its shear layer separated from a thick boundary layer at a free stream velocity of 15m/s. The study includes examining the cavity surface pressure and the associated flow structures. Pressure measurements were acquired from the cavity walls and the associated internal flow structures were studied using Particle Image Velocimetry (PIV). Several data processing techniques to study the flow structures were performed on the PIV data. These include time averaging quantities: velocities, vorticity and spatial correlation. In order to estimate the dynamics of the flow, the Proper Orthogonal Decomposition (POD) was applied to 900 independent PIV acquired velocities data set. The cavity wall surface pressure distribution indicated an open flow structure and was consistent with the mean velocity measurements which indicted a large re-circulating region within the cavity. Shear layer velocity profiles across the cavity revealed self-similarity beyond a distance of x/L=0.3. The shear layer growth rate of $d\theta/dx=0.031$ was close to the entrainment rate of a turbulent mixing layer, $d\theta/dx=0.035$. Two point spatial correlation coefficients of velocity fluctuations revealed a distinct pattern of alternating regions of positive and negative coefficient values, indicating the presence of organized coherent structures within the cavity. The modes one and two of the POD extracted structures indicated a flow structure of the closed cavity type. Mode three indicated the possibility of a large structure ejecting from the aft of the cavity.
Keywords: open cavity, coherent structures, proper orthogonal decomposition, particle image velocimetry, spatial correlation, self-similarity, recirculation.

WIT Transactions on Engineering Sciences, Vol 74, © 2012 WIT Press
www.witpress.com, ISSN 1743-3533 (on-line)
doi:10.2495/AFM120061

1 Introduction

Study of flow over cavities is motivated by its phenomena found in many areas such as in solar cells, slots between movable parts of ships, tandem arrangements of bluff bodies such as adjacent tall buildings or tractor-trailer combinations, gas dynamic lasers, hydraulic gates, control valves, landing gears of aircrafts, sunroofs or windows in automobiles [1, 2]. Though geometrically simple, these cavities are associated with complex phenomenon. When exposed to free stream, the cavities experience unsteady flow around them. According to Rockwell *et al* [3], aero acoustic tones are not present at low speed (Mach number less than 0.3); thus, unsteady flow behaviors are due to inherent interaction of the free stream fluid with the lower speed fluid within the cavity. Cavities flow in general can be defined as open, closed or transitional. In open cavity, the flow separates at the leading edge of cavity and spans the entire length of the cavity. For a closed cavity, the flow reattaches on the cavity floor downstream of the leading edge before separating again near the downstream edge. A schematic diagram depicting typical flow in open and closed cavity is shown in Figure 1. In the case of transitional cavity flow, the separated shear layer attaches close to the aft of the cavity.

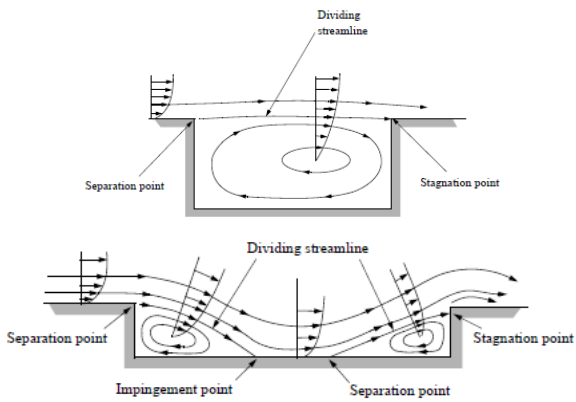

Figure 1: Schematic diagram of open cavity (left) and closed cavity (right) [4].

The current study was carried out on an open cavity with a length to depth ratio (L/D) of 4 at free stream velocity of 15m/s. It includes the measurement of pressure on cavity walls and the study of cavity internal flow structures through the use of Particle Image Velocimetry (PIV). Focus will be placed on investigating Reynolds stresses and coherent structures that develops within the cavity.

2 Experimental details

The experiments were carried out in an open loop wind tunnel with test section size of 220cm (length) by 40cm (width) by 40cm (height). The turbulence

intensity of the empty wind tunnel is about 1% at 30m/s. Operating speed of tunnel varies from 0m/s to 30m/s. The wind tunnel is represented schematically in Figure 2. The length of the cavity model is adjustable; L/D of 4 is used. Figure 3 shows the dimensions of the cavity structure. The cavity floor was instrumented with taps for pressure measurements along the centerline of the cavity floor. The width of the cavity spans the entire test section. The origin is taken to be at the leading edge of the cavity and at the middle of the cavity span.

The PIV system used consists of a double pulsed Nd:YAG laser, a HiSense MkII (Dantec Dynamics) camera and a system hub (FlowMap). The time between the laser pulses was set to be 50μs. The two images, captured during the laser pulses, were adaptive correlated successively starting from an initial interrogation window size of 64 by 64 pixels to a final size of 16 by 16 pixels with a 50% overlap ratio. A total of 900 time-independent images were captured in this study. The position of the PIV laser sheet is shown in Figure 4. The plane of interest lies on the x-y plane along the centreline of the cavity.

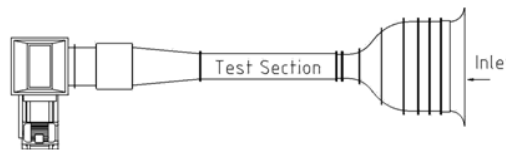

Figure 2: Schematic diagram of wind tunnel top view.

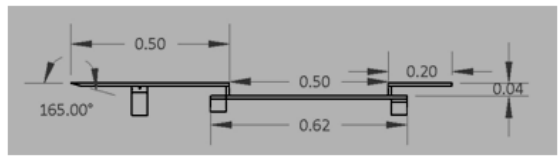

Figure 3: Dimensions of cavity model in metres.

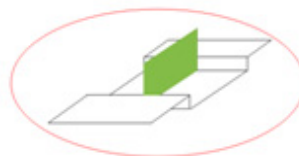

Figure 4: Location of the PIV laser sheet relative to the cavity.

3 Experimental results

3.1 Boundary layer and surface pressure measurements

The boundary layer at the leading edge of the cavity was found to conform to the 1/7 power law and hence is deduced to be turbulent. The boundary layer thickness, $\delta_{0.95}$, was found to be about 90mm. The large thickness could be attributed to both the blockage effect and the design of the leading plate before

the cavity. The pressure coefficient distribution along the centerline of the cavity floor is shown in Figure 5. The pressure gradient is slightly negative up to a x/L of ~ 0.4. After which, there is a gradual increase of pressure towards the cavity aft. These observations are typical of an open flow configuration.

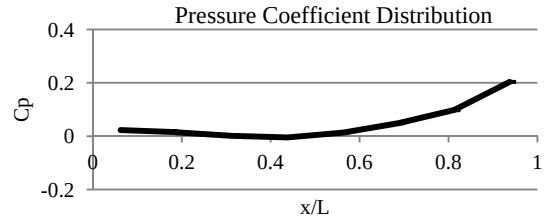

Figure 5: Pressure coefficient distribution along centerline of cavity floor.

3.2 PIV time-averaged results

The 900 independent images acquired from PIV were first averaged to obtain mean field variables. These included the mean flow field in the x and y direction, the in-plane streamlines, velocity fluctuations in the x and y direction, Reynolds shear stress, vorticity and spatial correlation. These quantities will be discussed below. Figure 6 shows the mean velocity in the x and y direction, U and V, as well as the in-plane streamlines. The contour distributions, as well as the large recirculating bubble within the cavity are typical of an open cavity configuration.

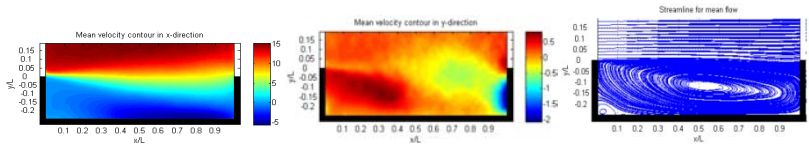

Figure 6: U (left), V (middle), in-plane streamlines (right).

Normalised velocity fluctuations for the cavity in x and y direction, $\frac{u'}{U_\infty}$ and $\frac{v'}{U_\infty}$ are shown in Figure 7 while the Reynolds shear stress, $\frac{u'v'}{U_\infty^2}$, is shown in Figure 8. In each figure, a similar study done by Ukeiley *et al.* [5] for L/D=5.16 at a Mach number of 0.2 is shown on the right for comparison. The general distribution of $\frac{u'}{U_\infty}$ for this study is similar to that of Ukeiley *et al.* [5] as shown in Figure 7. However, there is a region of high intensity above the cavity, especially at the top right corner of the contour plot of this study. This could be due to the thick boundary layer. If this region is ignored, a maximum value of about 0.3 is found along the lip line towards the trailing edge of the cavity. This is comparable to the maximum value of intensity found by Ukeiley *et al.* [5], which also occurs near the trailing edge of the cavity. Similar to the plots of $\frac{u'}{U_\infty}$, the two plots of $\frac{v'}{U_\infty}$ have the same distribution except for the patch of high intensity above the cavity

for this study. A maximum intensity of 0.2 is found for this study, which is comparable to the maximum value of 0.170 found by Ukeiley *et al.* [5]. The position of the maximum intensity occurs near the trailing wall of the cavity in both cases. From Figure 8, the Reynolds shear stress distribution of this study is also similar to that of Ukeiley *et al.* [5], with the maximum value occurring towards the trailing edge of the cavity. A maximum value of around 0.03 is obtained in this study while a maximum value of about 0.015 was obtained by Ukeiley *et al.* [5].

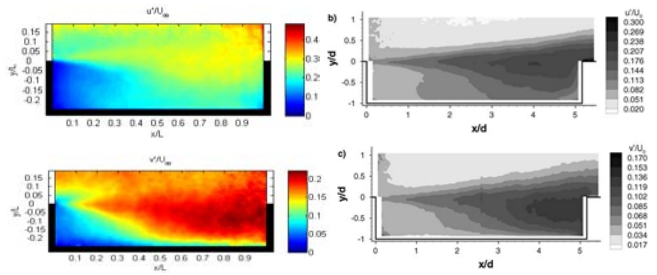

Figure 7: Contour plot of $\frac{u'}{U_\infty}$ and $\frac{v'}{U_\infty}$ (left: current study, right: Ukeiley *et al.* [5]).

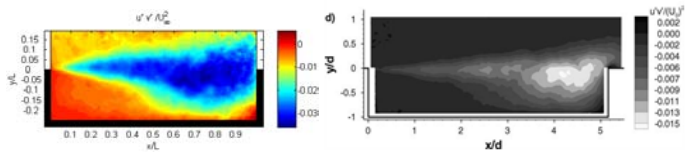

Figure 8: Contour plot of $\frac{u'v'}{U_\infty^2}$ (left: current study, right: Ukeiley *et al.* [5]).

Contour plot of normalized vorticity, $\frac{\omega_z D}{U_\infty}$ (D and U∞, denotes respectively the cavity depth and free stream velocity) was compared against that of Ukeiley *et al.* [5] in Figure 9. Region of higher vorticity was limited to the shear layer in both cases, with some levels of vorticity spreading towards the aft section of the cavity. This is due to the high speed free-stream fluid interacting with the low speed fluid inside the cavity. Both plots have vorticity values in similar range.

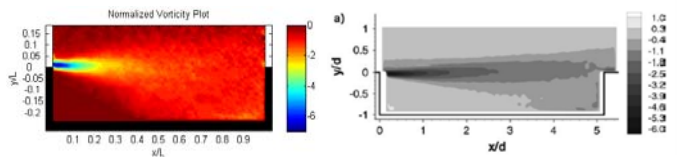

Figure 9: Contour plot of $\frac{\omega_z D}{U_\infty}$ (left: current study, right: Ukeiley *et al.* [5]).

In order to estimate the growth in length scales of coherent structures across the lip line of the cavity, two point spatial correlation coefficients of both the x and y velocity fluctuations were examined. The spatial correlation in x direction is represented by R_{uu} and the spatial correlation in y direction by R_{vv}. The spatial correlation for v' velocity is calculated as

$$R_{vv}(x_o, y_o) = \frac{<v'(x_o)v'(x)>}{\sqrt{v'(x_o)^2}\sqrt{v'(x)^2}} \quad (1)$$

where x_o and y_o denote the reference position for x and y respectively. For this calculation, a reference point was first chosen. The velocity fluctuation at all points in an individual image was correlated to the velocity fluctuation at this reference point. The same correlation procedure was carried out for all 900 images, the result of which was averaged to give the final image. Five reference positions were chosen for both R_{uu} and R_{vv}. These 5 positions lie on the lip line of the cavity and correspond to positions where x/L=0.1, 0.3, 0.5, 0.7 and 0.9. The aim of selecting these 5 positions was to track the growth of the shear layer across the lip. The results are presented in Figure 10, where the lengths of the structures were also measured and shown in cases when structures are smaller than the size of cavity.

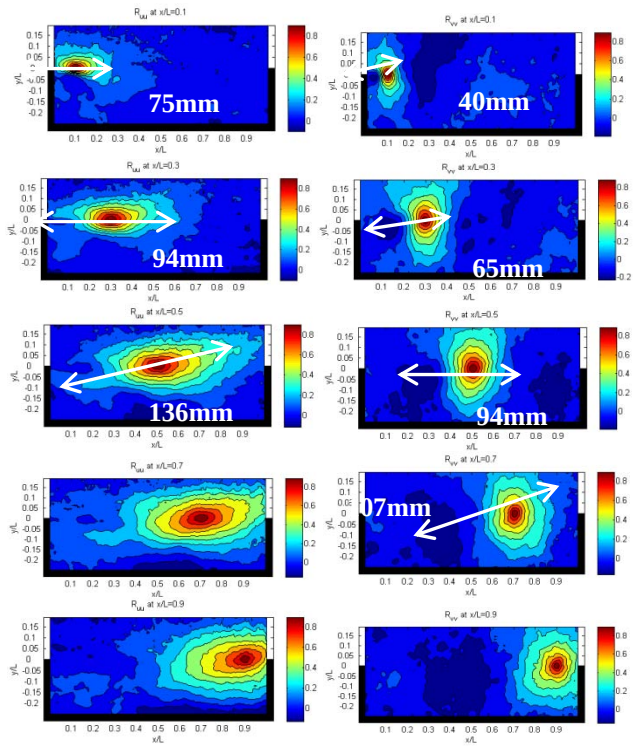

Figure 10: R_{uu} (left) and R_{vv} (right).

In R_{uu}, the length and height of the region of high positive correlation grows with increasing distance from the cavity leading edge. This is consistent with the amplification of disturbances by the shear layer to form large scale coherent structures. In R_{vv}, the correlated regions have roughly circular contours. There appears to be a distinct pattern of alternating regions of positive and negative coefficient values across the span of the cavity, shown by the red and dark blue regions. This reflects the organized nature of the coherent structures within the cavity. Again, the area of positive correlation grows across the cavity.

The velocity profiles across the shear layer as a function of x/L is shown in Figure 11. The plots indicate that the shear layer attains self-similarity beyond x/L=0.3. The growth in momentum thickness as shown in Figure 12 was estimated to be around 0.031. This is close to the entrainment rate of the mixing layer measured by Liepmann *et al* [6] which has $\frac{d\theta}{dx}$ value of 0.035.

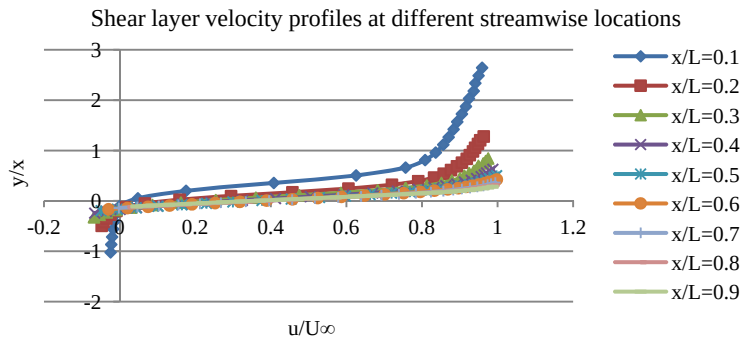

Figure 11: Velocity profiles at different streamwise locations.

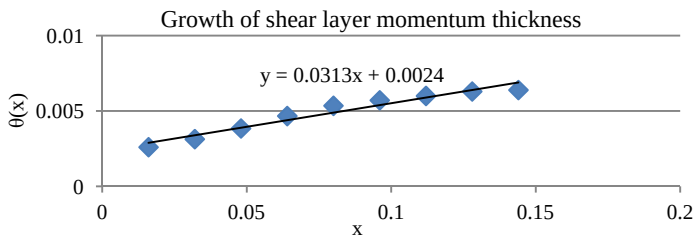

Figure 12: Growth of shear layer across the cavity lip line.

3.3 Proper Orthogonal Decomposition (POD)

3.3.1 Theory of POD

POD was first introduced in the context of turbulence by Lumley [7] as an unbiased way of extracting coherent structures from turbulent flows. It provides an empirical basis for representations of complex spatio-temporal fields that is optimal in the sense that it converges faster on average than any other representation. Detailed explanations of POD can be found in Holmes *et al*. [8]

and Delville *et al*. [9]. Sirovich [10] introduced the snapshot POD method that utilized spatially resolved but time un-correlated snapshots of the flow field like those obtained by PIV. The spatial modes associated with snapshot POD, φ, were assumed to have a special form in terms of the original velocity data:

$$\phi(x) = \sum_{n=1}^{N} a^{(n)} U_i^{(n)}(x) \tag{2}$$

where the temporal coefficients $a^{(n)}$, n=1,....,N are to be determined. A consequential eigenvalue problem is hence deduced to solve for $a^{(n)}$:

$$Ca^{(n)} = \lambda^{(n)} a^{(n)} \tag{3}$$

Flow reconstruction can then be done through the linear combination of spatial eigenfunctions with the temporal eigenfunctions as coefficients. Through POD, the spatial eigenfunctions are orthonormal and the temporal coefficients are orthogonal.

$$U_i(x) = \sum_{n=1}^{N} a^{(n)}(t) \phi_i^{(n)}(x) \tag{4}$$

3.3.2 Application of POD to PIV data

POD was applied to all 900 images from PIV, with the mean flow field subtracted from the images before decomposition. Figure 13 is a plot depicting the individual energy content of the modes, the sum of which contributes to 75% of the total energy in the flow. A total of about 74 modes were needed to make up 75% of the energy content in the field. The first mode has about 15.7% of the total energy. This is followed by a drop in energy for subsequent modes. Mode 2, 3 and 4 has about 7.3%, 5.6% and 4.5% of total energy respectively. For reconstruction of flow, the first 4, 7 and 14 modes are needed to recover 33%, 40% and 50% of the total energy content respectively.

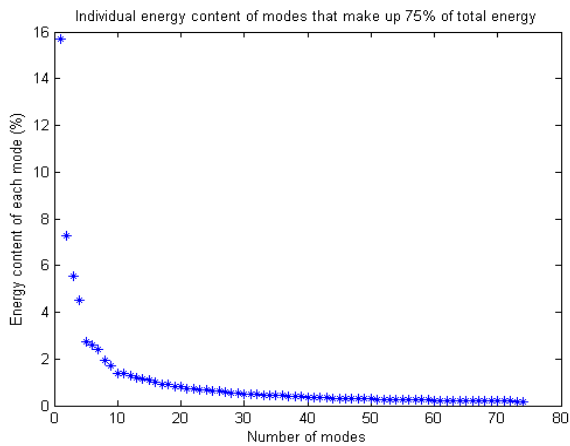

Figure 13: Individual energy content of modes.

The first 5 spatial modes in the y direction are shown in Figure 14. These plots reveal the structures that are contributing to each mode. From the spatial modes, the length scales of the structures were estimated, where clear structures could be identified. This is indicated by the white arrows in modes 2 to 5. From the figure, mode 1 has a structure that stretches through the entire cavity. Hence, the length-scale is taken to be the length of the cavity, 160mm. Mode 2 and mode 3 both have a length scale of about 114mm while mode 4 has a length scale of about 100mm and mode 5 has a length scale of about 83mm. The decrease in the length scale of structure with the increase in the mode number is expected as smaller structures contribute to a lesser percent of the total energy in the flow.

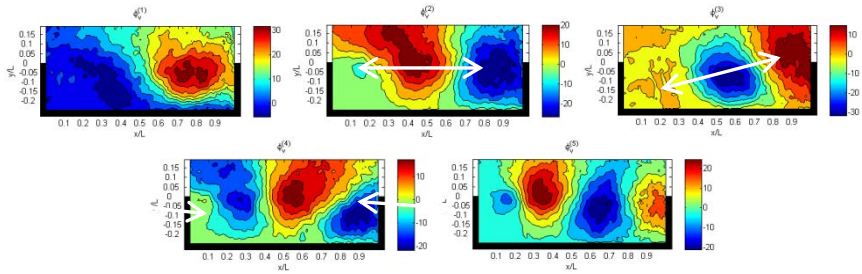

Figure 14: Plots of first 5 $\phi_v^{(n)}$.

The in-plane streamlines of modes 1 to 3 were also plotted in Figure 15. These streamlines represent the contribution of the modes in both the x and y direction. Inspection of the in-plane streamlines seems to indicate the flapping of the shear layer. One could deduce this fact from the super position of these modes onto the mean in-plane streamlines profile as shown in Figure 6 and eqn (4). Mode one and two indicated a flow structure of the closed cavity type while mode three indicated the possibility of a large structure ejecting from the aft of the cavity.

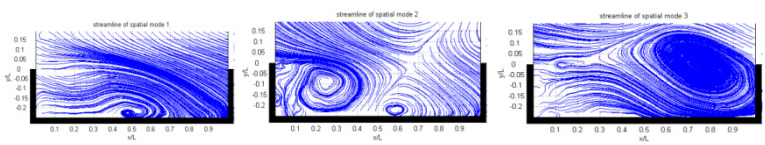

Figure 15: In-plane streamlines of individual spatial mode.

3.3.3 Reconstruction of flow with first four POD modes

Reconstruction of flow was done with the first 4 modes to see how well these modes can estimate the original mean flow field as well as whether the turbulent noise due to the thick boundary layer can be decoupled. The mean quantities are recalculated from the reconstructed field. Figure 16 shows the mean velocity in the x and y direction, U and V, as well as the in-plane streamlines. When comparing Figure 16 with Figure 6, it was observed that both U and V, and

hence the in-plane streamlines, have been successfully reconstructed. Reconstructed normalised velocity fluctuations in x and y direction, $\frac{u'}{U_\infty}$ and $\frac{v'}{U_\infty}$, are shown in Figure 17 while the reconstructed Reynolds shear stress, $\frac{u'v'}{U_\infty^2}$, is shown in Figure 18. In the contour plot of $\frac{u'}{U_\infty}$ and $\frac{v'}{U_\infty}$, it was observed that the region of high intensity above the cavity that was present in Figure 7 has now disappeared. This implies that we could decouple the turbulent background noise from the results. The general distribution of velocity fluctuations here is about the same as the original flow field in both x and y direction. For $\frac{u'}{U_\infty}$, a maximum value of 0.25 was obtained, which is comparable to the original value of 0.3. For $\frac{v'}{U_\infty}$, a maximum intensity of about 0.14 was obtained, which is slightly lower than the original value of 0.2. This loss of energy was expected as the background turbulent noise has been filtered by the POD procedure. In the contour plot of $\frac{u'v'}{U_\infty^2}$, the maximum value of 0.03 and its position is similar to the original flow shown in Figure 8. However, the intensity at the leading edge is lower here than in the original flow.

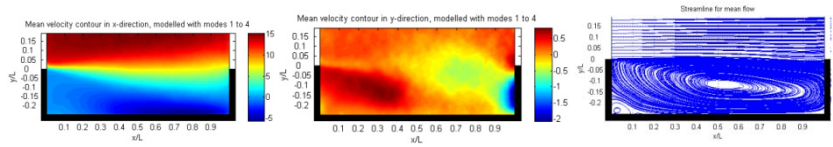

Figure 16: Contour of reconstructed U (left), V (middle) and in-plane streamlines (right), using the first 4 modes.

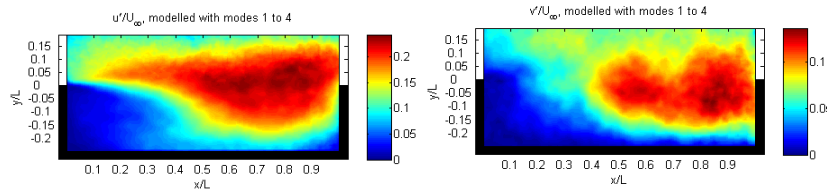

Figure 17: Contour plot of $\frac{u'}{U_\infty}$ (left) and $\frac{v'}{U_\infty}$ (right), modelled by first 4 modes.

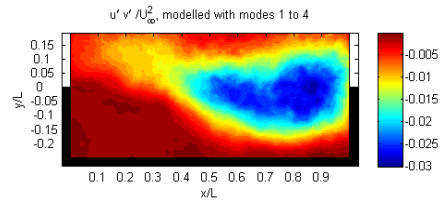

Figure 18: Contour plot of $\frac{u'v'}{U_\infty^2}$, modelled by first 4 modes.

Overall, it seems that the first 4 modes were able to replicate the mean flow field to a fairly accurate extent. This is an important feature of POD since using less number of modes to model the flow field accurately means that cost of computation can be reduced or that flow control studies could be carried out more efficiently.

4 Conclusion

The present work has made used of several data reduction tools to post process PIV data of an open cavity with L/D=4. The shear layer which grows across the cavity was found to attain self-similarity in the velocity profiles beyond x/L=0.3. The rate of growth in momentum thickness of this shear layer was estimated to be around 0.031, a value close to the entrainment rate of a turbulent mixing layer. Time-averaged quantities of the flow revealed the mean flow characteristics within the cavity while spatial correlations of velocity fluctuations indicated the presence of organized coherent structures which grew across the shear layer of the cavity. POD was applied to PIV data to derive the structures responsible for the different modes of flow. From the POD results, the first four modes were used to reconstruct the flow. This filtering process could remove the turbulent background noise successfully.

References

[1] Kook, H., Mongeau, L. , Brown, D.V. & Zorea, S.I., *Analysis of the interior pressure oscillations induced by flow over vehicle openings.* Noise Control Engineering Journal, **45**, pp. 223-234, 1997.

[2] Gharib, M. & Roshko, A., *The effect of flow oscillations on cavity drag.* Journal of Fluid Mechanics, **177,** pp. 501-30, 1987.

[3] Rockwell, D. & Naudascher, E., *Review-self-sustaining oscillations of flow past cavities.* Transactions of the ASME. Journal of Fluids Engineering, **100**, pp. 152-65, 1978.

[4] Plentovich, E.B., *Experimental Cavity Pressure Measurements at Subsonic and Transonic Speeds*. NASA Technical Paper 3358. 1993.

[5] Ukeiley, L. & Murray, N., *Velocity and surface pressure measurements in an open cavity.* Experiments in Fluids, **38**(5), pp. 656-671, 2005.

[6] Liepmann, H.W. & Laufer, J., *Investigation of free turbulent mixing*, National Advisory Committee for Aeronautics: Washington, DC, United States , 1947.

[7] Lumley, J., *The Structure of Inhomogeneous Turbulent Flows*. Atmospheric Turbulence and Wave Propagation, Moscow: Nauka, 1967.

[8] Holmes, P., Lumley, J. & Berkooz, G., *Turbulence, Coherent Structures, Dynamical Systems and Symmetry*, Cambridge, England: Cambridge University Press, 1996.

[9] Delville, J., Cordier, L. & Bonnet, J.P., *Large-Scale-Structure Identification and Control in Turbulent Shear Flows*, Springer Berlin / Heidelberg, pp. 199-273, 1998.

[10] Sirovich, L., *Turbulence and the dynamics of coherent structures. I. Coherent structures*. Quarterly of Applied Mathematics, **45**, pp. 561-70, 1987.

Section 2
Computational methods

This page intentionally left blank

On gauge fields in fluid turbulence

T. H. Moulden
The University of Tennessee Space Institute, USA

Abstract

A standard gauge velocity field is introduced into the constant density Navier–Stokes equations and extended to treat fluid turbulence. Some of the elementary properties of such gauge fields are explored and relationships between them established. In particular, the gauge fields separate out the irrotational motion from the vortical motion. An example that describes the inactive component of a turbulent flow is presented.
Keywords: gauge fields, turbulence models, energy estimates.

1 Background

Write the field equations for the flow of a constant density viscous fluid in the standard form:

$$\frac{\partial v_i}{\partial x_i} = 0; \qquad \frac{\partial v_i}{\partial t} + \frac{\partial}{\partial x_j}(v_i v_j) + \frac{\partial P}{\partial x_i} = \nu \frac{\partial^2 v_i}{\partial x_j \, \partial x_j} + f_i \qquad (1a, b)$$

where $P(\mathbf{x}, t)$ is the pressure field normalized by the constant fluid density. Equations (1*a*,*b*) define the field $(\mathbf{v}, P)$ in which $\mathbf{v}(\mathbf{x}, t)$ is the instantaneous velocity field at location $\mathbf{x}$ and time t. $\mathbf{f}(\mathbf{x})$ denotes a time independent body force in equation $(1b)$. Herein, the kinematic viscosity coefficient, ν, is taken to be constant. To be useful these equations must possess a unique regular solution for meaningful boundary conditions; and the existence of such a solution is assumed in the following discussion. Certain additional assumptions must be made before equations (1*a*,*b*) can be adopted to describe the turbulent flow of a viscous fluid. These assumptions include the need for the turbulent velocity and pressure fluctuations to be continuous and have bounded energy. It is also required that all velocity-related correlation functions be bounded. As is standard, the divergence of equation (1*b*) produces a Poisson equation to compute the pressure field directly:

$$\frac{\partial^2 P}{\partial x_i \, \partial x_i} = \frac{\partial f_i}{\partial x_i} - \frac{\partial^2}{\partial x_i \, \partial x_j}(v_i v_j) \qquad (1c)$$

WIT Transactions on Engineering Sciences, Vol 74, © 2012 WIT Press
www.witpress.com, ISSN 1743-3533 (on-line)
doi:10.2495/AFM120071

since, as stated above, it is assumed that all required derivatives exist. Some regularity results for the Navier–Stokes equations are given in Seregin [1].

Let the Reynolds decomposition be expressed in the standard form:

$$\mathbf{v} \mapsto \mathbf{V} + \mathbf{u}; \quad \mathbf{V} = \mathcal{E}(\mathbf{v}) \text{ and } \mathcal{E}(\mathbf{u}) = 0 \tag{2}$$

if $\mathbf{u}(\mathbf{x}, t)$ is the fluctuating velocity field and $\mathbf{V}(\mathbf{x}, t)$ the corresponding mean velocity. Equation (2) implies that the kinetic tensor, $\mathbf{R} = \mathbf{v} \otimes \mathbf{v}$ will be decomposed as $\mathbf{R} \mapsto \overline{\mathbf{R}} + \boldsymbol{\mathcal{R}}$ in the mean motion equations provided that $\overline{\mathbf{R}} = \mathbf{V} \otimes \mathbf{V}$ denotes the mean kinetic tensor. $\boldsymbol{\mathcal{R}}(\cdot)$ in the above represents an appropriate mean value operator whose specific form is not of significance for the present discussion and $\boldsymbol{\mathcal{R}} = \mathcal{E}(\mathbf{u} \otimes \mathbf{u})$ is referred to as the Reynolds tensor. As is well known, introduction of the Reynolds decomposition renders equations (1*a*,*b*) unclosed and hence unsolvable without an additional statement in the form of a *turbulence model*: $\boldsymbol{\chi}(\boldsymbol{\mathcal{R}}, \mathbf{V}, \boldsymbol{\alpha}) = \mathbf{0}$ (with a vector, $\boldsymbol{\alpha}$, of scalar constants). The constraints that must be placed upon such models, are not the present interest — for some of which see the discussion in Moulden [2]. Details of specific turbulence models are given in such references as Chen and Jaw [3], Wilcox [4] as well as in Launder and Sandham [5]. See also the discussion in Gatski [6].

Start by noting some fundamental properties of equations (1*a*,*b*) that will be required for subsequent developments:

a) As is standard, equations (1*a*,*b*), being based upon Newtonian mechanics, are covariant under the Galilean group, $\mathbb{G}_a$:

$$\mathbf{x}^* = \mathbf{Q}[\mathbf{x} + \mathbf{V}_T t + \mathbf{x}_0]; \qquad t^* = t + t_0$$

which implies a velocity transformation of the form $\mathbf{v}^* = \mathbf{Q}\,[\mathbf{v} + \mathbf{V}_T]$. Here, $\mathbf{Q} \in \mathbb{SO}_3$ is a *constant* coordinate rotation while $\mathbf{V}_T$ is the constant Galilean boost velocity while $\mathbf{x}_0$ and t_0 are constant space and time translations. The pressure field is invariant across inertial frames. Finally, note that the spatial and temporal gradients transform as:

$$\frac{\partial(\cdot)}{\partial x_i^*} \equiv Q_{ij} \frac{\partial(\cdot)}{\partial x_j}; \qquad \frac{\partial(\cdot)}{\partial t^*} = \frac{\partial(\cdot)}{\partial t} - (V_T)_k \frac{\partial(\cdot)}{\partial x_k}$$

under the group $\mathbb{G}_a$. The Reynolds averaged equations, like the Navier–Stokes equations, are fully covariant under the Galilean group.

b) Gurtin [7] gave a simple uniqueness result for the constant density Navier–Stokes equations (1*a*,*b*) under the assumption that certain regularity conditions are satisfied. In particular, that the norm of the stretching tensor $\mathbf{D} = sym(\mathbf{L})$ (if $\mathbf{L} = \boldsymbol{\nabla}(\mathbf{v})$ is the velocity gradient tensor) must be bounded for all $\mathbf{x}$, t of interest. This constraint implies that $\mathbf{D}$ must have bounded eigenvalues: a condition related to the requirements on the boundedness of the Reynolds tensor $\boldsymbol{\mathcal{R}}$. The theorem of Gurtin [7] showed that the velocity field, $\mathbf{v}(\mathbf{x}, t)$, must be unique but that the pressure field has the uniqueness property only up to an arbitrary function of time:

$$P(\mathbf{x}, t) \mapsto P(\mathbf{x}, t) + P^*(t)$$

say. This finding is nothing more than noting that the simple equality:

$$\frac{\partial}{\partial x} P(\mathbf{x}, t) = \frac{\partial}{\partial x}[P(\mathbf{x}, t) + P^*(t)]$$

must hold for any bounded function $P^* = P^*(t)$, only. Most important for practical applications is the velocity field uniqueness obtained from the theorem of Gurtin [7] and this result will be required herein.

It will be found below that certain gauge transformations introduced in the literature do not possess full Galilean covariance and so are not, to this extent, consistent with the Navier–Stokes equations. Some applications of one such gauge transformation will, however, be explored.

2 On the Reynolds decomposition

The instantaneous Navier–Stokes equations for constant density flow were written in equations (1*a*,*b*) (and formally constitute a well posed problem when appropriate boundary and initial conditions are appended: even though certain issues relating to uniqueness and regularity remain unresolved). The instantaneous kinetic tensor $\mathbf{R} = \mathbf{v} \otimes \mathbf{v}$, again normalized by the fluid density, has been introduced in equation (1*b*). Being symmetric the kinetic tensor has real eigenvalues one of which is $\lambda = \langle \mathbf{v}, \mathbf{v} \rangle$, the kinetic energy. It is assumed here that the velocity field is regular in that all required derivatives exist. The same is assumed of the pressure field.

With these definition in place the mean motion equations, corresponding to equations $(1a, b)$, can be written as:

$$\frac{\partial \mathbf{V}}{\partial t} + div(\overline{\mathbf{R}}) + div(\boldsymbol{\mathcal{R}}) + \boldsymbol{\nabla}(\overline{P}) = \nu \nabla^2(\mathbf{V}) + \mathbf{f}; \qquad div(\mathbf{V}) = 0 \qquad (3a, b)$$

when the velocity field $\mathbf{v}(\mathbf{x}, t)$ has been decomposed in the form $\mathbf{v} \mapsto \mathbf{V} + \mathbf{u}$ with $|\mathbf{u}|$ bounded. The corresponding equation for the fluctuating velocity, $\mathbf{u}(\mathbf{x}, t)$, with $div(\mathbf{u}) \equiv 0$, is given as:

$$\frac{\partial \mathbf{u}}{\partial t} + div[(\mathbf{V} \otimes \mathbf{u} + \mathbf{u} \otimes \mathbf{V}) + \mathbf{u} \otimes \mathbf{u} - \boldsymbol{\mathcal{R}}] + \boldsymbol{\nabla}(p') = \nu \nabla^2(\mathbf{u}) \qquad (4)$$

since the body force has been restrained as $\mathbf{f} = \mathbf{f}(\mathbf{x})$ only. Here the pressure field is given the usual decomposition as $P = \overline{P} + p'$. The standard evolution equation for the Reynolds tensor $\boldsymbol{\mathcal{R}} = (\mathcal{R}_{ij})$ can be established from equation (4) and has the form:

$$\frac{\partial \mathcal{R}_{ij}}{\partial t} + V_k \frac{\partial \mathcal{R}_{ij}}{\partial x_k} + \mathcal{R}_{jk} \frac{\partial V_i}{\partial x_k} + \mathcal{R}_{ik} \frac{\partial V_j}{\partial x_k} - \nu \frac{\partial^2 \mathcal{R}_{ij}}{\partial x_k^2} = -\Psi_{ij} \qquad (5)$$

(see, for example, Frost and Moulden [8]). The definition:

$$\Psi_{ij} = 2\nu \mathcal{E} \left[\frac{\partial u_i}{\partial x_k} \frac{\partial u_j}{\partial x_k} \right] + \frac{\partial}{\partial x_k} \mathcal{E}(u_i u_j u_k) + \psi_{ij} \equiv \mathbf{E}_T|_{ij} + \mathbf{D}_F|_{ij} + \psi_{ij}$$

has been included in equation (5). In this equation $\mathbf{E}_T$ denotes the turbulence dissipation and $\mathbf{D}_F$ the velocity diffusion term whose explicit form is not of importance in the present context. As usual, turbulence models are required for both of these terms. Finally ψ_{ij} denotes the standard pressure fluctuation terms in

the Reynolds stress equation:

$$\psi_{ij} = \mathcal{E}\left[\frac{\partial(u_j p')}{\partial x_i} + \frac{\partial(u_i p')}{\partial x_j}\right] - \mathcal{E}\left[p'\left(\frac{\partial u_j}{\partial x_i} + \frac{\partial u_i}{\partial x_j}\right)\right] \qquad (5a)$$

The velocity, $\mathbf{v}(\mathbf{x}, t)$, is unique and, for a *given* mean value operator, $\mathcal{E}$, so is the mean motion $\mathbf{V}$. Hence the fluctuations $\mathbf{u}(\mathbf{x}, t)$, must also be unique along with the Reynolds tensor $\boldsymbol{\mathcal{R}} = \mathcal{E}(\mathbf{u} \otimes \mathbf{u})$ *again when determined* from the unique instantaneous velocity field defined by the Navier–Stokes equations. Under the group $\mathbb{G}_a$ the well known transformations:

$$\mathbf{V}^* = \mathbf{Q}[\mathbf{V} + \mathbf{V}_T]; \qquad \mathbf{u}^* = \mathbf{Q}\mathbf{u}$$

hold (see Speziale [11] for a more general discussion of the invariance properties of turbulence models). Only the mean velocity is influenced by the Galilean boost velocity $\mathbf{V}_T$. In other words, the turbulent fluctuations are transparent to uniform rectilinear motion of the inertial frame.

3 A gauge decomposition

The experimental work of Bradshaw [10] studied the inactive component of the motion external to a turbulent shear layer. This motion contains irrotational velocity fluctuations as well as pressure fluctuations and the two relate via a Bernoulli-type equation. It is appropriate to introduce a gauge field $\boldsymbol{\omega}(\mathbf{x}, t)$ that describes the irrotational motion. That is equation $(1a)$, wherein $div(\mathbf{v}) = 0$, allows the specification of a *gauge velocity field* $\boldsymbol{\omega}$ in the form: $\mathbf{v} \mapsto \mathbf{s} + \boldsymbol{\omega}$ when:

$$div(\mathbf{v}) = 0 \equiv div(\mathbf{s}) + div(\boldsymbol{\omega}) \qquad (1d)$$

Since $\mathbf{v}$ is a function of space and time, it is assumed that $\mathbf{s}$ and $\boldsymbol{\omega}$ have that same dependence. The *nature* of the gauge field $\boldsymbol{\omega}(\mathbf{x}, t)$ is arbitrary within that constraint and could be stochastic. At this point there is nothing to specify that the above decomposition of the velocity field is unique. However, the variables $\mathbf{s}$ and $\boldsymbol{\omega}$ can at most, from equation (1d), differ by a divergence-free vector field. Clearly, when $\boldsymbol{\omega} = \boldsymbol{\nabla}(\varphi)$, for some scalar φ, the equality $\boldsymbol{\zeta} = curl(\mathbf{v}) \equiv curl(\mathbf{s})$ holds so that the $\mathbf{s}(\mathbf{x}, t)$ field captures all the vorticity in the flow. Now the condition $div(\mathbf{v}) = 0$ provides the Poisson equation $div(\mathbf{s}) + \nabla^2(\varphi) = 0$ and the $\boldsymbol{\omega}$ field is potential but not, in general, harmonic. Since the vector field $curl(\mathbf{s}) = \boldsymbol{\zeta}$ is known a (non-unique) velocity field can be generated from it. There is non-uniqueness since any $\beta \in \mathbb{R}$ such that $curl(grad(\beta)) \equiv 0$ can be introduced additively. However, since $div(\mathbf{v}) = 0$ has the physical meaning of mass conservation in constant density flow, the specification of $\mathbf{s}(\mathbf{x}, t)$ as the vorticity carrying component in the decomposition $\mathbf{v} = \mathbf{s} + \boldsymbol{\nabla}(\varphi)$ is unique: the scalar β can be combined with φ. For a discussion of the more specific Stokes–Helmholtz decomposition, which is not required herein, see Wu *et al.* [12]. Throughout it is assumed that all vector fields are bounded and, in unbounded regions, tend to zero in the far field.

For the application in mind in section 5, it is appropriate to take the vector $\boldsymbol{\omega}$ to be potential since it can then represent the irrotational component of a turbulent flow; both inside and outside of a turbulent shear layer. The appropriate boundary conditions to be appended to the definition of the $\mathbf{s}$ and $\boldsymbol{\omega}$ fields will be addressed in section 5 for a specific flow field.

From equation (1c) a Poisson equation for the pressure can be constructed, in the usual way, to give:

$$\frac{\partial^2 P}{\partial x_i\,\partial x_i} = \frac{\partial f_i}{\partial x_i} - \frac{\partial}{\partial x_i}(s_j + \omega_j)\frac{\partial}{\partial x_j}(s_i + \omega_i)$$

once the $\mathbf{s}(\mathbf{x}, t)$ and $\boldsymbol{\omega}(\mathbf{x}, t)$ variables are known.

The above gauge decomposition was introduced by Weinan E and Liu [13] and discussed by Wang and Liu [14] in the context of numerical solutions of the Navier–Stokes equations. The latter adopted a Crank–Nicolson, or backward Euler, time discretization to construct a stable finite difference formulation. The objective herein is to explore the possible use of such gauge fields in turbulent flow: specifically to isolate the inactive motion from the vortical motion inside a turbulent shear layer. As noted above, these irrotational velocity fluctuations exist outside the shear layer and the $\boldsymbol{\omega}$ field must also describe this external motion. Various aspects of the physics of the inactive motion are discussed in Bradshaw [10, 15] and Phillips [16] when restricted to the case of a statistically stationary flow field. The present interest lies in exploring the extension to non-stationary turbulent flows. In particular, evolution equations for the inactive motion are required but now expressed in terms of the gauge fields.

From equations (1a,b) there is an evolution of the velocity field $\mathbf{s}(\mathbf{x}, t)$ and a specification of the gauge $\boldsymbol{\omega}(\mathbf{x}, t)$ given by the equations:

$$\frac{\partial s_i}{\partial x_i} = -\frac{\partial \omega_i}{\partial x_i} \equiv -\frac{\partial^2 \varphi}{\partial x_i\,\partial x_i}; \qquad \frac{\partial s_i}{\partial t} + \frac{\partial}{\partial x_k}\left[v_i v_k\right] = \nu\frac{\partial^2 s_i}{\partial x_k\,\partial x_k} + f_i \qquad (6a, b)$$

if the variable $\omega_i \equiv \partial\varphi/\partial x_i$ is potential, so that $\mathbf{v} = \mathbf{s} + \boldsymbol{\nabla}(\varphi)$, then the pressure field $P(\mathbf{x}, t)$ is determined retrospectively from the equality:

$$\frac{\partial \varphi}{\partial t} + P = \nu\frac{\partial^2 \varphi}{\partial x_k\,\partial x_k} \qquad (7)$$

once the gauge field $\varphi(\mathbf{x}, t)$ has been determined. The regularity assumptions made in the theory demand that both quantities, $\partial\varphi/\partial t$ and $\nabla^2(\varphi)$, are bounded. The pressure field is then well defined in equation (7). It hardly requires stating that splitting the velocity $\mathbf{v}$ into a rotational and irrotational parts is artificial in the sense that flow experiments do not allow this separation of the measured velocity field. If equation (7) is looked upon as a non-homogeneous equation for the potential $\varphi(\mathbf{x}, t)$ then the constraints to be imposed upon the function $P(\mathbf{x}, t)$, for a unique solution to exist, must be specified. From Stakgold [17] a boundedness condition on $P(\mathbf{x}, t)$ is required.

The potential φ can be obtained from equation (6a) in terms of a Laplacian Green's function when the $\mathbf{s}(\mathbf{x}, t)$ field is known. If $\varphi(\mathbf{x}, t)$ is determined uniquely from equations (6a,b) then the pressure $P(\mathbf{x}, t)$ follows uniquely from equation (7). The classical vorticity transport equation for constant density fluid motion:

$$\frac{\partial \zeta_i}{\partial t} + v_j\frac{\partial \zeta_i}{\partial x_j} = \frac{\partial v_i}{\partial x_j}\zeta_j + \nu\frac{\partial^2 \zeta_i}{\partial x_j\,\partial x_j} + \epsilon_{ijk}\frac{\partial f_k}{\partial x_j}; \quad \boldsymbol{\zeta} = curl(\mathbf{v}) \equiv curl(\mathbf{s}) \qquad (V)$$

does not make reference to the fluid pressure. It is consistent with this observation that equation (7) determines the fluid pressure field from just the irrotational

motion. Equation (V) is covariant under $\mathbb{G}_a$ since the transformation $\boldsymbol{\zeta}^* = \mathbf{Q}\,\boldsymbol{\zeta}$ holds under that group.

Consider the Galilean transformation applied to the gauge decomposition introduced above when it is required that:

$$\mathbf{s}^* = \mathbf{Q}[\mathbf{s} + \mathbf{V}_T] \quad \text{and} \quad \boldsymbol{\omega}^* = \mathbf{Q}\,\boldsymbol{\omega} \quad \Rightarrow \quad |\boldsymbol{\omega}^*| \equiv |\boldsymbol{\omega}|$$

in addition $|\mathbf{s}^*|^2 \leq \left[|\mathbf{s}| + |V_T|\right]^2$ as a bound on the vector $\mathbf{s}^*(\mathbf{x}^*, t^*)$: a bound that must be boost velocity dependent. When $\boldsymbol{\omega}$ is potential there is the transformation: $\boldsymbol{\nabla}^*(\varphi^*) = \mathbf{Q}\,\boldsymbol{\nabla}(\varphi)$ under $\mathbb{G}_a$ so that $|\boldsymbol{\nabla}^*(\varphi^*)| = |\boldsymbol{\nabla}(\varphi)|$. It should be noted that the pair of equations (6b,7) are not Galilean covariant under boosts since the transformed equation (6b) has the form:

$$\frac{\partial s_i}{\partial t} + \frac{\partial}{\partial x_j}(v_i v_j) \left[+(V_T)_j \frac{\partial \omega_i}{\partial x_j}\right] = \nu \frac{\partial^2 s_i}{\partial x_j\, \partial x_j} + f_i \qquad (Ga)$$

while equation (7) transforms to:

$$\frac{\partial \varphi}{\partial t} \left[-(V_T)_k \frac{\partial \varphi}{\partial x_k}\right] + P = \nu \frac{\partial^2 \varphi}{\partial x_k\, \partial x_k} \qquad (Gb)$$

to demonstrate the lack of Galilean covariance in the gauge transformation: the terms in brackets in equations (Ga,b) destroying the covariance. The equations (6b,7) are, however, covariant under Galilean rotations. Equation (6a) is fully Galilean covariant. Equations (Ga,b) do not feature in the following discussion but must be recalled when transferring to a moving inertial frame.

4 The gauge Reynolds decomposition

Introduce a Reynolds decomposition into equations (6a,b) by specifying that:

$$\mathbf{s} \mapsto \mathbf{S} + \mathbf{r}; \quad \varphi \mapsto \Psi + \phi$$

where $\mathbf{S} = \mathcal{E}(\mathbf{s})$ and $\Psi = \mathcal{E}(\varphi)$. The vorticity field $\boldsymbol{\zeta}(\mathbf{x}, t) = curl(\mathbf{s})$ has two components: $curl(\mathbf{S})$ and $curl(\mathbf{r})$; the latter associating with the rotational part of the turbulent fluctuations. Given this decomposition, equation (6a) splits into:

$$\frac{\partial S_i}{\partial x_i} = -\frac{\partial^2 \Psi}{\partial x_i\, \partial x_i}; \qquad \frac{\partial r_i}{\partial x_i} = -\frac{\partial^2 \phi}{\partial x_i\, \partial x_i} \qquad (8a, b)$$

as statements of mean and fluctuating mass invariance in the current variables. Similarly equation (7) yields the pair of equations:

$$\frac{\partial \Psi}{\partial t} + \overline{P} = \nu \frac{\partial^2 \Psi}{\partial x_i\, \partial x_i}; \qquad \frac{\partial \phi}{\partial t} + p' = \nu \frac{\partial^2 \phi}{\partial x_i\, \partial x_i} \qquad (9a, b)$$

for the mean and fluctuating pressure fields when the potentials ϕ and Ψ are known. In addition, there is: $\mathcal{E}(p'\mathbf{v}) \equiv \mathcal{E}(p'\mathbf{r}) + \mathcal{E}(p'\boldsymbol{\nabla}(\phi))$. Hence the component $\mathcal{E}(p'\boldsymbol{\nabla}(\phi))$ depends only on the potential $\phi(\mathbf{x}, t)$. The component $\mathcal{E}(p'\mathbf{r})$, if it exists, is an interaction of the irrotational pressure fluctuations with the vortical

flow field. Finally, equation (6b) implies the following:

$$\left.\begin{aligned} \frac{\partial S_i}{\partial t} + \frac{\partial}{\partial x_k}\left[\overline{R}_{ik} + \mathcal{R}_{ik}\right] &= \nu \frac{\partial^2 S_i}{\partial x_k\, \partial x_k} + f_i \\ \frac{\partial r_i}{\partial t} + \frac{\partial}{\partial x_k}\left[V_i u_k + u_i V_k + u_i u_k - \mathcal{R}_{ik}\right] &= \nu \frac{\partial^2 r_i}{\partial x_k\, \partial x_k} \end{aligned}\right\} \quad (10a, b)$$

the field $\mathbf{r}(\mathbf{x}, t)$ being defined from equation (10b). Here $\boldsymbol{\mathcal{R}} = \mathcal{E}(\mathbf{u} \otimes \mathbf{u})$, the original Reynolds tensor, relates directly to correlations of the $(\mathbf{r}, \phi)$ fluctuations through the above transformations. Explicitly there is:

$$\boldsymbol{\mathcal{R}} = \boldsymbol{\mathcal{P}} + 2\mathcal{E}(\mathbf{r} \otimes \boldsymbol{\nabla}(\phi)) + \mathcal{E}(\boldsymbol{\nabla}(\phi) \otimes \boldsymbol{\nabla}(\phi)), \quad \text{where } \boldsymbol{\mathcal{P}} = \mathcal{E}(\mathbf{r} \otimes \mathbf{r})$$

Equation (8b) now gives the potential $\phi(\mathbf{x}, t)$ uniquely from the Poisson Green's function in the form:

$$\phi(\mathbf{x}, t) = -\int_{D(\xi)} G(\mathbf{x}, \boldsymbol{\xi}) \left[\frac{\partial r_i(\boldsymbol{\xi}, t)}{\partial \xi_i}\right] dV(\xi) + \Gamma(\mathbf{x}, t) \qquad (11)$$

where $\Gamma(\mathbf{x}, t)$ represents the contribution from the boundary conditions. The corresponding time derivative can be obtained as:

$$\frac{\partial \phi}{\partial t} = -\int_{D(\xi)} G(\mathbf{x}, \boldsymbol{\xi}) \left[\frac{\partial^2 r_i(\boldsymbol{\xi}, t)}{\partial t\, \partial \xi_i}\right] dV(\xi) + \frac{\partial \Gamma(\mathbf{x}, t)}{\partial t} \qquad (11a)$$

The domain of integration only extends over the support of the field $\mathbf{r}(\mathbf{x}, t)$ and that function must be such that the integrals in equations (11,11*a*) are bounded. Given the value of $\partial\phi/\partial t$ from equation (11*a*) the fluctuating pressure is determined directly from equations (8*b*,9*b*). In both equations (11) and (11*a*), the function $\mathbf{r}(\mathbf{x}, t)$ is only non-zero in any vortical region, such as turbulence, that is present in the domain of interest. The $\boldsymbol{\nabla}(\phi)$ term follows from equation (11) as:

$$\frac{\partial \phi(\mathbf{x}, t)}{\partial x_i} = -\int_{D(\xi)} \frac{\partial G(\mathbf{x}, \boldsymbol{\xi})}{\partial x_i} \left[\frac{\partial r_j(\boldsymbol{\xi}, t)}{\partial \xi_j}\right] dV(\xi) + \frac{\partial \Gamma(\mathbf{x}, t)}{\partial x_i} \qquad (11b)$$

for each component of $\mathbf{x}$.

Similar statements hold for the mean motion potential $\Psi(\mathbf{x}, t)$ in equations (8*a*) and (9*a*). That is, for example:

$$\Psi(\mathbf{x}, t) = -\int_{D(\xi)} G(\mathbf{x}, \boldsymbol{\xi}) \left[\frac{\partial S_i(\boldsymbol{\xi}, t)}{\partial \xi_i}\right] dV(\xi) + \Lambda(\mathbf{x}, t) \qquad (11c)$$

again with the integral taken over the support of the $\mathbf{S}(\mathbf{x}, t)$ function. Derivatives of $\Psi(\mathbf{x}, t)$ then follow as above.

The relationship between the different velocity decompositions that have been introduced above needs to be clarified in order to establish the gauge Reynolds decomposition equations. From the above definitions:

$$\mathbf{v} = \mathbf{V} + \mathbf{u} = \mathbf{s} + \boldsymbol{\omega} \equiv \mathbf{S} + \mathbf{r} + \boldsymbol{\nabla}(\Psi) + \boldsymbol{\nabla}(\phi)$$

It then follows from application of the operator $\mathcal{E}(\cdot)$ that:

$$\mathbf{u} = \mathbf{r} + \boldsymbol{\nabla}(\phi) \quad \text{and} \quad \mathbf{V} = \mathbf{S} + \boldsymbol{\nabla}(\Psi) \tag{12a,b}$$

to define the fluctuating and mean velocity fields. Associated with these velocity fields are the fluctuating and mean vorticity fields:

$$\boldsymbol{\zeta}' \equiv curl(\mathbf{u}) = curl(\mathbf{r}) \text{ and } \overline{\boldsymbol{\zeta}} \equiv curl(\mathbf{V}) = curl(\mathbf{S})$$

such that the $\mathbf{r}(\mathbf{x},t)$ and $\mathbf{S}(\mathbf{x},t)$ vector fields carry the vorticity of the turbulent fluctuations and the mean motion respectively. The irrotational motion is described by the mean, $\boldsymbol{\nabla}(\Psi)$, and fluctuating, $\boldsymbol{\nabla}(\phi)$, potential fields. The vortical motion, $\mathbf{r}(\mathbf{x},t)$ and $\mathbf{S}(\mathbf{x},t)$ act as sources for the inactive components $\phi(\mathbf{x},t)$ and $\Psi(\mathbf{x},t)$ in equations 8(*a,b*). The above Reynolds decomposition calls forth the transformations:

$$\mathbf{S}^* = \mathbf{Q}\,[\mathbf{S} + \mathbf{V}_T]; \quad \mathbf{r}^* = \mathbf{Q}\,\mathbf{r}; \quad \boldsymbol{\nabla}^*(\Psi^*) = \mathbf{Q}\,\boldsymbol{\nabla}(\Psi); \quad \boldsymbol{\nabla}^*(\phi^*) = \mathbf{Q}\,\boldsymbol{\nabla}(\phi)$$

under the Galilean group.

Equation (10b) allows the construction of an equation for the Reynolds gauge stress $\mathcal{P}_{ij} = \mathcal{E}(r_i r_j)$ associated with the vortical component of the flow. This requires the evaluation of correlations of the form:

$$\mathcal{E}(\mathbf{u} \otimes \mathbf{r}) \equiv \mathcal{E}(\mathbf{r} \otimes \mathbf{r}) + \mathcal{E}(\mathbf{r} \otimes \boldsymbol{\nabla}(\phi))$$

wherein the first term will, generally, predominate as discussed by Bradshaw [10]. Specifically, there is:

$$\frac{\partial \mathcal{P}_{ij}}{\partial t} + V_k \frac{\partial \mathcal{P}_{ij}}{\partial x_k} + \Pi_{ij} = \nu \nabla^2(\mathcal{P}_{ij}) - 2\nu \mathcal{E}\left(\frac{\partial r_i}{\partial x_k}\,\frac{\partial r_j}{\partial x_k}\right) \tag{13}$$

where $\Pi_{ij} = \Sigma_{\alpha=1,7}\Pi_{ij}^{(\alpha)}$, with the individual contributions given as:

$$\Pi_{ij}^{(1)} = \mathcal{P}_{jk}\frac{\partial V_i}{x_k} + \mathcal{P}_{ik}\frac{\partial V_j}{\partial x_k}; \qquad \Pi_{ij}^{(2)} = V_k\,\mathcal{E}\left[r_j \frac{\partial^2 \phi}{\partial x_i\,\partial x_k}\right] + V_k\,\mathcal{E}\left[r_i \frac{\partial^2 \phi}{\partial x_j\,\partial x_k}\right]$$

$$\Pi_{ij}^{(3)} = \frac{\partial V_i}{\partial x_k}\,\mathcal{E}\left[r_j \frac{\partial \phi}{\partial x_k}\right] + \frac{\partial V_j}{\partial x_k}\,\mathcal{E}\left[r_i \frac{\partial \phi}{\partial x_k}\right]; \qquad \Pi_{ij}^{(4)} = \mathcal{E}\left[\frac{\partial (r_i r_j r_k)}{\partial x_k}\right]$$

$$\Pi_{ij}^{(5)} = \mathcal{E}\left[r_j r_k \frac{\partial^2 \phi}{\partial x_i\,\partial x_k} + r_i r_k \frac{\partial^2 \phi}{\partial x_j\,\partial x_k}\right]; \qquad \Pi_{ij}^{(6)} = \mathcal{E}\left[\left[\frac{\partial (r_i r_j)}{\partial x_k}\right]\frac{\partial \phi}{\partial x_k}\right]$$

$$\Pi_{ij}^{(7)} = \mathcal{E}\left[\left[r_j \frac{\partial^2 \phi}{\partial x_k\,\partial x_i} + r_i \frac{\partial^2 \phi}{\partial x_k\,\partial x_j}\right]\frac{\partial \phi}{\partial x_k}\right]$$

If the correlations between the vortical and irrotational components are neglected then the quantity $\mathbf{\Pi}$ in equation (13) reduces to: $\mathbf{\Pi} = \mathbf{\Pi}^{(1)} + \mathbf{\Pi}^{(4)}$ only. Equation (13) then takes on the form:

$$\frac{d\mathcal{P}_{ij}}{dt}+\mathcal{P}_{jk}\frac{\partial V_i}{\partial x_k}+\mathcal{P}_{ik}\frac{\partial V_j}{\partial x_k}+\mathcal{E}\left[\frac{\partial(r_i r_j r_k)}{\partial x_k}\right] = \nu\nabla^2\mathcal{P}_{ij}-2\nu\mathcal{E}\left[\frac{\partial r_i}{\partial x_k}\frac{\partial r_j}{\partial x_k}\right] \quad (13a)$$

which can be compared to equation (5). It is seen that equation (5) contains the pressure term ψ_{ij} (given explicitly in equation (5*a*)) which is absent from (13*a*). This is due to the structure of the gauge decomposition revealed in equations (9*b*) and (10*b*). The pressure field does, in this gauge formulation, only relate directly to the irrotational part of the flow field. It can be noted that the linearized compressible flow equations (see Goldstein [18], for example) contain a similar splitting of the velocity field but with the possibility of vorticity production in higher order terms. However, the present discussion is restricted to constant density motion and, as such, there are no entropy changes to take into account (and no pressure component in the Beltrami diffusion equation to consider). The limit $\rho \rightarrow const$ of the compressible Navier–Stokes equations is not a trivial limit; see the discussion in Schochet [19] for the special case of a baratropic fluid. The relationship between the compressible and incompressible flow theories is not direct.

5 An example: inactive motion

It is well established that not all velocity fluctuations in a turbulent shear layer are vortical in nature. As mentioned above these irrotational velocity fluctuations, and the associated pressure fluctuations, propagate outside the turbulent shear layers. See the discussion in Bradshaw [10, 15] and Phillips [16]. The present interest lies in adopting the gauge fields introduced above to discuss the physics of the inactive motion both inside and outside a turbulent shear layer. Moyal [20] showed that in wave number space the pressure associates with velocity components that reside in the span of the wave number vector. A significant noise field arises in high speed turbulent shear layers as discussed, for example, in Phillips [21] and Tam [22] (with the latter showing photographs of Mach wave propagation external to a supersonic jet flow).

Outside the shear layer the equality $\mathbf{r} \equiv \mathbf{0}$ holds, but irrotational fluctuations do exist in that region where the quantity $\boldsymbol{\nabla}(\phi)$ is non-zero. Phillips [16] took the irrotational nature of the inactive motion (when statistically stationary) to imply that it could be explained in terms of a potential. Hence, under these assumptions, a solution of a Laplace equation was sought for that potential. The theory of Phillips [16] gave a $1/x^4$ decay of the energy $\mathcal{E}(u_i u_i)$ into the far field that was confirmed by the experiments reported by Bradshaw [15]. However, such a formulation does not allow the local time dependent external flow field to be described. The equations developed above allow a more general description of the irrotational motion.

Equations for region (A):

Refer to Figure 1 when the equations for region (A) are given as:

$$\left.\begin{aligned} \frac{\partial S_i}{\partial t} + \frac{\partial}{\partial x_k}[\overline{R}_{ik} + \mathcal{R}_{ik}] &= \nu \frac{\partial^2 S_i}{\partial x_k \, \partial x_k} \\ \frac{\partial r_i}{\partial t} + \frac{\partial}{\partial x_k}\left[V_i u_k + u_i V_k + u_i u_k - \mathcal{R}_{ik}\right] &= \nu \frac{\partial^2 r_i}{\partial x_k \, \partial x_k} \\ \frac{\partial \Psi}{\partial t} + \overline{P} = \nu \frac{\partial^2 \Psi}{\partial x_i \, \partial x_i}; \qquad & \frac{\partial \phi}{\partial t} + p' = \nu \frac{\partial^2 \phi}{\partial x_i \, \partial x_i} \\ \frac{\partial r_i}{\partial x_i} = -\frac{\partial^2 \phi}{\partial x_k \, \partial x_k}; \qquad & \frac{\partial S_i}{\partial x_i} = -\frac{\partial^2 \Psi}{\partial x_k \, \partial x_k} \end{aligned}\right\} \quad (14a, b, c, d, e, f)$$

The body force $\mathbf{f}(\mathbf{x})$ has not been included in the present discussion. Equations (11*a*,14*e*) allow the pressure fluctuations in region (A) to be given explicitly as:

$$p'(\mathbf{x}, t) = -\nu \, div(\mathbf{r}) + \int_{\mathcal{D}(\xi)} G(\mathbf{x}, \boldsymbol{\xi}) \left[\frac{\partial^2 r_i(\boldsymbol{\xi}, t)}{\partial t \, \partial \xi_i}\right] dV(\xi) - \frac{\partial \Gamma(\mathbf{x}, t)}{\partial t} \qquad (15)$$

when $div(\mathbf{r})$ is computed from equation (14*b*). Now it is found that the local pressure fluctuations in region (A) depend upon the local value of $div(\mathbf{r})$ and an integral over the domain defined by the support of $\mathbf{r}$. In addition, there is in equation (15) a local contribution from the boundary conditions. This contribution will vanish for steady flow. The mean pressure, both inside and outside the shear layer, follows in the same way from equation (9*a*) when the gauge function $\Psi(\mathbf{x}, t)$ is determined from equation (8*a*) and the function $\mathbf{S}(\mathbf{x}, t)$ from equation (10*a*).

Equations for region (B):

The mean external flow is assumed to lack a vortical component so that the (B) region flow is defined by the system:

$$\left.\begin{aligned} \mathbf{V} = \boldsymbol{\nabla}(\Psi); \qquad & \mathbf{u} = \boldsymbol{\nabla}(\phi) \\ \frac{\partial \Psi}{\partial t} + \overline{P} = \nu \frac{\partial^2 \Psi}{\partial x_i \, \partial x_i}; \qquad & \frac{\partial \phi}{\partial t} + p' = \nu \frac{\partial^2 \phi}{\partial x_i \, \partial x_i} \\ 0 = -\frac{\partial^2 \phi}{\partial x_k \, \partial x_k}; \qquad & \frac{\partial S_i}{\partial x_i} = -\frac{\partial^2 \Psi}{\partial x_k \, \partial x_k} \end{aligned}\right\} \quad (16a, b, c, d, e, f)$$

Note that equations (14*c*,*d*) and (16*c*,*d*) are identical so that boundary conditions $\boldsymbol{\nabla}(\phi) = 0$ are specified at $x_2 = 0$ and in the limit $x_2 \to \infty$ and a smooth solution can be sought on the whole domain. Equations (14*d*) and (16*d*) determine the fluctuating pressure field both inside, and external to, the turbulent shear layer once the potential $\phi(\mathbf{x}, t)$ has been determined. At the surface $x_2 = 0$ there is $\mathbf{v} \equiv \mathbf{0}$ which implies that both equalities $\mathbf{V} = \mathbf{0}$ and $\mathbf{u} = \mathbf{0}$ must hold. It further follows that $\mathbf{r} = \mathbf{0}$ while $\boldsymbol{\nabla}(\phi) = \mathbf{0}$ is also true on this surface. The condition $\mathbf{r} = \mathbf{0}$ also holds at the edge of the shear layer $x_2 = L$. It is assumed that all required fields are specified at the upstream boundary $x_1 = 0$ (which is taken to be some convenient origin for the computation as shown on Figure 1).

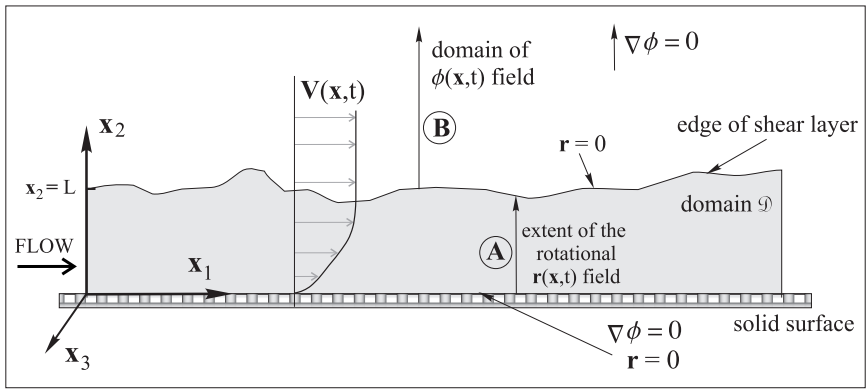

Figure 1: Regions in the flow field near a turbulent shear layer.

Equation (15) also defines the pressure fluctuations in the region external to the shear layer where, however, the local $div(\mathbf{r})$ term is identically zero. Alternatively, equation (16*d*,16*e*) define $p' = -\partial\phi/\partial t$ directly when equation (11*a*) applies. The integration is still over the support of the rotational motion but now the $(\mathbf{x}, t)$ values refer to this external region. For steady boundary conditions, the intensity of the pressure fluctuations external to the shear layer is given explicitly as:

$$\mathcal{E}(p'\,p') = \int_{\mathcal{D}}\int_{\mathcal{D}} G(\mathbf{x},\boldsymbol{\xi})\; G(\mathbf{x},\boldsymbol{\eta})\; \mathcal{E}\left[\frac{\partial^2 r_i}{\partial t\,\partial\xi_i}\;\frac{\partial^2 r_j}{\partial t\,\partial\eta_j}\right]\; dV(\eta)\,dV(\xi)$$

and a similar expression for the velocity correlation can be obtained from equation (11*b*). That is, *without* the contribution for the boundary conditions the correlation:

$$\mathcal{E}\left(\frac{\partial\phi}{\partial x_i}\;\frac{\partial\phi}{\partial x_j}\right) = \int_{\mathcal{D}}\int_{\mathcal{D}} \frac{\partial G(\mathbf{x},\boldsymbol{\xi})}{\partial x_i}\;\frac{\partial G(\mathbf{x},\boldsymbol{\eta})}{\partial x_j}\;\mathcal{E}\left[\frac{\partial r_k}{\partial\xi_k}\;\frac{\partial r_m}{\partial\eta_m}\right]\; dV(\eta)\,dV(\xi)$$

is obtained which, from the form of the Green's function, varies like $1/x_2^4$ for large distances from the shear layer. Pressure velocity correlations follow in the same way and need not be written down.

6 Final remarks

It has been shown that a non-Galilean invariant gauge velocity field can be defined for the Navier–Stokes equations when the fluid density is constant. These gauge fields are obtained from well defined boundary value problems and provide additional insight into the structure of the constant density Navier–Stokes equations. Of course, there is greater algebraic complexity in the gauge formulation. The decomposition has been illustrated with a discussion of the inactive motion outside a turbulent shear layer.

References

[1] Seregin, G. Local regularity theory of the Navier Stokes equations. *Handbook of mathematical fluid dynamics,* **IV**, Friedlander, S. and Serre, D. (Eds)., pp 159–200, Elsevier, Amsterdam, 2007.
[2] Moulden, T. H. On properties of turbulence models. *Advances in Fluid Mechanics VIII*, Algarve, Portugal, pp 15–26, 2010.
[3] Chen, C-J and Jaw, S-Y. *Fundamentals of turbulence modeling.* Taylor and Francis, Washington, 1998.
[4] Wilcox, D. C. *Turbulence modeling for CFD.* 2nd Edition, DCW, LaCañada, 1998.
[5] Launder, B. E. and Sandham, N. D. (Eds) *Closure Strategies for Turbulent and Transitional Flows.* Cambridge University Press, Cambridge, 2002.
[6] Gatski, T. B. Constitutive equations for turbulent flows. *Th. and Comp. Fluid Dyn.* **18**, pp 345–369, 2004.
[7] Gurtin, M. E. *An introduction to continuum mechanics.* Academic Press, New York, 1981.
[8] Frost, W. and Moulden, T. H. (Eds) *Handbook of Turbulence.* Plenum Press, New York, 1977.
[9] Moulden, T. H. A Uniqueness Theorem in Fluid Turbulence. *Proc. 8th HEFAT Conference*, Mauritius, 2011.
[10] Bradshaw, P. Irrotational fluctuations near a turbulent boundary layer. *JFM*, **27**, pp 209–230, 1967.
[11] Speziale, C. G. Invariance of Turbulent Closure Models. *Phys. Fluids*, **22** pp 1033–1037, 1979.
[12] Wu, J-Z, Ma, H-Y and Zhou, M-D. *Vorticity and Vortex Dynamics.* Springer, Berlin, 2006.
[13] Weinan E and Liu, J-G. Finite difference schemes for incompressible flows in velocity-impulse density formulation. *J. Comp. Phys*. **130**, pp 67–76, 1997.
[14] Wang, C. and Liu, J-G. Convergence of Gauge Method for Incompressible Flow. *Math. Comp*. **69**, pp 1385–1407, 2000.
[15] Bradshaw, P. 'Inactive' motion and pressure fluctuations in turbulent boundary layers. *JFM*. **30**, pp 241–258, 1967.
[16] Phillips, O. M. The irrotational motion outside a free turbulent boundary. *Proc. Camb. Phil. Soc.*, **51**, pp 220–229, 1955.
[17] Stakgold, I. *Green's functions and boundary value problems.* Wiley, New York, 1979.
[18] Goldstein, M. E. *Aeroacoustics.* McGraw Hill, New York, 1976.
[19] Schochet, S. The mathematical theory of the incompressible limit in fluid dynamics. *Handbook of mathematical fluid dynamics*, **IV**, Friedlander, S. and Serre, D. (Eds)., pp 159–200, Elsevier, Amsterdam, 2007.
[20] Moyal, J. E. The spectra of turbulence in a compressible fluid: eddy turbulence and random noise. *Proc. Camb. Phil. Soc*. **48**, pp 329–344, 1952.
[21] Phillips, O. M. On the generation of sound by supersonic turbulent shear layers. *JFM*. **9**, pp 1–28, 1960.
[22] Tam, C. K. W. On the noise of a nearly ideally expanded super sonic jet *JFM*. **51**, pp 69–95, 1972.

Preconditioned HLLC scheme for incompressible viscous flow simulation

Z. Qian[1,2] & C.-H. Lee[3]
[1]*AVIC Aerodynamics Research Institute, China*
[2]*AVIC Aeronautical Science and Technology Key Lab for High Speed and High Reynolds Number Aerodynamic Force Research, China*
[3]*National Laboratory for Computational Fluid Dynamics, School of Aeronautic Science and Engineering, Beihang University, China*

Abstract

A new HLLC approximate Riemann solver with preconditioning technique based on the pseudo-compressibility formulation for numerical simulation of the incompressible viscous flows has been proposed, which follows the HLLC Riemann solver (Harten, Lax and van Leer solver with contact resolution modified by Toro) for the compressible flow system. In the authors' previous work, the preconditioned Roe's Riemann solver was applied to the finite difference discretization of the inviscid flux. Although the Roe's Riemann solver is found to be an accurate and robust scheme in various numerical computations, the HLLC Riemann solver is more suitable for the pseudo-compressible Navier-Stokes equations, in which the inviscid flux vector is a non-homogeneous function of degree one of the flow field vector; however the Roe's solver is restricted to the homogeneous problems. Numerical investigations have been performed in order to demonstrate the efficiency and accuracy of the present procedure. The present results are found to be good agreement with the exact solutions, existing numerical results or experimental data.
Keywords: precondition, HLLC scheme, pseudo-compressibility, incompressible viscous flows, LU-SGS.

1 Introduction

The difficulty of numerically solving the incompressible Navier-Stokes (N-S) equations is the decoupling of the velocity and pressure fields while the zero


WIT Transactions on Engineering Sciences, Vol 74, © 2012 WIT Press
www.witpress.com, ISSN 1743-3533 (on-line)
doi:10.2495/AFM120081

divergence condition is hard to be satisfied. The pseudo-compressibility method proposed by Chorin [1] introduced an additional time derivative of the pressure field to the continuity equation, and so the continuity and momentum equations are solved in a coupling manner.

The precondition concept applied on the incompressible flow simulation was proposed by Turkel [2], then the authors [3] further developed this procedure and applied it to numerical simulation of the pseudo-compressible N-S equations. The influences of precondition parameter and pseudo-compressibility factors on the convergence rate were also investigated systematically, and the optimal parameters were identified in the author's previous paper [3].

Although the pseudo-compressibility method has been widely used for about three decades [4–7], only two classes of scheme, namely the Jameson's central scheme [8] and the Roe's upwind scheme [9], are employed for the inviscid flux terms. The author's previous work [3] shown that the Roe's upwind scheme is superior to the Jameson's central scheme for lower dissipation and free of turned parameter. However, since the inviscid flux vector F of the pseudo-compressible N-S equations is not homogeneous function of degree one of the flow field vector U, namely $\Delta F = A\Delta U$, and also the homogeneous property is a critical restriction in Roe's solver, consequently Roe's upwind scheme may be not proper in the pseudo-compressibility case.

In the present paper, a new approximate Riemann solver for upwind scheme for incompressible flow is derived following the HLL scheme propose by Harten *et al.* [10] and its modified form HLLC scheme proposed by Toro *et al.* [11] for compressible flow simulations. In this approximate Riemann solver we do not assume the homogeneous property of the inviscid flux, so the proposed approximate Riemann solver is more proper and general for incompressible flow simulation.

A numerical procedure using both the proposed HLLC upwind finite difference scheme and the precondition technology is then established for the viscous incompressible flow simulation. Several numerical test cases, including low Reynolds number flow over a circular cylinder, laminar flow over a flat plate, and high Reynolds turbulent flow over the S809 airfoil with the two equations k-ω SST turbulent model, are numerically investigated in this paper in order to demonstrate the efficiency and accuracy of the present procedure. The present results are found to be good agreement with the exact solutions, existing numerical results or experimental data.

2 Preconditioning for pseudo-compressibility Navier-Stokes equations

The pseudo-compressibility procedure and the preconditioning technique for convergence acceleration for stiff hyperbolic equations are employed to develop a highly efficient in-house code for solving two dimensional incompressible flows numerically in the author's previous work [3].

The preconditioned pseudo-compressibility Navier-Stokes equations in Cartesian coordinates can be given as below

$$\Gamma^{-1}Q_t + (E - E^v)_x + (F - F^v)_y = 0, \tag{1}$$

where

$$\Gamma^{-1} = \begin{pmatrix} 1/\beta^2 & 0 & 0 \\ \alpha u/\beta^2 & 1 & 0 \\ \alpha v/\beta^2 & 0 & 1 \end{pmatrix}, \tag{2}$$

The state variables Q and fluxes E, F, E^v, F^v are identical to those given in [3], where β denotes the pseudo-compressibility factor, and α denotes the parameter introduced by precondition. The selection of parameters α and β is critical to the accuracy and convergence rate, and some detailed discussions are already given in [3].

3 Numerical schemes

The semi-discretized finite difference method is used in the present paper. First, the spatial derivatives are discretized while the time variation remains continuous. Then, the time marching in temporal can be solved by the implicit LU-SGS (Lower-Upper Symmetric Gauss-Seidel) algorithm.

3.1 Spatial scheme

A new approximate Riemann solver for incompressible flow is derived following the HLL scheme propose by Harten, Lax and van Leer and its modified form HLLC scheme proposed by Toro, Spruce and Speares for compressible flow simulations.

3.1.1 The HLL approximate Riemann solver for incompressible flow

Harten *et al.* [10],Toro [12] put forward the following approximate Riemann solver

$$\hat{U}(x,t) = \begin{cases} U_L, if \quad x/t < S_L, \\ U_{hll}, \quad if \quad S_L \le x/t \le S_R, \\ U_R, \quad if \quad x/t > S_R. \end{cases} \tag{3}$$

where is U_{hll} is the integral average of the exact solution of the Riemann problem between the slowest and fastest waves, S_L and S_R are the fastest wave velocities perturbing the initial data states U_L and U_R respectively. Figure 1 shows the structure of this approximate solution of the Riemann problem.

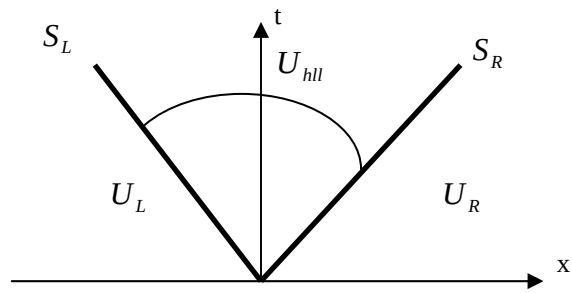

Figure 1: Approximate HLL Riemann solver.

Provided that the signal speeds S_L and S_R are known, U_{hll} can be given by

$$\mathrm{U}_{\mathrm{hll}} = \frac{S_R U_R - S_L U_L + F_L - F_R}{S_R - S_L} \tag{4}$$

following Harten, Lax and van Leer's formula. The corresponding flux at the cell interface for the HLL scheme is then given by

$$F_{i+1/2}^{hll} = \begin{cases} F_L, & if \quad 0 < S_L, \\ \dfrac{S_R F_L - S_L F_R + S_L S_R (U_R - U_L)}{S_R - S_L}, & if \quad S_L \le 0 \le S_R, \\ F_R, & if \quad 0 > S_R. \end{cases} \tag{5}$$

Given an algorithm to compute the speeds S_L and S_R one can have an approximate intercell flux. Procedures to estimate the wave speeds S_L and S_R in this paper are given by

$$S_L = \min\{u_L - a_L, u_R - a_R\}, \; S_R = \max\{u_L + a_L, u_R + a_R\}. \tag{6}$$

Following Harten, Lax and van Leer, the HLL scheme for the pseudo-compressibility Navier-Stokes equations can be derived. The artificial speed of sound is given by

$$a_{L,R} = \sqrt{u_{L,R}^2 + \beta^2} \; . \tag{7}$$

For incompressible flow the density is assumed to be constant and the energy equation is decoupled from the continuity and momentum equations. So the intermediate pressure p_* and normal velocity u_* can be obtained from the Rankine-Hugoniot Conditions across the two wave system similar to the original HLL scheme for compressible flow, which is given as

$$u_* = \frac{S_R u_R - S_L u_L + u_L^2 + P_L - u_R^2 - P_R}{S_R - S_L}, \tag{8}$$

$$p_* = \frac{S_R p_R - S_L p_L + \beta^2 u_L - \beta^2 u_R}{S_R - S_L}. \tag{9}$$

Also for incompressible flow, the two wave speeds are always satisfied that

$$u - a < 0,\ u + a > 0. \tag{10}$$

This means that the two approximate wave speeds S_L and S_R are always satisfied that

$$S_L < 0,\ S_R > 0, \tag{11}$$

consequently the corresponding cell interface flux of the HLL scheme for incompressible can be simplified as

$$F_{i+1/2}^{hll} = \frac{S_R F_L - S_L F_R + S_L S_R (U_R - U_L)}{S_R - S_L}. \tag{12}$$

Note that this Riemann solver consists of just three constant states separated by two waves. All intermediate states separated by intermediate waves are lumped into the single U_{hll} state without regard for the spatial variations of the solution of the Riemann problem in the Star region, so a shortcoming of the HLL scheme, with too serious dissipation, is exposed.

3.1.2 The HLLC approximate Riemann solver for incompressible flow

As pointed out by Harten *et al.* themselves [10], the too much dissipation of the HLL Riemann solver may be alleviated by restoring the missing waves. Accordingly, Toro *et al.* [11, 12] proposed the so called HLLC scheme, where C stands for Contact. In the HLLC scheme the missing middle waves are put back into the structure of the approximate Riemann solver.

Consider Figure 2, in which the complete structure of the solution of the Riemann problem is depicted. As shown in the figure, in addition to the slowest and fastest signal speeds S_L and S_R, we include a middle wave of speed S_*, corresponding to the shear wave with eigenvalue u.

Following Toro *et al.* [11], the HLLC flux can be written as

$$F_{i+1/2}^{hllc} = \begin{cases} F_L, & if \quad 0 < S_L, \\ F_{*L} = F_L + S_L(U_{*L} - U_L), & if \quad S_L \le 0 < S_*, \\ F_{*R} = F_R + S_R(U_{*R} - U_L), & if \quad S_* \le 0 \le S_R, \\ F_R, & if \quad 0 > S_R. \end{cases} \tag{13}$$

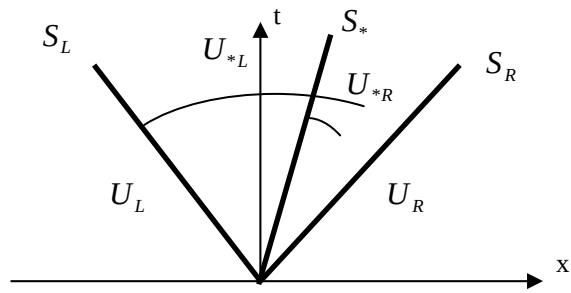

Figure 2: Approximate HLLC Riemann solver.

where U_{*L} and U_{*R} denote to the integral averages between the shear wave and the left and right waves respectively, which can be given by the following Rankine-Hugoniot conditions across each of the waves of speeds S_L, S_* and S_R.

$$F_{*L} = F_L + S_L(U_{*L} - U_L), \tag{14}$$

$$F_{*R} = F_{*L} + S_*(U_{*R} - U_{*L}), \tag{15}$$

$$F_{*R} = F_R + S_R(U_{*R} - U_R). \tag{16}$$

Here condition (14)–(16) are three equations for the four unknowns vectors U_{*L}, U_{*R}, F_{*L} and F_{*R}. The aim is to find the vectors U_{*L} and U_{*R}, so that the fluxes F_{*L} and F_{*R} can be determined from (14) and (16) respectively. For incompressible flow the following conditions are must guaranteed.

$$u_{*L} = u_{*R} = u_*, p_{*L} = p_{*R} = p_*, v_{*L} = v_L, v_{*R} = v_R. \tag{17}$$

Consequently, we can obtain that u_* and p_* are the same as equation (8) and (9) respectively, and $v_{*L} = v_L, v_{*R} = v_R, S_* = u_*$. Since $S_L < 0$ and $S_R > 0$, the corresponding intercell flux of the HLLC scheme for incompressible can be simplified as

$$F_{i+1/2}^{hllc} = \begin{cases} F_{L*} = F_L + S_L(U_{*L} - U_L), & if \quad 0 \le S_*, \\ F_{R*} = F_R + S_R(U_{*R} - U_L), & if \quad S_* < 0. \end{cases} \tag{18}$$

3.1.3 Second order accurate interface values U_L and U_R

In order to promote the accuracy, we employ the second order MUSCL scheme [13] in the present study. Accordingly, the left and right states are given respectively by

$$\left.\begin{aligned} U_L &= U_i + \varphi_L \Delta U_i, \\ U_R &= U_{i+1} - \varphi_R \Delta U_{i+1}, \end{aligned}\right\} \tag{19}$$

in which $\Delta U_i = U_i - U_{i-1}$, φ denotes to the limiter function. In the present paper, the minmod limiter is used unless specified.

3.1.4 Viscous term computations and numerical boundary conditions

The viscous terms of eq. (1) are discretized by the second-order central difference. The boundary conditions imposed on the solid wall are the no-slip condition for viscous flows, and the pressure on the wall is evaluated by extrapolation from the interior points. For the far field boundary, the conditions are specified according to the direction of the in-flow or out-flow, where the velocities are given, and the pressure is extrapolated from the interior nodes at the inflow boundary; whereas the pressure is given, and the velocities are extrapolated from the interior nodes at the outflow boundary.

3.2 Time advancement

The LU-SGS（Lower-Upper Symmetric Gauss-Seidel）formulation proposed by Yoon and Jameson [14] is used, which is one of the most commonly used implicit methods for compressible flows simulations. We generalize the formulation to the preconditioned pseudo-compressible Navier-Stokes equations, and details can be found in the authors' previous work [3].

4 Numerical results

Some validating tests are presented in this section, including low Reynolds number flow over a circular cylinder, laminar flow over a flat plate, and high Reynolds turbulent flow over the S809 airfoil with the two equations k-ω SST turbulence model. These cases are chosen for comparisons with exact analytic solutions or existing experimental data.

4.1 Low Reynolds number flow over circular cylinder

The low Reynolds number incompressible flow over a circular cylinder is a benchmark problem for incompressible flows, for which many experimental and computational results can be utilized for comparison [4, 15, 16]. In this section, the problem is simulated by the algorithm proposed in previous sections.

The characteristics of the flow field are sensitive to the Reynolds number. The case of Re=40 is computed, and the flow renders as a pair of symmetric separated vortices. The mesh used in this paper consists of a single gird zone with an O type topology, and is composed of 65×181 in the streamwise and wall normal direction, respectively, with the first grid spacing of 0.005 diameters and stretching to the outer boundary of 20 diameters in the normal direction.

The streamlines of the flow at Re=40 computed by the present scheme are depicted in Figure 3. The separation length measured from the rear stagnation point of the cylinder in cylinder diameters, the separation angle which defines the point of separation from the body, and the drag coefficient in each case are also shown in Table 1.They are consistent with the experimental data [15, 16] and the computational results listed in [4]. The errors of the separation length and separation angle relative to [16] are 2.35% and 0.37% respectively, and that of the drag coefficient relative to [15] is 2.42%. Moreover, all the errors of the numerical results relative to the experimental data are less than 5%, which demonstrate the reliability of the present method.

Table 1: Comparisons with experimental and other numerical results at Re=40.

	Length of separation (L/D) (Errors relative to [16])	Angle of separation (°) (Errors relative to [16])	Drag coefficient (Errors relative to [15])
Present	2.08 (-2.35%)	53.3 (-0.37%)	1.610 (-2.42%)
Reference [4] (Numerical)	2.29 (+7.51%)	53.0 (-0.93%)	1.549 (-6.12%)
Reference [15] (experimental)	—	—	1.65
Reference [16] (experimental)	2.13	53.5	—

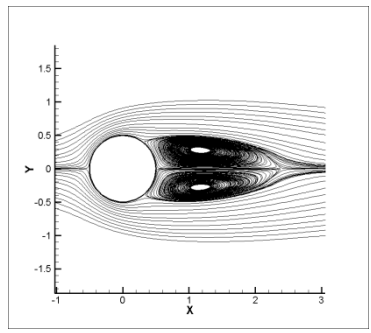

Figure 3: The streamlines at Re=40.

4.2 Laminar flow past flat plate

The incompressible laminar flow over a flat plate is commonly called a Blasius flow with an analytical similarity solution. This test case is used to validate the capability of the presently developed procedure for boundary layer flow simulation. The mesh is composed of 109×50 grids in the stream wise and wall normal direction, respectively, clustered at the leading and trailing edges of the flat plate. The computational region is stretched to the upper and upwind boundary of 5 times the length of the plate, and to the out flow boundary with 6 times the length. The Reynolds number defined by the length of the plate is 1.0×10^5. The grid is clustered near the wall due to great gradient in the boundary layer.

The velocity profile computed by the present scheme is plotted in Figure 4 together with the Blasius solution, where the abscissa $y' = y\sqrt{\mathrm{Re}_x}/x$, and the ordinate is the dimensionless velocity u. It is found that the present preconditioned HLLC scheme is capable of providing numerical solutions well consistent with the Blasius solution.

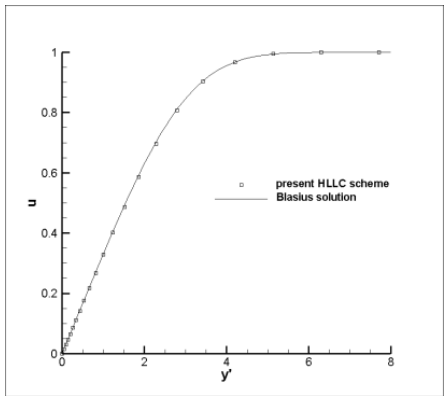

Figure 4: The velocity profiles of the laminar flat plate.

4.3 High Reynolds turbulent flow around S809 airfoil

The S809 airfoil was designed specially for wind turbine applications, the thickness ratio of which is 21%. A 0.6m chord length model of this airfoil has been tested in a 1.8m×2.5m low turbulence wind tunnel [17]. In this numerical test, the Reynolds number is 2.0×10^6 and the angle of attack is 9.22°. It shows the reliability of the proposed algorithm for turbulent flow simulation.

The mesh as shown in Figure 5 consists of a single gird zone with an O type topology, and is composed of 307×120 in the stream wise and wall normal direction, respectively, with the first grid spacing of 1.0×10^{-5} chord length and stretching to the outer boundary of 20 diameters. The Menter's $k-\omega$ SST turbulence model [18], which takes the advantages of the $k-\varepsilon$ model [19] and

Wilcox's $k-\omega$ model [20], is used. This model excludes the sensitivity to the inflow turbulence intensity and retains the numerical stability near the wall.

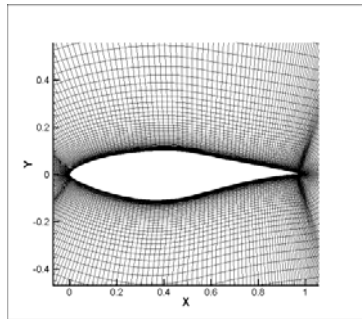

Figure 5: Mesh for S809 airfoil.

The computed contours of pressure, turbulence viscosity ratio and turbulence kinetic intensity are shown in Figure 6. Figure 7 depicts the comparison of the computed wall pressure coefficient and the experimental test data [17], and good agreement is shown.

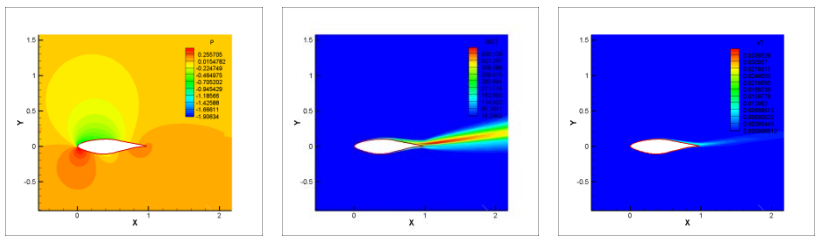

(a) Pressure (b) Turbulence viscosity ratio (c) Turbulence kinetic energy

Figure 6: The contours of pressure, turbulence viscosity ratio and turbulence kinetic intensity.

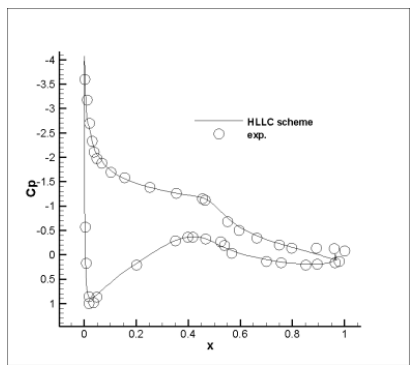

Figure 7: Comparison of the computed and experimental wall pressure coefficients.

5 Conclusions

This paper derives the preconditioned HLLC finite difference scheme for the incompressible flow by virtue of the pseudo-compressibility procedure. The proposed scheme does not assume the homogeneous property of the inviscid flux, so the proposed approximate Riemann solver is more proper and general for incompressible flow simulation. The preconditioned technique is used to accelerate the time marching, and the implicit LU-SGS time integration method is adopted to integrate temporally. The reliability of the present procedure are demonstrated by applications to low Reynolds number flow over a circular cylinder, laminar flow over a flat plate, and high Reynolds turbulent flow over the S809 airfoil. It is found that the numerical results of the present algorithm are in good agreement with theoretical solutions or experimental data.

References

[1] Chorin A J. A numerical method for solving incompressible viscous flow problems. J. Comput. Phys., 2: 12–26, 1967.
[2] Turkel E. Preconditioning methods for solving the incompressible and low speed compressible equations. J. Comput. Phys., 72: 227–298, 1987.
[3] Qian Zhansen, Zhang Jingbai, Li Chunxuan. Preconditioned pseudo-compressibility methods for incompressible Navier-Stokes equations. SCIENCE CHINA Phys. Mech. Astronomy., 53(11): 2090-2102, 2010.
[4] Rogers S E, Kwak D. An Upwind-Differencing Scheme for the Incompressible Navier-Stokes Equations. NASA TM-101051, 1988.
[5] Rogers S E, Kwak D. Upwind differencing scheme for the time-accurate incompressible Navier-Stokes equations. AIAA Journal, 28: 253–262, 1990.
[6] Kwak D, Chakravarthy S R. A three-dimensional incompressible Navier-Stokes flow solver using primitive variables. AIAA Journal, 24: 390–396, 1986.
[7] Tamamidis P, Zhang G, Assanis D N. Comparison of pressure-based and artificial compressibility methods for solving 3D steady incompressible viscous flows. J Computational Physics, 124: 1–13, 1996.
[8] Jameson A. Time dependent calculations using multigrid with application to unsteady flows past airfoils and wings. AIAA Paper 91-1596, 1991.
[9] Roe P L. Approximate Riemann Solvers, parameter vectors and difference schemes. J. Comput. Phys., 43: 357-372, 1981.
[10] Harten A, Lax P D, van Leer B. On upstream differencing and Godunov-type schemes for hyperbolic conservation laws. SIAM Review, 25(1): 35-61, 1983.
[11] Toro E F, Spruce M, Speares W. Restoration of the contact surface in the HLL-Riemann solver. Shock Waves, 4: 25-34, 1994.
[12] E.F.Toro. Riemann solvers and numerical methods for fluid dynamics: A practical introduction. Springer, 1997.

[13] van Leer B. Towards the ultimate conservation difference scheme: V. A second-order sequel to Godunov's method. Journal of Computational Physics, 32: 101-136, 1979.
[14] Yoon S, Jameson A. Lower-upper symmetric-Gauss-Seidel method for the Euler and Navier-Stokes equations. AIAA Journal, 26: 1025– 1026, 1988.
[15] Tritton D J. Experiments on the flow past a circular cylinder at low Reynolds numbers. J Fluid Mech, 6: 547–567, 1959.
[16] Contanceau M, Bouard R. Experimental determination of the main features of the viscous flow in the wake of a circular cylinder in uniform translation. Part 1. steady flow. J Fluid Mech, 79: 231– 256, 1972.
[17] Somers D M. Design and experimental results for the S809 airfoil. NREL/SR-440-6918, 1997.
[18] Menter F. Zonal two equation k-w turbulence models for aerodynamic flows. AIAA Paper 93-2906, 1993.
[19] Abid R. Evaluation of two-equation turbulence models for predicting transitional flows. International journal of Engineering Science, 131: 831-840, 1993.
[20] Wilcox D. Turbulence modeling for CFD. DCW Industries, Inc., La Canada, California, 1993.

An immersed boundary method for simulating compressible viscous flow in complex geometries

B. Jastrow & F. Magagnato
Institute of Fluid Machinery, Karlsruhe Institute of Technology, Germany

Abstract

This paper presents an immersed boundary method combined with a wall-layer approach implemented into an established flow solver. In the outer flow field, the compressible Navier-Stokes equations are solved using an approximate Riemann Solver whereas simplified boundary-layer equations are solved near the wall. Turbulence is accounted for by the one-equation model of Spalart-Allmaras in the outer flow region and by a mixing length eddy viscosity model with near wall damping in the wall layer. Computations performed for various test cases show good agreement with reference data found in literature.
Keywords: immersed boundary method, wall-layer model, compressible flow.

1 Introduction

Body-fitted grid generation for simulating flow in complex geometry can be very cumbersome especially when using a block-structured solver. Therefore the Cartesian-grid immersed boundary method (IBM) offers an interesting approach since automatic mesh generation can be realized easily. Furthermore, due to smoothness and orthogonality, Cartesian grids offer high accuracy and efficiency.

In the IBM a complex geometry is immersed into a regular Cartesian grid. The effect of the body on the flow is mimicked by the imposition of proper boundary conditions that act as forcing conditions [1, 2].

Several applications of the IBM use a linear interpolation for setting the boundary conditions as proposed in [1]. Their validity is therefore only given for grids resolved down to $\Delta y^+ < 1$. For flow of high Reynolds number these restrictions cannot be held in accordance with acceptable computing time. With


WIT Transactions on Engineering Sciences, Vol 74, © 2012 WIT Press
www.witpress.com, ISSN 1743-3533 (on-line)
doi:10.2495/AFM120091

the use of a wall-layer model one can overcome the need for high near wall resolution. Wall models based on incompressible turbulent boundary layer equations were proposed and tested by Balaras *et al.* [3], Cabot and Moin [4], Wang and Moin [5] in a body-fitted context. The applicability of such a wall-layer model in the framework of the IBM has been studied by Tessicini *et al.* [6]. Bond and Blottner [7] developed a compressible wall model, named the diffusion model.

The present paper studies the compressible wall-layer model within the framework of the IBM. It is shown, that the implementation in the in-house flow solver SPARC (Structured Parallel Research Code) [8], in the following referred to as SPARC-IBM, provides results for basic test cases in good agreement with literature.

2 Mesh generation

The mesh is automatically generated via a ray tracing technique. Based on a geometry described by a closed surface triangulation every cell center of a uniform Cartesian grid is marked as either internal or external [9]. Those internal cells having at least one external neighbor cell are marked as wall-layer cells. From the latter the normal to the closest wall is computed and stored together with the forcing point and the appropriate interpolation neighbors (figure 1). The current implementation of the mesh generator uses a block-refinement algorithm based on the wall distance.

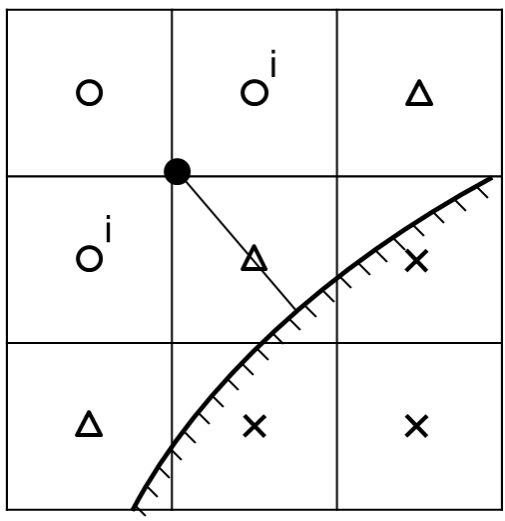

Figure 1: Mesh in the near wall region: ○: internal cell, Δ: wall-layer cell, x: external cell, ●: forcing point, i: interpolation neighbors.

3 Numerical method

The Reynolds-averaged Navier-Stokes (RANS) equations for compressible flow can be written as follows:

$$\frac{\partial \rho}{\partial t} + \frac{\partial (\rho u_j)}{\partial x_j} = 0 \tag{1}$$

$$\frac{\partial (\rho u_i)}{\partial t} + \frac{\partial (\rho u_i u_j + p\delta_{ij} - \tau_{ij})}{\partial x_j} = 0 \tag{2}$$

$$\frac{\partial (\rho e_t)}{\partial t} + \frac{\partial (\rho u_j e_t + p u_j - u_i \tau_{ij} + q_j)}{\partial x_j} = 0. \tag{3}$$

For the calculations carried out in this paper, the Spalart-Allmaras turbulence model has been used for closure. Details of the model are given in the paper by Spalart and Allmaras [10]. The discretization of the convective terms is obtained by an approximate Riemann solver (HLLC) [11] whereas the viscous terms are discretized with a central difference scheme. The solution vector is updated via a Runge-Kutta scheme.

Inside the wall-layer a simplified set of equations is solved. It is assumed that convection is negligible compared to diffusion, the normal pressure gradient is zero and the streamwise gradients are of orders lower than the gradients normal to the wall. Furthermore, the normal velocity is insignificant compared to the tangential velocity. This leads to the following equations for the x-momentum and the energy:

$$\frac{\partial (\rho u)}{\partial t} = \frac{\partial \left[(\mu + \mu_t) \frac{\partial u}{\partial y} - y \frac{\partial p}{\partial x} \right]}{\partial y} \tag{5}$$

$$\frac{\partial (\rho e_t)}{\partial t} = \frac{\partial \left[u(\mu + \mu_t) \frac{\partial u}{\partial y} + (\kappa + \kappa_t) \frac{\partial T}{\partial y} \right]}{\partial y}. \tag{6}$$

The properties μ_t and κ_t are the turbulent viscosity and the turbulent conductivity respectively. In a first stage of implementation, μ_t is obtained by a mixing length eddy viscosity model with near wall damping

$$\frac{\mu_t}{\mu} = \kappa y^+ \left(1 - e^{-\frac{y^+}{A}} \right)^2, \tag{7}$$

where $\kappa = 0.4$, $A = 19$ and y^+ defines the dimensionless distance to the wall [5]. At the wall, a no-slip boundary condition is applied. At the forcing point, that defines the outer edge of the wall-layer, the boundary condition is obtained through an interpolation from the flow values of the outer flow field. In this paper, the equations are further simplified by neglecting the time derivative terms and the streamwise pressure gradient. Two tridiagonal systems are created for the velocity and the temperature respectively and solved in a segregated way with the other dependent variables held constant. Subsequently the turbulent viscosity is updated. An outer loop runs over all equations until the full solution converges. Finally the flow values for the position of the center of the wall-layer cell is extracted and provided to the outer flow field as a boundary condition.

Assuming steady-state in the wall-layer corresponds to an instantaneous response of the wall-layer to the outer flow field which creates some error for unsteady flow calculations.

4 Results

4.1 Laminar flow past a flat plate

The first test case is the laminar flow past a flat plate. Since the wall-layer model also captures the linear near-wall behavior for low Reynolds number flow, this test case is perfectly suited for verifying the implementation. The computation was carried out on a structured multi-block mesh with refinement. The boundary layer was resolved with 32 cells making a total of 54,000 cells in the 2D plane.

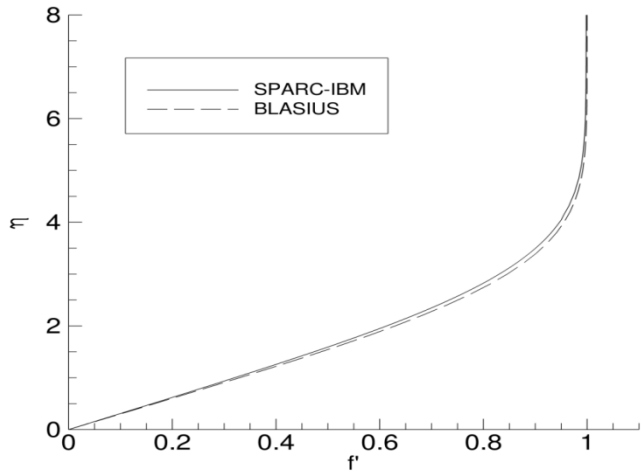

Figure 2: Comparison of the velocity profile in the boundary layer at Re_x=10,000$Re_x = 10{,}000$.

The Mach number was chosen to $Ma_\infty = 0.3$ and the velocity profile was extracted at a Reynolds number of $Re_x = 10{,}000$. In Figure 2 the profile is compared with the analytical results of the Blasius-equation [12] where f' is the dimensionless velocity and η is the dimensionless wall distance, defined as

$$f' = \frac{U}{U_\infty} \tag{8}$$

$$\eta = y\sqrt{\frac{U_\infty}{\nu x}}. \tag{9}$$

The numerical results show very good agreement with the analytic solution of Blasius.

4.2 Turbulent flow past a flat plate

The second test case was chosen to prove the consideration of turbulence in the wall-layer model. The mesh consists of 123,000 cells in the 2D plane which results in 27 cells resolving the boundary layer. Figures 3 and 4 show the

obtained velocity profile for $Re_x = 10{,}000{,}000$ and the skin friction coefficient along the flat plate together with the experimental data of [13]. The agreement is quite satisfactory.

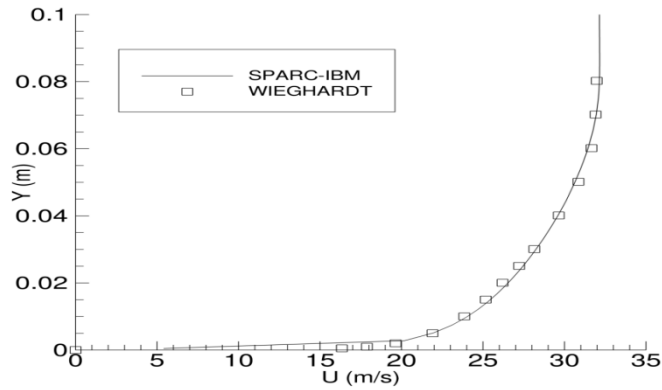

Figure 3: Comparison of the velocity profile in the boundary layer at Re_x=10,000,000.

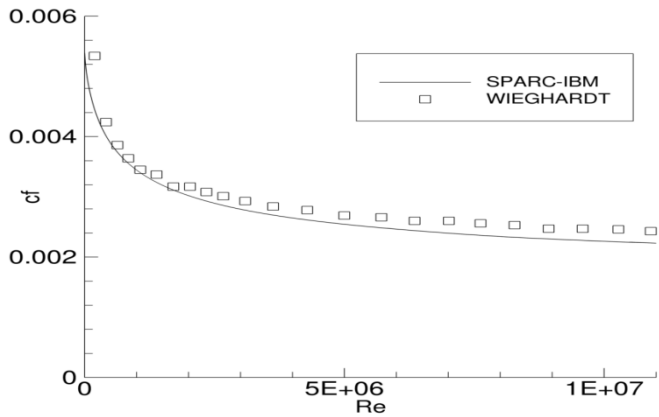

Figure 4: Comparison of the skin friction coefficient for various Reynolds numbers.

4.3 Laminar flow past a circular cylinder

To test the IBM together with curved surfaces, the flow past a circular cylinder was computed. Two flow regimes are shown, a steady flow at $Re = 20$ and an unsteady flow at $Re = 200$. A local view of the mesh is provided in Figure 5.

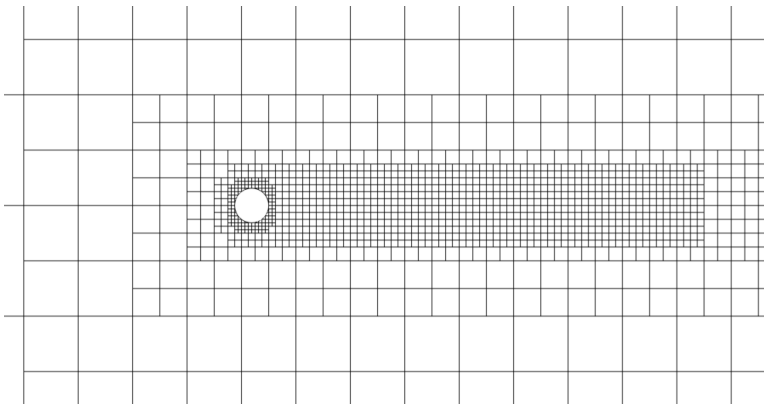

Figure 5: Local view of the mesh. Every eighth cell is plotted.

The wake region has been refined manually since a flow adaptive mesh refinement is subject to future work. The mesh consists of 105,000 cells in the 2D plane. The free stream Mach number in both cases was set to $Ma_\infty = 0.3$. The streamlines for the flow at $Re = 20$ are shown in Figure 6 whereas Table 1 lists the separation length and angle and the drag coefficient in comparison with reference values from literature [14, 15]. The agreement is quite satisfactory, only the separation angle is predicted too low, which might be due to the lack of considering the pressure gradient in the wall-layer.

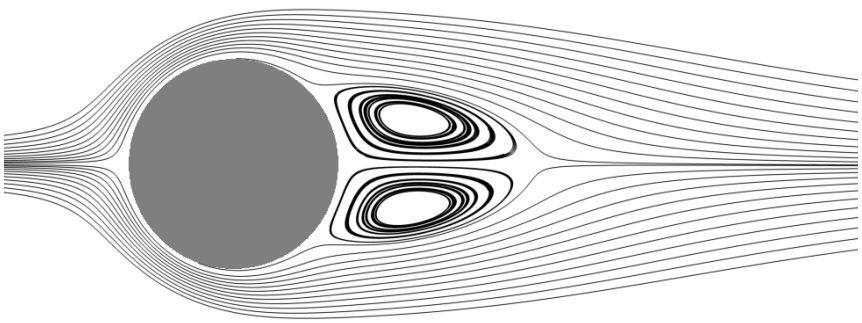

Figure 6: Streamlines for Re=20.

Table 1: Separation length L, separation angle θ_S and drag coefficient c_D for $Re = 20$.

	L	θ_S	c_D
Sucker and Brauer [14]	0.83	43.3°	2.02
Dennis and Chang [15]	0.94	43.7°	2.05
SPARC-IBM	0.93	41.8°	2.09

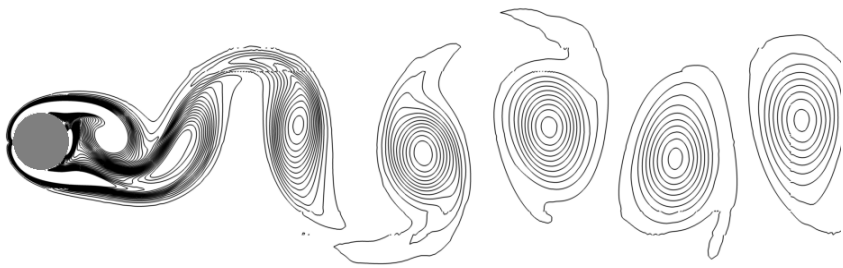

Figure 7: Instantaneous contours of the vorticity for $Re = 200$.

Figure 7 shows the instantaneous contours of the vorticity for an unsteady laminar flow around the cylinder at $Re = 200$. A comparison of the Strouhal number and the mean drag coefficient with results from literature [16, 17] is provided in Table 2.

Table 2: Strouhal number St and mean drag coefficient c_D for $Re = 200$.

	St	c_D
Linnick and Fasel [16]	0.197	1.34
Liu *et al.* [17]	0.192	1.31
SPARC-IBM	0.193	1.38

4.4 Turbulent flow past a circular cylinder

The unsteady turbulent flow around a circular cylinder at $Re = 140{,}000$ is provided as a further example. The mesh is taken from the previous stated calculations and the free stream Mach number was set to $Ma_\infty = 0.3$. Figure 8 shows the time averaged pressure distribution in terms of the pressure coefficient c_p in comparison with experimental results from Cantwell and Coles [18]. The angle α refers to the position on the surface of the cylinder beginning at the stagnation point. The calculation cannot predict the pressure distribution well.

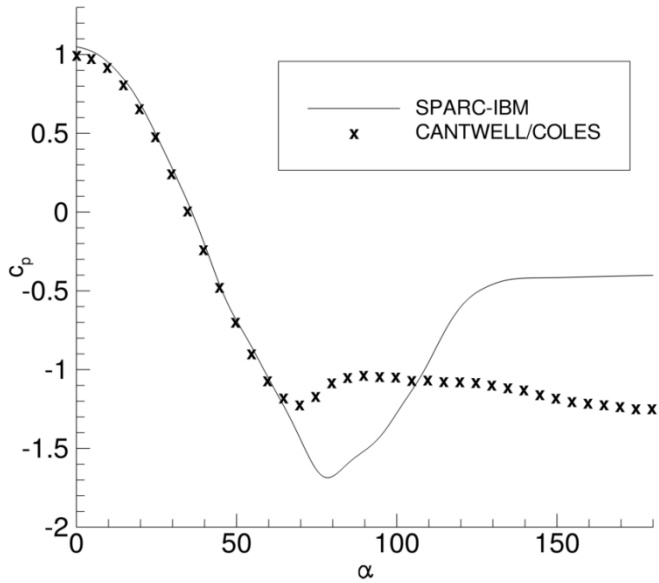

Figure 8: Pressure distribution at $Re = 140{,}000$.

The minimum c_p is about 40% lower than the measured value. In the separation area the pressure coefficient is determined too high resulting in a total drag coefficient of $c_D = 0.52$ which is much lower than the measured value of $c_D = 1.24$. Differences are also obtained for the Strouhal number. The computed value of $St = 0.23$ is much higher than the measured value of $St = 0.18$. The discrepancies are mostly due to the lack of the RANS turbulence model to predict the separation point correctly. Furthermore, turbulence is treated as isotropic which does not reflect reality.

5 Post processing

Plotting the flow field obtained by SPARC-IBM requires an additional post processing since there exists no information about a body-fitted shape of the wall-layer cells. Therefore the boundary knots of every wall-layer cell are moved onto the closest wall via a ray tracing technique similar to the one used for the mesh generation. Figure 9 shows a section of the mesh around a cylinder with and without the additional post processing. The appropriate flow values are obtained by an inverse distance interpolation or from the wall values directly if applicable.

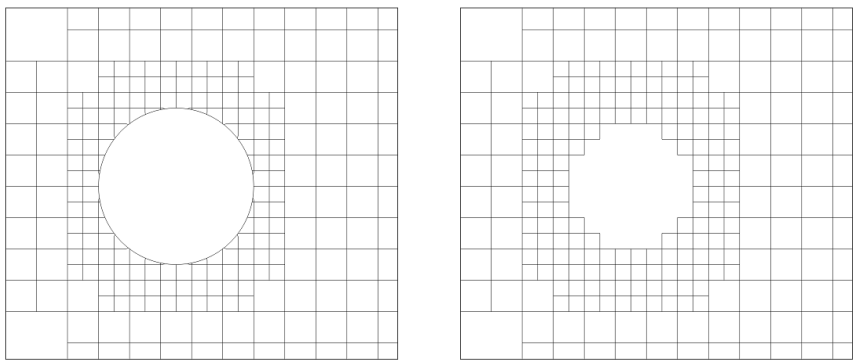

Figure 9: Local view of the mesh around a circular cylinder with (left) and without (right) the additional IBM-post processing. Every eighth cell is plotted.

6 Conclusions and ongoing work

The immersed boundary method (IBM) with a wall-layer approach has been implemented into an established block-structured code for solving compressible flow. The computation of basic test cases for laminar flow showed very good agreement with results found in literature. Viscosity dominated turbulent flow like the flow past a flat plate was also captured well. Discrepancies were obtained for turbulent flow with separation exemplarily shown for the flow past a circular cylinder. However, this is due to the well-known problem of turbulence modeling of bluff bodies rather than to the IBM.

To overcome the lack of consistency, future work comprises the testing of the simplified Spalart-Allmaras turbulence model for the wall-layer. It is believed that in contrast to using the algebraic model, the therewith associated full coupling of the outer flow field and the wall-layer provides better results for turbulent flows. Furthermore, the streamwise pressure gradient in the wall-layer and a flow adapted mesh refinement is about to be implemented.

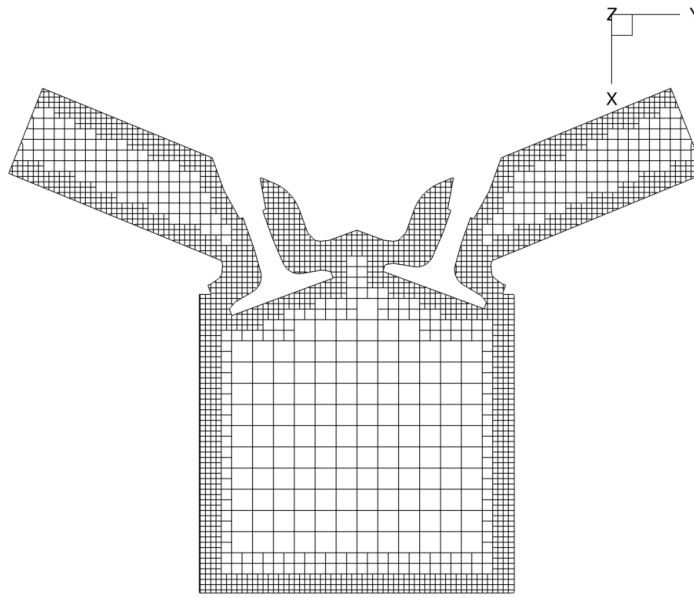

Figure 10: Slice through the IBM-mesh of an IC-engine. Every eighth cell is plotted.

Since the advantages of the IBM are only given for the simulation of complex geometries where the time for mesh generation is significant, the next step is to validate the implementation for 3D cases. As an example for a complex mesh a slice through the mesh of an internal combustion engine is shown in figure 10.

References

[1] Fadlun, E.A., Verzicco, R., Orlandi, P. and Mohd-Yusof, J., Combined immersed-boundary finite difference methods for three-dimensional complex flow simulations. *J. Comp. Phys.*, **161**, pp. 35-60, 2000.
[2] Mohd-Yosuf, J., Combined immersed-boundary/B-spline methods for Simulations of flow in complex geometries. *Annual Research Briefs, Center of Turbulence Research*, pp. 317-328, 1997.
[3] Balaras, E. *et al*. Two-layer approximate boundary conditions for large-eddy simulations. *AIAA Journal*, **34**, pp. 1111-1119, 1996.
[4] Cabot, W., Moin, P., Approximate wall boundary conditions in the large-eddy simulation of high Reynolds number flow. *Flow, Turbulence and Combustion*, **63**, pp. 269-291, 1999.
[5] Wang, M., Moin, P., Dynamic wall modeling for LES of complex turbulent flows. *Physics of Fluids*, **14**, pp. 2043-2051, 2002.

[6] Tessicini, F., Iaccarino, G., Fatica, M., Wang, M., Verzicco, R., Wall modeling for large-eddy simulation using an immersed boundary method. *Annual Research Briefs, Center of Turbulence Research*, pp. 181-187, 2002.
[7] Bond, R.B., Blottner, F.G., Derivation, implementation, and initial testing of a compressible wall-layer model. *Int. J. Numer. Meth. Fluids*, **66**, pp. 1183-1206, 2011.
[8] Magagnato, F., KAPPA – Karlsruhe Parallel Program for Aerodynamics, *TASK Quarterly Vol.2*, **2**, pp. 215-270, 1998.
[9] Verzicco, R., Iaccarino, G., Immersed Boundary Technique for Large-Eddy-Simulation. *Lecture series on "Large Eddy Simulation and related techniques: Theory and Applications"*, 2006.
[10] Spalart, P.R., Allmaras, S.R., A one-equation turbulence model for aerodynamic flows. *La Recherche Aerospatiale*, **1**, pp. 5-21, 1994.
[11] Toro, E.F., Spruce, M., Speares, M., Restoration of the contact surface in the HLL-Riemann solver, *Shock Waves*, **4**, pp. 25-34, 1994.
[12] Blasius, H., Grenzschichten in Flüssigkeiten mit kleiner Reibung. *Z. Math. Physik*, **56**, pp. 1-37, 1908.
[13] Wieghardt, K., Tillman, W., On the Turbulent Friction Layer for Rising Pressure. *NACA TM-1314*, 1951.
[14] Sucker, D., Brauer, H., Fluiddynamik bei quer angeströmten Zylindern. *Wärme- und Stoffübertragung*, **8**, pp. 149-158, 1975.
[15] Dennis, S.C.R., Chang, G.Z., Numerical solutions for steady flow past a circular cylinder at Reynolds numbers up to 100. *Journal of Fluid Mechanics*, **42**, pp. 471-489, 1970.
[16] Linnick, M.N., Fasel, H.F., A high-order immersed boundary method for unsteady incompressible flow calculations. *J. Comp. Phys.*, **204**, pp. 157-192, 2005.
[17] Liu, C., Zheng, X., Sung, C.H., Preconditioned Multigrid Methods for Unsteady Incompressible Flows. *J. Comp. Phys.*, **139**, pp. 35-57, 1998.
[18] Cantwell, B., Coles, D., An experimental study of entrainment and transport in the turbulent near wake of a circular cylinder. *J. Fluid Mech.*, **136**, pp. 321-374, 1983.

This page intentionally left blank

Computational design of the flow properties of foams

J. Skibinski[1], T. Wejrzanowski[1], J. Szumbarski[2] &
K. J. Kurzydlowski[1]
[1]*Warsaw University of Technology, Faculty of Materials Science and Engineering, Poland*
[2]*Warsaw University of Technology, Faculty of Power and Aeronautical Engineering, Poland*

Abstract

In the present studies the quantitative relationships between the structure and flow properties of porous materials are addressed. In order to investigate such relationships a series of foam structures with different porosity were characterized by computer tomography. Later, 3D image analysis was applied to obtain quantitative parameters of foam structures.

In order to calculate properties of the flow through porous structures, 3D images obtained by computer tomography were numerically processed and transformed into a finite element mesh. Simulation of fluid flow was performed using a Finite Volume Method. Both qualitative characterization and numerical simulation results, when compared, enabled us to establish structure-flow relationships.

The preliminary results show that the pressure drop is strongly related to the porosity of foams. The significant effect on flow properties exhibits also the diversity of pore sizes.

The results will be discussed with respect to foam structure optimization for several applications.
Keywords: ceramic foams, pressure drop, finite volume method.

1 Introduction

The industrial application of structures with open porosity such as ceramic or metallic foams has been growing over recent decade. Their favorable properties

WIT Transactions on Engineering Sciences, Vol 74, © 2012 WIT Press
www.witpress.com, ISSN 1743-3533 (on-line)
doi:10.2495/AFM120101

such as high specific surface area, high porosity, low density, low thermal conductivity and low specific heat capacity predestine them to serve as compact heat exchangers, reaction catalysts, flow stabilizers or casting filters [1]. These materials can also be found in nature, for example as porous rocks containing gas and oil. Those applications require new materials, which can be designed and investigated numerically before manufacturing. In order to understand quantitative nature of the structure-properties relationships in porous media relevant structural parameters must be defined. Open porosity and relative surface of pores are frequently used for this purpose [2]. These parameters give good general characteristics, however their meaning to the understanding of the material flow properties, such as pressure drop, is rather limited.

Many geometrical models have been developed to describe properties of real foam structures. Most of the models, such as the reproduction of a single type of polyhedron, or models based on Kelvin polyhedron (gives minimum specific surface) [3], exhibit anisotropy, which usually does not exist in real foams. Most of cellular structures are fabricated by techniques based on growth process. Poisson-Voronoi tessellation (PVT) is frequently used as an algorithm to obtain representative cellular structures of this type. However, geometrical parameters of real foams, such as average faces per cell, differ from those obtained by PVT. A representation of real foams structure can be obtained by application of Laguerre-Voronoi algorithm, where tessellations are performed on the set of spheres with pre-determined size distribution [4, 5].

This paper shows the preliminary numerical results of the modelling of fluid flow properties through real structures and the model structures obtained by Laguerre-Voronoi tessellation.

2 Geometries

2.1 Real structures

The commercially available alumina foams were used as a reference foam structures (further called real structures). The real structures were originally described by pores per inch number (ppi). Further 3d image analysis enabled for extended characterization, where other structural parameters such as porosity, specific surface, mean pore diameter, mean strut diameter were calculated.

Digitalized geometries of foams were obtained using Computer Tomography (CT). The vector-like structures were created from set of bitmaps. The surface of the foam is divided into a logical series of triangles. Each triangle is uniquely defined by its normal and three vertices. To create a valid volume, the surface geometry was converted to file of points cloud to simplify model in problematic areas. As a result, a valid 3D multi-surface mesh was created. The distribution of the strut diameter as well as specific surface area of each sample were calculated during post-processing.

Real ceramic foams have varying percentage of pores that are blocked. This is the effect of fabrication process, and the percentage of clogged pores increases with number of pores per inch. The resistance to the flow was expected to be higher in the structures with higher number of blocked pores.

In figure 1 a real geometry and its virtual representation is shown. Table 1 lists structural parameters of foams obtained after processing.

Table 1: Parameters of real ceramic foams.

Structure	Porosity [-]	Specific surface area [1/mm]	Mean strut diameter [mm]
10 ppi	0.740	0.77906	1.35222
30 ppi	0.702	1.22055	0.89627
50 ppi	0.754	1.84731	0.57974

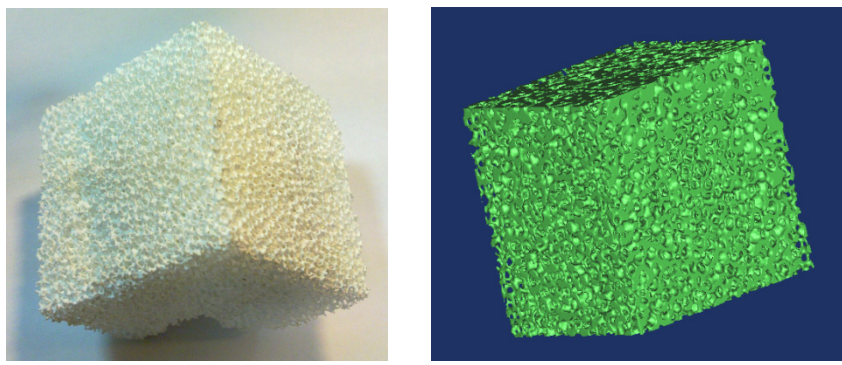

Figure 1: Ceramic foam and its computer model.

2.2 Foam numerical models

Foam models were created using Laguerre-Voronoi tessellation (LVT). LVT was applied to spheres with specified size distribution, which were packed in the cubic volume. The foam struts were created by cylinders with defined constant diameter generated along cell edges (see Figure 2a).

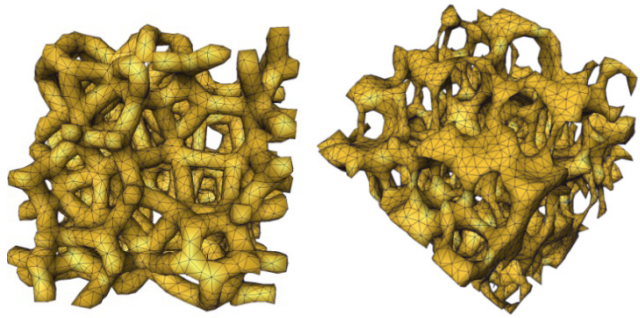

a) Model structure b) CT reconstructed real structure

Figure 2: Computer models of designed structure (a) and real structure (b).

Parameters of structures designed within these studies are shown in Table 2.

Table 2: Parameters of foam models.

Structure	Porosity [-]	Specific surface area [1/mm]	Mean strut diameter [mm]
CV 01	0.6964	0.76741	1.544
CV 03	0.7480	0.75987	1.278
Bimodal	0.8157	0.47446	1.459

The effect of pore clogging does not appear in the model structures. Blocked pores don't change porosity significantly, but the pressure drop is expected to be smaller regardless structural parameters.

3 Numerical method

Fluid flow calculations were performed using Finite Volume Method. This method represents partial differential equations in the form of algebraic equations. Values are calculated at discrete place on a meshed geometry. The key to the method is that the integral form of the conservation law (1) can be rewritten using the Gauss Divergence Theorem.

$$\frac{\partial}{\partial t}\int_{\Omega} U d\Omega + \int_{\Omega} \vec{\nabla} \cdot \vec{F} d\Omega = 0 \quad (1)$$

Volume integrals of divergence terms in a partial differential equation are converted to surface integrals of fluxes all around the control volume (2).

$$\frac{\partial}{\partial t}\int_{\Omega} U d\Omega + \oint_{\partial\Omega} \vec{F} \cdot \vec{n} d\Gamma = 0 \quad (2)$$

The resulting equations cannot be solved analytically and a numerical solution requires discretization into volumes. These terms are then evaluated as fluxes at the surfaces of each finite volume. The flux entering a given volume is

identical to that leaving the adjacent volume. This makes the FVM stable and flexible, yet relatively easy to implement. The main advantage of this method is it's applicability on unstructured meshes and the intrinsic local conservation properties of the resulting schemes, which suits very well the irregular geometries of porous structures.

The flows across real and designed structures were simulated. The computational domain was a channel with length of 20 mm and 15x15 mm square cross-section. Structural parameters of specimens are shown in Table 2. The size of specimens was 15mmx15mmx15mm block. The inlet velocities for FVM simulations range from 0.0002 to 0.02 m/s, which correspond to Reynolds number from 2 to 400.

4 Results

The results of the simulations of flows across real foams are compared with the designed structures. The hydraulic resistance of all structures is shown in Figure 3.

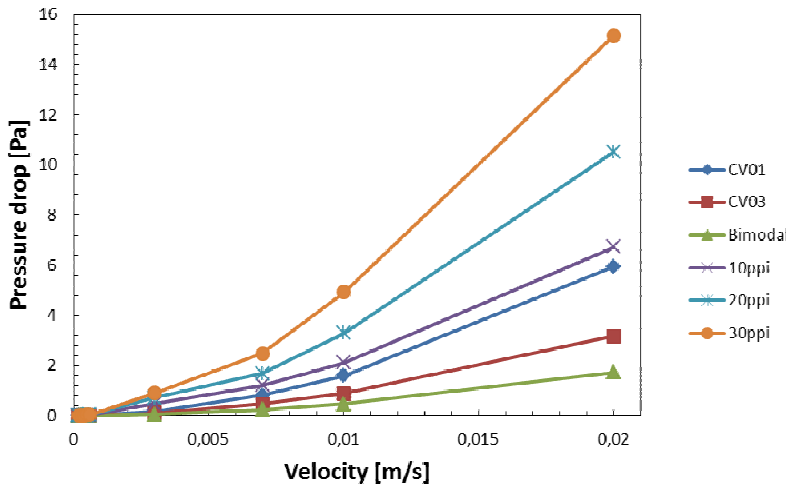

Figure 3: Comparison of simulated and experimental pressure drop in flow across different ceramic foams.

The structures that exhibit the closest similarity regarding structural parameters are 10ppi and CV03. These structures have been chosen for comparison of hydraulic properties of real and designed materials (Figure 4).

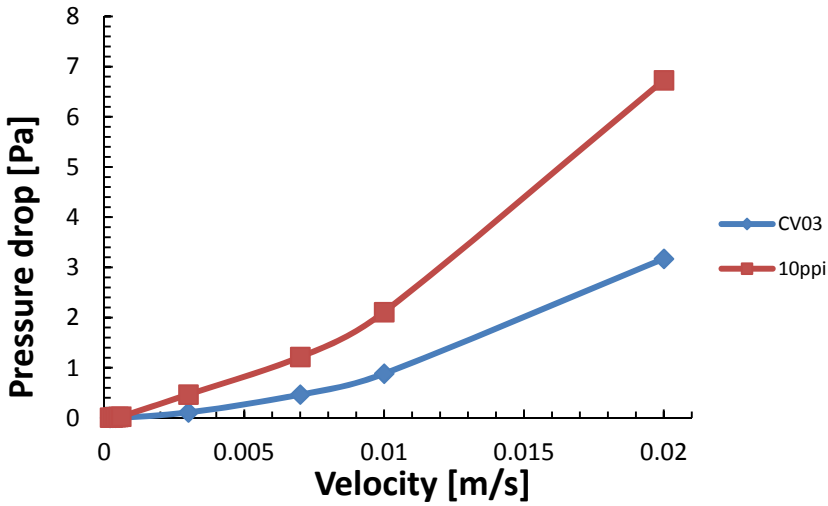

Figure 4: Comparison of pressure drop in flow across designed and real structures with similar structural parameters.

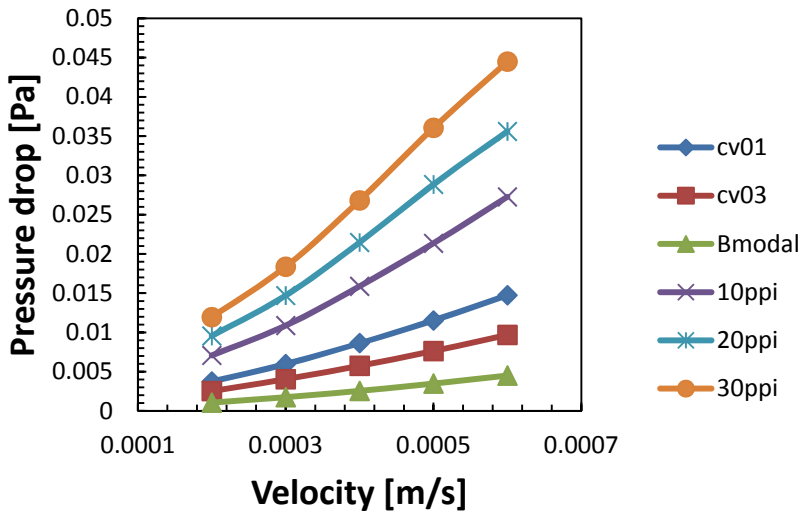

Figure 5: Pressure drop results for Darcy's flow regime.

Linear Darcy's model is most commonly used for describing flows through porous media. Darcy's law may be written as:

$$-\frac{dp}{dL} = \frac{\mu}{k} \cdot \vec{v} \tag{3}$$

where dL is a segment [m] along which a pressure drop dp [Pa] occurs, k permeability [m^2], μ dynamic viscosity [kg/ms] and v is the filtration velocity [m/s]. Darcy's law correctly describes the flow in porous media only for low velocity flows. As a basic criterion used to describe correct Darcy's regime is Reynolds number. The range of Reynolds number for Darcy's flow differs in dependence of sources [12–15], but Re = 10 is generally assumed to be a critical maximum value. Set of calculation results based on this criterion have been chosen to determine effective permeability of materials. Reynolds number valid for Darcy's law is equivalent to velocities of 0.0002 m/s to 0,0006 m/s for porous foams sizes used. Figure 5 shows the results of pressure drop for selected range of velocities.

For flows with Reynolds number exceeding the Darcy's law criterion, a discrepancy between experimental data and results obtained based on Darcy's law appears [16]. Forchheimer linked the latter to kinetic effect and suggested to modify (3) by an additive term $\rho\bar{U}^2$, representing kinetic energy [17]:

$$-\frac{dp}{dL} = \frac{\mu}{\kappa} \cdot \vec{v} + \beta\rho\vec{v} \tag{4}$$

where β [1/m] is Forchheimer's coefficient (also known as non-Darcy coefficient). The results of pressure drop in investigated structures for non-Darcy flow are shown in Figure 6.

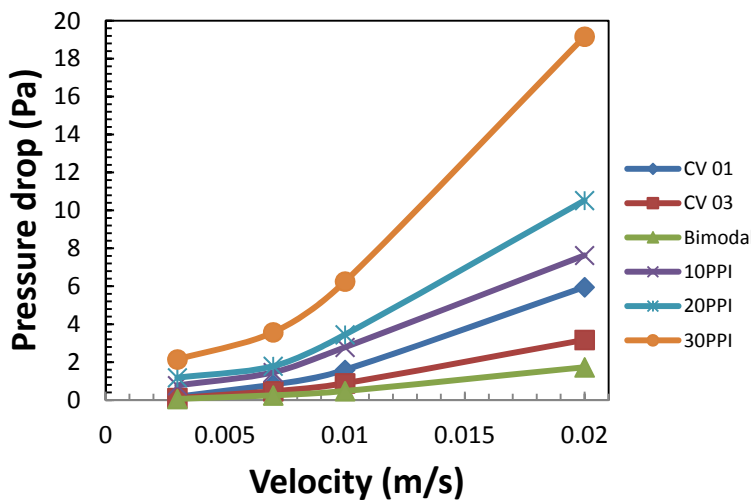

Figure 6: Pressure drop in porous structures for non-Darcy flow.

There is a good agreement between obtained results and the basic models describing flows through porous media. When the Reynolds number exceeds the

maximum value for Darcy's flow, the pressure vs. velocity curve changes from linear to polynomial for every investigated structure, which accords with Forchheimer's equation (4).

The effective permeability k_{eff} of materials have been determined from Darcy's law. The results are shown in Figure 7.

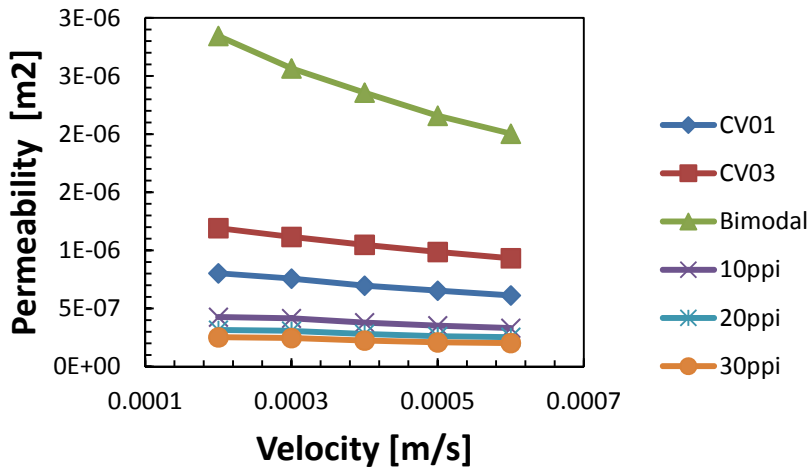

Figure 7: Effective permeability coefficient in function of velocity.

In general, k_{eff} takes into account not only permeability coefficient characterizing the medium, but also inertial effects. As the contribution of inertial effects grows with increasing velocity of flow, the effective permeability decreases.

5 Conclusions

Simulations of flows across porous structures were performed to determine hydraulic properties. Pressure drop difference between real and designed structures can be observed. This effect may be related with clogged pores, a result of the production process. The equivalent model structures considered in the simulations should be modified to implement blocked pores in the design process, which should result in more accurate model of real structure.

Acknowledgement

The work has been financially supported by the Polish Ministry of Science and Higher Education, research grant no. N N507 273636.

References

[1] A. Oscilowski, W. Plis, *Ceramic foam filters – using purpose, practical experience in Ferro-Term*, Archives of Foundry, Vol. 1, Book 1, PAN – Katowice, 2001.

[2] Edouard D., Lacroix M., Huu C.P., Luck F., Pressure drop modeling on SOLID foam: State-of-the art correlation. Chem. Eng. Journal 144, pp. 299-311, 2008.

[3] Weaire, D.; Phelan, R. (1994), "A counter-example to Kelvin's conjecture on minimal surfaces", Phil. Mag. Lett. 69: 107–110.

[4] Z. Fan, Y. Wu, X. Zhao, Y. Lu, *Simulation of polycrystalline structure with Voronoi diagram in Laguerre geometry based on random closed packing of spheres*, Computational Materials Science 29 (2004) 301–308.

[5] C. Redenbach, *Microstructure Models for Cellular Materials*, Computational Materials Science 44, 4 (2009) 1397-1407.

[6] Timothy Bart, Mario Ohlberger, *Finite Volume Methods: Foundation and Analysis*, Encyclopedia of Computational Mechanics, Chapter 9, 2004.

[7] M.R. Nangrejo, X. Bao, M.J. Edirisinghe, *The structure of ceramic foams produced using polymeric precursors*, Journal of Materials Science Letters 19 (2000) 787-789.

[8] J.G. Fourie, J.P. DuPlessis, Pressure drop modelling in cellular metallic foams, Chem. Eng. Sci. 57 pp. 2781–2789, 2002. [7] F.C. Buciuman, B. Kraushaar-Czarnetzki, Ceramic foam monoliths as catalyst carriers. 1. Adjustment and description of the morphology, Ind. Eng. Chem. Res. 42 pp. 1863–1869, 2003.

[9] V.N. Antsiferov, S.E. Porozova, *Foam ceramic filters for molten metals: reality and prospects*, Powder Metallurgy and Metal Ceramics, Vol. 42, Nos. 9-10, 2003.

[10] Luis Seminario, Roberto Rozas, Rodrigo Borquez, Pedro G. Toledo, *Pore blocking and permeability reduction in cross-flow microfiltration*, Journal of Membrane Science 209 (2002) 121-142.

[11] A. Santos, P. Bedrikovetsky, S. Fontoura, *Analytical micro model for size exclusion: Pore blocking and permeability reduction*,. Journal of Membrane Science 308 (2008) 115-127.

[12] Bear J., *Dynamics of Fluids in Porous Media*, Elsevier, 1972.

[13] Hansen T. E., *Flow in micro porous silicon carbide. Master Thesis*, Department of Micro and Nanotechnology, Technical University of Denmark, March 2nd, 2007.

[14] Hassanizadeh S.M., Gray W.G., *High Velocity Flow in Porous Media*, Transport in Porous Media (1987) 2: 521-531.

[15] Sawicki J., Szpakowski W., Weinerowska K., Woloszyn E., Zima P., *Laboratory of Fluid Mechanics And Hydraulics*, Gdansk University of Technology, 2004.

[16] Andrade J. S., Costa U. M. S., Almeida M. P., Makse H. A., Stanley H. E., *Inertial Effects on Fluid Flow through Disordered Porous Media*, Physical Review Letters, Vol. 82, No. 26, 28 June 1999.

[17] Ewing R., Lazarov R., Lyons S.L., Papavassiliou D.V., Pasciak J., Qin G.X., *Numerical Well Model For Non-Darcy Flow*, Computational Geosciences. 3(3-4). 185-204. 1999.

Assessment of two pressure-velocity coupling strategies for local meshless numerical method

G. Kosec[1,2], R. Vertnik[2, 3] & B. Šarler[2,4]
[1]*Jožef Stefan Institute, Laboratory for Parallel and Distributed Computing, Slovenia*
[2]*University of Nova Gorica, Laboratory for Multiphase Processes, Slovenia*
[3]*Štore steel, d.o.o. Research, Slovenia*
[4]*Centre of Excellence for Biosensors, Automation and Process Control, Laboratory for Advanced Materials Systems, Slovenia*

Abstract

The performance of two pressure-velocity coupling strategies, associated with the primitive variable solution of incompressible Newtonian fluid with the meshless Local Radial Basis Function Collocation Method (LRBFCM), is compared with respect to computational efficiency, stability, accuracy and spatial convergence. The LRBFCM is structured with multiquadrics on five noded support domains. The explicit time stepping is used. The Backward-Facing Step problem (BFS) has been selected as a benchmark problem, previously tackled by several numerical methods. The semi-local fractional step method (FSM) and completely local pressure-velocity couplings (LPVC) are compared. The numerical results are validated against previously published data. The results are represented and compared in terms of a convergence plot of the reattachment position. We show that both approaches provide reasonable results; however, LVPC is less computationally complex and less stable in comparison to FSM.
Keywords: meshfree methods, radial basis functions, collocation, convective-diffusive problems, adaptation, refinement, melting, fluid flow, Newtonian fluids.


WIT Transactions on Engineering Sciences, Vol 74, © 2012 WIT Press
www.witpress.com, ISSN 1743-3533 (on-line)
doi:10.2495/AFM120111

1 Introduction

The meshless methods belong to a class of numerical methods where an arbitrarily distributed set of nodes, without any additional topological relations between them, is used. There exist several meshless methods [1–5]; however, this work is focused on one of the simplest classes of meshless methods in development today, the point interpolation Radial Basis Function Collocation Method (RBFCM) [6]. In the present paper we use a local variant of RBFCM [6], the Local Radial Basis Function Collocation Method (LRBFCM). The main advantage of the local approach is in consideration of the multivariate data fitting and calculation of spatial derivatives through a local support domain. Consequently, the computational basis is simplified, since several small systems of algebraic equations are solved instead of a global algebraic equation system. Such approach has been already successfully applied to several thermo-fluid situations, ranging from the basic diffusion problems to complex highly non-linear and coupled technologically relevant situations [5, 7–14]. Important features of meshless methods represent straightforward application of dynamic node distribution [15], and stable behaviour on non-regular node distributions [11].

This paper is focused on application of LRBFCM in fluid mechanics, more precisely, in channel flow. In our past publications we have already demonstrated the applicability of LRBFCM in fluid flow computations. The LPVC (in the context of meshless methods) was for the first time introduced in [10] and further investigated regarding more complex physical systems in [12, 16, 17], where only closed and impermeable domains have been considered. The open domain problems were dealt with (in the context of meshless methods) the FSM approach in [14, 18].

In this paper we compare the performance of LPVC and FSM in open domain problems, which seems to appear more demanding than the closed ones. The well-known Backward-Facing Step problem [19–25] (BFS) is considered since its solution is well coped with in the literature, and is at the same time complex enough to challenge the proposed numerical techniques.

The principal message of the present paper is a quantitative comparison of two meshless based numerical procedures that differ only in pressure-velocity coupling strategies. The Chorin's FSM [21] is semi-global, and as such requires solution of a global system of algebraic equations for pressure, while LPVC is completely local. Both strategies show reasonably good convergence behavior as well as good agreement with already published data [22].

2 Problem definition

The BFS problem of the laminar incompressible Newtonian fluid flow over a backward-facing step in two dimensions is considered. It represents a standard test for investigating the flow separation and reattachment. It has been already used by numerous researchers as a benchmark test for various numerical methods [19–25]. The domain of the problem is characterized by a planar

channel with sudden change of the geometry (Figure 1), which governs the flow separation, and generation of several re-circulating zones downward the step, described by positions (p_{x1}, p_{x2}, p_{x3}). The flow is modelled by the Navier Stokes equations

$$\nabla \cdot \mathbf{v} = 0\,, \tag{1}$$

$$\rho \frac{\partial \mathbf{v}}{\partial t} + \rho \nabla \cdot (\mathbf{vv}) = -\nabla P + \nabla \cdot (\mu \nabla \mathbf{v})\,, \tag{2}$$

with t, $\mathbf{v}(v_x, v_y)$, P, μ and ρ standing for time, velocity, pressure, viscosity and density, respectively. The Cartesian coordinates are used, and the position vector is defined as $\mathbf{p} = (p_x, p_y)$. The rectangular domain is normalized to height $2h = 1$. Beginning of the computational domain is considered at the location of the step, where the flow enters the channel. The step height is set to h. The channel length is set to $30h$. The flow dynamics is characterized by the Reynolds number (Re), defined as

$$\mathrm{Re} = \frac{\rho v_0 2h}{\mu}\,, \tag{3}$$

with v_0 standing for the amplitude of the inlet velocity. At the inlet, the fully-developed velocity profile is set [22]

$$v_x(p_y) = v_0\, p_y(0.5 - p_y); 0.0 \le p_y \le 0.5\,. \tag{4}$$

At the outlet boundary, the Neumann boundary conditions for velocity components are prescribed and are all set equal to zero. At the walls, non-permeable and no-slip conditions are used. The schematics of the computational test are represented in Figure 1.

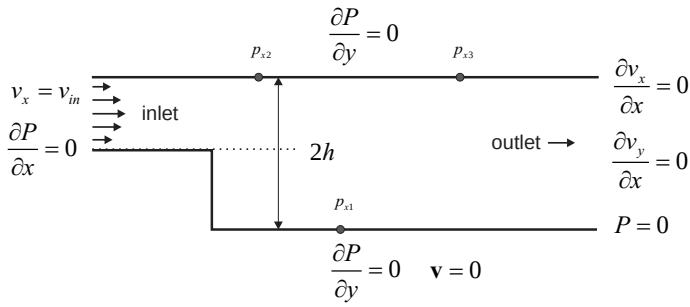

Figure 1: Problem schematics of the backward-facing step.

3 Solution procedure

A general idea in the local meshless methods is the use of local sub clusters of domain nodes, named local support domains, for the approximation of the fields. Complementary to the selected support domain, an approximation function is introduced as a sum of weighted basis functions

$$\theta(\mathbf{p}) = \sum_{n=1}^{N_{Basis}} \alpha_n \Psi_n(\mathbf{p}), \tag{5}$$

where θ, N_{Basis}, α_n and Ψ_n stand for the approximation function, the number of basis functions, the approximation coefficients, and the basis functions, respectively. The basis could be selected arbitrarily (monomials, radial basis functions, …). In this paper, Hardy's Multiquadrics (MQs),

$$\Psi_n(\mathbf{p}) = \sqrt{(\mathbf{p}-\mathbf{p}^n)\cdot(\mathbf{p}-\mathbf{p}^n)/\sigma_C^2 + 1}, \tag{6}$$

with σ_C standing for the free shape parameter of the basis function, are used. MQ's are selected. By taking into account all support domain nodes and equation (5) the approximation system is obtained. In this paper we use collocation (the number of support nodes is the same as the number of the basis functions). An arbitrary spatial differential operation L can be applied on the approximation function in the following way

$$L\theta(\mathbf{p}) = \sum_{n=1}^{N_{Basis}} \alpha_n L\Psi_n(\mathbf{p}) \tag{7}$$

In general, the system (5) has to be solved only when the support domain topology changes and therefore the computation can be optimized by computing $\mathbf{\Psi}^{-1}$ in a pre-process. Furthermore, the computation of the coefficients and the evaluation of differential operators can be combined. All information about the numerical approach and the local nodal topology can be stored in a predefined vector, which has to be re-evaluated only when the topology of the nodes changes. The differential operator vector χ_m^L is introduced as

$$\chi_m^L(\mathbf{p}) = \sum_{n=1}^{N} \Psi_{nm}^{-1} L(\Psi_n(\mathbf{p})). \tag{8}$$

The introduced formalism holds in general and therefore the general notation for partial differential operator (L) is used. However, in the present work, only operators ∇ and ∇^2 are employed

$$\chi_m^{\nabla^2}(\mathbf{p}) = \sum_{n=1}^{N} \Psi_{nm}^{-1} \sum_{\varepsilon} \frac{\partial^2}{\partial p_\varepsilon^2} \Psi_n(\mathbf{p}), \tag{9}$$

$$\chi_m^{\partial/\partial p_\varepsilon}(\mathbf{p}) = \sum_{n=1}^{N} \Psi_{nm}^{-1} \frac{\partial}{\partial p_\varepsilon} \Psi_n(\mathbf{p}). \tag{10}$$

The structured formulation is convenient since most of the complex and CPU demanding operations are performed in the pre-process phase. For all inner temporal loop operations only *N* floating point operations (FLOPS) are needed for evaluation of an arbitrary partial differential operator. The implementation of the Dirichlet boundary condition is straightforward. In order to implement Neumann and Robin boundary conditions, special interpolation is needed. In the present numerical framework, the computation of Neumann and Robin boundary conditions can be simplified through the use of the differential operator vector. Consider Neumann boundary condition

$$a\frac{\partial\theta}{\partial\mathbf{n}} + b\theta = \theta_{BC}, \tag{11}$$

$$\theta_0 = \frac{\theta_{BC} - a\sum_{m=2}^{N_{Sub}} \chi_m^{\partial/\partial\mathbf{n}}\,\theta_m}{a\,\chi_0^{\partial/\partial\mathbf{n}} + b}, \tag{12}$$

where θ_0 stands for the boundary node. Equation (12) simplifies to Neumann boundary condition computation if b is set to zero. Such approach makes the Neumann and the Robin boundary condition computation straightforward and CPU effective. Again, only N flops are needed to evaluate it, without any kind of special computational treatment on or near the boundaries.

3.1 Local pressure-velocity coupling

A two-level explicit time stepping is used, thus equation (2) is discretized as

$$\hat{\mathbf{v}} = \mathbf{v}_0 + \frac{\Delta t}{\rho}\left(-\nabla P_0 + \nabla\cdot\left(\mu\nabla\mathbf{v}_0\right) + \mathbf{b}_0 - \rho\nabla\cdot(\mathbf{v}_0\mathbf{v}_0)\right), \tag{13}$$

with Δt standing for time step, index zero marks the initial time step values and $\hat{\mathbf{v}}$ stands for intermediate velocity. Equation (13) does not take into account the mass continuity and therefore the pressure and the velocity corrections are added

$$\hat{\mathbf{v}}^{m+1} = \hat{\mathbf{v}}^m + \tilde{\mathbf{v}}, \quad \hat{P}^{m+1} = \hat{P}^m + \tilde{P}, \tag{14}$$

where m, $\tilde{v}$ and $\tilde{P}$ stand for pressure velocity iteration index, velocity correction, and pressure correction, respectively. By combining the momentum and the mass continuity equations, the pressure correction Poisson equation emerges

$$\nabla\hat{\mathbf{v}}^m = \frac{\Delta t}{\rho}\nabla^2\tilde{P}. \tag{15}$$

Instead of solving the global Poisson equation problem, the pressure correction is directly related to the intermediate velocity divergence

$$\hat{P} = \ell^2 \frac{\rho}{\Delta t} \nabla \cdot \hat{\mathbf{v}}^m. \tag{16}$$

The proposed assumption enables direct solving of the pressure velocity coupling iteration. It is thus very fast due to only one spatial discretization operation needed in each node to evaluate the new iteration pressure and the velocity corrections. With the computed pressure correction, the pressure and the velocity can be corrected as

$$\hat{\mathbf{v}}^{m+1} = \hat{\mathbf{v}}^m - \zeta \frac{\Delta t}{\rho} \nabla \hat{P}, \qquad \hat{P}^{m+1} = \hat{P}^m + \zeta \hat{P}, \tag{17}$$

where ζ stands for the relaxation parameter. The iteration is performed until the criterion $\nabla \cdot \hat{\mathbf{v}} < \varepsilon_V$ is met in all computational nodes. After successful pressure-velocity iteration, the algorithm continues with the next time step. The LPVC approach is similar to the artificial compressibility method (ACM), which has been recently under intense research in connection with Finite Volume Method [26, 27] and in connection with Finite Element Method [28]. A similar approach, in the framework of the FDM, is SOLA algorithm [29]. However, the proposed LPVC approach retains the correct time transient which is, in general, not the case in SOLA and ACM approaches.

3.2 Fractional step approach

The pressure is omitted from temporally discretized form of momentum equation in FSM approach

$$\hat{\mathbf{v}} = \mathbf{v}_0 + \frac{\Delta t}{\rho} \left(\nabla \cdot \left(\mu \nabla \mathbf{v}_0 \right) + \mathbf{b}_0 - \rho \nabla \cdot (\mathbf{v}_0 \mathbf{v}_0) \right). \tag{18}$$

Again, the equation (18) does not take into account the mass continuity. In a similar manner as in 3.1, the pressure Poisson equation is constructed.

$$\nabla^2 P = \frac{\Delta t}{\rho} \nabla \hat{\mathbf{v}}. \tag{19}$$

The equation (19) is directly solved in the FSM approach. However, the locality of spatial discretization simplifies the computations to solution of a sparse system of algebraic equations. With the solved pressure, the intermediate velocity is corrected as

$$\mathbf{v} = \hat{\mathbf{v}} - \frac{\Delta t}{\rho} \nabla P. \tag{20}$$

In FSM, the internal iterations are not performed. The computed pressure and corrected velocity are therefore new values and simulation proceeds to the next time step. FSM does not provide a correct time transient in general.

4 Results

The results are presented in terms of velocity field plot and velocity, pressure and shear stress cross section profiles for $\mathrm{Re} = 800$ case. The convergence is monitored at the reattachment position p_{x1} with respect to the number of computational nodes, ranging from 150x40 to 325x110. The reattachment position is defined as a point where the wall shear stress equals zero

$$\tau = \mu \frac{\partial v_x}{\partial p_y} = 0 \tag{21}$$

Steady state velocity field is represented in Figure 2. The x axis is on the plot limited to 10 (for the sake of better visibility), although the computations are performed on domain with length 15.

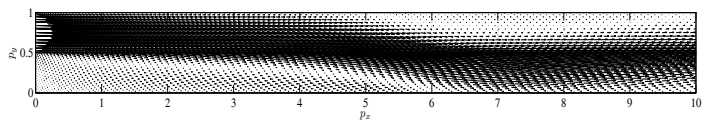

Figure 2: Problem schematics of the backward-facing step.

All computations were performed with time step $\Delta t = 10^{-3}$, relaxation parameter $\zeta = 10^{-7}$ and MQ shape parameter $\sigma_C = 32$, normalized to the maximum distance between the nodes within the support domain.

A comparison of the results is done on velocity cross-section profiles with the already published data [22], presented as "Gartling" in Figures. Two different cross-sections are examined, at $p_x = 7$ and $p_x = 15$ (Figure 3). In Figure 4, the shear stress profiles at the bottom and the top walls are represented. A good agreement is achieved in all analyses. Finally, the convergence plot for both meshless based solutions is represented in Figure 5. Both solution procedures converge at the same rate with minimal differences. However, it can be seen that LPVC develops minor instabilities in the convergence plot. The behaviour is to be investigated in our future work. Our preliminary analyses show that the instabilities can be mitigated by usage of an additional stability term in pressure correction.

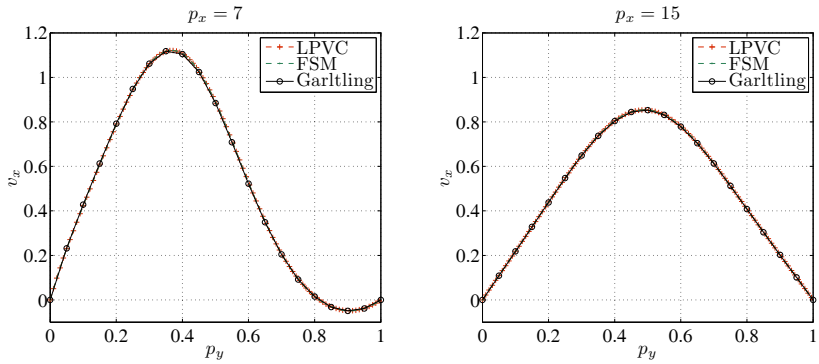

Figure 3: Comparison of vertical velocity profiles at $p_x = 7$ and $p_x = 15$.

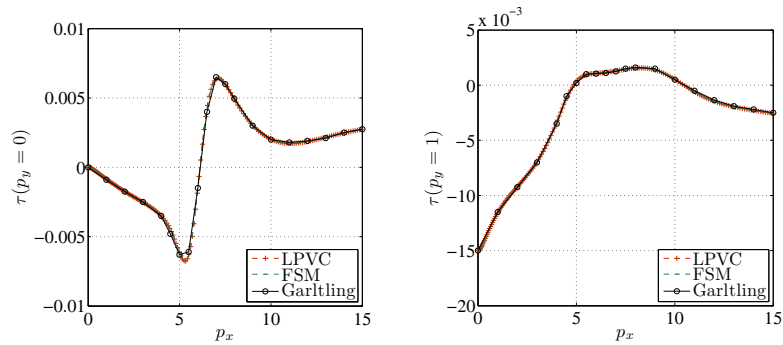

Figure 4: Comparison of shear stress profiles at the top and at the bottom wall.

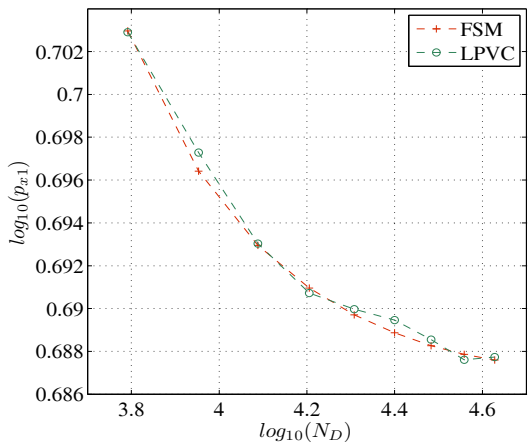

Figure 5: Convergence plot for reattachment position p_{x1} with respect to the number of the nodes N_D.

5 Conclusions

Two different strategies for pressure-velocity coupling in meshless solution of laminar, incompressible Newtonian channel flow are presented. Both strategies provide good results. Comparison with published data shows good accuracy of both presented methods. The semi-local FSM behaves more stable as the LPVC. The main advantages of the LPVC approach are: ease of implementation, straightforward parallelization, and low computational cost. On the other hand, the global FSM pressure-velocity strategy does not require a consideration of any extra relaxation parameter, at the cost of higher computational complexity. The FSM approach also shows more stable convergence behavior. The main drawback of FSM as compared to the LPVC is global solution of pressure equation. First, the global system has to be constructed. This is not problematic as long as the static node distribution is used, as it can be done in preprocess. The solution of the system remains the task to be done in each time step, however. With proper iterative algorithms and pre-conditioning this overhead can be minimized. Still, the complexity is proportional to $O(N_D)$, while for LPVC this step is omitted. Besides a higher computational complexity, the important factor is ease of parallelization since the multicore computers are common today. The LPVC is almost ideally parallelizable as it is completely local. There is minimal communication with other parts of the computational domain. For the shared memory systems the OpenMP parallelization is trivial and extremely effective [30]. At the cost of computational complexity, however, the FSM offers more stable numerical scheme. The FSM also does not provide a proper time transient. These conclusions are preliminary and will be further investigated and supported with more analyses in the archival version of the present paper, that will be submitted to EABE.

Acknowledgements

The research was funded through Slovenian state research projects J2-4120, P2-0379 and P2-0095. The Centre of Excellence for Biosensors, Instrumentation and Process Control is an operation financed by the European Union, European Regional Development Fund and Republic of Slovenia, Ministry of Higher Education, Science and Technology. The financial support is kindly acknowledged.

References

[1] Kansa, E. J., Multiquadrics - a scattered data approximation scheme with application to computational fluid dynamics, part I. *Computers and Mathematics with Applications*, **19**, pp. 127-145, 1990.

[2] Chen, W., New RBF collocation schemes and kernel RBFs with applications. *Lecture Notes in Computational Science and Engineering*, **26**, pp. 75-86, 2002.

[3] Liu, G.R., *Mesh Free Methods*, CRC Press: Boca Raton, 2003.
[4] Trobec, R., Šterk, M. and Robič, B., Computational complexity and parallelization of the meshless local Petrov-Galerkin method. *Computers & Structures*, **87**, pp. 81-90, 2009.
[5] Šterk, M. and Trobec, R., Meshless solution of a diffusion equation with parameter optimization and error analysis. *Engineering Analysis with Boundary Elements*, **32**, pp. 567-577, 2008.
[6] Šarler, B., From global to local radial basis function collocation method for transport phenomena. *Advances in Meshfree Techniques*, pp. 257-282, 2007.
[7] Šarler, B. and Vertnik, R., Meshfree explicit local radial basis function collocation method for diffusion problems. *Computers and Mathematics with Applications*, **51**, pp. 1269-1282, 2006.
[8] Vertnik, R. and Šarler, B., Meshless local radial basis function collocation method for convective-diffusive solid-liquid phase change problems. *International Journal of Numerical Methods for Heat and Fluid Flow*, **16**, pp. 617-640, 2006.
[9] Divo, E. and Kassab, A. J., Localized meshless modeling of natural-convective viscous flows. *Numerical Heat Transfer*, **B129**, pp. 486-509, 2007.
[10] Kosec, G. and Šarler, B., Solution of thermo-fluid problems by collocation with local pressure correction. *International Journal of Numerical Methods for Heat and Fluid Flow*, **18**, pp. 868-882, 2008.
[11] Trobec, R., Kosec, G., Šterk, M. and Šarler, B., Comparison of local weak and strong form meshless methods for 2-D diffusion equation. *Engineering Analysis with Boundary Elements*, **36**, pp. 310-321, 2012.
[12] Kosec, G., Založnik, M., Šarler, B. and Combeau, H., A Meshless Approach Towards Solution of Macrosegregation Phenomena. *Computers, materials & continua*, **580**, pp. 1-27, 2011.
[13] Vertnik, R., Založnik, M. and Šarler, B., Solution of transient direct-chill aluminium billet casting problem with simultaneous material and interphase moving boundaries by a meshless method. *Engineering Analysis with Boundary Elements*, **30**, pp. 847-855, 2006.
[14] Vertnik, R. and Šarler, B., Local collocation approach for solving turbulent combined forced and natural convection problems. *Advances in Applied Mathematics and Mechanics*, **3**, pp. 259-279, 2011.
[15] Kosec, G. and Šarler, B., H-Adaptive Local Radial Basis Function Collocation Meshless Method. *CMC: Computers, Materials & Continua*, **26**, pp. 227–254, 2011.
[16] Kosec, G. and Šarler, B., Local RBF collocation method for Darcy flow. *CMES: Computer Modeling in Engineering & Sciences*, **25**, pp. 197-208, 2008.
[17] Kosec, G. and Šarler, B., Solution of phase change problems by collocation with local pressure correction. *CMES: Computer Modeling in Engineering & Sciences*, **47**, pp. 191-216, 2009.

[18] Vertnik, R. and Šarler, B., Solution of incompressible turbulent flow by a mesh-free method. *CMES: Computer Modeling in Engineering & Sciences*, **44**, pp. 66-95, 2009.
[19] Armaly, B. F., Durst, F., Pereira, J. C. F. and Schönung, B., Experimental and theoretical investigation of backward-facing step flow. *Journal of Fluid Mechanics*, **127**, pp. 473–496, 1983.
[20] Chiang, T. P. and Sheu, T. W. H., A numerical revisit of backward-facing step flow problem. *Physics of fluids*, **11**, pp. 862, 1999.
[21] Chorin, A.J., A numerical method for solving incompressible viscous flow problems. *Journal of Computational Physics*, **2**, pp. 12-26, 1967.
[22] Gartling, D. K., A test problem for outflow boundary conditions—flow over a backward-facing step. *International Journal for Numerical Methods in Fluids*, **11**, pp. 953–967, 1990.
[23] Gresho, P. M., Gartling, D. K., Torczynski, J. R., Cliffe, K. A., Winters, K. H., Garratt, T. J., Spence, A. and Goodrich, J. W., Is the steady viscous incompressible two-dimensional flow over a backward-facing step at Re= 800 stable? *International Journal for Numerical Methods in Fluids*, **17**, pp. 501–541, 1993.
[24] Ramšak, M. and Škerget, L., A subdomain boundary element method for high-Reynolds laminar flow using stream function-vorticity formulation. *International Journal for Numerical Methods in Fluids*, **46**, pp. 815–847, 2004.
[25] Zhang, X. H, Ouyang, J. and Zhang, L., Characteristic based split (CBS) meshfree method modeling for viscoelastic flow. *Engineering Analysis with Boundary Elements*, **34**, pp. 163–172, 2010.
[26] Rahman, M. M. and Siikonen, T., An artificial compressibility method for viscous incompressible and low Mach number flows. *Internation Journal of Numerical Methods in Engineering*, **75**, pp. 1320-1340, 2008.
[27] Malan, A. G. and Lewis, R. W., An artificial compressibility CBS method for modelling heat transfer and fluid flow in heterogeneous porous materials. *International Journal for Numerical Methods in Engineering*, **87**, pp. 412-423, 2011.
[28] Traivivatana, S., Boonmarlert, P., Thee, P., Phongthanapanich, S. and Dechaumphai, P., Combined adaptive meshing technique and characteristic-based split algorithm for viscous incompressible flow analysis. *Applied Mathematics and Mechanics*, **28**, pp. 1163-1172, 2007.
[29] Hong, C. P., *Computer Modelling of Heat and Fluid Flow Materials Processing*, Institute of Physics Publishing Bristol, 2004.
[30] Kosec, G., Trobec, R., Depolli, M. and Rashkovska, A.: Multicore parallelization of a meshless PDE solver with OpenMP, ParNum 11, 2011.

This page intentionally left blank

Numerical investigation of swirl flow inside a supersonic nozzle

E. Eslamian, H. Shirvani & A. Shirvani
Faculty of Science and Technology, Anglia Ruskin University, UK

Abstract

This study reports the Computational Fluid Dynamics (CFD) results of a swirling flow induced by introducing a helical insert inside a supersonic nozzle. The CFD simulation shows a very complex unsteady, non-axisymmetric flow pattern for the swirl flow inside the nozzle. The flow is investigated by solving the Reynolds averaged Navier Stokes (RANS) equations with k-ω and Reynolds Stress Model (RSM) turbulence models to predict the flow patterns and the type of swirling flow. Computations are conducted for a range of nozzle pressure ratios with and without swirl inside the converging–diverging nozzle. The study has revealed a new understanding and data for flow features such as shock location, mass flow rate and anisotropic turbulence.
Keywords: swirl flow, supersonic nozzle, flow separation, CFD.

1 Introduction

Investigation of supersonic flow inside converging–diverging (C–D) nozzles has been the subject of several numerical and experimental studies in the past [1, 2] but there is not that much research on the effect of swirl flow inside C–D nozzles. Swirling flows which are very common in technical applications, such as turbo machinery, cyclones or separators, and they require sophisticated modeling.

The effect of swirl inside a nozzle can improve the mixing features of the flow by increasing turbulence and vorticity in the nozzle, which can be useful in combustion injectors and sand blast techniques; also swirl flow will change the shock structure and its interaction with the boundary layer and create a larger separation zone at the exit of a nozzle. These viscous and compressible phenomena affect the flow behavior inside and outside of a nozzle. Since

WIT Transactions on Engineering Sciences, Vol 74, © 2012 WIT Press
www.witpress.com, ISSN 1743-3533 (on-line)
doi:10.2495/AFM120121

experimental data for the swirl flow inside a high speed nozzle are scare, numerical results are vital for understanding the flow and for further analysis.

In this study the finite volume method is utilized (Fluent), to solve the governing equations of flow.

2 Numerical analysis

2.1 Nozzle geometry

The dimension of the nozzle with the flow inside which has been investigated is shown in Figure 1a. The length of the nozzle is 200mm and it has three sections. The first 64mm is the convergence section, then comes a 16mm section with constant 11mm diameter and this is followed by the divergence section with length 120mm and outlet diameter of 15mm. The computational domain which consists of the helical inlet and the nozzle is illustrated in Figure 1b. The helical section, Figure 1c, is used to create swirl flow inside the nozzle. The helical section has a 31.75mm diameter with length of 76.45mm; the spiral part has two revolutions with a start angle of 45 degrees.

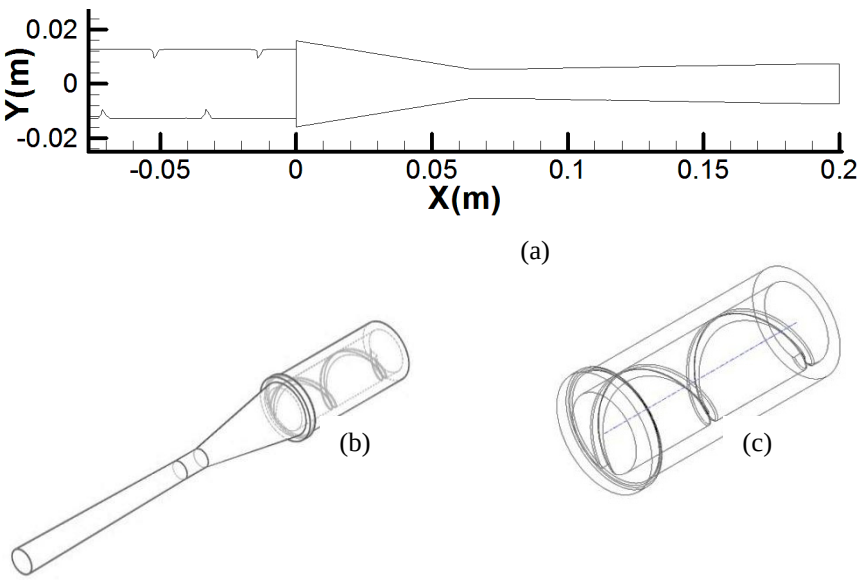

Figure 1: Geometry and dimensions of the computational domain.

2.2 Numerical model

Turbulence modelling is still one of the main problems of Computational Fluid Dynamics (CFD). The models mostly used for fluid phenomena are the standard k-ε and k-ω models. These Reynolds averaged Navier Stokes (RANS) models give adequate results for isotropic turbulence flows, and have been validated

with many experimental tests (Wilcox [3]). However, as we have highly swirling flow inside nozzle, there will be a considerable degree of anisotropy in the stress and dissipation tensors which causes a highly anisotropic eddy viscosity (Yajnik and Subbaiah [4]), so the isotropic turbulence model will not give precise results. To be able to capture anisotropic turbulence inside a nozzle we have to consider all Reynolds stress equations. The highest accuracy in turbulence is acheived by Direct Numerical Simulations (DNS), but this needs huge processing power. Large Eddy Simulations (LES) is another major turbulence model which lately has begun to grow in popularity and many academic and industry users deploy it for their research and applications. LES resolves all anisotropic turbulent structures both in time and space, and just leaves the small scales to be modelled by simple turbulence models (Ogor *et al.* [5]). However, we still need a lot of precessing power and a very fine mesh to use LES modelling.

The RANS models for anisotropic turbulence are limited to the modified k-ε and Reynolds Stress Model (RSM). We have used a realizable k-ε model, which contains an alternative formulation for eddy viscosity and uses a modified transport equation for dissipation rate (Shih *et al.* [6]) but the RSM model solves all six transport equations. In this research, the RSM gave more consistent results, and for a realizable k-ε method we need to carry out more research with a higher order scheme; therefore the focus is more on the RSM and the results shown here are based on the RSM.

For the RSM a second oreder upwind scheme is applied to the flow equations, but the turbulent kinetic energy, turbulent dissipation rate and Reynolds Stress are considered first order upwind.

The initial simulations were conducted with a steady method, but the convergence history of residuals showed unsteadiness which is in agree with the results of Xiao *et al.* [7]; the main reason for this is the separation of the flow at the exit of the nozzle. Therefore a transient solver is considered for the flow with 1e-5 time step intervals.

The air in the nozzle will reach $Ma > 1$, so compressibility is one of the main factors for the flow solver. The density based solver in Fluent gives more accurate results and has better convergence rate for compressible flows. It also captures more precicely the shock waves in the nozzle .

2.3 Governing equations

The density based solver from Fluent has been used to solve the governing equations of the flow. The conservative integral form of the continuity, momentum and energy equations for a single component fluid in an infinitesimal control volume is (Fluent [8]):

$$\frac{\partial}{\partial t}\int W dV + \oint [F - G].\, dA = \int H dV \tag{1}$$

where the vectors *W*, *F* and *G* are defined as:

$$W = \begin{Bmatrix} \rho \\ \rho u \\ \rho v \\ \rho w \\ \rho E \end{Bmatrix}, F = \begin{Bmatrix} \rho v \\ \rho v u + P\hat{\imath} \\ \rho v v + P\hat{\jmath} \\ \rho v w + P\hat{k} \\ \rho v E + P v \end{Bmatrix}, G = \begin{Bmatrix} 0 \\ \tau_{xi} \\ \tau_{yi} \\ \tau_{zi} \\ \tau_{ij} v_j + q \end{Bmatrix} \quad (2)$$

The vector H contains all of the source terms such as the body forces. In the above equation ρ is density, v is velocity, E is total energy per unit mass and P is pressure. τ and q are the viscous stress tensor and heat flux, respectively. In the density based solver of Ansys Fluent, to overcome the poor convergence rate of high speed flows, a preconditioning technique has been deployed. The preconditioning technique modifies the time derivative term of equation (1) by multiplying it with a preconditioning matrix. This will rescale the acoustic speed of the governing equations in order to mitigate the numerical stiffness encountered in low Mach numbers.

2.3.1 Turbulence equations

In Reynolds averaging the variables of exact N-S equations are substituted with mean and fluctuation components. By substituting $u_i = \overline{u_\iota} + u'_i$ into the momentum equation, where $\overline{u_\iota}$ is the mean and u'_i is the fluctuating velocity components, the time average of the momentum equation can be shown as:

$$\frac{\partial}{\partial t}(\rho u_i) + \frac{\partial}{\partial x_j}(\rho u_i u_j) = -\frac{\partial P}{\partial x_i} + \frac{\partial}{\partial x_j}\left[\mu\left(\frac{\partial u_i}{\partial x_j} + \frac{\partial u_j}{\partial x_i} - \frac{2}{3}\delta_{ij}\frac{\partial u_l}{\partial x_l}\right)\right] + \frac{\partial}{\partial x_j}(-\rho\overline{u'_\iota u'_j}) \quad (3)$$

In order to close equation (3), the Reynolds stress term $(-\rho\overline{u'_\iota u'_j})$ must be modelled. In this study we have used the RSM, which uses the exact transport equation for the transport of the Reynolds stresses, $-\rho\overline{u'_\iota u'_j}$, which can be written as:

$$\frac{\partial}{\partial t}\left(\rho\overline{u'_\iota u'_j}\right) + C_{ij} = D_{T,ij} + D_{L,ij} + P_{ij} + G_{ij} + \phi_{ij} - \epsilon_{ij} + F_{ij} \quad (4)$$

where C_{ij} is the convection term, $D_{T,ij}$ stands for turbulent diffusion, $D_{L,ij}$ is the molecular diffusion term, P_{ij} equals the stress production, G_{ij} is buoyancy production, ϕ_{ij} stands for pressure strain, ϵ_{ij} is the dissipation and F_{ij} is production by the system rotation. Four parameters, $D_{T,ij}$, G_{ij}, ϕ_{ij} and ϵ_{ij}, have to be modelled in order to close equation (4), but the rest of the parameters do not required modelling. The turbulent diffusion $(D_{T,ij})$ has been modelled with the simplified model of Daly and Harlow [9]:

$$D_{T,ij} = \frac{\partial}{\partial x_k}\left(\frac{\mu_t}{\sigma_k}\frac{\partial\overline{u'_\iota u'_j}}{\partial x_k}\right) \quad (5)$$

where μ_t is the turbulent viscosity. The pressure strain term has been modelled according to the proposal by Gibson and Launder [10]. Buoyancy production (G_{ij}) for an ideal gas is modelled as:

$$G_{ij} = -\frac{\mu_t}{\rho Pr_t}\left(g_i \frac{\partial \rho}{\partial x_j} + g_j \frac{\partial \rho}{\partial x_i}\right) \quad (6)$$

The dissipation rate (ϵ_{ij}) is modelled as follows:

$$\epsilon_{ij} = \frac{2}{3}\delta_{ij}(\rho\varepsilon + Y_M)\,,\; Y_M = 2\rho\varepsilon M_t^2 \quad (7)$$

In equation (7) Y_M is an additional dilatation dissipation term according to the model by Sarkar and Balakrishnan [11].

2.4 Numerical results

The results for two pressure ratios (P_{in}/P_{out}) of 2 and 3 are shown here. At both pressure ratios there is an overexpanded supersonic nozzle, where the shock waves occur inside the nozzle. The Mach number contours for a pressure ratio of 2 in two time steps are illustrated in Figure 2. Experimental and numerical simulations represent two separation patterns for an overexpanded nozzle, the Free Shock Separation (FSS) and Restricted Shock Separation (RSS) (Hadjadj and Onofri [12]). In FSS the separation region extends from the separation point to the end of the nozzle, but in RSS the separation zone reattaches to the surface and creates recirculation bubbles. For a pressure ratio of 2 the FSS pattern can be seen at the upper side of the nozzle wall (Figure 2).

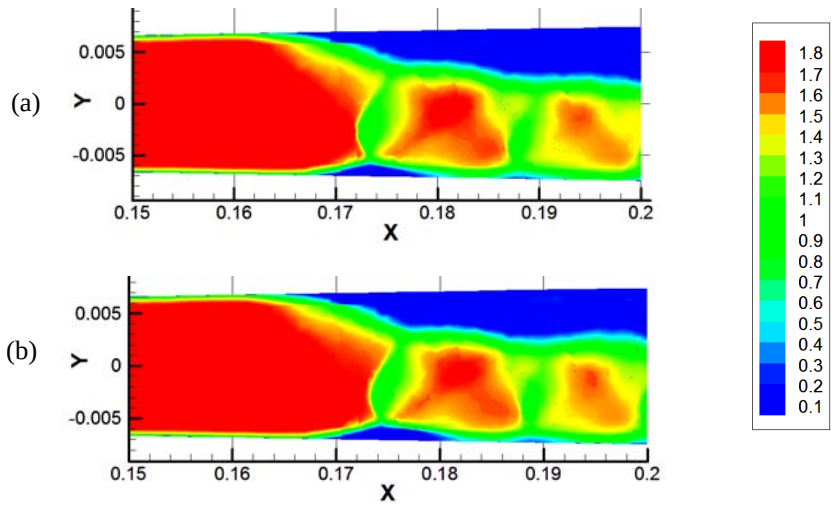

Figure 2: Mach number contours for a pressure ratio of 2 at (a) t=0.8e-2s and (b) t=1.8e-2s.

Because of asymmetry which is due to the Coanda effect, flow tends to attach to the surface and creates a RSS pattern on the down side of the nozzle wall. The separation zone starts at the interaction point between the oblique shock wave and the nozzle wall which creates an adverse pressure gradient. Reflection of the

oblique shock wave on the shear layer generates expansion fans. To provide more detail of the separation nozzle, Figure 3 illustrates the flow and shock wave pattern for the pressure ratio of 2. Since the separation zone is large the flow remains attached to the down side of the nozzle wall, and therefore the difference between two time steps is mostly about the change in the shear layer position.

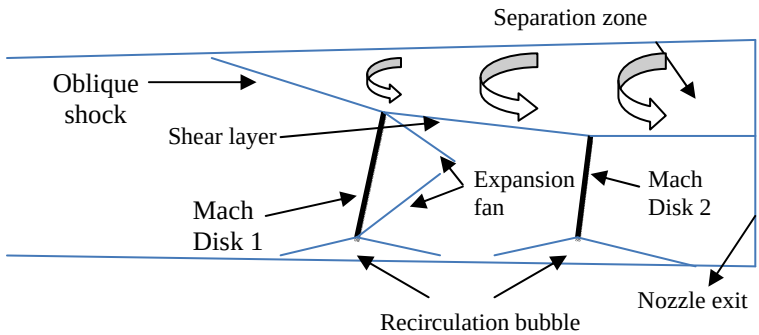

Figure 3: Schematic of the shock wave structure for the pressure ratio of 2 at the exit of the nozzle.

By increasing the pressure ratio to 3 the oblique shock waves become weaker so the pressure gradient behind it will significantly reduce and the separation point moves downstream of the nozzle. Contours of Mach number for two time steps at the exit of the nozzle are shown in Figure 4.

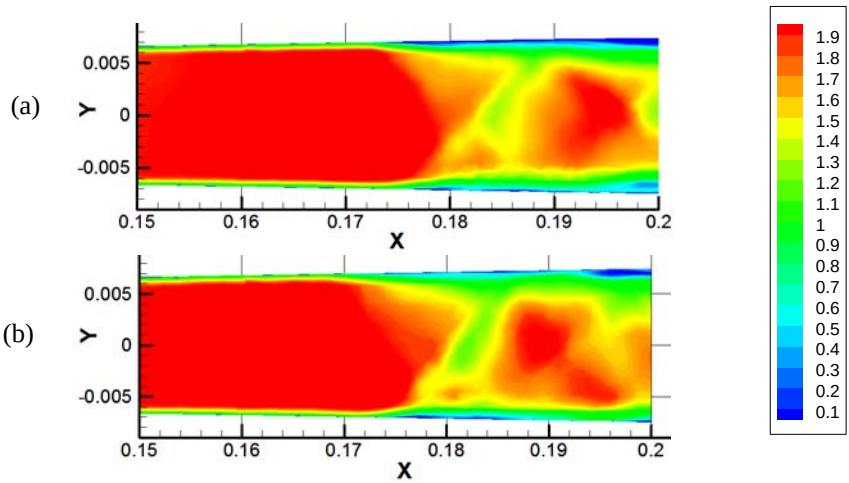

Figure 4: Mach number contours for the pressure ratio of 3 at (a) t=o.8e-2s, (b) t=2.8e-2s.

The flow pattern still remains asymmetric, and the second Mach disk moves out of the nozzle. At t=0.8e-2, Figure 4a, the second Mach disk is at the exit of the nozzle but in t=2.8e-2, Figure 4b, it is completely out of the nozzle. Calculation of 1000 more time steps does not show any major change to the shock wave structure apart from the shear layer movement. The reflection of the shock wave on the shear layer creates expansion fans.

By adding swirl to the flow the shock wave structure becomes weaker, and instead of one strong shock wave there will be series of shock waves and expansion fans at the exit of the nozzle. This can be seen from the static pressure diagram at the centre of the nozzle which for a pressure ratio of 2 is shown in Figure 5. Also the start point of the shock wave has been moved upstream for the swirl flow. The results are compared with experimental data from Abbasalizadeh [13] for the same nozzle without the swirl that shows good agreement with CFD calculations.

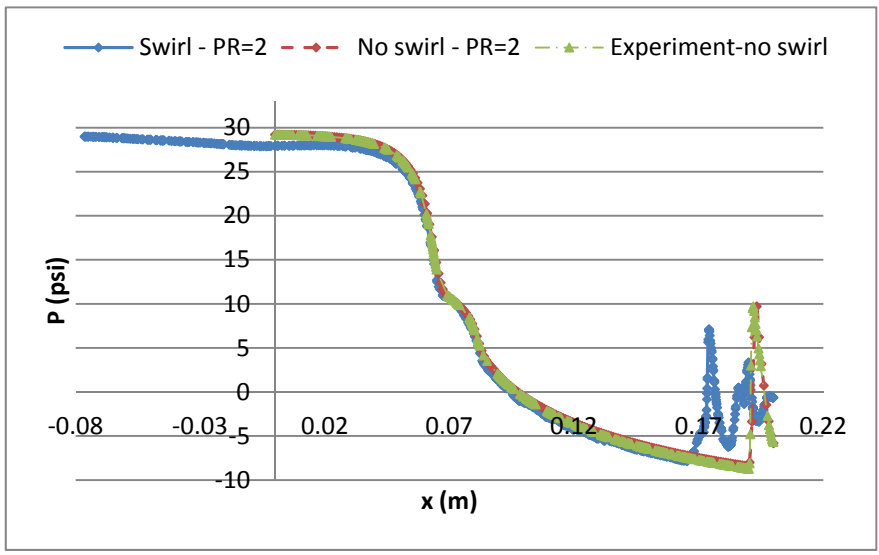

Figure 5: Static pressure diagram for pressure ratio 2 at the centre of nozzle.

For a pressure ratio of 3 the static pressure diagram is shown in Figure 6. We can see that for the nozzle without swirl there is no shock wave inside the nozzle, but by adding swirl conditions, the nozzle remains overexpanded; however, the shock waves become weaker compared to those for a pressure ratio of 2. The experimental data from Abbasalizadeh [13] for the nozzle without swirl also show that there is no shock wave inside the nozzle and the nozzle is in an underexpanded condition.

Apart from the exit of the nozzle for both pressure ratios the rest of the centre line static pressure of the nozzle with swirl matches that of the nozzle without swirl.

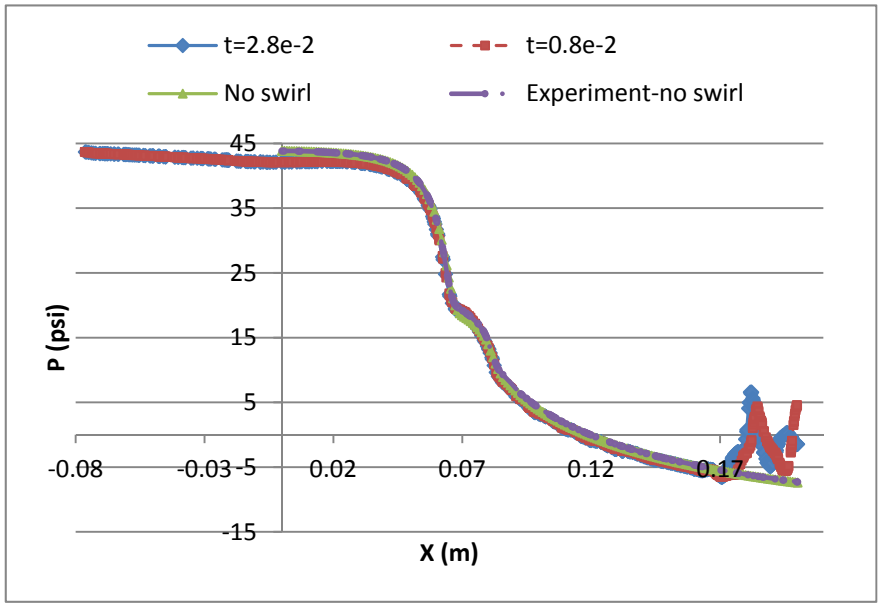

Figure 6: Static pressure diagram for the pressure ratio of 3 at the centre of the nozzle.

2.5 Numerical validation

Since it is very difficult to carry out experimental tests inside a nozzle and there are little experimental data for supersonic swirl flow inside a nozzle, the validation process is very important to gain confidence in the results. To check grid dependency all the simulations have been run for 200k, 450k and 800k cells with refinement at the boundaries and exit of the nozzle to capture the boundary layer and shock waves. We obtain similar results for three different meshes. Considering the computational effort, the results shown here are based on a 400k mesh. The residuals are all reduced at least by an order of 4. Because of the 3D complex geometry, it was difficult to get a high quality hexahedral mesh; therefore to obtain a good quality mesh a tetrahedral mesh with a prism layer at the boundaries has been used. The minimum quality for the mesh was 0.84. In addition, the mass flow rate through the inlet and outlet is checked to ensure that conservation of mass is observed. The net mass flow rate through the system is under 1%.

The maximum wall yplus value for the CFD tests was 50, and the RSM which is a core-turbulent model gives better results with a yplus value in the log-low region (y+>30 to 60) (Salim and Cheah [14]), so the yplus value is satisfied for most of the nozzle wall.

3 Conclusion

The CFD analysis of swirling flow inside a converging–diverging nozzle is studied at pressure ratios of 2 and 3. For turbulence modelling, the RSM has been used to solve seven Reynolds stress equations. The following conclusions can be drawn:

1. Numerical solutions show swirling flow has unsteady asymmetric behaviour, with a separation zone at the exit of the nozzle, and the main reason for asymmetry is the Coanda effect.
2. Because of anisotropic turbulence, a two equation model will not solve all the scales of turbulent flow, so the RSM with a second order scheme is selected for turbulence modelling.
3. By increasing the pressure ratio to 3 the shock waves move out of the nozzle in no swirl conditions, but by adding swirl condition to the flow the nozzle design criteria will be changed and the nozzle still remains overexpanded.
4. The centre line static pressure shows in swirl conditions that, instead of having one strong shock wave, there are a series of weak shock waves and expansion fans.

References

[1] Anderson, J. D., Modern compressible flow with historical perspective, New York: McGraw-Hil, 2003.
[2] Anderson, J. D., Hypersonic and high temperature gas dynamics, American Institute of Aeronautics and Astronautics, 2000.
[3] Wilcox, D. C., Turbulence Modelling for CFD, California: Griffin, 1994.
[4] Yajnik, K. and Subbaiah, M., "Experiments on swirling turbulent flows. Part 1. Similarity in swirling flows," *Journal of Fluid Mech*, vol. 60, no. 4, pp. 665-687, 1973.
[5] Ogor, I. B., Gyllenram, W., Ohlberg, E., Nilsson, H. and Ruprecht, A., "An Adaptive Turbulence Model for Swirling Flow," in *Conference on Turbulence and Interactions*, Porquerolles, France, 2006.
[6] Shih, T., Liou, W., Shabbir, A., Yang, Z. and Zhu., J., "A New k -e Eddy-Viscosity Model for High Reynolds Number Turbulent Flows - Model Development and Validation," *Computers Fluids*, vol. 24, no. 3, pp. 227-238, 1995.
[7] Xiao, Q., Tsai, H. and Papamoschou, D., "Numerical Investigation of Supersonic Nozzle Flow Seperation," *AIAA*, pp. 532-541, 2007.
[8] Ansys, "Ansys Fluent 13 User's Guide," Ansys, Inc, 2010.
[9] Daly, B. and Harlow, F. H., "Transport Equations in Turbulence," *Physics of Fluids*, vol. 13, no. 11, p. 2634–2649, 1970.
[10] Gibson, M. and Launder, B., "Ground Effects on Pressure Fluctuations in the Atmospheric Boundary Layer," *Journal of Fluid Mechanics*, vol. 86, no. 3, p. 491–511, 1978.

[11] Sarkar, S. and Balakrishnan, V, "Application of a Reynolds-Stress Turbulence Model to the Compressible Shear Layer," NASA Langley Research Center, Virginia, 1990.
[12] Hadjadj, A. and Onofri, M., "Nozzle Flow Separation," *Shock Waves*, pp. 163-169, 2009.
[13] Abbasalizadeh, M., Investigation of Three Phase Nozzle flow In an Innovative Sand Blasting System, Chelmsford: Anglia Ruskin University, 2011.
[14] Salim, M. S. and Cheah, S., "Wall yplus Strategy for Dealing with Wall-bounded Turbulent Flows," in *Proceeding of the International MultiConference of Eng. and Comp.*, Hong Kong, 2009.
[15] Guo, H.-F., Chen, Z.-Y. and Yu, C.-W., "3D numerical simulation of compressible swirling flow induced by means of tangential inlets," *International Journal For Numerical methods in Fluids*, pp. 1285-1298, 2008.
[16] Najafi, A., Saidi, M., Sadeghipour, M. and Souhar, M., "Numerical analysis of turbulent swirling decay pipe flow," *International Communications in Heat and Mass Transfer*, pp. 627-638, 2005.

Numerical study of battle damaged two-dimensional wings

S. Djellal, T. Azzam, M. Djellab & K. Lakkaichi
Fluid Mechanics Laboratory Polytechnical School Bordj El Bahri, Alger, Algeria

Abstract

The flow around a NACA 64_1-412 airfoil with circle damage is numerically investigated using the Ansys Fluent package. Several diameter values are considered for the damage which is located at either quarter or mid chord. The numerical domain is covered with a multiblock structured hexagonal grid consisting of 344,680 cells in the undamaged case and 351,540 cells in the damaged case. Inside the damage hole, a structured tetragonal mesh is used. Turbulence effects are taken into account via the k-ε model. The results show that the presence of the damage hole decreases the lift coefficient and increases the drag coefficient, resulting in a loss of airfoil performance (fineness decrease). The numerical simulations show that the flow through the damage corresponds either to a weak or a strong jet. In the first case an attached wake forms giving the smallest change in the force coefficients whereas the second case shows a separated wake with a reverse flow giving the highest force coefficient change. The present paper also compares the structure of the damage through flow with previously published experimental results. Finally, the numerical solution is qualitatively and quantitatively validated using available experimental results.
Keywords: damage, drag, lift, strong jet, weak jet, undamaged.

1 Introduction

The survivability of an aircraft is becoming one of the key aircraft design requirements [1] and is dependant upon its vulnerability to damage caused by a variety of threats. Published works to date in this field focus mainly on two-dimensional wings.

WIT Transactions on Engineering Sciences, Vol 74, © 2012 WIT Press
www.witpress.com, ISSN 1743-3533 (on-line)
doi:10.2495/AFM120131

The first study by Irwin at Loughborough University was extensively reported [2, 3] and by many other authors; Render *et al*. [4], Mani and Render [5] and Djellal and Ouibrahim [6]. Recently Saaedi *et al*. [7] published a numerical study in this field.

In this investigation, we are interested in the aerodynamic performance losses caused to a two dimensional wing by the impact of battle damage. For this matter, we investigate by means of numerical methods the undamaged case and damaged case by considering the variation of the hole diameter and its chordwise position.

In this work, we analyse the flow field inside the damage hole and also around the undamaged and damaged aerofoil. In order to validate the numerical results, obtained values have been compared with those of experimental investigations led by the previous authors [2, 5, 6, 8].

2 Damage modelling

The most common type of damage used in simulations is the circular hole [6]. The study of other shapes reported by Mani and Render [5] has not shown noticeable differences.

Damage size can be expressed in terms of a percentage diameter *d* to the local chord length *c*. The range of damage sizes varies from 0.1 to 0.4 c [2] and, for our simulations, two diameters, 0.2, 0.3, have been considered and both were located at mid span.

NACA 64_1-412 aerofoil experimented firstly by Render and his colleagues serves as the model's cross section. The aerofoil's chord and the wing's span are 200 mm and 450 mm respectively (Fig. 1).

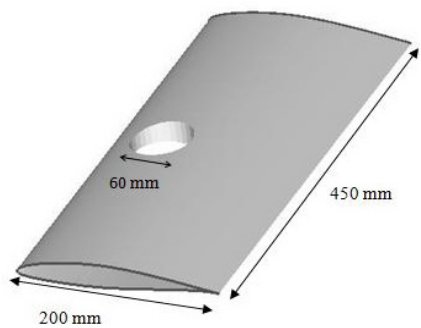

Figure 1: Circle damaged wing at quarter chord.

We only considered wing damaged at the quarter and the mid-chord, because they produced the greatest adverse influence on aerodynamic performance [2].

3 Modelling and grid generation

The numerical domain is made discrete by two approaches: (1) structured tetragonal cells for circle damage (2) multiblock structured hexagonal cells are applied for the remainder damaged aerofoil. The finite volume discretisation method is used in 'Fluent' numerical code.

Following a suitable study of grid sensitivity, Number of cells applied in this numerical domain is 344,680 cells in the undamaged case and 351,540 cells in the damaged case. It is worth mentioning that the used structured mesh that is able to capture the boundary layer was a complicated and time consuming process. The multiblock approach generated in Gambit allows via the interface condition to reduce the cells number and consequently the time process.

The results did not show a major difference between aerodynamic coefficients, pressure distribution or other phenomena in three grid types. The calculations with such amount of grids are made possible with the use of an ordinary 2-core processors, 2.5 GHz computer.

4 Boundary conditions

Five types of boundaries are used in this model: Velocity inlet, pressure outlet, symmetry, interface and wall. Dimensions of numerical domain are considered big enough to damp turbulences before reaching the domain boundaries. The boundary conditions for lower and upper surface of the aerofoil are considered as solid wall.

The wind tunnel used for the experiments is a low subsonic low turbulence (0·1% of turbulence intensity) wind tunnel at Loughborough University and the dimensions of the test section are: 45cm × 45cm× 1·2m. The test section velocity is $35ms^{-1}$.

5 Numerical solution characteristics

The flow in this analysis is assumed to be steady, incompressible, and turbulent. For modelling the viscous turbulent flow, *k*-ε turbulence model is applied. SIMPLE algorithm is applied to solve these two equations. Standard wall functions are also used for the areas close to wall (parietal distance $y^+ = 40$). For the turbulence parameters at the inlet and the outlet, we use the method which gives the intensity (0.1%) [2] and the viscosity ratio $\nu_t/\nu = 5$ after tests. This value is chosen for a stall detection reason.

6 Qualitative discussion and validation

In this part the velocity vectors and pressure coefficient contours are used to provide a good understanding of the flow field.

As evident in Figure 3, the pressure difference is higher and this will lead to a stronger jet which will be explained later. The sudden changes in the rear portion of the damage hole are because of the local stagnation of the flow. The gap in the damage results was where the damage hole cut through the surface.

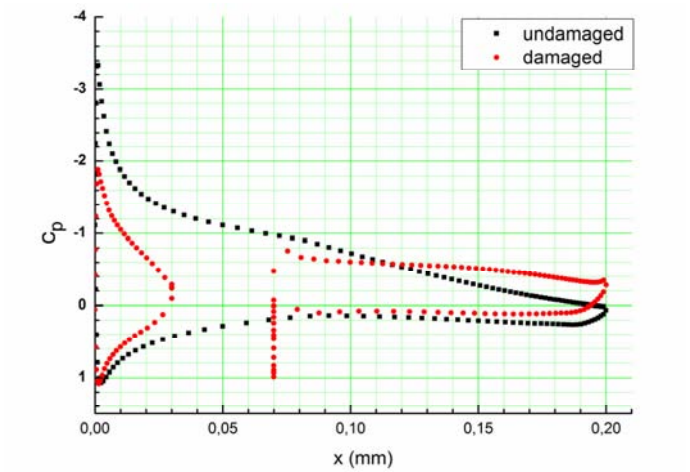

Figure 2: Wing centreline pressure coefficient [20%c at quarter-chord for 8°].

Figure 3(a) shows the velocity vectors around the damaged aerofoil from lateral view for 0°deg incidence angle.

There is a weak jet exiting the damage hole which formed an attached wake behind the damage hole.

Because of the pressure difference between two surfaces of the aerofoil, the flow would like to penetrate from the lower surface of the aerofoil to the upper surface and this flow through the damage is pushed through the damage hole and added to the damage wake.

Figure 3(b) shows the velocity vectors of the numerical solution on the upper surface of the aerofoil. At the rear edge of the damage hole, there are two vortex centres, observed to be contra-rotating vortices approximately symmetrical about the hole centreline.

These vortices are the results of interaction between jet flow exiting the damage and free stream. The weak jet exited from the rear edge of the hole was immediately bent over, forming an attached wakes to the upper surface. When the incidence angle is increased higher than 0° degree, the jet no longer immediately bent over upon exiting the hole and penetrated to the free stream. Finally a separated region is formed between the jet and upper wing surface.

Figures 4(a) and 4(b) that are for incidence angle of 8°, show the separated region and detached wake of strong jet.

It is noticeable that the stall angle of an undamaged aerofoil is normally 12°deg but for damaged aerofoil this angle shifted to 14°deg.

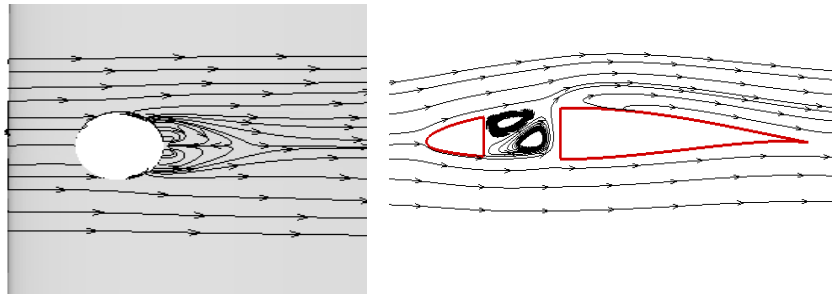

a) Upper view b) Lateral view

Figure 3: Velocity vectors for damaged aerofoil (0° deg).

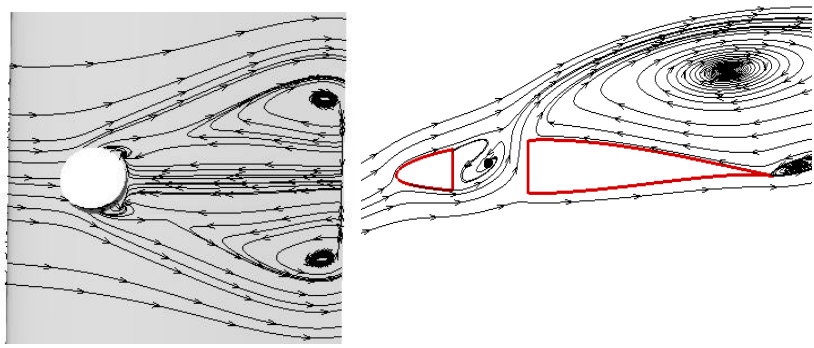

a) Upper view b) Lateral view

Figure 4: Velocity vectors for damaged aerofoil (+8 deg).

The above numerical results for the velocity vectors on the upper surface of the aerofoil are compared to the results of flow visualisation that was implemented by Render *et al.* [4] and Mani and Render [5]. In Figure 5 that is for damaged aerofoil, it represents experimental results. The results are presented for incidence angles of 0°deg and 8°deg that represent weak and strong jet respectively.

As evident, the general feature of the flow fields obtained by numerical analysis (figures 3 and 4) are in a suitable consistency with experimental results. It is clear in both flow visualisations that the width of the wake behind the damage hole increases with incidence angle because of the strength of exiting jet.

There are also two large surface wakes in 8°deg incidence angle behind the damage hole which are clear in experimental and numerical results. In both cases they are counter rotating vortices.

Some phenomena such as laminar separation and transition and thus, the laminar bubble can not be captured by the software which are visible in the side of the damage hole in experimental results.

The differences between experimental and numerical results are due to numerical error associated with numerical solution.

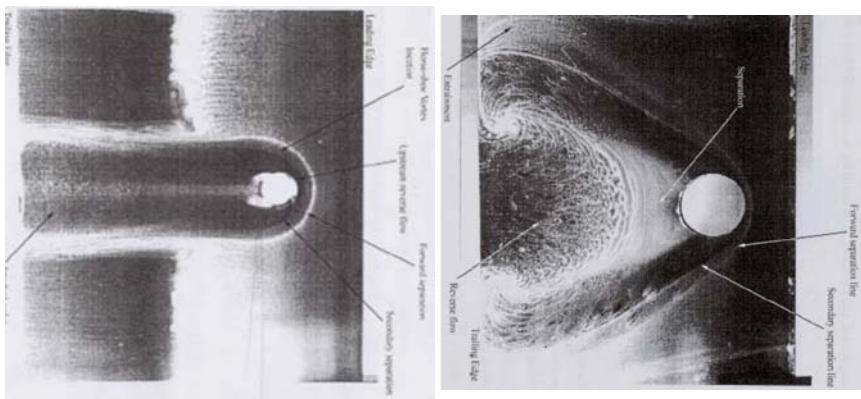

a) Weak jet b) strong jet

Figure 5: Experimental flow field for damaged aerofoil at 0° deg and 8 deg incidence angles.

7 Quantitative discussion and validation

In this section the quantitative results are investigated using dC_L and dC_D, *vs* α diagrams. For a better perception and assessment of the effects of the damage; the corresponding above results are transcribed in terms of increments of losses of C_L and C_D. The increments dC_L and dC_D are defined from the undamaged state as follows:

$$dC_L = C_{L_{damaged}} - C_{L_{undamaged}}$$

$$dC_D = C_{D_{damaged}} - C_{D_{undamaged}}$$

Before studying the influence of damaged aerofoil, analysis on the undamaged model was done. The results obtained were found to agree reasonably well with those found in the literature [2].

This numerical procedure allows us to capture the stall phenomenon, for instance, the lift coefficient reaches a maximum value of 1.20 for an angle of stall of 12°. Also, the angle of zero lift is close to -2.5°, which is consistent with this non symmetric profile. The coefficient of drag reaches a minimal value of 0.016 for the angle 0°.

Now we consider the damaged aerofoil to explain the influence of the damage on the aerodynamic characteristics of the aerofoil and the effect of both diameter and chordwise position of damage expressed only in increments of lift and drag coefficients as explained above.

In figures 6 and 7, we present, simultaneously, the influence of both diameter and chordwise position of damage with the experimental and numerical curves. One can see an increase of the C_D over most of the incidence range except close to the stall angle where part of the jet goes through the hole. The strength of the jet is in direct relation with incidence angle.

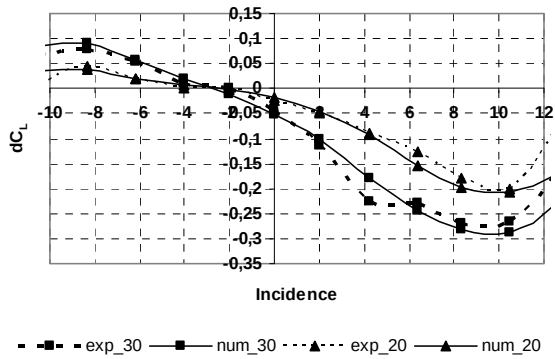

Figure 6: Influence of damage diameter at quarter chord on lift coefficient (experimental and numerical solutions).

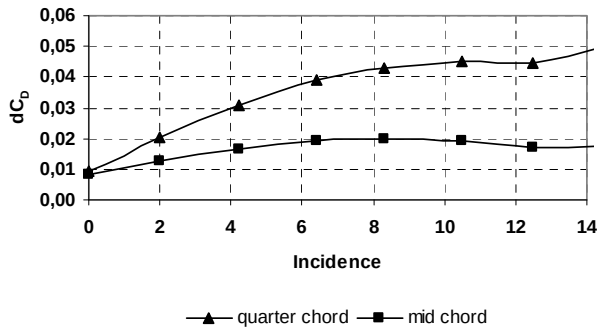

Figure 7: Chordwise influence of damage on drag coefficient (numerical results).

There are two mechanisms for the drag increase. For small angles of incidence, the attached jet increases friction drag while for higher angles of incidence, the strong jet forms a separated wake which increases form drag. An additional pressure drag is produced by the damaged hole which creates a positive pressure increment on the wing internal surface.

Results also show a reduction in the amplitude of C_L over the entire range of positive incidence angle. This reduction in C_L is due to the hole through flow which affects the distribution of pressure at the upper surface.

Lift loss for the quarter chord damage is higher than the mid-chord damage. This is expected because when we approach the leading edge; the suction pressure on the upper surface is strongly reduced affecting consequently the lift coefficient. The drag increase is higher for the quarter chord damage, where the chord wise extent of the wake is greater than seen for the mid-chord.

For the effect of diameter, results show that lift increments dC_L against incidence for different values of the diameter and over the positive incidence range ($\alpha > -2.5°$), an increase of the hole size results in a decrease of the lift coefficient.

This is expected because a larger damage size allows a greater through flow, and perturbs even more the pressure distribution at the upper surface. Increasing the hole diameter changes the jet shape from weak-jet to strong-jet.

The drag also increases with hole diameter over the entire incidence range. Indeed, an increase of the diameter increases the wake area size. In order to validate the numerical results and to assess that the numerical procedure is performed truly, the experimental coefficients are also required.

The aerodynamic coefficients for damaged aerofoil from numerical solution are compared to experimental coefficients of circle damaged aerofoil that were available in [2] and [3]. It is observed that the trends of experimental and numerical curves in the two figures are so similar to each other and there is a very good consistency between the curves. In the worst case, the difference between the values of C_L and C_D at the high incidence close to the stall is less than 10%. In this incidence angle, the numerical error is at the highest value because of stall phenomenon and causes this difference.

The difference between numerical and experimental results that is observable in figure 6 is because of numerical error. Generally, the results show that the numerical solution has no major error in modelling and solving the equations.

The constant difference between two curves is originated from numerical sources such as turbulence modelling, boundary-layer capturing and truncation error. It can be concluded from this diagram that numerical solution has been performed truly and physical phenomena are correctly captured.

8 Conclusion

In this paper the various damages have been studied comprehensively by numerical investigation and the results have been validated using the relevant experimental results. The multi-block grid allows us to reduce time consumption and enhances consistency and accuracy. It is concluded that the damages (circle damage) give a reduction in lift and an increase in drag. These variations depend on the incidence angle and the diameter (jet exiting from the damage hole). The numerical simulation gives accurate results comparatively to experimental results.

References

[1] Ball, R. E., *The Fundamentals of Aircraft Survivability Analysis and Design*, 2nd ed., AIAA Education Series: Reston, VA, 2003.
[2] Irwin, A. J. & Render, P. M., The influence of mid-chord battle damage on the aerodynamic characteristics of two-dimensional wings, *The Aeronautical Journal*, **104(1033)**, pp.153–161, 2000.
[3] Irwin, A. J., Render, P. M., McGuirk, J. J., Probert, B. & Alonze, P. M., Initial investigation into the aerodynamic properties of a battle damaged wing. *13th AIAA Applied Aerodynamics Conference*, AIAA Paper No. 95-1845, 1995.
[4] Render, P. M., De Silva, S., Walton, A. J. & Mani, M., Experimental investigation into the aerodynamics of battle damaged airfoils, *Journal of Aircraft*, **44(2)**, pp.539–549, 2007.
[5] Mani, M., & Render, P. M., Experimental investigation into the aerodynamic effects of airfoils with triangular and star shaped through damage," AIAA Paper 2005-4978, June 2005.
[6] Djellal, S., & Ouibrahim, A., Aerodynamic performances of battle-damaged and repaired wings of an aircraft model", *Journal of Aircraft*, **45(6)**, pp.2009–2023, 2008.
[7] Saaedi, M., Ajalli, F. & Mani, M., A., Comprehensive numerical study of battle damage and repairs upon the aerodynamic characteristics of an aerofoil, *The Aeronautical Journal*, **114(1158)**, August 2010.
[8] Djellal, S., Effects of Battle Damage Repairs on Aerodynamic of a wing, Sabbatical leave report, Aeronautical and Automotive Engineering Department, Loughborough University, 2004.

This page intentionally left blank

Simulation of fluid-structure interaction for an elastic cylinder in an axial flow

Z. G. Liu[1], Y. Liu[1] & J. Lu[2]
[1]*Department of Mechanical Engineering, Hong Kong Polytechnic University, China*
[2]*College of Engineering, City University of Hong Kong, China*

Abstract

The fluid-structure interaction for an elastic cylinder in an axial flow was studied numerically with the ALE method and the LES turbulence model. The commercial CFD software Fluent is used as the fluid solver and the Euler-Bernoulli beam solver is embedded into Fluent by its user defined functions (UDF). Two types of cylinder are included in this study. The motion for the first type of cylinder is constrained in one lateral direction and for the second in two lateral directions. The two types of cylinder are both released from their equilibrium state. When the stiffness is kept large enough, only weak oscillatory is induced by the flow. However, the motion of the cylinder induced by the flow may become unstable in the form of either buckling or oscillatory, when the stiffness becomes small enough. In this study, it is found that with the same simulation parameters the first type of cylinder is buckled and the second has an oscillatory. When buckled, the cylinder is located at a new state with weak oscillatory. The oscillatory after the instability has much larger amplitude than that before the instability.
Keywords: CFD, fluid-structure interaction, fluidelastic instability, buckling, flutter.

1 Introduction

One of the most classical subjects in fluid mechanics is the flow over cylinder, by which many interesting and significant phenomena are discovered such as Karman vortex streets [1] and also by which, for example, one can get the Kutta-Joukowski theorem, one of the most basic theorems in aerodynamics [2].


WIT Transactions on Engineering Sciences, Vol 74, © 2012 WIT Press
www.witpress.com, ISSN 1743-3533 (on-line)
doi:10.2495/AFM120141

However, this is almost for a rigid cylinder and the flow past a deformable cylinder attracts more and more interest of researchers due to not only its academic importance but also a lot of applications in engineering such as nuclear station design, building and so on. In this case, the fluid-structure interaction (FSI) will arise. FSI is a big topic and includes many aspects, nevertheless in this paper we just focus on a slender deformable cylinder subjected to axial flow.

This problem has been studied by many researchers and a good recent review was conducted by Wang and Ni in [3], where they also reviewed other FSI systems besides the system in this paper. In 1966, Paidoussis [4] developed a theory to deal with the dynamics for a single cylinder subjected to axial flow based on the Lighthill theory [5], which was used to get the force related to added mass, and Taylor's theory [6], which was applied to calculate viscous force imposed on the cylinder. The two kinds of force related to fluid flow and other kinds of force all were imposed on the cylinder regarded as an Euler-Bernoulli beam in his theory [4]. Based on his theory, Paidoussis [4] concluded that the stability of the system is determined partly by the dimensionless velocity, the definition of which will be written in the following, i.e. the flow damps the vibration for small dimensionless velocity while the cylinder may become instable, either in the form of buckling or flutter, when this parameter becomes large enough. He also conducted experiment to check his theory [7]. Taking gravity into account and modifying frictional force, Paidoussis also developed his theory further [8], however still a linear theory, which was mended further by Lopes *et al*. [9] into a nonlinear one for cantilevered cylinder in axial flow. The basic conclusion based on this nonlinear theory and that based on the linear theory have no crucial differences [10, 11]. In addition, the idea of Paidoussis's deriving his theory can be extended to several cylinders subjected to axial flow [12–14].

When the flow velocity is small, the cylinder could vibrate but with small amplitude. This kind of vibration, often called sub-critical vibration, is related to the perturbation of flow field [15, 16]. Some former researchers used semi-empirical methods to predict the amplitude of this kind of vibration [17–19]. But one must have the loading distribution available from experiments in order to adopt those methods in practice.

It is very manifest that one should consider both the fluid flow field and the structure dynamics when he deals with FSI. In some simple cases, one can get an analytic solution for the FSI system [20]. But unfortunately, on the other hand, in the most cases one can not get a fluid flow field solution to give enough information to the structure, even if the structure is not of complexity, e.g. the FSI system in this paper, a cylinder subjected to axial flow. Even in the theories mentioned above, the flow field is actually obtained based on some assumptions. Thus in this paper, we simulate numerically the FSI system shown in fig. 1, namely solve the fluid flow field in the arbitrary Lagrange-Euler (ALE) frame with CFD and the cylinder dynamics equation numerically. The paper is divided into four parts. The model and governing equations will be introduced in the

second part, followed is the third part, where the numerical details will be illuminated. In the last part, we will discuss the results and make a brief conclusion.

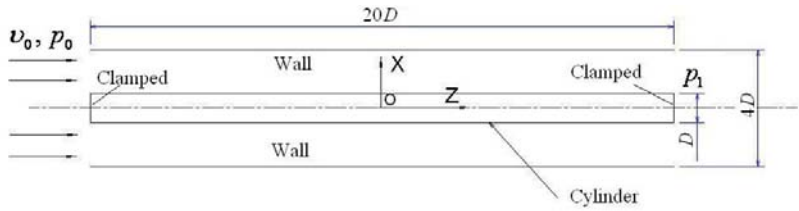

Figure 1: Schematic model.

2 Model and governing equations

The FSI system is shown in fig. 1, where D denotes the outer diameter of the cylinder. The cylinder clamped at its two ends, 20D long with its inner diameter 0.88D, is located in the fluid flow confined by a cylindrical pipe that is the same long as the cylinder with 4D diameter. The fluid could flow from one end to the other, inducing the vibration of the cylinder. In this paper, we study two cases for the model, in the first of which the cylinder is constrained only to vibrate in one lateral direction, while in the second of which the cylinder can vibrate in two lateral directions.

For the different cases respectively, the same parameters are adopted in the simulation. The main parameters are listed in table 1, where the dimensionless velocity υ and the mass ratio β are defined by eqns. (7) in section 4. The Reynolds number Re is based on the hydraulic diameter, which is 3D, and the inlet flow velocity υ_0.

Table 1: The parameters of calculation.

Case	1		2	
Re	8×10^4			
υ	6.0173	8.8997	6.0173	8.8997
β	0.4699	0.4699	0.4699	0.4699

First, it should be noted that the fluid flow velocity here is small and there is no need to consider the compression of the fluid. Therefore the incompressible Navier-Stokes (N-S) equations are one of the bases. Generally speaking, the fluid domain deforms in the process of simulation due to the deformation of the interfaces between the fluid and structure domains. To take into account the deformation of the fluid domain essentially, one method for CFD is rewriting the N-S equations as arbitrary Lagrange-Euler form, i.e. ALE N-S equations [20, 21]:

$$\begin{cases} \nabla \cdot \boldsymbol{\upsilon} = 0 \\ \rho \dfrac{\partial \boldsymbol{\upsilon}}{\partial t} + \rho(\boldsymbol{\upsilon} - \hat{\boldsymbol{\upsilon}}) \cdot \nabla \boldsymbol{\upsilon} = -\nabla p + \mu \nabla^2 \boldsymbol{\upsilon} \end{cases} \tag{1}$$

where t, $\boldsymbol{\upsilon}$, p, ρ and μ are time, fluid velocity, pressure, density and viscosity respectively; $\hat{\boldsymbol{\upsilon}}$ refers to mesh node velocity, which related to the deformation of the fluid domain. One can find the detailed derivation in [20]. In eqns. (1), the flow variables are solved in Euler frame as usual while the mesh nodes are regarded in Lagrange frame. This is why eqns. (1) are called ALE N-S equations. It is easily seen that eqns. (1) become the common N-S equations if the mesh node velocity $\hat{\boldsymbol{\upsilon}} = 0$. The large eddy simulation (LES) model [22, 23] is adopted to deal with the turbulence and the Smagorinsky-Lilly model [22, 23] is utilized as the subgrid-scale model.

The cylinder is considered as an Euler-Bernoulli beam and currently the axial loading and gravity are ignored here. The coordinates system is shown in fig. 1 and right-hand. The dynamic equation is [24]

$$\rho_b A \frac{\partial^2 u}{\partial t^2} + EI \frac{\partial^4 u}{\partial z^4} = q(z,t) \tag{2}$$

with $u(z)$ being the displacement of cross sections in beam, EI, A, ρ_b being the modulus of flexural rigidity, cross-sectional area, density of the beam, respectively, $q(z, t)$ being the loading on beam and calculated after the fluid field is solved. Eqn. (2) is just for the vibration of cylinder in one plane (for example x-z plane) and the dynamic equation for the other plane is ignored here, because they have the same form. Eqn. (2) can be solved numerically by finite element method (FEM), and the numerical details are explained in the following part. The boundary conditions at two ends of the cylinder are both clamped as mentioned above, which give

$$u\big|_{z=-L/2} = \left.\frac{\partial u}{\partial z}\right|_{z=-L/2} = u\big|_{z=L/2} = \left.\frac{\partial u}{\partial z}\right|_{z=L/2} = 0 \tag{3}$$

with $L = 20D$ being the length of the cylinder (see fig. 1).

In addition, the mesh is remeshed at each simulating step by spring analogy [23], in which the nodes of mesh are considered as being connected by fictitious springs whose stiffnesses are concerned with the locations of nodes. In this paper, the fictitious spring constant between two nodes is assumed being inverse proportion of their distance [23].

3 Numerical approach

The simulation on FSI actually needs to treat three distinct fields coupled together [25]. The first field is fluid flow field governed by N-S equations, the second is related to the structure deformation and the last one refers to the mesh

motion. These three coupled fields give rise to three equations sets still coupled together after discretization, making a great challenge for numerical simulation. In the past years, to overcome this challenge, many researchers [25–28] proposed many available numerical approaches, which, however generally speaking, can be classified roughly into two major categories, monolithic [26] and partitioned [25, 27, 28]. The monolithic approaches do not uncouple three numerical equations sets and solve them simultaneously as one, while the partitioned approaches solve them in sequence. The monolithic approaches have better numerical stability [27] but cost more computational resources than the partitioned ones. In practice, one of major difficulties in adopting the monolithic approaches is that the programming codes for them should usually be rewritten and can not reuse efficiently the already existing CFD or structure solvers. Therefore, the partitioned approaches are still popular and applied in this study.

The applied partitioned scheme is shown in fig. 2 and the same as CSS in [28]. The commercial software Fluent is utilized as the CFD solver, in which the ALE N-S equations are discretized by finite volume method (FVM) [23], and the structure codes by finite element method [29] based on eqns. (2) and (3) are embedded into the former by its providing user-defined functions (UDF) [23], some of which provide the access to controlling the motion of fluid domain mesh in simulation. The algorithm of updating mesh has been explained above and is implemented in Fluent. Firstly, the flow field is calculated by Fluent and sequentially obtained is the loading exerted on the cylinder (regarded as a beam), by which the structure codes determine the deformation of the cylinder, forming new boundary for the fluid domain. Then Fluent updates the mesh and a new cycle begins if needed. It should be noted that the fluid flow in all cases is simulated with turbulence model.

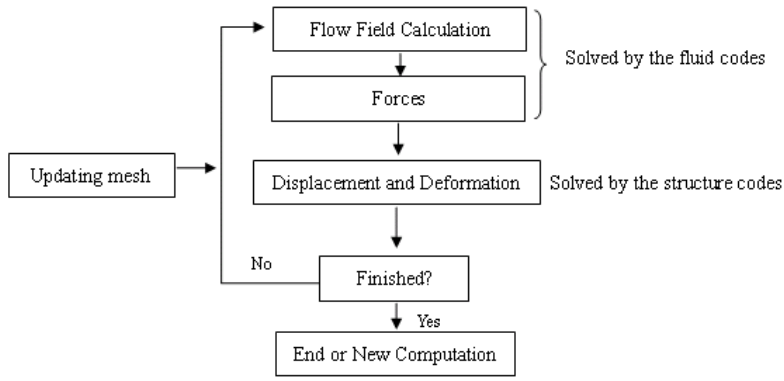

Figure 2: Simulation steps.

For the flow simulation, the first order implicit method for temporal discretization and the bounded central differencing scheme for spatial discretization are adopted with the PISO method for pressure-velocity coupling [23]. For turbulent flow, the LES model is utilized with Smagorinsky-Lilly as subgrid-scale model [22, 23].

Now, we focus on the discretization of eqn. (2). Through the standard Galerkin procedure of FEM [29], it with eqn. (3) can be discretized as one ordinary differential equations set

$$\mathbf{M}\ddot{\mathbf{u}} + \mathbf{K}\mathbf{u} = \mathbf{Q} \tag{4}$$

where **M** and **K** are global mass and stiffness matrices respectively; $\mathbf{u} = [\mathbf{u}_1, \mathbf{u}_2, \cdots, \mathbf{u}_N]^T$, a function of time *t* and *z*, is generalized displacements vector of N nodes including two end nodes. For one certain node, its generalized displacement consists of its displacement and rotation, i.e.

$$\mathbf{u}_i = [v_i, \theta_i] \tag{5}$$

with v_i and θ_i being displacement and rotation of *i*th node, respectively. **M** and **K** are assembled by local mass and stiffness matrices respectively. One can find the details on these local mass and stiffness matrices and how to assemble them to global ones as well as how to get **Q** in [29, 30]. Eqn. (4) is solved by the generalized-α method, an extension version of HHT-α and WBZ-α method, having the second-order accuracy and being unconditional stable if its parameters are set appropriately [31].

The loading here includes pressure and frictional force, the same as proposed by Paidoussis [4, 16] except the ignored axial force, i.e.

$$q_i = \int_C (-p\delta_{ij} + \tau_{ij}) n_j dl \,. \tag{6}$$

where q_i is the loading in eqn. (2) with $i = x, y$, τ_{ij} is the deviatoric stress tensor and n_j refers to the normal vector of the cylinder, and C is its lateral perimeter.

4 Results and discussion

For convenience, following Paidoussis [4, 16], we define dimensionless velocity υ, the mass ratio β, the dimensionless time τ and displacement by

$$\upsilon = \upsilon_0 L\sqrt{\frac{\rho A_t}{EI}}, \beta = \frac{\rho A_t}{\rho A_t + \rho_b A_e}, \tau = \frac{t}{L^2}\sqrt{\frac{EI}{\rho_b A_e + \rho A_t}},$$

$$d_x = \frac{u_x(z)}{D},\ d_y = \frac{u_y(z)}{D} \tag{7}$$

where υ_0 and ρ are the flow inlet velocity and fluid density respectively; L, ρ_b, A_t, and A_e are respectively the length, density, total cross-sectional area and effective cross-sectional area of the cylinder; d_x and d_y are the dimensionless displacement in x direction and y direction respectively with u_x and u_y being the corresponding displacement. Note that A_e is actually A in eqn. (2) and different from A_t since the cylinder is hollow.

The simulation parameters are shown in table 1, in which case 1 is related to the case where only one direction vibration is calculated and case 2 to the other one where the vibrations in two directions are both calculated. For different cases, the cylinder is located initially at its equilibrium state and only induced by fluid flow to vibrate. By increasing or decreasing stiffness of the cylinder, we can make the dimensionless velocity smaller or lager and thus focus on the effect of the latter for generalizing, by which the effect of the former can be easily and clearly concluded. In this paper, the effect of β is not discussed.

Fig. 3 shows the displacement histories of two cross sections of the cylinder in x direction for the case 1, where ζ is dimensionless length based on the diameter of the cylinder and ζ = 0, 20 means two ends of the cylinder respectively. These two cross sections have the almost most maximum displacement and thus the following results also focus on them.

It can be found from fig. 3 (a) that the oscillation amplitudes are small, about maximum 0.01D with D diameter of the cylinder, when the dimensionless velocity υ equals 6.0173. This kind of oscillation is almost around the initial equilibrium position of the cylinder and attributed to the turbulence as we mentioned above and called sub-critical vibration. However, when υ is increased to 8.8997, or equivalently the stiffness of the cylinder is decreased, as shown in fig. 3 (b) one dramatic vibration is induced distinct from that shown in fig. 3 (a). At the beginning, the oscillations with small amplitudes are induced till τ = 1.0 as they are when υ = 6.0173, after which the displacements rapidly increase to a large value about maximum 0.6D within a short time and then will never do visibly. Consequently, the cylinder oscillates around a new position with an approximate maximum amplitude 0.025D lager than that when υ = 6.0173. It indicates that the cylinder is buckled at a new position. This phenomenon is one type of fluidelastic instability and in particular discussed for the cylinder subjected to axial flow by Paidoussis [4, 7, 16].

We now move on to the case 2, where the cylinder can vibrate in two directions. Fig. 4 shows the vibrations of two same selected cross sections in two directions when υ = 6.0173. The oscillating amplitudes in two directions are also small, about maximum 0.05D in x direction and 0.03D in y direction. No matter in x and y directions, the oscillating is almost around the initial equilibrium position of the cylinder. This is similar to that shown in fig. 3 (a) and also this oscillation should be related to the turbulence. Nevertheless, when υ = 8.8997, the difference between case 1 and case 2 is apparent. Fig. 5 shows the vibrations in two directions when υ = 8.8997. Initially, the cylinder vibrates around its equilibrium position and then deviates rapidly from this position. The deviation is followed by an oscillation with the amplitude approximately maximum 0.1D in x direction and 0.2D in y direction both much larger than that after rapid increasing of the displacement shown in fig. 3 (b). This oscillation is different from the initial oscillation that should be only about 10^{-3} to $10^{-2}D$ [16] and thus could not be mainly associated with the turbulence but due to another kind of fluidelastic instability called flutter. Comparing fig. 3 (b) and fig. 5, one can further find that the time of the displacement rapidly increasing onset in the former is after that in the latter, together with the fact that the buckling usually

occurs at a smaller value of the dimensionless velocity than the flutter [4, 16] concluding that the FSI system here is more stable when the cylinder is constrained only to vibrate in one direction than when it can vibrate in two directions.

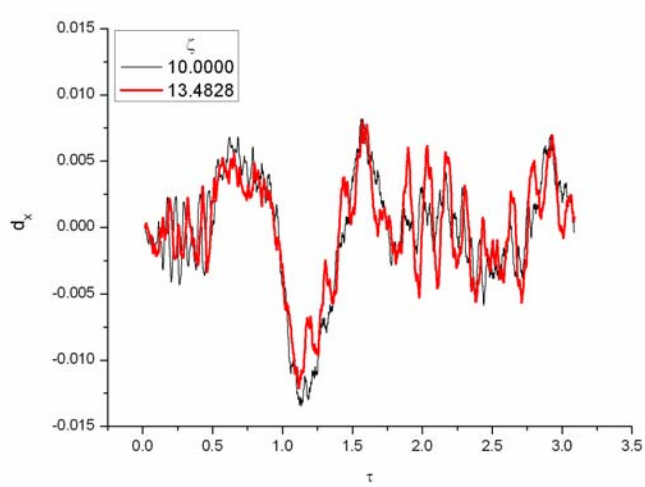

(a)

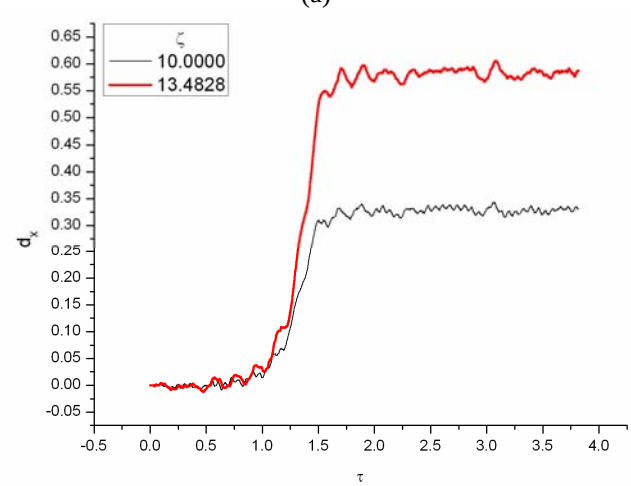

(b)

Figure 3: Dimensionless x-displacements of two cross sections of the cylinder in the case 1 when (a) $\upsilon = 6.0173$ and (b) $\upsilon = 8.8997$.

The buckling is not predicted by Paidoussis theory [4] for his considering a specific model similar to the model in this paper, but by recent nonlinear theory [32], the buckling is possible for a similar clamped-clamped system. The value 8.8997 of the dimensionless velocity for buckling (in case 1) or flutter (in case 2) is different from that of fluidelastic instability onset suggested by Modarres-

Sadeghi *et al*. [32], which is about 2π for buckling and 21.6 for flutter. It should be noted that the numerical method in this paper is much difficultly applied to predict the value of the dimensionless velocity after which the fluidelastic instability occurs, since it is impossible to simulate sufficient cases for different dimensionless velocities due to long time cost in numerical simulation. The value 8.8997 may not be one of fluidelastic instability onsets for the FSI system in this paper. Another reason for this difference should be attributed to the difference between the FSI systems in this paper and [32]. However, the results here are qualitatively consistent with those in [4, 16, 32].

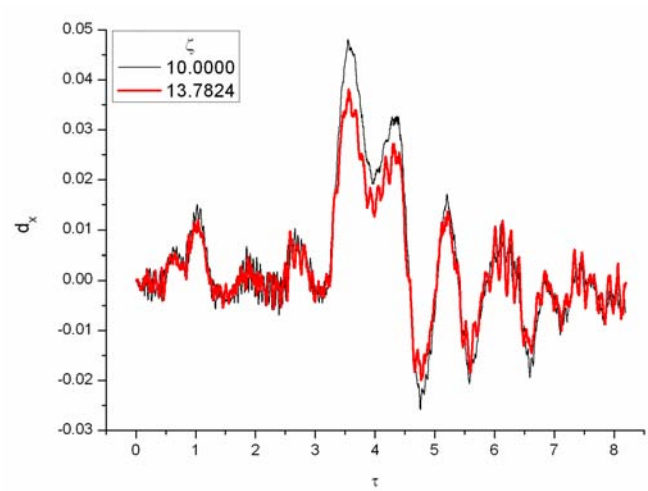

(a)

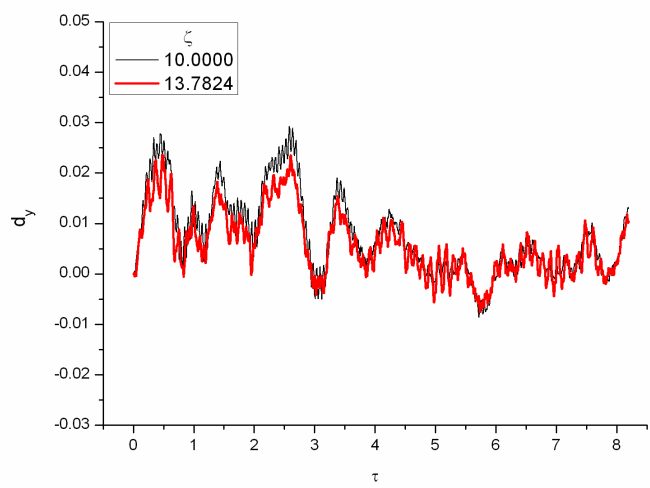

(b)

Figure 4: Dimensionless (a) x-displacements and (b) y-displacements of two cross sections of the cylinder in the case 2 when $\upsilon = 6.0173$.

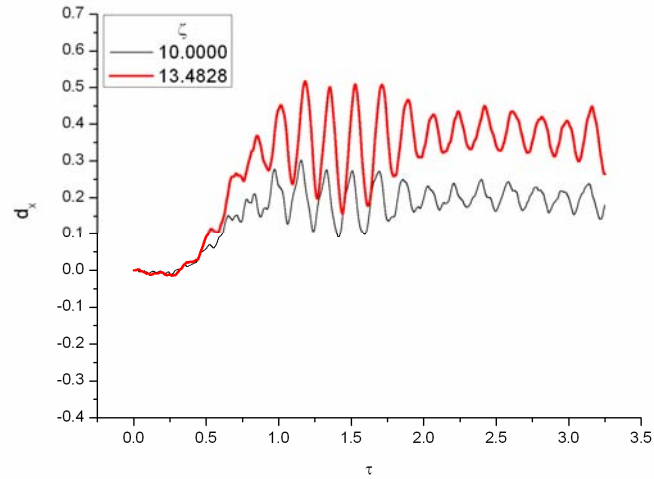

(a)

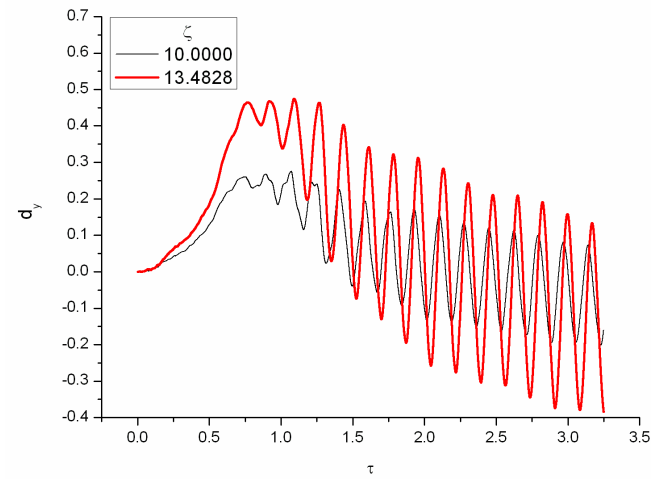

(b)

Figure 5: Dimensionless (a) x-displacements and (b) y-displacements of two cross sections of the cylinder in the case 2 when $\upsilon = 8.8997$.

In summary, for the FSI system in this paper, the numerical results shows that only small oscillation of the cylinder is induced when the dimensionless velocity is small enough while the fluidelastic instability occurs when it is large enough. However, due to the fluidelastic instability, the cylinder is buckled when it can vibrate only in one direction and oscillates with large amplitude when it can vibrate in two directions. This is qualitatively consistent with the conclusions of [4, 16, 32]. By the definition of the dimensionless velocity (see eqn. (7), it is can be concluded that when the stiffness is kept large enough, only weak oscillatory is induced by the flow, however, the FSI system becomes unstable if it is small.

Acknowledgement

Support given by the HKPolyU/AREVA collaboration under grant No.RPQ4 is gratefully acknowledged.

References

[1] White F.M., *Viscous Fluid Flow*, McGraw-Hill: New York, pp. 4-15, 2006.
[2] Anderson J.D., *Fundamentals of Aerodynamics*. McGraw-Hill: New York, pp. 232-239, 2001.
[3] Wang L. and Ni Q., Vibration of Slender Structures Subjected to Axial Flow or Axially Towed in Quiescent Fluid. *Advances in Acoustics and Vibration*, 2009, pp. 1-19, 2009.
[4] Paidoussis M.P., Dynamics of Flexible Slender Cylinders in Axial Flow, part 1: theory. *Journal of Fluid Mechanics*, 26, pp. 717-736, 1966.
[5] Lighthill M.J., Note on the Swimming of Slender Fish. *Journal of Fluid Mechanics*, 9, pp. 305-317, 1960.
[6] Taylor G., Analysis of the Swimming of Long and Narrow Animals. *Proceedings of the Royal Society of London, Series A, Mathematical and Physical Science*, 214, pp. 158-183, 1952.
[7] Paidoussis M.P., Dynamics of Flexible Slender Cylinders in Axial Flow, part 2: experiments. *Journal of Fluid Mechanics*, 26, pp. 737-751, 1966.
[8] Paidoussis M.P., Dynamics of Cylindrical Structures Subjected to Axial Flow. *Journal of Sound and Vibration*, 29, pp. 365-385, 1973.
[9] Lopes J.L., Paidoussis M.P. and Semler C., Linear and Nonlinear Dynamic of Cantilevered Cylinders in Axial Flow, part 2: The Equation of Motion. *Journal of Fluids Structures*, 16, pp. 715-737, 2002.
[10] Paidoussis M.P., Grinevich E., Anamovic D. and Semler C., Linear and Nonlinear Dynamic of Cantilevered Cylinders in Axial Flow, part 1: Physical Dynamics. *Journal of Fluids Structures*, 16, pp. 691-713, 2002.
[11] Semler C., Lopes J.L., Augu N. and Paidoussis M.P., Nonlinear Dynamic of Cantilevered Cylinders in axial flow, part 3: Nonlinear Dynamics. *Journal of Fluids Structures*, 16, pp. 739-759, 2002.
[12] Chen S.S., Vibration of Nuclear Fuel Bundles. *Nuclear Engineering and Design*, 35, pp. 399-422, 1975.
[13] Paidoussis M.P. and Suss S., Stability of a Cluster of Flexible Cylinders in Bounded Axial Flow. *Journal of Applied Mechanics*, 44, pp. 401-408, 1977.
[14] Paidoussis M.P., The Dynamics of Clusters of Flexible Cylinders in Axial Flow: Theory and Experiments. *Journal of Sound and Vibrations*, 65, pp. 391-417, 1979.
[15] Paidoussis M.P. and Curling L.R., An Analytical Model for Vibration of Clusters of Flexible Cylinders in Turbulent Axial Flow. *Journal of Sound and Vibrations*, 98, pp. 493-517, 1985.
[16] Paidoussis M.P., *Fluid-Structure Interactions: Slender Structure and Axial Flow*, Vol. 2, Elsevier: London and California, pp. 787-877, 2004.

[17] Reavis J.R., Vibration Correlation for Maximum Fuel-Element Displacement in Parallel Turbulent Flow. *Nuclear Science and Engineering*, 38, pp.63-69, 1969.
[18] Reavis J.R., WVI-Westinghouse Vibration Correlation for Maximum Fuel-Element Displacement in Parallel Turbulent Flow. *Transactions of the American Nuclear Society*, 10, pp. 369-371, 1967.
[19] Gorman D.J., An Analytical and Experimental Investigation of the Vibration of Cylindrical Reactor Fuel Elements in Two-Phase Parallel Flow. *Nuclear Science and Engineering*, 44, pp. 277-290, 1971.
[20] Wang X.D., *Fluid-Solid Interactions: Analytical and Computational Approaches*, Elsevier: Amsterdam and Oxford, pp. 163-169, 2008.
[21] Stein E., De Borst R. and Hughes J.R., (eds). Encyclopedia of Computational Mechanics, Vol. 1 (Chapter 14). *Arbitrary Lagrangian-Eulerian Methods*, ed. Donea J. etc, John Wiley and Sons, Ltd., pp. 1-25, 2004.
[22] John V., *Large Eddy Simulation of Turbulent Incompressible Flows*. Springer-Verlag: Berlin and Heidelberg, pp. 21-62, 2004.
[23] *ANSYS FLUENT 12.0 Documentation*, ANSYS, Inc.
[24] Chen Y., *Vibrations: Theoretical Methods*. Addison-Wesley Publishing Company, Inc.: Reading and Massachusetts, pp. 204-208, 1966.
[25] Piperno S., Farhat C. and Larrouturou B., Partitioned procedures for the transient solution of coupled aeroelastic problems, part 1: Model problem, theory and two-dimensional application. *Computer Methods in Applied Mechanics and Engineering*, 124, pp. 79-112, 1995.
[26] Blom F.J., A monolithical fluid-structure interaction algorithm applied to the piston problem. *Computer Methods in Applied Mechanics and Engineering*, 167, pp. 369-391, 1998.
[27] Matthies H.G. and Steindorf J., Partitioned but strongly coupled iteration schemes for nonlinear fluid-structure interaction. *Computers and Structures*, 80, pp. 1991-1999, 2002.
[28] Farhat C. and Lesoinne M., Two Efficient Staggered Algorithms for the Serial and Parallel Solution of Three-Dimensional Nonlinear Transient Aeroelastic Problems. *Computer Methods in Applied Mechanics and Engineering*, 182, pp. 499-515, 2000.
[29] Zienkiewicz O.C., Taylor R.L. and Zhu J.Z., *The Finite Element Method: Its Basis and Fundamentals*. Elsevier Butterworth-Heinemann: Oxford and New York, pp. 54-95, 2005.
[30] Zienkiewicz O.C. and Taylor R.L., *The Finite Element Method for Solid and Structural Mechanics*. Elsevier Butterworth-Heinemann: Oxford and New York, pp. 278-320, 2005.
[31] Chung J. and Hulbert G.M., A Time Integration Algorithm for Structural Dynamics with Improved Numerical Dissipation: The Generalized-α Method. *Journal of Applied Mechanics*, 60, pp. 371-375, 1993.
[32] Modarres-Sadeghi Y., Paidoussis M.P. and Semler C., The Nonlinear Behavior of a Slender Flexible Cylinder Pinned or Clamped at Both Ends and Subjected to Axial Flow. *Computers and Structures*, 85, pp. 1121-1133, 2007.

Numerical simulation of vortex-induced vibration of a pivoted cylinder using the spectral element method

H. Gun Sung[1], H. Baek[2], S. Hong[1] & J.-S. Choi[1]
[1]*Maritime and Ocean Engineering Research Institute (MOERI; formerly KRISO), KORDI, Daejeon, Korea*
[2]*Department of Mathematics, MIT, Cambridge, USA*

Abstract

The present paper describes preliminary results of numerical simulation of VIV (vortex-induced-vibration) phenomenon around a pivoted circular cylinder subject to steady flow. The present flow model is based upon the Navier-Stokes equations with velocity-pressure formulation. The governing equations are solved through the Spectral Element Method (SEM), which possesses the property of high-order spatial accuracy as proposed by Karniadakis and Sherwin in their book *Spectral/hp Element Methods for CFD*. The solution procedure and characteristic aspects of the present modelling and numerical method are briefly stated. The coupling method of the body motion with the flow problem is restated from the viewpoint of the present problem. A series of numerical estimation of VIV flow characteristics have been carried out for varying parameters of the problem such as the reduced velocity and damping parameter, etc.
Keywords: vortex-induced vibration, pivoted cylinder, spectral element method, coupling of body motion with flow.

1 Introduction

In general, VIV (vortex-induced-vibration) problem is focused upon reduction and suppression of VIV as noted in Blevins [2] and Sarpkaya [3]. As indicated by Raghavan [4], and Bernitsas and Raghavan [5], however, it seems to be probable to extract considerable energy from VIV phenomena. For example, Professor Bernitsas has developed an energy extraction device known as

WIT Transactions on Engineering Sciences, Vol 74, © 2012 WIT Press
www.witpress.com, ISSN 1743-3533 (on-line)
doi:10.2495/AFM120151

VIVACE (Vortex Induced Vibration Aquatic Clean Energy) which converts ocean and river current energy to electricity (Bernitsas *et al.* [6]). MOERI/KORDI is also developing its own energy extraction device which utilizes a pivoted circular cylinder subject to background current flows.

The present paper consists as follows. The physical problem under consideration is introduced. Flow model and governing equation are briefly explained. Numerical method and solution procedure are addressed. Some of numerical results of a specified configuration are presented.

2 Physical problem under consideration

As shown in Fig. 1, a submerged cylindrical body is pivoted to a column and exposed to VIV due to background fluid flow such as ocean currents. As stated above, the present device is conceptually associated with the earlier development done by Prof. Bernitsas' group in the University of Michigan.

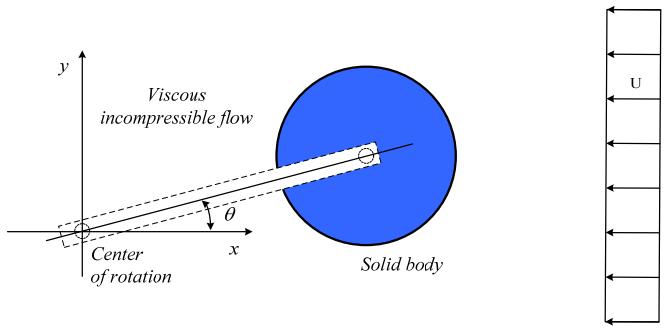

Figure 1: A schematic diagram of the VIV problem of a pivoted circular cylinder subject to steady flow.

3 Flow model and governing equation

Coordinate system and modeling of present problem is shown in Fig. 2. Rotation vector of the body can be denoted by $\vec{\Omega}(t) = (0,0,\theta(t))$ for the present case of 2D. So, the angular velocity and acceleration can be obtained by time derivative of the rotation vector as $\dot{\vec{\Omega}}(t)$ and $\ddot{\vec{\Omega}}(t)$, respectively. We also assume the flow domain has rectangular shape, and there is no free surface.

We describe the present flow problem by using the viscous incompressible flow model. For the present problem in which we need to describe the grid movement due to vortex induced body motion, we can apply ALE (Arbitrary Lagrangian-Eulerian) framework. Hence, the corresponding set of governing equations can be modified as follows.

$$\frac{\partial \vec{u}}{\partial t} + N(\vec{u}, \vec{w}) = -\frac{1}{\rho}\nabla p + \nu L(\vec{u}) + \vec{f} \ in\ V(t) \tag{1}$$

$$\nabla \cdot \vec{u} = 0 \ in\ V(t) \tag{2}$$

where $\vec{u}(\vec{x},t) = (u,v,w)$ is the velocity vector, $\vec{w}(\vec{x},t)$ the ALE mesh velocity vector, $p(\vec{x},t)$ the pressure field, ρ the density of the fluid, ν the kinematic viscosity of the fluid, and $\vec{f}$ the body force that can include the effect of non-inertial reference frame. The underlying Cartesian coordinates is denoted by the spatial coordinates $\vec{x}$ and by the time coordinate t. We can define as $N(\vec{u},\vec{w}) = (\vec{u}-\vec{w})\cdot\nabla\vec{u}$ and $L(\vec{u}) = \nabla\cdot\left[\nabla\vec{u} + (\nabla\vec{u})^T\right]$. So, the partial time derivative of the velocity is taken for a given fluid particle or a pseudo-particle in general. It is also assumed that the fluid domain, $V(t)$ can be time-varying for generality of the formulation. With ALE concept, the partial time derivative in the above is taken on the mesh frame under consideration.

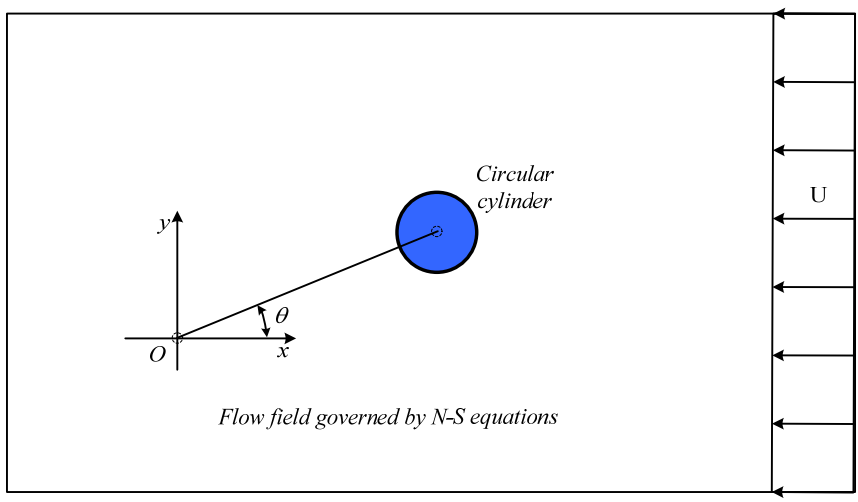

Figure 2: Coordinate system and modeling of the problem.

For the body boundary condition, we specify the impermeable condition as follows.

$$\vec{u} = \vec{u}_b \ in\ \Gamma_b(t) \tag{3}$$

where $\vec{u}_b = \dot{\vec{\Omega}}(t)\times(\vec{r}-\vec{r}_{CR})$ with $\vec{r}_{CR} = (x_{CR}, y_{CR}, z_{CR})$ to denote the position vector of the center of rotation, *i.e.* the pinned position of the rod.

In the present paper, we apply the boundary conditions at truncation boundaries as follows.

$$u = U,\ w = 0 \ in\ x = x_L \tag{4}$$

$$w = 0, \vec{s} \cdot \nu\left[\nabla\vec{u} + (\nabla\vec{u})^T\right] \cdot \vec{n} = 0 \; in \; z = z_L, z_H \tag{5}$$

$$u = U, \vec{s} \cdot \nu\left[\nabla\vec{u} + (\nabla\vec{u})^T\right] \cdot \vec{n} = 0 \; in \; x = x_L \tag{6}$$

where U denotes the outflow velocity, and $x = x_L$, $x = x_R$, $z = z_L$, $z = z_H$ mean the left, right side and low, high side of the truncated rectangle of the flow domain. The vectors $\vec{s}$ and $\vec{m}$ (pointing to z-axis in 2D problems) are an orthonormal vector pair lying on the tangent plane, and related to the unit normal vector as $\vec{n} = \vec{s} \times \vec{m}$. Hence, the vector pair, $(\vec{s}, \vec{m}, \vec{n})$ constitutes the orthonormal curvilinear coordinates.

With the ALE methodology, the motion of the mesh nodes, $\vec{X}$ is described as

$$\frac{d\vec{X}}{dt} = \vec{w} \tag{7}$$

with an operator equation for the mesh velocity vector,

$$\boldsymbol{E}\vec{w} = 0 \tag{8}$$

where $\boldsymbol{E}$ stands for the elliptic operator which governs the grid motion. Its type is chosen depending upon the problem in consideration. For example, the Laplace equation was utilized by Ho and Patera [7], and Robertson *et al.* [8]. On the other hand, Rabier and Medale [9] adopted a Lagrangian-Eulerian kinematic method by the way of an elastic problem for the mesh displacement field rather than a standard ALE formulation. A similar approach can be found in Bouffanais and Deville [10].

The boundary condition on the ALE mesh motion is also to be carefully specified. On the free-slip boundary, ALE mesh nodes move with the fluid particle as follows.

$$\vec{w} = \vec{u} \equiv (\vec{u} \cdot \vec{n})\vec{n} + (\vec{u} \cdot \vec{s})\vec{s} + (\vec{u} \cdot \vec{m})\vec{m} \;\; in \; \Gamma_s \tag{9}$$

This guarantees the velocity compatibility on the free-slip boundary. The Dirichlet-type boundary specifies the velocity vector and the corresponding boundary is stationary in space and time. So, we may apply the following constraint.

$$\vec{w} = \vec{0} \;\; in \; \Gamma_D \tag{10}$$

4 Equation of body motion

In the case of 2D problem, the equation of body motion can be written as follows.

$$J_b\ddot{\theta} + C_b\dot{\theta} + K_b\theta = T_{ext}(t) \tag{11a}$$

where θ denotes the angle of rotation of the body. The coefficients J_b, C_b, K_b are the moment of inertia, damping factor, and stiffness of rotation, respectively. The external moment, T_{ext} can be obtained from the equation.

$$T_{ext}(t) = \vec{e}_3 \cdot \int_{S_b(t)} (\vec{r} - \vec{r}_{CG}) \times \left[-p\vec{n} + \nu\left(\nabla\vec{u} + \nabla\vec{u}^T\right) \cdot \vec{n}\right] ds \tag{12}$$

where $\vec{r}_{CR}$ means the position vector of the center of rotation, *i.e.* the pinned position of the rod, and $\vec{e}_3 = (0,0,1)$ for the present case. For simplicity of the derivation and notation, the equation (11a) can be normalized as follows:

$$\ddot{\theta} + 2\omega_0\zeta_b\dot{\theta} + \omega_0^2\theta = T_{ext}^*(t) \tag{11b}$$

with definitions such as $\omega_0 = \sqrt{K_b / J_b}$, $\zeta_b = C_b / 2\omega_0 J_b$, $T_{ext}^* = T_{ext}(t) / J_b$.

Based upon the proposed values of preliminary design, some variations of the parameters such as the length of the connection rod, mass moment of inertia, damping factor, and stiffness are compared with in this study by numerical simulation.

In order to couple the body motion with the fluid flow, we need to transfer the velocity and acceleration on the body surface to the flow solver. Thus, we can use the following relationship.

$$\vec{u}_b = \dot{\theta}(t)(-y + y_{CR}, x - x_{CR})\ in\ \Gamma_b(t) \tag{13}$$

where we use $\dot{\vec{\Omega}}(t) = (0,0,\dot{\theta})$. The acceleration is written as follows.

$$\vec{a}_b = \ddot{\vec{\Omega}}(t) \times (\vec{r} - \vec{r}_{CR}) + \dot{\vec{\Omega}}(t) \times \left[\dot{\vec{\Omega}}(t) \times (\vec{r} - \vec{r}_{CR}) \right] \tag{14}$$

Thus, in the present case we have

$$\vec{a}_b = \ddot{\theta}(t)(-y + y_{CR}, x - x_{CR}) + \dot{\theta}(t)^2(-x + x_{CR}, -y + y_{CR},)\ in\ \Gamma_b(t) \tag{15}$$

For the present case of rotating circular cylinder, the body boundary can be defined as

$$\left(x - x_{CR} - R_r \cos\vartheta\right)^2 + \left(y - y_{CR} - R_r \sin\vartheta\right)^2 = R_c^2 \tag{16}$$

where the parameter ϑ is the angle of the point on the cylinder surface, R_r means the distance from the center of rotation and center of the cylinder, and R_c the cylinder radius.

5 Higher-order splitting scheme and SEM

For numerical solution of the ALE N-S equations, we utilized the high-order splitting scheme for pressure and velocity coupling by using stiffly-stable time integrators. It was originally developed by Professor G.E. Karniadakis (Karniadakis and Sherwin [1]), which is utilized in this study with some modification. Detailed procedure is thus omitted and a brief introduction is given.

The high-order splitting scheme is applied as follows.

$$\tilde{\tilde{u}} - \sum_{q=0}^{J_i-1} \alpha_q \vec{u}^{n-q} = \delta t \left[- \sum_{q=0}^{J_i-1} \beta_q N\left(\vec{u}^{n-q}, \vec{w}^{n-q}\right) + f^{n+1} \right] in\ \Omega^n \tag{17}$$

$$\tilde{\tilde{\tilde{u}}} - \tilde{\tilde{u}} = -\frac{\delta t}{\rho} \nabla p^{n+1} \quad in\ \Omega^n \tag{18}$$

$$\gamma_0 \vec{u}^{n+1} - \tilde{\tilde{\tilde{u}}} = \nu \delta t L\left(\vec{u}^{n+1}\right) \quad in\ \Omega^n \tag{19}$$

The superscript refers to the time level index, and J_i the order of the time integration, and γ_0, α_q and β_q the coefficients for stiffly stable time integration. Readers are referred to Karniadakis and Sherwin [1] for values of the integration coefficients for different orders. The time step size, δt is fixed throughout the time marching in this study.

The primary reason for using the present time integration scheme is due to necessity of attaining the high-order accuracy and robustness in time. The stiffly-stable time integration scheme is known to be very accurate and stable. Particularly in SEM, the condition number is very large compared with other discretization schemes and so the conventional time integration scheme such as the Adams-Bashforth and Runge-Kutta methods may give rise to numerical instability.

The present study is based upon the previous development known as Nektar which was originally due to Prof. Karniadakis at Brown University, USA. Thus in this paper, we can skip most of the details and just cite relevant references such as Karniadakis and Sherwin [1]. Etc. It should be noted that the grid motion is directly obtained by using ALE concept which is implemented on the framework of NEKTAR.

6 Coupling method of FSI (fluid-structure-interaction)

Coupling of the flow dynamics with body motion is realized mainly through time marching procedure. In the above, we mentioned the type of time-stepping for fluid flow. So, the remaining part is the equation of body's rotational motion, and data transfer and connection between fluid part and structure part, which are discussed below.

The conventional method is based upon the Newmark-family time marching as in Papaioannou *et al.* [11] and Placzek *et al.* [12], etc. When we are interested in explicit time marching, any type of time integration scheme can be utilized in principle only if it guarantees numerical stability. However, the practical issue seems to be efficiency and accuracy as well; i.e. a choice is preferred when the type of time marching algorithm for structure part does not deteriorate the level of accuracy of solution method of fluid part, particularly in time-axis. The present method for this FSI problem is briefly explained in the below.

At first, the angular motion of the pivoted cylinder can be described by

$$J_b \ddot{\theta}\Big|^{n+1} + C_b \dot{\theta}\Big|^{n+1} + K_b \theta\Big|^{n+1} = T_{ext}\Big|^{n} \tag{20}$$

where the superscript denotes the time step, while the subscript means sub-iteration step. Hence, $T_{ext}\Big|^{n}$ stands for the hydrodynamic torque that can be calculated by using the previous time step.

Within this framework, the way to describe $\dot{\theta}^n$ and $\ddot{\theta}^n$ can construct the time integration scheme and also can determine its temporal accuracy and stability. The present choice for time discretization is a Newmark scheme which can be written as

$$\theta^{n+1} = \theta^n + \delta t\dot{\theta}^n + \frac{\delta t^2}{2}\left[(1-2\beta)\ddot{\theta}^n + 2\beta\ddot{\theta}^{n+1}\right] \tag{21a}$$

$$\dot{\theta}^{n+1} = \dot{\theta}^n + \delta t\left[(1-\gamma)\ddot{\theta}^n + \gamma\ddot{\theta}^{n+1}\right] \tag{21b}$$

It is known that the accuracy of the scheme is dependent upon the parameter set of (β,γ). In this study, $(\beta,\gamma) = (0.25,0.5)$ is used.

The whole process for each time step can be summarized as follows.

i) Solve the equation for the solid part with the last solutions of the fluid part.
ii) Obtain the angular displacement, velocity, and acceleration using Eqs. (21a) and (21b).
iii) Calculate the translational velocity and acceleration for the next time-step on the body boundary and transfer those values to fluid flow solver.
iv) Solve the governing equation of fluid motion, and the corresponding mesh field.
v) Compute the traction on the interface between and the solid and the fluid and find the torque acting upon the body.
vi) Repeat the processes i) to v) up to the termination time.

7 Numerical results and discussion

In this section, we discuss the numerical results of the present VIV problem of a pivoted circular cylinder for varying parameters with the developed numerical method. A typical grid system for present VIV simulation is shown in Fig. 3. As shown, rectangular grids are utilized, and the order of the interpolation of spectral elements was 5 or 6 for most of the cases of simulation.

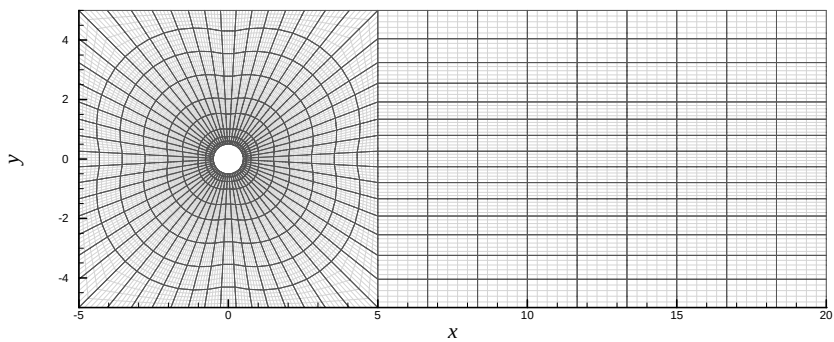

Figure 3: A typical grid system for present VIV simulation.

We restrict ourselves to the case of $R_r / R_c = 3$ for preliminary test simulation for which we have experimental data. In this case, the flow is incident from the upstream side and the pivoting point is located downstream. The normalized mass moment of inertia was 9.089 for the present case.

In the first place, an example of computational time series data of angular displacement, velocity, acceleration, and hydrodynamic torque of the cylinder is shown in Fig. 4. The Reynolds number was 200, the reduced velocity was 5, and the damping factor was 0.07 for this case. Figure 5 depicts how the cylinder is moving in the plane for the same case. Figure 6 and 7 correspond to pressure and vorticity contour plots for this case at a specified time instant. It is noted that the vorticity contour plot shows some discontinuities around mesh boundary because of relatively coarse grid density in the downstream side.

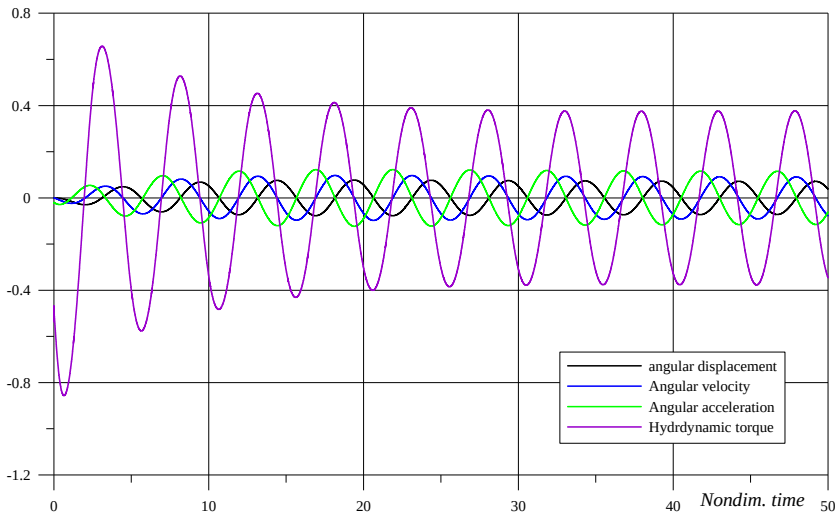

Figure 4: Time series of variables such as angular displacement, velocity, acceleration, and hydrodynamic torque of the cylinder ($R_r / R_c = 3.0$, $\mathrm{Re} = 200$, $U_r = \pi U / \omega_0 R_c = 5$, $\zeta_b = 0.07$).

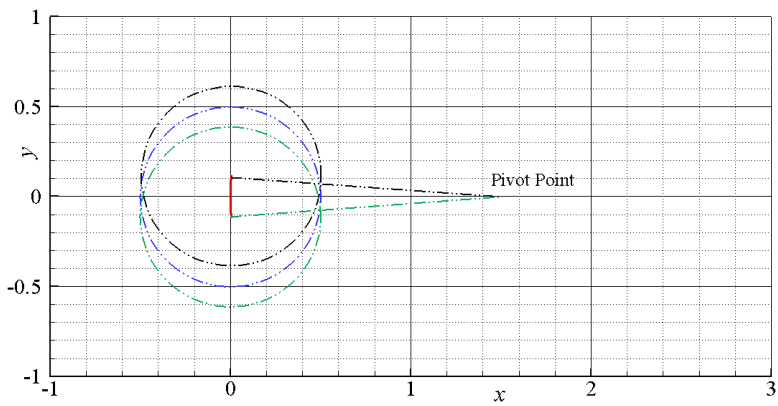

Figure 5: Trajectory of the cylinder ($R_r / R_c = 3.0$, $\mathrm{Re} = 200$, $U_r = \pi U / \omega_0 R_c = 5$, $\zeta_b = 0.07$).

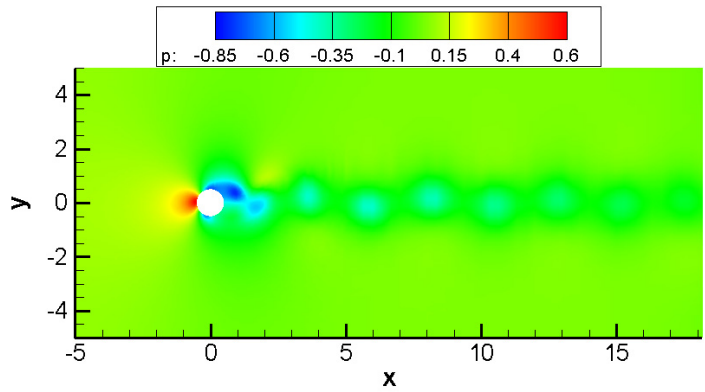

Figure 6: Pressure contour plot ($t = 49.4$, $R_r / R_c = 3.0$, $\mathrm{Re} = 200$, $U_r = \pi U / \omega_0 R_c = 5$, $\zeta_b = 0.07$).

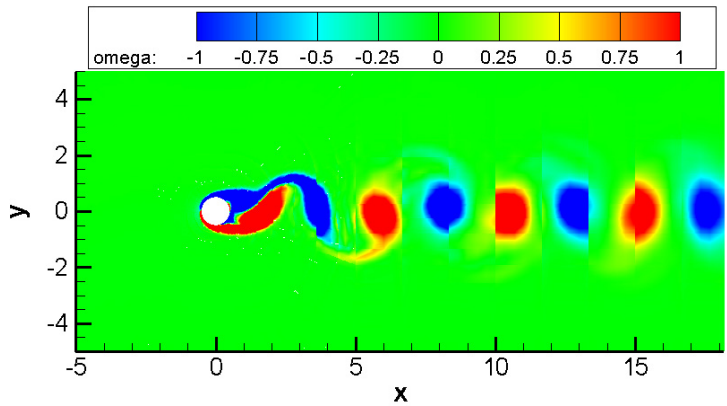

Figure 7: Vorticity contour plot ($t = 49.4$, $R_r / R_c = 3.0$, $\mathrm{Re} = 200$, $U_r = \pi U / \omega_0 R_c = 5$, $\zeta_b = 0.07$).

We compared the present numerical results in Fig. 8 with the experiment performed by Choi *et al.* [13]. It is noted that in the experiment the cylinder is connected to the multi-hinged bars which is also guided to a generator unit. The detailed features of the experiment are referred to the paper cited in the above. The figure indicates that the present numerical method under-predicts the performance of the rotational VIV motion of the cylinder. We note that the present value of damping factor in simulation was found by some series of decay test in the experiment. We suppose that the present numerical method contains appreciable level of numerical damping because the numerical results is similar to the no load case rather than to the zero resistance case.

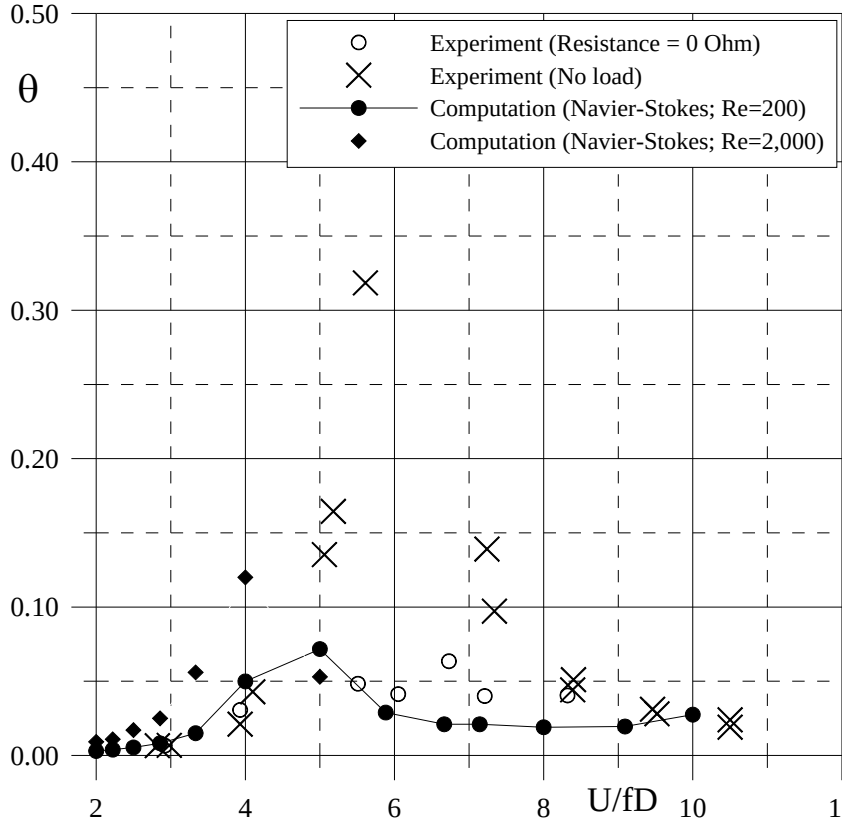

Figure 8: VIV response for various reduced velocity ($R_r / R_c = 3.0$, for the computation, the damping factor was chosen as $\zeta_b = 0.07$).

The actual range of Reynolds number of the experiment was $4.74 \times 10^4 \leq \mathrm{Re} \leq 1.625 \times 10^5$, while for present simulations we tested the case of $200 \leq \mathrm{Re} \leq 2{,}000$. Since the higher Reynolds numbers cause the present numerical method to show an unstable motion in time. As an intermediate conclusion, it is required to utilize the strong coupling scheme as noted in Baek [14], and Baek and Karniadakis [15]. By resorting to this robust method, it is expected that we can go up to a very high Reynolds number case without unstable solutions. Another reason for this discrepancy is attributed to the one dimensional simplification to the experimental arrangement of multi-hinge connection. A significant feature to be addressed further is the effect of the generator unit on the VIV motion of the cylinder. These three aspects will be studied further.

8 Summary and conclusion

The present paper described some preliminary results of numerical simulation of VIV phenomenon around a pivoted circular cylinder subject to steady flow. The present flow model and method utilized an SEM-based N-S solver, which are originally developed by Professor G.E. Karniadakis' group. Numerical treatment for movement of the body was done by using ALE approach. The solution procedure and characteristic aspects of the present modeling and numerical method were briefly stated. The present method of coupling of the body motion with the flow problem is based upon a kind of weak coupling scheme. A series of numerical estimation of VIV flow characteristics were carried out for a given parameter set. By comparing with experimental results, it has been found out that there is a great need to utilize a strong coupling scheme and to refine the modeling of the multi-hinge connection of the system, which will be sought sincerely for the forthcoming paper.

Acknowledgements

The present study is supported by the "Development of key-technology of ocean renewable energy using Vortex-Induced Vibration (VIV) in water flow" granted by Ministry of Knowledge Economy of Korea and the principal R&D program of KORDI: "Performance Evaluation Technologies of Offshore Operability for Transport and Installation of Deep-sea Offshore Structures" granted by Korea Research Council of Public Science and Technology. The authors express deep gratitude to Professor Karniadakis for permission of the computer code, known as NEKTAR.

References

[1] Karniadakis, D., and S.J. Sherwin, Spectral/hp Element Methods for CFD, Oxford University Press, 2nd Ed., London, 2005.
[2] Blevins, R. D. Flow-Induced Vibration, Malabar, FL Krieger Publishing Company, 1994.
[3] Sarpkaya, T. A critical review of the intrinsic nature of vortex-induced vibrations, Journal of Fluids and Structures, Vol. 19, pp. 389–447, 2004.
[4] Raghavan, K, "Energy Extraction from a Steady Flow Using Vortex Induced Vibration", Ph.D. Dissertation, The University of Michigan, 2007.
[5] Bernitsas, M.M. and Raghavan, K. "Reduction/Suppression of VIV of Circular Cylinders through Roughness Distribution at $8\times10^3 < Re < 1.5\times10^5$", Proc. OMAE Conference, pp. 1-5, 2008.
[6] Bernitsas, M.M., Raghavan, K., Ben-Simon, Y. and Garcia, E.M.H. "VIVACE (Vortex Induced Vibration for Aquatic Clean Energy): A New Concept in Generation of Clean and Renewable Energy from Fluid Flow", Proc. OMAE Conference, pp. 1-18, 2006.
[7] Ho, L.-W., and Patera, A.T., "A Legendre Spectral Element Method for Simulation of Unsteady Incompressible Viscous Free-Surface Flows,"

Computer Methods in Applied Mechanics and Engineering, Vol. 80, No. 1/3, pp. 355-366, 1990.
[8] Robertson, I., Sherwin, S.J., and Graham, J.M.R., "Comparison of Wall Boundary Conditions for Numerical Viscous Free Surface Flow Simulation," Journal of Fluids and Structures, Vol. 19, No.4, pp. 525-542, 2004.
[9] Rabier, S., and Medale, M., "Computation of Free Surface Flows with a Projection FEM in a Moving Mesh Framework," Computer Methods in Applied Mechanics and Engineering, Vol. 192, No. 41/42, pp. 4703-4721, 2003.
[10] Bouffanais, R., and Deville, M.O., "Mesh Update Techniques for Free-Surface Flow Solvers Using Spectral Element Method," Journal of Scientific Computing, Vol. 27, No.1/3, pp.137-149, 2006.
[11] Papaioannou, G.V., D.K.P. Yue, M.S. Triantafyllou, G.E. Karniadakis, On the effect of spacing on the vortex-induced vibrations of two tandem cylinders, Journal of Fluids and Structures 24, pp. 833–854, 2008.
[12] Placzek A., Sigrist J.-F., Hamdouni A. Numerical simulation of an oscillating cylinder in a cross-flow at low Reynolds number: Forced and free oscillations, Computers & Fluids 38, pp. 80–100, 2009.
[13] Jong-Su Choi, Sup Hong, Tae-Kyeong Yeu and Hyung-Woo Kim, 2010, "Experimental Study on Vortex-Induced Vibration Clean Energy Extraction Device Model using Circular Cylinder Pivoted with a Lever (in Korean)", Proc. KSOE Spring conference, pp. 2516 – 2519, 2010.
[14] Baek, H. 2010, A spectral element method for fluid-structure interaction: new algorithm and application to intracranial aneurysms. Ph.D. Thesis, Brown University.
[15] Baek, H. and G.E. Karniadakis, 2010, Stabilization of fluid-structure interactions via fictitious added mass and damping in physical and biological applications, submitted to Elsevier.

Droplet interaction and dynamic wettability of advanced materials used in aeronautics

O. Gohardani & D. W. Hammond
Department of Power and Propulsion, Cranfield University, UK

Abstract

In aircraft icing applications the interaction of Super-Cooled Liquid Droplets (SLD) with the forward facing surfaces of an aircraft is of outmost importance, as it influences the consequent icing that ensues on the structure. In this study, empirical results are shown that characterize different droplet splashing scenarios onto polymeric matrix composites reinforced with carbon nanotubes. Results are presented for droplet interaction upon advanced pristine and eroded aerospace materials based on a numerical scheme, that identifies different splashing features into distinct categories. The purpose of utilizing the dynamic wetting analysis scheme is to numerically represent the type of splashing events that are evident on the experimental photographs. Images are presented for splashing features on different surfaces and their similarities and differences are discussed based on the analysis. Hydrophobicity and hydrophilicity of the different specimen surfaces are further examined based on both static and dynamic contact angle measurements and a correlation between the two modes of wetting is presented for the aforementioned materials.
Keywords: dynamic wettability, contact angle, droplet interaction, carbon nanotubes, aeronautics.

1 Introduction

The potential usage of advanced materials such as polymeric matrix composites and carbon nanotubes have widely been recognized due to the number of possible applications where these materials may present desired characteristics. In aerospace applications, composite materials are widely being considered because of their higher stiffness and strength [1]. The present study investigates the


WIT Transactions on Engineering Sciences, Vol 74, © 2012 WIT Press
www.witpress.com, ISSN 1743-3533 (on-line)
doi:10.2495/AFM120161

interaction of droplets on advanced materials and the resulting splashing that occurs empirically. This interaction is comparable to the splashing that occurs upon the airframe of an aircraft, flying through a cloud formation or when subjected to precipitation. Weathering effects due to extended service operations of aircraft in flight may occasionally result in structural wear on the airframe and erosion as described in an extensive review by Gohardani [2]. For this purpose the considered specimens have been modified by erosion, in order to investigate the role of surface morphology on the ensuing splashing structures.

Wetting characteristics outside aerospace sciences have been examined in a wide range of applications, where in particular the role of wetting on micro and nano-structures in biological applications, has been studied for plant surfaces [3], insect wing structures [4] and animal locomotion on the surface of water layers [5].

2 Experimental details

2.1 Experimental setup

The experiments in this study are carried out at the vertical droplet tunnel located at Cranfield University, United Kingdom. The tunnel is located next to the main Icing Tunnel, with the flow in both tunnels powered by a centrifugal backward curved suction fan, capable of producing flow rates, $\dot{m} \in [30, 100]$ kg·s^{-1}. The temperature range $T \in [-30, +5]$ °C is attained by the refrigeration plant which has a capacity of 400 kW. Upon generation of the flow, the air from the fan is directed through a duct into a heat exchanger for cooling and directed into a steering dish in the adjacent vertical tunnel where it gets accelerated toward the test section. A droplet generator equipped with an interchangeable platinum nozzle orifice disk is placed on top of the steering dish.

Upon entering the contraction section of the vertical droplet tunnel, the mono dispersed droplets are accelerated towards the test section, where the gentle contraction length of 5 meters, ensures that no aerodynamic breakup of the droplets occurs. The test section is situated on top of two control valves, capable of regulating the locus of the stagnation point. The target specimen is placed on a designed target holder, that allows for vertical position adjustment of the specimen. This is essential in order to account for the range of different specimen thicknesses within the study. The incident angle of the oncoming air in relation to the target is $\alpha = 70°$. Upon contact with the target area the flow is bifurcated and exits the tunnel through the control valves into the air inlet of the main Icing Tunnel, where it gets regenerated by the fan. The droplet diameter in this study has been confined to $d = 400$ μm, with three different free stream velocities $U_\infty \approx \{35, 50, 60\}$ m $\cdot$ s^{-1}, in accordance with expected number of splashing structures for statistical purposes. The mono dispersed droplets are ejected from the orifice of the droplet generator at a frequency of $f_d \approx 12$ kHz. Figure 1 shows the experimental setup for the dynamic wettability experiments.

The illumination of the target area is attained by directing the light from an LED through a collimating lens system. The LED device is strobed with a pulse

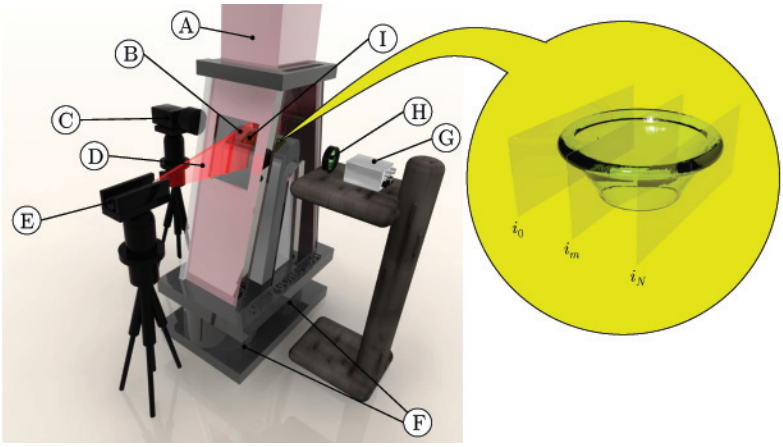

Figure 1: The experimental setup for the dynamic wettability experiments with notations: (A) Vertical droplet tunnel, (B) droplet cloud, (C) CCD camera, (D) laser sheet, (E) laser, (F) control valves, (G) LED strobing device, (H) collimating lens, and (I) specimen target. The right hand side image depicts a schematic corona structure with virtual planes $i_0, \ldots, i_N$, with i_m showing the mid-plane.

period $T = 40$ ms and pulse length of $\tau = 5$ μs which results in approximately one strobe per acquired frame of the experiment. The image acquisition is actualized by employing a Sony XCD-SX90 camera operated at 30 FPS. The camera is equipped with a 50 mm lens and 13 mm extension. The distance between the camera and the wall of tunnel $d_W = 50$ mm, the LED and the collimating lens $d_C = 40$ mm, and further between the collimating lens and the wall of the tunnel is 100 mm.

The optical magnification of the experimental image is hence 0.32. The images are acquired upon utilizing a graphical user interface on a personal computer.

2.1.1 Integrated view

As the LED light is captured along the length of the specimens, splashing features are apparent in the volume of space along the width of each specimen. The image acquisition camera is focused on the mid-plane of the specimen surface as denoted by i_m in Figure 1. This entails that any structure appearing within this plane of sight will appear entirely in focus on the experimental photographs. Equally, a deviation from this plane will result in structures appearing not entirely in focus. However, as the employed illumination within the depth of field is adequate, even off-plane splashing features are distinguishable. This approach hence results in capturing of most splashing events, at the expense of them appearing simultaneously on similar locations along the width of the specimen which may result in distinction of certain features becoming intricate. It is notable

that as the LED light travels through all virtual planes $i_0, \ldots, i_N$, an integrated view is visible upon image acquisition.

2.1.2 Planar view

In order to estimate the local liquid water content on the specimen surface, a laser sheet with a 2 mm width was used to illuminate the exact half-width of the specimen, where the camera was focused parallel to the oncoming droplets. Upon entering the laser sheet, the droplets were illuminated and visible as distinct features upon image acquisition. The finite thickness of the laser sheet further implied that very few unfocused droplets were observed.

3 Experimental specimens

A total number of 8 different materials referred to hereafter as specimens A−H were utilized in this study in two different prescribed conditions; as supplied and in an eroded condition. The majority of these are established epoxy resins commonly used within the aerospace industry with addition of carbon nanotubes as a reinforcing agent. Specimens A and B are both combinations of Araldite® LY564/Aradur® 2954 with the exception that specimen B also features multi-walled carbon nanotubes (MWCNT) at a 0.5% wt. Graphistrength® C100. Specimen C is Araldite® DBF/Aradur® HY956EN base resin with 10% wt. aluminium nitride nanoparticles. Specimens D−G are Araldite® MY0510/Aradur® 976-1 combinations where D and F have 0.5% wt. MWCNT. Finally specimen H is a gelcoat consisting of a SW404/ XB5173 combination. All considered material specimens have dimensions, $(L \times W) = (30 \times 20)$ mm^2 with different thickness values of $H \in [1, 9]$ mm.

In the pristine state, no morphological treatment to the specimen surface is applied. This condition replicates instances where no material degradation has been observed upon implementation of the material on an aircraft during flight. The second state is an eroded state of the material, which is attained upon its wet blasting by using alumina. The choice of this abrasive stems from the need to obtain a fine degradation of the material without catastrophic failure. An eroded state of the material is obtained from an accelerated testing technique. However, this approach allows for establishment of surface morphology modifications on the resulting wetting characteristics of the materials. The surface roughness of the specimens prior and after wet blasting is measured by a Surtronic instrument. The average value of the surface roughness pre-erosion R_a^p, surface roughness post-erosion R_a^e and the percentage change in surface roughness ΔR_a are shown in Table 1.

3.1 Methodology

The methodology comprises of determining the type of specimen based on its wetting characteristics, by employing the flowchart in Figure 2.

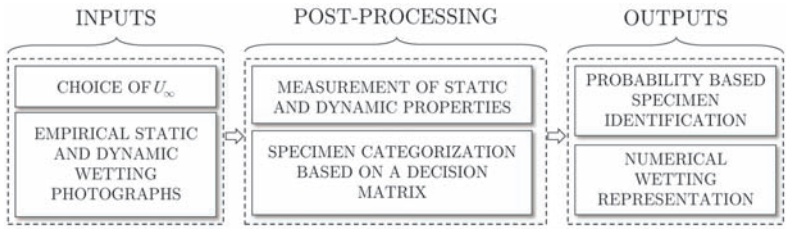

Figure 2: Flowchart for the data processing methodology based on empirical results.

Initially, a predefined free stream velocity U_∞ at which the sample photographs are acquired is chosen by the user. This velocity determines the local liquid water content based on a numerical scheme that identifies the droplet cloud distribution from experimental photographs and provides an averaged histogram of the cloud spatial distribution on the target. Static and dynamic wetting photographs in the pre- and post-erosion state of the specimen are further used as inputs to the numerical specimen detection scheme. The resulting photographic information is upon input, processed based on a number of Graphical User Interfaced tools developed in MATLAB®, as shown in Figure 3. Upon post-processing of the data, a decision matrix determines a probability factor which is attributed to a specific specimen.

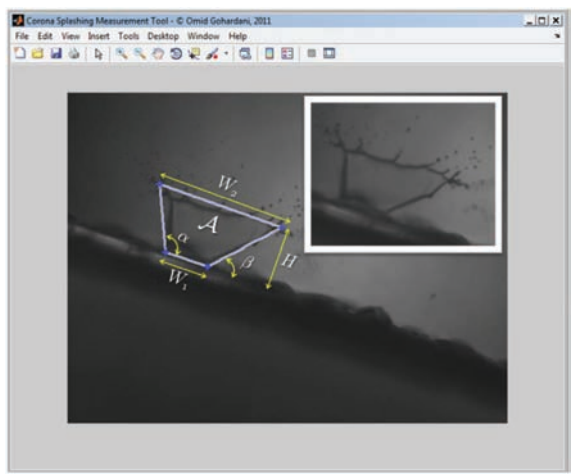

Figure 3: Autonomous corona measurement tool developed in MATLAB®. The tool outputs the projected area of the corona $\mathcal{A}$, angles α and β, and distances H, W_1, W_2 and other image related properties.

4 Data acquisition

4.1 Liquid Water Content

By utilizing a laser sheet for a given free stream velocity U_∞, a sequential monitoring of the cloud scatter was actualized. The acquired photographs were digitally processed based a numerical approach which subdivided each photograph into 10 regions with the same size along the length of the specimen. The photographic stack of 347 images, was after contrast enhancement, processed by a droplet counting scheme which determined the number of droplets in each sub-region. The averaged number of droplets within a sequence of images, in a given zone were further given by

$$\overline{R}_j = \frac{1}{n}\left\{\sum_{i=1}^{n} D_i\right\}_j \tag{1}$$

where $i = \{1, 2, \ldots, n\}$, $j = \{1, 2, \ldots, 10\}$ and n is the number of frames equal to 347. Upon known number of droplets, a similar approach for estimation of the local Liquid Water Content (LWC) as Ide [6] was employed. For a constant droplet diameter, d and total sample area for the bins $\widetilde{A}$, the LWC can be expressed as

$$LWC \cong \frac{\rho\pi d^3}{6\widetilde{A}U_\infty t}\sum_i R_j \tag{2}$$

where ρ is the water density, t is the sampling time, U_∞ is the free stream velocity, and the sum refers to the total number of droplets. The local liquid water content for free stream velocities $U_\infty \approx \{35, 50, 60\}\ \mathrm{m \cdot s^{-1}}$ was estimated to $LWC \cong \{0.38, 0.16, 0.02\}\ \mathrm{g \cdot m^{-3}}$. Figure 4 shows the averaged number of droplets within 10 equally sized bins at three different free stream velocities for a sampling duration of 10 seconds. The lack of droplets between the first and last bin for free stream velocities above 35 $\mathrm{m \cdot s^{-1}}$ indicate that lower local LWC values are observed with an increasing U_∞. For statistical purposes $U_\infty \approx 35$ $\mathrm{m \cdot s^{-1}}$ hence provides more reliable empirical results compared to the other free stream velocities.

4.2 Contact angle measurements

Both static and dynamic sessile drop methods were employed, in order to obtain angles at which the droplets move along the surface of the specimen. These methods convey results about the surface energy using Young's equation

$$\gamma_{\mathrm{SG}} - \gamma_{\mathrm{SL}} - \gamma\cos(\varphi) = 0 \tag{3}$$

where γ is the surface energy and the subscripts SG and SL denote solid-gas and solid-liquid respectively. In the static sessile drop method, the angles between the

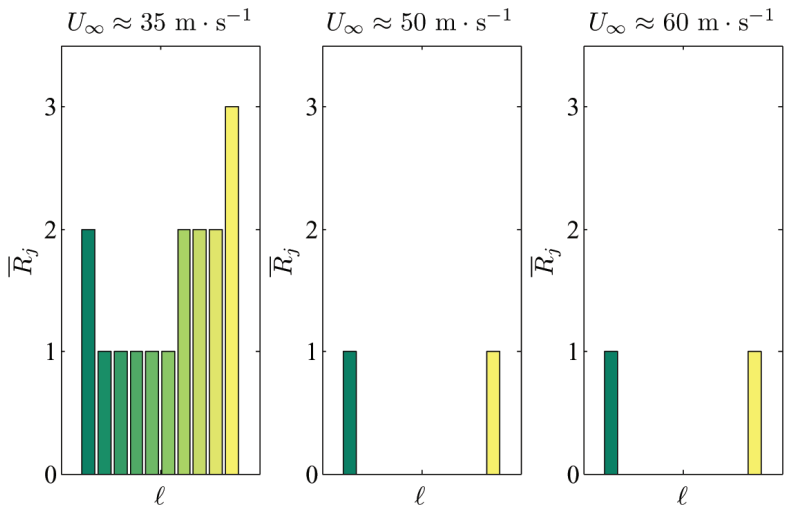

Figure 4: The number of averaged droplets within each bin $\overline{R}_j$, designated by a dark color for the first bin and a bright color for the last bin, for different free stream velocities $U_\infty \approx \{35, 50, 60\}\ \mathrm{m \cdot s^{-1}}$ along the non-dimensional specimen length, ℓ.

interfaces at SG and SL are measured by utilizing a protractor. For the dynamic sessile drop method, the drop is modified by either dispensing or retracting its volume, resulting in an advancing angle θ_A or a receding angle θ_R, measured by a protractor. This method allows for an assessment of the homogeneity of the specimen, as droplets can be deposited on different locations on the specimen surface. In this study an averaged value of five measurements placed on different locations on the surface are presented. Hysteresis ψ, can in this context be defined as $\psi \equiv \theta_A - \theta_R$. The equilibrium Young contact angle θ_C can also be expressed in terms of the advancing and receding angles [8] as

$$\theta_C = \arccos\left\{\frac{\Gamma_A \cos(\theta_A) + \Gamma_R \cos(\theta_R)}{\Gamma_A + \Gamma_R}\right\} \tag{4}$$

where $\Gamma_{A,R} \equiv \{\sin^3(\theta_{A,R})/(2 - 3\cos(\theta_{A,R}) + \cos^3(\theta_{A,R}))\}^{1/3}$. Table 1, shows the advancing, receding, equilibrium Young contact angle and their corresponding hysteresis.

4.3 Image analysis

4.3.1 Static wetting

The static wetting of the specimens is assessed by employing contact angle measurements on both pristine and eroded specimen surfaces. The experimental setup for the contact angle measurements is shown in Figure 5. The specimen is

Table 1: Surface roughness on the specimens in the pre- and post-erosion state given by R_a^p and R_a^e respectively. The percentage increase and decrease is given by $\Delta R_a = (R_a^p - R_a^e)/R_a^p$. The advancing angle θ_A, receding angle θ_R, hysteresis ψ and the equilibrium Young angle θ_C for each specimen are shown with the pristine value in the left and the eroded value to the right in each column.

Notation	R_a^p [μm]	R_a^e [μm]	ΔR_a	θ_A [°]		θ_R [°]		ψ [°]		θ_C [°]	
A	5	4.24	−0.152	110	75	22	11	88	64	22	11
B	0.74	4.4	4.946	93	90	33	6	60	84	35	6
C	0.8	3.74	4.946	80	90	17	10	64	80	18	10
D	0.2	3.98	3.675	87	80	28	10	58	70	30	10
E	1.2	3.92	2.267	93	70	32	8	62	62	33	8
F	0.2	4.06	19.30	90	68	28	13	62	55	30	14
G	0.8	2.32	1.90	82	110	32	22	50	88	34	22
H	0.6	2.98	3.967	117	90	60	8	57	82	63	8

positioned on a table with a vertical adjustment capability and illuminated by a light emitting diode with a diffuser, which provides a uniform illumination of the droplet.

The setup is utilized for measurement of the advancing and receding contact angles on the different specimen surfaces.

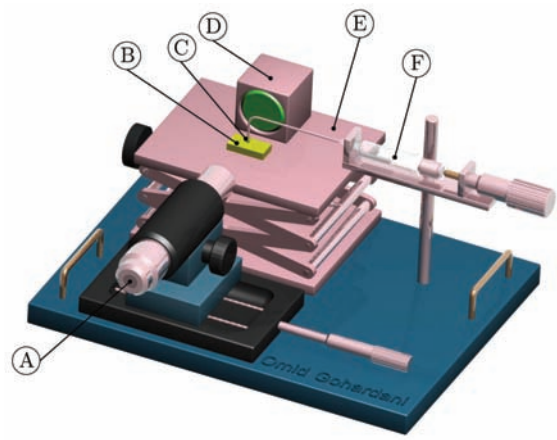

Figure 5: The experimental setup for the contact angle measurements, with notations: (A) Eye piece fitted with a protractor, (B) specimen, (C) generated droplet, (D) LED with diffuser, (E) vertical adjustable table, and (F) syringe and spring device fitted with a micrometer.

Table 2: Non-dimensional parameters for the prescribed free stream velocities, U_∞ in $\mathrm{m} \cdot \mathrm{s}^{-1}$.

U_∞	Re	We	K	Ca	ξ^*
35	12 271	6 725	49 856	0.55	$3.03 - 3.04$
50	17 530	13 725	101 747	0.78	3.32
60	21 035	19 764	146 567	0.94	3.47

4.3.2 Dynamic wetting

The splashing phenomenon is often related to different non-dimensional parameters such as the Reynolds number $Re \equiv (\rho U_\infty d)/\mu$, the Weber number $We \equiv (\rho U_\infty^2 d)/\sigma$, the Ohnsorge number $Oh \equiv \sqrt{We}/Re$, and the Capillary number $Ca \equiv We/Re$, where d is the droplet diameter, ρ defines the density, U_∞ is the free stream velocity, μ is the dynamic viscosity and σ denotes the surface tension. The spreading factor $\xi^* \equiv d_{\max}/d$, can further be expressed as [7]

$$\xi^* = \sqrt{\frac{We + 12}{3\left(1 - \cos(\theta_A) + \frac{4We}{\sqrt{Re}}\right)}} \tag{5}$$

Table 2, shows the non-dimensional parameters for the considered free stream velocities.

It is notable that the influence of the advancing angle on the spreading factor is nominal for the considered cases as it influences the maximum spread diameter, $d_{\max}$ with less than 5%. From Table 2, it is evident that $d_{\max} \in [3.0d, 3.5d]$ where d, is the initial diameter of the droplet. Representative photographs for each specimen in its pristine and eroded state respectively, are shown in Figure 6.

5 Discussion

The general observation for the wetting characteristics of the considered materials exhibits that specimens in the pre-eroded state are mainly hydrophobic as indicated by the formation of discrete water beads upon wetting. With modifications to the surface morphology by erosion, a partial or complete water film is apparent on all specimens.

The difference between the specimens in the post-eroded state is therefore, solely determined by the number of streams along the specimen surface. For the specimens exhibiting completely continuous water films, these streams merge to one coherent water film flowing along the specimen surface. By contrast, specimens with partial wetting characteristics have a discrete number of streams separated by non-wetted regions between them.

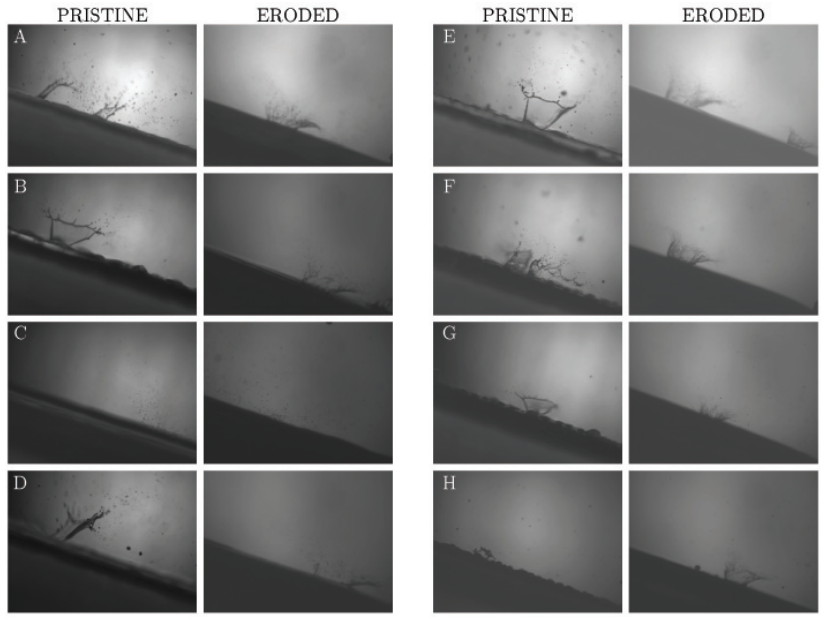

Figure 6: Pre- and post-erosion photographs of splashing structures on specimens A−H. The brightness and contrast of the images have digitally been enhanced for visualization purposes.

6 Conclusions

Dynamic wettability of the considered materials exhibit seemingly similar wetting characteristics in the pristine state of each material, with the materials being largely hydrophobic. Upon erosion, the formation of water films on the specimen surfaces, indicate a more hydrophilic behavior. Despite the complexities of image processing for different static and dynamic wettability arrangements, a methodology has been developed that discriminates between different empirical photographs of hydrophobic and hydrophilic specimens based on a numerical scheme. This scheme has thus far provided satisfactory results based on post-processing of the empirical photographs. For more adequate results however new modules have to be added to this methodology that would allow for better identification rules of different materials, based on their wetting characteristics.

Acknowledgement

The authors greatly acknowledge the financial support from the European Union for conducting this research as a part of multi-functional layers for safer aircraft composite structures (LAYSA) project, under the Seventh Framework Programme (FP7), including aeronautics.

References

[1] Shalin RE. Polymer matrix composites. 1995; Springer, pp 440. ISBN 0412613301.
[2] Gohardani O. Impact of erosion testing aspects on current and future flight conditions. 2011; Progress in Aerospace Sciences. Volume 47, Issue 4, Elsevier, pp. 280–303. doi:10.1016/j.paerosci.2011.04.001.
[3] Neinhuis C and Barthlott W. Characterization and distribution of water-repellent, self-cleaning plant surfaces. 1997; Ann Bot, 79(6): pp 667–677.
[4] Byun D, Hong J, Saputra, Ko JH, Lee YJ, Park HC, Byun BK, Lukes JR. 2009; Wetting Characteristics of Insect Wing Surfaces. J Bionic Eng, Vol 6(1), pp 63–70.
[5] Hu DL, Prakash M, Chan B, and Bush JWM. Water-walking devices. In; Animal locomotion. 2010; Springer. Eds: Taylor G, Triantafyllou MS, Tropea C, pp 350. ISBN 3642116329.
[6] Ide RF. Comparison of Liquid Water Content measurement techniques in an icing wind tunnel. 1999; NASA/TM–1999-209643.
[7] Pasandideh-Fard M, Qiao YM, Chandra S, and Mostaghimi J. Capillary effects during droplet impact on a solid surface. 1996; Phys Fluids 8(3), pp 650–659.
[8] Tadmor R. Line Energy and the Relation between Advancing, Receding, and Young Contact Angles. 2004; Langmuir 20(18), pp 7659-7664.

This page intentionally left blank

Section 3
Multiphase flow

This page intentionally left blank

On radiation absorption effects and air humidity influence on evaporating water droplets and vapour condensation intensity

G. Miliauskas, S. Sinkunas & K. Sinkunas
Department of Thermal and Nuclear Energy,
Kaunas University of Technology, Lithuania

Abstract

This paper discusses modelling of water droplet heating and evaporation in humid air. The effect of black body spectral radiation of the air temperature on the combined heat transfer in the water droplet has been evaluated. A combined analytical and numerical method of investigation is applied. Securing the balance of energy fluxes in the droplet with a confidence of one hundredth of a percent, the method of fastest descent has been used to determine the droplet surface temperature. Thermal state and phase transformation dynamics for the warming droplets heated in a humid air environment are modelled under conductive and combined conductive-radiative heating.
Keywords: humid air, water droplet, combined heat and mass transfer, droplet heating and evaporation, condensation.

1 Introduction

The research of water droplet heat and mass transfer is connected with application of sprayed water technology in power energy and other industries. The problem of droplet evaporation has been researched for more than a hundred years [1]. Demand to improve technology which employs liquids in the sprayed form requires further understanding of combined heat and mass transfer processes in liquid droplets under wide range of conditions. Applied methods for investigation of heat and mass transfer in liquid droplet are systematically reviewed in [2]. There has been an objective for particular consideration of unsteady combined heat and mass transfer processes in recent years [3–9]. The methods developed for analytical and numerical investigation of droplet combined heat and mass transfer allows modelling of more complex processes and their interactions.

WIT Transactions on Engineering Sciences, Vol 74, © 2012 WIT Press
www.witpress.com, ISSN 1743-3533 (on-line)
doi:10.2495/AFM120171

The above mentioned phenomenon is relevant to nuclear industry and specifically to durability of boiler tubes. Hence, understanding of factors affecting tube metal degradation is significant to nuclear safety of the plant. The relevant degradation mechanism depends on tube wall metal and the environment properties it operates in. The risk of stress corrosion cracking is applicable to stainless steel tubes, which normally operate with superheated steam, but under certain operational conditions have likelihood of droplet carryover into that section of the boiler.

Water droplet heating and evaporation can be modelled in different ways. Various aspects of heat and mass transfer can be considered: droplet slipping in steam flow will affect convection, droplets in steam are also heated by convection, but radiation of the surroundings determines if heating is combined heating. Sprayed droplet initial temperature and dispersity are also very important factors affecting heat and mass transfer. The condensation process requires the presence of vapour in the droplet surroundings. The initial droplet temperature affects if heat and mass transfer on the droplet surface will be for condensation or evaporation. For small droplets of diameter of microns range it is necessary to evaluate the influence of Knudsen layer to droplet evaporation. In the case when droplets are large the influence of surroundings radiation must be evaluated. Each of these factors contributes essential peculiarities for heat and mass transfer modelling [9–11].

The results of analysis of heating and phase transformation for larger droplets on their surface in humid air are presented in this paper.

2 Formulation of the problem

The intensity of phase transformations at the droplet surface determines water vapour flux [12]:

$$m_v^+ = \frac{D_{vg}\mu_v}{T_{vg,R}R_\mu R}\left[p_{v,R} - p_{v,\infty} + \frac{\mu_v}{\mu_g}\left(p\ln\frac{p - p_{v,\infty}}{p - p_{v,R}} + p_{v,\infty} - p_{v,R}\right)\right]. \quad (1)$$

The influence of Knudsen layer for large-scale droplets evaporation is negligibly small, and steam and gas mixture temperature near the droplet in expression (2) is comparable to the droplet surface temperature: $T_{vg,R} \equiv T_R$. The droplet surface temperature determines the regime of phase transformations – when it is below the dew point temperature the water vapour of humid air condenses on the droplet surface. When heated droplet surface temperature reaches dew point temperature the regime of phase transformation changes and droplet starts to evaporate. Air humidity is defined by volumetric part of water vapour $\overline{p}_v = p_{v,\infty} / p$. The driving force of diffusive evaporation is defined by the water vapour pressure difference near the droplet and in humid air. The effect of Stefan hydrodynamic flow on the intensity of evaporation is evaluated by logarithm in expression (1). The droplet surface temperature is determined by heat flow interaction at the surface. This temperature must secure the heat flux

in-flow and out-flow balance. Assumption of heat and mass transfer process quasi-stationarity enables to describe the heat flow balance by the condition:

$$\vec{q}_k^{+} + \vec{q}_k^{-} + \vec{q}_f^{+} \equiv 0; \frac{\lambda_{vg}}{R}\left(T_g - T_R\right)\cdot \ln\frac{1+B_T}{B_T} - \lambda\left.\frac{\partial T(r,\tau)}{\partial r}\right|_{r=R^-} = m_v^{+} L\,. \tag{2}$$

Logarithmic function of Spalding heat transfer number in the expression (2) takes into account effect of Stefan hydrodynamic flow on the intensity of convective heating of evaporating droplet. Water circulation in the droplet has not been considered. It is assumed that there is no phase slippage in humid air flow carrying water droplets. The incident spectral radiation onto droplet is partially reflected and partially absorbed in the semitransparent droplet. The direction of vapour flux is determined by the logarithmic function in expression (1), and it is considered being positive in the case of evaporative regime. The temperature gradient for combined conductive-radiative heat transfer process in the droplet is described by expression [10]:

$$\left.\frac{\partial T(r,\tau)}{\partial r}\right|_{r=R^-} = \frac{2\pi}{R^2}\sum_{n=1}^{\infty} n(-1)^n \int_0^{\tau}\left[(-1)^n \frac{R}{n\pi}\frac{dT_R}{d\tau_*} + \frac{1}{R\rho c_p}\int_0^{R}\left(\sin n\pi\eta - n\pi\eta\cdot\cos n\pi\eta\right)q_r\,dr\right]\exp\left[-a\left(\frac{n\pi}{R}\right)^2(\tau-\tau_*)\right]d\tau_*. \tag{3}$$

Flux density of radiation in spherical semitransparent droplet is calculated according to methodology [10] and the complex refractive index of water is used in accordance with [13, 14] recommendations. The Spalding heat transfer number takes into account the radiation absorption by droplet and temperature gradient in it [15]. The expression (2) is solved numerically. The time step is chosen freely. Instant droplet surface temperature is determined by the iterative method of fastest descent. Imbalance of heat fluxes on the droplet surface is achieved to less than one hundredth of a percent. After calculating the vapour flux on droplet surface in accordance with expression (1) the volume change of spherical droplet in time step $\Delta\tau$ is determined by:

$$\frac{\partial(\rho V)}{\partial\tau} = -4\pi R^2 m_v^{+}. \tag{4}$$

To determine the droplet surface temperature its volume is assumed constant during time step $\Delta\tau$ while conducting iterative calculations. This ensures the stability of the numerical iterative scheme. The droplet volume is revised for every next time step.

3 Results and discussion

The analysis has been conducted for water droplets of various initial temperatures in the humid air (of $\overline{p}_v \equiv 0.2 \div 0.95$) of 700 K and 0.1MPa. Conductive heating has been modelled assuming that droplets in air are stagnant.

In the case of combined heating by conduction and radiation the external black body radiative source with air temperature has been assumed. Droplet evaporation process is significantly influenced by the degree of moisture in the air (Fig. 1). Curves describing the change of heat and mass transfer parameters presented in the dimensionless form of Fourier number scale are general for all conductively heated droplets. The initial water temperature and air parameters must be defined.

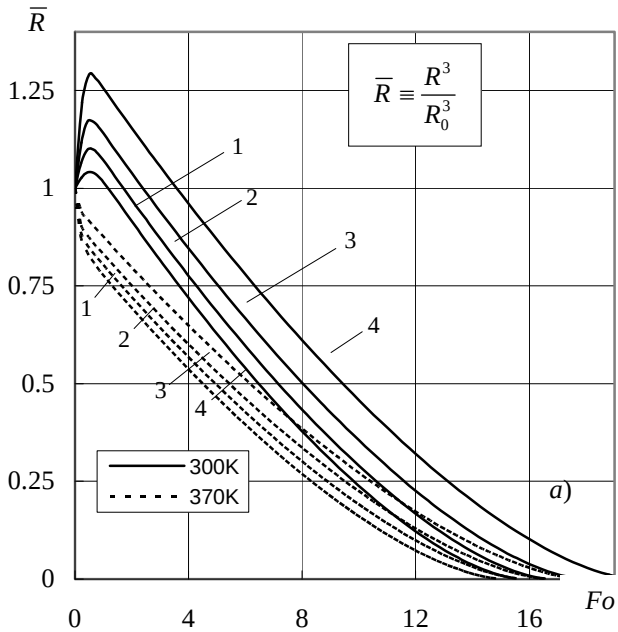

Figure 1: Evaporation of conductively heated water droplets in humid air. $\Delta\overline{p}_{v,\infty}$: (1) 0.2, (2) 0.4, (3) 0.6, (4) 0.8.

The droplet volume dynamics $R^3(Fo)/R_0^3 \equiv \overline{R}(Fo)$ strongly depends on air humidity and sprayed water temperature. Volume of the low initial temperature droplets increases during the primary stage of phase transformations due to vapour condensation on their surfaces and expansion of warming water. The droplet volume is increasing for certain duration due to expansion of warming water during the initial stage of the droplet evaporation regime. The evaporating droplet volume starts to decrease when the process of water evaporation exceeds water expansion process. The effects of above mentioned competing processes to the dynamics of droplet volume reach equality and are visible on the volume dynamics curve $\overline{R}(Fo)$ as an extremum point (Fig. 1). The droplet volume of high initial water temperature does not have volume expansion stage and its volume starts to decrease immediately. Rapid volume decrease is caused by

intensive evaporation process and shrinkage of cooling water. Water droplets quite quickly reach equilibrium evaporation regime. Equilibrium evaporation is defined as a phase transformation regime during which heat delivered to the droplet by the surroundings is solely consumed for droplet evaporation, i.e. $q_f^+\left(Fo \equiv Fo_e\right) \equiv q_\Sigma^+$. The beginning of equilibrium evaporation for conductively heated droplets is also indicated as convergence of curves $q_f^+\left(Fo\right)$ and $q_k^+\left(Fo\right)$.

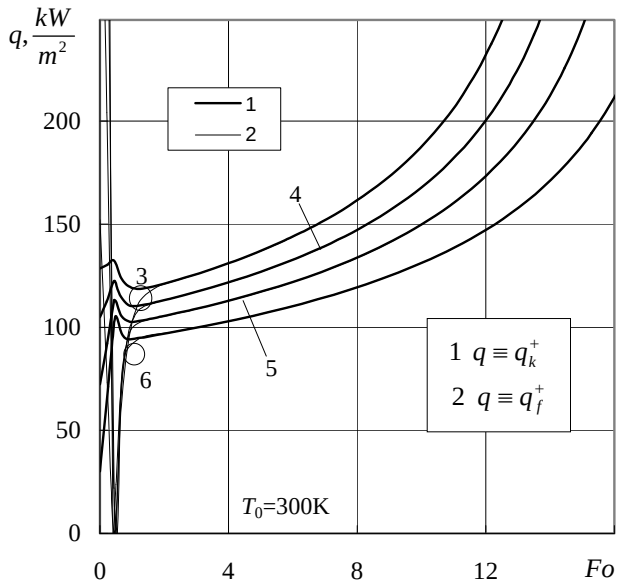

Figure 2: Heat fluxes on the droplet surface for conductively heated cold droplets. $\Delta\overline{p}_{v,\infty}$: (3) 0.2, (4) 0.4, (5) 0.6, (6) 0.8; $R_0 = 0.0001$m.

The temperature of the conductively heated droplets does not change during the equilibrium evaporation regime (Fig. 3). The equilibrium evaporation temperature is reached by intensive droplet heating for low initial temperature droplets (Fig. 3*a*) and intensive cooling for high initial temperature droplets (Fig. 3*b*). The distinct non-isothermality is observed during the initial stage of phase transformations. The droplet non-isothermality diminishes when approaching the regime of equilibrium evaporation. The near equilibrium temperature is first reached by the subsurface layers in the droplet and later by the central layers of the droplet.

During the unsteady phase transformations not only the droplet temperature changes rapidly, but also the heat fluxes at the droplet surface change significantly (Fig. 4). This is caused by the initial water droplet temperature and their way of heating.

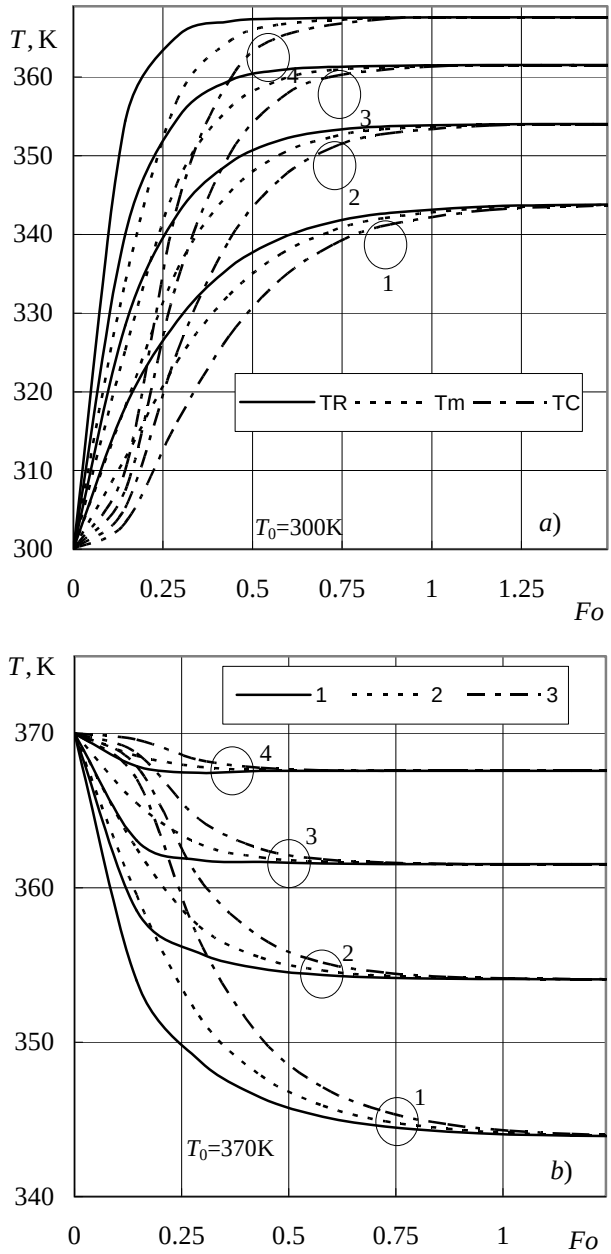

Figure 3: The influence of initial water temperature to the droplet temperature dynamics for conductively heated droplets during the initial stage of phase transformations. $\Delta\overline{p}_{v,\infty}$: (1) 0.2, (2) 0.4, (3) 0.6, (4) 0.8.

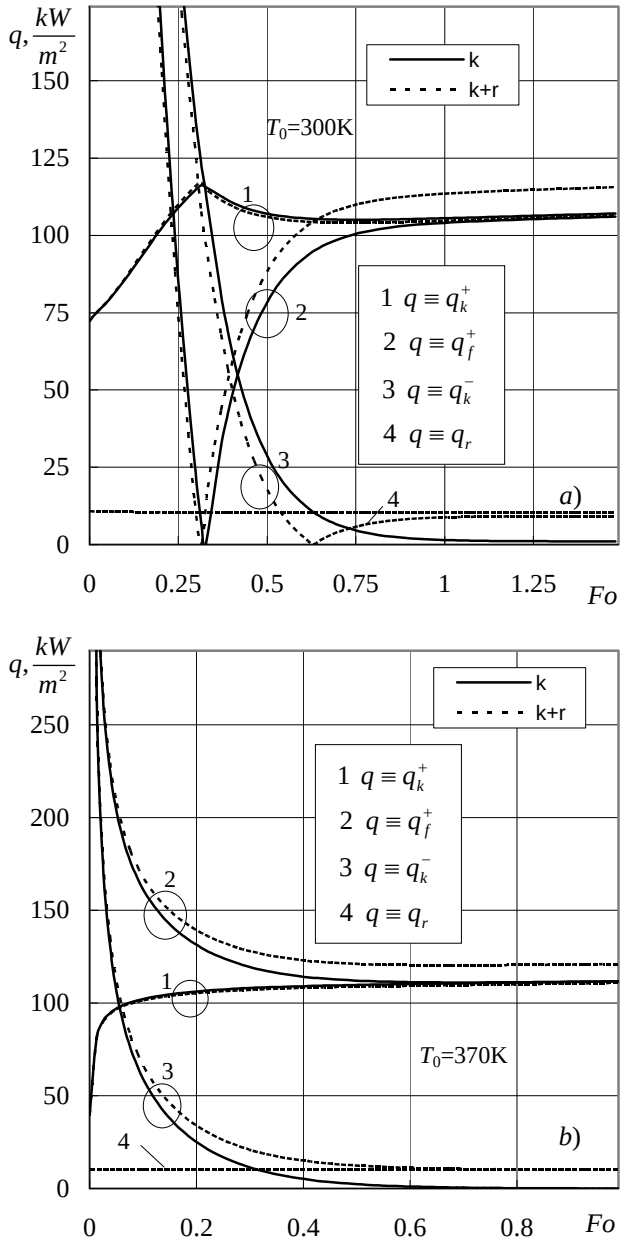

Figure 4: Heat fluxes at the droplet surface for low and high temperature droplets during unsteady phase transformation regime for the conductive heating case (k) and the combined heating case (k+r). $\Delta\overline{p}_{v,\infty}$: (1) 0.2, (2) 0.4, (3) 0.6, (4) 0.8.

The influence of radiation to phase transformations for larger droplets is more significant (Fig. 5). Intensive heating of low initial temperature droplets up to dew point temperature is caused by intensive vapour condensation process (Fig. 4*a*). When the droplet is heated conductively, then the intensity of water warming is determined by conductive heat flux on the internal side of the droplet surface, and in the case of combined heating – by the total heat flux. The total heat flux on the internal side of the droplet surface during the regime of condensational phase transformation is $q_{\Sigma}^{-}\left(0 \div Fo_{co}\right) \equiv q_{k}^{+} + q_{r}^{+} + q_{f\equiv co}^{+}$, where term q_{co}^{+} approaches zero. At the moment of phase transformation regime changeover the condition $q_{k}^{-} \equiv q_{k}^{+}$ is valid. Accelerating process of evaporation inhibits water warming in the droplet: $q_{h}\left(Fo_{co} \div Fo_{e}\right) \equiv q_{k}^{+} + q_{r}^{+} - q_{f}^{+}$. The phase transformation heat flux during the unsteady evaporation regime is $q_{f}\left(Fo_{co} \div Fo_{e}\right) \equiv q_{\Sigma}^{+} - q_{\Sigma}^{-}$. The dynamics of heat fluxes during the unsteady evaporation regime determines the initial spayed water temperature and the ways droplet are heated (Fig. 4). The influence of heating manner is especially distinct for low temperature droplets (Fig. 4*a*). Conditions for absorbed radiation in the semitransparent droplet to participate in the water evaporation process establish only when droplet temperature field of negative gradient is formed. The conductive heat flux becomes zero at the moment of the vector direction

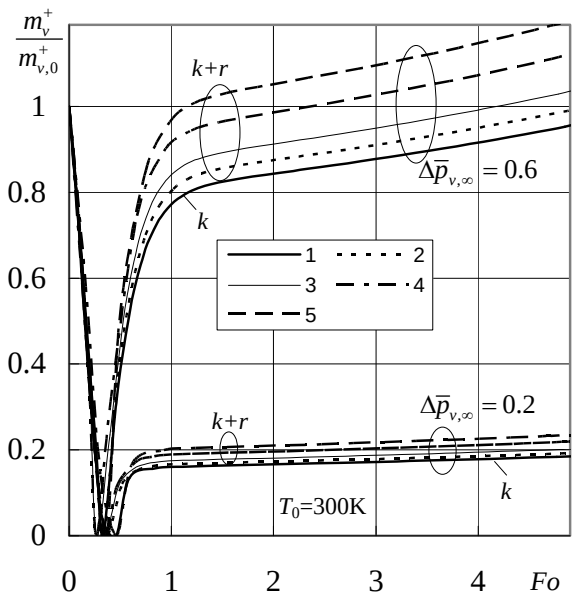

Figure 5: Influence of radiation on droplets phase transformations. R_0, m: (2) 0.00005, (3) 0.0001, (4) 0.0002, (5) 0.0003.

changeover for droplet temperature field gradient. Later it increases to $q_{k,e}^{-} \equiv q_r$ (Fig. 4*a*). The condensational phase transformation regime for the high initial water temperature droplets is impossible. The temperature field of negative gradient is formed immediately at the start of evaporation. The rapid cooling of the droplet is caused by very intensive evaporation process (Fig. 4*b*), which is associated with the participation of cooling droplet internal energy. The droplet cooling is slowing with approach to the equilibrium evaporation regime and the influence of the droplet internal energy reduces. For equilibrium evaporation regime the gradient of temperature field in the droplet ensures participation of the droplet absorbed radiation flux in the evaporation process.

4 Conclusions

The regime of unsteady phase transformations for water droplets in humid air is short and droplets rapidly reach the characteristic equilibrium evaporation temperature. Nonetheless, the regime of unsteady phase transformations for interaction of heat and mass transfer processes in sprayed water systems is very significant. The way of droplet heating and water initial temperature play an important role during this phase transformation regime.

The process of water vapour condensation, which is contained in air, causes rapid warming of low initial temperature droplets to the equilibrium evaporation temperature. The participation of droplet internal energy in the evaporation process determines rapid cooling of high initial temperature droplets. The initial water droplet temperature does not influence heat transfer processes during the equilibrium evaporation regime.

The effect of radiation to temperature dynamics and phase transformations is more significant for droplets of bigger size than for smaller ones. The influence of radiation is very significant for conductive heat flux dynamics in the cold water droplets.

5 Nomenclature

a – thermal diffusivity, m^2/s; B_T – Spalding heat transfer number; c_p – specific heat, J/(kg K); D – mass diffusivity, m^2/s; Fo – Fourier number; k – conductive heating; $k+r$ combined heating; L – latent heat of evaporation, J/kg; m – vapour mass flux, kg/(s·m^2); n – number of terms in the infinite sum; p – pressure, Pa; q – heat flux, W/m^2; R – radius of a droplet, m; R_μ – universal gas constant, kg/(kmol K); r – radial coordinate, m; T – temperature, K; V – droplet volume, m^3; η – non-dimensional coordinate; λ – thermal conductivity, W/(m K); μ – molecular mass, kg/kmol; ρ– density, kg/m^3; τ – time, s;

Subscripts: C – droplet centre; co – condensation; e – equilibrium evaporation; f – phase transformation; g – gas; k – conductive; m – mass average; r – radiative; R – droplet surface; rt – dew point; v – vapour; vg – vapour-gas mixture; 0 – initial state; ∞ – far from a droplet; Σ – total.

Superscripts: + – external side of the surface; - – internal side of the surface.

References

[1] N.A. Fuks. Evaporation and Droplet Growth in Gaseous Media. London: Pergamum Press, 1959.
[2] Sazhin S.S., 2006, Advanced models of fuel droplet heating and evaporation, Progress in Energy and Combustion Science, Vol. 32, pp. 162-214.
[3] Miliauskas G., Sinkūnas S. and Norvaisiene K., 2011, Influence of thermal radiation to the interaction of heat and mass transfer processes under evaporation of water droplets. ICCHMT'2011: 7th Inter-national Conference on Computational Heat and Mass Transfer. Turkey: Istanbul, pp. 1–8.
[4] Dombrovsky L.A., Solovjov V.P. and Webb B.W., 2011, Attenuation of solar radiation by a water mist from the ultraviolet to the infrared range. J. Quant Spectroscopy Radiative Transfer, Vol. 112, pp. 1182–1190.
[5] William F., Godoy and Paul E., 2009, Radiation driven evaporation for polydisperse water sprays. Int. J. of Heat and Mass Transfer, Vol. 52, pp. 2893–2901.
[6] Miliauskas G., Sinkūnas S. and Miliauskas G., 2010, Evaporation and condensing augmentation of water droplets in flue gas. Int. J. of Heat and Mass Transfer, Vol. 53, pp. 1220–1230.
[7] Arias P.G., Im H.G., Narayanan P. and Trouve A., 2011, A computational study of non-premixed flame extinction by water spray. Proceedings of the Combustion Institute, Vol. 33, pp. 2591–2597.
[8] Hitoshi Fujimoto, Yosuke Oku, Tomohiro Ogihara and Hirohiko Takuda, 2010, Hydrodynamics and boiling phenomena of water droplets impinging on hot solid. International Journal of Multiphase Flow, Vol. 36, pp. 620–642.
[9] Tseng C. C. and Viskanta R., 2006, Enhancement of water droplet evaporation by radiation absorption. Fire Safety J., Vol. 41, pp. 236-247.
[10] Miliauskas G., 2001, Regularities of unsteady radiative-conductive heat transfer in evaporating semitransparent liquid droplets. Int. J. of Heat and Mass Transfer, Vol. 44, pp. 785-798.
[11] Miliauskas G. and Garmus V., 2009, The peculiarities of hot liquid droplets heating and evaporation. Int. J. of Heat and Mass Transfer, Vol. 52, pp. 3726–3737.
[12] Kuzikovskij A.V., 1970, Dynamic of spherical particle in powerful optical field. Izv. VUZ Fizika, Vol. 5, pp. 89–94.
[13] Hale G.M. and Querry M.R., 1973, Optical constants of water in the 200-nm to 200-μm wavelength region. Appl. Opt., Vol. 12, pp. 555–562.
[14] Hale GM, Querry MR, Rusk AN and Williams D 1972 Influence of temperature on the spectrum of water. J. Opt. Soc. Am., Vol. 62, pp. 1103–1108.
[15] Miliauskas G and Sabanas V 2006 Interaction of transfer processes during unsteady evaporation of water droplets *Int. J. Heat Mass Transfer* **49** 1790–1803.

Emulsion compression and coalescence under enhanced gravity studied with in-situ microscopy

T. Krebs[1,2], J. J. Slot[3], C. P. G. H. Schroen[2],
H. W. M. Hoeijmakers[3] & R. M. Boom[2]
[1]*Institute for Sustainable Process Technology, The Netherlands*
[2]*Wageningen University, Food Process Engineering Group, The Netherlands*
[3]*University of Twente, Engineering Fluid Dynamics Group, The Netherlands*

Abstract

We report the results of experiments and numerical calculations of compression and coalescence in a monodisperse oil-in-water emulsion upon centrifugation. A custom-built setup allows in-situ monitoring of a rotating bilayer of emulsion droplets using an optical microscope. The oil volume fraction in a compressed layer of oil droplets stabilized against coalescence was measured experimentally as a function of time for different radial accelerations. The sedimentation was simulated using CFD in order to test the applicability of the computational method and the Ishii-Zuber drag law for very high dispersed phase volume fractions. Quantitative agreement of emulsion sedimentation as a function of time between the experiments and simulations is good at higher accelerations, but decreases with decreasing accelerations. Coalescence in a centrifuged emulsion, which was destabilized prior to centrifugation by adding sodium chloride, was also quantified. The growth of a pure oil phase on top of the droplet layer was measured as a function of time. From the growth rate, a characteristic time for droplet coalescence with the pure oil phase was deduced. The experimental method may serve as a tool to study the compression and coalescence kinetics of emulsions under enhanced gravity, which may be of use to assess emulsion stability for industrial applications. Possible improvements of the current experimental setup are also discussed.

Keywords: emulsion, compression, coalescence, microscopy, droplet, CFD, drag law.

WIT Transactions on Engineering Sciences, Vol 74, © 2012 WIT Press
www.witpress.com, ISSN 1743-3533 (on-line)
doi:10.2495/AFM120181

1 Introduction

The behavior of dense emulsions in flow fields with radial accelerations is of major importance for separation processes using cyclonic devices or centrifuges. Major examples are separation of crude oil and water during oil production, and milk processing in the food industry. The design of these separation processes is often strongly based on the results of Computational Fluid Dynamics, which has become an important tool for the process industry in recent years. For reliable modeling, information about the sedimentation rate, and kinetics of coalescence and breakup of droplets in a dense emulsion under enhanced gravity is needed.

A key parameter for modeling is the choice of the drag law for droplets as it will impact the calculated rate of sedimentation. For dense droplet-laden flows, the drag law of Ishii and Zuber is often used [1]. The Ishii-Zuber drag law is an extension of the well known Schiller-Naumann drag law [2]. It can be applied to flows with higher volume fractions of the disperse phase by incorporating hindered settling. As a droplet moves through the fluid it will induce a motion of the continuous phase and thereby deform the surrounding fluid. When other droplets are present in this surrounding fluid they will be subjected to this deformation as well. Due the Laplace pressure, the surrounding droplets will resist deformation more than the continuous fluid, leading to a higher local viscosity acting on the moving droplet. Therefore, the drag for these dense systems is modeled by assuming similarity to the single droplet case and using an expression for the mixture viscosity instead of the continuous phase viscosity. Besides the Ishii-Zuber drag law, other drag laws have been proposed for dense systems [3]. Still, the Ishii-Zuber law is a popular choice for CFD since it can be applied for a wide range of multiphase systems and flow parameters.

In addition to applying proper relation for the drag law, a correct prediction of the droplet size distribution and its effects on the flow field will increase the accuracy of multiphase flow CFD. In multiphase CFD, droplet breakup and coalescence kinetics can be taken into account using the approach of population balance equations (PBE) [4]. Analytical hydrodynamic models to predict the timescale of coalescence between two droplets have been proposed, which cannot generally be applied to dense flowing emulsions under enhanced gravity, however. Apart from analytical models, input for the coalescence functions in PBE modeling can also be provided by experiments, in principle. For oil/water separation applications, the kinetics of coalescence between droplets will impact the rate of separation. The mean droplet size will increase in the system when coalescence dominates over breakup, which will then accelerate the separation.

The dynamics of coalescence in centrifuged emulsions have been recently investigated by us using a tabletop centrifuge [5]. From the experiments, we derived characteristic coalescence times of the droplets in the emulsion as a function of the radial acceleration and surfactant concentration. Analysis of the samples was performed ex-situ, however, which increased the experimental error and made the experiments time-consuming.

In this paper, we present a study of compression and coalescence in an emulsion under enhanced gravity using a custom-built centrifuge, which allows in-situ microscopic observation of the emulsion during centrifugation. The degree of compression in a stable emulsion is expressed as the oil volume fraction in the compressed droplet layer. We compare the experimental results with CFD calculations to test the applicability of the computational method and the Ishii-Zuber drag law to high dispersed phase fractions. Further, we measure the rate of coalescence in an unstable emulsion as a function of the radial acceleration. From the coalescence experiments, characteristic times for coalescence of a droplet with a pure oil phase under enhanced gravity can be derived.

2 Experimental and computational methods

2.1 Chemicals

Sodium n-dodecyl sulfate (SDS, ACS reagent, $\geq$ 99%) and sodium chloride (NaCl, ACS reagent, $\geq$ 99%) were purchased from Sigma Aldrich. Sylgard 184 Silicone Elastomer kit was purchased from Dow Corning. As dispersed phase Sil180 silicone oil (Dow Corning) was used. At 293 K, the density of Sil180 is 931 kg m^{-3} and the viscosity 10.4 mPa s. Aqueous solutions of NaCl (5 wt%) and SDS (10 mM) were prepared with Millipore water. The density of the 5 wt% aqueous NaCl solution was 1032 kg m^{-3} at 293 K. The density difference between pure water and the oil is $\Delta\rho = 69$ kg m^{-3}, and for the salt solution and the oil $\Delta\rho = 101$ kg m^{-3}.

2.2 Microcentrifuge experiments

For the microcentrifuge experiments, a custom-made setup was used. Figure 1A displays a photo of the experimental setup. The setup consists of a disk, which is connected to a DC motor. The range of accessible rotation frequencies f is 1.5 Hz $< f <$ 100 Hz. A sample holder can be mounted on the disk. The distance r between the center of the sample holder and the motor axis is 10 cm. The radial acceleration a is given by $a = (2\pi f)^2 r$. The range of accelerations is thus 3.95 m s$^{-2} < a <$ 39500 m s^{-2}, or $0.402 < a/g < 4020$, if expressed in multiples a/g of the normal gravitational acceleration $g = 9.81$ m s^{-2}. For the entire range of a/g the induction time of the motor to reach 95% of the desired acceleration was < 0.5 s. The disk and the motor are enclosed in a protective housing. The entire assembly is placed on a custom-made plate, which is mounted on an inverted optical microscope (Axiovert 200, Zeiss). Three set screws allow to align the sample with the objective of the microscope. A high-speed camera (Y4-S2, IDT Inc.) is connected to the microscope. A software trigger was used (Motion Pro Studio, IDT Inc), which triggered recording when at least one pixel in the image was not black, indicating that the sample chamber, which is transparent, is passing by the microscope. A frame rate of 5000 Hz and an exposure time of 100 ns were

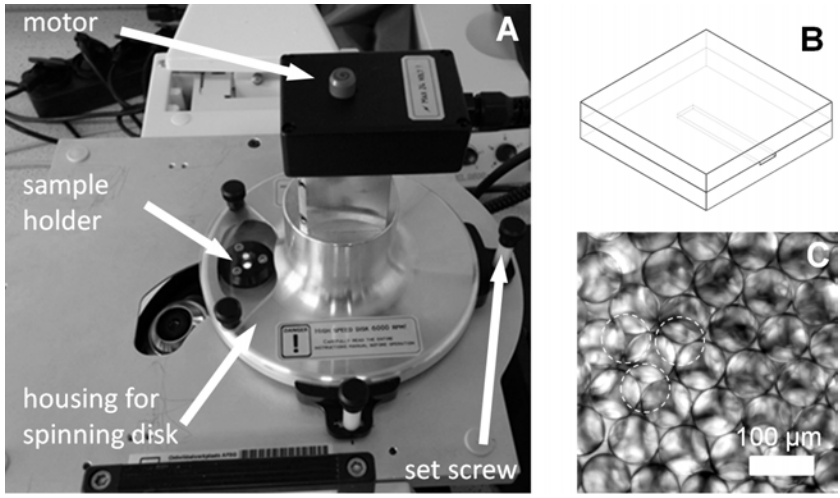

Figure 1: Panel A: photograph of the experimental setup. Panel B: sketch of the sample chamber used for the centrifuge experiments. The chamber is made from two PDMS disks. The bottom disk contains a channel of dimensions $5.25 \times 1 \times 0.2$ mm^{-3}, where the emulsion is inserted. Panel C: photograph of a oil-in-water emulsion in the sample chamber. The oil phase was Sil180 silicone oil, the aqueous phase a 10 mM SDS solution. The top layer of a bilayer of monodisperse droplets with a mean diameter 79.3 µm is displayed. The position of the second droplet layer is indicated by the dotted circles.

used for the experiments. The recorded images were processed with the program ImageJ using custom-written scripts.

A drawing of the sample chamber, which is placed in the sample holder, is displayed in Figure 1B. The sample chamber consists of two parts, which are made from polydimethylsiloxane (PDMS). The bottom part contains a channel (dimensions $5.25 \times 1 \times 0.2$ mm^3), which is open to one side. The top part of the sample holder contains no features. The parts are made from mold casting using the Sylgard Elastomer Kit, which consists of liquid PDMS and a curing agent [6]. The top and bottom part are chemically bonded together after exposure to an oxygen plasma. Before each experiment, the sample chamber was exposed to an oxygen plasma to render the chamber walls hydrophilic, in order to enable wetting of the channel walls with the continuous phase [6].

Monodisperse droplets of Sil180 silicone oil in a 10 mM aqueous SDS solution were produced with a microfluidic T-junction. The experimental setup and parameters have been described previously [7]. An oil-in-water emulsion with a mean droplet diameter $d = (79.3 \pm 0.8)$ µm was obtained. The emulsion was stable for the entire duration (~ 4 weeks) of the experimental work. The emulsion creamed in the storage flask; droplets were removed from the dense layer using a pipette and injected into the sample chamber. The mean oil volume fraction ϕ_0

in the creamed emulsion layer was measured by removing 1 μl of sample and counting the number of droplets after spreading of the test volume on a microscope slide. From ten measurements $\phi_0 = 0.72 \pm 0.03$ was obtained. Figure 1C displays a photograph of the emulsion in the sample chamber. The droplets have a circular cross section and form a bilayer. In the image shown, the image was focussed on the top layer of droplets. The second layer of droplets is visible only diffuse, the position of the droplets relative to the first is sketched by the dotted circles in Figure 1C.

2.3 Numerical calculations

$$C_D = \frac{24}{Re_m}(1 + 0.15 Re_m^{0.687}) \tag{1}$$

The Reynolds number based on the mixture viscosity is defined as $Re_m = \rho_w \mid \mathbf{u_o} - \mathbf{u_w} \mid d/\eta_m$. Finally, the mixture viscosity is given by

$$\eta_m = \eta_w (1 - \phi)^{-2.5 \frac{\eta_o + 0.4\eta_w}{\eta_o + \eta_w}} \tag{2}$$

Here η_o and η_w are the dynamic viscosities of the oil and water respectively.

The governing equations were solved using the commercial CFD package Ansys CFX 13.0. A mesh of 3.3 million hexahedral elements and the use of double precision executables are required to capture the steep gradients in volume fraction and to avoid strong oscillations near that gradient in the numerical solution. A no slip condition is imposed on the walls. The use of a spatially varying centrifugal force lead to numerical oscillations in volume fraction. Therefore, a constant body force is used here. Due the large radius at which the chamber is placed compared to its dimensions of the error made here is smaller than 1%. All other parameters used in the calculation, such as d, a and ϕ_0 are matched with the experimental values. As initial condition a homogeneous emulsion with ϕ_0 is used.

3 Results and discussion

3.1 Emulsion compression

Figure 2A displays a contour plot of the oil volume fraction ϕ in the sample chamber during centrifugation obtained from the CFD calculations at 103g after 10 s of centrifugation as an example. Due to the density difference between the two phases ($\Delta\rho = 69$ kg m^{-3}), oil is concentrated at the right side of the sample chamber. At the left side of the sample chamber, pure continuous phase is accumulated. The transition between the oil-rich and oil-free layer is sharp, as can be seen from a cross-sectional plot of ϕ along the y-axis (Figure 2B). In the oil-rich layer, $\phi(y)$ increases with increasing distance from the boundary between the two layers, and eventually reaches unity. From the $\phi(y)$ profiles we calculate an average oil volume fraction ϕ_c of the oil-rich layer, in order to compare the

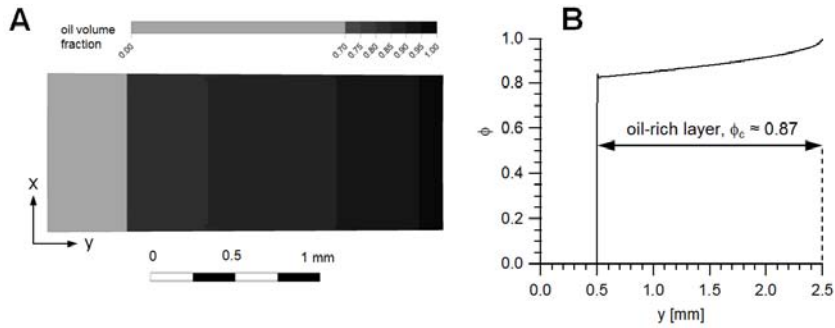

Figure 2: Examples of results of the numerical calculations. Panel A: Contour plot of the oil volume fraction in the sample chamber during centrifugation at 103g, 10 s after the start of centrifugation. Panel B: cross-sectional profile of the oil volume fraction along the y-axis at $x = 0.5$ mm, extracted from the contour plot in Panel A.

CFD results with the experiments. For the example shown in Figure 2B, $\phi_c = 0.87$ is obtained.

Two images from the compression experiments are shown in Figure 3 as an example. Panel A displays the emulsion at rest before centrifugation. The mean volume fraction of oil is $\phi \approx 0.72$. Panel B displays a snapshot of the emulsion during centrifugation at $231g$, 5 s after the start of centrifugation. Upon centrifugation, droplets are accelerated towards the axis of rotation, thereby forming a dense layer. From the height of the compressed droplet layer h_c and the total height of the liquid column h_t we can calculate the averaged oil volume fraction ϕ_c in the compressed layer, $\phi_c = \phi_0 h_t / h_c$. For the example shown in Figure 3B, we obtain $\phi_c \approx 0.83$. Figure 3 displays ϕ_c as a function of time, obtained from the experiments and CFD calculations, for three different radial accelerations. The experimentally measured $\phi_c(t)$ increase with time, but eventually approach asymptotic values. For a given time, ϕ_c increases with increasing acceleration. The maximum volume fraction for hard spheres is ≈ 0.74, which is close to the experimentally measured value of the monodisperse dense droplet layer from where the emulsion was sampled. For droplets, higher packing fractions can be achieved, as droplets are deformable. The Bond number $Bo = \Delta\rho g d^2/\sigma$ compares the magnitude of body forces and interfacial tension forces. For our system, at the smallest acceleration of 103g, we obtain $Bo \approx 0.11$, which indicates that droplet deformation will take place [9], and that the measured values of $\phi_c > 0.72$ are physically reasonable. The maximum oil volume fractions at the corresponding Bo are: $\phi_{c,max}(Bo = 0.11) = 0.75$, $\phi_{c.max}(Bo = 0.25) = 0.79$ and $\phi_{c,max}(Bo = 0.55)$ = 0.90. The $\phi_c(t)$ curves obtained from the CFD calculation also increase with increasing t, and $\phi_c(t)$ also increases with acceleration for a given t. The curves do not approach an asymptotic value, however, and for $103g$ and $231g$ also differ quantitatively from the experimental data.

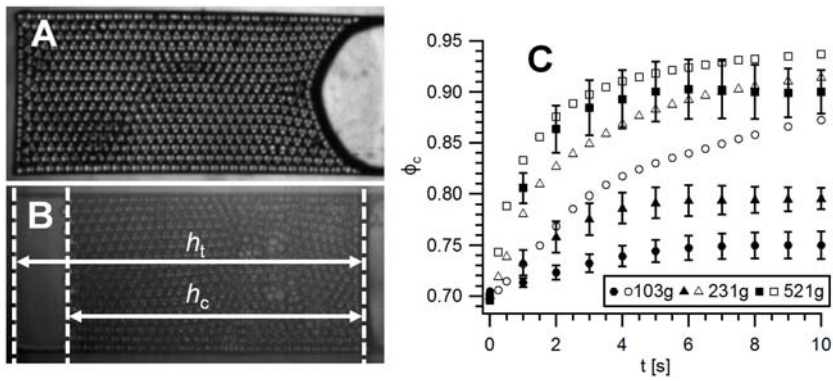

Figure 3: Panel A: photograph of the emulsion at rest. The droplet diameter is 79.3 μm, the oil volume fraction is 0.72. Panel B: Photograph of the same emulsion as in panel A after 5 s of centrifugation at 231g. h_c and h_t indicate the height of the compressed emulsion layer and total height of the liquid column, respectively. Panel C: mean oil volume fraction ϕ_c in the compressed droplet layer as a function of time for different accelerations. Filled symbols are the results from microcentrifuge experiments. Each data point is the average of 4 individual measurements. The error bars are 95% confidence intervals. Open symbols are the results from the CFD calculations.

The agreement between the $\phi_c(t)$ curves which were experimentally measured and calculated from CFD is not good, both from a quantitative and qualitative point of view. Generally, the calculated values overestimate the experimental values. One reason for the discrepancy is the fact that in the computational model the oil volume fraction will eventually approach unity for any radial acceleration, as the dispersed phase is not treated as discrete particles, but as a continuous medium. This is a direct consequence of the averaging procedure carried out in the derivation of the two-fluid model. In the experiments, on the other hand, there will be a maximum value of the oil volume fraction for a given *Bo*, for each radial acceleration. The applicability of the computational method for high dispersed phase fractions may be enhanced by imposing a maximum dispersed phase fraction ϕ_{max} that can be reached in a given volume element for the CFD calculations.

In addition, the expression for the mixture viscosity was derived for a dilute suspension of liquid spherical droplets by Taylor [10]. Later, Roscoe derived an expression for the mixture viscosity for solid spheres at higher volume fraction [11]. The two expressions are combined in the mixture viscosity in the Ishii-Zuber drag law. However, Taylor assumes spherical droplets, while in the present experiments considerable deformations are seen. Furthermore, while some deviations from the spherical shape are permitted according to Roscoe, his derivations of the mixture viscosity assumes a very wide particle size distribution.

Here, a monodisperse emulsion is used. These deviations in the experiments from the assumptions in the model derivation also contribute to the observed discrepancies in the results.

3.2 Emulsion coalescence

The kinetics of emulsion breakup were investigated with the same system that was used for the compression experiments. Oil-in-water emulsions stabilized by 10 mM SDS are highly stable due to the colloidal forces that prevent droplets from coalescing [12]. The addition of inorganic electrolytes is known to promote coalescence in emulsions stabilized by ionic surfactants such as SDS, due to a decrease of the electric double layer repulsion between the droplet interfaces [12].

One drop of emulsion with a volume of 350 nl and $\phi = 0.72$ was added to the sample chamber. The sample was then briefly centrifuged to push all liquid to the bottom of the chamber. Then, a droplet of a 5 wt% NaCl aqueous solution (350 nl) was added to the sample chamber. A snapshot of the sample chamber after addition of the two solutions is displayed in Figure 4 (photo at the left). The concentration of SDS after addition of the NaCl solution changed to 5 mM and the concentration of NaCl to 2.5 wt%. The interfacial tension of Sil180 and an aqueous phase with this composition was measured to be 5.4 mN m^{-1}. Emulsions prepared in this way were centrifuged for 10 minutes at different accelerations in the range $64 < a/g < 2260$. Figure 4 displays snapshots of an emulsion centrifuged at $864g$ at different times. The droplets are compressed at the top of the emulsion. A layer of pure oil, which grows with time, is visible after 1 minute of centrifugation. As continuous phase is flowing from top to bottom in the emulsion due to the enhanced gravitational acceleration, the film of continuous phase between droplets is always thinnest in the top layer of the emulsion. A thinner film is more likely to rupture, hence coalescence takes place mostly in the top layer of the emulsion. In addition to coalescence between oil droplets and the pure oil homophase, coalescence between droplets in the emulsion layer was also observed. This is best visible in the snapshot in Figure 4 taken after 10 minutes. The extent of drop-drop coalescence was not evaluated in this work, as the presence of a droplet bilayer causes problems for automated image analysis.

The volume fraction of coalesced oil $x_c = V_c/V_t$ was evaluated. V_c and V_t are the volumes of coalesced oil and total volumes of oil in the system, respectively. Figure 5A displays three curves $x_c(t)$ as examples. Curve 1 was recorded at $2260g$ acceleration, curves 2 and 3 were recorded at $1282g$ acceleration. For curve 1, $x_c(t)$ increases approximately linearly until $x_c = 1$ is reached, which indicates that all oil from the emulsion has coalesced. From a linear fit to the data points for which $x_c < 1$ we calculate a mean coalescence rate $r_c = dx_c/dt$. For curve 2, $x_c < 1$ for the duration of the experiment. The difference in slopes between curves 1 and 2 indicates that the coalescence rate is larger for $2260g$ acceleration as compared to $1282g$. It was often observed that coalescence took place before centrifugation was started, as a few seconds passed between addition of the NaCl solution and the start of centrifugation. Curve 3 in Figure 5A displays an example where significant coalescence occurred before centrifugation and thus the intercept of the linear fit

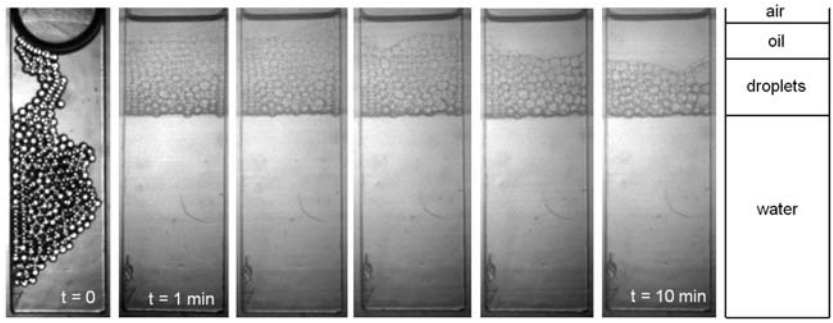

Figure 4: Snapshots of an emulsion after addition of a 5 wt% NaCl aqueous solution during centrifugation at $864g$ centrifugal acceleration. The picture at the left displays the sample chamber after additions of 350 nl emulsion and 350 nl NaCl solution. The other photos display the sample chamber at different times of centrifugation. The sketch at the right schematically displays the distribution of phases during centrifugation.

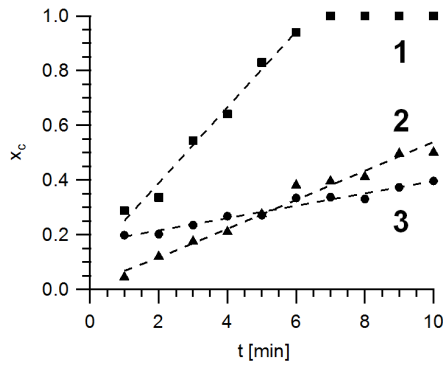

Figure 5: Relative volume fraction of coalesced oil x_c as a function of centrifugation time for three individual experiments as examples. The dotted lines are linear fits to the data points. The curves are discussed in detail in section 3.2.

$x_c(t)$ at $t = 0$ would deviate strongly from zero. The first data point was taken after one minute centrifugation, $x_c(t)$ increased approximately linear from this point on.

The slopes of curves 2 and 3 differ significantly from each other, even though experiments were performed at the same acceleration. The scatter of the data points was generally large, which is visualized in Figure 6A displaying r_c as a function of the relative radial acceleration a/g obtained from individual measurements. The reason for this large scatter is currently not known. For each value a/g, 5-7 individual measurements were performed and the average value $\langle r_c \rangle$ was calculated. Even though the error bars in Figure 6A are large, $\langle r_c \rangle$ increases

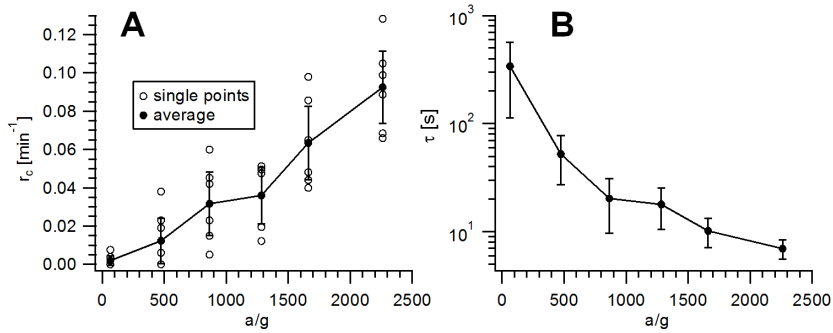

Figure 6: Mean relative coalescence rate r_c (panel A) and mean coalescence time τ (panel B) between a droplet and the pure oil phase as a function of the relative acceleration a/g. The open circles in Panel A are results of individual measurements, the filled circles are average data points from 5-7 measurements. Error bars are 95% confidence intervals.

approximately linearly with increasing a/g. The coalescence rate r_c is not a universal property, as it depends on the area of the pure oil/emulsion interface A_i. A more general parameter is the characteristic coalescence time τ, which is the time it takes for the thin film of continuous phase between the droplet and the pure oil phase to drain and rupture. We have shown previously that τ can be calculated as $\tau = A_i\phi_t/4V_0q_tr_c$ [5]. A_i is given by $A_i = hw$, where h and w are the channel height and width, respectively. ϕ_t is the dispersed phase volume fraction in the top layer of the emulsion, for which we will assume $\phi_t = 1$. V_0 is the total volume of oil in the system, q_t is the ratio of cross-sectional area A_d and volume V_d of a droplet in the top layer of the emulsion, $q_t = A_d/V_d$.

From the images we see that the droplets in the top layer are deformed. If we assume the droplets to be in the shape of a rhombic dodecahedron, which is a common approximation for deformed droplets in a dense emulsion layer, then we obtain $q_t \approx 2.29/d$, where d is the diameter of an undeformed droplet of the same volume. The coalescence time τ is displayed in Figure 6B as a function of the relative radial acceleration a/g; τ decreases with increasing a/g.

In the simplest model for film drainage, a circular film forms at the droplet interface which is parallel with the pure oil interface. The coalescence time τ is then given by: $\tau = 12\pi\eta_c r_f^4/Fh_c^2$ [13]. η_c is the continuous phase viscosity, r_f the film radius, F the compressive force and h_c the critical film thickness, at which coalescence will occur. The equation predicts a decrease of τ with increasing compressive force, which was observed in our experiments.

Several factors will cause quantitative deviation of the experimental data from this simple model, however. Firstly, the film radius itself will depend on the compressive force, an estimate is given by $r_f^2 = Fr_d/2\pi\sigma$, where r_d is the droplet radius and σ the interfacial tension [12]. Due to the confinement of droplets in a dense emulsions, r_f cannot increase arbitrarily with F, but will take on a maximal

value at a certain force. Secondly, the critical film thickness is mostly only known as an order-of-magnitude estimate, and is thus a considerable source of error, as $\tau \propto h^{-2}$. Thirdly, as the coalescing droplet is surrounded by a dense emulsion, the flow of continuous phase may be significantly impeded due to the high hydraulic resistance of the network of channels of continuous phase that is formed between the emulsion droplets, as compared to film drainage between an isolated drop and the pure oil interface. Fourthly, the experiments were performed with a micellar solution as the continuous phase. The presence of micelles may further modulate the interaction force between the droplets at distances < 100 nm [12], which is difficult to quantify. Hence, a quantitative description of the coalescence dynamics cannot be done in a reliable manner, and we restrict ourselves to the qualitative discussion given above.

4 Conclusions

We investigated the sedimentation and coalescence of monodisperse emulsions under enhanced gravity using in-situ microscopy. The novelty of the experimental approach is that it allows direct optical monitoring of emulsion droplets during centrifugation at high g-forces.

The agreement between the emulsion compression experiments and numerical simulations was not good for two of the three employed radial accelerations. Possible reasons for this are the loss of interfacial physics due to the averaging procedure used for the two-fluid model and also the disagreement of the experiments with some of the modeling assumptions. We would like to point out that the results demonstrate that the Ishii-Zuber drag law, which is very popular, should be employed critically in CFD calculations simulating multiphase systems with high dispersed phase fractions and/or under conditions where enhanced gravity would cause significant droplet deformation.

In the coalescence experiments it was found that the coalescence rate increased approximately linearly with a/g. This behavior was explained qualitatively with a simple film drainage model.

Improvements of the current experimental setup are possible for future work. In order to study coalescence between droplets in the emulsion, a monolayer of droplets must be produced to allow for a better visibility of individual droplets. As we want to work with droplet diameters < 100 μm because of their relevance for industrial applications, the height of the sample chamber needs to be ≤ 100 μm. When using PDMS as chamber material, we observed that channels of height ≤ 100 μm and width $= 1$ mm collapsed due to downward bending of the lid. To avoid this, the sample chamber can be made from glass. The procedure of destabilizing the emulsion by addition of salt may cause coalescence before the start of centrifugation. The destabilization can be triggered in a more reproducible way by choosing a photo-destructible surfactant, that will lose its emulsifying capability upon irradiation of the sample with light [14]. This is expected to reduce the statistical uncertainty of the measured coalescence rate.

Acknowledgements

This work is carried out as part of a project of the Institute for Sustainable Process Technology: development of an Ω^2R separator focusing on oil/water separation (project number OG 00-04). We thank Laurens van Campen from Delft University of Technology, Johanna Bos from Frames and Paul Verbeek from FMC Technologies for helpful discussions.

References

[1] Ishii, M. & Zuber, N., Drag coefficient and relative velocity in bubbly, droplet or particulate flows. *AIChE Journal*, **25**, pp. 843–855, 1979.
[2] Schiller, L. & Naumann, A., Uber die grundlegenden Berechnungen bei der Schwerkraftaufbereitung. *Zeitschrift des Vereines Deutscher Ingenieure*, **77**, p. 318, 1933.
[3] Rusche, H., *Computational fluid dynamics of dispersed two-phase flows at high phase fractions*. Ph.D. thesis, Imperial College of Science, Technology & Medicine, Department of Mechanical Engineering, London, UK, 2002.
[4] Jakobsen, H., *Chemical Reactor Modeling: Multiphase Reactive Flows*. Springer, 1st edition, 2008.
[5] Krebs, T., Schroen, C. & Boom, R., Separation kinetics of an oil-in-water emulsion under enhanced gravity. *Chemical Engineering Science*, **72**, pp. 118–125, 2012.
[6] Qin, D., Xia, Y. & Whitesides, G., Soft lithography for micro- and nanoscale patterning. *Nature Protocols*, **5**, pp. 491–502, 2010.
[7] Krebs, T., Schroen, C. & Boom, R., A microfluidic method to study demulsification kinetics. *Lab on a Chip*, 2012. doi:10.1039/C2LC20930F.
[8] Drew, D., Mathematical modeling of two-phase flow. *Annual Review of Fluid Mechanics*, **15**, pp. 261–291, 1983.
[9] Griggs, A., Zinchenko, A. & Davis, R., Gravity-driven motion of a deformable drop or bubble near an inclined plane at low Reynolds number. *International Journal of Multiphase Flow*, **34**, pp. 408–418, 2008.
[10] Taylor, G., The viscosity of a fluid containing small drops of another fluid. *Proceedings of the Royal Society of London, Series A*, **138**, pp. 41–48, 1932.
[11] Roscoe, R., The viscosity of suspensions of rigid spheres. *British Journal of Applied Physics*, **3**, pp. 267–279, 1952.
[12] Birdi, K., *Handbook of Surface and Colloid Chemistry*. CRC Press, 2nd edition, 2003.
[13] Chesters, A., The modelling of coalescence processes in fluid-liquid dispersions: A review of current understanding. *Trans IChemE*, **69A**, pp. 259–270, 1991.
[14] Eastoe, J., Photo-destructible surfactants in microemulsions. *Progress in Colloid and Polymer Science*, **133**, pp. 106–110, 2006.

Steady state numerical model for critical two-phase flow in a nozzle

S. Martel[1], Y. Mercadier[1] & M. Dostie[2]
[1]*Department of Mechanical Engineering, Université de Sherbrooke, Canada*
[2]*Laboratoire des technologies de l'énergie, Hydro-Québec, Shawinigan, Canada*

Abstract

This paper presents a steady state two-phase flow model including new choking criteria for one-dimensional conservative systems. As a first step, this model is used to study the flow in the motive nozzle of an ejector. Mechanical disequilibria and momentum exchange between phases are taken into account and the numerical scheme uses the SIMPLE algorithm. Numerical results are compared to experimental and previous numerical results from the literature.
Keywords: critical two-phase flow, critical location, steady state model.

1 Introduction

The steady state flow of compressible fluid through convergent-divergent nozzles covers various important flow phenomena like the occurrence of critical flow conditions, transition from subsonic to supersonic flow or the occurrence of flow discontinuities. One phenomena still of interest is the choking condition in a critical flow such as in supersonic ejectors. Supersonic ejectors are widely used in a range of applications such as aerospace, propulsion, refrigeration and many thermal systems. In this paper, a one-dimensional compressible steady state two-phase flow model is presented with new choking criterions that are directly related to optimal flux conditions developed by [1]. As a first step, this model is used to study the flow in the motive nozzle of an ejector.

WIT Transactions on Engineering Sciences, Vol 74, © 2012 WIT Press
www.witpress.com, ISSN 1743-3533 (on-line)
doi:10.2495/AFM120191

2 Numerical model

This is a one-dimensional two-fluid single pressure model using one temperature and mechanical disequilibria between phases in which no phase changes occurred. The procedure used for the calculation of the flow field is the standard SIMPLE algorithm developed for steady state flow conditions [2]. A constant liquid density and perfect gas law for compressible component are assumed. In addition, droplets in gas flow for momentum exchange between phases are assumed to be uniform and with constant diameter. In order to take account of the mechanical disequilibria, the slip ratio between phases must be obtained using drag source term.

With these assumptions, the following four equations model is obtained:

$$\frac{\partial}{\partial x}\sum_k \left(f_{Mk}\right) a_s \alpha_1 \rho_1 u_1 = 0 \tag{1}$$

$$\frac{\partial}{\partial x}\sum_k \left(f_{Mk} s_k\right) a_s \alpha_1 \rho_1 u_1^2 + \frac{d}{dx}\left(a_s p\right) = p\frac{\partial a_s}{\partial x} \tag{2}$$

$$\frac{\partial}{\partial x}\left[A\alpha_1\rho_1 u_1\left(\sum_k \left(f_{Mk} s_k^2\right)\frac{u_1^{\ 2}}{2} + \sum_k \left(f_{Mk} f_{Tk}\right)\frac{C_{p1}P}{R_1\rho_1}\right)\right] = 0 \tag{3}$$

$$\frac{\partial}{\partial x}\left(A\alpha_2\rho_2 u_2^2\right) + \frac{\partial}{\partial x}\left(a_s\alpha_2 p\right) = \Gamma_{2,J} + \Gamma_{2,J}^c \tag{4}$$

where $\Gamma_{2,J}$ is the drag force between phases and $\Gamma_{2,J}^c$ is the force cause by the variable section:

$$\Gamma_{2,J} = -\frac{V_2}{V_p}\frac{A_2^D}{\Delta x}\frac{C_D}{2}\rho_1\left(u_2 - u_1\right)\left|u_2 - u_1\right| \tag{5}$$

$$\Gamma_{2,J}^c = p\frac{\partial}{\partial x}\left(a_s\alpha_2\right) \tag{6}$$

In these equations, s_k is the slip ratio, f_{Mk} the mass flow ratio, and f_{Tk} enthalpy ratio of phase k. These ratios can be respectively defined by:

$$s_k = \frac{u_k}{u_1} \tag{7}$$

$$f_{Mk} = \frac{a_k\rho_k u_k}{a_1\rho_1 u_1} \tag{8}$$

$$f_{Tk} = \frac{Cp_k T_k}{Cp_1 T_1} \tag{9}$$

In the previous equations, a_s is the sectional area, α_k the volumetric fraction of each phase k, ρ_k the density of each phase, u_k the velocity of each phase, p the

flow pressure, C_{p1} the heat capacity of compressible phase, and R_1 the specific gas constant of compressible phase. For compressible phase, k is 1 and for incompressible phase, k equal 2. Volumetric fraction and geometrical section are linked by the following equations representing a global constraint that all phases must occupy the total nozzle section:

$$\alpha_k = \frac{a_k}{a_s}$$
$$\sum_k \alpha_k = 1 \tag{10}$$

3 Validation

At the inlet of the nozzle, homogeneous equilibrium flow is assumed from reservoir. For this reason, each phase have the same temperature and pressure. The inlet volume fraction is imposed. For the outlet boundary condition a constant exit pressure is applied. The initial conditions in the nozzle are identical with the upstream reservoir conditions which imply that the transient calculation starts with a strong discontinuity at the nozzle exit. The model has been validated with experimental data from Elliot and Weinberg [3] and with Carofano and McManus [4]. Finally, results have been compared to numerical results from Städtke [5].

3.1 Elliot and Weinberg comparison

Experimental results were obtained using a 1.27 m experimental nozzle. Authors show one pressure profile and a table resuming experimental results obtained for different mass flow ratio such as mass flow rate, exit velocity, and thrust measurement. Inlet conditions for all tests are p_0= 10.3421 (MPa), T_0=293K and an exit pressure of 0.1013 MPa. The Figure 1 shows that numerical pressure

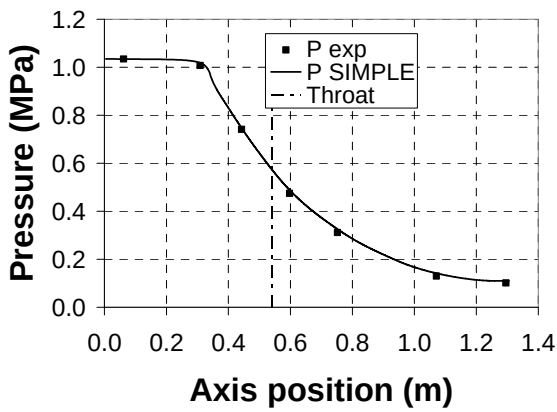

Figure 1: Pressure profile in the nozzle.

profile is in good agreement with experimental results. For this test, mass flow ratio is 39.1 and experimental mass flow rate is 67.33 kg/s. The numerical mass flow rate obtained is 67.64 which give an error of 0.45%.

Table 1 shows comparison between numerical and experimental results for mass flow ratio range of 15.3 – 64.9. For all tests, results are in good agreement for mass flow rate since error varies from 0.11 to 2.77%. However, comparison of experimental and numerical thrust results give an overestimation in all cases between 4.96 to 8.28%. From Elliot and Weinberg numerical results, the difference between wall frictionless flow velocity and the velocity with friction is about 5.6%. From this observation, the wall frictionless flow assumption resulting in a higher mean velocity used in the calculation of the thrust is the cause of this overestimation.

Table 1: Comparison with results of Elliot and Weinberg.

Experimental results				Numerical results					
Mass flow ratio	M (kg/s)	Exit velocity (m/s)	Thrust (N)	M (kg/s)	Error (%)	Exit velocity (m/s)	Error (%)	Thrust (N)	Error (%)
15.3	44.5	143	6334	45.8	2.77	147	3.35	6748	6.54
17.2	47.7	131	6236	48.1	0.83	140	7.07	6753	8.28
21.1	51.8	125	6441	52.5	1.27	129	3.34	6760	4.96
22.3	53.6	118	6308	53.7	0.14	126	6.73	6762	7.21
28.3	57.7	109	6308	59.3	2.76	114	4.34	6773	7.38
30.1	60.9	104	6334	60.8	0.11	111	6.83	6776	6.97
39.1	67.7	94	6334	67.3	0.59	100	7.30	6760	6.72
51.6	74.5	85	6334	75.4	1.13	90	6.27	6813	7.55
64.9	81.4	78	6334	82.2	1.00	83	6.73	6844	8.04

3.2 Carofano and McManus comparison

The nozzle used by Carofano and McManus [4] to obtain experimental two-phase flow results is used to validate numerical results. They obtain a pressure profile for p_0 = 0.3440 MPa, T_0 = 289 K and an exit pressure of 0.1455 MPa. The mass flow ratio used in this case is 0.1013. The experimental mass flow rate is 0.4141 kg/s and the numerical mass flow rate obtained is 0.4103 which implies a difference under 1%. The pressure profile is in good agreement with experimental.

3.3 Städtke comparison

The ASTAR nozzle geometry presented by Städtke [5] is used to compare numerical results. For this case, fixed upstream reservoir pressure and temperature of p_0 = 1 MPa, T_0 = 400 K, $u_1 = u_2$ is used with a mass flow rate

ratio (F_{Mk}) of unity and an exit pressure of 0.6 MPa. Numerical results obtained with this scheme are in good agreement with those of [5] as shown on Figure 1.2. Total mass flow rate obtained by [5] is 5.68 kg/s compared to 5.70 kg/s obtained with this model which implied a difference of 0.35%. It is interesting to see that the numerical scheme is able to capture choc wave in the nozzle. The differences between velocity profiles can be explained by the fact that no information about the droplet assumptions are given by Städtke. Droplet diameter and drag correlation have a direct effect on the slip ratio and the velocity profiles. In addition, Städtke are using a two temperatures model giving some differences in the phase velocity results.

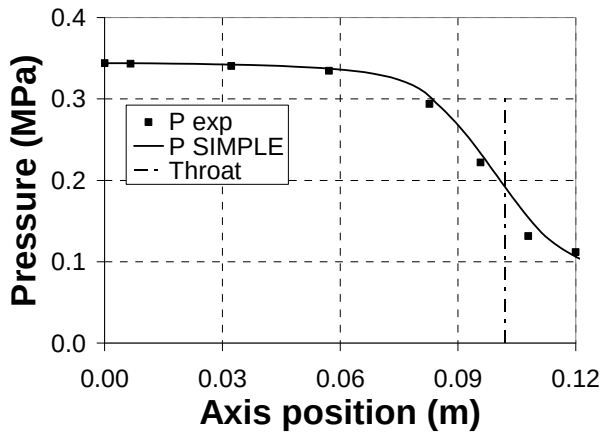

Figure 2: Pressure profile in the nozzle.

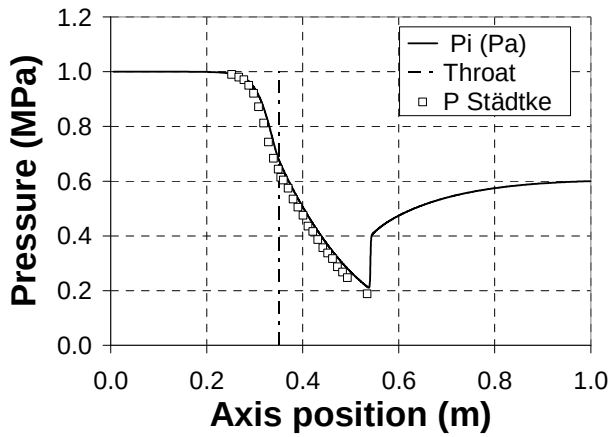

Figure 3: Pressure profiles in the ASTAR nozzle.

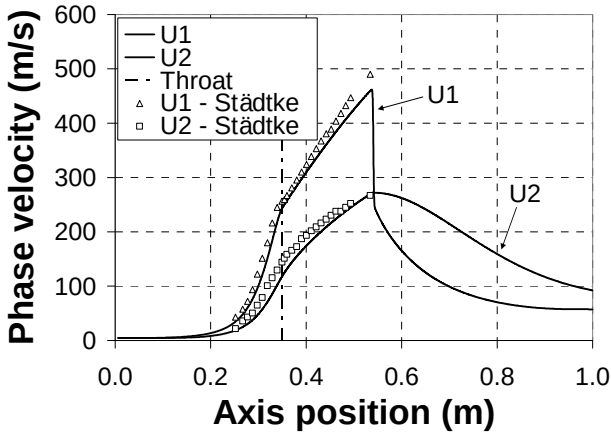

Figure 4: Velocity profiles in the ASTAR nozzle.

4 Conclusions

Multiphase systems present significant scientific challenges and the choking phenomenon has to be taken into account properly to achieve an accurate model of two phase flow. More results are obtained concerning super-critical behavior in comparison with mono-phase compressible flow. This numerical scheme give good results and the numerical study have given a lot of information about critical two-phase flow behavior. It also shows that steady state models are achievable for critical two-phase flow. Such an approach is in some cases simpler that using transient models which involve much more complex propagation phenomenon. This model allows a good range of inlet void fraction from droplet flow (void fraction close to 1) to bubble flow (void fraction close to 0.4). Numerical results also validate the fact that critical location is not necessary at the throat section. For variable slip ratio, this is not necessary the case since mass, momentum and energy exchanges between phases give a different behavior and critical location appear after the throat. Numerical study and theoretical consideration are into progress to predict critical position and effect of mass flow ratio and thermical disequilibria on flow behavior.

Acknowledgements

The work described here was supported by NSERC, FQRNT and NSERC Chair in Industrial Energy Efficiency (chairholder: N. Galanis) at Université de Sherbrooke with the support of Hydro-Quebec (Energy Technology Laboratory, LTE), Rio Tinto Alcan and the CANMET Energy Technology Center (CETC-Varennes, Natural Resources Canada).

References

[1] Dostie M., Mercadier Y., Critical fluxes in conservative systems: application to multiphase flow. *Submitted to Journal of Fluid Mechanics*, 2011.
[2] Patankar, S.V. (1980). *Numerical heat transfer and fluid flow*, Hemisphere Publishing Corporation, New-York, 197 p.
[3] Elliot, D. G. and Weinberg, E. *Acceleration of Liquids in Two-Phase Nozzles*, JPL Tech. Rep. 32-987, 1968.
[4] Carofano, G. C. and McManus, H. N. (1969). An analytical and experimental study of the flow of air-water and steam-water mixtures in a converging-diverging nozzle, *Progress in Heat and Mass Transfer*, Vol. 2, Pergamon Press, Oxford.
[5] Städtke, H. *Gasdynamic Aspects of Two-Phase Flow*. WILEY-VCH, Weinheim, 273 p, 2006.

This page intentionally left blank

Experimental and numerical investigation of boiling flow in a vertical pipe with phase change using a multi-fluid modelling approach

R. Kopun[1] & L. Škerget[2]
[1]*AVL-AST d.o.o., Maribor, Slovenia*
[2]*Faculty of Mechanical Engineering, University of Maribor, Slovenia*

Abstract

Multi-phase boiling flow inside a vertical pipe is simulated as part of a preliminary study of the heat transfer characteristics of coolant flow inside water cooling jackets in IC engines. Based on increasing demands for higher efficiency inside the engine cooling block, heat transfer plays an important role in a conceptual and thermal analysis used to provide efficient cooling. The simulations of thermal and flow phase change characteristics inside a vertical pipe boiling system were made to prevent component failure and to create a uniform temperature distribution inside the water cooling jacket. The developed boiling mass transfer model, such as the BDL (Boiling Departure Lift-off) model, has empirically correlated heat transfer coefficients and is implemented within the commercial computational fluid dynamics code AVL FIRE®. Governing equations are based on the Eulerian multi-fluid approach which treats each phase as interpenetrating continua coexisting in the flow domain, with inter-phase transfer terms accounting for phase interactions. Turbulence is modelled by using an advanced $k\text{-}\zeta\text{-}f$ model. In this paper, we focus on comparison and suitability of the mentioned boiling model with two different boundary condition approaches to determine the HTC (heat transfer coefficient) for multi-phase boiling flow inside the vertical pipe. Temperature measurements along the height of the pipe were performed at three different positions. Comparison with the available experimental data for different boundary conditions is presented. Simulation results exhibit good agreement with the experimental data.
Keywords: multiphase flow, boiling, vertical pipe, HTC, CFD, IC engines.

WIT Transactions on Engineering Sciences, Vol 74, © 2012 WIT Press
www.witpress.com, ISSN 1743-3533 (on-line)
doi:10.2495/AFM120201

1 Introduction

Detailed knowledge of flow and heat transfer analysis is essential in order to achieve a controlled boiling over a wide range of working conditions. Heat transfer applications such as those introduced in automotive industries often play an important role in conceptual and thermal analysis of cooling system (Dong *et al.* [1]). Vapour bubbles usually start growing in superheated zones near the walls and are normally able to condense harmlessly back into the cooler liquid, but under certain conditions (flow geometry, fluid conditions, est.) Transition from nucleate to film boiling regime occurs. That kind of behaviour dramatically reduces heat transfer rate which leads to large rise (upturn) of component temperature and contributes to the failure of the device. Hence, efficient cooling is essential to prevent component failure and provide even temperature distribution. This leads to reduction of thermal stresses and higher durability and has consequently influence on power requirements (Campbell *et al.* [2]).

Modelling of flow boiling heat transfer usually relies on the empirical approaches. It is based on the superposition of convective and boiling components, as first suggested by Rohsenow, i.e. represented by simple addition of the nucleate and convective coefficient. This approach was afterwards extended by Chen (Steiner and Taborek [3]). In recent years many new approaches and correlations have been proposed. One of them is the newly developed model for mass transfer function based on the assumption that the mass transfer parameters are proportional to the heat transfer coefficient from the fluid system as proposed by Srinivasan and Wang [4]. The model has already been successfully implemented and applied to the quenching boiling heat transfer process showing significant improvement as reported by Wang *et al.* [5].

Heat transfer of coolant flows inside water cooling jacket often involves a phase change which can be simulated, as a preliminary study, with the horizontal and the vertical pipe for easier explanation of flow characteristics. Recently, Srinivasan [6] has developed the new mass transfer model to simulate thermal and phase change characteristics for binary mixture during flow boiling process inside a horizontal channel. Good agreements of numerical predictions with experiments are presented and the applicability of developed model shows that it can be easily extended to automotive applications.

In this work we simulate the multi-phase boiling flow inside a vertical pipe with commercial CFD code AVL FIRE. A brief overview of the governing equations of the newly developed mass transfer model is described first. Boundary conditions, numerical setups and simulation results are presented and compared with the available experimental values. Results are discussed and summarized in the concluding.

2 Numerical background

Eulerian multi-fluid methods consider each phase as interpenetrating continua coexisting in the flow domain, with inter-phase transfer terms accounting for

phase interactions where conservation laws apply. From the theoretical work of Lahey and Drew [7] the averaged continuity and momentum equations are presented as follows:

2.1 Continuity

$$\frac{\partial \alpha_k \rho_k}{\partial t} + \nabla \cdot \alpha_k \rho_k \mathbf{v}_k = \sum_{l=1, l\neq k}^{N} \Gamma_{\mathrm{kl}} \qquad k = 1, \ldots, N \tag{1}$$

where α, ρ and v stand for volume fraction, density and velocity. Phase change rate (in this particular case, boiling) is Γ_{k} and the subscript k is a phase indicator ($k = l$ or $k = v$).

2.2 Momentum

$$\frac{\partial \alpha_k \rho_k \mathbf{v}_k}{\partial t} + \nabla \alpha_k \rho_k \mathbf{v}_k \mathbf{v}_k = -\alpha_k \nabla p + \nabla \alpha_k \tau_k + \alpha_k \rho_k g + \boldsymbol{M}_k + \mathrm{v}_{int} \Gamma_{\mathrm{k}} \tag{2}$$

while p, τ and v_{int} are respectively the pressure, stress and interfacial velocity. Interfacial momentum transfer term M_k with the drag is being the most important force and due to boiling initiated along the solid and liquid interface, mass interfacial exchange occurs. Interfacial momentum exchange term is given as:

$$M_c = C_D \frac{1}{8} \rho_c A_{int} |\mathbf{v}_r| \mathbf{v}_r = -M_d \tag{3}$$

where C_D is the drag coefficient, A_{int} is the interfacial area density and $\mathbf{v}_r = \mathbf{v}_d - \mathbf{v}_c$ is the relative velocity. Subscripts c and d denote the continuous and dispersed phases of the given flow. Drag of coefficient is defined as

$$C_D = \begin{cases} \dfrac{24}{Re_b}(1 + 0.15 Re_b^{0.687}) & Re_b \leq 1000 \\ 0.438 & Re_b > 1000 \end{cases} \qquad Re_b = \frac{\mathrm{v}_r D_b}{\nu_c} \tag{4}$$

Presented model does not account for the turbulence dispersion force on the momentum interface. In the framework of the two-fluid model, an individual energy equation is be solved for each phase, where it is assumed that two phases are in thermal equilibrium, because the heat transfer rate between vapour and liquid phase is relatively rapid. Further details concerning modelling interfacial mass exchange can be obtained from AVL FIRE Multi-fluid model, solver theory guide [8].

2.3 Energy

An advanced k-ζ-f model developed by Hanjalic *et al.* [9] was implemented inside the code to model the effects of turbulence within the multiphase system.

$$\frac{\partial \rho_m h}{\partial t} + \nabla \rho_m \mathbf{v} h = \nabla q + \rho_m q''' + \rho_m g \mathbf{v} + \nabla \tau \mathbf{v} + \alpha_m \frac{\partial p}{\partial t} + \sum_{l=1, l \neq k, l \notin N}^{N} H_{kl} + h \sum_{l=1, l \neq k, l \notin N}^{N} \Gamma_{kl} \tag{5}$$

with

$$\alpha_m = \sum_{k=1}^{N} \alpha_k \qquad \mu_m = \sum_{k=1}^{N} \alpha_k \mu_k \qquad \rho_m = \sum_{k=1}^{N} \alpha_k \rho_k \qquad \kappa_m = \sum_{k=1}^{N} \alpha_k \kappa_k \tag{6}$$

enthalpy volumetric flow is denoted as with q''', energy interfacial exchange between phases k and l is denoted as H_{kl} and α, μ and κ represent volume fraction, dynamics viscosity and conductivity, respectively heat flux q is given by

$$q = \frac{\kappa_m}{\tilde{C}_{p,m}} \nabla h \tag{7}$$

where $\tilde{C}_{p,m}$ is the mixture specific heat. Eqn. for turbulent kinetic energy and dissipation rate are given by

$$\frac{\partial \alpha_k \rho_k k_k}{\partial t} + \nabla(\alpha_k \rho_k \mathbf{v}_k k_k) = \nabla \alpha_k \left(\mu_k + \frac{\mu_k'}{\sigma_k}\right) \nabla k_k + \alpha_k P_k - \alpha_k P_k \varepsilon_k + \sum_{l=1, l \neq k}^{N} K_{kl} + k_k \sum_{l=1, l \neq k}^{N} \Gamma_{kl} \tag{8}$$

$$\frac{\partial \alpha_k \rho_k \varepsilon_k}{\partial t} + \nabla(\alpha_k \rho_k \mathbf{v}_k \varepsilon_k) = \nabla \alpha_k \left(\mu_k + \frac{\mu_k'}{\sigma_k}\right) \nabla \varepsilon_k - \alpha_k C_1 P_k \frac{\varepsilon_k}{k_k} + \sum_{l=1, l \neq k}^{N} D_{kl}' + \varepsilon_k \sum_{l=1, l \neq k}^{N} \Gamma_{kl} - \alpha_k C_2 \rho_k \frac{\varepsilon_k^2}{k_k} - \alpha_k C_4 \rho_k \varepsilon_k \nabla \mathrm{v}_k \tag{9}$$

further details about turbulence modelling and poly-dispersed bubble flow equations can be obtained from AVL FIRE Multi-fluid model, solver theory guide [8].

2.4 Boiling model

Based on the assumption that the heat transfer rate is proportional with the phase change rate, since the mass transfer predominantly controls heat transfer, the phase change rate due to boiling process can be written as

$$\Gamma_c = \frac{C_m \cdot C_b \cdot \tilde{h}_b \cdot A_{int} \cdot \Delta T'}{H_{fg}} \tag{10}$$

where $C_m, C_b, \tilde{h}_b$ and H_{fg} are the closure coefficient, the boiling correction coefficient, the boiling heat transfer coefficient and the latent heat of vaporization, respectively. Wall superheat temperature $\Delta T'$, the interfacial area density A_{int} and the closure coefficient C_m used to correct the interfacial area density in eqn. (10) are defined by

$$\Delta T' = T'_w - T'_{sat} \qquad A_{int} = \frac{6\alpha_d}{D_b} \qquad C_m = 1 - \sqrt{\frac{\alpha_d + \alpha_{min}}{\alpha_{pack} + \alpha_{min}}} \tag{11}$$

with α_{pack} being the dispersed dry phase packing limit and α_{min} being the minimum volume fraction. The boiling correction coefficient C_b is imposed to correlate nature of boiling process such as film, partial nucleate, transition boiling model etc. The heat transfer coefficient $\tilde{h}_b$ in the eqn. (10) is used for computing the mass transfer exchange rates and assumes the computed value of boiling heat transfer coefficient for different boiling regimes. Heat transfer coefficient for binary mixture is evaluated with the Chen correlation [10] as

$$\tilde{h}_b = h_{mic} \cdot S \tag{12}$$

where the microscopic heat transfer coefficient h_{mic} is modelled as

$$h_{mic} = 0.00122 \left[\frac{{k_l}^{0.79} \cdot {c_{pl}}^{0.45} \cdot {\rho_l}^{0.79}}{\sigma^{0.5} \cdot {\mu_l}^{0.79} \cdot {H_{fg}}^{0.24} \cdot {\rho_v}^{0.24}} \right] [T_w - T_b]^{0.24} \cdot [p_{sat}(T_w) - p_{sat}(T_b)]^{0.75} \tag{13}$$

From eqn. (13) parameters like k_l, c_{pl}, σ, μ_l, h_{fg}, T_w, T_b, $p_{sat}(T_w)$, $p_{sat}(T_b)$ refer to liquid thermal conductivity, liquid specific heat at constant pressure, surface tension, liquid dynamics viscosity, latent heat of vaporization, wall temperature, bubble point temperature, saturation pressure at T_w and saturation pressure at T_b.

Recent modification of the Chen model were made by Steiner *et al.* [11] with combination of Zeng *et al.* [12] and the model was fully implemented into FIRE as the BDL model. The main difference between the two models is in determination of suppression factor where the Chen model cannot take local fluid state into account as a function of a reference Reynolds number of the global geometry. The BDL model is a recent improvement in which the suppression factor is computed from local velocity and length scales. The boiling suppression factor used in eqn. (12) is decomposed in two parts as

$$S = S_{BDL1} \cdot S_{BDL2} \tag{14}$$

where the first suppression faction S_{BDL1} is based on study of bubble dynamics and growth and the second suppression factor S_{BDL2} correlates correction to the defined heat transfer coefficient h_{mic} modelled in eqn. (14) as

$$S_{BDL1} = \left(\frac{D_{dep}}{D_{lift}}\right)^{\phi} \qquad S_{BDL2} = \frac{S_{BDL1} \cdot h_{mic}}{1 + C_{BDL} \cdot Nu} \tag{15}$$

The departure diameters D_{dep} and lift-off diameters D_{lift} in eqn. (18) are calculated as a function of local velocity and differences in saturation to local cell temperature, where C_{BDL} and Nu in eqn. (19) stand for local coefficient and Nusselt number. Detailed information about parameters can be found in AVL FIRE Multi-fluid model, solver theory guide [8].

3 Experimental and numerical simulation set up

The present study consists of the experimental and numerical investigation on the vertical pipe boiling case. The experimental setup is schematically demonstrated in Fig. 1.

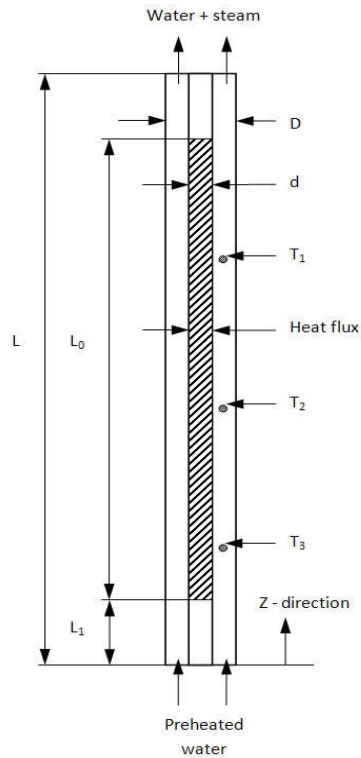

Figure 1: Schematic of vertical pipe experimental cross-section in z-direction.

The total length L of the pipe is 1.9 m with the outer diameter D of 0.03 m. Heated section, length L_0 of 1.5 m with the inner diameter d of 0.012 m, has a measured constant heat flux q of 44139 W/m^2. At the inlet and outlet there are small parts of the pipe with length L_1 of 0.2 m which are blind, i.e. not exposed to heat flux.

There are three thermo-sensors known as IEC 584, tip-K with working temperature ranged from -200℃ to $+800$℃ with measurement deviations of ± 1.5℃ or $0.004 \cdot |T|$. Thermo-sensors T_1, T_2 and T_3 are placed on three different positions along the pipe, where length in z direction to T_3 is 0.415 m, 0.885 m to sensor T_2 and 1.35 m to sensor T_1. Inlet water is preheated to the temperature of 80℃ and it enters the inlet domain with different velocities. The volumetric flow range varied from $\dot{V}_1 = 1.04\ L/min$ to $\dot{V}_2 = 2.18\ L/min$, corresponding to velocities from $v_1 = 0.04148\ m/s$ to $v_2 = 0.08695\ m/s$. Mixture of two-phases (water and steam) exits the vertical pipe at the top with static pressure of 1 bar. Data measurements were perform at the surrounding temperature of $T_\infty = 21$℃.

Basic elements of the numerical model configuration, shown in Fig. 2, include flow inlet and outlet section, heated wall, non-heated wall and wall. Heated wall area (in Fig. 1 marked with parameter L_0) selection is available to present constant heat flux $q = 44139\ W/m^2$ as in the original experimental set up, where the wall boundary condition consists of a natural convection to surrounding temperature $T_\infty = 21$℃ with the heat transfer coefficient $\alpha = 10\ W/m^2K$. The non-heated wall is modelled with $q = 0\ W/m^2$ adiabatic boundary condition. The entire domain is meshed by using a hexahedral type structure to a count of 160,000 cells.

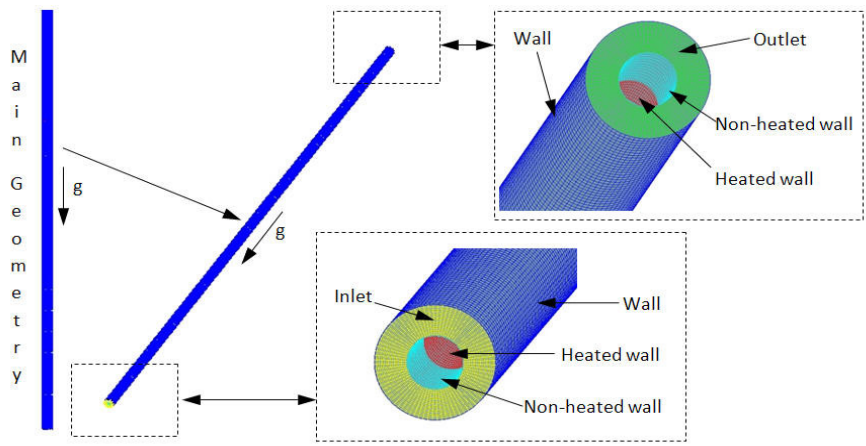

Figure 2: Computation domain set up and boundary conditions.

At the pipe inlet the fluid velocity is set only for z-direction (in our case in the liquid flow direction) with different velocities v_1 and v_2 with preheated water to 80°C as it is described in the experimental set up. The minimum volume fraction admissible for each phase in the entire domain is set to $1 \cdot 10^{-6}$ and phase one stands for water and phase two is vapour. Transient simulations with different time steps are conducted to compare with the experiment which lasted for 100 sec.

The numerical simulations were performed with the commercial CFD code AVL FIRE® v2010.1 in which the Finite Volume approach was used to solve governing equations and where numerical solution procedure was based on SIMPLE algorithm extended for a multiphase flow case. The normalized residual limit for mass, momentum, and volume fraction were set to $2 \cdot 10^{-3}$, while the turbulence was allowed to drop until it reaches $1 \cdot 10^{-4}$, where the energy relaxation was extended to the value of $1 \cdot 10^{-5}$. Turbulence was modelled with an advanced $k\text{-}\zeta\text{-}f$ model, where homogeneous turbulence interface exchange between different phases was used.

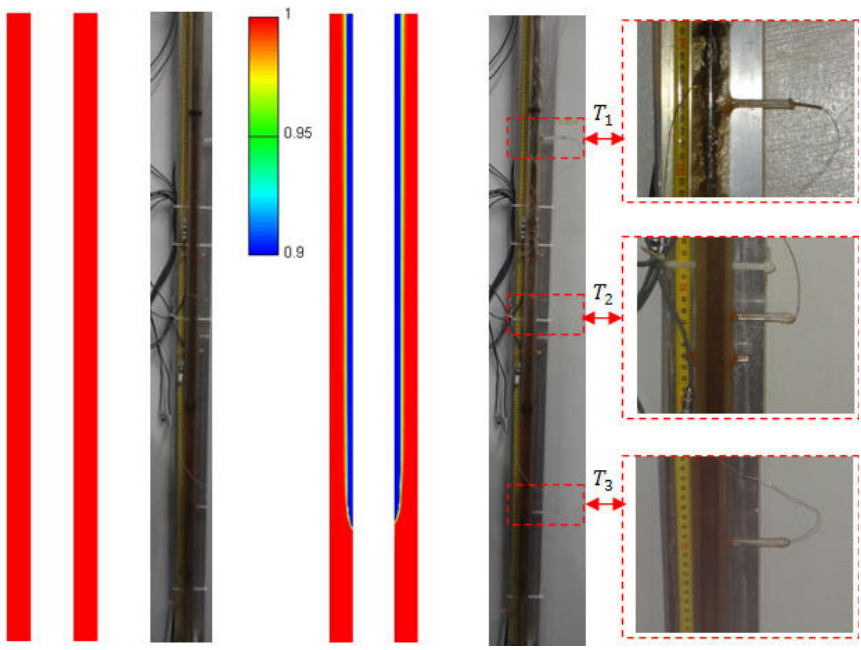

a) b)

Figure 3: Contour plots of liquid volume fraction at inlet velocity $v_1 = 0.04148\ m/s$ with experiment for different times, a) $t_1 = 1\ sec$ and b) $t_2 = 100\ sec$ with zoom area of the thermocouples T_1, T_2 and T_3.

4 Simulation results

The 3D results presented in the following section focus around the monitoring points T_1, T_2 and T_3 for easier visualization purpose and to observe the flow variable and physic effects on details between numerical and experimental results.

The effect of constant heat flux on the growth and propagation of volume fraction, for a given inlet velocity condition $v_1 = 0.04148\ m/s$, can be identified from Fig. 3. It can be seen that after $t_1 = 1\ sec$ (Fig. 3a) no vapour bubble is generated because the heat flux produces a temperature that is lower than the saturation temperature. By a close look at the experimental results in Fig. 3a, it is observed that there is also no vapour bubbles generated, whereas at the time $t_2 = 100\ sec$ (Fig. 3b) vapour bubbles are initiated in the heated wall area section and develops to the upstream of the tube.

Good agreement between experimental and numerical results can be observed in Figs. 3a and b. From the Fig. 3b at $t_2 = 100\ sec$ of heating time, it can be seen that heavy boiling occurs in area T_1 by zooming thermocouples T_1, T_2 and T_3 areas. It is found that the temperature has almost reached the saturation temperature in the area of T_2 as some bubbles can be observed in the heated area, whereas in the area T_3 no vapour bubbles are observed which implies that the temperature at this height is lower than the saturation temperature. Similar results were generated with other inlet velocity conditions ($v_2 = 0.08695\ m/s$). The results are not presented here.

Detailed comparison of experimentally measured temperatures and the corresponding simulated ones for two different inlet velocity cases ($v_1 = 0.04148\ m/s$ and $v_2 = 0.08695\ m/s$) on 3 different positions along the height of the pipe are displayed in Figs 4 and 5. Fluctuations of the experimental values appearing in Figs. 4 and 5 could be partly caused by noise during the measurement as expected.

At the lower inlet velocity ($v_1 = 0.04148\ m/s$), Fig. 4 shows the deviation in temperature predicted by the model against the measured values, noted for all 3 positions along the height of the pipe in transition area, between the beginning and before calculation reaches a steady state. In general, the model captures the trend of the experimental temperature histories. It can be seen that when calculation reaches a steady state ($t = 100\ sec$), for the position of thermocouple T_1, it has just the absolute deviation of $\Delta T = 0.8\ K$ from the experiment, and deviations of $\Delta T = 0.2\ K$ and $\Delta T = 0.5\ K$ for the thermocouples T_2 and T_3, respectively. The maximum deviation for thermocouple T_1 is $\Delta T = 5.7\ K$ at around $t = 5$ sec, whereas the deviation for the thermocoupleT_2 is $\Delta T = 5.9\ K$.

Similar results are obtained also with higher velocity ($v_2 = 0.08695$ m/s, see Fig. 5), where the difference between the measured and simulated values are presented at the same positions along the height of the pipe. Good agreement is obtained in this case. The maximum deviation reaches $\Delta T = 3.5\ K$ at t=100 s (relative deviation of 1%) in the area of thermocouple T_1. When the calculation reaches a steady state in the area of thermocouple T_2, the absolute deviation is

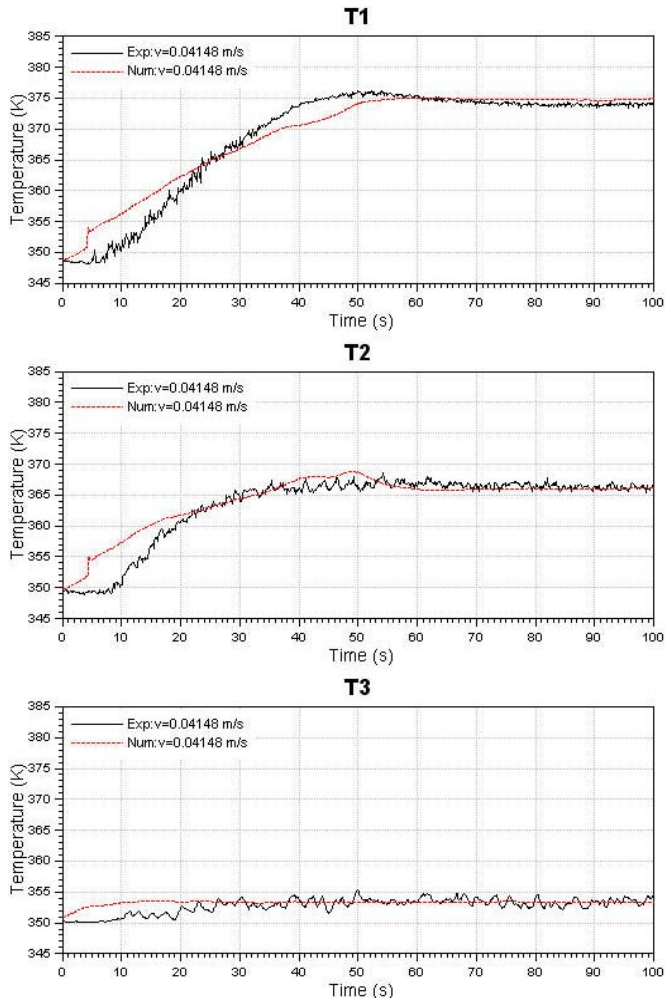

Figure 4: Comparison of thermocouple temperatures (T_1, T_2 and T_3) predicted by the numerical model (red dashed line) against the experimentally measured values (black solid line) with inlet liquid velocity $v_1 = 0.04148\ m/s$.

$\Delta T = 1.2\ K$, and $\Delta T = 0.3\ K$ for the thermocouple T_3. The maximum absolute deviation appears in developing stage at around $t = 5\ sec$ and has a value of $\Delta T = 4.9\ K$ for the area of thermocouples T_3.

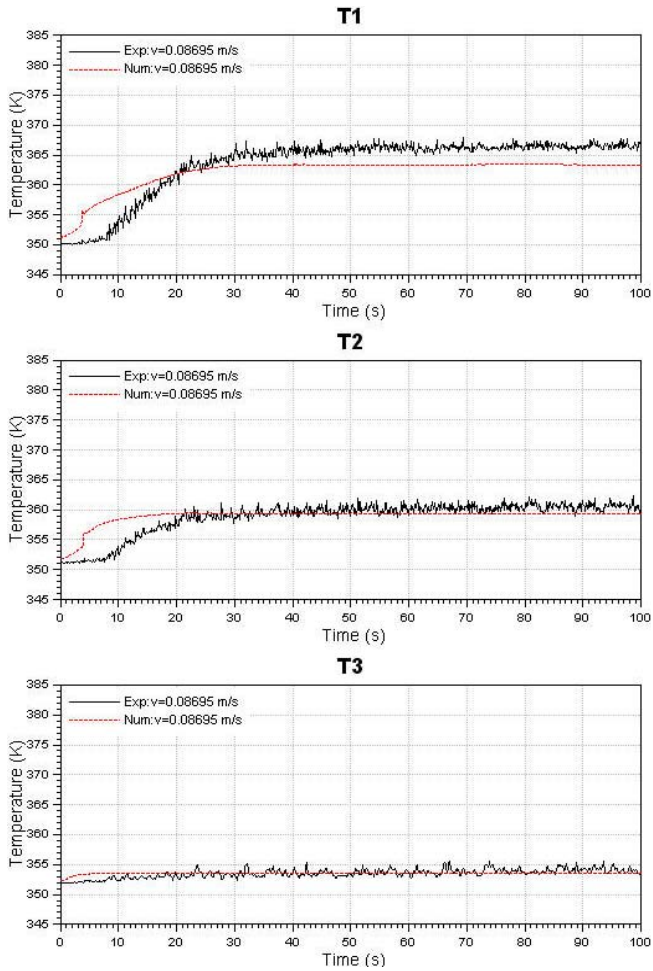

Figure 5: Comparison of thermocouple temperatures (T_1, T_2 and T_3) predicted by the numerical model (red dashed line) against the experimentally measured values (black solid line) with inlet liquid velocity $v_2 = 0.08695\ m/s$.

5 Conclusion

A new BDL model based on the multi-fluid modelling approach implemented within the commercial CFD code AVL FIRE® is capable of predicting boiling under different conditions in a vertical pipe. It can be concluded that all numerical results show a good agreement with the available experimental data. While better trends and lower deviations were observed for lower inlet velocities, higher inlet velocities can have a maximum relative deviation of 1.4% during the whole boiling process. In the current contest all calculations were performed

with the advanced k-ζ-f turbulent model, but the forthcoming work will perform present simulation with the variety of turbulence models and different inlet velocities to identify flow pattern predictions. Comparison of the vapour size and volume fraction with measurements will be performed. The computational method and workflow discussed in this article are capable of reporting the temperature values in combination with phase characteristics in the flow domain and can be used as a preliminary study of heat transfer characteristics of coolant flow inside water cooling jackets in internal combustion engines.

References

[1] Dong F., Fan Q., Cai Y., Jiang S., Guo C., Norihiko W., Lee W.T., Numerical simulation of boiling heat transfer in water jacket of DI engine, *SAE International, 2010.*

[2] Campbell N.A.F., Charlton S.J., Wong L., *Designing towards nucleate boiling in combustion engines*, *IMechE* C496/092, 1995, pp. 587-595.

[3] Steiner D., Taborek J., Flow boiling heat transfer in vertical tubes correlated by an asymptotic model, *Heat Transfer Engineering*, Vol. 13, No.2, 1992, pp. 43-69.

[4] Srinivasan V., Wang D.M., Modelling and simulation of the heat and mass transfer characteristics of binary mixtures for boiling flow applications, *J. ASTM international*, Vol.8, No.2, 2011, pp. 1-22.

[5] Wang D.M., Alajbegovič A., Su X.M., Jan J., Numerical simulation of water quenching process of an engine cylinder head, *Proceedings of ASME FEDSM 2003, 4th ASME JSME Joint Fluids Engineering Conference*, Honolulu, Hawaii, USA, July 6-10, 2003.

[6] Srinivasan V., Numerical simulation of flow boiling of binary mixtures using multi-fluid modelling approach, *ASME international Mechanical Engineering Congress and Exposition*, Colorado, 2011, pp. 1-12.

[7] Lahey R.T.Jr., Drew D.A., An Analysis of Two-Phase Flow and Heat Transfer Using a Multidimensional, Multi-Field, Two-Fluid Computational Fluid Dynamics (CFD) Model, *Japan/US Seminar on Two-Phase Flow Dynamics*, Santa Barbara, California, 2000.

[8] AVL LIST GmbH, *FIRE CFD* Solver, Eulerian Multi-fluid model. *Solver Theory Guide*. 2010, Graz, Austria.

[9] Hanjalic K., Popovac M., Hadziabodic M., A robust near-wall elliptic-relaxation eddy-viscosity turbulence model CFD, *Int. J. Heat and Fluid Flow*, 25, 2004, pp. 1047-1051.

[10] Chen J.C., Correlations for boiling heat transfer to saturated liquids in convective flow, *I&EC Process Design and Development*, Vol.5, No.3, 1966, pp. 322-329.

[11] Steiner H., Kobor A., Gebhard L., A wall heat transfer model for subcooled boiling flow, *Int. J. Heat and Mass Transfer*, vol.48, 2005, pp. 4161-4173.

[12] Zeng L.Z., Klausner J.F., Bernhard D.M., Mei R. A unified model for the prediction of bubble detachment diameters in boiling systems-II. Flow boiling, *Int. J. Heat Mass*, Vol. 36, No.9, 1993, pp. 2271-2279.

Validation of the CFD model for prediction of flow behaviour in fluidized bed reactors

R. K. Thapa & B. M. Halvorsen
Department of Process, Energy and Environmental Technology, Telemark University College, Norway

Abstract

The aim of this study is to develop a robust CFD model for predicting fluid dynamics in a gasification reactor. Experimental tests are performed. A cylindrical bed with pressure sensors is used in the experimental study. A series of simulations are performed using the commercial CFD tool ANSYS Fluent 12.1. A multi-fluid Eulerian model incorporating the kinetic theory of granular flow is applied in the simulations. Fluidized bed reactors in biomass gasification processes use steam as a fluidizing gas. High temperature makes it difficult to study the flow behaviour under the operating conditions. A cold flow model is constructed to study the fluid dynamics. Air at ambient conditions is used as the fluidizing gas for the cold model. The density and viscosity variation between air at ambient temperature and steam at high temperature results in different flow behaviour. The CFD model is developed to also be able to predict the flow behaviour of steam fluidized beds. Computational minimum fluidization velocity, bed expansion ratio pressure drop and pressure standard deviation agree well with experimental measurements. A computational model has been developed and validated against experimental data. The validated CFD-model can be useful in the study of flow behaviour of high temperature steam fluidized gasification reactors.
Keywords: fluidized bed, CFD, multi-fluid Eulerian model.

1 Introduction

Gas-solid fluidized bed reactors are widely used in biomass gasification technology. The fluidizing gas in the reactors is steam at high temperature. Study of the flow behaviour inside the hot bed is difficult. Most of the design and

WIT Transactions on Engineering Sciences, Vol 74, © 2012 WIT Press
www.witpress.com, ISSN 1743-3533 (on-line)
doi:10.2495/AFM120211

optimization of the reactors are still based on the empirical methods. Alternatively, down-scaled pilot plants and cold flow models are constructed. In the cold flow model, air at ambient conditions is used as the fluidizing gas. Air at ambient condition and high temperature steam has different density and viscosity. The density and viscosity effect in the flow behaviour and fluidization properties. The computational fluid dynamics (CFD) offers an approach to the prediction of the flow behaviour. A validated model can be applied in the simulation of flow behaviour in a hot steam fluidized reactor. This can reduce the task of constructing pilot-scale and cold flow models.

Eulerian multi-fluid model is becoming more and more accepted in gas-solid fluidized bed simulations [1]. The model incorporating kinetic theory of granular flow considers both gas and solid as interpenetrating fluids. The objective is to establish a comparatively validated model. This requires agreement between the experimental and simulated results on parameters such as pressure drop, pressure standard deviation, bed expansion, minimum fluidization velocity and bubble behaviour.

A number of works on validation of the model have been published [2–6]. A reasonably good agreement between experimental and computational results is reported. The governing equations are mass and momentum balance. However, different drag models and constitutive equations have been used in the models.
A set of the constitutive equation with drag model has been finalized by Jayarathna, S.A. [7]. This option is applied in this work. The computational analysis of minimum fluidization velocity and bubble behaviour using pressure standard deviation and fluctuation of solid volume fraction has been introduced.

2 Experimental set up

Experiments are performed in a Plexiglas cylinder with 1.4 m height and 0.084 m diameter. The pressure sensors are located along the height of the cylinder and connected to the lab-view program for data storage as shown in Figure 1.

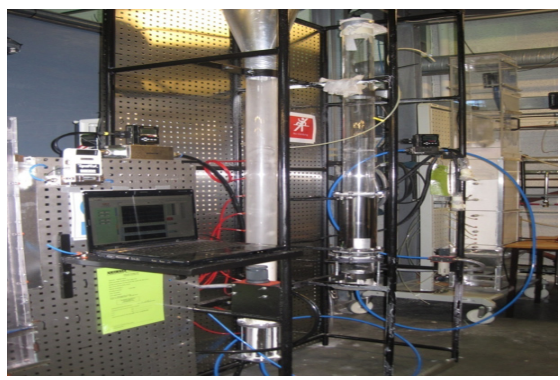

Figure 1: Experimental set-up: fluidized bed with pressure reduction valve, digital flow controller, pressure sensors.

The air flowing through a uniform air distributer is controlled by the lab-view program in order to maintain a steady flow of gas. The air flow rate is controlled by air flow meter and the data are saved in the lab-view program.

The particles in biomass gasification reactors are quartz sand of mean particle size 500 μm and density 2500 kg/m^3. Similar particles are selected in the experimental work.

The physical properties of gas and particles used in the experiments are presented in Table 1. A series of experiments are performed for a wide range of superficial air velocity.

Table 1: Gas and solid properties.

Parameters	Value	Remarks
Particle density [kg/m^3]	2500	Glass
Gas density [kg/m^3]	1.225	Air
Gas viscosity	1.78x10^{-5}	Air
Particle diameter [μm]	500	Mean
Initial bed height [m]	0.32	

The pressure sensors are located at 0.03, 0.13, 0.23, 0.33 m above the air distributor as shown in Figure 2.

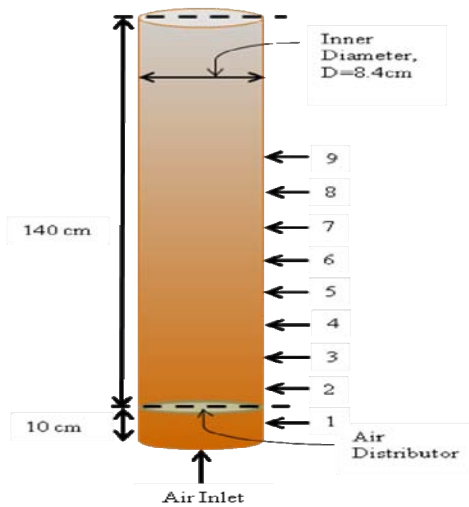

Figure 2: Sketch of 0.084 m bed with pressure sensors.

3 Computational model

A multi-fluid Eulerian model incorporating kinetic theory of solid particles is applied to simulate the transient behavior of the bed. The governing equations

are the conservation of mass and momentum. The kinetic theory of granular flow considers the conservation of solid fluctuation energy [8]. Simulations are performed with air as fluidizing gas. The particles and properties are consistent to those used in the experiments. The simulation parameters used for the model are presented in Table 2.

Table 2: Simulation parameters.

Parameters	Value	Remarks
Particle density [kg/m^3]	2500	Glass
Gas density [kg/m^3]	1.225	Air
Gas viscosity [Ps.s]	1.78x10^{-5}	Air
Particle diameter [μm]	500	Mean
Restitution coefficient	0.9	
Initial solid packing	0.6	
Maximum solid volume fraction [-]	0.63	
Bed diameter [m]	0.084	
Static bed height [m]	0.32	
Time step	1x 10^{-3}	
Number of iterations per time step	40	

The combination of the models used in the work is summarized in Table 3. The combination of model is validated against the experimental data for different flow conditions [7].

Table 3: Models used in the simulation.

Drag model	Symlal O'Brien
Grannular Bulk Viscosity	Symlal O'Brien
Frictional Viscosity	Constant
Frictional Pressure	Based-ktgf
Solid Pressure	Ma-ahamadi
RadialDistribution Function	Ma-ahmadi

4 Results and discussion

Minimum fluidization velocity is regarded as the most important parameter in the design of fluidized bed reactors [9]. Minimum fluidization velocity (u_{mf}) is experimentally determined plotting average pressure drop across the bed height as a function of superficial air velocity as shown in Figure 3. Experimental measurement of minimum fluidization velocity for the glass particles is about 0.24 m/s. The pressure drop is 129 mbar and the bed expansion ratio is 1.03. The pressure drop is proportional to the gas velocity below minimum fluidization condition.

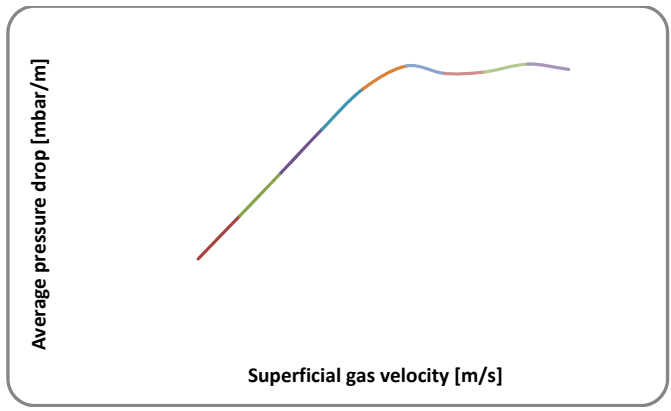

Figure 3: Experimental average pressure drop as a function of superficial gas velocity.

Fig. 4 compares the experimental and computational pressure standard deviation at different level of the bed height. After fluidization conditions, the pressure fluctuation across the bed increases significantly. Pressure standard deviation can be used to determine the minimum fluidization velocity from experimental and computational results. Before fluidization the pressure standard deviation is about zero. It increases with the particle movement in the bed. The experimental and simulated minimum fluidization velocities are about 0.24 and 0.26 m/s respectively. The experimental u_{mf} is similar to that in Figure 3. The deviation between experimental and computational u_{mf} is 8%. The increase in pressure standard deviation with increasing superficial air velocity indicates increasing bubble frequency. The Figure indicates a good agreement of experimental and simulated results concerning the minimum fluidization velocity.

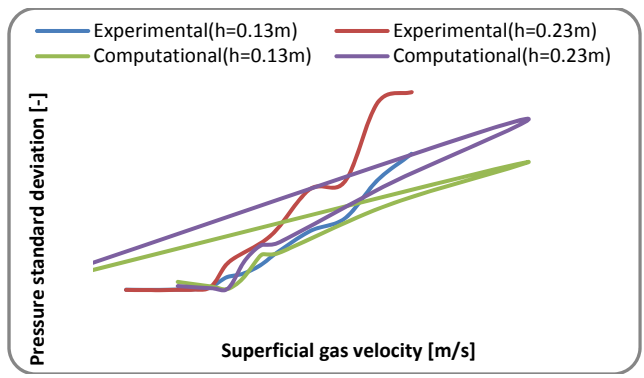

Figure 4: Comparison of experimental and computational pressure standard deviation as a function of superficial air velocity. Bed height = 0.13m.

The contour of solid volume fraction at the height of 0.13m is presented in Figure 5. The contours are at different superficial air velocity and at 8s of real time simulation. Bubbles start to appear at the superficial air velocity 0.28 m/s. The predicted minimum bubbling velocity is slightly higher than minimum fluidization velocity. The particles used in the study are characterized as Geldart B particles. For Geldart B particles, the minimum fluidization and minimum bubbling velocities are almost the same [9]. Bubble frequency is increased with increasing air velocity. Small bubbles are formed at the bottom of the bed and the size is increased as they rise along the bed height.

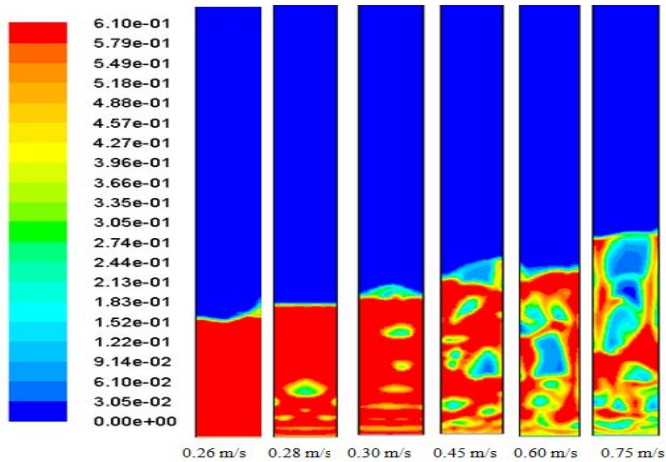

Figure 5: Contours of solid volume fraction at different superficial air velocities.

The minimum bubbling velocities are also studied from the plot of time average solid volume fraction from simulation data at the bed height 0.13m and 0.23m. Figure 6 shows the solid volume fraction variation against time at the bed height of 0.23 m/s.

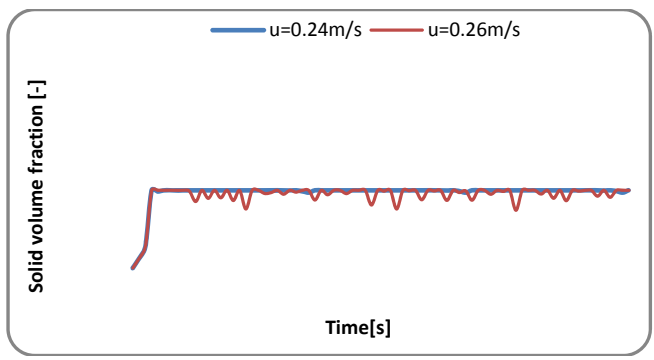

Figure 6: Solid volume fraction fluctuation at lower air velocities.

At the air velocity of 0.24 m/s, the solid volume fraction is almost constant as shown in Figure 6. Slight fluctuation of the solid volume fraction starts at the air velocity of 0.26m/s indicating the inception of fluidization.

The solid volume fraction at the superficial air velocity 0.28 m/s shows significant fluctuation indicating bubble formation. The bubble frequency is increased at the air velocity 0.30m/s.

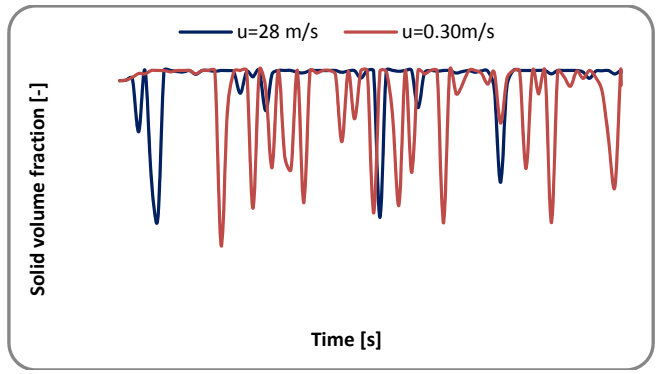

Figure 7: Solid volume fraction as a function at the higher air velocities.

In Fig. 8 computational and experimental pressure drops are compared at the bed height of 0.13m.The pressure drop show good agreement at the gas velocity above the minimum fluidization. The deviation between the computational and experimental results is 7% at minimum fluidization. Above the minimum fluidization condition, the deviations are less than 7%. However, below minimum fluidization the deviation is significant. Eulerian multiphase model considers both the solid and gas as fluids. The model considers the bed fluidizing even at the gas velocity lower than minimum fluidization.

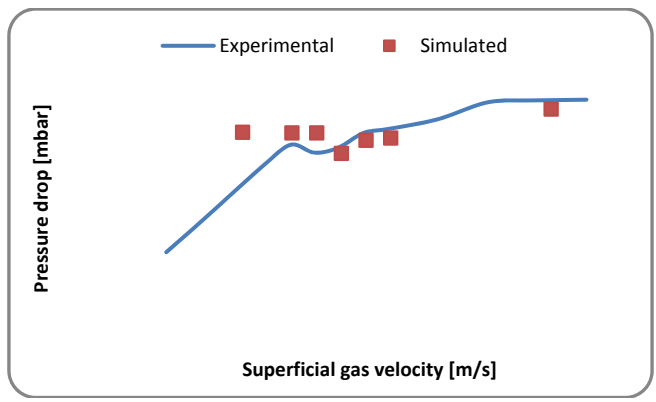

Figure 8: Comparison of experimental and computational pressure drop as a function of air velocity.

Figure 9 shows a comparison of bed expansion in experiment and simulations. In both cases the bed expansion ratio is increased consistently with superficial air velocity. Simulated bed expansion is slightly lower than experimental. The average deviation of bed expansion between computational and experimental results is about 5%. At the higher air velocities, the experimental bed expansion is an average expansion. The bed height in the experiments is fluctuating and not constant at higher air velocities.

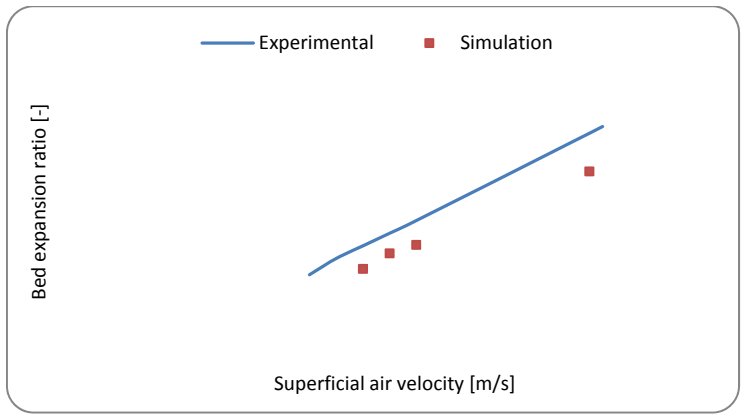

Figure 9: Experimental and simulated bed expansion as a function of superficial air velocity.

5 Conclusions

A multifluid Eulerian model incorporating the kinetic theory of granular flow is applied for computational prediction of gas-solid flow behaviour. The results are compared with the experimental measurements. The computational and experimental minimum fluidization velocities are 0.24m/s and 0.26 m/s with 8% deviation. Experimental and computational pressure standard deviation also gives the same results for minimum fluidization velocity. The computational and experimental pressure drops are about 29 and 27 mbar respectively at the minimum fluidization condition. The deviation is about 7%. Computational and experimental bed expansions at the minimum fluidization condition are 8% and 10% respectively. Computational solid volume fraction fluctuation is studied to predict bubble formation and bubble frequency.

For the given operating conditions, the model predictions are in good agreement with the experimental measurement. The model can be the basis for the study of flow behaviour in high temperature steam fluidized gasifiers.

References

[1] V.Mathiesen, T.S., B.J. Hjertager, *Prediction of gas particle flow with an Eulerian model including a realistic particle size distribution.* Power Technology, 2000. **112**: p. 34-45.
[2] Taghipour, F., Ellis, N., Wong, C., *Experimental and computational study of gas-solid fluidized bed hydrodynamics.* Chemical Engineering Science, 2005. **60**: p. 6857-6867.
[3] Hamzehei, M., Rahimzadeh, H, Ahmadi, G., *Studies of gas velocity and particle size effects on fluidized bed hydrodynamics with CFD modeling and experimental investigations*. Journal of Mechanics, 2010. **26**.
[4] Wachem, v.B.G.M., Schouten J.C., Krishna, R., Bleek den van C. M., *Validation of the Eulerian simulated dynamic behavior of gas-solid fluidized bed.* Chemical Engineering Science, 1999. **54**: p. 2141-2149.
[5] Sahoo, A., Ch, R., Biswal, K.C., *Experimental and computational study of the bed dynamics of semi-cylindrical gas-solid fluidized bed.* Canadian Journal of Chemical Engineering, 2009. **87**: p. 11-18.
[6] M.M. Kumar, E.N., *CFD simulation for two-phase mixing in 2D fluidized bed.* Int J Adv Manf Technol, 2008.
[7] Jayarathna, S.A., *Recommendation of a model for simulating and analysis of the influence of particle size distribution on the simulation of bubbling fluidized bed, in Department of Process, Energy and Environment.* 2008, Telemark University College: Prosgrunn. p. 22-46.
[8] Gidaspow, D., *Multiphase Flow and Fluidization.* 1994, California: Academic Press Inc.
[9] Kunii, D., Levenspiel, O., *Fluidization Engineering*. Second ed. 1991, London: Butterworth-Heinemann.

This page intentionally left blank

Study of a fluidized bed reactor for gasification of biomass

K. Kleiva, R. K. Thapa & B. M. Halvorsen
Department of Process, Energy and Environmental Technology, Telemark University College, Norway

Abstract

Experimental studies have been performed on a cold fluidized bed with glass and plastic particles emulating the properties of wood and olivine particles. The purpose of the experimental studies was to find the fluidization properties of the particles. These experimental studies have founded the background for conducting computational studies of multiphase flows of particles with the same properties. The computational studies are performed in ANSYS Fluent 12.0. The mathematical model has been verified with an experimental study to validate the simulations. A combination of steam, olivine particles and wood chips has then been simulated based on the results from the experimental and computational studies. The results from the computational studies show that the minimum fluidization velocity in the Fluent-simulations is higher than in the physical experiments, which is expected to a certain degree because of the wider distribution of particle sizes in the physical experiment. The pressures in the simulations scale well with the experimental results with increasing superficial velocity; more than one solid phase in the simulation gives a higher difference in pressure between the simulated and experimental values.
Keywords: fluidized bed, CFD, multi-phase Eulerian model, multiple density simulations, biomass, CHP.

1 Introduction

The behavior of biomass particles inside a fluidized bed is an essential part of the efficiency of a gasification combined heat and power-plant (CHP-plant), and for simulations of the behavior to be accurate, physical experiments are vital. The computational model used in fluent is based on already published models [1].

WIT Transactions on Engineering Sciences, Vol 74, © 2012 WIT Press
www.witpress.com, ISSN 1743-3533 (on-line)
doi:10.2495/AFM120221

In order for a gasifying facility to be efficient and the gasifying temperatures to be adequately high, good mixing is necessary in the fluidized bed unit. The process itself should be able to generate enough heat so that external energy is not required to feed the process when it is up and running. A big span in size and density between the reacting particles and the inert particles in the bed lead to a natural segregation of the lighter and denser particles. The biomass tends to float on top of the bed, volatiles are released into the freeboard and the requirements for heating the steam inside the bed might be unfulfilled, making it difficult to maintain sufficient gasification temperature. This results in a much lower efficiency of the gasification process than what is possible with a more uniform mixing [2].

2 Multiphase modeling in ANSYS fluent

The adaptation of a mathematical model to a fluidized bed is already covered by Sanoja and Ariyarathna [3]. The setup used in Fluent is presented in Table 1.

Table 1: Mathematical model parameters in ANSYS fluent.

Type of force	**Mathematical model**
Solid-fluid drag model	Syamlal-O'Brien
Solid-solid drag model	Syamlal-O'Brien Symmetric
Granular viscosity	Syamlal-O'Brien
Granular bulk viscosity	Constant
Frictional viscosity	Schaeffer
Frictional pressure	Based-ktgf
Solids pressure	Ma-ahmadi
Radial distribution function	Ma-ahmadi

The multiphase model used in the simulations is the Euler-Euler approach. The different mathematical models are presented in this section. Multiphase simulation solves the continuity, momentum and energy equations for each phase. For this study, the two most important are the continuity equation and the momentum equation as there is no transfer of heat between the phases. The minimum fluidization velocity (u_{mf}) of a mixture characterizes its fluidization properties and is a way to compare the experiments with the simulations [4].

2.1 Experimental setup for pressure drop measurements

A small scale fluidized bed is used in the experimental study. The bed has pressure sensors located on the walls with a vertical distance of 10 cm between them. A drawing of the bed setup is shown in Figure 1.

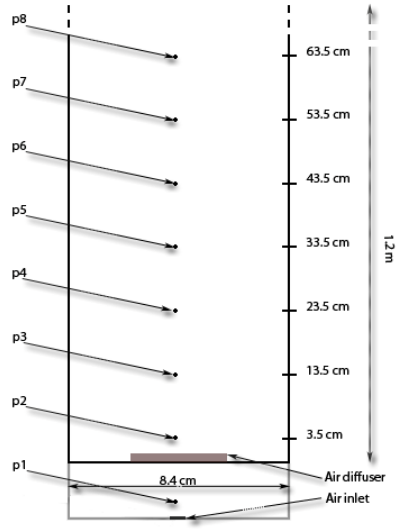

Figure 1: 2-D representation of the circular fluidized bed with dimensions and pressure sensor alignments (not drawn to scale).

The air diffuser, seen in Figure 1, in the bottom of the bed gives a uniform air distribution at the inlet of the bed. The eight pressure nodes are connected to a hub which again is connected to LabVIEW. The diameter of the circular bed is 8.4 cm and the height is 1.2 m.

2.2 Fluidized bed experiments

Two types of particles were used in the experiments; their respective characteristics as well as the air phase characteristics used in the Fluent simulations are displayed in Table 2.

Table 2: Phase characteristics for the G, GP-1 and GP-2 simulations.

Phase	Mean particle size (μm)	Density (kg/m^3)	Viscosity (kg/m-s)	Geldart classification [5]
Glass	182	2485	-	B
Plastic	3000	964	-	D
Air	-	1.225	1.7894e-05	-

Three sets of experiments were run with different mixtures of glass and plastic particles, as seen in Table 3.

Table 3: Mixture ratios of glass and plastic in the G, GP-1 and GP-2 simulations.

Simulation	Volume of glass particles (l)	Volume of plastic particles (l)	Total mixture	Weight of plastic particles
G	2	0	0 vol% plastic	0 wt%
GP-1	2	0.6	23 vol% plastic	10.5 wt%
GP-2	2	1	33 vol% plastic	17.5 wt%

To transfer the experimental studies and simulation to a relevant case with material properties that are of the same kind that appear in a real situation, a steam/olivine/charred wood simulation has been performed. The characteristics of the different elements of this simulation are presented in Table 4.

Table 4: Phase characteristics for the steam/olivine/charred wood simulation.

Phase	Mean particle size (μm)	Density (kg/m^3)	Viscosity (kg/m-s)	Geldart classification
Steam (800°C)	-	0.29	4.1e-05	-
Olivine	400	2500	1.7894e-05	B
Charred wood	3000	400	1.7894e-05	D

The mixture ratio of the olivine-charred wood mixture is displayed in Table 5. The weight-percentage of the charred wood particles is set to 10 wt-%, giving a vol-% of 38.5 of the wood particles patched uniformly with olivines in the initial conditions in the fluidized bed simulation.

Table 5: Mixture ratios of olivine and charred wood in the simulation.

Volume of olivine (l)	Volume of charred wood (cw) (l)	Total mixture	Weight of cw-particles
2	1.25	38.5 vol% cw	10 wt% cw

2.3 Results and discussion

The snapshots from the simulations of the GP-1 mixture, Figure 2, show that small bubbles appear in the bed at around 8 cm/s, showing that u_{mf} is reached.

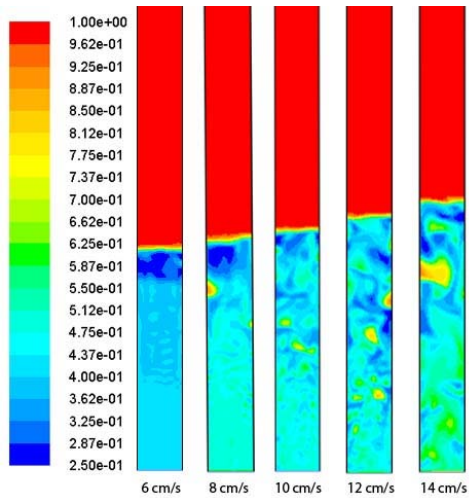

Figure 2: Volume fraction of air in a simulation of the GP-1 mixture.

The course of the volume fraction of air as a function of time in point p3, 13.5 cm above the air-inlet, of the GP-1 mixture for a superficial velocity of 6 and 8 cm/s are shown in Figure 3 and Figure 4 respectively. Fluctuations in the volume fraction of air are a sign of fluidization.

Figure 3 and Figure 4 indicate, as the snapshot in Figure 2 that the u_{mf} is reached before a superficial velocity of 8 cm/s.

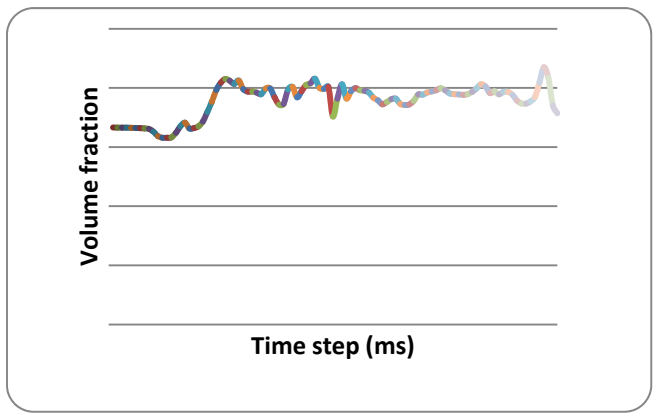

Figure 3: Course of the facet average volume fraction of air in p3 of the bed for the simulation of the GP-1 mixture at a superficial velocity of 6 cm/s as a function of time.

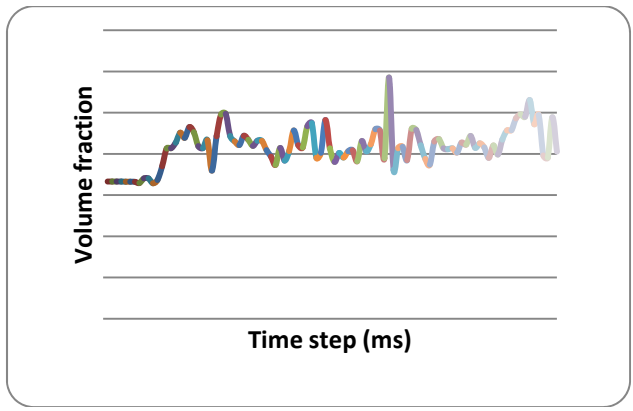

Figure 4: Course of the facet average volume fraction of air in p3 of the bed for the simulation of the GP-1 mixture at a superficial velocity of 8 cm/s as a function of time.

The difference in the particle properties of the glass and plastic particles is clearly seen in Figure 5. The plastic particles float to the top because of their lower density and larger diameter, as also was visually apparent in the physical experiment. The snapshot at 14 cm/s has a more uniform mixture of glass and plastic particles, suggesting that the vertical mixing of the two particle types is better with increased superficial velocity from u_{mf}. The expansion of the bed is also making the distribution of plastic particles more uniform.

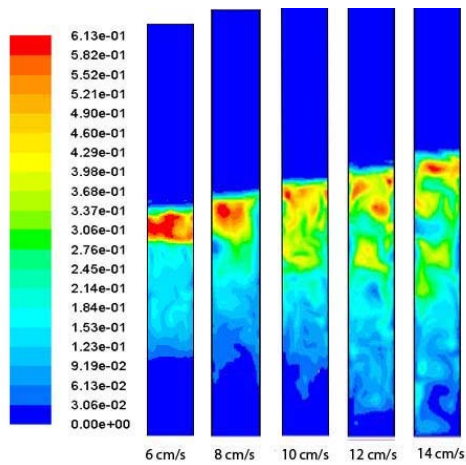

Figure 5: Volume fraction of plastic particles in a simulation of the GP-1 mixture.

The GP-2 mixture, Figure 6, has a slightly lower u_{mf} than the GP-1 mixture, and this picture also shows bubble appearance at 6 cm/s in the top part of the

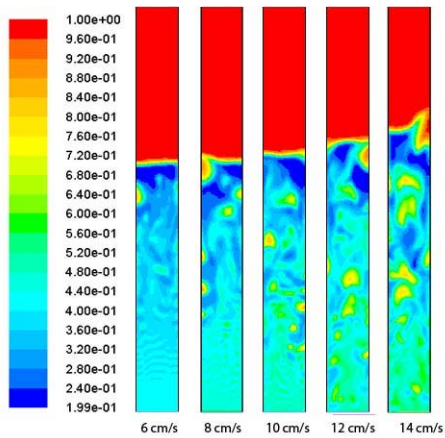

Figure 6: Volume fraction of air in a simulation of the GP-2 mixture.

bed. This holds true until enough light particles are added to the mixture to reduce the u_{mf} once again when the packing no longer is optimal.

Ramakers *et al*. [6] stated that a mixture of 10 wt-% of wood particles in a olivine-wood mixture is an optimal mixture for uniform mixing of the particles in a fluidized bed. This theory is arguably notable in the comparison of Figure 5 and Figure 7 which have a wt-% of 10.5 and 17.5 respectively. The gathering of plastic particles in the top part of the bed is much higher in the GP-2 mixture in Figure 7 at a superficial velocity of 14 cm/s, which in a gasifier would result in a

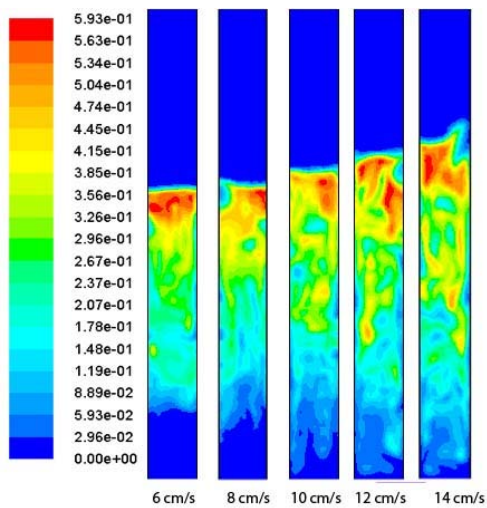

Figure 7: Volume fraction of plastic particles in a simulation of the GP-2 mixture.

poorer energy transfer from the non-reacting olivine particles to the wood particles. Both particle mixtures have a uniform concentration in the bottom part of the bed, but the GP-1 mixture have a more uniform concentration overall.

3 Particle mixing in a steam/olivine bed

The simulation of the steam/olivine/charred wood-combination has been done to transfer the proven model to a case that is closer to a real gasifier in a CHP-plant.

A simplified theoretical value of the u_{mf} for this mixture has been calculated using the Ergun equation [4] to be approximately 0.48 m/s. The course of the volume fraction of steam in the lowest superficial velocity simulation of 0.24 m/s, Figure 8, shows that the u_{mf} already is superceded. The large peaks in the volume fraction of steam are an indication of bubbles and the amplitude of the peaks are a sign of a well fluidized bed.

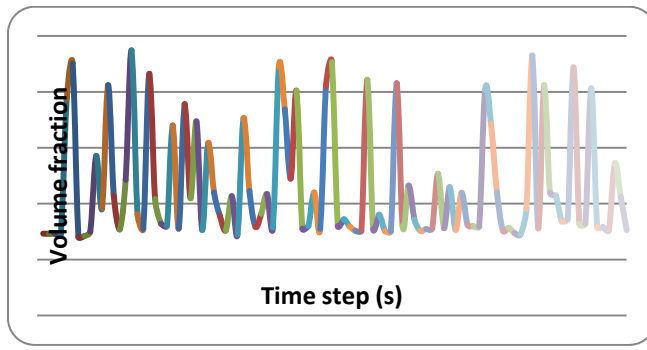

Figure 8: Volume fraction of steam in the steam/olivine/charred wood simulation, with a superficial velocity of 0.24 m/s as a function of time.

When steam is used as a fluidizing medium, the superficial velocity required to achieve fluidization is increased when compared to cold air as a fluidization medium. This is because of the lower density of the steam. The lowest simulated velocity of 0.24 m/s gives a proper fluidized bed, as can also be seen in Figure 9. The bubbles are comparable to the GP-1 simulation, but it is apparent that the superficial velocity of 0.24 m/s is slightly higher than the u_{mf} for the particle-gas mixture. The most homogenous mixing of the combination of olivine and charred wood particles, see Figure 10, seems to be somewhere in between a superficial velocity 0.48 m/s and 0.72 m/s. This can be stated because the area on the top the bed with charred wood at 0.72 m/s has a higher concentration of wood particles than the top part at 0.48 m/s. This also supports that a higher superficial velocity to a certain points increases the buoyancy forces working on the lighter particles in the fluidized bed. The assumed u_{mf} of slightly below 0.24 m/s along with the fact that the most uniform mixing happens in between 0.48

m/s and 0.72 m/s further supports the suggestion by Ramakers *et al*. [6], that a superficial velocity of 3-4 times the u_{mf} is the ideal superficial velocity for optimal mixing of wood particles and non-reactive particles in a fluidized bed.

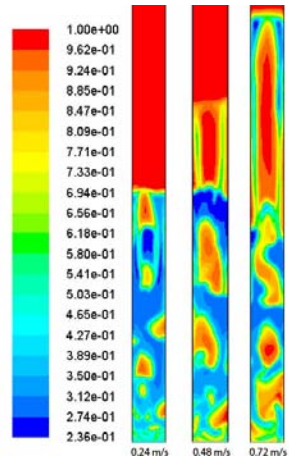

Figure 9: Volume fraction of steam in the fluidized bed.

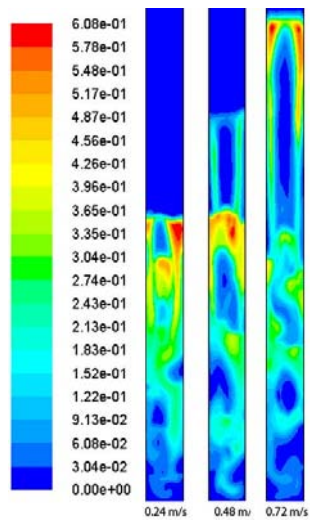

Figure 10: Volume fraction of charred wood in the fluidized bed.

4 Conclusion

The glass and plastic experiments show that adding plastic particles to the mixture causes an increase of the minimum fluidization velocity (u_{mf}) to a certain

point, before it decreases again. The addition of larger particles causes the packing factor of the glass particle mixture to increase to a degree, and hence the u_{mf} to increase. When more light density and large particles are added to the mix, the u_{mf} will start decreasing again as they have a smaller theoretical u_{mf}, the mixture of 23 vol-% plastic was found to have a u_{mf} of 0.05 m/s, while the 33 vol-% plastic mixture was found to have a u_{mf} of 0.045 m/s. In the case of mixed glass and plastic particles, the fluidization seemed to appear in both the top and bottom region of the fluidized bed simultaneously.

The simulations gave a higher u_{mf} than the experiments for both mixtures of glass and plastic particles as well as for glass particles only. This is an effect of not having a particle distribution in the particles, only a mean diameter. The 23 vol-% plastic mixture has a simulated u_{mf} of 0.09 m/s, while a simulated 33 vol-% plastic mixture has a u_{mf} of 0.075 m/s.

The 23 vol% plastic mixture correlates to a 10.5 mass% mixture, which is assumed to be the optimum mixture between large light density particles and small high density particles. This mixture gives a more uniform distribution of reacting and catalytic particles in the bed. When a 10 mass% mixture of wood chips in a steam, olivine and charred wood mixture is simulated, it is apparent that the uniformity of the mixture does not get better with a large superficial velocity. Large superficial velocities increase the buoyancy effect, causing the light particles to gather in the top of the particle region in the bed. A superficial velocity of 3-4 times the u_{mf} seems to be the optimal conditions for a steam/olivine/wood chip gasifier.

References

[1] P. L. N. Ramesh and M. Raajenthiren, “A Review of Some Existing Drag Models Describing the Interaction Between the Solid-Gaseous Phases In a CFB,” *International Journal of Engineering Science and Technology*, vol. 2, pp. 1047-1051, 2010.

[2] J. X. Laihong Shen, Fredrik Niklasson, Filip Johnsson, “Biomass mixing in a fluidized bed biomass gasifier for hydrogen production,” *Chemical Engineering Science,* pp. 636-643, 2006.

[3] D. G. A. Sanoja U. Ariyarathna, “Recommendation of a Model for Simulating & Analysis of the Influence of Particle Size Distribution on the Simulations of Bubbling Fluidized Beds,” Master Thesis, Telemark College University, 2008.

[4] D. Kunii and O. Levenspiel, *Fluidization Engineering*: Butterworth-Heinemann, 1991.

[5] D. Geldart, “Types of Gas Fluidization,” *Powder Technology,* pp. 285-295, 1973.

[6] Bram J. Ramakers, Ronny de Ridder and Piet J.A.M. Kerkhof “Fluidization behavior of wood/sand mixtures,” *Drying,* pp. 1337-1344, 2004.

Liquid–gas interface under hydrostatic pressure

A. Gajewski
Bialystok University of Technology, Faculty of Civil Engineering and Environmental Engineering, Department of Heat Engineering, Poland

Abstract

The surface-tension forces and the pressure force at a gas–liquid interface were balanced. This was done at a differential control surface under hydrostatic pressure. As a result, three quadratic and two linear equations were derived representing the conditions for equilibrium at the interface. These equations have eight roots describing eleven different equilibrium states. The most important is the Young-Laplace formula under hydrostatic pressure which is denoted in the spherical coordinate system. Hence, it is a quadratic equation. The first root of this equation describes a pendant drop, drop or bubble, while the second one circumscribes a sessile drop. There are two solutions for the uniform pressure, where one of them is the Young-Laplace formula. It is concluded that the surface existence depends on the pressure difference between both bulk phases. A plane is formed when the surface-tension forces equilibrate themselves. Under uniform pressure the interface is a sphere and its other shapes need a pressure gradient. To form a drop or a bubble the pressure difference must be higher than its border value. A sessile drop exists if the gauge pressure is negative, while a pendant drop requires a positive value. A comparison with experimental results is done for the bubble.
Keywords: Young-Laplace equation in spherical coordinates, static equilibrium, drop, bubble.

1 Introduction

To describe the force balance on the liquid–gas interface, the Young-Laplace equation is usually applied. The equation must be solved for each point separately. Hence, it is computationally difficult to balance the surface-tension

WIT Transactions on Engineering Sciences, Vol 74, © 2012 WIT Press
www.witpress.com, ISSN 1743-3533 (on-line)
doi:10.2495/AFM120231

and hydrodynamic forces on a differential surface or volume. The Young-Laplace equation was derived from work involving the expansion of a soap-bubble surface. The same formula can be also applied as a condition of static equilibrium because the surface tension is considered simultaneously as a surface-tension force per unit length and, following Tolman [1], either as the quotient of the energy change with the change in surface area at constant entropy, constant composition and constant volumes for the two phases (measured at the surface of tension) or as the rate of free energy change with the change in surface area at constant temperature, constant composition and constant volumes. The theory of wetting phenomena on curved surfaces has been developed to date by the derivation of formulas or theorems originating from an "energetic" definition and their application in force balances. Hence, this solution is limited to one scalar equation. Because a force may have three components, this equation may not be applied as a condition for equilibrium in the case of an unsymmetrical shape, nor can the shape of the surface be described using only the force balance due to the lack of the corresponding equations along the tangents to the surface directions.

The main goal of the current work is to develop a wetting theory of curved gas-liquid interfacial surfaces beginning directly from the surface tension defined as the unit force. This was expected to yield two equations of force balance for the symmetric shapes for the droplet or bubble under hydrostatic pressure.

2 Mathematical model

The topic of discussion here is the prediction of the shape of the liquid–gas interface under hydrostatic pressure. To do it, the forces applied on the surface at rest are balanced. As surface forces shape the surface, they should be balanced at the surface. While the fixed coordinate system is used, the hydrostatic pressure creates a changing radius of curvature. Therefore, the surface with a varying radius along the depth of the liquid must be described.

The surface presented in fig. 1 is defined in the spherical parameterisation in which the radial distance changes along the θ coordinate:

$$f(\theta,\varphi) = \left(r(\theta)\sin\theta\cos\varphi, r(\theta)\sin\theta\sin\varphi, r(\theta)\cos\theta\right) \tag{1}$$

The versors of the surface-coordinate system are

$$\vec{\delta}_\theta = \cos(\theta-\omega)\cos\varphi\vec{i} + \cos(\theta-\omega)\sin\varphi\vec{j} - \sin(\theta-\omega)\vec{k} \tag{2}$$

$$\vec{\delta}_\varphi = -\sin\varphi\vec{i} + \cos\varphi\vec{j} \tag{3}$$

where ω is defined in fig. 3.

Moving along the tangential vector, the surface curves in the direction of the movement. The curvature is described by the unit vector perpendicular to the surface. It arises from the structure of the surface, which is a two-dimensional object existing in three-dimensional space. Taking the above into account, it is necessary to define the normal unit vector:

$$\vec{\delta}_n = \sin(\theta-\omega)\cos\varphi\vec{i} + \sin(\theta-\omega)\sin\varphi\vec{j} + \cos(\theta-\omega)\vec{k} \tag{4}$$

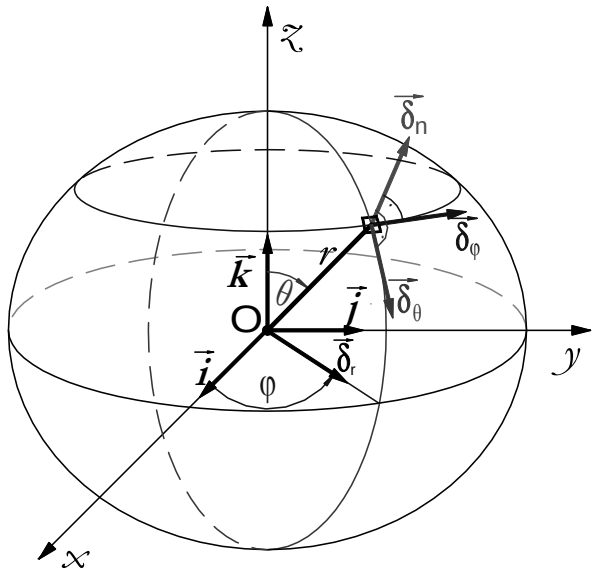

Figure 1: The assumed surface coordinates and the versors.

2.1 The force system

No matter how small, a fluid is a substance that deforms continuously under the application of tangential stress. In the considered case, the shear stresses equal zero. Therefore, only the normal stresses are sustained. As a result, the resultant force acting on the surface is normal to the surface. The resultant pressure force that tends to expand the surface, acts in the centre of the area. Because the force system has to satisfy Newton's third law, the directions and senses of the resultant surface forces preventing expansion must be oriented out from the surface. However, the components of the resultant surface-tension forces must be applied at the boundary arc of the surface, and these are tangential to the surface.

The force system is shown in fig. 2. In this case, the resultant pressure force is the active force. Therefore, the resultant of the tangential surface forces is the reactive force. A differential surface element is defined using two arcs with radii r and $r\sin\theta$ (cf. fig. 2). Therefore, this surface is a curvilinear rectangle (fig. 1 and fig. 2). Hence, we have four infinitesimal surface-tension forces (fig. 2). As a result, we obtain two resultants, one each of each pair of these forces. These resultants equilibrate the infinitesimal pressure force.

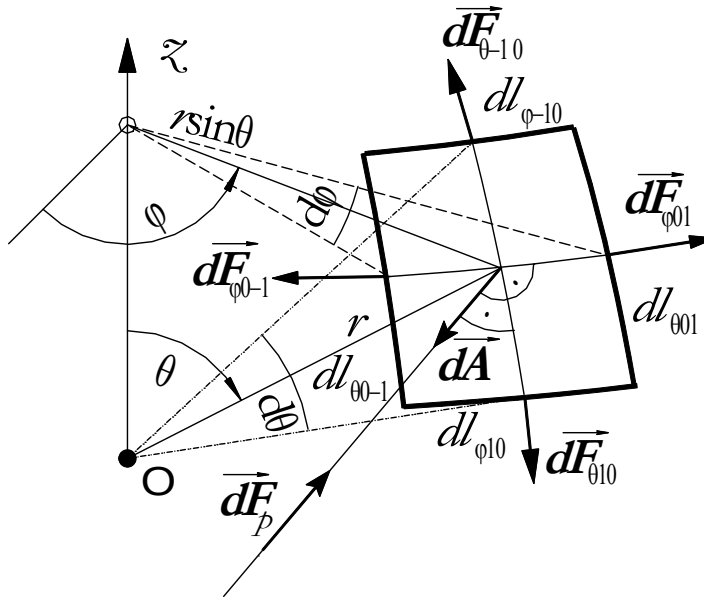

Figure 2: The force system for an infinitesimal element.

The pressure force is expressed by the formula

$$\vec{dF}_p = -p\vec{dA} = p\frac{r^2 \sin\theta d\theta d\varphi}{\cos\omega}\vec{\delta}_{n00} \tag{5}$$

The surface tension forces in the φ component are presented

$$\vec{dF}_{\varphi 01} = \left(\sigma r d\theta / \cos\omega\right)\vec{\delta}_{\varphi 01} \tag{6}$$

$$\vec{dF}_{\varphi 0-1} = \left(-\sigma r d\theta / \cos\omega\right)\vec{\delta}_{\varphi 0-1} \tag{7}$$

Next, the components in the θ direction are obtained:

$$\vec{dF}_{\theta 10} = \sigma\left(r + dr/2\right)\sin\left(\theta + d\theta/2\right)d\varphi\vec{\delta}_{\theta 10} \quad , \tag{8}$$

$$\vec{dF}_{\theta -10} = -\sigma\left(r - dr/2\right)\sin\left(\theta - d\theta/2\right)d\varphi\vec{\delta}_{\theta -10} \quad . \tag{9}$$

The resultant force in the θ direction is:

$$\vec{dF}_\theta = \sigma\left(r\sin d\theta\cos\theta + dr\sin\theta\cos^2\frac{d\theta}{2}\right)d\varphi\vec{\delta}_{\theta 00} - \sigma r\sin\theta\sin d\theta d\varphi\vec{\delta}_{n00} \tag{10}$$

and in the φ direction:

$$\vec{dF}_\varphi = -2\sigma\frac{rd\theta}{\cos\omega}\cos\theta\sin\frac{d\varphi}{2}\vec{\delta}_{\theta 00} - 2\sigma\frac{rd\theta}{\cos\omega}\sin\theta\sin\frac{d\varphi}{2}\vec{\delta}_{n00} \tag{11}$$

The system of the resultant forces and the cross section of the investigated surface are showed in fig. 3. Hydrostatic pressure is calculated as follows:

$$p = \rho g\left(r_0 - r\cos\theta\right) \quad . \tag{12}$$

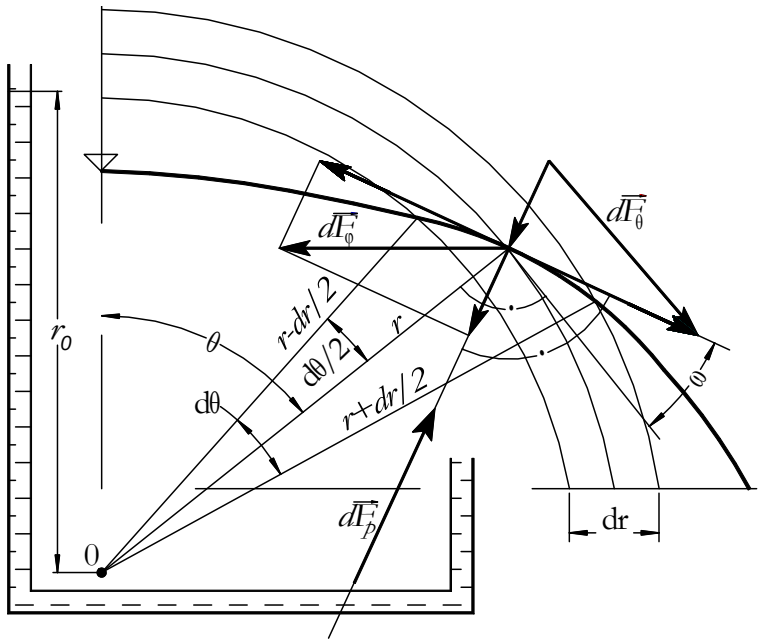

Figure 3: The force system resolved into meridian and normal directions.

2.2 The force balance

The resultant surface tension forces and pressure force are balanced. Respectively, their components along the meridian and normal directions to the surface must equal zero. First we obtain the force balance in tangential direction:

$$1+\frac{dr}{rd\theta}\tan\theta=\sqrt{1+\left(dr/rd\theta\right)^2} \tag{13}$$

and the balance of the forces in the normal direction:

$$\frac{dr}{d\theta}=r\sqrt{\frac{1}{\left(\frac{\rho g r\left(r_0-r\cos\theta\right)}{\sigma}-1\right)^2}-1} \tag{14}$$

Substituting the relationship

$$r^+=r/\sqrt{\sigma/\rho g} \tag{15}$$

into Eqs. (13) and (14), we obtain a system of dimensionless equations as follows:

$$\begin{cases}\dfrac{dr^+}{r^+d\theta}\left[\dfrac{dr^+}{r^+d\theta}\left(\tan^2\theta-1\right)+2\tan\theta\right]=0\\ \dfrac{dr^+}{r^+d\theta}-\sqrt{\dfrac{1}{\left(r^+\left(r_o^+-r^+\cos\theta\right)-1\right)^2}-1}=0\end{cases} \tag{16}$$

for which the solution is the product of the left sides of the five equations:

$$r^+\left(r_o^+ - r^+ \cos\theta\right) - 2 = 0 \tag{17}$$

$$r^+ = 0 \tag{18}$$

$$r_o^+ - r^+ \cos\theta = 0 \tag{19}$$

$$r^+\left(r_o^+ - r^+ \cos\theta\right) - 2\sin^2\theta = 0 \tag{20}$$

$$r^+\left(r_o^+ - r^+ \cos\theta\right) - 2\cos^2\theta = 0 \tag{21}$$

These equations can be expressed in dimensional form as

$$\rho g\left(r_0 - r\cos\theta\right) = 2\sigma/r \tag{22}$$

$$r = 0 \tag{23}$$

$$\rho g\left(r_0 - r\cos\theta\right) = 0 \tag{24}$$

$$\rho g\left(r_0 - r\cos\theta\right) = 2\sigma\sin^2\theta/r \tag{25}$$

$$\rho g\left(r_0 - r\cos\theta\right) = 2\sigma\cos^2\theta/r \tag{26}$$

Formulas (17) and (22) are the Young-Laplace equation for the hydrostatic pressure written in spherical coordinates. These formulas can be solved as a quadratic equation with r as the variable. Hence, the shape of the surface can be found easily.

In contrast, their solution in the Cartesian coordinate system, in which the double surface tension is divided by the radius of curvature, requires the solution of a second-order differential equation. It can be concluded that the surface can exist if the resultant surface-tension force equals zero (cf. Eq. (24)), but it cannot be formed if the hydrostatic pressure is equal to zero. The last conclusion arises from the analysis of Eqs. (22), (24), (25) and (26) and is expressed implicitly by Eq. (23).

2.3 The shapes of the interfaces

As the shapes of the liquid–gas interfaces are presented by the solutions of Eqs. (17)–(21), we can distinguish four kinds of surface equilibrium. The first is described the Young-Laplace formula, i.e., Eq. (17). The second is the flat surface, expressed by Eq. (19), with a lack of a surface as its particular case (cf. Eq. (18)). The third and fourth kinds of equilibria have not been connected with any real situation so far. Therefore, they can be only the solutions of the force balance without any physical meaning.

Although the analysis is made in the surface-coordinate system, the graphs are plotted in Cartesian coordinates:

$$x^+ = r^+ \sin\theta \tag{27}$$

$$z^+ = r^+ \cos\theta \tag{28}$$

where the variables are defined in fig. 1. Because these solutions have axisymmetric shapes, they are plotted as cross-sections in the x^+z^+ plane.

2.3.1 The Young-Laplace equation

The solution of Eq. (17), i.e., the Young-Laplace formula with hydrostatic pressure in spherical coordinates, has two roots:

$$r_1^+ = \frac{r_o^+ - \sqrt{r_o^{+2} - 8\cos\theta}}{2\cos\theta} \tag{29}$$

$$r_2^+ = \frac{r_o^+ + \sqrt{r_o^{+2} - 8\cos\theta}}{2\cos\theta} \tag{30}$$

Because these solutions have discontinuities at $\theta = \pi/2$, the limits of the functions at this point must be calculated. To do so, we represent the square roots in Eqs. (29) and (30) as Taylor series. If $r_0^+ \Big/ \sqrt{r_0^{+2}} = 1$, the limits of the roots r_1^+ and r_2^+ are calculated as follows:

$$\lim_{\theta \to \pi/2} r_1^+ = \frac{2}{r_o^+} \tag{31}$$

$$\lim_{\theta \to \pi/2} r_2^+ = -\infty \tag{32}$$

If $r_0^+ \Big/ \sqrt{r_0^{+2}} = -1$, these limits are presented below:

$$\lim_{\theta \to \pi/2} r_1^+ = \infty, \tag{33}$$

$$\lim_{\theta \to \pi/2} r_2^+ = \frac{2}{r_o^+} \tag{34}$$

Hence, in the case of a positive hydraulic head, r_0^+, the root r_1^+ is a continuous function. If the hydraulic head has a negative value, the solution for r_2^+ has no discontinuity. We can summarise that the hydraulic head is the asymptote for some solutions. Note that r_1^+ and r_2^+ can generally be complex numbers. To return a real number for the square root over the interval $0 \le \theta \le \pi$, $\left|r_0^+\right|$ cannot be less than $2\sqrt{2}$. Over the domain $\pi/2 < \theta \le \pi$, cosine θ is less than zero, and so the discriminant has a positive value. The solutions of these equations for this positive border values are presented in fig. 4. The graphs for r_1^+ and for r_2^+ over the interval $0 \le \theta < \pi/2$ show the shapes of the interfaces when the pressure inside is higher than their surroundings. The plots for r_2^+ over the interval $\pi/2 < \theta \le \pi$ present the surface limited in volume with internal pressure lower than the surroundings.

In the case of higher gauge pressure, the drop has no tangent point with the upper layer, but its shape is almost spherical because the vertical diameter is slightly longer than the horizontal one. These diameters will be equal if $r_0^+ = 55.2$, and so the drop will then be a sphere.

The sample solution for $0 < r_0^+ < 2\sqrt{2}$ is presented in fig. 4b). The intervals in which the real roots of eqs. (29) and (30) can be found are noted in this figure. The results for r_1^+ model the case of a pendant drop that is still connected to the solid phase. We can conclude that the drop will form if the dimensionless gauge-pressure value reaches $2\sqrt{2}$. Although gaps in the plots are observed for r_2^+ in

the domain $0 \le \theta < \pi/2$, this does not indicate a lack of the surface at the gap period in this case; rather, it only means the lack of a state of the equilibrium for the surface with the assumed force system. The surface could thus accelerate, or other forces could be introduced to the analysis. A different situation is observed in the interval $\pi/2 < \theta \le \pi$. Because cosine θ is less than zero here, the discriminant in Eq. (30) is a positive value. Thus, there is no gap for r_2^+ within this interval.

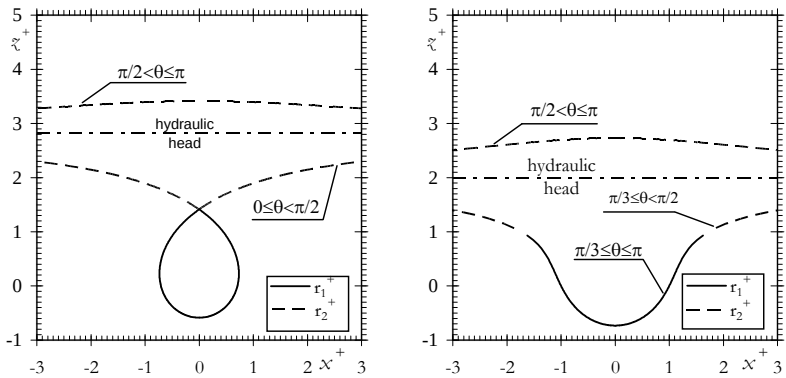

a) b)

Figure 4: The plots of eqs. (29) and (30) for: a) $r_0^+ = 2\sqrt{2}$, b) $r_0^+ = 2$.

The plots for $-2\sqrt{2} < r_0^+ < 0$ are the mirror image of the plots for their modulus values. There occurs the shift between solutions for Eqs. (29) and (30). The second root describes the sessile drop well. Therefore, the plots for $r_0^+ = -2$ are the mirror image of the plots in fig. 4b), where the hydraulic head line is the axis of symmetry.

2.3.2 The flat surface and the lack of surface

The flat surface is the solution of Eq. (19):

$$r_4^+ = \frac{r_o^+}{cos\,\theta} \tag{35}$$

The height of the surface or the depth of the liquid is equal to hydraulic head, r_0^+ . As the right side of Eq. (19) is zero, there is no resultant surface-tension force. However, this does not mean that these forces are not present but rather that the surface-tension forces achieve equilibrium on the plane and only their resultant does not exist.

The most extreme state is the lack of a surface if the hydraulic head equals zero, which is expressed by Eq. (20). This is an important finding of this work. The surface can exist if the surface-tension forces balance each other, but the surface cannot be shaped if there is no pressure difference between two sides of the surface (i.e., between the two bulk phases). This conclusion is confirmed by

the limit of the function calculated by Eq. (32). A liquid–gas surface will not reach the level of the hydraulic head if the surface-tension forces do not achieve equilibrium. These situations are presented in figs. 4, 5.

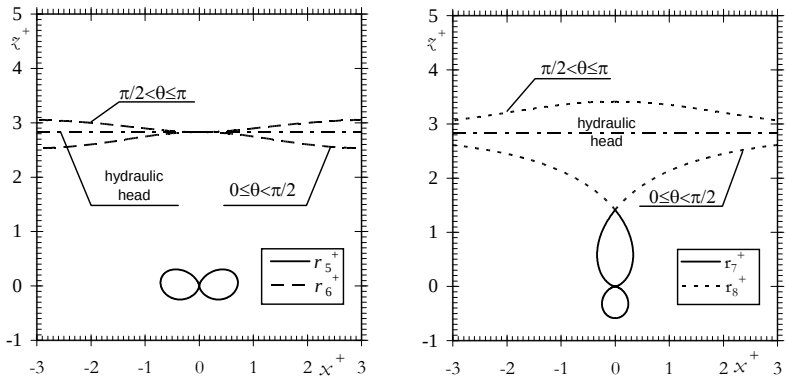

a) b)

Figure 5: a) The graphs of Eqs. (36) and (37) for $r_0^+ = 2\sqrt{2}$, b) The graphs of Eqs. (38) and (39) for $r_0^+ = 2\sqrt{2}$.

2.3.3 The third kind of equilibrium state

This solution has not been connected with any experimental observations so far, and its properties have not been described in detail.

The third equilibrium state, defined by Eq. (20), has two roots:

$$r_5^+ = \frac{r_o^+ - \sqrt{r_o^{+2} - 8\sin^2\theta\cos\theta}}{2\cos\theta} \tag{36}$$

$$r_6^+ = \frac{r_o^+ + \sqrt{r_o^{+2} - 8\sin^2\theta\cos\theta}}{2\cos\theta} \tag{37}$$

The graphs of Eq. (36), plotted in fig. 5a) have shapes similar to a horn torus. The plots of Eq. (37) are tangent to the line of the hydraulic head because sine θ for $\theta = 0$ in Eq. (20) is equal to zero. For that reason, this equation is decomposed into two: (18) and (19) (i.e., the lack of a surface and a flat surface, respectively) in this point. The solution for the plane is plotted in fig. 5a) at $\theta = 0$, which makes this solution different from the cases described in Sections 2.3.1 and 2.3.4. The depth of the lower layer (i.e., the difference between the hydraulic head and the vertical coordinate of the lower surface) is tangent to the upper plate (the solution for $0 \le \theta < \pi/2$), and it increases up to its maximum value (for $\theta = 0.9553$) then approaches the hydraulic-head line. The height of the upper layer (the solution for $\pi/2 < \theta \le \pi$) rises from 0 (for $\theta = \pi$) to its maximum (for $\theta = 2.186$) and then approaches the hydraulic-head line.

2.3.4 The fourth kind of equilibrium state

The fourth equilibrium state, given by Eq. (21), has two roots:

$$r_7^+ = \frac{r_o^+ - \sqrt{r_o^{+2} - 8\cos^3\theta}}{2\cos\theta} \tag{38}$$

$$r_8^+ = \frac{r_o^+ + \sqrt{r_o^{+2} - 8\cos^3\theta}}{2\cos\theta} \tag{39}$$

The seventh root of the general force balance given by Eq. (38) has the shape of a thin drop suspended within another one, cf. fig. 5b). The upper layer (the solution for $\pi/2 < \theta \le \pi$) is largest for $\theta = 0$, and then it decreases and approaches the hydraulic-head line. The lower layer (the solution for $0 \le \theta < \pi/2$ is deepest for $\theta = 0$, and it monotonically approaches the hydraulic-head line.

2.3.5 Surface under uniform pressure

Eq. (14) under uniform pressure takes the form

$$\frac{dr}{d\theta} = r\sqrt{\frac{1}{\left(\frac{pr}{\sigma} - 1\right)^2} - 1}\ , \tag{40}$$

while eq. (13) does not change. There are two solutions of eqs. (13) and (40):

$$p = \frac{2\sigma}{r}\ , \tag{41}$$

$$p = \frac{2\sigma}{r}\cos^2\theta \quad . \tag{42}$$

Formula (41) is well known Young-Laplace equation and describes bubble under uniform pressure that shape is spherical. Although, it is common known result, for the first time this shape was derived from the complete force balance directly. Eq. (42) seems to be only mathematical solution that has not been observed experimentally, which cross-section is two equal bubbles where second bubble is attached under the first one.

3 Summary and discussion

It was proven that it is possible to obtain a complete system of equations for the static equilibrium of a surface under hydrostatic pressure for all fluids that do not sustain shear stresses when at rest. To predict the shape of this surface, a new differential surface with a varying radial distance along the meridian direction was defined. The pressure force and surface-tension forces were balanced on this surface. In the method presented herein, it was possible to balance the surface forces and the surface-tension forces on the control surface. This had not previously been possible, and it represents the major finding of this work. As a result, a system of two equations was obtained: one each in the radial and tangential directions. Their solutions were decomposed into three quadratic and two linear equations with eight roots. Due to the existence of discontinuities, they can describe eleven different situations. The first solution is the Young-

Laplace equation with the interface under hydrostatic pressure. To obtain the results in the traditional way, a second-order differential equation must be solved. In the achieved method, a simple quadratic equation is instead solved, which makes the calculations quite simple. The linear solutions are the flat surface and the lack of a surface. Although they are both trivial, their presence proves the generality of the developed model. Furthermore, two new solutions were obtained that seem to be unconnected with any physical situation.

3.1 Conclusions

We drew the following conclusions for a surface under pressure and surface-tension forces only:

- A surface under uniform pressure is a sphere.
- A plane is formed if the surface-tension forces equilibrate themselves.
- Other shapes occur if a pressure gradient exists and the surface-tension forces equilibrate pressure force.
- A surface cannot exist without a pressure difference across both of its sides.
- The pressure forces are the active forces, whereas the surface-tension forces are the reactive forces, which only act to curve the surface.
- To form a closed interface (e.g., a drop or a bubble), the interior pressure cannot be less than its border value; i.e., the modulus of the hydraulic head must be a factor of $2\sqrt{2}$ or more times higher than the capillary constant.

Acknowledgement

This scientific research was financed from the resources of the National Centre for Science.

References

[1] R.C. Tolman, Consideration of the Gibbs Theory of Surface Tension, The Journal of Chemical Physics, Vol. 16, No. 8, 1948, 758-774.
[2] Thoroddsen S.T., Etoh T.G., Takehara K., High-Speed Imaging of Drops and Bubbles, Annu. Rev. Fluid Mech. 2008, 40:257-85.

This page intentionally left blank

Multifield hybrid approach for bubble to slug flow transition modelling

R. Denefle[1], S. Mimouni[1], J.-P. Caltagirone[2] & S. Vincent[1]
[1]*EDF R&D, France*
[2]*I2M, Université Bordeaux 1, UMR 5295, France*

Abstract

This paper aims to assess a conservative interface locating method based on level-set adapted to two fluid model for two phase flow. The objective of the work is twofold: first to check out the prediction of the model on bubble coalescence cases and then to introduce a first description of the multifield hybrid approach for two-phase flow modelling. The interface locating method is part of a model dedicated to the simulation of large and distorted bubbles. At different liquid viscosities and densities, the model yields reasonable predictions of terminal velocities and shapes for rising bubble experiments. The overall method relies also on an existing building block, consisting of a set of averaged models dedicated to dispersed bubbles, which has already been validated and has given a reasonable agreement with experimental data in cases where the spherical shape assumption is still valid for the dispersed phase. As a consequence, we present the first step toward a new approach consisting of modelling the small bubbles as a dispersed field and simulating the large and distorted ones.

The main outcome is the simulation of bubble coalescence where the distortion of the interface during the coalescence phenomena is followed. The capability to simulate correctly coalescence phenomena is an important point of the modelling of slug flows with interface locating methods.
Keywords: multifield model, surface tension, interface sharpening, bubble rising, coalescence.

1 Introduction

Two-phase flows are featuring many industrial applications such as nuclear power plants, heat exchangers and chemical reactors. Based on the interface structure,

WIT Transactions on Engineering Sciences, Vol 74, © 2012 WIT Press
www.witpress.com, ISSN 1743-3533 (on-line)
doi:10.2495/AFM120241

topological classification commonly separates two-phase flow regimes into three main groups. The first group would be separated flows such as annular, film or stratified flows, the second the dispersed flows such as bubbly, droplet or particle flows, and the last group would be the flows such as bubbly annular, churn turbulent or slug flow. Although these regimes have been experimentally confirmed since a few decades [1], their numerical simulation is still challenging and an universal model remains to be established.

There are several approaches for two-phase flow Eulerian modelling, that may be classified by the successive numerical choices, such as the number of fields, the use of space or time averages, the filtering of some space scales, and the way the interfaces are dealt with. As described by Bestion [2], the capability of these approaches to model the different flow regimes are far from being similar. The RANS approach, which is today of widespread use in CFD for industrial applications presents the drawback of filtering every intermittency scales. This means that besides this approach can deals with all flow regimes, it requires a large amount of work on the closure laws models, currently limited to dispersed and separated flows. The DNS and LES without interface filtering are nowadays too expensive to treat high Reynolds number flows such as churn. According to Bestion, an hybrid method so called Hybrid LES, both filtering and simulating interfaces may be a promising way to describe all flow regimes at a reasonable CPU cost without filtering the two-phase structures as RANS approach does.

We present here the first steps building the Hybrid LES method. We propose to treat statistically the interfaces small enough to be considered as spherical, and to simulate the distorted interfaces. This naturally leads to a filter scale imposed by the flow conditions.

This method is implemented in the multifield code NEPTUNE_CFD. The modeling of dispersed phase flows has already been validated [3] and has given a reasonable agreement with experimental data in cases where the spherical shape assumption is still valid for the dispersed phase. As a consequence, we concentrate here our work on the simulation of large and deformed bubbles. A first step toward the Hybrid LES method is to build a set of equations to model the large interface field. Numerical model and its application to bubble rising are summarized here and can be found in [4] for more details.

After proving the efficiency of the method on well-known bubble rising cases, we will test the model on two-bubble coalescence experimental cases. This will comfort the extension of the interface locating model toward slug flows studying.

2 State of the art for interface treatment and coalescence

Rise of bubbles in viscous liquids/fluids remains a fundamental problem in fluid physics. Despite several theoretical [5], experimental [6] and over these recent years numerical [7, 8] studies, this paradigm is still a topic of major interest.

Most of the current techniques applied to interface flows such as large bubble rising have been developed taking into account two major aspects:

capturing/tracking the interface and stabilizing the flow solver to handle discontinuous fluid properties at the interface.

Several categories of interface locating exist. The first one is Lagrangian grid methods [9] where the background grid is following the interface. The main limitation is that this method cannot track surfaces that break apart or intersect. The second category is the front tracking method [10]. The motion equation for the flow field is solved on a fixed grid and the interface position is tracked explicitly by markers distributed evenly on the interface. Difficulty generally comes from the repartition of the markers which should ideally be kept equidistant, especially for coalescence of interfaces applications. The third category of these methods consists in capturing the interface using various volume functions defined on the fixed grid used to solve the governing equations of the flow. The volume of fluid [11] method and level-set [12] approaches are parts of this group. VOF methods are conservative, but interface properties such as normal and curvature are difficult to calculate accurately. Level-set methods automatically deal with topological changes but are not conservative. Several techniques have been developed to ensure volume conservation and improve the locating method, such as a combination of Level-set and VOF method [13], or the augmented Lagrangian method coupled to VOF techniques [14].

Olsson and Kreiss [15] introduced a level set method with an artificial compression step performed after the advection of the level set function to ensure that the thickness of the transition layer is preserved.

In our work, the Eulerian approach is use. This approach of the two-fluid model allows the direct use of the volume fraction as an interface function. Thus, the equivalent to the level-set function is self-transported by the resolution of the momentum balance equation. To keep a good location of the interface over time, the same artificial compression step as Olsson's is used.

Concerning coalescence, only few experiments present results on two-bubble coalescence such as Brereton and Korotney's experiment [16]. Numerical works on this phenomena usually follow interface treatment methods and can be found with marker approach, Singh and Shyy [17], and VOF approach, van Sint Annaland *et al.* [18].

3 Mathematical formulation and numerical method

3.1 Governing equations

The two-fluid model is based on Eulerian multifield balance equations. Further information can be found in Ishii and Hibiki [19]. The balance equations for isothermal two-fluid model can be written as mass and momentum balances:

$$\partial_t(\alpha_k\rho_k) + \partial_{x_i}(\alpha_k\rho_k U_{k,i}) = \Gamma_k \quad \text{with} \sum_k \Gamma_k = 0 \tag{1}$$

$$\begin{aligned}\partial_t(\alpha_k\rho_k U_{k,i}) + \partial_{x_j}(\alpha_k\rho_k U_{k,i}U_{k,j}) = \quad & \partial_{x_j}(\alpha_k\tau_{k,ij}) - \alpha_k\partial_{x_i}(P) \\ & +\alpha_k\rho_k g_i + I_{k,i}\end{aligned} \tag{2}$$

where ρ_k , U_k, α_k, Γ_k and $\tau_{k,ij}$, P and $I_{k,i}$ denote respectively the density, the mean velocity, the volumetric fraction, the mass transfer and the total stress tensor including laminar and turbulent contribution, the mean pressure and the interfacial momentum exchange between phases. The interfacial momentum exchange is constituted here by two interfacial forces : surface tension force and drag force. This later appears in momentum balance equations due to averaging. Its local sum over phases is equal to zero and depends on the relative velocity between the phases.

$$\overrightarrow{F}_{drag,1} = \frac{\alpha_1\alpha_2(\overrightarrow{v_2} - \overrightarrow{v_1})(\alpha_1\rho_1 + \alpha_2\rho_2)}{\tau} \tag{3}$$

As we consider in the paper a local separated flow in the two fluid model, the role of the drag force is to enforce a no slip condition and so equality of the phase velocities at the bubble interface. The closure law, eqn. (3), is applied with a very short relaxation time τ to achieve large interface drag ($\tau = \Delta t/100$).

3.2 Surface tension

Large bubbles are no longer considered as a dispersed, but as a continuous field, therefore the surface tension, eqn. (4), has to be taken into account in the model. From an Eulerian point of view, a surface force has to be implemented in volume:

$$\overrightarrow{F}_{sta} = \sigma\kappa\overrightarrow{n} \tag{4}$$

where σ, κ and $\overrightarrow{n}$ denote respectively the surface tension, the curvature and the normal vector. The curvature κ is defined as the divergence of the unit normal vector at the interface. A color function c locating the interface, such as a level set function, is a descriptor of this normal vector. The unit normal vector and the curvature can be calculated with the color function, obtain by diffusion of .the volume fraction. Here it becomes important that the thickness of the interface is kept constant so that the color function gives a good approximation of the local curvature. The Continuum Surface Force (CSF) method described by Brackbill *et al.* [20] allows the reformulation of the surface tension into an equivalent volume force, eqn. (5), that can be added to the momentum balance equation. In the two-fluid model, this force is split between the two phases occupying the cell, since two momentum equations are solved. The average model is here the volume one.

$$\overrightarrow{F}^k_{st} = \alpha_k\sigma\left[\nabla.\left(\frac{\nabla c}{\|\nabla c\|}\right)\right]\nabla c dV \tag{5}$$

3.3 Interface sharpening

As already discussed in the previous section, the curvature calculation requires to pay some attention to the interface thickness. Olsson and Kreiss [15] coupled an

artificial compression method to a level set method to obtain volume conservation. The interface sharpening method consists in resolving the following eqn. (6) on a non physical time step between two physical steps to ensure the interface thickness to be kept constant.

$$\partial_\tau(\alpha_k) + \nabla\left(\alpha_k(1-\alpha_k)\overrightarrow{n}\right) = \varepsilon\Delta\alpha_k \tag{6}$$

The parameter ε controls the final interface width at convergence and is here chosen so that the interface thickness is 2 cells. The non-physical time $\Delta\tau$ is chosen to ensure CFL and Fourier numbers under 0.5 and to minimize the number of iteration leading to a steady interface width: $\varepsilon = \Delta x/2$ and $\Delta\tau = \Delta x/32$.

4 Application to bubble rising: Rosant's experiment

4.1 Experiment description

The capturing interface process described in the previous section is validated against the experiments of Raymond and Rosant [6]. Bubbles are released in still water at time $t = 0\ s$. The reference pressure is the atmospheric pressure $1013\ hPa$. The fluid viscosity and density (blend of water and glycerol) are given in table 1. The final bubble velocity and shape (ratio between height h and width w of the bubble) are studied as functions of the bubble initial diameter. An axisymmetric geometry is used, reproducing the experiment situation of bubbles rising in a pipe. The air density and viscosity are respectively $1.29\ kg.m^{-3}$ and $1.84 * 10^{-5}\ Pa.s$. A Dirichlet's condition on the pressure field is imposed at the top boundary.

4.2 Sensitivity analysis, size of the computational domain

The experiments were conducted in a rectangular Plexiglas tank of $0.3 \times 0.2\ m^2$ inside cross section and $0.5\ m$ height. Wall confinement effects on the bubbles can be considered as negligible. As modelling such a huge domain will cost a lot of calculation time, the aim of this analysis is to find the smallest possible computational domain in which walls have negligible effect on the terminal velocity and shape of the simulated bubbles. Radius from 2 to 6 times the bubble

Table 1: Fluid properties for the Raymond and Rosant's experiment [6].

Series	Viscosity $[Pa.s]$	Density $[kg/m^3]$	Surface tension $[N/m]$
S1	0.687	1250	0.063
S3	0.242	1230	0.063
S5	0.0733	1205	0.064
S6	0.0422	1190	0.064

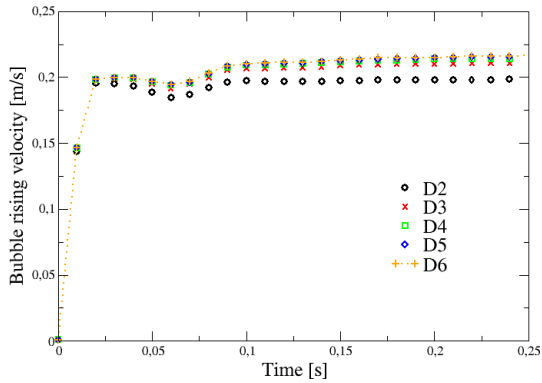

Figure 1: Effect of computational domain size on the bubble shape for an initially 8 mm diameter spherical bubble in the S5 experiment (see table 1).

diameter were tested for the simulation of the experimental case S5 (see table 1) with an 8 mm diameter bubble. The fig. 1 presents the terminal bubble shape for the tested computational domain size. The terminal velocity can be considered as independent from the domain size D when $D \leq 4\ D_b$.

4.3 Sensitivity to the mesh refinement

A grid-independent test was carried out on the axisymmetric rise of a single bubble in a liquid on six different meshes. According to the previous sensitivity analysis on the domain size, the domain is chosen to have a four bubble diameter radius, and twelve bubble diameter height. The six grids are M2 ($h = D_{bubble}/\Delta x = 15$), M3 ($h = 20$), M4 ($h = 25$), M5 ($h = 30$), M6 ($h = 35$) and M7 ($h = 40$).

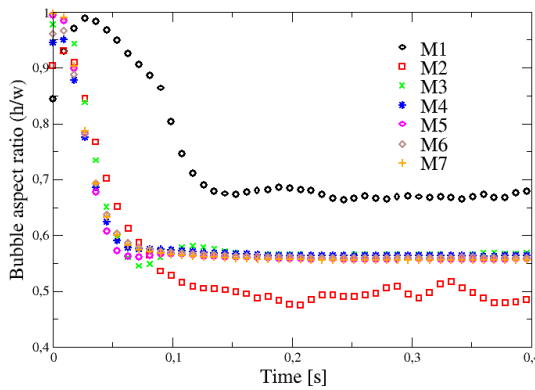

Figure 2: Effect of the mesh refinement on the bubble rising velocity for an initially 8 mm diameter spherical bubble in the S3 experiment. D is the domain radius given here in number of bubble diameter.

Fig. 2 shows that the mesh M5 provides a nearly grid-independent solution. This grid will be used in all other runs.

4.4 Model validation with experiments

Fig. 3 and 4 present the evolution of terminal velocities and shapes versus the initial bubble diameter for the 4 experiments S1, S3, S5 and S6. The predicted velocities are found to be in a good agreement with the experimental data, the deviation being lower than 10%. Concerning the bubble aspect ratio, the deviation is lower than 10% for experiment S1 and S3, lower than 23% for experiment S5 and lower than 30% for S6. For the most distorted cases (experiment case S6 and bubble diameters greater than $6\ mm$), part of the gap between measures and numerical prediction could be explained by the difficulty to reproduce the exact initial conditions. In the simulation, the bubble is initiated as a still sphere whereas in the experiment the bubble may not be spherical at time $t = 0\ s$, especially for experiments where the bubble is large and the fluid less viscous.

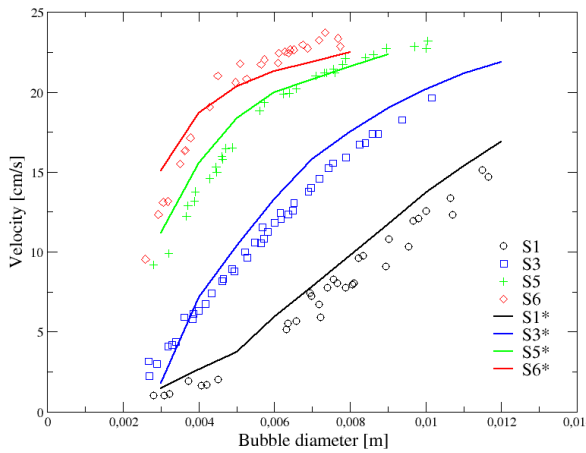

Figure 3: Predicted bubble velocities (solid lines) compared to experimental data (symbols) versus the equivalent diameter for various liquid properties.

5 Bubble coalescence

5.1 Experiment description

The predictions of the model prove to be in reasonable agreement with the experimental observations for bubble rising cases. For the simulation of slug flows, we need to be able to describe large bubble coalescence phenomena. The experiments of Brereton and Korotney [16] provide a good qualitative description

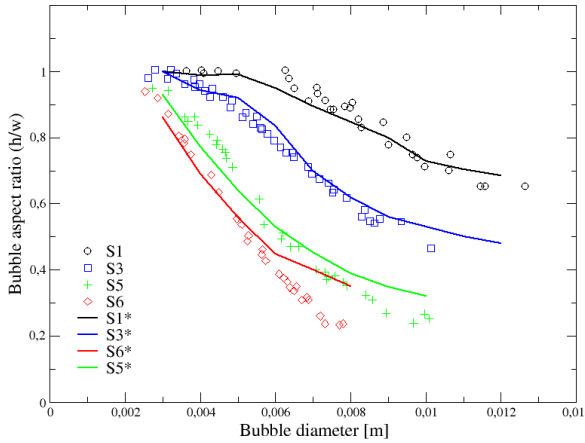

Figure 4: Predicted bubble aspect ratio (solid lines) compared to experimental data (symbols) versus the equivalent diameter for various liquid properties (see table 1).

of the coalescence of two rising bubbles. Four cases are calculated: two cases of coaxial coalescence and two cases of oblique coalescence, each type of coalescence being treated in two dynamic conditions, described by Reynolds, Morton and Eötvos numbers: case (a), $(Re = 43, Mo = 2.10^{-4}, E\ddot{o} = 16)$ and case (b), $(Re = 1, Mo = 30, E\ddot{o} = 16)$. The two initial bubbles have the same volume.

5.2 Results

Numerical results are presented in figs. 5 and 6. The computational domain is a rectangular 3D box of size $0.04 \times 0.04 \times 0.08\ m^3$, the origin is placed at the center of the bottom face. The initial bubble have a radius of $5\ mm$ and are placed at positions {(0,0,0.025) (0,0.08,0.125)} and {(0,0,0.025) (0,0,0.125)} respectively for the oblique and the coaxial coalescence experiments. Regarding the discretization, the space scale is $\Delta x = 5.10^{-3}\ m$ for the case (a) and $\Delta x = 2.5.10^{-3}\ m$ for the case (b), the fact that the most viscous case need the finest grid is due to the difficulty to reproduce the sharp tail of the second bubble observed on fig. 6 at 0.09 and $0.12\ s$. The time scale of the coalescence is well predicted by the numerical simulations for all cases, as the time between each experimental photograph is approximatively $30\ ms$. Despite the difficulty of the phenomena, the shapes of both leading and trailing bubbles are in excellent agreement with the experimental observations.

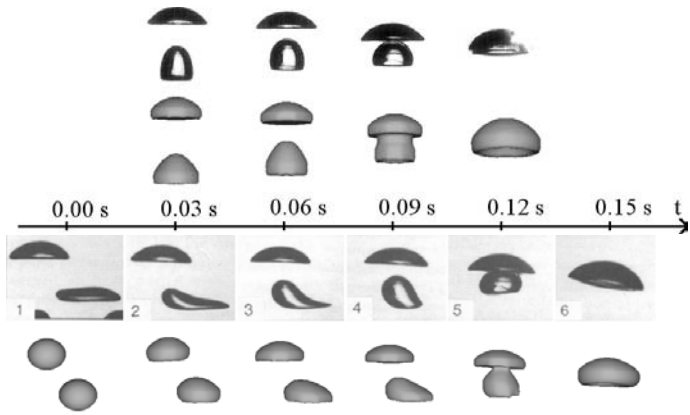

Figure 5: Comparison between the experimental observations from Brereton and Korotney [16] and numerical predictions for coaxial and oblique coalescence of two bubbles: $Re = 43, Mo = 2.10^{-4}, E\ddot{o} = 16$.

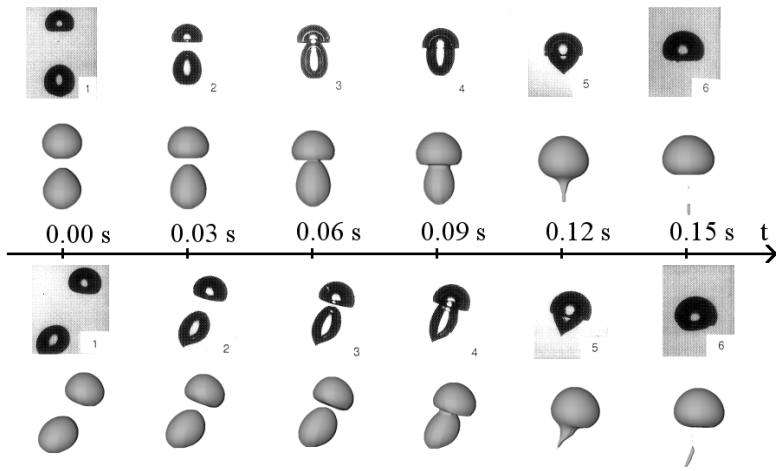

Figure 6: Comparison between the experimental observations from Brereton and Korotney [16] and numerical predictions for coaxial and oblique coalescence of two bubbles: $Re = 1, Mo = 30, E\ddot{o} = 16$.

6 Conclusion

The dynamics of a deformed bubble has been studied using a two-fluid model adapted to cases with located interfaces. Experimental validations have been carried out. Quantitatively for bubble rising, the predicted terminal shape and velocity of bubbles are in reasonable agreement with the experiments of Raymond and Rosant [6]. Qualitatively for two-bubble coalescence, the coalescence time

scale and bubble behavior are found to be quite similar to Brereton and Korotney's experiments [16]. The model dedicated to large distorted bubbles was successfully applied to coalescence cases in different liquid conditions. This is comforting us in the way of an hybrid three field model to address regime transitions such as bubbly to slug flow.

Acknowledgements

This work has been achieved in the framework of the NEPTUNE project, financially supported by CEA (Commissariat à l'Energie Atomique et aux Energies Alternatives), EDF, IRSN (Institut de Radioprotection et de Sûreté Nucléaire) and AREVA-NP, in collaboration with I2M laboratory (Bordeaux, France).

References

[1] Weisman, J. and Kang, S.Y., Flow pattern transitions in vertical and upwardly inclined lines. *International Journal of Multiphase Flow*, **7**, pp. 271–291, 1981.
[2] Bestion, D., Applicability of two-phase CFD to nuclear reactor thermalhydraulics and elaboration of best practice guidelines. *Nuclear Engineering and Design*, *In Press*, p. Corrected proof, 2011.
[3] Mimouni, S., Archambeau, F., Boucker, M., Laviéville, J. and Morel, C., A second order turbulence model based on a reynolds stress approach for two-phase boiling flow and application to fuel assembly analysis. *Nuclear Engineering and Design*, **240**, pp. 2225–2232, 2009.
[4] Denefle, R., Mimouni, S., Caltagirone, J.P. and Vincent, S., Multifield hybrid LES approach for two-phase flow modelling - part 1: Adiabatic bubble rising. *Work in progress*.
[5] Clift, R., Grace, J.R. and Weber, M.E., *Bubbles, drops, and particles*. Academic Press, New York, 1978.
[6] Raymond, F. and Rosant, J.M., A numerical and experimental study of the terminal velocity and shape of bubbles in viscous liquids. *Chemical Engineering Science*, **55**, pp. 943–955, 2000.
[7] Hua, J. and Lou, J., Numerical simulation of bubble rising in viscous liquid. *Journal of Computational Physics*, **222**, pp. 769–795, 2007.
[8] Koebe, M., Bothe, D. and Warnecke, H.J., Direct simulation of air bubbles in water/glycerol mixtures : shapes and velocity fields. *Proceedings of FEDSM'03: 4th ASME_JSME Joint Fluids Engineering Conference*, Honolulu, Hawaii, USA, 2003.
[9] Hyman, J.M., Numerical methods for tracking interfaces. *Physica D*, **12**, pp. 396–407, 1984.

[10] Unverdi, S.O. and Tryggvason, G., A front-tracking method for viscous, incompressible, multi-fluid flows. *Journal of Computational Physics*, **100**, pp. 25–37, 1992.
[11] Hirt, C.W. and Nichols, B.D., Volume of fluid (VOF) method for the dynamics of free boundaries. *Journal of Computational Physics*, **39**, pp. 201–225, 1981.
[12] Osher, S. and Sethian, J.A., Fronts propagating with curvature-dependent speed: Algorithms based on Hamilton-Jacobi formulations. *Journal of Computational Physics*, **79**, pp. 12–49, 1988.
[13] Sussman, M. and Puckett, E., A coupled level set and volume-of-fluid method for computing 3D and axisymmetric incompressible two-phase flows. *Journal of Computational Physics*, **162**, pp. 301–337, 2000.
[14] Vincent, S., Caltagirone, J.P., Lubin, P. and Randrianarivelo, T.N., An adaptive augmented lagrangian method for three-dimensional multimaterial flows. *Computers and Fluids*, **33**, pp. 1273–1289, 2004.
[15] Olsson, E. and Kreiss, G., A conservative level set method for two phase flow. *Journal of Computational Physics*, **210**, pp. 225–246, 2005.
[16] Brereton, G. and Korotney, D., Coaxial and oblique coalescence of two rising bubbles. *Proceedings of AMD-Vol. 119: The ASME Applied Mechanics Conference*, Columbus, Ohio, USA, 1991.
[17] Singh, R. and Shyy, W., Three-dimensional adaptive grid computation with conservative, marker-based tracking for interfacial fluid dynamics. *44th Aerospace Science Meeting*, Reno MV, USA, 2006.
[18] van Sint Annaland, M., Deen, N. and Kuipers, J., Numerical simulation of gas bubbles behaviour using a three-dimensional volume of fluid method. *Chemical Engineering Science*, **60**, pp. 2999–3011, 2005.
[19] Ishii, M. and Hibiki, T., *Thermo-fluid Dynamics of Two Phase Flow*. Springer-Verlag, 2006.
[20] Brackbill, J., Kothe, D. and Zemach, C., A continuum method for modeling surface tension. *Journal of Computational Physics*, **100**, pp. 335–354, 1992.

This page intentionally left blank

Development of a computationally efficient bubble column simulation approach by way of statistical bubble micro-flow modelling

W. Coetzee[1], R. L. J. Coetzer[2] & R. Rawatlal[1]
[1]*Department of Chemical Engineering, University of Cape Town, South Africa*
[2]*Sasol Technology Research and Development, South Africa*

Abstract

Bubble columns are extensively used in the chemical process industry, however their hydrodynamics are computationally expensive to simulate, severely restricting design and optimisation studies. A novel discrete-phase bubble column modelling approach is proposed where the flow-field in the immediate vicinity of individual bubbles is predicted from the Reynolds number *via* an algebraic bubble flow model, i.e. the Bubble Cell Model (BCM). This contrasts to the traditional Euler–Lagrange approach, where the flow structure is resolved at a larger scale using the Navier–Stokes equations. The construction of the BCM involves generating the micro-flow fields through solving the analogous case of the flow over a fixed sphere with the Navier–Stokes equations at 22 equally spaced Reynolds numbers in the operating range of $Re \leq 270$. The model construction then occurs in two stages, i.e. stage one: the fitting of each velocity vector field at the discrete Reynolds numbers, and stage two: the cross correlation of the stage one model parameters with respect to Reynolds number. For stage one, a hybrid between analytical and statistical models was found to provide accurate fits, resulting in R^2 values ranging from 0.9968 to 0.9999. The Reynolds dependence of the parameters was found to be described through simple polynomial and exponential models in the second stage construction, producing a model which generates the velocity vector field around a bubble for a given Reynolds number as the result of a single algebraic evaluation. The integration of the BCM with a Eularian macro fluid model has also been investigated for a single bubble pilot test case.

Keywords: bubble flow, Euler–Lagrange, cell model.

WIT Transactions on Engineering Sciences, Vol 74, © 2012 WIT Press
www.witpress.com, ISSN 1743-3533 (on-line)
doi:10.2495/AFM120251

1 Introduction

Bubble column simulation requires the resolution of complex hydrodynamic interactions between the gas and liquid phases. This can be modelled with the Navier–Stokes equations, however, the solving of the Navier–Stokes equations at bubble scale, e.g. Volume-Of-Fluid method, is impractical with regards to computational expense when considering any more than a few bubbles [1]. The momentum source generated by the bubbles on the continuum fluid phase is subsequently modelled through experimentally correlated force models i.e. drag, lift and added mass, which is used in coupling the gas phase to the continuum [2]. The gas phase can then either be tracked as individual bubbles, i.e. the Euler–Lagrange approach, or approximated as a continuum i.e. the Euler-Euler approach. These approaches enable larger grid sizes and make the simulation of entire bubble columns possible. However, the bubble scale flow detail is severely reduced and computational efficiency remains a problem [3]. Furthermore, the question of which physical effects to include in the coupling model, is still under debate [4].

It follows that the choice of bubble column simulation approach depends on the level of flow detail required and the size of the geometry, as illustrated in Figure 1. The computational expense required for large sized problems can subsequently inhibit the choice of smaller scale models.

In an attempt to address these issues, relating to multiphase flow simulation in general, it has been proposed by the authors to substitute the flow-fields in the direct vicinity of the bubbles in a Euler–Lagrangian framework, with an algebraic micro-flow model correlated to the Navier–Stokes solution for the appropriate flow situations. The algebraic flow model will be referred to as the Bubble Cell Model (BCM). The computationally expensive regions around individual bubbles are therefore accounted with the BCM, which can be rapidly evaluated, in contrast to the computationally expensive partial differential Navier–Stokes equations. In addition, the BCM can be used to determine the force acting on the bubble

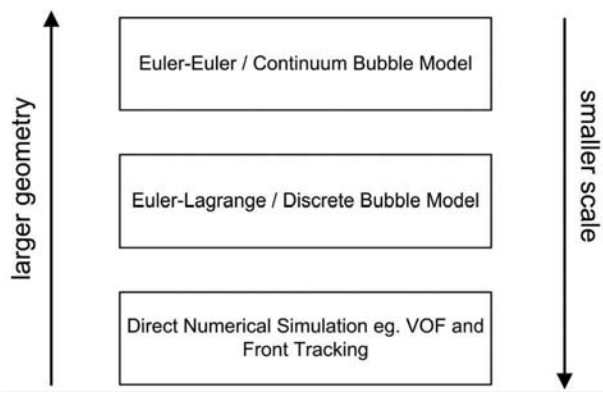

Figure 1: CFD bubble column simulation framework.

in the equation of motion and allows the bubble scale flow information to be approximated.

2 Bubble cell model development

The aim of the BCM is to provide a model of the velocity vector field, $\mathbf{u}^{\mathbf{M}}$, with respect to spatial position, $\mathbf{x}$, around a bubble as a function of Reynolds number, $Re = \frac{\rho D u_{rel}}{\mu}$ (where ρ, D, u_{rel} and μ represent the fluid density, bubble diameter, bubble relative velocity and fluid viscosity respectively). The solution to the Navier–Stokes equations for the flow over a fixed sphere with appropriate boundary conditions (as discussed in Section 2.1), is regarded as the "true velocity field", $\mathbf{u}^{\mathbf{true}}$, with respect to the construction of the BCM. To approximate $\mathbf{u}^{\mathbf{true}}$ as a function of Reynolds number, a two stage fitting strategy has been devised. Stage one involves fitting the velocity vector fields at discrete Reynolds numbers, whilst stage two aims to cross correlate the parameters of the stage one model w.r.t. Reynolds number. This strategy is schematically presented in Figure 2.

2.1 Flow over fixed sphere: data generation

To set up the case, the boundary condition at the bubble surface and the bubble shape is considered:

- If the liquid is pure enough, it is possible for it to slip along the surface of the bubbles (free slip condition), in contrast to the flow past rigid bodies, where slip will not occur (no-slip condition). This very often makes the flow unseparated in circumstances where the flow around a solid body of similar shape would be separated (i.e. the fluid flow becomes detached from the surface of the object at higher Reynolds numbers) or even turbulent [5]. Consequently, the boundary condition for a contaminant free system,

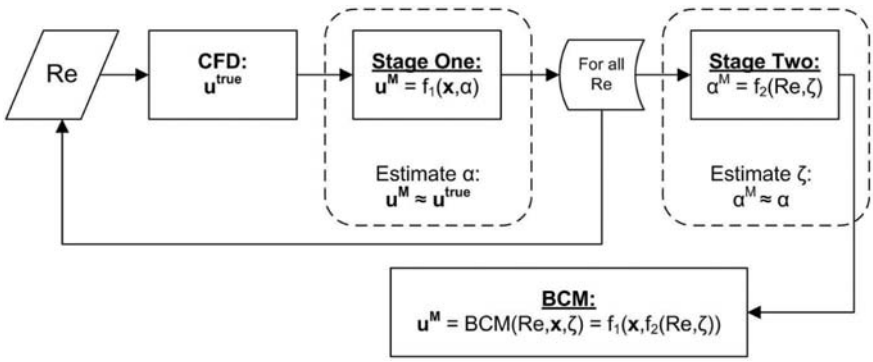

Figure 2: BCM two stage fitting strategy, where f_1, α, f_2 and ζ represent the overall stage one model, stage one parameters, stage two model and stage two parameters respectively.

imposed at the bubble surface on the tangential component of the liquid velocity, is a zero-shear-stress one rather than a no-slip one [6].

- The shape of the bubble directly influences the local hydrodynamics and can be transient during bubble motion. According to the research of Tomiyama *et al.* [7], bubble motion, shape and velocity are remarkably sensitive to initial shape deformation. The researchers subsequently proposed a steady state drag model which is dependent on bubble shape through the dimensionless Eötvös number ($E\ddot{o} = \frac{\Delta\rho g D^2}{\sigma}$, with $\Delta\rho$, g and σ representing the density difference, gravity vector and surface tension respectively). It has become apparent that bubble shape is an important parameter which adds new degrees of freedom to an already complex problem.

For the development of the BCM approach, we restrict the focus onto spherical bubbles in a contaminant free system. It follows from experimental data [8], that the spherical assumption is valid for $Re \leq 270$ for an air-water system, whilst the clean system will be accounted for with an zero-shear-stress boundary condition on the bubble surface. Furthermore, to allow for faster development of the concept, the work will be carried out in two dimensions. It should be noted that the approach could be extended to different shaped bubbles occurring in heterogeneous bubble columns through parametrization of the $E\ddot{o}$ number, higher Reynolds numbers and three dimensions.

The Navier–Stokes equations are solved with the Finite-Volume method, using the SIMPLE pressure-velocity coupling scheme [9] and 2nd order UPWIND spatial discretization in the Fluent 12 solver (FLUENT INC, USA). The mesh is created according to the geometry depicted in Figure 3, and its resolution optimized according to the convergence of the drag force on the bubble surface.

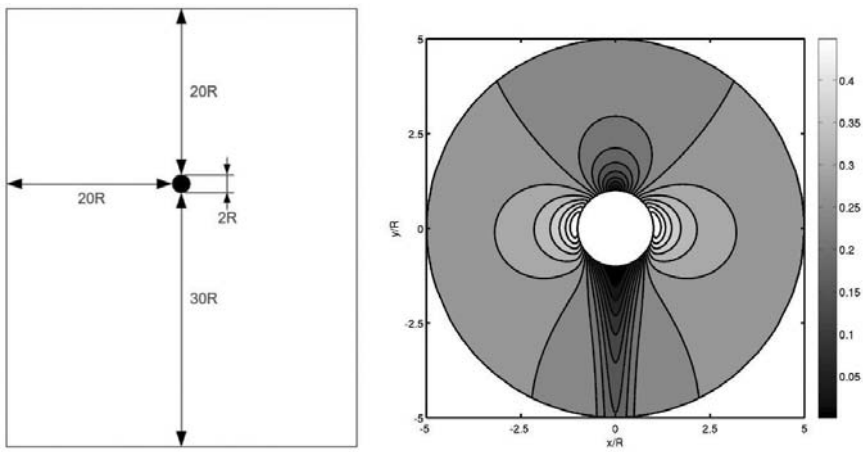

Figure 3: Case geometry and resulting velocity magnitude contours following CFD simulation. The geometry is set up with respect to the radius (R) of the bubble and the ratios chosen to allow flow dynamics to sufficiently develop across the domain.

This resulted in 164,983 data points in the BCM region, which was chosen as 5 times the bubble radius. The drag coefficients for the Reynolds numbers evaluated, corresponded to the experimental data for bubbles in pure systems [10].

2.2 Stage one model

2.2.1 Analytical solutions

Analytical solutions provide a good starting point to the development of the BCM, since they capture useful features of the flow structure. Solutions are possible through simplifying assumptions, such as either creeping flow (i.e. zero advective terms), or potential flow (i.e. zero viscous terms), making analytical evaluation of the steady state, incompressible Navier–Stokes equations (eqn. (1) and (2)) possible. Here $\mathbf{u}$, p and $\mathbf{S}$ refer to the fluid velocity vector, fluid pressure and the body force vector respectively.

$$\nabla \cdot \mathbf{u} = 0 \tag{1}$$

$$\underbrace{\rho(\mathbf{u} \cdot \nabla \mathbf{u})}_{advective\ terms} = -\nabla p + \underbrace{\mu \nabla^2 \mathbf{u}}_{viscous\ terms} + \underbrace{\mathbf{S}}_{body\ forces} \tag{2}$$

The creeping flow solution (valid at $Re \ll 1$) was derived by Stokes [11], by assuming axisymmetric flow and writing the Navier–Stokes equations in terms of the Stokes stream function ψ (the two velocity components are expressed as derivatives of ψ such that continuity is automatically satisfied) in spherical coordinates (where $\mathbf{r}$ and $\boldsymbol{\theta}$ correspond to the radial and angular spatial components, centred around the centre of volume of the bubble), simplifying the problem considerably. Following the solution strategy by Slattery [12], the stream function is proposed as a fourth order polynomial whose coefficients are obtained through the substitution of the boundary conditions. Applying the zero-shear-stress boundary conditions, eqn. (3)–(5), the stream function is obtained, which upon differentiation with respect to $\boldsymbol{\theta}$ and $\mathbf{r}$ leads to radial and angular velocities, $\mathbf{u_r}$ and $\mathbf{u}_\theta$, which are subscripted for the creeping flow solution as $\mathbf{u_{r,CF}}$ and $\mathbf{u}_{\theta,\mathbf{CF}}$ in eqn. (6) and (7). The free stream velocity here, u_∞, corresponds to the relative bubble velocity u_{rel}.

$$\mathbf{u_r}_{|\mathbf{r}\to\infty} = u_\infty \cos(\theta) \tag{3}$$

$$\mathbf{u_r}_{|\mathbf{r}=\mathbf{R}} = 0 \tag{4}$$

$$\frac{d\mathbf{u}_{\theta|\mathbf{r}=\mathbf{R}}}{d\mathbf{r}} = 0 \tag{5}$$

$$\mathbf{u_{r,CF}}(r,\theta) = u_\infty \left[1 - \frac{3}{4}\left(\frac{R}{\mathbf{r}}\right) - \frac{1}{4}\left(\frac{R}{\mathbf{r}}\right)^3\right] \cos(\boldsymbol{\theta}) \tag{6}$$

$$\mathbf{u}_{\theta,\mathbf{CF}}(r,\theta) = u_\infty \left[1 - \frac{3}{8}\left(\frac{R}{\mathbf{r}}\right) + \frac{1}{8}\left(\frac{R}{\mathbf{r}}\right)^3\right] \sin(\boldsymbol{\theta}) \tag{7}$$

Although zero viscosity fluids do not actually exist, the assumption (valid at $Re \rightarrow \infty$) provides a reasonably good description of the velocity profile, except near the body and beyond the line of flow separation [13]. The potential flow solution is derived by defining velocity potential Φ, such that $\mathbf{u} = -\nabla\Phi$, the zero-shear-stress boundary condition, is automatically satisfied by the inviscid assumption. For incompressible potential flows, Φ satisfies Laplace's equation which can be solved with the method of separation of variables [12], and upon differentiation yields the potential flow velocity fields, $\mathbf{u_{r,PF}}$ and $\mathbf{u_{\theta,PF}}$, as presented in eqn. (8) and (9).

$$\mathbf{u_{r,PF}}(r,\theta) = u_\infty \left[-1 + \left(\frac{R}{\mathbf{r}}\right)^3 \right] \cos(\boldsymbol{\theta}) \tag{8}$$

$$\mathbf{u_{\theta,PF}}(r,\theta) = u_\infty \left[1 + \frac{1}{2}\left(\frac{R}{\mathbf{r}}\right)^3 \right] \sin(\boldsymbol{\theta}) \tag{9}$$

The solutions for both simplifying assumptions are simple algebraic expressions which allow for rapid numerical function evaluation. However, neither of these solutions are able to capture the flow separation and wake features which are artefacts arising when $Re > 1$, resulting in poor flow prediction at the rear of the bubble and incorrect hydrodynamic force calculation which limits the practical applicability of these solutions.

2.2.2 Statistical modelling

The need for statistical modelling arises from an attempt to bridge the gap between the two extrema cases of the analytical solutions i.e. $Re = 0$ and $Re = \infty$, by accounting for features occurring in the non-idealized flow regimes. Since the aim of the BCM is rapid functional evaluation, a semi-analytical model, expressed through algebraic expressions, would be justified.

The two analytical models, associated with creeping and potential flow, is to be combined to take account of a significant portion of the flow structure. A linear combination of the two solutions is used, i.e. eqn. (10) and (11), where $\alpha_{1,1}$ to $\alpha_{2,2}$ represents the weighting coefficients obtained through linear least squares with respect to $\mathbf{u^{true}}$. For this purpose, only data from the region $\pi/2 \leq \theta \leq 3\pi/2$ is considered, since this region is best represented by the two solutions, whereas the wake feature at the rear of the bubble negatively impacts the least squares fit by attempting to take account of a structure the model is not capable of representing.

$$\mathbf{u^M_{r,A}} = \alpha_{1,1}\mathbf{u_{r,CF}} + \alpha_{1,2}\mathbf{u_{r,PF}} \tag{10}$$

$$\mathbf{u^M_{\theta,A}} = \alpha_{2,1}\mathbf{u_{\theta,CF}} + \alpha_{2,2}\mathbf{u_{\theta,PF}} \tag{11}$$

The residuals to these solutions, i.e. eqn. (12) and (13), require statistical modelling to be accounted for. This has been achieved by considering each of the residual velocity surfaces, $\mathbf{u_{r,res}}$ and $\mathbf{u_{\theta,res}}$ across the Reynolds operating range, and identifying regions following simple functional forms. In addition, the

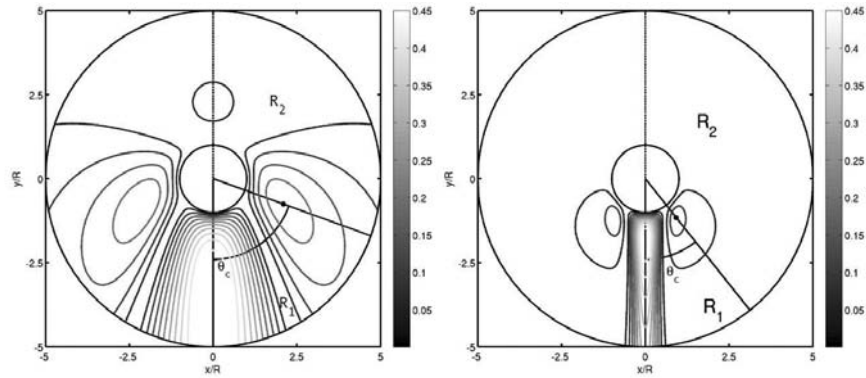

Figure 4: Contours of $|\mathbf{u_{r,res}}|/u_\infty$, illustrating the change of θ_c w.r.t. Reynolds number . R_1 and R_2 denote region 1 and region 2.

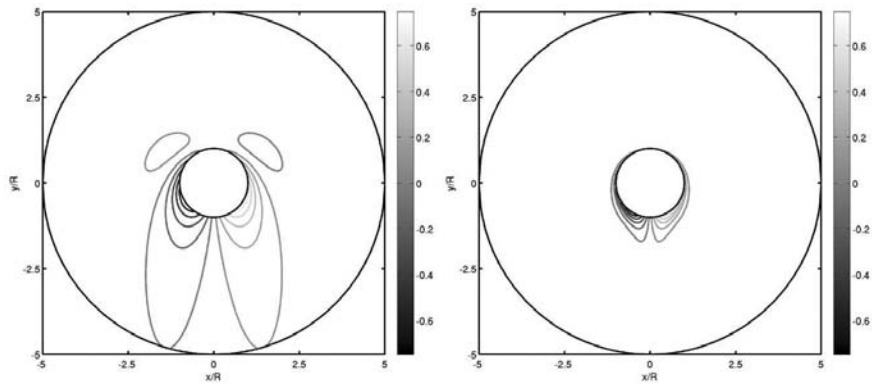

Figure 5: Contours of $\mathbf{u}_{\theta,\mathbf{res}}/u_\infty$ at two different Reynolds numbers.

symmetry across the $x = 0$ line, was also used to simplify the problem.

$$\mathbf{u_{r,res}} = \mathbf{u_r^{true}} - \mathbf{u_{r,A}^M} \tag{12}$$

$$\mathbf{u}_{\theta,\mathbf{res}} = \mathbf{u}_\theta^{\mathbf{true}} - \mathbf{u}_{\theta,\mathbf{A}}^{\mathbf{M}} \tag{13}$$

The residual of to the radial velocity, was largely focussed in the bubble wake region. This was captured by identifying a critical angle, θ_c, corresponding to the maximum of the local peak at the rear of the bubble, which divides the domain into two regions, as illustrated in Figure 4. These regions were subsequently captured through a series of exponential models. The final model for $\mathbf{u_r^M}$ had a total of 17 parameters ($\alpha_{1,i}$) and resulted in R^2 values between 0.9968 - 0.9999. The residual of the angular velocity was a maximum at the bubble surface, which decayed into the radial direction. This surface was approximated through finding the appropriate model to represent $\mathbf{u}_{\theta,\mathbf{res}}|_{\mathbf{r=R}}$ and fitting the exponential decay of this model

Table 1: Surface fit results of $\mathbf{u}_{\mathbf{r}}^{\mathbf{M}}$ and $\mathbf{u}_{\theta}^{\mathbf{M}}$ with varying Reynolds number.

Re	$\mathbf{u}_{\mathbf{r}}^{\mathbf{M}}$: MSE	$\mathbf{u}_{\mathbf{r}}^{\mathbf{M}}$: R^2	$\mathbf{u}_{\theta}^{\mathbf{M}}$: MSE:	$\mathbf{u}_{\theta}^{\mathbf{M}}$: R^2
0.1	3.1015e-12	0.9968	8.1015e-12	0.9974
15	7.2915e-08	0.9989	2.9301e-07	0.9978
75	3.9737e-07	0.9998	1.7457e-06	0.9995
135	7.0539e-07	0.9999	3.9877e-06	0.9997
195	1.2357e-06	0.9999	6.9260e-06	0.9997
270	2.2273e-06	0.9999	1.1348e-05	0.9998

radially. This resulted in a reasonable approximation of the data with $R^2 = 0.9974$ to 0.9998, with 11 parameters ($\alpha_{2,i}$). (Please note that due to space restrictions it is not possible to expand on the residual models i.e. $\mathbf{u}_{\mathbf{r},\mathbf{res}}^{\mathbf{M}}$ and $\mathbf{u}_{\theta,\mathbf{res}}^{\mathbf{M}}$. They will however be discussed in more detail in an upcoming paper by the authors.)

The overall results are presented in Table 1. It is seen that the accuracy of the approximation increases with Reynolds number. This is due to the deviations from the potential flow solution, mainly consisting of the wake feature, becoming concentrated in a smaller region as Re increases, thereby allowing for a more accurate fit. At the lower range the wake is more spatially spread out, and whilst the $\mathbf{u}_{\mathbf{r},\mathbf{A}}^{\mathbf{M}}$ and $\mathbf{u}_{\theta,\mathbf{A}}^{\mathbf{M}}$ approximations becomes better as the creeping flow solution is approached at $Re = 0.1$, the $\mathbf{u}_{\mathbf{r},\mathbf{res}}^{\mathbf{M}}$ and $\mathbf{u}_{\theta,\mathbf{res}}^{\mathbf{M}}$ models are not as accurate at lower Reynolds numbers. Response surface strategies have also been evaluated for the same data, however they resulted in higher MSE's with more parameters [14].

2.3 Stage two model

To ensure a smooth response of the first stage parameters, $\alpha_{i,j}$, with respect to Reynolds number, each first stage fit was carried out using the parameter estimations from the previous fit as initial guesses, thereby warm starting the optimization e.g. the parameter estimates for the $Re = 270$ surface is used as initial guesses for the $Re = 255$ surface. Carrying out the procedure from high to low Reynolds numbers provided the most well behaved curves. The dependence of the $\alpha's$ w.r.t. Re was found to be described by first and second order polynomial and exponential models. A typical example of the behaviour of the $\alpha's$ is given in Figure 6.

The final parameters to the BCM was found by optimizing all of the ζ parameters with respect to the original CFD surfaces i.e. $\mathbf{u}^{\mathbf{true}}$. This results in a bubble flow field model dependent on the Reynolds number (Re), spatial position (r and θ) and the stage two fitting parameters (ζ).

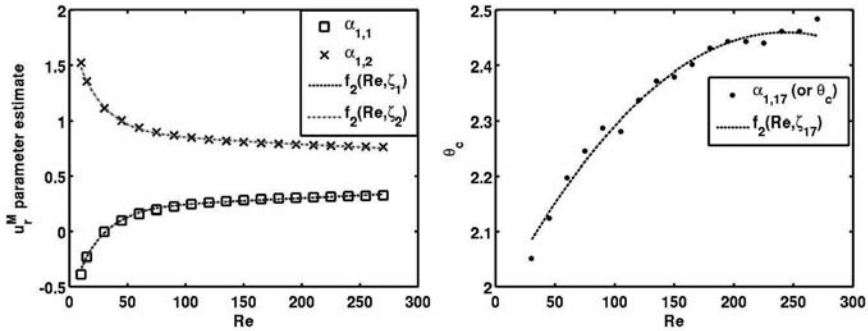

Figure 6: Second stage fit of parameters $\alpha_{1,1}$, $\alpha_{1,2}$ and $\alpha_{1,17}$.

3 Integration of bubble cell model with macro flow model: single bubble test case

With the BCM constructed, the next step is to integrate it with a macro flow model to account for the continuum outside of the BCM regions. For the development of this model, the Openfoam C++ libraries where used [15]. The BCM regions are tracked in a Lagrangian framework, and the Navier–Stokes equations solved on a structured grid for the continuum. A structured grid is used such that the computational cells falling within the BCM regions can be identified, through their structured relationship, in a computationally efficient manner. To exclude the BCM regions from the Eularian flow computations, the linear system of equations is modified. The corresponding values are set to that of the BCM and the cells are eliminated from the equations. Furthermore, the edges of the BCM regions neighbouring the computational cells, act as "internal boundary conditions", thereby closing the problem.

As a pilot test to the BCM approach, the case of a single bubble rising is considered with a fixed Reynolds number as illustrated in Figure 7. The resulting flow field in the continuum qualitatively follows experimental and numerical modelling trends [16, 17]. A rigorous analysis and validation of the results however, remain to be completed at this stage. Furthermore, the equation of motion for the BCM case needs to be developed.

4 Conclusion

A novel bubble column modelling approach is proposed, with the goal to offer bubble scale flow information at reduced computational expense. This is aimed to be achieved through the introduction of an algebraic flow model which approximates the flow field around individual bubbles, i.e. the BCM, in contrast to having to solve a set of non-linear PDE's. The BCM was constructed through a two stage fitting process, where the parameters are correlated with CFD generated

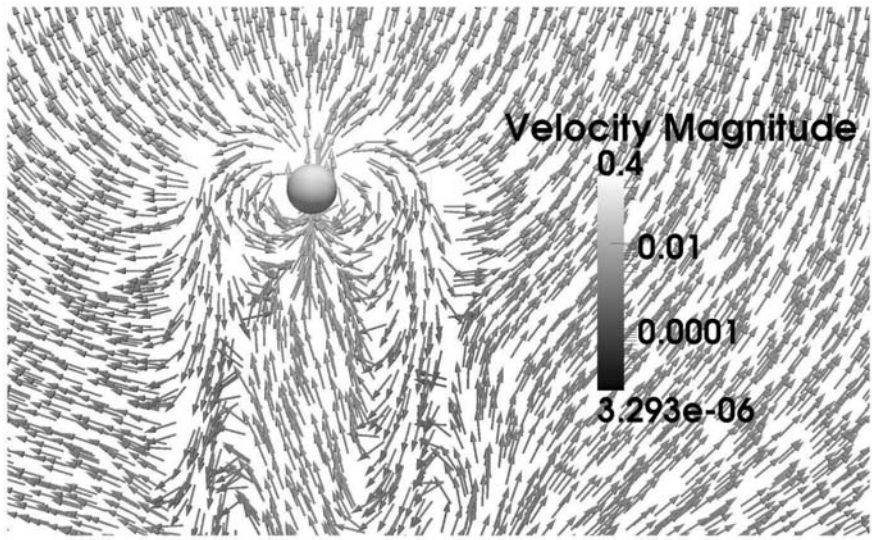

Figure 7: Resulting velocity vector field of a single bubble rising in a Euler–Lagrange framework following the BCM approach. The bubble is simulated as $Re = 120$.

data, for the analogues situation of flow over a fixed fluid sphere. The combination of the creeping and potential flow analytical solutions provided a good starting point by taking account of a large portion of the flow field. The non-linear deviations occurring outside of their idealized operating regimes however, required the introduction of statistical models. The combination of these models resulted in a semi-analytical model capable of approximating the flow field very accurately in the range examined. Furthermore, the cross correlation of the stage one parameters with Reynolds number proved to be successful with simple polynomial and exponential functions, thereby arriving at the BCM.

The BCM has been integrated with a "macro Eularian" flow model, whereby the BCM regions are tracked in a Lagrangian framework. This has been performed successfully with a pilot test case, where a single bubble rising is simulated with a fixed Reynolds number. Rigorous validation remains outstanding, however, the results qualitatively appear realistic and illustrates the potential of the approach.

References

[1] Brenner, C.E., *Fundamentals of Multiphase Flow*. Cambridge University Press, 2005.
[2] Michaelides, E.E., *Particles, Bubbles & Drops: Their Motion, Heat and Mass Transfer*. World Scientific, 2006.
[3] Joshi, J.B., Computational flow modelling and design of bubble column reactors. *Chemical Engineering Science*, **56**, pp. 5893–5933, 2001.

[4] Sokolichin, A., Eigenberger, G. & Lapin, A., Simulation of buoyancy driven bubbly flow: Established simplifications and open questions. *American Institute of Chemical Engineers*, **50**, pp. 24–45, 2004.
[5] Magnaudet, J. & Eames, I., The motion of high-Reynolds-number bubbles in inhomogeneous flows. *Annual Review: Fluid Mechanics*, **32**, pp. 659–708, 2000.
[6] Batchelor, G.K., *An Introduction to Fluid Dynamics*. Cambridge University Press, 1967.
[7] Tomiyama, A., Celata, G.P., Hosokawa, S. & Yoshida, S., Terminal velocity of single bubbles in surface tension force dominant regime. *International Journal of Multiphase Flow*, **28**, pp. 1497–1519, 2002.
[8] Clift, R., Grace, J.R. & Weber, M.E., *Bubbles, Drops and Particles*. Academic Press, 1978.
[9] Pantankar, S.V., *Numerical Heat Transfer and Fluid Flow*. Taylor & Francis, 1980.
[10] Haberman, W.L. & Morton, R.K. *David Taylor Model Basin Rep*, **802**, 1953.
[11] Stokes, G.G., On the effect of the internal friction of fluids on the motion of a pendulum. *Transactions of the Cambridge Philosophical Society*, **9**, pp. 8–106, 1851.
[12] Slattery, J.C., *Advanced Transport Phenomena*. Cambridge University Press, 1999.
[13] Bird, R.B., Steward, W.E. & Lightfoot, E.N., *Transport Phenomena: second edition*. John Wiley & Sons Inc, 2002.
[14] Coetzee, W., Coetzer, R.J.L. & Rawatlal, R., An analysis of response surface strategies in developing statistical models for application in bubble column modelling. *submitted to: Computers & Chemical Engineering*, 2010.
[15] OpenCFD, http://www.openfoam.com/, *OpenFoam - The Open Source CFD Toolbox*, 2009.
[16] Ellingsen, K. & Risso, F., On the rise of an ellipsoidal bubble in water: oscillatory paths and liquid-induced velocity. *Journal of Fluid Mechanics*, **440**, pp. 335–268, 2001.
[17] Deen, N.G., van Sint Annaland, M. & Kuipers, J.A.M., Multi-scale modeling of dispersed gas-liquid two-phase flow. *Chemical Engineering Science*, **59**, pp. 1853–1861, 2004.

This page intentionally left blank

Computational and experimental analysis of the churning power losses in an industrial planetary speed reducer

F. Concli & C. Gorla
Politecnico di Milano, Dipartimento di Meccanica, Milan, Italy

Abstract

Advantages of planetary speed reducers are well known and due to their compact design and power density they are suitable for a wide range of applications. Efficiency is becoming more and more of a main concern in the design of power transmissions and the demand for high efficiency gearboxes is continuously increasing. For this reason it is important to have some models in order to quantify the power losses of those already during the design stage. Some theoretical or semi-empirical models that allow us to estimate losses like those of bearings, of seals, of gear meshing (due to sliding) and, for ordinary gears, those of churning are available in literature. In the case of planetary speed reducers, where the motion of the planet carrier causes a rotatory motion of the planets around the axis of the gearbox, the oil splash lubrication is an important source of losses. This report introduces a multiphase CFD model for the prediction of the churning losses characteristic of planetary gears. The analysis has been carried out by means of an unsteady Volume of Fluid (VOF) model and implemented on a commercial software (Fluent). The whole geometry of the speed reducer and many operating conditions like the rotational speed, the oil level and the operating temperature have been taken into account. Moreover the results of an experimental testing campaign on an especially designed gearbox are presented and compared with the computation ones in order to validate the model. The two approaches give results in good agreement.
Keywords: planetary speed reducers, churning losses, multiphase flow simulation, VOF.

WIT Transactions on Engineering Sciences, Vol 74, © 2012 WIT Press
www.witpress.com, ISSN 1743-3533 (on-line)
doi:10.2495/AFM120261

1 Introduction

In the last years, efficiency is becoming more and more a main concern also in the design of power transmissions and the demand for high efficiency gearboxes is continuously increasing. Just having appropriate models to predict the final efficiency of the speed reducer [1] it is possible to take the correct choices since the design step, avoiding waste of time and money. Some models for the estimation of the different sources of losses like those of bearings [2], of seals [3], of gear meshing (due to sliding) [3] and, for ordinary gears, those of churning [4] already exist. What is still missing, is an appropriate model for the prediction of the churning losses in planetary speed reducers. In this kind of gearing, in fact, the motion of the planetary gears due to the planet carrier rotation is an additional source of losses.

Aim of this study is to provide a model for the correct estimation of this kind of losses and, consequently, for the correct estimation of the efficiency of the whole transmission. The model has been performed by mean of a computational fluid dynamic (CFD) analysis that simulates the behaviour of the air-oil lubricant mixture.

To validate the numerical model, an industrial planetary speed reducer has been conveniently modified in order to be able to measure the churning losses alone caused by the motion of the planetary gears. This gearbox has been tested on an especially designed test rig.

2 Problem definition

Figure 1 shows an example of a planetary gearing: it can be seen the sun gear, the planetary gears, the planet carrier and the external crown.

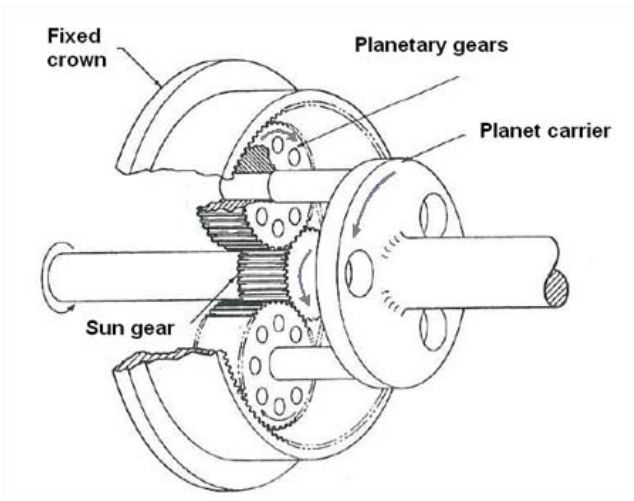

Figure 1: Planetary gearing.

In the common configuration, the power flows from the sun gear shaft to the planet carrier shaft. The planetary gears have therefore two rotatory motion components: the first one is a rotation around their axis and the second one is a motion with a circular path around the gearbox axis due to the planet carrier rotation on which they are mounted.

The planetary speed reducers are generally oil splash lubricated and it is just the interaction between the rotating elements and the lubricant air-oil mixture the source of losses investigated by the presented model.

The influence parameters are the oil level and its properties, such as the viscosity and the density (functions of the temperature), the geometry and, of course, the rotational speed. The transmitted torque influences this kind of losses indirectly: increasing the transmitted torque means more load dependent power losses (like the meshing ones and part of the bearing ones) and, consequently, a higher regime temperature of the lubricant.

3 Geometry modifications

The initial geometry of the analysed speed reducer is shown in figure 2.

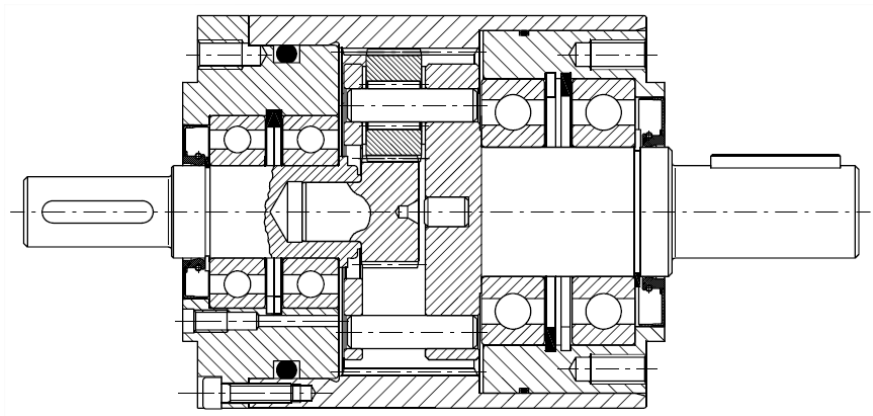

Figure 2: Initial geometry of the speed reducer.

The speed reducer is composed by a sun gear, 3 planetary gears and a “double disk” planet carrier. Both, the input and the output shaft, are mounted by mean of 2 bearings. Two contact seal are also present to avoid leakage of lubricant. In order to evaluate the churning power losses related to the motion of the planetary gears around the gearbox axis due to the rotation of the planer carrier only, the originary geometry of the speed reducer has been modified. The teeth of the external crown have been removed by machining and the sun gear has been substituted with a smaller and cylindrical (without teeth) component. The aim of these modifications is to prevent the engaging of the gears, avoiding sliding losses and churning losses due to the rotation of the gears around their axis. This modified geometry has been used both for the numerical model and the experimental testing campaign.

4 Model set up

4.1 Geometry and mesh

The domain for the CFD analysis is the internal free volume of the speed reducer after the above described geometry modifications. Figure 3 shows this volume marked in grey.

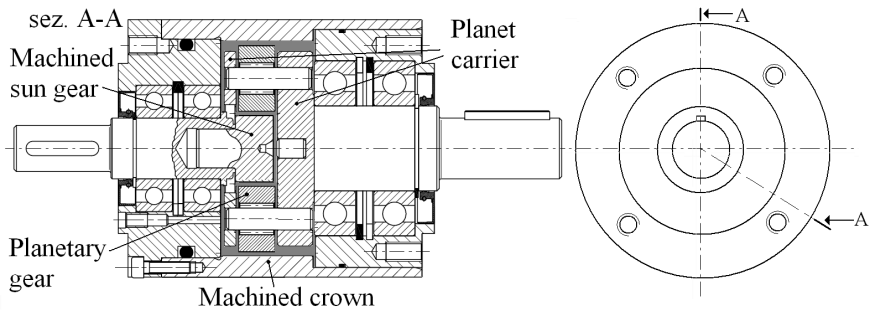

Figure 3: Modified geometry of the speed reducer: the computational domain is marked in yellow.

The computational domain for the CFD analysis has been modelled by means of 3D cad software and discretized with a swept mesh. This meshing technique consists in creating a mesh on one side of the region, known as the source side, and then copying the nodes of that mesh, one element layer at a time, until the final side, known as the target side, is reached.

The whole model has been discretized with about 500000 hexahedral cells. This kind of elements allows a larger aspect ratio compared with the tetrahedral cells in which it will invariably affects the skewness of the cell, which is undesirable as it may impede accuracy and convergence.

4.2 Parameter setting

A VOF multiphase approach has been chosen for the analysis. The VOF formulation relies on the fact that two or more fluids (or phases) are not interpenetrating. The fields for all variables and properties are shared by the phases and represent volume-averaged values, as long as the volume fraction of each of the phases is known at each location. Thus the variables and properties in any given cell are either purely representative of one of the phases, or representative of a mixture of the phases, depending upon the volume fraction values. The tracking of the interface between the phases is accomplished by the solution of a continuity equation for the volume fraction of one of the phases

$$\frac{\partial}{\partial t}\left(\alpha_q \rho_q\right) + \nabla \cdot \left(\alpha_q \rho_q \vec{v}_q\right) = S_{\alpha_q} + \sum_{p=1}^{n}\left(\dot{m}_{pq} - \dot{m}_{qp}\right) \quad (1)$$

where ρ_q is the density of the q^{th} phase, α_q the volume fraction of that phase, $\dot{m}_{pq}$ and $\dot{m}_{qp}$ the mass transfer from phase q to phase p and vice versa

respectively. This volume fraction equation has been solved be mean of an explicit scheme discretisation in order to avoid the numerical diffusion. That means solving

$$\frac{\alpha_q^{n+1}\rho_q^{n+1}-\alpha_q^n\rho_q^n}{\Delta t}V + \sum_f\left(\rho_q U_f^n \alpha_{q,f}^n\right) = \left[S_{\alpha_q} + \sum_{p=1}^n\left(\dot{m}_{pq} - \dot{m}_{qp}\right)\right]V \quad (2)$$

where $n+1$ and n are the indexes for the new time step and the preious one, $\alpha_{q,f}^n$ is the face value of the q^{th} volume fraction computed with the Geo-Reconstruction scheme, V is the volume of the cell and U_f^n is the volume flux on the face. The Geo-Reconstruction approach is an accurate scheme that assumes that the interface between two fluids has a linear slope within each cell, and uses this linear shape for the calculation of the advection of fluid through the cell faces. This scheme avoids the numerical diffusion but needs an accurate grid.

The properties appearing in the above transport equations are determined by the presence of the component phases in each control volume. In a two-phase system, if the phases are represented, for example, by the subscripts $_{air}$ and $_{oil}$, and if the volume fraction of the second of these is being tracked, the density in each cell is given by

$$\rho = \rho_{oil}\alpha_{oil} - \rho_{air}(1-\alpha_{oil}) \quad (3)$$

All other properties are calculated in the same manner.

The two phases properties are summarized in table 1.

Table 1: Properties of the two phases at 40°C.

	$\rho_{40°C}$ [Kg/m^3]	$\nu_{40°C}$ [Kg/ms]
Air	1.225	1.7894E-05
Lubricant Oil	1041	0.2082

As operating density has been chosen the lowest one.

A single momentum equation is solved throughout the domain, and the resulting velocity field is shared among the phases

$$\frac{\partial}{\partial t}(\rho\vec{v}) + \nabla\cdot(\rho\vec{v}\vec{v}) = -\nabla p + \nabla\cdot[\mu(\nabla\vec{v} + \nabla\vec{v}^T)] + \rho\vec{g} + \vec{F} \quad (4)$$

One limitation of the shared-fields approximation is that in cases where large velocity differences exist between the phases, the accuracy of the velocities computed near the interface can be adversely affected. The energy equation si also shared among the phases

$$\frac{\partial}{\partial t}(\rho E) + \nabla\cdot\left(\vec{v}(\rho E + p)\right) = \nabla\cdot\left(k_{eff}\nabla T\right) + S_h \quad (5)$$

The VOF model treats energy, E, and temperature, T, as mass-averaged variables. As with the velocity field, the accuracy of the temperature near the interface is limited in cases where large temperature differences exist between the phases.

For the pressure-velocity-couplig a SIMPLE scheme has been adopted as suggested for flows in closed domains. This algorithm uses a relationship between velocity and pressure corrections to enforce mass conservation and to obtain the pressure field.

In order to reproduce the operating conditions of the speed reducer, a rigid motion of the mesh has been applied. The motion has been defined by mean of an UdF (User defined Function). All the boundaries has been set to no slip walls: the internal boundaries, corresponding to the planet carrier and planetary gears surfaces, rotate together with the mesh (marked in dark grey in the figure 4) while the other boundaries, corresponding to the external crown and the case of the gearbox (marked in black in the figure 4), are stationary in the absolute reference frame.

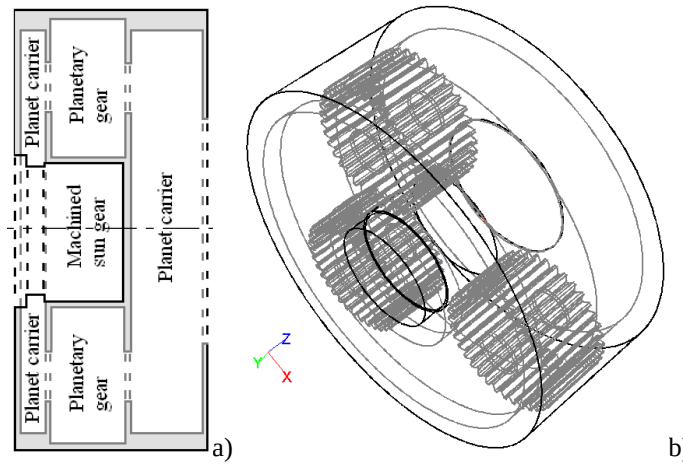

Figure 4: a) 2D schematization of the computational domain (section A-A fig. 3) b) 3D representation of the computational domain.

The time step for the transient analysis has been evaluated as

$$\Delta t = \frac{V_{cell,min}^{\frac{1}{3}}}{U} \tag{6}$$

where $V_{cell,min}$ is the volume of the smallest cell in the computational domain and U is the velocity scale of the problem.

4.3 Operating conditions

The purpose of the simulations is to analyze the resistant torque on the planet carrier shaft. This moment is calculated with a surface integral on the moving walls with respect to the gearbox axis and it is composed by two parts: the first given by pressure and the second by the viscous effects. Some simulations have been computed with different combinations of oil level, operating temperature and rotational speed. Table 2 shows the combinations of parameters for each

simulation. ***T*** is the operating temperature in °C, ***ω*** the rotational speed of the planet carrier in rpm and ***L*** is the oil level in mm measured from the gearbox axis (positive if higher than the axis, negative if lower).

Table 2: Parameters for each simulation.

T [°C]	L[mm]	ω[rpm]
40	20	500
40	0	500
40	0	1500
40	20	1000
40	20	1500
40	0	1000
40	-20	500
40	-20	1000
40	-20	1500
20	0	1000
65	0	1000

The analysis has been stopped after the resistant torque had no more sensible fluctuations and has stabilized. By multiplying the mean value of the torque by the imposed rotational speed, it is possible to determine the churning power losses.

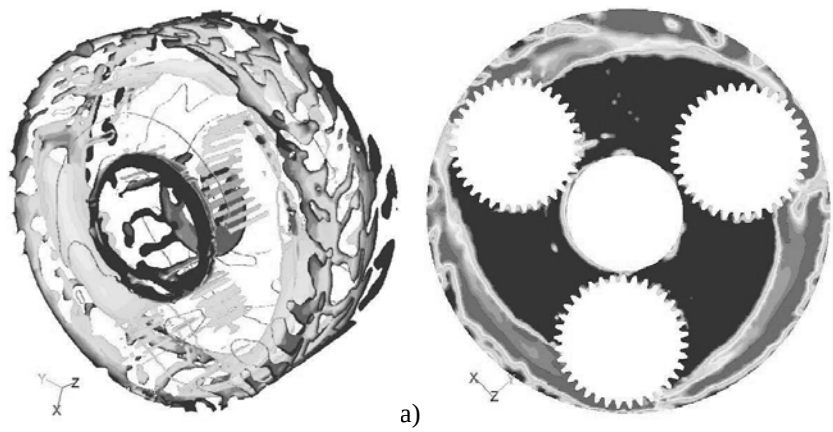

Figure 5: a) Contours of velocity magnitude for the oil phase b) Contours of volume fraction for the oil phase in the mid-section.

5 Experimental tests

In order to provide a validation of the numerical model, a real industrial planetary speed reducer has been modified as already described and tested. After the modifications, the input shaft and the output shaft are completely uncoupled. That allows us to move the planet carrier and reproduce the condition in which the meshing losses and the churning losses due to the rotations of the gears around their axis are avoided.

A schematic layout of the test rig is shown in figure 6. The speed reducer is fixed to the ground by mean of a specially designed structure. The planet carrier shaft is connected to a HBM T12 torque meter with a telemetric transmission of the signal by mean of a double cardan shaft in order to avoid bending. The torque meter, in turn, is connected to a 35KW DC motor by means of a coupling.

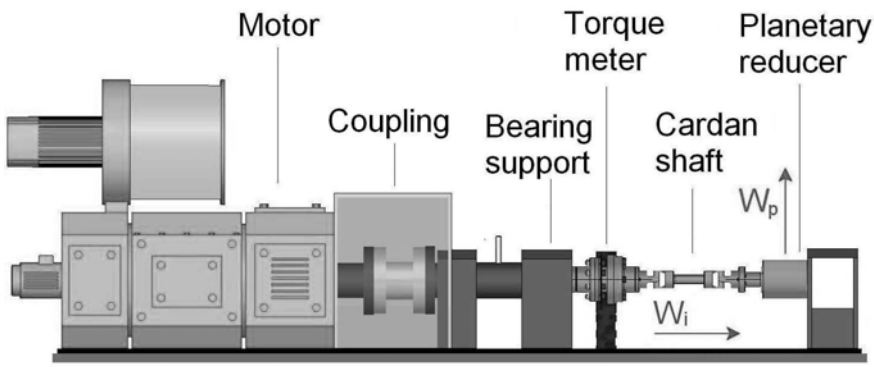

Figure 6: Schematic layout of the test rig.

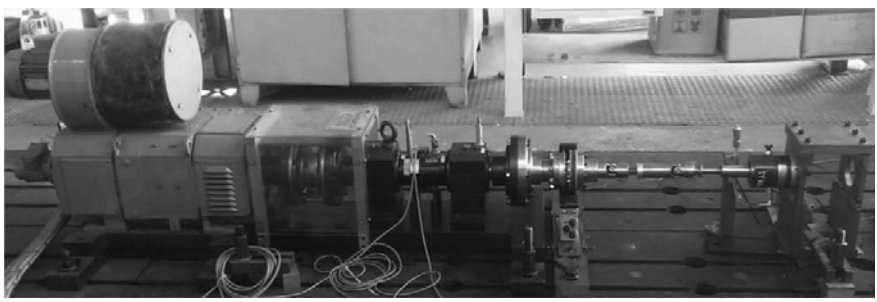

Figure 7: Test rig with the tested speed reducer.

A transparent pipe allows the monitoring of the actual oil level. The operating temperature can be imposed by a special heating system (insulated chamber with a heating source) and measured by mean of a thermocouple. The rotational speed can be controlled by the motor PLC (programmable logic controller). For each of the 3 oil levels, 4 different temperatures have been tested. For all this coupled

operating conditions (oil level + temperature) the power losses have been measured in a rotational speed range between 100 rpm and 1500 rpm.

6 Results

Before comparing the experimental results with the computation ones, it is necessary to subtract the seal losses and the bearing losses from the measured values. The torque meter, in fact, measures the input power of the reducer. A little fraction of this power is dissipated by the two internal bearings of the planet carrier shaft and by its seal. This part of losses can be easily calculated by mean of some proved models [2, 3] as function of the testing conditions.

Figure 8 to 13 show both the experimental and the computation results for the different oil levels and as a function of temperature and rotational speed.

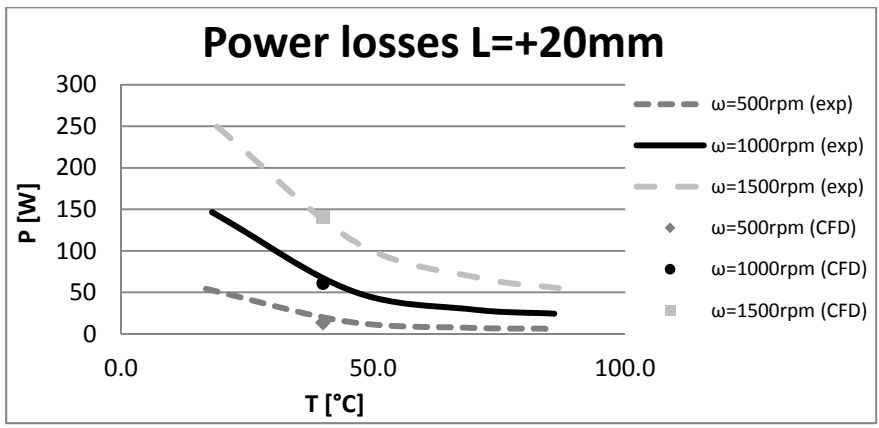

Figure 8: Experimental and computation results for L=20mm.

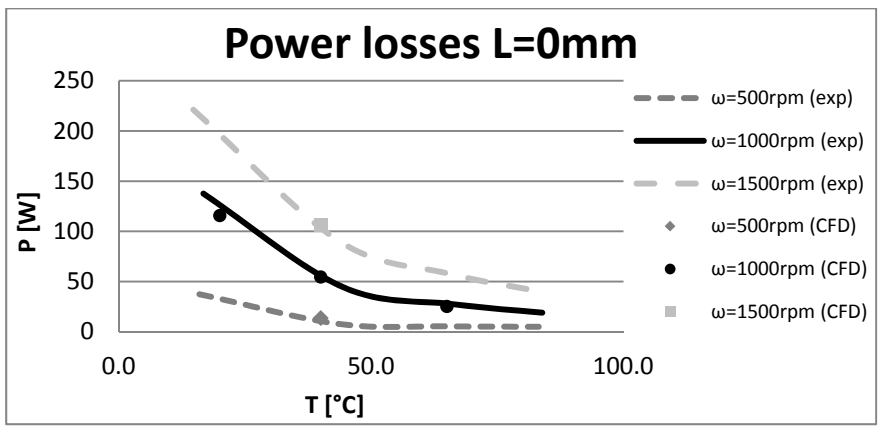

Figure 9: Experimental and computation results for L=0mm.

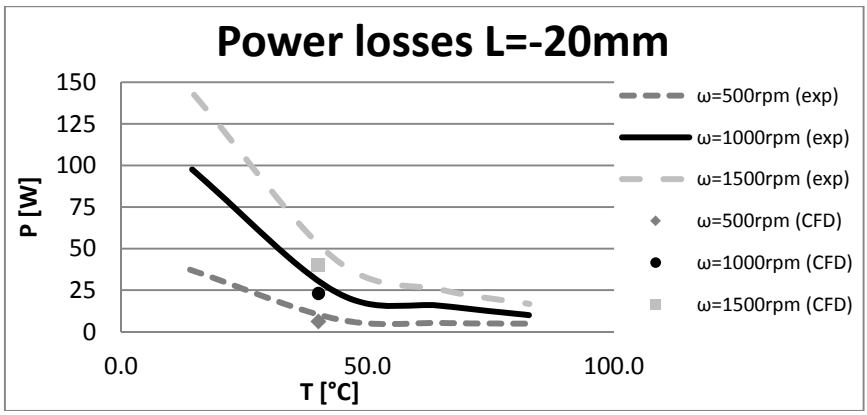

Figure 10: Experimental and computation results for L=-20mm.

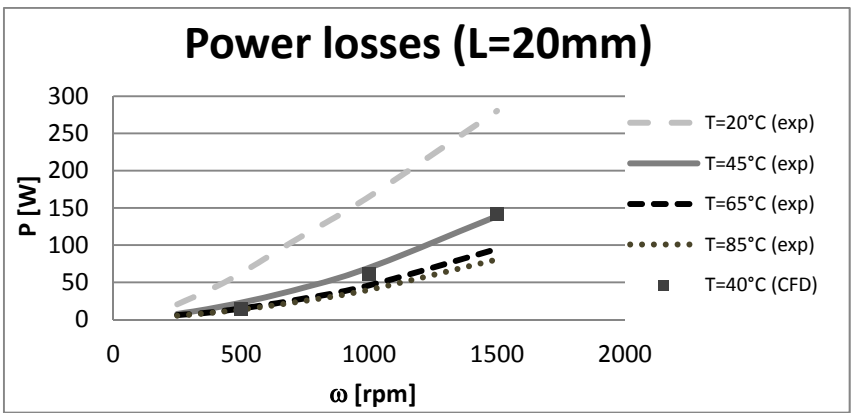

Figure 11: Experimental and computation results for L=20mm.

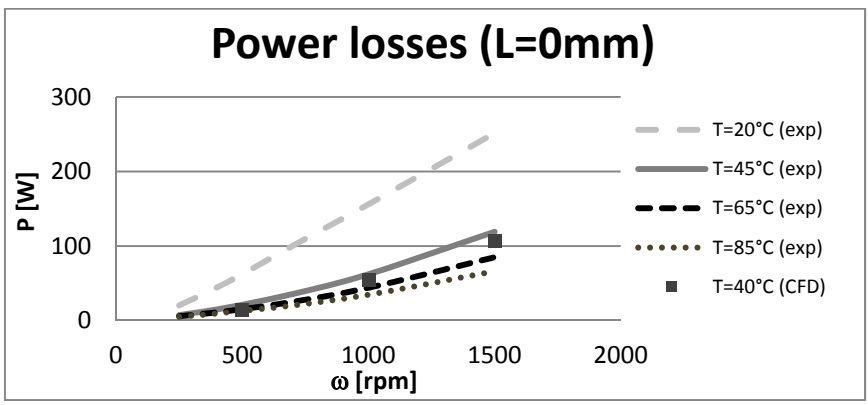

Figure 12: Experimental and computation results for L=0mm.

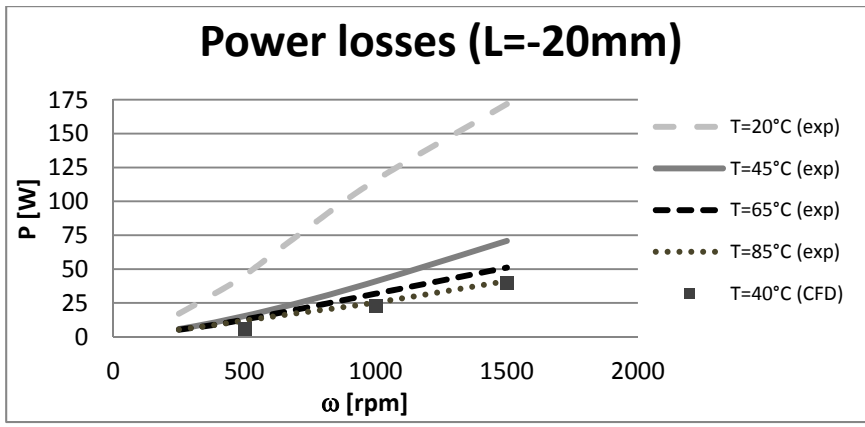

Figure 13: Experimental and computation results for L=-20mm.

Due to the high computational time needed for the solution of the numerical models, not all the experimentally tested conditions have been also computed with the CFD analysis.

It can be seen that the numerical results are in good agreement with the numerical ones.

7 Conclusions

As reliable models to predict the churning losses of the planetary gears are still not available, a CFD model has been applied in order to predict this important component of losses of epicycloid gear reducers, starting from the geometry and the operating conditions. The results of the model are well supported by the experiments (except for extremely low temperatures). The losses increase, as expected, with static lubricant level and rotational speed and decrease with the temperature. The decrease rate of the power losses with the temperature is very high for low temperature and decreases with the temperature growth.

The increase rate of the losses with the rotational speed is more than linear.

Future development is the investigation of other influence parameters like the oil type and the geometry of the reducer.

References

[1] Concli, F., Gorla, C., Arigoni, R., Cognigni, E., Musolesi, M., *Planetary Speed Reducers: Efficiency, Backlash, Stiffness*, International conference on gears, Munich 2010.

[2] *General Catalogue SKF* — SKF Group, December 2006.

[3] Niemann, G., Winter, H., *Maschinenelemente – Band 2: Getriebe Allgemein, Zahnradgetriebe – Grundlagen, Stirnradgetriebe – 2. Auflage* , Springer, Berlin 2003.

[4] *ISO/TR 14179-1* and -2.
[5] Patankar, S.V., *Numerical heat transfer and fluid flow*, Taylor&Francis, USA 1980.
[6] Versteeg, H.K., Malalasekera, W., *An introduction to computational fluid dynamics – The finite volume method*, Longman Group, London 1995.
[7] Comini, G., *Fondamenti di termofluidodinamica computazionale*, SGEditoriali, Padova 2004.
[8] Concli, F., Gorla, C., Arigoni, R., Musolesi, M., *Riduttori di precisione a gioco ridotto ed alta efficienza*, Organi di trasmissione – febbraio 2011, Tecniche Nuove, Milano 2011.
[9] Csobàn, A., Kozma, M., *Influence of the Oil Churning, the Bearing and the Tooth Friction Losses on the Efficiency of Planetary Gears*, Journal of Mechanichal Engineering 56(2010)4, pp.231-238.

Section 4
Environmental fluid mechanics

This page intentionally left blank

Water and contaminant flux estimation from multi-layer passive flux meter measurements

H. Klammler[1,2,3], K. Hatfield[2,3], J. Luz[1], M. Annable[3,4], M. Newman[2,3], J. Cho[3,4], A. Peacock[5], V. Stucker[6], J. Ranville[6] & C. Clark II[7]
[1]*Department of Environmental Science and Sustainable Development, Federal University of Bahia, Brazil*
[2]*Department of Civil and Coastal Engineering, University of Florida, USA*
[3]*Inter-Disciplinary Program in Hydrologic Sciences, University of Florida, USA*
[4]*Department of Environmental Engineering Sciences, University of Florida, USA*
[5]*Microbial Insights, Inc., Rockford, USA*
[6]*Department of Chemistry and Geochemistry, Colorado School of Mines, USA*
[7]*Department of Civil and Environmental Engineering, Florida A&M University, USA*

Abstract

The passive flux meter (PFM) enables the measurement of cumulative water and contaminant mass fluxes in porous aquifers. It consists of a sorbent material, which is installed in a monitoring well to intercept groundwater flow. Tracer losses and contaminant retention on the sorbent are used to estimate water and contaminant mass fluxes through the device. In the multi-layer PFM different (sorbent) materials are used in an annulus (layer-type) configuration. This allows leached tracers inside the PFM (no tracer release into aquifer) to be retained and facilitates simultaneous deployment of different sorbent types in a single device. In order to estimate undisturbed ambient fluxes in the aquifer, measurements need to be corrected for flow convergence or divergence induced by the well and PFM components. We make use of an analytical solution to the potential flow

WIT Transactions on Engineering Sciences, Vol 74, © 2012 WIT Press
www.witpress.com, ISSN 1743-3533 (on-line)
doi:10.2495/AFM120271

problem of uniform flow disturbed by a system of concentric rings of contrasting hydraulic conductivities. A flow convergence factor is defined as a function of PFM ring conductivities and radii, where tracer elution and contaminant sorption may occur in arbitrary layers. The results are used for calibration of convergence factors of a multi-layer PFM to laboratory sand box experiments.
Keywords: aquifer, groundwater, plume, flow convergence, sand box.

1 Introduction

Groundwater contamination is recognized as a dangerous threat to ecosystems and human drinking water supplies. Besides contaminant concentrations (mass per volume), contaminant mass fluxes (mass per cross sectional area per time) have been used more recently as relevant measures for contaminant source identification, risk assessment, decision making and remediation performance control (ITRC [1]). Currently, three fundamental approaches are available for measuring contaminant fluxes: (1) Multi-level sampling (MLS; Einarson and Mackay [2]), which is based on separate measurements of contaminant concentrations and water fluxes for subsequent multiplication to obtain contaminant fluxes. (2) Integral pump tests (IPT; Bockelmann *et al*. [3]), which extract contaminated groundwater from the aquifer through pumping from a well and monitor contaminant concentrations at the well head over time. (3) Passive flux meter measurements (PFM; Hatfield *et al*. [4], Annable *et al*. [5]) based on the installation of sorbent materials in observation wells, where the sorbents initially contain known amounts of resident tracers. From detected tracer losses from a sorbent and contaminant masses sorbed onto a sorbent through laboratory analyses, cumulative (i.e., time integrated or averaged over the period of installation) water and contaminant fluxes may be obtained simultaneously as depth profiles along the well.

PFMs have typically been deployed in observation wells as self-contained units consisting of a single sorbent material, which acts as both a leaching tracer reservoir and a contaminant trap. As a consequence, it has to be assured that (1) the sorption properties of the sorbent material are appropriate for both tracer(s) and target contaminants, and (2) that the chemical properties of the tracer(s) are such that tracer release (even though minimal) into the aquifer does not cause legal or environmental problems. In an effort to circumvent these two issues (e.g., for measuring water and contaminant fluxes at Rifle, CO, USA) a multi-layer PFM has been developed and tested, which consists of multiple concentric rings (layers) of different materials (which may be sorbents or not).

Figure 1 compares the two different PFM configurations, where figure 1a shows a single sorbent installed inside a well screen, while figure 1b illustrates the annular composition of a multi-layer PFM installed in a screened well. From the periphery towards the center k_i [L/T] and r_i [L] denote the hydraulic conductivities and outer radii of the different rings. k_0 corresponds to the aquifer, k_1 is the well screen, k_2 an outer sorbent layer for contaminant sorption (e.g., Lewatit resin for uranium), k_3 an intermediate sorbent layer (e.g., granular activated carbon (GAC) for alcoholic tracers) to retain tracers eluded from an

inner sorbent layer of k_5 (e.g., also consisting of GAC for alcoholic tracers). Between the two GAC layers, there is a thin perforated stainless steel pipe of conductivity k_4, which serves to separate the inner GAC from the outer one for installation and laboratory analysis. The center circle of radius r_6 is an impermeable pipe for physical stabilization and water evacuation during PFM

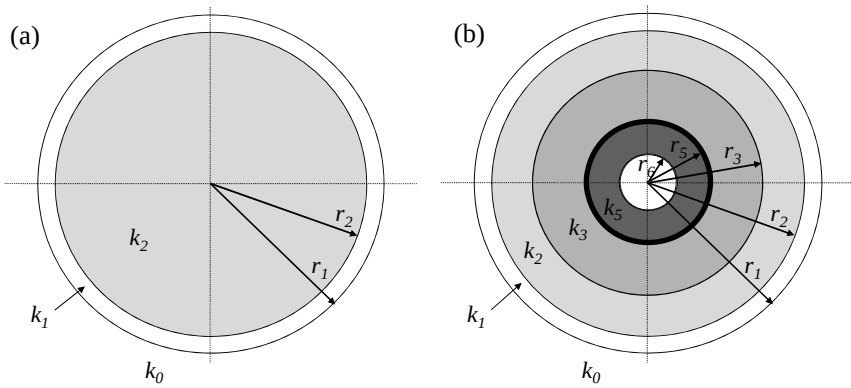

Figure 1: Horizontal cross sections of well screens and (a) a PFM consisting of a single sorbent and (b) a multi-layer PFM as used in laboratory testing. Bold black circle is of outer radius r_4 and conductivity k_4.

Table 1: Summary of multi-layer PFM properties as depicted in figure 1b with k_1 and k_4 to be determined from laboratory box experiments.

Ring n^o. i [-]	Conductivity k_i [m/day]	Outer radius r_i [cm]	Material / purpose
0	33	infinite	Aquifer (sand)
1	k_1	5.7	Well screen (slotted PVC pipe)
2	250	5.1	Lewatit resin for uranium sorption
3	350	3.8	GAC for tracer retention
4	k_4	2	Perforated pipe for separation
5	350	1.9	GAC for tracer elution
6	0	0.8	Impermeable center pipe

installation and removal. Table 1 summarizes the properties of the multi-layer PFM configuration used in laboratory sand box experiments for determination of k_1 and k_4 and subsequent deployment for measuring water and uranium fluxes at the uranium field site in Rifle.

Similar to the simple PFM, the multi-layer PFM provides data in terms of tracer losses from sorbent ring 5 and contaminant masses retained from sorbent ring 2. Following the method of Hatfield *et al*. [4] the apparent flux $q_{PFM,i}$ [L/T] through the *i*-th ring of a PFM may be found as

$$q_{PFM,i} = \frac{(1-m_{ri})(r_i^2 - r_{i+1}^2)\pi\theta_i R_i}{2r_i t} \tag{1}$$

where m_{ri} [-] is the relative mass of a tracer remaining (with respect to the initial mass of that tracer) after time of exposure t [T] in the *i*-th ring of relative water content θ_i [-] and retardation factor R_i [-]. The attribute "apparent" indicates that flow is generally not uniform inside a multi-layer PFM and $q_{PFM,i}$ is to be understood as a discharge per unit transect area of the *i*-th ring perpendicular to incident flow direction. In analogy, an apparent contaminant mass flux $J_{PFM,i}$ [M/(TL^2)] trough the *i*-th ring may be obtained from

$$J_{PFM,i} = \frac{M_{si}}{2r_i bt} \tag{2}$$

where M_{si} [M] is the mass of contaminant sorbed in the *i*-th layer over a PFM interval of length b [L]. Eqn (1) is valid as long as none of the stream tubes through the *i*-th layer are completely cleared (empty) of tracer, while eqn (2) is valid as long as none of the contaminant previously sorbed onto the *i*-th layer is again released from it. As a consequence, within their ranges of validity eqns (1) and (2) do not depend on the properties (e.g., non-uniformity) of the flow field in the respective rings. Note that for $r_{i+1} = 0$ (i.e., the *i*-th layer is the center circle) eqn (1) reduces to eqn (18) of Hatfield *et al*. [4], whose coefficient of 1.67 appears as $\pi/2 \approx 1.57$ here. This is a consequence of the range of validity stipulated (an analogous observation applies to eqn (2)).

However, due to the more complex configuration of the multi-layer PFM and flow refraction between layers of different conductivities, an assessment of undisturbed ambient water and contaminant fluxes in the aquifer is not straightforward. Klammler *et al*. [6] present an analytical solution to the potential flow problem through the multi-layer PFM and they develop flow convergence factors for estimation of undisturbed (uniform) ambient fluxes. These factors, however, are with respect to the inner-most ring (center circle) only and are not applicable to other rings. The present work generalizes the convergence factors of Klammler *et al*. [6] to arbitrary layers in a multi-layered PFM configuration and uses the result for calibration of unknown parameters (well screen and perforated pipe conductivities k_1 and k_4) through a laboratory sand box experiment, such that they may be applied to the multi-layer PFM deployment at Rifle for measuring water and uranium fluxes.

2 General flow field solution

The solution of Klammler *et al*. [6] is based on potential flow through porous media (Strack [7]). It makes use of a flow field analogy between uniform flow

disturbed by a cylindrical inhomogeneity in hydraulic conductivity and uniform flow disturbed by an impermeable or infinitely permeable cylinder. Its application is best illustrated by a numerical example, for which we use the flow domain of figure 1b (table 1) with values of k_1 = 2.3 m/d and k_4 = 3.2 m/d. This leads to the flow field (stream lines) of figure 2 with the stream function Ψ_i [L^3/T] in the i-th ring given by

$$\Psi_i = q_i r b \left(1 - \frac{a_i^2}{r^2}\right) \sin\gamma \tag{3}$$

where r [L] and γ [-] are the radial and angular coordinates, respectively, b [L] is the thickness of the flow domain (length of PFM interval in eqn (2)) and the parameters a_i [L] and q_i [L/T] are given in table 2 and obtained as follows: Starting with an initial value of $a_6 = 0$ in table 2, the columns of k_{ia} [L/T] and a_i are populated from bottom up by alternately applying eqns (4) and (5). Subsequently, the column of q_i is populated from top down by consecutive use of eqn (6). Most parameters in table 2 are auxiliary variables without direct physical equivalences (some of them complex/ imaginary). Exceptions are q_0 (undisturbed flux in the aquifer; assumed uniform), k_{6a} (equal to conductivity k_6 of inner ring), k_{0a} (equal to aquifer conductivity k_0) and q_6 (specific discharge in inner ring). Since $k_6 = 0$, it is further seen that a_5 is equal to the center pipe radius r_6. Following this example, the step-wise solution scheme of eqns (3) through (6) is generally applicable to an arbitrary number of layers.

$$k_{ia} = k_i \frac{1 - \left(\frac{a_i}{r_i}\right)^2}{1 + \left(\frac{a_i}{r_i}\right)^2} \tag{4}$$

$$a_{i-1} = r_i \sqrt{\frac{1 - \frac{k_{ia}}{k_{i-1}}}{1 + \frac{k_{ia}}{k_{i-1}}}} \tag{5}$$

$$q_i = q_{i-1} \frac{1 + \frac{k_i}{k_{ia}}}{1 + \frac{k_{i-1}}{k_{ia}}} \tag{6}$$

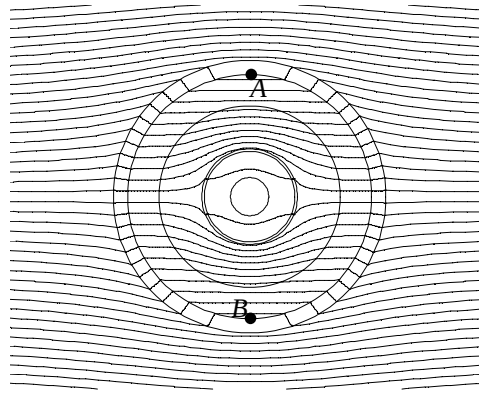

Figure 2: Flow field solution depicted as stream lines (lines of constant Ψ_i) for flow domain of figure 1b (table 1).

Table 2: Summary of flow field parameters and convergence factors for multi-layer PFM of figure 1b for k_1 = 2.3 m/d and k_4 = 3.2 m/d. $j = \sqrt{-1}$ is the imaginary unit.

Ring n°. i [-]	a_i [cm]	k_{ia}[m/day]	q_i/q_0 [-]	α_i [-]
0	2.94	33	$\boldsymbol{q_0/q_0 = 1}$	1
1	5.05j	19.12	0.41	0.73
2	0.79	238.38	0.83	0.81
3	1.73	229.46	1.01	0.80
4	1.88j	49.78	0.13	0.25
5	0.80	244.59	0.32	0.26
6	$\boldsymbol{a_6 = 0}$	0	0	0

3 Flow convergence factors for arbitrary layers

Using the solution of Ψ_i from eqn (3) for an arbitrary number of layers, the apparent flux $q_{PFM,i}$ [L/T] through the i-th ring of eqn (1) may be found. It is equal to the difference of the stream function between the lateral-most points (e.g., for i = 2 points A and B in figure 2) of the ring divided by the cross sectional area perpendicular to flow.

$$q_{PFM,i} = \frac{\Psi_i(r_i, \frac{\pi}{2}) - \Psi_i(r_i, -\frac{\pi}{2})}{2r_i b} = \frac{\Psi_i(r_i, \frac{\pi}{2})}{r_i b} = q_i\left(1 - \frac{a_i^2}{r_i^2}\right) \tag{7}$$

In the undisturbed aquifer the flow is assumed to be of uniform flux q_0, such that a flow convergence (or divergence) factor α_i [-] for the i-th ring may be defined by

$$\alpha_i = \frac{q_{PFM,i}}{q_0} = \frac{q_i}{q_0}\left(1 - \frac{a_i^2}{r_i^2}\right) \tag{8}$$

In other words, the flow convergence factor expresses how much flow crosses the i-th ring of a multi-layer PFM with respect to the ambient flow through a ring of the same size, if the aquifer was not disturbed by the well and PFM components. A value of α_i larger than one may be viewed as a situation of flow convergence, while a value smaller than one reflects a condition of flow divergence. For a single layer PFM, flow convergence occurs when the PFM sorbent is more permeable than the aquifer and flow divergence occurs when the contrary is true. For multi-layer PFMs, however, $\alpha_i \geq 1$ and $\alpha_i \leq 1$ may occur simultaneously in different layers of a single device depending on the sequence of k_i. Returning to the example of figure 1b and using values of r_i from table 1 with values of q_i/q_0 and a_i from table 2, the values of α_i as given in the last column of table 2 are directly obtained from eqn (8) (note hereby that some values of a_i are imaginary).

The flow convergence factor α_i from eqn (8) is a generalization over that of Klammler *et al*. [6], because it is applicable to any layer. If i is equal to the total number of layers present, such that α_i applies to the center circle of the flow domain as shown in figure 1, for example, then eqn (8) becomes equal to α_i from Klammler *et al*. [6]. Moreover, for i = 1, 2 and 3 (and an arbitrary total number of layers), eqns (3), (12) and (13) of Klammler *et al*. [6] may be written in a generalized form by using k_{1a}, k_{2a} and k_{3a} from eqn (4) instead of k_1, k_2, and k_3 resulting in

$$\alpha_1 = \frac{2}{1 + \frac{k_0}{k_{1a}}} \tag{9}$$

$$\alpha_2 = \frac{4}{\left(1 + \frac{k_0}{k_1}\right)\left(1 + \frac{k_1}{k_{2a}}\right) + \left(1 - \frac{k_0}{k_1}\right)\left(1 - \frac{k_1}{k_{2a}}\right)\left(\frac{r_2}{r_1}\right)^2} \tag{10}$$

$$\alpha_3 = \frac{8}{\left(1 + \frac{k_0}{k_1}\right)\left(1 + \frac{k_1}{k_2}\right)\left(1 + \frac{k_2}{k_{3a}}\right) + \left(1 - \frac{k_0}{k_1}\right)\left(1 - \frac{k_1}{k_2}\right)\left(1 + \frac{k_2}{k_{3a}}\right)\left(\frac{r_2}{r_1}\right)^2 + \left(1 + \frac{k_0}{k_1}\right)\left(1 - \frac{k_1}{k_2}\right)\left(1 - \frac{k_2}{k_{3a}}\right)\left(\frac{r_3}{r_2}\right)^2 + \left(1 - \frac{k_0}{k_1}\right)\left(1 + \frac{k_1}{k_2}\right)\left(1 - \frac{k_2}{k_{3a}}\right)\left(\frac{r_3}{r_1}\right)^2} \tag{11}$$

For i = 4, the result of Appendix B in Klammler *et al*. [6] is incomplete and after substituting k_4 by k_{4a} it should be

$$\alpha_4 = \frac{16}{A + B + C + D + E + F + G + H} \tag{12}$$

with

$$A = \left(1+\frac{k_0}{k_1}\right)\cdot\left(1+\frac{k_1}{k_2}\right)\cdot\left(1+\frac{k_2}{k_3}\right)\cdot\left(1+\frac{k_3}{k_{4a}}\right)$$

$$B = \left(1-\frac{k_0}{k_1}\right)\cdot\left(1-\frac{k_1}{k_2}\right)\cdot\left(1+\frac{k_2}{k_3}\right)\cdot\left(1+\frac{k_3}{k_{4a}}\right)\cdot\left(\frac{r_2}{r_1}\right)^2$$

$$C = \left(1+\frac{k_0}{k_1}\right)\cdot\left(1-\frac{k_1}{k_2}\right)\cdot\left(1-\frac{k_2}{k_3}\right)\cdot\left(1+\frac{k_3}{k_{4a}}\right)\cdot\left(\frac{r_3}{r_2}\right)^2$$

$$D = \left(1-\frac{k_0}{k_1}\right)\cdot\left(1+\frac{k_1}{k_2}\right)\cdot\left(1-\frac{k_2}{k_3}\right)\cdot\left(1+\frac{k_3}{k_{4a}}\right)\cdot\left(\frac{r_3}{r_1}\right)^2$$

$$E = \left(1+\frac{k_0}{k_1}\right)\cdot\left(1+\frac{k_1}{k_2}\right)\cdot\left(1-\frac{k_2}{k_3}\right)\cdot\left(1-\frac{k_3}{k_{4a}}\right)\cdot\left(\frac{r_4}{r_3}\right)^2$$

$$F = \left(1+\frac{k_0}{k_1}\right)\cdot\left(1-\frac{k_1}{k_2}\right)\cdot\left(1+\frac{k_2}{k_3}\right)\cdot\left(1-\frac{k_3}{k_{4a}}\right)\cdot\left(\frac{r_4}{r_2}\right)^2$$

$$G = \left(1-\frac{k_0}{k_1}\right)\cdot\left(1+\frac{k_1}{k_2}\right)\cdot\left(1+\frac{k_2}{k_3}\right)\cdot\left(1-\frac{k_3}{k_{4a}}\right)\cdot\left(\frac{r_4}{r_1}\right)^2$$

$$H = \left(1-\frac{k_0}{k_1}\right)\cdot\left(1-\frac{k_1}{k_2}\right)\cdot\left(1-\frac{k_2}{k_3}\right)\cdot\left(1-\frac{k_3}{k_{4a}}\right)\cdot\left(\frac{r_2 r_4}{r_1 r_3}\right)^2 \qquad (13)$$

Note that eqns (9) through (13) are equivalent formulations to the step-wise procedure of eqns (4) through (6). While closed form expressions of α_i for $i > 4$ may be derived, they become increasingly lengthy and computational implementation of eqns (4) through (6) (e.g., in a spreadsheet) may be more convenient.

Not immediately obvious from eqns (9) through (13) and more easily verifiable using eqns (5), (6) and (8) is that the ratio α_i/α_{i-1} is only a function of k_m and r_m, where $m \geq i - 1$. More intuitively, this means that flow refraction between two adjacent layers does not depend on the radii and conductivities of any outside layers or the aquifer. This may be convenient for comparing flux estimates from different layers independent of the perhaps uncertain aquifer conductivity k_0 and will be explored for estimating k_1 and k_4 below. However, it also precludes the possibility of estimating an unknown k_0 from two flux estimates in different layers (as may be attempted in analogy to the method presented in Klammler *et al.* [6]).

Assuming that contaminant transport is dominated by advection (i.e., contaminant particles travel along the same stream tubes as water particles and effects of diffusion and dispersion are neglected), $q_{PFM,i}$ and q_0 in the first equality of eqn (8) may be substituted by $J_{PFM,i}$ from eqn (2) and the undisturbed ambient contaminant mass flux J_0 [M/(L^{2}T)], respectively. It is recalled that m_{ri} for estimation of $q_{PFM,i}$ and M_{si} for estimation of $J_{PFM,i}$ do not have to stem from the same PFM layer (i.e., index i in eqns (1) and (2) generally takes different

values). However, if m_{ri} and M_{si} are obtained from the same layer, then the same flow convergence factor α_i applies.

4 Laboratory experiments and calibration

For application of the multi-layer PFM configuration of figure 1b at the uranium site in Rifle and determination of unknown conductivities k_1 and k_4, laboratory sand box experiments are performed. Box size is 39 x 30.5 x 17.9 cm (length L x width W x height H) and table 1 contains the sand conductivity as well as well screen and PFM parameters. "Ambient" water fluxes q_0 and uranium fluxes J_0 through the box are obtained from

$$q_0 = \frac{Q_0}{WH} \tag{14}$$

$$J_0 = q_0 C_u \tag{15}$$

where Q_0 [L^3/T] is the independently measured water discharge through the box and C_u [M/L^3] is the uranium concentration in the influent water. Eleven tests of different durations were run for water flux obtaining estimates $q_{PFM,5}$ from eqn (1) for comparison to q_0 of eqn (14). In five of these tests uranium was added at $C_u \approx 200$ µg/l for comparison of $J_{PFM,2}$ from eqn (2) with J_0 of eqn (15).

Table 3: Summary of results from sand box experiments.

t [days]	q_0 [cm/day]	$q_{PFM,5}$ [cm/day]	α_5 [-]	J_0 [µg/(cm^{2}day)]	$J_{PFM,2}$ [µg/(cm^{2}day)]	α_2 [-]
3.00	15.95	4.12	0.26	N/A		
2.87	16.85	4.03	0.24			
2.92	16.85	3.44	0.20			
2.99	18.48	4.13	0.22			
4.24	17.03	3.84	0.23			
4.05	19.44	4.09	0.21			
5.92	7.87	2.40	0.30	1.68	1.86	1.11
3.94	11.52	3.64	0.32	2.38	1.80	0.76
1.95	25.02	6.17	0.25	5.05	2.16	0.43
1.51	31.78	7.93	0.25	6.15	2.96	0.48
12.00	3.87	1.68	0.43	0.80	1.05	1.30
		Average α_5 =	0.26		Average α_2 =	0.81

Table 3 summarizes the results of the sand box experiments and indicates average values of $\alpha_2 = J_{PFM,2}/J_0 = 0.81$ and $\alpha_5 = q_{PFM,5}/q_0 = 0.26$. At this point we return to table 2 and revert the previous assumption that the conductivities k_1 and k_4 of the well screen and the perforated pipe are known. Instead, the experimental values of α_2 and α_5 are used to determine effective values of k_1 and k_4 to be used in the interpretation of field deployments. For this purpose,

advantage is taken of the previous conclusion that the ratio $\alpha_5/\alpha_2 = 0.32$ is not affected by k_1. Thus, k_4 may be directly found, which is most conveniently achieved by systematically varying k_4 for an arbitrary value of k_1 and observing the results in terms of α_5/α_2. Figure 3 shows the outcome of this process and leads to two possible values of $k_4 = 3.2$ and 18851 m/day. For each of the values found for k_4, the same process is repeated with k_1 to reach the required value of $\alpha_2 = 0.81$ (or equally $\alpha_5 = 0.26$). This is illustrated in figure 4 and shows that again two values of k_1 may be combined with each value of k_4, thus resulting in the four solutions given in the first two rows of table 4.

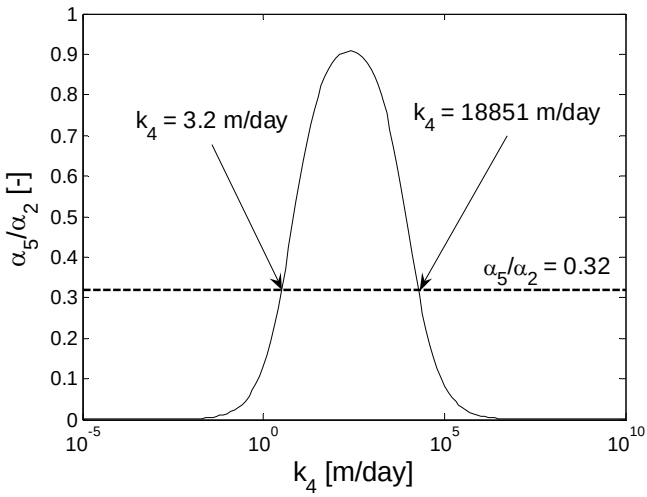

Figure 3: α_5/α_2 as a function of k_4 for arbitrary k_1 to achieve target value $\alpha_5/\alpha_2 = 0.32$.

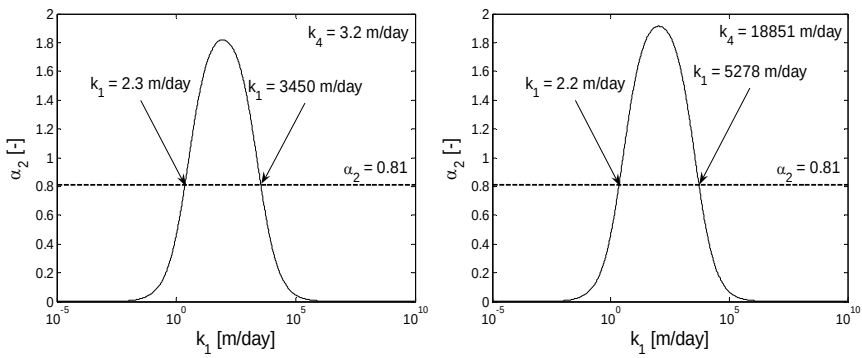

Figure 4: α_2 as a function of k_1 for $k_4 = 3.2$ and 18851 m/day to achieve target value $\alpha_2 = 0.81$.

Table 4: Possible combinations of k_1 and k_4 in m/day to achieve $\alpha_2 = 0.81$ and $\alpha_5 = 0.26$ from box experiments and resulting α_q and α_J for the Rifle deployment.

k_1	2.3	3450	2.2	5278
k_4	3.2		18851	
α_q	0.20	0.36	0.20	0.37
α_J	0.61	1.13	0.61	1.16

For each of the four solutions pairs, a flow convergence factor α_q for water flux and a flow convergence factor α_J for uranium may be computed for the deployment conditions at the Rifle site. These conditions are identical to those of figure 1b, except for the presence of a filter pack of radius 10.2 cm and conductivity 160 m/day around the well screen and inside an aquifer of conductivity of approximately 2.5 m/d. Considering these modifications, results for α_q and α_J from application of eqns 4, 5, 6 and 8 are given in the last two rows of table 4. It may be seen that $\alpha_q/\alpha_J = \alpha_5/\alpha_2 = 0.32$ remains constant and, more interestingly, that the solutions are pair wise identical (up to chart reading and rounding errors). It appears that this is not a coincidence as the same behaviour may be observed for other hypothetical values of aquifer and filter pack conductivities and radii. From the remaining two solution, $\alpha_q = 0.20$ and $\alpha_J = 0.61$ are proposed for use at the Rifle site, since they are associated with a low value of $k_1 = 2.3$ (and either value of k_4). This choice is justified by two related arguments: (1) From an independent borehole dilution test (no PFM installed) in the sand box a value of $k_1 = 87$ m/day is estimated. This may be regarded as an upper bound for k_1 as flow in the vicinity of an open borehole is radial. Flow components in the tangential direction through the well screen are hindered by the fact that screen slots are not continuous along the circumference of a PVC screen. (2) As illustrated by the flow field in figure 2, low k_1 and k_4 cause flow in the respective rings to be essentially radial, which is in agreement with the geometric properties of the screen slots and the pipe perforations acting as water conduits. Large values of k_1 and k_4, in turn, would lead to a certain degree of flow short circuiting along these rings, which is considered less plausible, particularly since the sorbents are granular and tend to settle into the well and close possible voids along the pipe or screen surfaces.

5 Summary

Based on an existing solution to the potential flow problem of uniform flow disturbed by an arbitrary number of concentric rings of contrasting conductivities, flow convergence (or divergence) factors are developed for interpretation of multi-layer PFM measurements. Flow convergence factors convert water and contaminant fluxes measured in an arbitrary layer of the PFM into estimates of respective undisturbed ambient fluxes (i.e., unaffected by the

presence of well and PFM). Using the results in combination with laboratory sand box experiments, effective conductivities of a well screen and another separation screen between layers are determined. With these conductivities, flow convergence factors for measuring water and uranium fluxes at a site in Rifle, CO, USA, are proposed.

Acknowledgements

This research was partially funded by the first author's fellowship of the Bahia State Science Foundation (FAPESB; DCR 0001/2009), Brazil, the U.S. National Science Program (award number 0804134), the Environmental Remediation Science Program (ERSP), U.S. Department of Energy (grant number DE-FG02-08ER64585), the U.S. Department of Defense (project number ER0831) under the Environmental Security Technology Compliance Program (ESTCP) and the Florida Water Resources Research Center under a grant from the U.S. Department of the Interior (Grant Number G11AP2007).

References

[1] ITRC, *Use and Measurement of Mass Flux and Mass Discharge. MASSFLUX-1*. Interstate Technology & Regulatory Council: Washington, D.C., 2010.
[2] Einarson, M.D., Mackay, D.M., Predicting impacts of groundwater contamination. *Environmental Science and Technology*, **35(3)**, pp. 66A-73A, 2001.
[3] Bockelmann, A., Zamfirescu, D., Ptak, T., Grathwohl, P. and Teutsch, G., Quantification of mass fluxes and natural attenuation rates at an industrial site with a limited monitoring network: a case study. *Journal of Contaminant Hydrology*, **60(1-2)**, pp. 97-121, 2003.
[4] Hatfield, K., Annable, M., Cho, J., Rao, P.S.C. and Klammler, H., A direct passive method for measuring water and contaminant fluxes in porous media. *Journal of Contaminant Hydrology*, **75(3-4)**, pp. 155-181, 2004.
[5] Annable, M., Hatfield, K., Cho, J., Klammler, H., Parker, B., Cherry, J. and Rao, P.S.C., Field-scale evaluation of the passive flux meter for simultaneous measurement of groundwater and contaminant fluxes. *Environmental Science and Technology*, **39(18)**, pp. 7194-7201, 2005.
[6] Klammler, H., Hatfield, K., Annable, M., Agyei, E., Parker, B., Cherry, J. and Rao, P.S.C., General analytical treatment of the flow field relevant to the interpretation of passive flux meter measurements. *Water Resources Research*, **43(4)**, W04407, 2007.
[7] Strack, O.D.L., *Groundwater Mechanics*, Prentice Hall: Englewood Cliffs, N.J., 1989.

Meridional flow of grounded abyssal currents on a sloping bottom in spherical geometry

G. E. Swaters
Applied Mathematics Institute, Department of Mathematical & Statistical Sciences and Institute for Geophysical Research, University of Alberta, Canada

Abstract

A steady nonlinear planetary-geostrophic model in spherical coordinates is presented describing the hemispheric-scale meridional flow of grounded abyssal currents on a sloping bottom. The model, which corresponds mathematically to a quasi-linear hyperbolic partial differential equation, can be solved explicitly for a cross-slope isopycnal field that is grounded (i.e., intersects the bottom on the up slope and down slope sides). The abyssal currents possess decreasing thickness in the equatorward direction while maintaining constant meridional volume transport and exhibit westward intensification as they flow toward the equator.

1 Introduction

Many of the abyssal currents in the oceans associated with the equatorward motion of deep water masses produced in high latitudes due to atmospheric cooling, are organized as mesoscale topographically-steered geostrophically-balanced grounded gravity currents that flow along sloping continental boundaries. These currents form an important component in the deep "leg" of the meridional overturning circulation in the oceans. The mesoscale dynamics of these currents has been described in a series of papers [1–11]. All of these studies have implicitly assumed either an f or β-plane approximation in which the dynamics is modelled in a Cartesian coordinate system with the implicit assumption that the horizontal length scales are not too much larger than the internal deformation radius (on the order of about 10–100 km in the ocean).

WIT Transactions on Engineering Sciences, Vol 74, © 2012 WIT Press
www.witpress.com, ISSN 1743-3533 (on-line)
doi:10.2495/AFM120281

However, the spatial extent of these abyssal currents is well known to be hemispheric in scale. This raises the question about the role of planetary sphericity in determining the large scale kinematic structure of these flows.

The principal purpose of this paper is to present a preliminary report on a simple, but nevertheless illuminating, reduced-gravity shallow-water model for the meridional, or equatorward, steady flow of grounded abyssal currents on a longitudinally-sloping bottom on a rotating sphere. A complete discussion of the dynamical properties as well as a specific oceanographically-relevant example of the solution briefly described here will be published elsewhere in a venue more suitable for research problems in geophysical fluid dynamics.

2 Model derivation

The reduced-gravity shallow-water equations for a stably-stratified abyssal water mass overlying variable bottom topography on a rotating sphere can be written in the form

$$u_t + \frac{uu_\lambda}{a\cos\theta} + \frac{vu_\theta}{a} - \frac{u\,v\tan\theta}{a} - 2\Omega\,v\sin\theta$$

$$= -\frac{g'}{a\cos\theta}\left(h + h_B\right)_\lambda, \tag{1}$$

$$v_t + \frac{uv_\lambda}{a\cos\theta} + \frac{vv_\theta}{a} - \frac{v^2\tan\theta}{a} + 2\Omega\,u\sin\theta = -\frac{g'}{a}h_\theta, \tag{2}$$

$$h_t + \frac{1}{a\cos\theta}\left[\left(h\,u\right)_\lambda + \left(h\,v\cos\theta\right)_\theta\right] = 0, \tag{3}$$

where u and v are the zonal (positive eastward) and meridional (positive northward) velocities, respectively, λ is the longitude (positive eastward) and θ is the latitude (positive northward), t is time, Ω is the angular frequency associated with Earth's rotation (2π rads/day), a is the radius of Earth (about 6300 km), $h\left(\lambda,\theta,t\right)$ is the thickness of the abyssal layer, $h_B\left(\lambda\right)$ is the longitudinally-varying height of the bottom topography above a constant reference depth and $g' = g\left(\rho_2 - \rho_1\right)/\rho_2 > 0$ is the (stably-stratified) reduced gravity where ρ_1 and ρ_2 are the densities of the (infinitely deep and motionless) overlying fluid and dynamically active abyssal layer, respectively, and g is the gravitational acceleration (9.81 m/s^2). Typical oceanographic values for the reduced gravity are in the range $10^{-4}-10^{-2}$ m/s^2. The *dynamic* pressure (i.e., the total pressure minus the hydrostatic pressure) in the abyssal layer is given by $p = g'\rho_1\left(h + h_B\right)$.

Further analysis is facilitated by introducing the scalings

$$\lambda = \frac{L}{a}\widetilde{\lambda},\; t = \frac{a}{V}\widetilde{t},\; u = \frac{LV}{a}\widetilde{u},\; v = V\,\widetilde{v},$$

$$\left(h, h_B\right) = \frac{2\Omega VL}{g'}\left(\widetilde{h}, \widetilde{h}_B\right),\; p = 2\Omega VL\rho_1\,\widetilde{p}, \tag{4}$$

into (1)–(3), yielding (after dropping the tildes)

$$\varepsilon\,\delta^2\left[u_t+\frac{uu_\lambda}{\cos\theta}+v\,u_\theta-u\,v\tan\theta\right]-\,v\sin\theta\,=$$

$$-\frac{1}{\cos\theta}\,(h+h_B)_\lambda\,, \tag{5}$$

$$\varepsilon\left[v_t+\frac{uv_\lambda}{\cos\theta}+v\,v_\theta-v^2\tan\theta\right]+\,u\sin\theta\,=-h_\theta, \tag{6}$$

$$h_t+\frac{1}{\cos\theta}\left[(h\,u)_\lambda+(h\,v\cos\theta)_\theta\right]=0, \tag{7}$$

where ε and δ are, respectively, the Rossby number and aspect ratio given by

$$\varepsilon=\frac{V}{2\Omega L}\text{ and }\delta=\frac{L}{a},$$

and where the dynamic pressure is given by

$$p=h+h_B.$$

Assuming typical scales [12] of

$$V\simeq 5\times10^{-2}\text{ m/s, }L\simeq10^5\text{ m and }g'\simeq3\times10^{-3}\text{ m/s}^2,$$

suggests that

$$\varepsilon\simeq3.4\times10^{-4}\text{ and }\delta\simeq1.6\times10^{-2},$$

with the additional scalings

$$\frac{a}{V}\simeq145\text{ days, }\frac{LV}{a}\simeq8\times10^{-4}\text{ m/s and }\frac{2\Omega VL}{g'}\simeq240\text{ m.}$$

Thus, to leading order in the Rossby number, the model reduces to

$$u\,=-\frac{1}{\sin\theta}h_\theta, \tag{8}$$

$$v\,=\frac{1}{\sin\theta\cos\theta}\,(h+h_B)_\lambda\,, \tag{9}$$

$$\sin^2\theta\,h_t+\tan\theta\,h_{B_\lambda}h_\theta-h\,h_\lambda=h_{B_\lambda}h. \tag{10}$$

Equations (8)–(10) corresponds to a planetary-geostrophic model in which the velocities are geostrophically determined but for which order-one dynamic variations in the thickness in the abyssal layer are permitted, i.e., the thickness field can intersect the bottom allowing for groundings. It is important to point out that the model is singular at the equator ($\theta=0$) and thus cannot be used to described inter-hemispheric or cross-equatorial flow. The dynamic pressure $p=h+h_B$ forms the geostrophic stream function for the flow as seen in (8) and (9).

3 Steady state solution

We briefly describe the equilibrium solution to the model (8)–(10) in which $h(\lambda, \theta)$ will be determined by the steady-state quasi-linear hyperbolic equation

$$\tan\theta\, h_\theta - \frac{h}{h_{B_\lambda}} h_\lambda = h. \tag{11}$$

The model (11) can be solved using the method of characteristics with the boundary condition

$$h(\lambda, \theta_0) = h_0(\lambda), \tag{12}$$

where θ_0 is a given reference latitude and $h_0(\lambda)$ is a prescribed abyssal height profile that varies only in the latitudinal direction.

The solution to (11) subject to (12) can be written in the form

$$h(\lambda, \theta) = \frac{\sin\theta}{\sin\theta_0} h_0(\tau), \tag{13}$$

$$h_B(\tau) + \frac{\sin\theta_0 - \sin\theta}{\sin\theta_0} h_0(\tau) = h_B(\lambda). \tag{14}$$

Given λ and θ, one solves (14) for $\tau(\lambda, \theta)$ and then determines $h(\lambda, \theta)$ from (13).

4 Some properties of the solution

The first thing to note is that the abyssal height monotonically decreases in the equatorward direction and in the limit as $\theta \to 0$, it follows from (13) that $h(\lambda, \theta) \to 0$.

The characteristics associated with the quasi-linear model (11) are the curves in (λ, θ)-space along which τ is constant, as determined by (14). Along these characteristic curves

$$\left.\frac{d\theta}{d\lambda}\right|_{\tau=\text{constant}} = -\frac{h_B'(\lambda)\sin\theta_0}{\cos\theta\, h_0(\tau)}. \tag{15}$$

We are interested in the physical situation where $h_B'(\lambda) < 0$ with $\theta > 0$ corresponding to flow in the northern hemisphere along a topographic slope in which the depth of the fluid increases as λ increases, i.e., eastward. This is a model for the equatorward flow of a grounded abyssal water masses along a continental slope on the western side of an ocean basin. In this situation the characteristics are, generally speaking, aligned in the southwest to the northeast direction since

$$-\frac{h_B'(\lambda)\sin\theta_0}{\cos\theta\, h_0(\tau)} > 0.$$

In fact, the characteristics correspond to the geostrophic streamlines. Equations (13) and (14) can be combined into the form

$$p(\lambda, \theta) \equiv h_B(\lambda) + h(\lambda, \theta) = h_B(\tau) + h_0(\tau). \tag{16}$$

Thus, when τ is constant, i.e., along a characteristic, the geostrophic stream function is constant and the characteristics coincide with the streamlines. The characteristics, therefore, describe the path lines in the flow and given the orientation of the characteristics associated with (15) when $h'_B(\lambda) < 0$ with $\theta > 0$, the equatorward flow is, generally speaking, moving in the northeast to the southwest direction as it is, nevertheless, topographically steered.

The corresponding velocity components, determined by (8) and (9) are given by, respectively

$$u(\lambda,\theta) = -\frac{[h'_B(\tau)+h'_0(\tau)]\,\tau_\theta}{\sin\theta}$$

$$= -\frac{\cot\theta\, h_0(\tau)\,[h'_B(\tau)+h'_0(\tau)]}{\sin\theta_0\, h'_B(\tau)+(\sin\theta_0-\sin\theta)\,h'_0(\tau)}, \tag{17}$$

$$v(\lambda,\theta) = \frac{[h'_B(\tau)+h'_0(\tau)]\,\tau_\lambda}{\sin\theta\cos\theta}$$

$$= \frac{\sin\theta_0\, h'_B(\tau)\,[h'_B(\tau)+h'_0(\tau)]}{\sin\theta\cos\theta\,[\sin\theta_0\, h'_B(\tau)+(\sin\theta_0-\sin\theta)\,h'_0(\tau)]}, \tag{18}$$

where (14) and (16) have been used. Observe that as $\theta \to 0$, both u and v become unbounded as a consequence of the fact that the geostrophic balance ((8) and (9)) breaks down at the equator. The meridional and zonal mass fluxes given by vh and uh, respectively, remain bounded over the entire domain (including at the equator).

Another general property of the solution is that the position of the groundings in the abyssal height field, that is, the location(s) where $h(\lambda,\theta)=0$, i.e., h intersects the bottom, are invariant with respect to θ once set by their location in the boundary condition (12). This means that throughout the domain the groundings will simply correspond to the fixed λ-values for which $h_0(\lambda)=0$. To see this suppose that a grounding in the solution occurs along the curve $\lambda = \widetilde{\lambda}(\theta)$ (allowing for a possible θ-dependence). It follows from (13) that

$$h\left(\widetilde{\lambda}(\theta),\theta\right) = 0 = \frac{\sin\theta}{\sin\theta_0} h_0\left(\tau\left(\widetilde{\lambda}(\theta),\theta\right)\right)$$

$$\Longrightarrow h_0\left(\tau\left(\widetilde{\lambda}(\theta),\theta\right)\right) = 0.$$

But it therefore follows from (14) that

$$h_B\left(\tau\left(\widetilde{\lambda}(\theta),\theta\right)\right) = h_B\left(\widetilde{\lambda}(\theta)\right) \Longrightarrow \tau\left(\widetilde{\lambda},\theta\right) = \widetilde{\lambda}, \tag{19}$$

since $h_0\left(\tau\left(\widetilde{\lambda},\theta\right)\right) = 0$. Thus, along a grounding we necessarily have $\lambda = \widetilde{\lambda}$ where $h_0\left(\widetilde{\lambda}\right) = 0$, i.e., the λ-location of a grounding is independent of θ and is set by the boundary data along $\theta = \theta_0$.

The fact that the meridional location of the groundings does not vary with latitude θ, together with the fact as previously established, that the streamlines are oriented in the northeast to the southwest direction (when $h'_B(\lambda) < 0$ with

$\theta > 0$) means that the flow exhibits a westward intensification, i.e., as the flow moves equatorward the streamlines shift westward or in the onshore or up slope direction. In fact, as shown below, it is possible, depending on the initial conditions for a "shock" to form in the solution on the western or up slope or western flank. The formation of such a shock could result in mixing on the up slope flank of the abyssal water mass as it propagates equatorward. This would be a decidedly different "instability mechanism" than baroclinic destabilization, which preferentially occurs on the down slope or offshore side of grounded abyssal currents [7, 8, 10].

The *net* meridional volume transport is also constant with respect to θ. Suppose that the abyssal current height $h_0(\lambda)$ is only nonzero in the region $\lambda_1 < \lambda < \lambda_2$, i.e., $h_0(\lambda_{1,2}) > 0$ only for $\lambda \in (\lambda_1, \lambda_2)$ with $h_0(\lambda_{1,2}) = 0$. The net meridional volume transport as a function of θ is given by

$$T \equiv \int_{\lambda_1}^{\lambda_2} h(\lambda,\theta)\, v(\lambda,\theta)\, \cos(\theta)\, d\lambda$$

$$= \int_{\lambda_1}^{\lambda_2} \frac{h\, (h+h_B)_\lambda}{\sin(\theta)}\, d\lambda$$

$$= \frac{1}{\sin\theta_0} \int_{\lambda_1}^{\lambda_2} h_0(\tau)\, [h_0(\tau) + h_B(\tau)]_\lambda\, d\lambda$$

$$= \frac{1}{\sin\theta_0} \int_{\lambda_1}^{\lambda_2} h_0(\tau)\, [h_0'(\tau) + h_B'(\tau)]\, d\tau$$

$$= \frac{1}{\sin\theta_0} \int_{\lambda_1}^{\lambda_2} h_0(\tau)\, h_B'(\tau)\, d\tau, \tag{20}$$

which is independent of θ, where (13), (14) and (19) have been used.

As discussed previously, the westward intensification of the streamlines or characteristics as the flow moves equatorward (when $h_B'(\lambda) < 0$ with $\theta > 0$) could result in shock formation on the western flank of the propagating abyssal water mass. The formation of a shock in the solution will correspond to the first θ-value (as θ decreases from $\theta_0 > 0$) where $|h_\lambda| \to \infty$ (assuming flow in the northern hemisphere with $h_B'(\lambda) < 0$). From (13) it follows that

$$h_\lambda = \frac{\sin\theta}{\sin\theta_0} h_0'(\tau)\, \tau_\lambda$$

$$= \frac{\sin\theta\, h_0'(\tau)\, h_B'(\tau)}{\sin\theta_0\, h_B'(\tau) + (\sin\theta_0 - \sin\theta)\, h_0'(\tau)}, \tag{21}$$

where (14) has been used. Thus, the shock will occur for the first value of $\theta \le \theta_0$ for which

$$\sin\theta = \left[1 + \frac{h_B'(\tau)}{h_0'(\tau)}\right] \sin\theta_0,$$

which we denote by θ_s, and is given by

$$\sin\theta_s = \left[1 + \max_{\tau}\left(\frac{h'_B(\tau)}{h'_0(\tau)} \mid h'_0(\tau) > 0\right)\right]\sin\theta_0,$$

where we assume $h'_B(\tau) < 0$. Should it be the case that

$$\max_{\tau}\left(\frac{h'_B(\tau)}{h'_0(\tau)} \mid h'_0(\tau) > 0\right) < -1,$$

then $\theta_s < 0$ and this is not physically relevant since the solution is singular at the equator $\theta = 0$ in any event and cannot be extended into the southern hemisphere where $\theta < 0$. Thus, the only physically relevant case is when

$$-1 < \max_{\tau}\left(\frac{h'_B(\tau)}{h'_0(\tau)} \mid h'_0(\tau) > 0\right) < 0.$$

In only this case is it possible that a shock forms on the up slope or western flank of the equatorward propagating abyssal water mass (in the northern hemisphere) and the potential for mixing by nonbaroclinic instability processes can develop. This is an interesting idea that requires further study.

5 Summary

A preliminary report on a simple, but nevertheless illuminating, reduced-gravity shallow-water model for the meridional, or equatorward, flow of grounded abyssal currents on a longitudinally-sloping bottom on a rotating sphere has been given. For oceanographically relevant parameter values it was shown that the abyssal layer height satisfies a quasi-linear hyperbolic equation with the velocities being geostrophically determined. The model corresponds to a planetary-geostrophic dynamical balance that permits the abyssal height field to intersect the bottom, i.e., a so-called grounding. Due to the fact that model is singular at the equator, it cannot be used to investigate cross-equatorial or inter-hemispheric flow.

The steady-state limit of the equation governing the abyssal layer height could be solved exactly. For a physical configuration corresponding to flow in the northern hemisphere on topography associated with increasing ocean depth in the eastward direction, the abyssal current flows equatorward from the northeast to southwest direction. The characteristics associated with the quasi-linear hyperbolic model were shown to be co-parallel with the geostrophic streamlines. It was shown that the groundings could not vary with latitude and are therefore set by the northern boundary condition. The meridional volume transport was shown to be independent of latitude. Finally, conditions for possible shock formation in the solution were established. If a shock forms, it is possible that this could lead to mixing on the up slope or western flank of these propagating abyssal water masses, which would be quite different than the instability and mixing associated with baroclinic destabilization. These and other issues require further study.

Acknowledgement

Preparation of this paper was partially supported by the Natural Sciences and Engineering Research Council of Canada.

References

[1] Choboter, P. F. & Swaters, G. E., Two layer models of abyssal equator crossing flow. *Journal of Physical Oceanography,* **33**, pp. 1401–1415, 2003.
[2] Choboter, P. F. & Swaters, G. E., Shallow water modeling of Antarctic Bottom Water crossing the equator. *Journal of Geophysical Research,* **109**, C03038, doi:10.1029/2003JC002048, 2004.
[3] Ha, S. J. & Swaters, G. E., Finite amplitude baroclinic instability of time varying abyssal currents. *Journal of Physical Oceanography*, **36**, pp. 122–139, 2005.
[4] Mooney, C. J. & Swaters, G. E., Finite amplitude baroclinic instability of a mesoscale gravity current in a channel. *Geophysical and Astrophysical Fluid Dynamics,* **82**, pp. 173–205, 1996.
[5] Poulin, F. J. & Swaters, G. E., Sub-inertial dynamics of density-driven flows in a continuously stratified fluid on a sloping bottom. I. Model derivation and stability conditions. *Proceedings of the Royal Society of London A*, **455**, pp. 2281–2304, 1999.
[6] Reszka, M. K., Swaters, G. E. & Sutherland, B. R., Instability of abyssal currents in a continuously stratified ocean with bottom topography. *Journal of Physical Oceanography,* **32**, pp. 3528–3550, 2002.
[7] Swaters, G. E., On the baroclinic instability of cold-core coupled density fronts on sloping continental shelf. *Journal of Fluid Mechanics,* **224**, pp. 361–382, 1991.
[8] Swaters, G. E., Nonlinear stability of intermediate baroclinic flow on a sloping bottom. *Proceedings of the Royal Society of London A*, **442**, pp. 249–272, 1993.
[9] Swaters, G. E., Numerical simulations of the baroclinic dynamics of density-driven coupled fronts and eddies on a sloping bottom. *Journal of Geophysical Research*, **103**, pp. 2945–2961, 1998.
[10] Swaters, G. E., On the meridional flow of source-driven abyssal currents in a stratified basin with topography. Part I. Model development and dynamical characteristics. *Journal of Physical Oceanography*, **36**, pp. 335–355, 2006.
[11] Swaters, G. E., On the meridional flow of source-driven abyssal currents in a stratified basin with topography. Part II. Numerical Simulation. *Journal of Physical Oceanography*, **36**, pp. 356–375, 2006.
[12] Swaters, G. E., Mixed bottom-friction-Kelvin-Helmholtz destabilization of source-driven abyssal overflows in the ocean. *Journal of Fluid Mechanics*, **626**, pp. 33–66, 2009.

The Italian Data Buoy Network (RON)

M. Bencivenga[1], G. Nardone[1], F. Ruggiero[2] & D. Calore[2]
[1]*ISPRA - Italian Institute for Environmental Protection and Research, Rome, Italy*
[2]*Envirtech S.p.A., Venice, Italy*

Abstract

The *Italian Data Buoy Network* consists of 15 oceanographic buoys, deployed along Italian coasts, on a seabed 100 meters deep. It collects directional sea wave data, meteorological data, sea surface temperature and in some cases quality parameters. Acoustic Doppler Current Profilers (ADCP) and hyperspectral probes will be added in the future. The network will be also the main framework for tsunami wave study in the central Mediterranean Sea, and an early technological platform to study low-frequency sea motion detected in open sea using high-precision, multichannel, multisatellite GPS/Glonass/Galileo receivers and sea bottom instrumentation equipped with nano-resolution pressure sensors.
Keywords: data buoys, coastal management, directional wave measurement, gravity waves, physical oceanography, iSSH, SST, tide, tidal waves, tsunami.

1 Introduction

The Italian Data Buoy Network (RON) owned and managed by ISPRA, was completely redesigned by Envirtech in 2009 to acquire more oceanographic parameters and to increase nautical capabilities, reducing accidental buoy adrift events. The network goals comprise the Mediterranean Tsunami Assessment System (MeTAS) project. Since 1989, a network has been in place along Italian coasts, but this was only able to measure directional sea waves and sea surface temperature. It consisted of eight 'slope-following' *Datawell Wavec buoys*, and was called the *Rete Ondametrica Nazionale* (RON). It was a semi-real-time network with reduced capabilities in terms of prompt data accessibility, as only a small part of the collected data was available at the control centre. All data were stored at shore stations and manually downloaded on a quarterly basis using magnetic disks. In 1999, the number of buoys was increased to 10, introducing


WIT Transactions on Engineering Sciences, Vol 74, © 2012 WIT Press
www.witpress.com, ISSN 1743-3533 (on-line)
doi:10.2495/AFM120291

two more *Datawell Waverider buoys*; furthermore, the data management system was centralised and upgraded to real-time. In 2002, all buoys were changed to 'particle-following' *Triaxys*, and the number of buoys was increased to 14. A new Control Centre architecture was introduced to maintain a stable, fault-tolerant SQL database to centralise all measures and to generate easier data access and processing. The *Triaxys* network was in place until 2009, when a completely renewed network was deployed based on 15 new *Watchkeeper buoys*, using the same sensor technology (Triaxys).

2 Network description

Figure 1 shows the buoys' positions along Italian coasts.

Figure 1: Buoys' location.

Buoys transmit data to shore stations within 15 NM and a small dataset via Inmarsat. All shore stations are connected to the control centre based in Rome, using 2 Mbps xDSL channels, implementing a virtual private network. Users can

access data via the Web, GTS, the Italian Broadcast Teletext Service (Rai-1 televideo) and via scheduled FTP uploads. At the control centre, a server array based on six quad-processors nodes, in a cluster configuration, processes and stores all data collected using a Microsoft SQL Server.

Table 1 shows the shore stations names, the buoys' positions and sea bottom depths.

Table 1: Buoys' coordinates and sea bottom depth.

BUOY CODE	SHORE STATION	LATITUDE	LONGITUDE	Depth (meters)
61207	CATANIA	37°26'24'N	15°08'48'E	90
61208	MAZARA	37°31'05'N	12°32'00'E	85
61209	PALERMO	38°15'30'N	13°20'00''E	145
61210	CROTONE	39°01'25'N	17°13'12'E	80
61211	CETRARO	39°27'12'N	15°55'06'E	100
61212	SINISCOLA	40°37'00'N	09°53'30'E	130
61213	ALGHERO	40°32'55'N	08°06'25'E	85
61214	PONZA	40°52'00'N	12°57'00'E	115
61215	MONOPOLI	40°58'30'N	17°22'40'E	85
61216	CIVITAVECCHIA	42°14'41'N	11°33'14'E	62
61217	ORTONA	42°24'24'N	14°32'12''E	72
61218	ANCONA	43°49'26'N	13°43'10'E	70
61219	LA SPEZIA	43°55'45'N	09°49'40'E	85
61220	VENEZIA	45°20'00'N	12°31'00'E	17
61221	CAGLIARI	39°06'54'N	09°24'18'E	150

2.1 Network goals

According to Shih [1], surface gravity waves provide the principle energy inputs related to many near-shore processes such as longshore currents, changes in beach profiles and the longshore transportation of sand. Further interest in coastal wave information comes from environmental managers, the engineering and scientific communities and maritime commerce.

It has been found that surface wave observations and forecasts are usually one of the top three variables requested or used by marine users. The other two variables are surface winds and currents. Moreover, waves have number three priority under physical observations, following temperature and salinity.

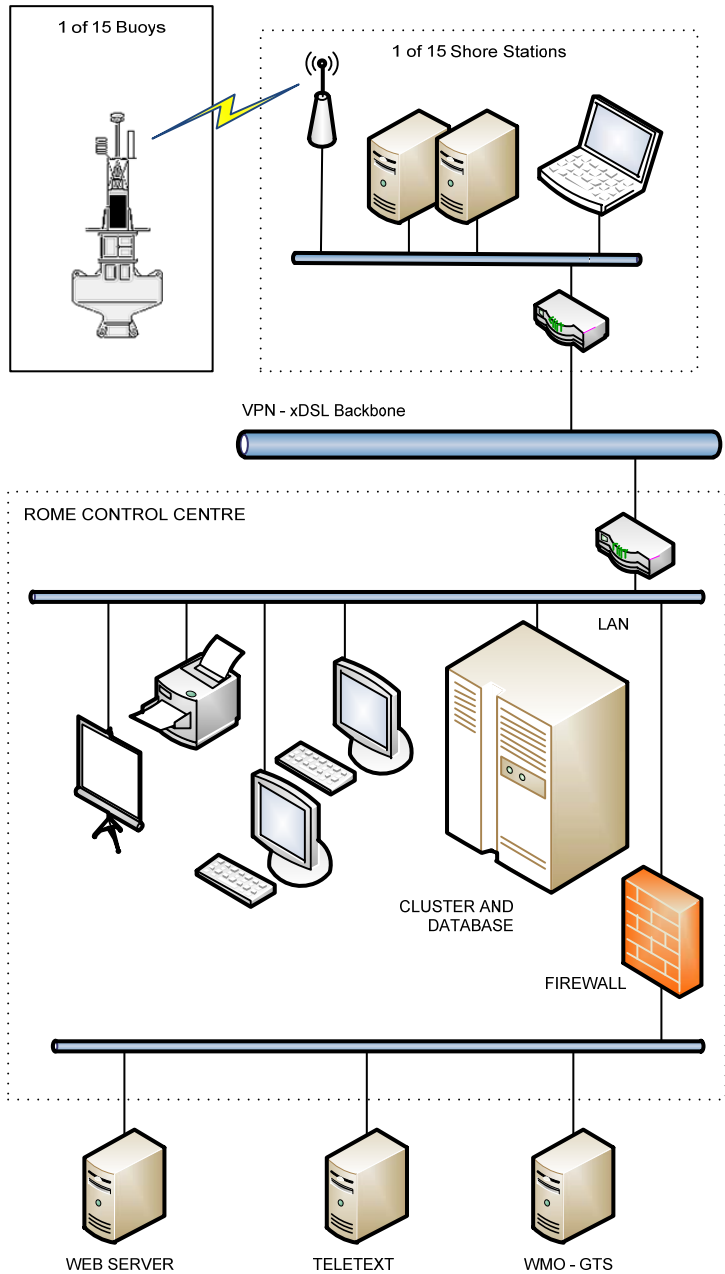

Figure 2: Network scheme.

Further applications include wave nowcast/forecast model verification, determining marsh restoration and shore erosion, hazardous material spill response, assessing coastal storm induced flooding, engineering design and construction, dredging, ship routing and scheduling, cargo loading and unloading and recreational boating.

The new Italian Data Buoy Network was designed with the above-mentioned priorities in mind, and new buoys were acquired to implement the following measurements:

- Directional sea waves
- High-accuracy Sea Surface Temperature (SST) and salinity
- Meteorological parameters like wind speed and direction, air temperature and barometric pressure.

New buoys have been equipped with a special *moon-pool* to improve the implementation of quality multiparameter probes and Acoustic Doppler Current Profiler (ADCP).

The redesign of the data management architecture, as well as the implementation of a shore station network that is well connected to the control centre located in Rome, will allow for the further increase of data buoys and sensors to monitor low-frequency sea motion, including infragravity waves, to be measured in open sea using GPS buoys and nano-resolution pressure transducers deployed on the sea bed. According to Webb *et al*. [2], tsunamis are large-amplitude infragravity waves generated by the displacement of the seafloor during earthquakes or because of landslides. Since 2002, after the Stromboli Volcano Tsunami Event, the authors started to project and build a new class of underwater modules, called the 'Vulcan Class', which are able to collect both high-resolution pressure data and seismic waves in real-time. The device was the leading part of the MeTAS project, after the Tsunami Event in the Indian Ocean. Figure 3 shows all the data that will be collected by the network within the next five years. At present, Surface Gravity Waves, SST and meteorological measurement data are being taken. By the end of the year, the first Envirtech MKIII buoy [3], for the study of very low frequency waves will be moored. At present, an MKI-2 [4] is under testing for tide measurements in open sea and biochemical data collection.

2.2 Nautical capabilities of buoys

After the first five years of network operation, it was clear that having four or five buoys off-mooring every year was acceptable in consideration of the very high level of fishing boat traffic. This means more or less one buoy adrift episode for each two buoys moored per year. Buoys adrift and vandalization are well recognized problems worldwide as reported by Teng *et al.* [5] and highlighted by the Data Buoy Cooperation Panel (DBCP).

Unfortunately, the small dimensions of Triaxys and Waverider hulls did not fulfil the necessary nautical capabilities, taking into account the increased fishing boat traffic revealed during the first years of the 21st century. In 2001–2003, the

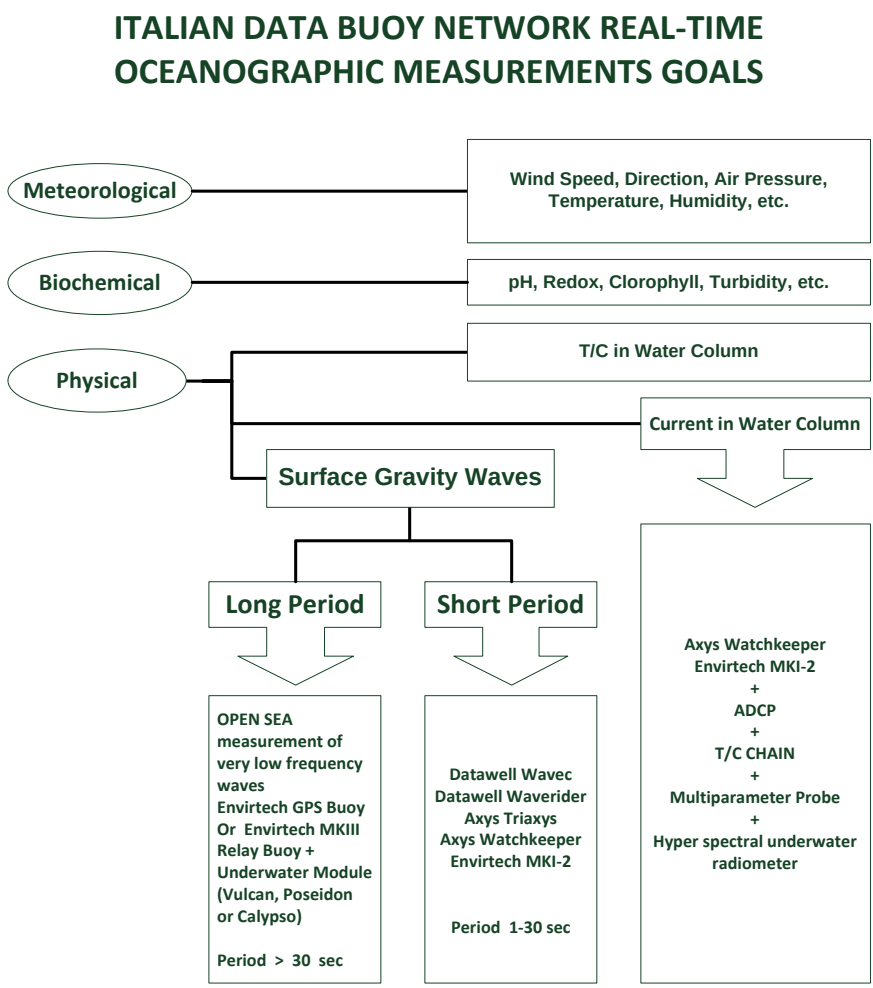

Figure 3: Network goals.

data buoy network, based on 15 Triaxys buoys, reported about 100 off-mooring cases (more than two adrift events per moored buoy per year), mainly due to fishing boats or acts of vandalism. As a consequence, the network produced a very low volume of data.

To address this unplanned adrift rate, in 2005, experimentation began regarding the use of bigger buoys with good nautical capabilities in terms of stronger mooring and visibility, but with acceptable sea wave measurement accuracy at the same time. The Watchkeeper buoys from Axys were chosen. These buoys have proven hull visibility in any condition, and embed the same payload as Triaxys buoys. The experiment consisted of mooring a Triaxys buoy and a Watchkeeper buoy sufficiently close to one another and collecting the same data from both of them, which was sampled at 4 sps for one year.

The test showed acceptable compatibility in the period range of 2–15 seconds, and the new buoys were proposed as potential substitutes for Triaxys buoys in the network.

2.3 Data Buoys in the Italian Network

One of the very basic requirements of a data buoy network is to maintain as many buoys as possible in position for a long time to collect an uninterrupted, good-quality data series. This goal can easily be reached in sea water that is not crossed by too many fishing boats or vandals. Unfortunately, this is not the standard situation in Italian seas or, generally speaking, in Mediterranean coastal waters. Moreover, to collect an accurate sea wave series, it is mandatory to ensure that the buoy hulls are as small as possible. This further condition conflicts with the requirement of having good visibility (night and day) to avoid collisions, and is the main issue that needs to be addressed to create a stable data buoy network.

To find the best performat buoy, in terms of accuracy and nautical capabilities, in the last 15 years, the authors have tested many buoys from different manufacturers. To better understand the differences between all available systems, the principal method of collecting directional sea wave data using buoys is now briefly described.

2.3.1 Slope-following buoys

Heave-pitch-roll buoys such as the old Wavec and Fugro Oceanor Wavescan.
Advantages: The buoys have great dimensions. This was the only available way to measure waves in open sea until the 1990s.

Disadvantages: The hull and mooring system are expensive; accurate measurement requires that the buoy be designed to follow the water's surface and ensuring that the accelerometer remains vertical. The cardanic suspension of the heave sensor could results in many mechanical faults as a consequence of impact during land transportation and small collisions at sea.

2.3.2 Small Particle-following buoys

These include Waverider and Triaxys.

Typically spherical shape; use a compliant mooring system; the Waverider sensing package consists of a gyroscopically stabilised platform, accelerometers (heave), surface slope (pitch and roll) and a compass.

The Triaxys sensing package consists of accelerometers, rate gyros and a compass.

Advantages: Less expensive; very high accuracy; widely used.

Disadvantages: Susceptible to theft, vandalism and damage from shipping; could be overturned by steep breaking waves (this often occurs in shallow waters less than 8 m); accurate measurement requires that the buoy be designed to follow water particles; accuracy degrades in the very highest waves or short crest seas, and measuring nonlinear wave properties.

2.3.3 Big Particle-following buoys

These include Watchkeeper and Envirtech Deep Sea MKI-2 buoys.

To address the issues related to the small dimensions of Triaxys buoys, a class of medium displacement buoys has been developed (by Axys Canada and Envirtech Italy), embedding inertial platform sensors. In these buoys, the transfer function is very important to assure a good response in frequency over the classical frequency band; the hull shape also has a relevant impact on the accuracy of wave height measurement.

To increase the accuracy of sea wave measurement, in 2000, Triaxys buoys were introduced to substitute for Datawell Wavec and Waverider buoys.

As mentioned, Triaxys buoys, like the Datawell Directional Waverider buoys, the Watchkeeper and the Envirtech Deep Sea MKI-2, are 'particle-following' buoys that measure the water particle motion in three orthogonal directions. While Axys and Envirtech sensors work similarly to one another, the wave-measuring techniques of the Waverider are different.

The Triaxys buoy uses three accelerometers to measure total accelerations along the mutually orthogonal X, Y, Z axes of the buoy; three angular rate sensors to measure rotation rates about the roll, pitch and yaw axes; and a gimbaled compass to measure sensor heading. An algorithm for a six-degrees-of-freedom non-linear equation of motion of the sensor and the Maximum Entropy Method (Kalman filter) are used to derive wave height and directional frequency spectra. In comparison, the Waverider buoy uses heave-pitch-roll sensors, two horizontal hull-fixed accelerometers and a compass to determine directional wave information.

Starting in 2009, the new network has been composed of Watchkeeper buoys. In 2011, an Envirtech buoy, Deep Sea MKI-2, was introduced to the network to collect more sea water quality data and to test high-precision, multichannel, multisatellite receivers to implement instantaneous Sea-Surface Height (iSSH) measurement in open sea and to start a comparative test with the Watchkeeper buoys. The new buoy is in addition to the next deployment of Envirtech MKIII Tsunami Buoy, which have been built to study very low frequency sea motion within the MeTAS project, which began in 2005.

3 Directional wave data acquisition and processing

Since the year 2000, it has been clear that a permanent data buoy network should be built to allow for data acquisition from sea wave measurement payloads produced by different manufacturers.

It was decided to implement new, manufacturer-independent wave data management architecture to allow for the use of any buoy available on the market. This should also use an open format to access raw data collected directly by the sensors with little or no post-processing.

The data acquisition architecture is shown in Figure 4.

Basically, any manufacturer implements software to process data starting from the sensor up to the final result. For many reasons, the software runs within the payload on board the buoy, and only the final result is transmitted to the

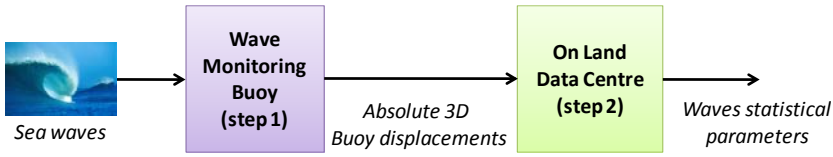

Figure 4: Data acquisition architecture.

control centre. Because of the different algorithms implemented, the results are not always completely cross-comparable; in particular, directional spectral analyses could give different results.

In the new network architecture, the measurement chain has been split into two flows: one on board the buoy, on charge to the manufacturer software, and the other at the control centre. In this way, the independent maintenance of the second process, independent from the specific buoy, has been assured. To address the goal, manufacturers have been requested to implement the supply, in addition to their data and calculations, time domain data files containing the following information for each record: sample time, Heave, Displacement North-South and Displacement East-West. These data are acquired with the maximum available data sample rate, and further decimated to comply with the network standard of 1,536 samples spaced at 0.78 seconds. The file, transmitted to shore stations every 30 minutes has been named HNE displacement file.

Figure 5 shows the first data process on board an Envirtech MKI-2 buoy. It is similar to the data processing of Triaxys sensors.

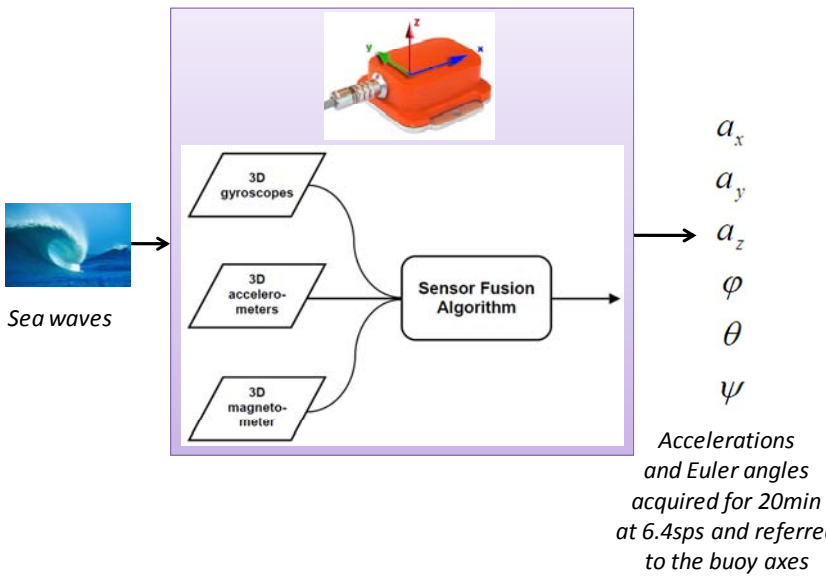

Figure 5: First data process on board the buoy.

The sensor is programmed to produce accelerometric samples (three accelerations and three Euler angles) with a rate of 6.4 sps. In the Italian network, 20 minute series are collected every 30 minutes.

The technique used to produce a motion history from these data consists of the following steps:

- Acquiring data for 20 minutes
- Preprocessing raw data (filtering, anti-spike, etc.)
- Finding the rotational matrix
- Finding the inertial accelerations
- Applying a mirror to the last samples to obtain a 2^N sample vector
- Applying the Hamming window
- Applying band-pass filtering in the frequency domain
- Double-integrating accelerations to obtain the motion history.

These steps are explained in detail in Figures 6 and 7.

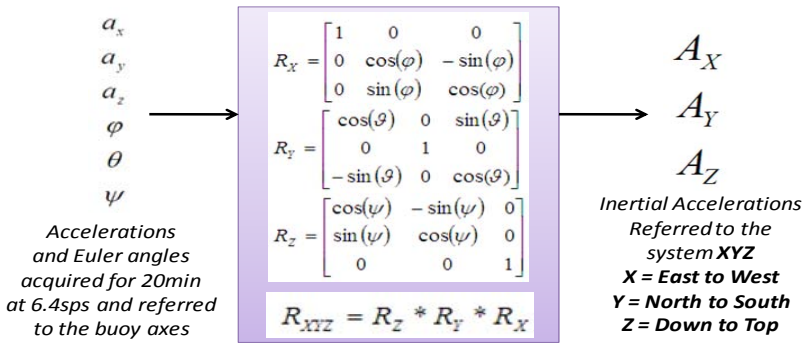

Figure 6: Reference system transformations to get the inertial accelerations.

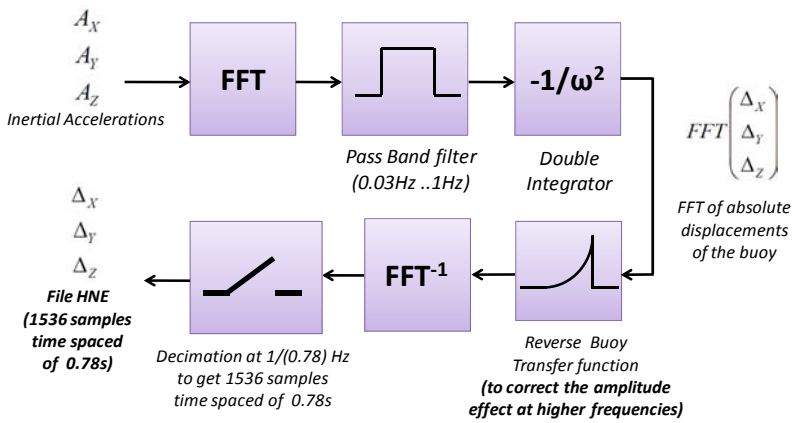

Figure 7: Processing steps to get buoy displacements in the frequency domain, correction of buoy characteristic effect, passage to the time domain and decimation to get HNE data file.

3.1 Manufacturer-independent open architecture HNE processing

The next illustrations show the calculation chain implemented at the Control Centre, which is able to transform the above-mentioned HNE files received from the buoy each 30 minutes to the final statistical data output and directional power spectra. Modelling the HNE sequences as ergodic stochastic signals, it is possible to get related auto, cross and quadrature spectral correlations with the following relationships where $\Im_X$, $\Im_Y$ and $\Im_Z$ are the Fourier transformations of the displacements in the HNE data file:

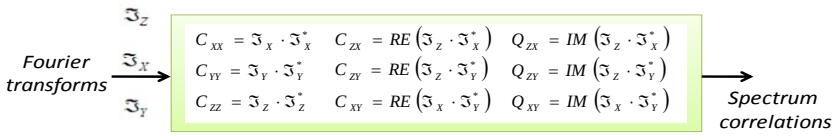

The spectrum correlations allow us to get the typical waves statistical parameters with the following formulas:

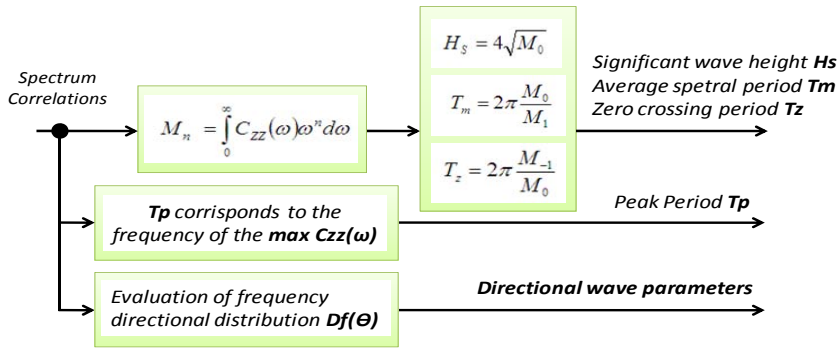

The frequency directional distribution $D_f(\theta)$ provides for each frequency the wave probability distribution along the direction range [0, 2π]. We refer to Kahama *et al.* [6] for the derivation of $D_f(\theta)$ that assumes $D_f(\theta) = E(f,\theta)/C_{zz}(f)$ where $E(f,\theta)$ is the energy directional spectrum and $C_{zz}(f)$ the elevation auto-spectrum also called energy density: it is possible to get $D_f(\theta)$ with the following approximation:

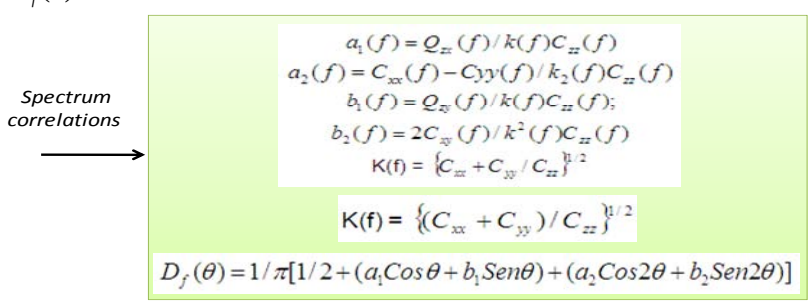

The mean propagation direction for frequency band is obtained as:

$$\theta_0(f) = \arctan(b_1(f)/a_1(f))$$

It is clear to the user that the energy directional spectrum $E(f,\theta)$ allows to get all statistical parameters of the wave as function of the period and direction. It contains all information related to the wave data collected.

4 Conclusions

In this paper, the state-of-the-art Italian Data Buoy Network has been described, along with further improvements planned for the next five years. Collected data are accessible via GTS, Web [7] and Televideo-RAI teletext service [8]. The network capabilities will be extended to infragravity wave measurement and biochemical data gathering. The manufacturer-independent data processing algorithm implemented at the Control Centre in Rome was also described; this allows for experimentation on all devices available on the market while maintaining the legacy data structure.

References

[1] Shih, H.H., Triaxys Directional Wave Buoy for Nearshore Wave Measurements - Test and Evaluation Plan, NOAA Technical Report NOS CO-OPS 38, Silver Spring, Maryland, Jan 2003.
[2] Spahr C. Webb, X.Zhang, W.Crawford, Infragravity Waves in the Deep Ocean, Journal Of Geophysical Research, Vol. 96, No.C2, Pages 2723-2796, February 15, 1991.
[3] Envirtech Tsunami Warning System: Technical Specifications of Surface Buoy. Doc 20003-SPE-200.0 – Venice February 15, 2011, Envirtech S.p.A., Italy.
[4] Envirtech Deep Sea MKI-2 Directional Wave buoy – Technical Specification. Doc 21004-001.1 – Venice March 1, 2010 Envirtech S.p.A., Italy.
[5] C.C. Teng, S.Cucullu, S. McArthur, C. Kohler, B. Burnett, L. Bernard, Buoy Vandalism Experienced by NOAA National Data Buoy Center, June 2010, Office of Naval Research, 875 N. Randolph St., Arlington, VA 22203-1995.
[6] Kahma, Hauser, Krogstad, Lehner, Monbaliu, Wyatt, 2005. Measuring and Analysing Directional Spectra of Ocean Waves, COST Action 714, Bruxells.
[7] The Italian Data Buoys network web site: www.telemisura.it
[8] Rete Ondametrica Nazionale, Pag. 719 – Televideo Rai-1.

Section 5
Turbulent flow

This page intentionally left blank

PIV measurements on the formation of the flow field and aerosol particle distribution in a turbulent square duct flow

T. Barth, M. Banowski & U. Hampel
Institute of Safety Research,
Helmholtz-Zentrum Dresden-*Rossendorf e.V., Germany*

Abstract

The formation of the flow field and spatial aerosol particle distribution play an important role in various industrial applications. Regarding experiments on aerosol particle transport phenomena in turbulent flows it is of essential interest to generate a homogeneously mixed air stream. Particle Image Velocimetry (PIV) measurements have been conducted in order to characterize the turbulent mixing process in a small-scale gas/aerosol test facility which is designed for the investigation of deposition and resuspension of nuclear aerosol particles. The turbulent flow field in a square duct (Re_d = *8.9k..43k*) is seeded with DEHS droplets in the size range of approximately d_{Paero} = *2 µm*. Firstly, the downstream formation of particle mixing is quantified in terms of the spatial distribution of the scatter light intensity of the PIV images. It is found that sufficient mixing of the aerosol particles is accomplished at *8* to *10* hydraulic diameters downstream of the injection point. Furthermore, the formation of the flow field is evaluated in terms of the time mean averaged velocity as well as velocity fluctuations. These values are presented at successive downstream positions and display the development of the turbulent boundary layer. It is shown that the near wall turbulent region of the test section nicely follows the universal slope of a well developed turbulent boundary layer. Nevertheless, the flow field formation still takes place after *20* hydraulic diameters.
Keywords: aerosol particles, particle image velocimetry, turbulent flow, quadrant count method.

WIT Transactions on Engineering Sciences, Vol 74, © 2012 WIT Press
www.witpress.com, ISSN 1743-3533 (on-line)
doi:10.2495/AFM120301

1 Introduction

The nature of turbulent flows in stacks and ducts has been comprehensively explored in the past by all kinds of scientists but is not yet fully understood. Huser and Biringen [4] described the nature of turbulent duct flow as a mean flow, which is superimposed by eight counter rotating edge vortices. They performed a direct numerical simulation at a bulk Reynolds number of *10320*, which displays the interaction between corner near-wall effects and the distortion of the mean flow field. Quadrant analysis of the instantaneous turbulent structures shows a dependency between the stress-driven secondary flow field with respect to pressure-strain and velocity-pressure gradient correlations.

Another direct numerical simulation of a turbulent duct flow at Reynolds number of *6000* was done by Nikitin [5] who focussed on the characterization of near-wall turbulence statistics. Comparison of the time mean averaged flow field between Nikitin's data and present results show relatively good agreement.

Recently, Winkler *et al.* [10] performed a Large Eddy Simulation (LES) of a turbulent square duct flow at Reynolds numbers of *360* based on the friction velocity. It is shown that aerosol particles tend to accumulate in regions of low vorticity magnitude. Nevertheless, the time mean averaged flow field is in good agreement to the present results with respect to the state of flow formation.

In this work, Particle Image Velocimetry (PIV) measurements have been conducted in a new small-scale gas/aerosol test facility whose results will be presented hereafter. For experimental studies, it is of essential importance to understand how well developed the flow field in the test section of a facility is. Unknown flow disturbances due to flow formation processes may have a crucial impact on the quality of the experimental results. Thus, the state of flow development and particle mixing in the present facility are quantified experimentally. The experiments have been conducted in an air driven wind tunnel, which is specifically designed for the investigation of the transport behaviour of nuclear aerosol particles. The flow field is recorded successively at different downstream positions and Reynolds numbers. Analysis of scattered light intensity distribution of the PIV raw data images by means of quadrant count techniques characterizes the particle mixing process. It is shown that the aerosol particles are homogeneously distributed *8* hydraulic diameters downstream of the injection point which is in good agreement to published data (Cohen [2]). The flow field formation is illustrated in terms of time averaged velocity plots in channel centre section. It will be shown that the velocity profiles nicely approach existing numerical data approximately after *40* to *50* hydraulic diameters. However, the turbulent boundary layer is in excellent agreement to results from direct numerical simulations.

2 Experimental setup

The facility is an air driven open loop wind tunnel in suction mode. The inlet of the tunnel is equipped with a HEPA for air cleaning purposes. Afterwards, a nozzle contracts the flow into a *10 x 10 cm²* square duct formation zone of *15*

diameters length. The test section is located downstream of the flow formation zone and has a length of *5* hydraulic diameters. Both the formation zone and test section are made of Plexiglas in order to allow optical access. Finally, the particle laden air stream is decelerated in a diffuser stage and filtered by an electrostatic precipitator before entering a radial fan at the outlet of the facility.

Aerosol particles, which are used as PIV seeding, are made of DEHS by means of a Condensation Aerosol Generator SLG 270 and injected into the flow upstream of the flow formation zone. The aerodynamic diameter of the aerosol particles was measured using an Aerodynamic Particle Sizer Spectrometer (TSI, APS 3321) and isokinetic sampling ($d_{P,aero} = 2\ \mu m$).

The LaVision 2C2D-PIV system consists of a Nd:YAG double pulse laser source (New Wave Gemini 200-15) and a CCD camera (Imager intense, *1376 x 1040 pxl*) focusing normal to the laser sheet as further described in Raffel *et al.* [8]. Both, the laser and the camera are mounted on a 3D linear traversing system in order to record the flow field at different downstream positions using the same calibration. The double frame, double exposure technique is used and the images have been processed with LaVision DaVis 7.

The signal-to-noise ratio of the images is increased substantially by calculating the mean pixel-image of a data set and then subtracting it from every individual image. This eliminates background noise, e.g., due to scatter light reflections. The images were then cross-correlated. As correlating attributes were chosen an interrogation window size of *32 x 32 pixels* at positions $x = [1,3,5]d$ and *16 x 16 pixels* further downstream due to more homogeneous mixing of the tracer particles. The images were correlated with *75%* overlap. Thereby the spatial resolution of the velocity field was about *0.4* down to *0.2 mm* per interrogation frame. According to Prasad *et al.* [7], the relative uncertainty of the velocity is about *4%* of the measured value. *400* sections were recorded and time averaged to have sufficient statistical convergence of the turbulent flow field.

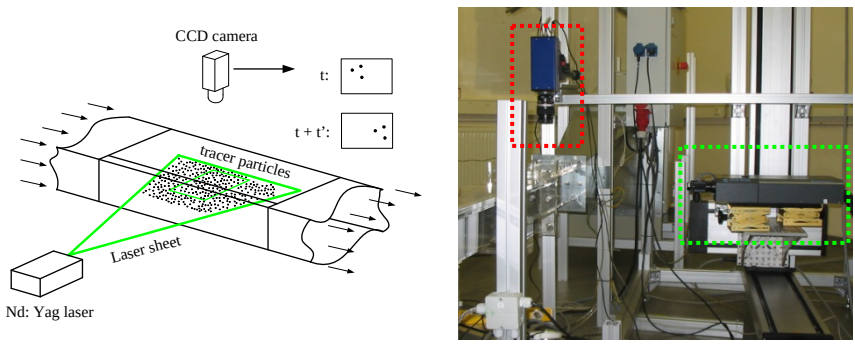

Figure 1: Left: general setup of 2C2D PIV system (Raffel *et al.* [8]), right: test section including Nd:YAG laser (green) and CCD camera (red).

3 Results

3.1 Spatial distribution of aerosol particle mixing

The quality of the PIV data is mainly influenced by an evenly distributed tracer material, which is illuminated by two well aligned laser sheets. At the entrance to the flow formation zone, the tracer particles are irregularly distributed, as can be seen in Figure 2. PIV raw image data display the kind of vortex shedding in the wake of the particle injection nozzle. Particles tend to accumulate in the vicinity of the vortices. Eventually the turbulent mixing leads to a homogeneous spatial distribution of the tracer particles in the downstream region. This process is quantified by spatial point pattern analysis using quadrant count method (Diggle [3]).

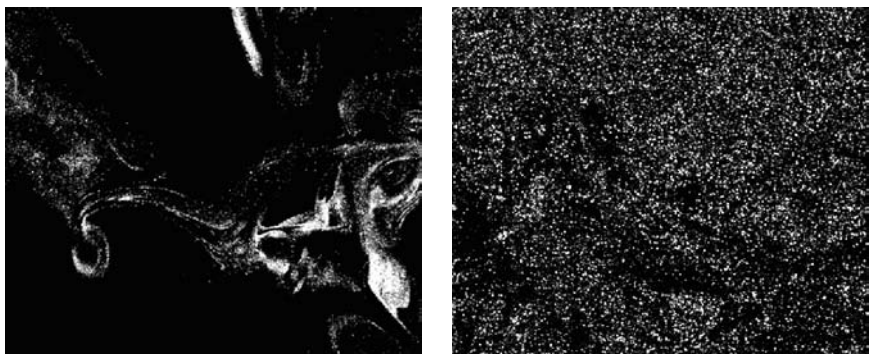

Figure 2: PIV raw data images, left: $x = 1d$, right: $x = 17d$.

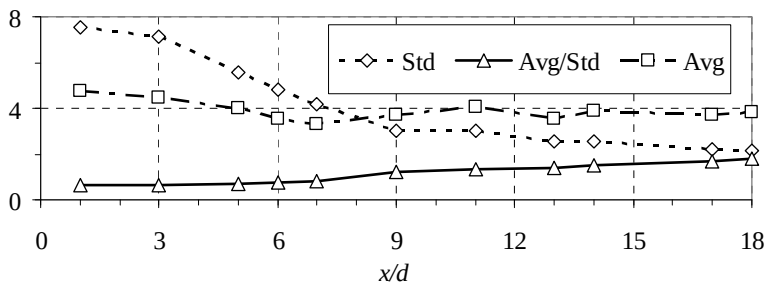

Figure 3: Downstream formation of particle distribution and concentration in terms of scatter light intensity.

The PIV raw images are post processed by means of Image J. *50* snapshots are uploaded and discretized into *40 x 32* interrogation windows. Then, the stack of *50* images is treated with a threshold to suppress optical noise and mean average of particle light intensity (*Avg*), as well its standard deviation (*Std*) are evaluated. The standard deviation of particle light intensity decreases

continuously from *7.5* down to *2.13* which is probably the result of continuous turbulent mixing downstream.

The average light intensity between inlet and test section decreases slightly to about *20%* which might be induced by the deposition of the tracer particles at the channel walls. Assuming that there is constant light sheet intensity, the downstream gradient average light intensity might be a parameter, which could be used in order to quantify particle deposition rates. Nevertheless, normalizing the mean average particle light intensity (*Avg*) by standard deviation (*Std*) leads to a particle number independent value for the correct assessment of spatial distribution. The ratio *Avg/Std* increases from *9%* at *x/d = 1* to about *49%*, but the uptake from *x/d = 9 to 18* reduces to *31 %*. According to that change, the tracer particles are roughly well distributed after *8* hydraulic diameters, but there is still progress in the mixing process due to particle deposition and turbulent mixing. However, the aerosol particles seem to be evenly distributed *8* hydraulic diameters downstream of the injection point, which is in good agreement with the empirical values of Cohen [2] who also stated that homogeneously mixing is evident after *5* to *8* hydraulic diameters downstream of a disturbance.

3.2 Formation of the velocity field

The development of the flow field is illustrated in terms of non-dimensional velocity plots across the channel centre plane at different downstream positions. The time-averaged mean velocities, as well as its fluctuations are computed from *400* instantaneous velocity fields (Figure 4).

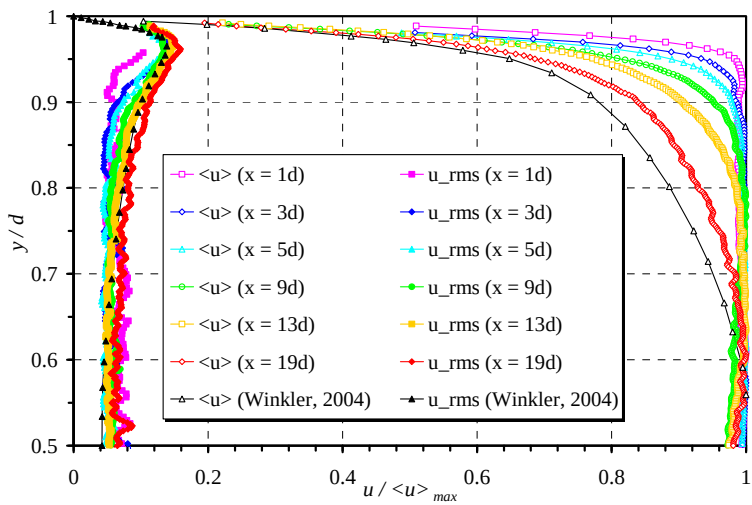

Figure 4: Time mean averaged velocity profiles and root mean square values across channel centre plane at $Re_d = 8.9k$.

The velocity profile at *x = 1d* (magenta line) is considerably sharp, whereas the slope with increasing downstream position continuously changes to a well-

curved profile. Note that the development of the flow has not yet been completed at $x = 19d$ (red line).

There is a slight shift of $<u>_{max}$ to $y/d = 0.6$, but $<u>_{max}$ should usually be in channel centre. One possible reason for this is the asymmetric injection of the tracer particles in order to concentrate the tracer particles in the measurement area. The SLG 270 is driven by a N_2 gas flux of about $dV/dt = 150$ l/h, which is a contribution to the overall volume flux in the test section of approximately 1%. However, the time-averaged mean velocity profiles seem to approach the slope of LES data published by Winkler *et al.* [10]. It is assumed that this approach might be approximately finished after 20 hydraulic diameters further downstream.

The profiles of the root mean square velocities in Figure 4 match the data of Winkler *et al.* [10]. The slope of u_{rms} corresponds to the slope of Winkler's data at a downstream position of $x = 3d$. The maximum of $u_{rms}(x = 3d)$ in the near-wall region is nicely reproduced. Further downstream the magnitude of u_{rms} overshoots the level of Winkler (Winkler *et al.* [10]), which might be an effect of higher wall roughness and surface irregularities of the experimental facility.

The velocity fluctuations could not be resolved in the viscous sublayer of the wall-near region due to reflexions and laser sheet distortion at the wall.

Furthermore, the non-dimensional, time-averaged mean velocity u^+ is plotted against the wall units y^+ in Figure 5 in order to compare the data with the universal slope of a turbulent boundary layer (tbl). The dotted line represents the ideal tbl, whereas in the viscous sublayer ($y^+ < 5$) the velocity is proportional to the wall units ($u^+ = y^+$). For $y^+ > 12$ the velocity u^+ departs from the linear relationship and above $y^+ > 20$ it enters the logarithmic law of the wall ($u^+ = 1/\kappa \ ln(y^+) + B$), which is called the log-law region. The intermediate region between viscous sublayer and log-law region is called buffer layer (Pope [6]).

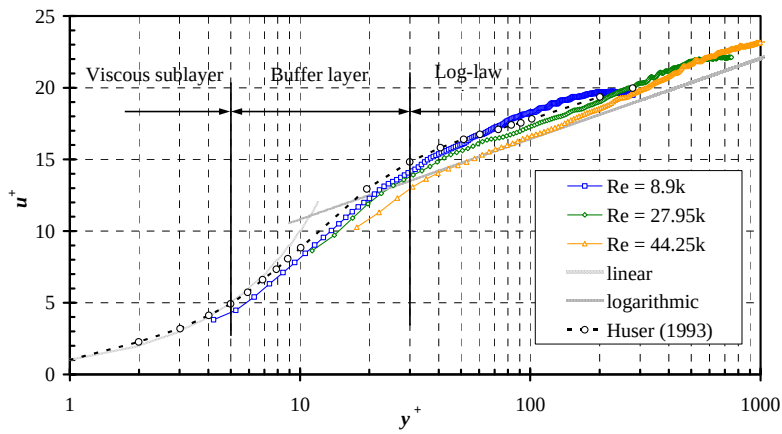

Figure 5: Time mean averaged dimensionless velocity u^+ against wall units y^+ in channel centre plane at $x = 17d$.

The first measurement point of the low Reynolds number $Re_d = 8.9k$ is at $y^+=4$ which is fairly well within the viscous sublayer. In comparison to the law of the wall (hatched gray line) the measured velocity falls below the $u^+ = y^+$ slope in the viscous sublayer and slightly exceeds the log law above $y^+ > 20$. This might be related to the unfinished development of the turbulent flow field at this position downstream of the inlet. Note that by increasing the Reynolds number from $Re_d = 8.9k$ to $Re_d = 27.95k$ and finally $Re_d = 44.25k$ the first useable measurement point changes from $y^+ = 4$ to $y^+ = 11$ and finally to $y^+ > 18$. By increasing the Reynolds number, the viscous length scale decreases and thus the layers of the tbl shrinks by then. Therefore, the application of a constant geometrical measurement grid defined by the settings of the PIV system leads to the spatial resolution of the tbl to decrease with increasing Reynolds number. However, the data from Huser and Biringen [4] show excellent agreement to the present data and also overshoot the log-law region at $y^+ > 20$. They state that the overshooting in the log-law region might be due to the higher turbulence production near the walls away from the corners compared to channel and boundary layer flows without pressure gradient.

4 Discussion

The time-averaged mean velocity plots in channel centre (Figure 4 and Figure 5) show reasonably good agreement with the numerical results published by Winkler *et al.* [10] and Huser and Biringen [4]. Note the non dimensional velocity in channel centre is proportional to Reynolds number. This relationship is consistent to the numerical results of Ciofalo and Collins [1], which is quantified in Table 1. In contrast, the time-averaged mean fluctuations in channel centre are assumed to be $u^+' = 1.4$ by Nikitin [5] and $u^+' = 2.2$ by Truckenbrodt [9]. In the present work the time-averaged mean fluctuations increase from the inlet $u^+' (x/d = 1) = 0.85$ up to $u^+' (x/d = 17) = 2.45$ in the test section, which suits well with the value from Truckenbrodt [9]. The increase in the magnitude of the fluctuations is assumed to be an indication of an increasing turbulence in the downstream region.

Table 1: Comparison of non dimensional maximal velocity against Reynolds number.

present study		Ciofalo and Collins [1]	
Re (k)	u^+_{max} (-)	*Re (k)*	u^+_{max} (-)
8.9	19.77	10	20.5
27.95	21.92	20	21
44.25	22.68	40	22

Considering the time-averaged mean flow field presented in Figure 4 and Figure 5 , it is visible that in terms of downstream length the near-wall turbulent boundary layer develops much faster than the core region. The root mean square

of the mean velocity already meets the curve progression of Winkler *et al.* [10] after *3* hydraulic diameters downstream of the inlet whereas the slope of the time mean averaged velocity still changes after *20* hydraulic diameters.

5 Conclusion

In the present work a PIV measurement of a turbulent flow in a square duct was done in order to assess the aerosol particle mixing process and the flow development in terms of velocity profiles at the channel centre. At first, a brief overview on published data about turbulent square duct flow was given. Following the remarks of Huser and Biringen [4] a turbulent square duct flow consists of eight counter-rotating edge vortices which deform the mean flow field accordingly. The downstream particle mixing process was analyzed by quadrant count method. The distribution of the scattered light intensity of the PIV raw data images was analyzed by dividing the image into separate interrogation frames and assessing the scattered light intensity of each frame, respectively. It was shown that particle mixing is complete after *8* hydraulic diameters, which is in good agreement to previous investigations on turbulent particle mixing.

The flow field formation was illustrated in terms of time-averaged mean velocity profiles in the channel centre. The curve progression of the mean velocity right after the inlet is relatively sharp and thereafter the slope continuously approaches a parabolic shape. However, the present velocity field in the test section ($x = 15..20d$) is not fully developed, but it seems to approach the flow field of Winkler *et al.* [10] after approximately further *20* hydraulic diameters downstream. On the other hand, the velocity root mean square already agrees well with Winkler's data after *3* hydraulic diameters, which raises the suggestion that the wall-near turbulent boundary layer develops faster than the core flow. Furthermore, this assumption was endorsed by the plot of non dimensional velocity u^+ against wall units y^+. In comparison to the universal law of the wall (Pope [6]) and DNS data published by Huser and Biringen [4], there is excellent agreement between these data and the present results. In addition, the overshooting of the velocity in the log-law region can be explained by additional turbulence production in the channel corner. This turbulent production may have an impact on the channel core flow. In relying on the present data, it is assumed that the turbulent boundary layer region converges much earlier a constant state with respect to downstream formation compared to the channel core flow. In the present facility, the particle mixing is complete after *8* hydraulic diameters downstream of the injection point. The near-wall turbulent boundary layer nicely follows the universal law of the wall after *17* hydraulic diameters but the core flow probably needs *40* to *50* hydraulic diameters to approach an equilibrium state between the pressure and the shear forces.

References

[1] Ciofalo, M. and Collins, M.W., Large-Eddy Simulation of turbulent Flow and Heat Transfer in plane and rib-roughened Channels. *International Journal for numerical Methods in Fluids*, **15(4)**, pp. 453-489, 1992.
[2] Cohen, B.S, *Air Sampling Instruments for Evaluation of Atmospheric Contaminants*. American Conference of Governmental and Industrial Hygenists, p. 595, 2001.
[3] Diggle, P., *Statistical analysis of spatial point patterns*, Arnold, 2003.
[4] Huser, A. and Biringen, S., Direct numerical simulation of turbulent flow in a square duct. *Journal of Fluid Mechanics*, **257**, pp. 65-95, 1993.
[5] Nikitin, N.V., Statistical Characteristics of Wall Turbulence. *Fluid Dynamics*, **31(3)**, pp. 361-370, 1996.
[6] Pope, S.B., *Turbulent Flows.* Cambridge University Press, 2009.
[7] Prasad, A. K.,; Adrian, R. J.; Landreth, C. C. and Offutt P. W., Effect of resolution on the speed and accuracy of particle image velocimetry interrogation, *Experiments in Fluids*, **13**, pp. 105-116, 1992.
[8] Raffel, M.; Willert, C. E.; Werely, S. T. and Kompenhans, J., *Particle Image Velocimetry - A Practical Guide.* Springer-Verlag: Berlin and Heidelberg, 2007.
[9] Truckenbrodt , E., *Fluidmechanik Band 1 - Grundlagen und elementare Strömungsvorgänge dichtebeständiger Fluide*. Springer-Verlag: Berlin and Heidelberg, 2008.
[10] Winkler, C. M.; Rani, S. L. and Vanka, S. P., Preferential concentration of particles in a fully developed turbulent square duct flow. *International Journal of Multiphase Flow*, **30(1)**, pp. 27–50, 2004.

This page intentionally left blank

Numerical simulation of coaxial turbulent jet with and without discrete particles

K. Kumaran & R. Sadr
Micro Scale Thermo Fluids (MSTF) Laboratory,
Mechanical Engineering Program,
Texas A&M University at Qatar, Qatar

Abstract

Three dimensional, steady, turbulent flow RANS simulations are carried out to study the near flow field characteristics of a particle laden coaxial water jet. Spherical glass particles of 240 micron diameter are added to the central jet flow at two mass loading ratios of 0.074% and 0.22%. Numerical results for single phase flow are first compared with experimental data obtained using Molecular Tagging Velocimetry (MTV). The predictions of the axial velocity, axial turbulent intensity, correlation coefficient and vorticity are compared for single-phase and two-phase flow cases to bring out the effect of addition of particles on the fluid phase, while the numerical results show that the influence of the particles on the continuous phase flow field is minimal.
Keywords: coaxial turbulent jets, particle laden, numerical simulation.

1 Introduction

The study of particle laden, coaxial turbulent jets in a confined environment has been a subject of interest due to its implications in several applications such as jet mixers, sprays, particle separators, and combustion chambers in the field of chemical, industrial and mechanical engineering. The near field region of a coaxial jet, typically extending up five to six diameters from the nozzle exit, plays a crucial role in shaping the turbulent characteristics of the jet. This has a direct effect on the mixing process of the particle in a particle-laden coaxial jet. It is therefore important to understand the flow field in this region to better understand the details of particle-laden coaxial jets. A review of the literature pertaining to coaxial jet flows with and without the dispersed phase is presented next.

WIT Transactions on Engineering Sciences, Vol 74, © 2012 WIT Press
www.witpress.com, ISSN 1743-3533 (on-line)
doi:10.2495/AFM120311

Ko and Kwan [1] experimentally investigated the initial region of single phase coaxial jets at different mean velocity ratios. Based on the length of the inner and outer potential cores, they categorized the initial region of coaxial jet flow field into three zones namely, the inner merging zone, intermediate zone and the fully merged zone. Also, they reported that the outer mixing region resemble close to that in a single phase jet. Dahm *et al.* [2] investigated the vortex dynamics in the near field of the coaxial water jet for velocity ratios ranging from 0.59 to 4.16. They reported that the sudden momentum change across the shear layer is an important aspect of the dynamics of coaxial jet. Later on, several studies [3, 4] were carried out to investigate the effect of inner wall thickness and diameter ratio on the flow field dynamics and mixing characteristics of single phase turbulent coaxial jets.

Mostafa *et al.* [5] investigated the initial region of coaxial jet flows with and without the glass beads of 110μm diameter and reported that the discrete particles attenuate the continuous phase turbulence. Fan *et al.* [6] investigated the effect of velocity ratio and particle mass loading on coaxial jets. The spreading rate of two phase coaxial jet was observed to be smaller than that of the single phase coaxial jet. Later, Fan *et al.* [7] confirmed these results using RANS simulations with k- ε turbulence model. Recently, Virdung and Rasmuson [8] investigated the hydrodynamics of a liquid single jet dispersed with glass beads of 1.5mm diameter. They carried out the numerical simulations with three different turbulent models and compared them with experimental data. It was reported that the realizable k- ε turbulence model was able to predict the mean axial velocity better with the drag correction term suggested by Brucato *et al.* [9] when compared to the other turbulent models. Despite the drag correction, the results were reported to be under- and over-predicted in the initial jet region. Stakic *et al.* [10] numerically investigated the influence of sand particles (of diameter 0.25mm and 0.9mm) on the gas phase using the k- ε turbulence model. The particle size was reported to have an influence on the mechanism of momentum exchange between the continuous phase and the particles. However, the under prediction of the results was attributed to the assumption of isotropic nature of turbulence in the modeling. Later, in the same configuration, Sijercic *et al.* [11] numerically investigated the effect of turbulence anisotropy using a higher-order, Reynolds-stress turbulence model. However, the axial and radial turbulent intensities were under-predicted near the jet exit.

In recent years, the high end numerical methods such as large eddy simulation (LES) and direct numerical simulation (DNS) are used to solve the turbulent flow field either completely (DNS) or partially (LES) in contrast to RANS simulations wherein the turbulent eddies are modeled. The flow field predictions of particle laden coaxial turbulent jets using the LES (Liu *et al.* [12]) and DNS (Ahmed and Elghobashi [13]) methods have demonstrated to be superior to the RANS calculations. Nevertheless, these numerical methods are computationally too expensive to apply in practical applications at a time that RANS models are able to predict the two phase flows reasonably well within the scope of turbulent closure modeling.

Although, several investigations were carried out in the past, most of them are case specific and demand further investigation to understand the performance of the modeling scheme to study the flow field. Thus in the present work, RANS calculations in conjunction with realizable *k- ε* turbulence model are carried out to investigate the effect of discrete particles on the continuous phase coaxial turbulent jet flow field at two different velocity ratios. The single phase numerical results are validated with experimental data of Sadr and Klewicki [14] herein after called *the experiment*. Later, predictions of the discrete phase results are compared with single phase results to highlight the influence of addition of particles on the continuous phase flow field.

2 Experimental methodology

Figure 1 shows a schematic of the experiment facility with its major system components. The test section measures 0.5m in height and width and 0.6m in length. The coaxial jet orifice located in the center of the upstream wall of the test section issues fluid horizontally into the test section. The central and annular jets are d_i=30mm and d_o=75mm in diameter, respectively. The wall thickness of the central jet nozzle, t, is 1.5mm. The central and the annular jet flows are driven by two pumps. The particles are made of clear spherical glass beads with a specific gravity of 2.46 and a mean diameter of 240μm. A novel particle injection system, Sadr and Klewicki [15], is used to introduce particles into the central jet flow upstream of the jet orifice.

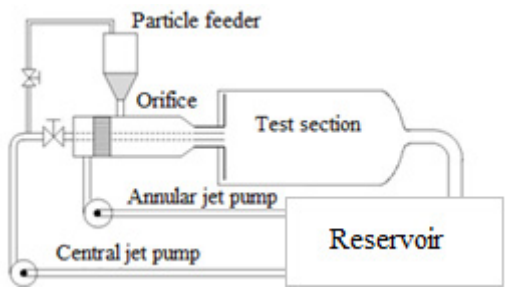

Figure 1: Schematic of the coaxial jet configuration.

Molecular tagging velocimetry (MTV), a whole field optical technique, is used to non-intrusively map the fluid flow velocities simultaneously at many points over a plane. It works by premixing the flowing medium and/or solid phase with molecules having long-lived luminescence lifetime. Typically, a pulsed UV laser is used to tag a region of interest in the flow. The tagged region is imaged at two successive times to record its displacement caused by the fluid flow. From this deformation, the kinematics of the flow may be obtained. The method is especially attractive for particulate flow studies since it does not require seeding, which may raise some complications with the presence of the

solid phase. More details of the method and various parameters involved in it can be found in several review articles by Koochesfahani and Nocera [16].

Two different laser patterns are commonly used in MTV method: multiple lines and a grid. The major advantage of the multiline method is its fine spatial resolution. This method, hence, relies on finding the best fit to the laser line intensity profile near its peak. Figure 2 shows an example of the MTV images used by Sadr and Klewicki [17] to study the flow field in the particle- laden coaxial jet. The multiple line method is most accurate in flows dominated by a single velocity component. In this method, a series of coplanar MTV laser lines are used to measure single component of instantaneous velocity profiles.

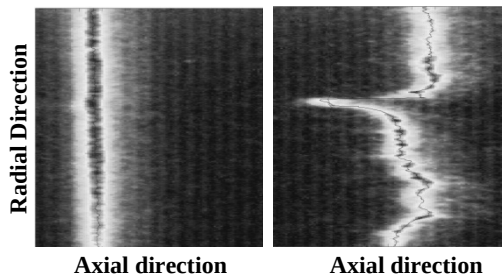

Figure 2: Sample undeformed (left) and deformed (right) MTV images at x/d_i=0.07 and velocity ratio of 1.11. Black line indicates the center of the laser line. Flow is from left to right.

3 Numerical formulation and methodology

Figure 3 shows a slice of the schematic of the computational domain considered here and it is only part of that shown in fig. 1. The central and coaxial jets issue into the test section at $x/d_i = 0$ where, x is the axial distance and d_i is the inner pipe diameter. More details about the experimental facility are discussed in section 2. In this study, three dimensional, steady, incompressible, turbulent flow calculations are carried out in half domain (as shown in fig. 3) from symmetry considerations at two velocity ratios (ratio of outer to inner jet mean velocity) η = *1.11* and *0.18*. The inner jet velocity is held constant and the velocity ratio is varied by varying the outer jet velocity. In all the simulations, the working fluid is taken as water and mass and momentum equations (Reynolds-averaged Navier-Strokes (RANS)) are solved. The Reynolds stress, $(-\rho\overline{u_i'u_j'})$ is modeled using the Boussinesq's approximation.

Initially, the single phase simulations were carried out using two turbulence models namely SST k-ω (Menter [18]) and realizable *k-ε* (Shih *et al.* [19]) turbulence models. Since the axial velocity profile and the turbulent intensity predictions at $x/d_i = 0$ are better with the realizable *k-ε* turbulence model, the two phase simulations are carried out with the realizable *k-ε* turbulence model alone. Hence, the results obtained using realizable *k-ε* turbulence model alone is discussed here. The turbulent kinetic energy, *k* and the dissipation rate, *ε* are

calculated using the realizable *k-ε* turbulence model with default model constants ($C_{1\varepsilon} = 1.44, C_2 = 1.9, \sigma_k = 1.0$ and $\sigma_\varepsilon = 1.2$) where, σ_k and σ_ε are the turbulent prandtl numbers for the turbulent kinetic energy and dissipation rate respectively.

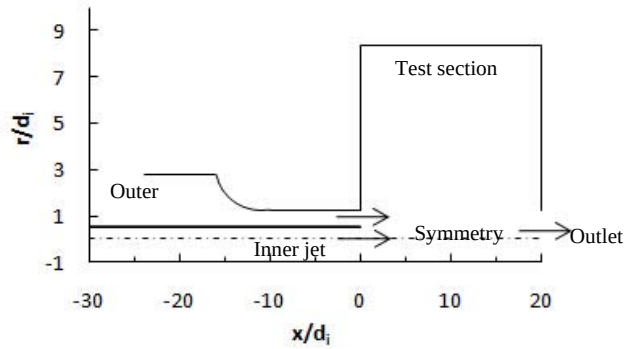

Figure 3: Schematic of the coaxial jet configuration (slice of a 3D domain).

The calculations with the discrete phase are carried out using Euler-Lagrangian approach where the continuous phase is solved in Eulerian mode and the discrete phase in Lagrangian mode. This is based on the fundamental assumption that the second phase (here discrete solid particles) volume fraction is small (typically <5%) when compared to the continuous phase in spite of the second phase having higher mass. The trajectory of the discrete phase is calculated based on the force balance of the particle as follows,

Particle Inertial force = Drag force + gravity force + additional forces (1)

The additional force could be due to virtual mass (when fluid density is more than the particle density), thermophoretic, brownian and Saffman's lift force. Based on the experimental condition, in this work only the drag force is accounted in the calculation. Consequently, the force balance results in the form,

$$\frac{du_p}{dt} = F_D(u - u_p) \ , \text{ where } F_D = \frac{18\mu}{\rho_p d_p^2}\frac{C_D Re}{24}. \quad (2)$$

Here, u is the fluid phase velocity, u_p is the particle velocity, μ is the molecular viscosity of the fluid, ρ and ρ_p are the fluid and particle densities respectively. C_D is the Drag coefficient and Re is the relative Reynolds number, Re ≡ $(\rho d_p|u_p\text{-}u|)/\mu$. The drag force is calculated using the spherical drag law.

In discrete phase simulations, the effect of continuous phase turbulent velocity fluctuations on the particles is predicted using the stochastic tracking model. In addition to turbulent dispersion, two-way coupling is also considered to include the effect of particle fluctuations on the continuous phase. The particle-particle collision is not considered as the discrete phase concentration is below 0.3% (Hardalupas *et al.* [20]). The coupling between the continuous phase and the discrete phase is carried out using the particle-source-in-cell (PSI-CELL)

approach. In all the simulations reported here, second order, upwind scheme is used for the spatial discretization and Roe-flux difference splitting scheme (Roe [21]) is used for the convective and diffusive flux terms. The pressure-velocity coupling is carried out using the coupled solver. All the calculations are carried out using the ANSYS-FLUENT [22].

3.1 Boundary conditions

The central and coaxial pipe inlets upstream of the test section inlet are defined as mass flow inlets where, the mass flow rates are adjusted until velocities at $x/d_i = 0.07$ and $r/d_i = 0$ matches with the experimental values. Since the exact values of the inlet turbulent quantities at either of these pipe inlets are not available from experiments, a uniform specification of the turbulent intensity and the hydraulic diameter are specified. The Reynolds number for the inner jet is maintained at 4.1×10^4 (center line jet exit velocity U_c=1.39 m/s) same as that of experiments. The outlet is defined as an outflow boundary condition with zero diffusive flux for all the variables and extrapolated from the interior of the domain. The mid-plane is specified as symmetry and all the walls are defined as stationary with no slip condition. At the plane of symmetry, the radial velocity and the radial gradients of other variables are defined to be zero.

For the discrete phase simulations, the discrete particles (glass beads of 240μm diameter) are injected in the central jet at two mass loading ratios (ratio of particle mass to continuous phase mass) of 0.074 % and 0.22 % similar to the experimental case of Sadr and Klewicki [17]. Volume fraction at this range is encountered in many practical applications. For example the primary stream of a pulverized coal burner operates at a volume fraction of 0.05% (Hardalupas *et al.* [20]) at standard condition.

3.2 Convergence metrics

All the calculations are carried out until the mass and momentum balances are within the acceptable limits. For all the results reported here, the difference in mass and momentum balance between the inlets and the outlet is within 1% and 5% respectively. All the results reported here is second order accurate.

3.3 Grid independence

The computational domain is completely meshed using the structured mesh. The near wall regions are resolved using the boundary layer mesh. In the test section, the first node from the wall is placed at about 50 microns and the following nodes are placed at different lengths using a progressive ratio. A top view of the node distribution on the test section symmetry plane and a close up view of the inner wall region are shown in fig. 4. A coarse mesh is generated first and then refined progressively until no significant change (i.e., less than 5%) in the results was observed and that resulted in a total cell count of 799500, that herein after is called the base mesh.

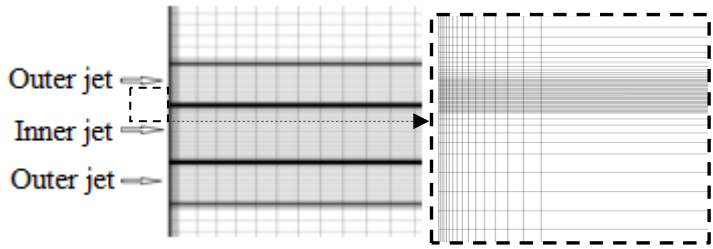

Figure 4: Top view of the node distribution in the symmetry plane (left) and a close up view of the inner wall region (right).

In order to attest to the fact that the results are grid independent, the base mesh was further refined in the region of interest, i.e., $x/d_i > 0$, by reducing the distance between the cells in the radial and axial direction by half. This has resulted in a cell count of 1909500. Since the wall refinement has been done adequately for the base mesh, the near wall refinement is retained the same in the refined mesh. As a result, the wall y^+ values between the meshes are almost the same ($y^+ \approx 40$). Grid independence study is carried out only for the high velocity ratio. Figure 5 shows the comparison of radial profiles of the mean axial velocity and axial turbulent intensity at several locations downstream of the test section inlet between the base mesh and refined mesh.

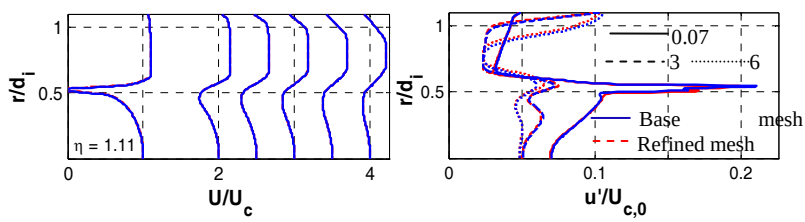

Figure 5: Comparison of axial mean velocity (left) and axial turbulent intensity (right) at different axial locations (x/d_i = 0.07, 2, 3, 4, 5 and 6) between the base mesh (blue line) and refined mesh (red line) at velocity ratio, $\eta = 1.11$. Here, $U_{c,0}$ is the inner jet velocity at $x/d_i = 0$.

The variation of mean axial velocity between the meshes is almost the same. On the other hand, the difference in the variation of turbulent intensity profiles between the meshes is only marginal. These results clearly suggest that the base mesh is able to resolve the flow features adequately. Hence, all the results reported here are calculated using the base mesh.

4 Results and discussions

In this section, results from the continuous phase simulations with and without considering the discrete particles at two velocity ratios (η = 1.11 and 0.18) are presented and discussed. First, the results of single-phase are compared with that of experimental data to establish the validity of the numerical procedure. Later, results from two phase flow calculations are compared with single phase results to highlight the influence of discrete particles on the continuous phase.

4.1 Single phase flow

Figure 6 shows the comparison of predicted radial profiles of the axial velocity at several axial locations downstream of the jet exits with experimental data. Here, the velocity profiles (except at x/d_i = 0.07) are offset by a factor of $0.5*x/d_i$ to show the variation. In both the cases, the inner jet ($0 \le r/d_i \le 0.5$) velocity profile at x/d_i =0.07 is a fully developed velocity profile and the outer jet ($0.55 \le r/d_i \le 1.25$) is almost like a top-hat profile similar to that observed in the experiment. Since the velocity ratio is varied by varying the outer jet, the inner jet velocity profile is the same at all velocity ratios. The inlet jet velocity profile shows small deviation from experimental data in the region, $0.15 < r/d_i < 0.4$. This could be due to the difference in the jet inlet conditions between the experiment and numerical simulation as mentioned in section 3.1. However, the velocity gradient near the inner jet wall region is predicted well (in the region $0.5 \le r/d_i \le 0.55$).

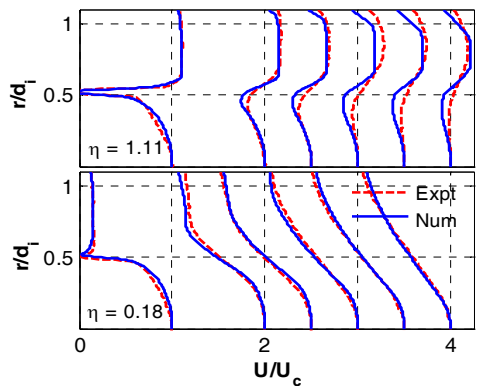

Figure 6: Radial variation of axial velocity at different axial locations (from left, x/d_i = 0.07, 2, 3, 4, 5 and 6) and velocity ratios.

In both velocity ratios, the outer jet velocity profile predictions at x/d_i = 0.07 are very close to experimental data. Further downstream, at η = 1.11, the predictions show a greater deviation from experimental data in the inner shear region where the difference is close to 5 % elsewhere, the deviation is within 3%. This could be due to the over prediction of the wake effect when compared

to experimental data. This difference decreases with decrease in velocity ratio. At low velocity ratio, the radial profile predictions agree with experimental data within 2%.

Figure 7 shows the decay of the axial velocity and axial turbulent intensity comparison between the prediction and experimental data, along the centerline $r/d_i = 0$ (left) of the inner jet and along the midpoint of the coaxial jet $r/d_i = 0.86$ (right), both normalized by the inner jet exit velocity at $x/d_i = 0$. It is observed that in all the cases, the axial decay of mean axial velocity is predicted well within 5% of the experimental data. Along the centerline of the inner jet, the turbulent levels are under-predicted however, the trends are predicted well while at $r/d_i = 0.86$, the turbulent intensity levels are predicted closer to experimental data at both velocity ratios (near $x/d_i = 0$). In both lines the difference between the experimental data and prediction increases with axial distance. This under prediction could be due to the difference of the turbulent intensity, between the experiments and simulation, at the jet inlets. The under prediction of turbulent quantities at the jet exit could be either due to the lack of turbulence level information from the experiments or due to the turbulent closure modeling. From all the above results it is evident that the RANS simulations are able to predict the trend and the magnitude at a reasonable level. Having these in mind, the numerical simulations are extended further to study the influence of discrete particles on the continuous phase. This is discussed next.

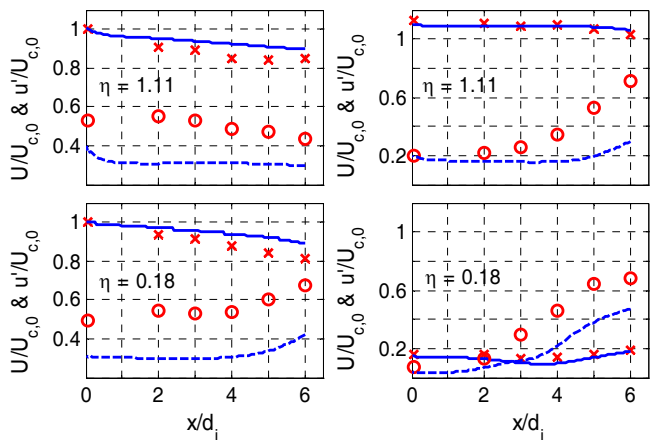

Figure 7: Comparison of axial velocity and axial turbulent intensity decay along the centerline of the inner (left) and outer (right) jets. (x) Expt ($U/U_{c,0}$); (o) Expt ($6*u'/U_{c,0}$) ; continuous line - Num ($U/U_{c,0}$) and dashed line - Num ($6*u'/U_{c,0}$). Here, $U_{c,0}$ are the inner jet velocity at $x/d_i = 0$.

4.2 Two phase flow

In this section results pertaining to the two phase simulations are presented and discussed. The effect of discrete particles on the continuous phase flow field is

discussed by comparing the two phase results with the single phase results. Although the simulations are carried out at two mass loading ratios, the difference in the predictions between the mass loadings are marginal and hence not presented here for the sake of brevity. The high mass loading results are compared with the single phase results.

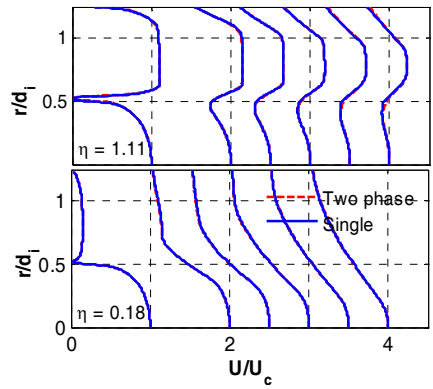

Figure 8: Comparison of the radial variation of axial velocity predictions of two phase and single phase at different axial locations (from left x/d_i = 0.07, 2, 3, 4, 5 and 6).

Figure 8 shows the variation of the axial velocity component along the radial direction predicted with and without the discrete particles. The rate of decrease in continuous-phase centerline velocity is seen to be similar in the single phase as well as in two phase flow predictions. It is evident from fig. 8 that overall the difference between the dispersed phase and the single phase predictions is almost nil except a few regions near the inner shear layer at η = 1.11. This is found to be consistent with the experimental observation by Arai *et al.* [23], and later, Sadr and Klewicki [17], and Virdung and Rasmuson [8] wherein the effect of mass loading at 0.21% on the continuous phase was reported as insignificant.

Figure 9 shows comparison of the axial turbulent intensity predicted along the radial direction with and without the dispersed phase. It is observed that at η = 1.11, the turbulent intensity gradually decreases in the outer mixing region with increase in axial distance, whereas, the axial turbulent intensity is considerably affected in the inner jet alone as the particles are injected in the inner jet. At x/d_i = 0.07, the axial turbulent intensities predicted (in the inner jet region) with the dispersed phase are lower than the single phase predictions at all velocity ratios. This can be attributed to the fact that the particles seem to attenuate the continuous phase turbulent intensities as experimentally observed by Fan *et al.* [24]. Further downstream, the dispersed phase turbulent intensity is marginally lower than single phase only in the outer mixing region elsewhere; the values are comparable to the single phase results. Overall, the difference in turbulent intensity between the dispersed phase and the single phase is predicted to be high

only in the immediate vicinity of the jet exit. Far downstream, the difference is marginal. Gore and Crowe [25] related such a trend for the small particle size, and low stokes number, which is the case in this study.

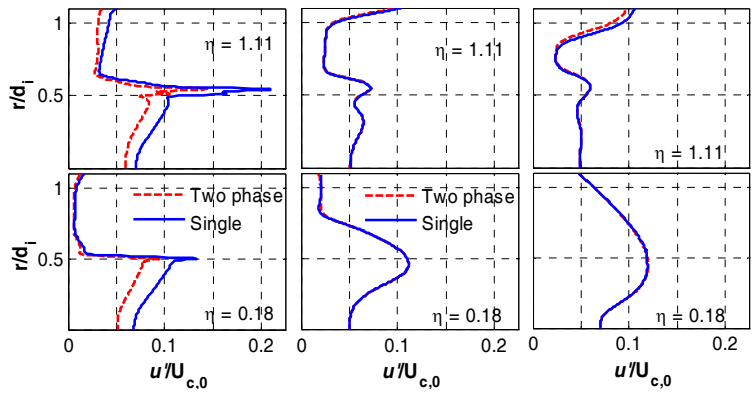

Figure 9: Comparison of axial intensity at stream-wise locations x/d_i = 0.07 (left), 3 (center) and 6 (right) at different velocity ratios.

Figure 10 shows the comparison of the predictions of correlation coefficient, $C_{uv} = \overline{uv}/(u'v')$ with and without the dispersed phase. The predictions are different only in a few regions in the inner mixing region elsewhere, the difference is insignificant. This corroborates with the fact that the axial and radial turbulent intensities are almost the same and marginally different from the single phase predictions. At η = 0.18, the difference is almost nil at all axial locations investigated here.

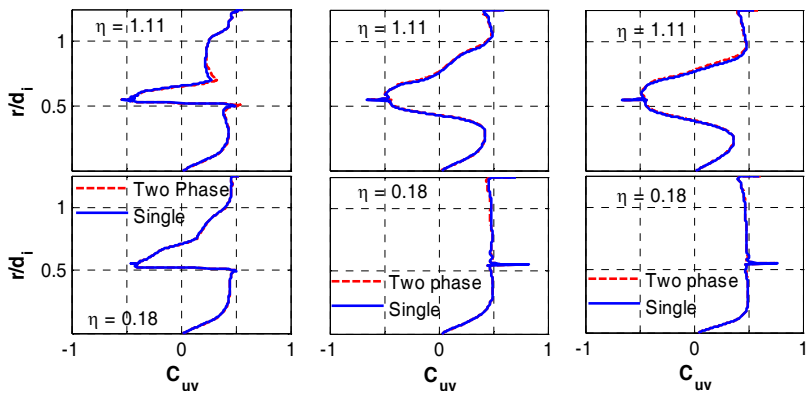

Figure 10: Comparison of correlation coefficient at stream-wise locations x/d_i = 0.07 (left), 3.67 (center) and 6 (right) at different velocity ratios for the single and two phase flows.

In addition to the axial velocity and turbulent intensity, the comparison of the vorticity field between the single-phase and two-phase results is also discussed. Since the difference between two phase and single phase predictions is small, only the normalized difference is presented instead of the absolute values to facilitate the discussion. The vorticity is normalized using the central jet velocity and central jet diameter. Then the difference, $\Delta\xi_{21}$ is calculated between the single phase and two phase conditions. The difference, $\Delta\xi_{21}$ at a given condition is then normalized using the maximum value of the difference, $(\Delta\xi_{21})_{max}$= 6.1 at η = 1.11. Hence, the difference presented here is the difference between the normalized vorticities not the difference in absolute value of vorticity.

Figure 11 shows the normalized vorticity difference between two-phase and single-phase. It is worth noting that at x/d_i = 0.07 in the inner mixing region, the maximum difference is in the negative direction implying that the single phase prediction is higher than the two phase prediction at η = 1.11. This in turn implies that the particles in the continuous phase influence adversely in the inner side of the inner mixing region. However, the peak in the outer side of the inner mixing region is positive when compared to the inner side. This could be due to the restricted spread of the inner jet and in turn the particles by the outer jet.

At low velocity ratio η = 0.18, the difference is only marginal which indicates that the fluid rotation is not affected by the presence of particles. However, at downstream locations, the difference increases gradually. This could be due to the effect of the solid particles on the entrainment in the outer jet at η = 0.18. At x/d_i = 0.07, the difference is seen to increase with increase in velocity ratio. At x/d_i = 6, the difference is high at low velocity ratio when compared to η = 1.11. This is due to the entrainment of the outer jet into the inner jet. Interestingly, from this trend it can be inferred that the particles in the inner mixing region tend to reduce the fluid rotation possibly owing to the transfer of momentum from the continuous phase to the particles. The influence of particles on the fluid rotation is minimal at all conditions. Away from the jet exits, the difference is seen to decrease at both velocity ratios.

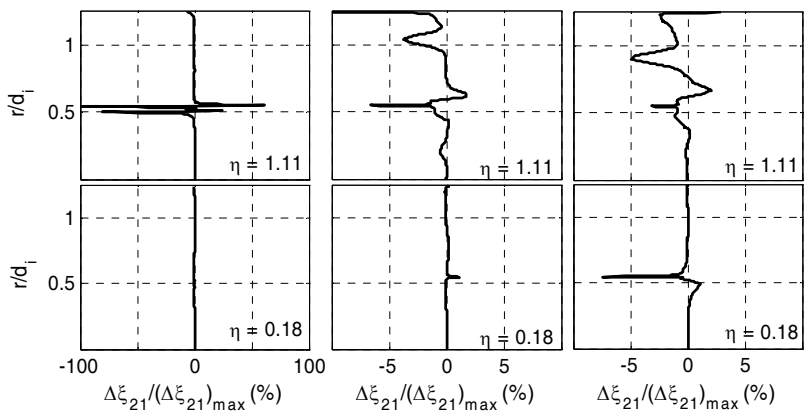

Figure 11: Variation of vorticity difference at different axial locations, x/d_i = 0.07 (left), 3 (center) and 6 (right).

All these results clearly demonstrate that velocity ratio has a major contribution in the development of coaxial jet flow field. Furthermore, the addition of discrete particles alters the continuous phase flow field. However, it is evident only in the turbulent quantities rather than the mean quantities.

5 Conclusions

In this work, the flow field dynamics of the particle laden coaxial, turbulent jets are numerically investigated at two different velocity ratios. To this end, 3D, incompressible discrete phase turbulent flow calculations are carried out. In this study, glass beads of 240μm diameter are injected in the inner jet alone. For the mass loading studied in this work, the overall difference in the prediction between two phase and single phase is seen to be minimal which in turn implies that the influence of discrete particles on the continuous phase flow field is insignificant. However, close to the jet exits, the presence of discrete particles is seen to attenuate the continuous phase turbulence along the pipe. The results from this study demonstrate that the velocity ratio is an important parameter in the development of coaxial jet flow field and particles (of the size considered) will have an influence on the continuous phase only in the near flow field of the coaxial jets.

Acknowledgement

This work was partially supported by Qatar Science and Technology Park.

References

[1] Ko, N.W.M. and Kwan, A.S.H., The initial region of subsonic coaxial turbulent jets, Journal of Fluid Mechanics, **73**, pp. 305–332, 1976.
[2] Dahm, W.J.A., Frieler, C.E. and Tryggvason, G., Vortex structure and dynamics in the near field of a coaxial jet, Journal of Fluid Mechanics, **241**, pp. 371-402, 1992.
[3] Buresti, G., Petagna, P. and Talamelli, A., Experimental investigation on the turbulent near-field of coaxial jets, Experimental Thermal and Fluid Sciences, **17**, pp. 18-36, 1998.
[4] Balarac, A., Si-Ameur, M., Lesieur, M. and Metais, O., Direct numerical simulations of high velocity ratio coaxial jets: mixing properties and influence of upstream conditions, Journal of Turbulence, **8**, pp. 1–14, 2007.
[5] Mostafa, A.A., Mongia, H.C., McDonell, V.G. and Samuelsen, G.S., An experimental and numerical study of particle-laden coaxial jet flows, International Journal of Heat and Fluid Flow, **11 (2)**, pp. 90-97,1990.
[6] Fan, J., Zhao, H. and Jin, J., Two-phase velocity measurement in particle-laden coaxial jets, Chemical Engineering Journal, **63**, pp. 11-17, 1996.

[7] Fan, J., Zhang, X., Chen, L. and Cen, K., New stochastic particle dispersion modeling of a turbulent particle-laden round jet, Chemical Engineering Journal, **66**, pp. 207-215, 1997.
[8] Virdung, T. and Rasmuson, A., Hydrodynamic properties of a turbulent confined solid-liquid jet evaluated using PIV and CFD, Chemical Engineering Science, **62**, pp. 5963-5978, 2007.
[9] Brucato, A., Grisafi, F. and Montante, G., Particle drag coefficients in turbulent fluids, Chemical Engineering Science, **53**, pp. 3295–3314, 1998.
[10] Stakic, M.B., Zivkovic, G.S. and Sijercic, M.A., Numerical analysis of discrete phase influence on gas flow in a two-phase turbulent free jet, Proc. of the ASME FED, FED-244, pp. 501-506, 1997.
[11] Sijercic, M., Belosevic, S. and Stevanovic, Z., Simulation of free turbulent particle-laden jet using Reynolds-stress gas turbulence model, Applied Mathematical modeling, **31**, pp. 1001-1014, 2007.
[12] Liu, Y., Zhou, L.X. and Xu, C.X., Numerical simulation of instantaneous flow structure of swirling and non-swirling coaxial jet particle-laden turbulence flows, Physica A, **389**, pp. 5380-5389, 2010.
[13] Ahmed, A.M. and Elghobashi, S., Direct numerical simulation of particle dispersion in homogeneous turbulent shear flows, Physics of Fluids, **13**, pp. 3346-3364, 2001.
[14] Sadr, R. and Klewicki, J.C., An experimental investigation of the near-field flow development in coaxial jets, Physics of Fluids, **15**, pp. 1233-1246, 2003.
[15] Sadr, R. and Klewicki, J.C., A Multi Purpose Feed System for Fluids and Solid Particles, Measurement Science and Technology, **14**, N33-N35, 2003.
[16] Koochesfahani, M.M. and Nocera, D.G., Handbook of Experimental Fluid Dynamics, Springer-Verlag, Chapter 5.4, 2007.
[17] Sadr, R. and Klewicki, J.C., Flow field characteristics in the near field region of particle-laden coaxial jets, Experiments in Fluids, **39**, pp. 885-894, 2005.
[18] Menter, F.R., Zonal Two Equation k-ω Models for Aerodynamic Flows, AIAA Paper 93-2906, 1993.
[19] Shih, T.H., Liou, W.W., Shabbir, A., Yang, Z. and Zhu, J., A New k- ε Eddy-Viscosity Model for High Reynolds Number Turbulent Flows - Model Development and Validation, Computers Fluids, **24 (3)**, pp. 227-238, 1995.
[20] Hardalupas, Y., Taylor, A.M.K.P. and Whitelaw, J.H., Velocity and particle flux characteristics of turbulent particle-laden jets, Proc. of Royal Society London A, **426**, pp. 31–78, 1989.
[21] Roe, P.L., Characteristic based schemes for the Euler equations, Annual Review of Fluid Mechanics, **18**, pp. 337-365, 1986.
[22] ANSYS – Fluent 12.0, 2010.
[23] Arai, T., Kudo, N., Ishima, T., Youssef, I.M. and Obokata, T., Turbulence structure of a liquid–solid two-phase jet by means of laser techniques. In: Proc. of 4th ASME-JSME Conference, USA, July 6–10,pp. 847–853, 2003.

[24] Fan, J., Zhao, H. and Cen, K., An experimental study of two-phase turbulent coaxial jets, Experiments in Fluids, **13**, pp. 279–287, 1992.
[25] Gore, R.A. and Crowe, C.T., Effect of particle size on modulating turbulent intensity. International Journal of Multiphase Flow, **15 (2)**, pp. 279–285, 1989.

This page intentionally left blank

Three-dimensional mixture theory simulations of turbulent flow over dynamic rippled beds

A. M. Penko & J. Calantoni
Marine Geosciences Division, Naval Research Laboratory, USA

Abstract

The highly turbulent, sediment-laden flow above rippled beds in the wave bottom boundary layer (WBBL) is poorly understood and difficult to quantify mainly because of our failure to understand the fundamental interaction forces driving sediment transport. However, recent advances in high performance computing allow for highly resolved simulations of fluid-sediment dynamics in the WBBL to examine the small-scale fluctuations of boundary layer processes and characterize seabed morphology. A three-dimensional mixture theory model, SedMix3D, solves the unfiltered Navier-Stokes equations for the fluid-sediment mixture with an additional equation describing sediment flux. Mixture theory treats the fluid-sediment mixture as a single continuum with effective properties parameterizing the intra- and inter-phase interactions with closure relations for the mixture viscosity, diffusion, hindered settling, and particle pressure. We validate results obtained with SedMix3D using temporally and spatially resolved fluid velocity measurements acquired with a particle image velocimetry (PIV) system in a free-surface laboratory flume. Measured two-dimensional velocity fields are compared to two-dimensional vertical slices from the three-dimensional simulation domain. We examine the hydrodynamics of the flow by comparing bulk flow statistics, and swirling strength. In general, results from SedMix3D were in excellent agreement with the observations. We believe SedMix3D captures the essential physics governing two–phase turbulent flow over ripples for the conditions represented by the experiments and should provide us with a powerful research tool for studying the dynamics of seafloor bedforms.
Keywords: ripples, bedforms, numerical modeling, turbulence, multiphase flow, mixture theory, model-data comparison.

WIT Transactions on Engineering Sciences, Vol 74, © 2012 WIT Press
www.witpress.com, ISSN 1743-3533 (on-line)
doi:10.2495/AFM120321

1 Introduction

Despite advances in computing and laboratory observational technology, there still exist many unknowns about the small-scale interactions driving two-phase hydrodynamics in the seafloor boundary layer. Past work has extensively studied the flow structure over static (or fixed) sand beds [1–5]. These studies have broadened our knowledge on vorticity dynamics of oscillatory flow over ripples; however, they lack the dynamic coupling between the fluid and sediment, which influences turbulence production/dissipation and resulting bed morphology. Because strong correlations exist between the sediment transport, near bed fluid velocity, and bed morphology, coupling these processes will be necessary to accurately model bottom boundary layer flow and the resulting sediment entrainment/deposition.

A three-dimensional numerical model solving the unfiltered Navier-Stokes equations using mixture theory is presented here. Mixture theory treats the fluid-sediment mixture as a continuum with the inter- and intra-phase interactions parameterized with closure relations. The model is validated quantitatively through comparisons of time-dependent and spatially varying velocities as well as bulk flow statistics measured under scaled laboratory conditions.

2 Experimental set-up

The observations were made in a wave flume at the Fluid Mechanics Laboratory at Delft University of Technology, Netherlands using a particle image velocimetry technique [6]. The wave flume is 42 m in length, 0.8 m in width, and 1 m in height, with the bottom covered with a layer of sediment. A material typically used for sand blasting was chosen for the sediment with a mean grain diameter of 0.054 cm and a specific gravity of 1.2. A Dantec particle image velocimeter (PIV) system consisting of a 120 mJ Nd-Yag pulsed laser synchronized with a 1 MegaPixel camera was used to capture two-dimensional vertical (x-z) plane optical images. The sampling window (11 cm × 11 cm) was located approximately 29 m from the wave generator in a water depth of about 0.31 m. For this experiment, the wave generator produced regular waves 5 cm in height with a period of 2 s.

The laser was placed in a watertight housing located approximately 27 cm above the bed and the camera was placed outside the flume. An Acoustic Doppler Velocimeter (ADV) time-synchronized with the PIV system measured the free-stream velocity approximately 17 cm above the bed. The camera captured image pairs (10 ms time lag between pair members) of the sampling window for 60 s bursts at approximately 12 Hz. Suspended sediment, organic matter, and micro-bubbles acted as seeding agents in the water column. The velocity vectors were calculated by correlating the image pairs using 64 × 32 pixel interrogation windows with 50% overlap. The resulting spatial resolution of the vector field was 3.48 mm × 1.74 mm. Outliers were removed with a three standard deviation filter and replaced with the local ensemble average.

3 Methodology

SedMix3D solves the unfiltered Navier-Stokes equations with an additional sediment flux equation for a fluid-sediment mixture resulting in the time-dependent sediment concentration and three-component velocity vector field [7]. The model treats the fluid-sediment mixture as a single continuum with effective properties that parameterize the fluid-sediment and sediment-sediment interactions including a bulk hindered settling velocity, a shear-induced diffusion, an effective viscosity, and a particle pressure. The sediment flux equation models the concentration of sediment by describing the balance between advection, sedimentation due to gravity, and shear-induced diffusion. Grid spacing was on the order of a sediment grain diameter and time step was $O(10^{-5}$ s). The model only simulates flow in the boundary layer (i.e., no free surface). The numerical scheme is finite difference with second-order central differences employed on a staggered grid. The boundary conditions for the velocities and concentration are periodic in the horizontal. At the top of the domain, the *u* velocity is assumed to follow the free-stream while the *v* and *w* velocities are set to zero. A no-slip condition exists for the velocities at the bottom boundary (i.e., deep inside the sand bed). The initial concentration is equal to the concentration of a fully packed bed at the bottom boundary (ϕ = 0.63) and zero at the top boundary.

The modeling framework of SedMix3D includes governing equations for sediment flux, mixture continuity, and mixture momentum. The mixture continuity equation was derived by combining the fluid and sediment phase continuity equations,

$$\frac{\partial \rho}{\partial t} + \nabla \cdot (\rho \mathbf{u}) = 0, \tag{1}$$

where **u** is the mixture velocity and ρ is the mixture density,

$$\rho = \phi \rho_s + (1-\phi)\rho_f, \tag{2}$$

where ϕ is the sediment volumetric concentration, and ρ_s and ρ_f are the sediment and fluid densities, respectively. The mixture momentum equation was derived from the sum of the individual phase momentum equations,

$$\rho \frac{\partial \mathbf{u}}{\partial t} + \rho \mathbf{u} \cdot \nabla \mathbf{u} = -\nabla P + \nabla \cdot (\mu \nabla \mathbf{u}) + \mathbf{F} - \rho \mathbf{g}, \tag{3}$$

where *P* is the mixture pressure, μ is the effective viscosity, **F** is the external driving force vector per unit volume, and **g** is gravitational acceleration (981 cm s^{-2}). SedMix3D employs a modified Eilers [8] equation to represent effective viscosity, μ, here scaled by the pure water viscosity, μ_f

$$\frac{\mu}{\mu_f} = \left[1 + \frac{0.5[\mu]\phi}{1 - \phi/\phi_m} \right]^2, \tag{4}$$

where [μ] is the intrinsic viscosity, a dimensionless parameter representing the sediment grain shape, and $0.0 < \phi < 0.63$, where the lower bound represents pure water and upper bound roughly corresponds to the maximum concentration of unconsolidated sediment. Here, we fix the maximum value of the effective viscosity by specifying $\phi_m = 0.66$. The intrinsic viscosity parameter, $[\mu]$, was 2.5 to represent spherical particles [9].

The concentration of sediment is modeled with a sediment flux equation [10] that balances the temporal gradients in sediment concentration with advection, gravity, and shear-induced diffusion,

$$\frac{\partial \phi}{\partial t} + \mathbf{u} \cdot \nabla \phi = D \nabla^2 \phi - \frac{\partial \phi W_t}{\partial z}, \tag{5}$$

where W_t is the concentration specific settling rate,

$$W_t = W_{t0}(1-\phi)^q, \tag{6}$$

where W_{t0} is the settling rate of a single particle in a clear fluid and q is an empirical constant [11]. The shear-induced diffusion of sediment, D, is a function of grain size, volumetric concentration, and mixture stresses [12].

4 Results

The model forcing was derived from the free stream velocity measured by the ADV in the experiment (Fig. 1). The first four wave periods were considered model spin-up periods. All quantities used in the following comparisons were calculated after discarding the four model spin-up periods. Flow quantities were

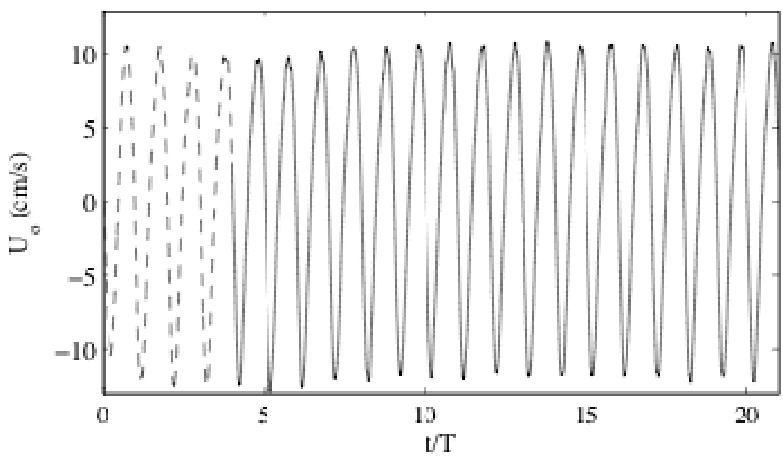

Figure 1: Free-stream velocity recorded by the ADV in the experiment (solid lines) and the four model spin-up periods (dashed lines).

time- and ensemble-averaged over a total of 17 wave periods. We compared a two-dimensional velocity field (x-z plane) from the simulation to the two-dimensional velocity field extracted from the PIV measurements. The simulated x-z plane chosen for comparison here resulted from the minimization of the temporal RMS deviation of the horizontal and vertical velocity RMS deviation. Here we examine the difference between the simulated and observed mean and standard deviation of the horizontal velocity and the ensemble-averaged swirling strength.

4.1 Horizontal velocity mean and standard deviation

The simulated and observed horizontal mean flow profiles at varying locations over the bed are plotted in fig. 2. The maximum difference between the simulated and observed mean flow is less than 2 cm/s at all locations along the ripples. The simulated mean flow agrees very well with the observations over the peaks of the ripples (e.g., x = 3 cm, 7 cm, and 8.5 cm), matching the maximum, minimum, and shape of the mean horizontal velocity profile. In the first and last

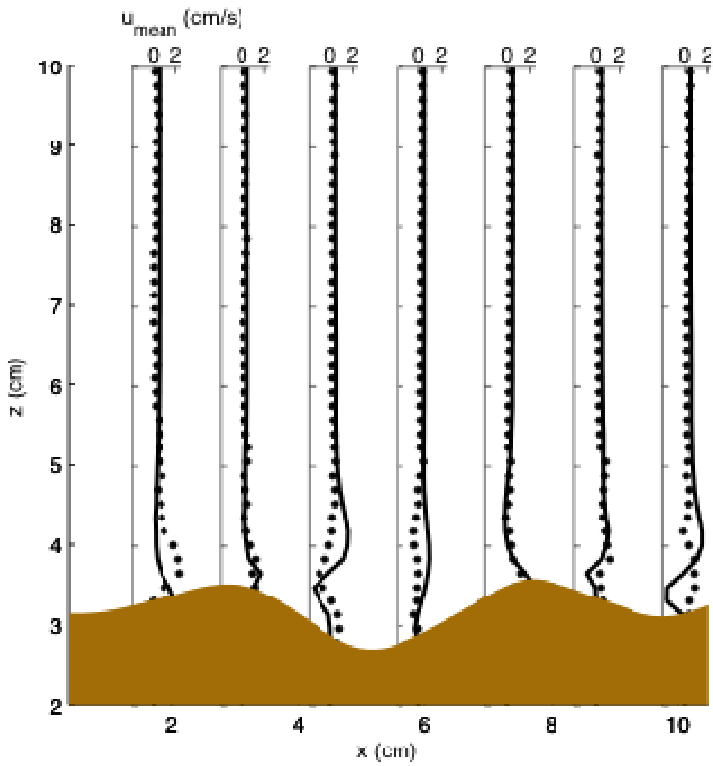

Figure 2: Mean horizontal velocity profiles from the simulation (lines) and observations (dots) at varying locations above the bed.

profiles (x = 1.5 and 9.8 cm), there is about a 2 cm/s difference between the simulated and observed horizontal maximum and minimum mean velocity. Fig. 3 is a plot of the standard deviation of the horizontal velocity at the same locations as fig. 2. Contrary to the mean flow, there is better agreement between the simulated and observed standard deviation of the velocity in the troughs of the ripples. In the troughs, the simulated and observed standard deviations are within 2 cm/s. The model overestimates the standard deviation above the crests of the ripples by a maximum of 5 cm/s. Except at the crests, there is very good agreement between the simulated and observed standard deviation profile shape. Above the boundary layer (i.e., z > 6), the simulated and observed mean and standard deviation of the horizontal velocity are in very good agreement with the velocities differing less than 0.3 cm/s.

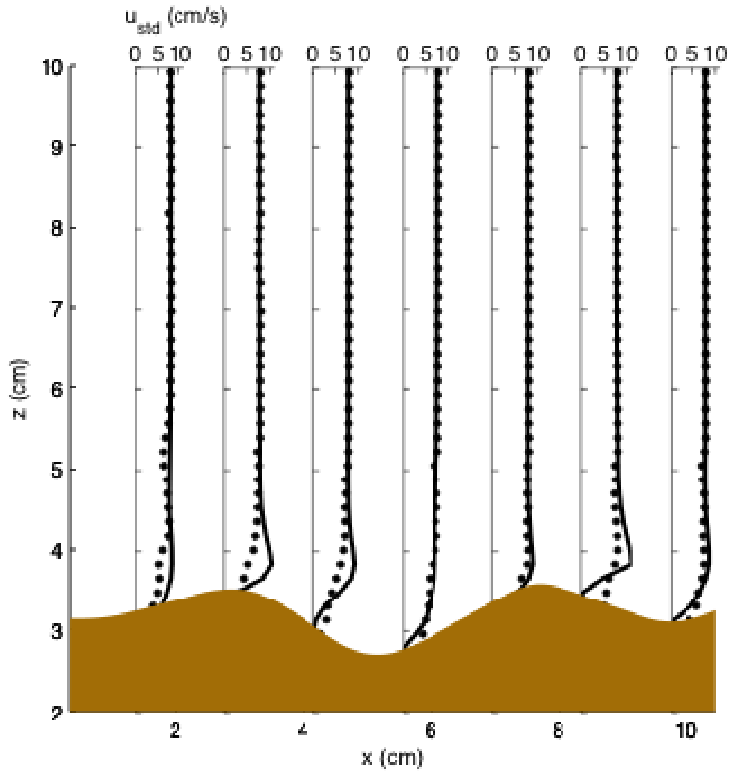

Figure 3: Profiles of the standard deviation of the horizontal velocity from the simulation (lines) and observations (dots) at varying locations above the bed.

4.2 Swirling strength

In complex, three-dimensional, and oscillatory flows, the vortex structures are often difficult to distinguish from the vorticity due to the boundary-generated

shear. The swirling strength, λ_{ci}, is used to identify the coherent closed rotational vortex structures excluding the interference from boundary-generated shear (fig. 4). The swirling strength is calculated as the imaginary part of the complex eigenvalues of the velocity gradient and is zero if the eigenvalues are not complex [13]. The method is effective in determining the location of vortex cores in boundary layer shear flow, but does not identify the rotational direction. The ensemble-averaged swirling strength plotted in Fig. 4 illustrates that the time-varying quantities from the simulation and observations are also in good agreement. The horizontal and vertical positions of the vortices and the timing relative to the wave phase predicted by the model are in good agreement with the observations. The strength of the vortices predicted by the model is only slightly greater than the observations. The observations show less coherent vortex structures and are noisier than the simulation.

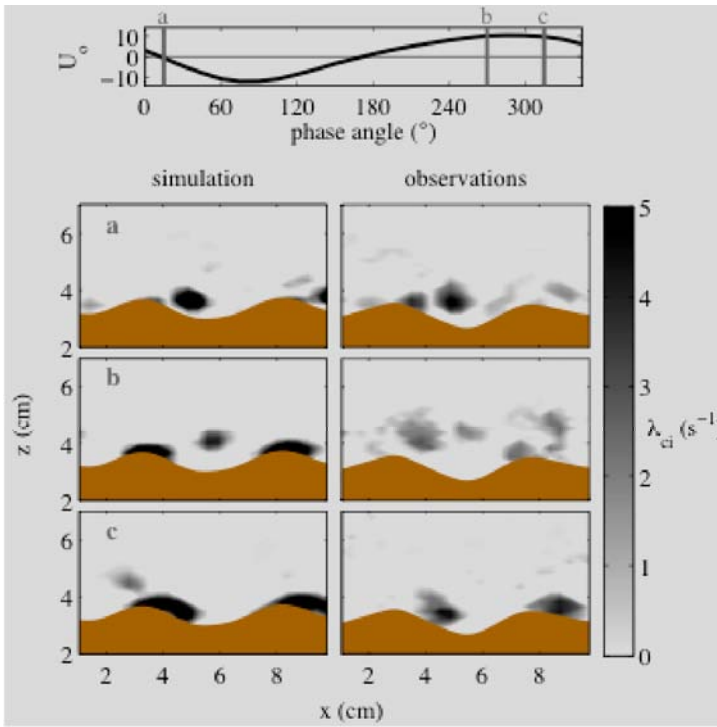

Figure 4: Ensemble-averaged simulated and observed swirling strength, λ_{ci} (s^{-1}), at three phase locations of a wave. Flow is initially directed to the left. Darker areas indicate coherent vortex structures. A time-average of the simulated and observed bed profile is plotted for reference.

5 Discussion

Coherent vortex structures in bottom boundary layer flow over rippled beds have been found to play a significant role in erosion and deposition of sediment on the seafloor. Therefore, a numerical model examining the dynamics of bottom boundary layer flow must accurately predict the temporally and spatially varying velocity fields. While differences in the magnitude of the velocity and swirling strength exist, the simulated vortex location, size and shape agreed remarkably well with the observed vortex structures. The noise associated with making measurements in a laboratory forces the need to smooth the data to remove any outliers. Data smoothing damps out the closed streamline paths of the observed flow measurements, decreasing the strength of the coherent vortices. Typically only very strong circulation events are recorded in situ [14]. In addition, large light reflections at the fluid-sediment interface result in a decreased peak correlation and a lower confidence in the velocity estimates near the bed. The inherent ability of the model to calculate velocities with equal resolution everywhere, even in the highly concentrated layer of moving sediment at the bed would account for some of the differences between the simulated and observed velocity.

6 Conclusions

The turbulent, three-dimensional nature of the wave bottom boundary layer forces the need for three-dimensional, time-dependent simulations in order to fully capture the physics of the flow over ripples. While two-dimensional models are typically less computationally expensive and generally require less storage and processing, they must compensate for their deficiencies in the physics by introducing non-physical terms. Our three-dimensional mixture model has been validated with laboratory data and provides an unprecedented level of detail about sand ripple dynamics that exceeds field and laboratory technologies. Future work will examine the complex, three-dimensionality of the turbulent bottom boundary layer flow over rippled beds.

References

[1] Blondeaux, P. and Vittori, G., Vorticity dynamics in an oscillatory flow over a rippled bed, *Journal of Fluid Mechanics*, 226, pp. 257-289, 1991.
[2] Scandura, P., Vittori, G., and Blondeaux, P., Three-dimensional oscillatory flow over steep ripples, *Journal of Fluid Mechanics*, 412, pp. 355-378, 2000.
[3] Barr, B. C., Slinn, D. N., Pierro, T., and Winters, K. B., Numerical simulation of turbulent, oscillatory flow over sand ripples, *Journal of Geophysical Research*, 109(C9), pp. 1-19, 2004.
[4] Chang, Y. S. and Scotti, A., Entrainment and suspension of sediments into a turbulent flow over ripples, *Journal of Turbulence*, 4, 2003.

[5] Zedler, E. A. and Street, R. L., Sediment transport over ripples in oscillatory flow, *Journal of Hydraulic Engineering*, 132(2), pp. 180-193, 2006.
[6] Rodriguez Abudo, S. and Foster, D.L., Characterization of the wave bottom boundary layer over movable rippled beds, *Eos Trans. AGU*, Ocean Sci. Meet. Suppl., Abstract PO21B-05, 2010.
[7] Penko, A. M., Slinn, D. N., and Calantoni, J., Model for mixture theory simulation of vortex sand ripple dynamics, *Journal of Waterway Port Coastal and Ocean Engineering- ASCE,* in press.
[8] Eilers, H., The viscosity of the emulsion of highly viscous substances as function of concentration, *Kolloid-Zeitschrift*, 97(3), pp. 313-321, 1941.
[9] Einstein, A., Eine neue Bestimmung der Moleküldimensionen (German) [A new determination of molecular dimensions], *Annalen der Physik*, 19, pp. 289-306, 1906.
[10] Nir, A. and Acrivos, A., Sedimentation and sediment flow on inclined surfaces, *Journal of Fluid Mechanics*, 212, pp. 139-153, 1990.
[11] Richardson, J. F. and Zaki, W. N., Sedimentation and fluidisation: part 1, *Transactions of the Institution of Chemical Engineers*, 32, pp. 35-53, 1954.
[12] Leighton, D. and Acrivos, A., Viscous resuspension, *Chemical Engineering Science*, 41(6), pp. 1377-1384, 1986.
[13] Zhou, J., Adrian, R. J., Balachandar, S. and Kendall, T. M., Mechanisms for generating coherent packets of hairpin vortices in channel flow. *Journal of Fluid Mechanics*, 387, pp. 353–396, 1999.
[14] Nichols, C. S. and Foster, D. L., Full-scale observations of wave-induced vortex generation over a rippled bed, *Journal of Geophysical Research*, 112(C10), 2007.

This page intentionally left blank

Validation of a stochastic droplet breakup model applied to a liquid jet in turbulent crossflow

R. Blanchard[1] & S. Shi[2]
[1]*GE Global Research, USA*
[2]*GE Power & Water, USA*

Abstract

Coal gasification technology has the potential to reduce the environmental impact of coal power by enabling technologies like integrated gasification combined cycle (IGCC) and carbon capture for sequestration (CCS) for power generation. Numerical simulations of the various components of a coal gasification plant using validated CFD models enables faster configuration improvement cycles and thereby increased component performance, reliability, and overall cycle efficiency. Many such computations require the simulation of turbulent, multi-phase flows where the atomization and agglomeration of liquids play a critical role in plant processes. This paper focuses on the development and validation of a stochastic droplet breakup and agglomeration model for use in a steady-state RANS simulation of a liquid jet in a turbulent cross-flow. The models aim to accurately predict the trajectories and sizes of liquid droplets without incurring the computational cost of more expensive methodologies such as LES or VOF which are currently too computationally intensive to be used in the design cycle. The model builds on similar models proposed by Apte and Kuan by proposing a new probability density function (PDF) for the break-up process and adapting the methodology to a steady-state framework. The model is then validated against measurements made by Wu. The model shows good qualitative and quantitative agreement with measurement of the downstream mass flux distribution of the liquid droplets. An agglomeration model is added to the simulation which improves the agreement between predicted and measured Sauter-mean diameter (SMD) of the liquid droplets downstream of the initial atomization region.
Keywords: atomization, agglomeration, stochastic, gasification.

WIT Transactions on Engineering Sciences, Vol 74, © 2012 WIT Press
www.witpress.com, ISSN 1743-3533 (on-line)
doi:10.2495/AFM120331

1 Introduction

Coal-derived power plays a major role in meeting the world's energy needs and will continue to do so for many years. Technologies can make coal-derived power generation with fewer emissions than traditional coal plants. Coal gasification technology has the potential to reduce the environmental impact of coal power by enabling technologies like integrated gasification combined cycle (IGCC and carbon capture for sequestration (CCS) for power generation. Numerical simulations of the various components of a coal gasification plant using validated CFD models enables faster configuration improvement cycles and thereby provide increased component performance, reliability, and overall cycle efficiency. Many such computations require the simulation of turbulent, multi-phase flows where the atomization and agglomeration of liquids play a critical role in plant processes.

This paper focuses on the development and validation of a stochastic droplet breakup and agglomeration model for use in a steady-state RANS simulation of a liquid jet in a turbulent cross-flow. The goal of the current study is to accurately predict the trajectories and sizes of the atomized particles using a discrete phase model (DPM) coupled with a 2-equation turbulence model without incurring the computational cost of more expensive methodologies such as large eddy simulation (LES) or volume of fluid (VOF) which are currently too computationally intensive to be used in the design cycle.

2 Breakup model formulation

The proposed breakup model is similar to the previously-published models by Apte [1] and Kuan [2] in that breakup events are triggered when a droplet's Weber number exceeds a critical value (this work assumes that $We_{CR} = 6$) and the and the size of the child droplets are determined by a stochastic sampling of a probability density function (PDF) based on Weber number. The current model differs from previous versions in 3 key areas:

1. The breakup PDF formulation prevents particle growth (child droplets cannot be larger than their parents).
2. The model is implemented for steady-state spray simulations.
3. Droplet parcelization is held constant throughout the atomization process.

2.1 Breakup PDF

The proposed breakup function from which new particle diameters are sampled, exhibits many of the same self-similar properties described by Apte [1] but is formulated such that no child droplet can be larger than its parent. The function is formulated such that the ratio of droplet Weber number to critical Weber number is the key parameter that drives the rate of breakup during the atomization process and is shown in cumulative distribution function (CDF) form in equation (1), where i and i+1 subscripts respectively denote parent and

child droplet characteristics. The timescale of droplet breakup is given in equation (2), where ρp, ρg, dp, and Vp-g denote droplet density, gas density, droplet diameter, and the magnitude of relative velocity between the droplet and gas respectively. No further breakup events are allowed to occur until during the time interval ΔtBU after a breakup event is triggered. The value of the constant C in equation (2), is taken to be $\sqrt{1/3}\sqrt{1/3}$ from O'Rourke [3]. The definition of Weber number is given in (3), where σ denotes droplet surface tension.

$$CDF = p_o\left(\frac{We_{i+1}}{We_i}\right)^{\left(\frac{We_i}{We_{CR}}\right)} \tag{1}$$

$$\Delta t_{BU} = C\sqrt{\frac{\rho_p}{\rho_g}}\frac{d_p}{V_{p-g}} \tag{2}$$

$$We = \frac{\rho_p V_{p-g}^2 d_p}{\sigma_g} \tag{3}$$

2.2 Numerical implementation and parcelization

The droplet breakup model algorithm is implemented in the following steps:

1. A new particle parcel stream is introduced into the simulation with diameter equal to the injector orifice diameter.
2. As the particle is marched through the steady-state flow field, the particle's Weber number is calculated at each time step, if the Weber number is ever greater than We_{CR} and the elapsed time since the last breakup event (or injection) is greater than Δt_{BU}, a breakup event is triggered.

When a breakup event is triggered and a new particle diameter is sampled from equation (1) but the parcelization of the stream is held constant as the new particle diameter is applied to the entire parcel stream.

3 Validation

The current model was applied to a simulation of an experiment by Wu *et al.* [4, 5], which consisted of a liquid jet injected into a turbulent crossflow of gas at low Mach number. Measurements of mass flux, particle velocity, and particle size were made along the spray centerline 300 nozzle diameters downstream of the injection point.

The CFD simulation of the experimental test section was modelled as shown in as a 12.5 x 40.6 x 7.5 cm rectangular domain with 1.0e6 grid cells and wall y+

of approximately 20 for the baseline simulation. The baseline conditions consisted of a .5 mm diameter liquid jet (all distance normalization of the results is done based on this diameter) being injected at 19.3 m/s into a 103 m/s gas crossflow. Turbulence was modelled using the standard k-epsilon model and droplet-turbulence interaction was accounted for using Fluent's default stochastic random walk model. The spray was parcelized into 1e5 streams of equal mass flow. The liquid jet of pure water, was assumed to have surface tension and viscosity of 7.19e-2 N/m 1.003e-3 Pa-s respectively. The gas flow was assumed to have properties of air at standard sea-level conditions.

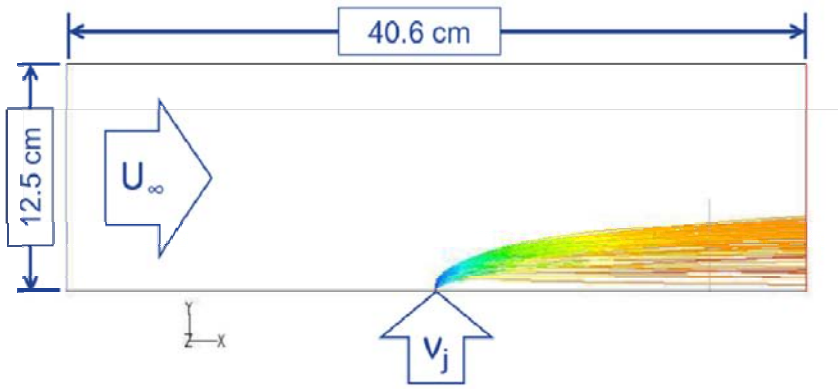

Figure 1: Schematic of wind tunnel and liquid jet.

In addition to the baseline case, case A, four additional runs were completed, shown in , to evaluate the sensitivity of the results to changes in liquid jet velocity (at 12.3 and 29 m/s respectively) and changes in crossflow velocity (69 and 137 m/s respectively). The mass flux profiles of these streams were also sampled along the spray centerline 300 injector diameters downstream of the liquid jet.

Table 1: 5 cases comprising this study.

Case	U (m/s)	v_j (m/s)
A	103	19.3
B	103	12.8
C	103	29
D	69	19.3
E	137	19.3

The droplet flux of the simulated spray showed good first- and second-moment agreement with the measured flux profiles as can be seen in Figure 2. While certainly some discrepancy exists between the vertical location of the measured and simulated peaks in the flux profiles, the centroids of the profiles match each other within 3-10% in all five cases as shown in Figure 3. The half-widths of the profiles are likewise similar between simulation and measurement.

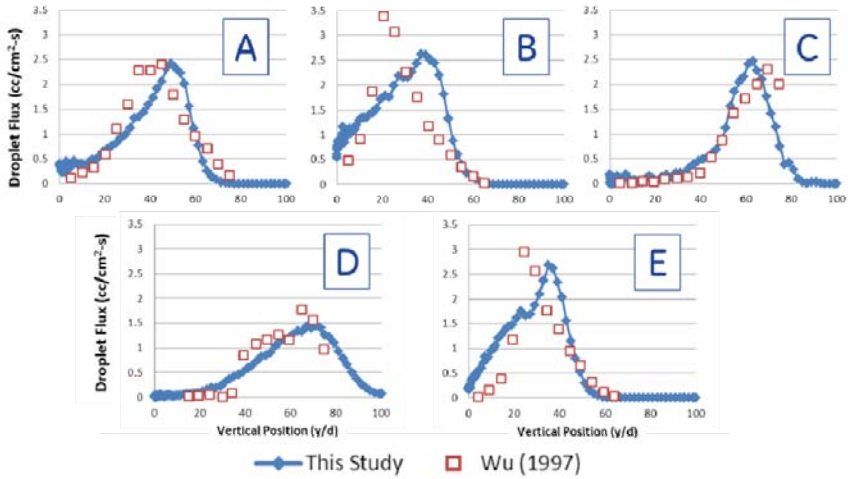

Figure 2: Droplet flux profiles at x/d = 300 downstream of the injection point.

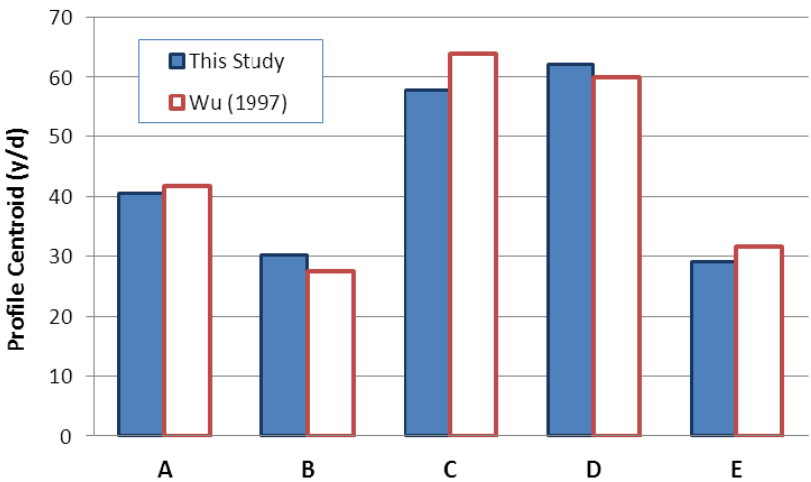

Figure 3: Comparison of profile centroids between the current study and measurements.

Table 2: Comparison of profile centroids between current study and measurements.

			Centroid Height (y/d)	
Case	U (m/s)	v_j (m/s)	Current Work	Wu (1997)
A	103	19.3	40.6	41.9
B	103	12.8	30.1	27.5
C	103	29	57.9	63.8
D	69	19.3	62.1	60.0
E	137	19.3	29.0	31.5

4 Agglomeration model

While the simulated particle trajectories showed good agreement with the measured profiles of particle mass flux, the profiles of Sauter-mean diameter (SMD) of the simulated sprays showed consistently smaller droplet sizes than were measured. It was hypothesized that the droplets were breaking and very rapidly reaching their final height above the injection plane but were coalescing to form larger droplets farther downstream before being measured. This hypothesis, if true, would explain how a droplet's height at the measurement plane could be decoupled somewhat from its size.

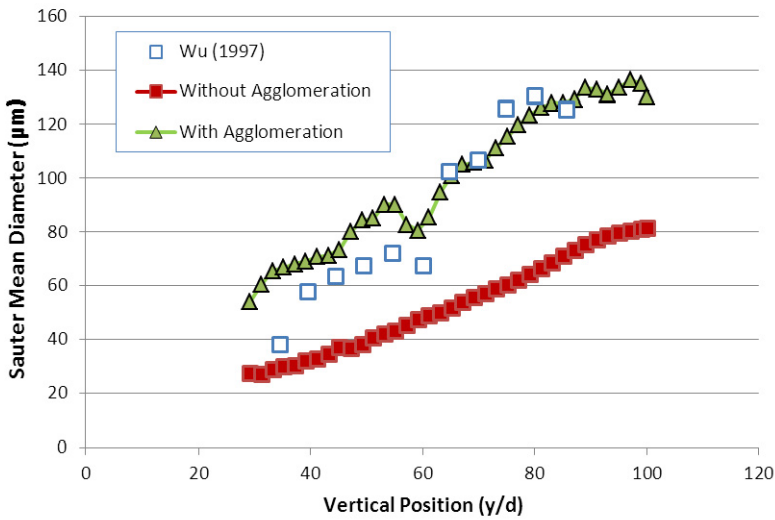

Figure 4: Sauter-mean diameter profiles at x/d = 300.

To account for agglomeration of droplets a simple droplet collision and coalescence model, originally developed by O'Rourke [3] for unsteady sprays, was adapted to a steady-state formulation as shown in equations (4) and (5), where K_T Δt_p m_p, C_{DPM}, and smd denote, local turbulent kinetic energy, droplet trajectory integration timestep, parcel mass, local droplet concentration, and the local SMD of the spray respectively. The effect of this model on the size distribution of the simulated spray is shown in Figure 4, which shows how the inclusion of the agglomeration model significantly improves the agreement between measured and simulated SMD profiles.

$$V = \frac{3}{2}\sqrt{K_T}\Delta t_p\left(\frac{m_p}{d_p} + \frac{C_{DPM}}{smd}\right) \tag{4}$$

$$\frac{d_{i+1}}{d_i} = \sqrt[3]{1+V} \tag{5}$$

5 Conclusions

The proposed steady state breakup model showed good agreement with measurements of droplet flux profiles downstream of the injector. When a simple droplet agglomeration model was incorporated into the simulation, the size distributions of the simulated spray matched the corresponding measurements as well. This simple set of models allows for the atomization process to be modelled with reasonable accuracy in a steady state framework that significantly reduces calculation time compared to other, more computationally intensive methods like volume-of-fluid or large eddy simulation, thus providing the designer with a low-cost option for simulating jet breakup.

References

[1] Apte S.V., Gorokhovski, M., Moin, P., LES of atomizing spray with stochastic modeling of secondary breakup, *International Journal of Multiphase Flow*. **29**, pp. 1503-22, 2003.
[2] Kuan, B., CFD Modelling of Liquid Jet and Cascade Breakup in Crossflows, *Seventh Seventh International Conference on CFD in the Minerals and Process Industries,* CSIRO: Melbourne, Australia, 2009.
[3] O'Rourke, P.J., Collective Drop Effects on Vaporizing Liquid Sprays, *PhD Thesis, Princeton University:* Princeton, New Jersey, 1981.

[4] Wu, P.K., Kirkendell, K.A., Fuller, R.P., "Spray Structures of Liquid Jets Atomized in Subsonic Crossflows" Journal of Propulsion and Power, **13(2)**, pp. 64-73, 1997.
[5] Wu, P.K., Kirkendell, K.A., Fuller, R.P., Spray Structures of Liquid Jets Atomized in Subsonic Crossflows. *Journal of Propulsion and Power*, **14(21)**, pp. 173-182 1998.

Section 6
Bubble and drop dynamics

This page intentionally left blank

Air–water: two phase flow behavior in a horizontal pipe using computational fluids dynamics (CFD)

F. Vásquez, M. Stanko, A. Vásquez, J. De Andrade & M. Asuaje
Laboratory of Mechanical Energy Conversion, Simón Bolívar University, Venezuela

Abstract

Two-phase flow is an area of primary interest, particularly for the petroleum industry, where a fair amount of these kinds of flows can be found in the production of oil wells. This study refers to the evaluation of two-phase flow air–water through a horizontal pipe of 0.0508m (2in) diameter and 1.016m (40in) length. A 3D CFD approach was used for reproducing the behavior of the dispersed bubble, stratified smooth and slug flow in a horizontal pipe. The pressure drop and liquid holdup associated with it were estimated. Data of the superficial velocities of the liquid and gas were taken from the literature; and then many CFD simulations were carried out using different multiphase flow models. The results were validated with the available experimental data from the literature. For the case in which the liquid is the continuous phase and the gas behaves as the dispersed one, the results show that the bubble disperse flow behaves homogeneously. In these simulations, for a 0.01mm gas bubble diameter the pressure drop presented a deviation of 6.12% over that reported in the literature. For the liquid holdup value a difference of 0.001% was obtained. An inhomogeneous approach with the free surface model reproduced satisfactorily the stratified smooth behavior. In addition, the influences of increasing water superficial velocity on the energy losses and the liquid holdup were obtained. However, for the studied numerical domain, the slug flow pattern could not be reproduced. All these results above allowed us to establish the great applicability of CFD modeling in the problem resolution of two-phase flow in a horizontal pipe.
Keywords: two-phase flow, CFD, flow patterns, liquid holdup, pressure drop.

WIT Transactions on Engineering Sciences, Vol 74, © 2012 WIT Press
www.witpress.com, ISSN 1743-3533 (on-line)
doi:10.2495/AFM120341

1 Introduction

In the petroleum industry, the two-phase flow characterization has an essential importance due to its presence during the production and transportation of crude oil and natural gas. The gas and liquid phases are distributed in the pipe in a variety of flow configuration, called flow patterns. The flow pattern prediction is a major problem in two-phase flow analysis. Indeed, main variables like: pressure drop, liquid holdup, heat and mass transfer coefficients are strongly dependent on the existing flow pattern. These variables have to be predicted in order to reduce the main potentially hazardous problems that such parameters could cause.

The explanation above is why many researchers study the two-phase flow behavior in horizontal and vertical pipes, trying to predict accurately the flow pattern. In that sense, Aziz and Petalas [1] proposed a mechanistic model applicable to all pipe geometries and fluid properties. Thus, new empirical correlations were proposed for: liquid/wall and liquid/gas interfacial friction in stratified flow, the liquid fraction entrained and the interfacial friction in annular-mist flow, and the distribution coefficient used in the determination of holdup in intermittent flow. The model application has shown the ability to predict reasonably accurate pressure drops and holdup under different operating conditions. Wongwises *et al.* [2] presented new correlations to predict the liquid holdup with horizontal concurrent stratified flow in a circular pipe. Also, they demonstrated that the liquid holdup can be predicted by using Taitel and Dukler momentum balance between both phases. Recently, Shoham [3] presented an approach for flow patterns prediction. The mathematical mechanistic model was based on the physical phenomena of the two-phase behavior analysis. The model allows its application to diverse operational conditions, showing results with significant confidence.

With nowadays computer performances and dedicated codes, numerical simulations of tridimensional two-phase flow calculation in a horizontal pipe are proposed with reasonable precision, providing a close look at the flow development through the pipe. In this new direction of two-phase flow understanding, the present study assesses the two-phase air-water flow in a horizontal pipe by means of 3D CFD flow simulations. The study mainly focus on predicting the behavior of the flow patterns, the pressure drop in the flow line, as well as on predicting the liquid holdup changes throughout the pipe. The specific objectives of the study are to:

- Reproduce the flow patterns behavior, for air–water mixture in a horizontal pipe by means of CFD techniques.
- Determine the pressure drop associated to the flow pattern under study.
- Determine the liquid holdup associated to each flow pattern through the pipe.
- Validate with literature data, the results obtained by the simulations.
- Establish the applicability of CFD techniques in the calculation of two-phase flow in a horizontal pipe.

2 Verification of flow patterns existence

Based on the Taitel and Dukler [4] flow patterns map, the studied flow patterns were selected. Due to the complexity of the flow patterns identification by means of visual observations, it was important to verify the flow patterns predicted by Taitel and Dukler for all the selected values of superficial velocities of water and air, against some correlations. This verification was carried out using the specific correlations presented in table 1, which are widely used in this research area [5].

Table 1: Test case values of water and air superficial velocity, for each flow pattern considered.

Taitel and Dukler flow pattern	V_{SL} [m/s]	V_{SG} [m/s]	Verification correlations
Dispersed bubble	8.429	0.100	Beggs and Brill
	6.629	0.100	
	8.408	1.000	
	6.881	1.000	
Stratified	0.100	0.100	Guzhov
	0.062	0.100	
	0.010	0.100	
	0.100	1.000	
	0.062	1.000	
	0.010	1.000	
Slug	6.458	10	Guzhov
	4.734	10	
	2.915	10	
	1.000	10	

For dispersed bubble the Beggs and Brill correlation [6] was used. On the other hand, to verify the presence of the flows stratified smooth and slug the correlation of Guzhov was used [3].

3 Numerical approach

Numerical simulations were carried out on a horizontal pipe of L/D coefficient equal to twenty (20). Furthermore, as in any CFD problem, a sensibility analysis was performed to guarantee the independence of the results with respect to the numerical grid. For the calculations, unstructured tetrahedral cells with inflated layers were created. The total number of elements in the final grid was 644,620. The simulations were performed using the software package ANSYS CFX v.11. To reproduce all the flow patterns above mentioned, an air-water two-phase mixture at 25°C and an Eulerian approach were used. The turbulence and the two-phase flow models were selected according to the three studied flow patterns

as it is shown in table 2. For dispersed bubble flow several gas bubble diameters were studied, among them are: 1, 0.1, 0.01 and 0.001 mm.

Table 2: Specification of numerical models used for each studied flow pattern.

Flow pattern	Two-phase flow model	Turbelence model	Temporal approach
Dispersed bubble	*Homogeneous:* mixture and particle	K-épsilon	Steady state
Stratified	*Inhomogeneous:* mixture and particle	Shear Stress Transport	Steady state
Slug	*Inhomogeneous:* free surface and particle	K-épsilon	Unsteady & steady state

The equations describing the fluid flow through a specific domain need to be numerically closed stipulating the so-called boundary conditions. At the inlet of the domain, a total pressure condition and the volumetric fractions of the air and water were set. This condition is the most accurate due to the inflow energy is defined and the software is allowed to obtain gradients in velocity and pressure. At the outlet the mass flow was specified. Each flow rate of interest corresponds to a different superficial velocity. The viscous fluxes are computed with a "high resolution" scheme, which means that in regions with low variable gradients, a second order scheme is used. In areas where the gradients change sharply, a first order upwind scheme is used to maintain robustness. Furthermore, root mean squared convergence criteria with an average residual target of 1×10^{-4} in mass, momentum and turbulence (k-ε) equations was used.

In order to validate the results obtained by CFD calculation, the pressure drop and holdup were compared with values calculated from experimental data in the literature. These values were estimated by using the Wallis homogeneous flow model [7] for dispersed bubble, Lockhart and Martinelli separated flow model [8] for stratified smooth and finally the Dukler and Hubbard model [9] for slug.

4 Results and discussion

All flow patterns existence was verified using the mentioned correlations criteria. The conditions of the used correlations for verifying the flow patterns existence were satisfied in all the studied points of the disperse bubble, stratified and slug flow. Afterward, in this section the fluid dynamic behavior of the flow patterns in the horizontal pipe is addressed for the operating conditions in Table 1. First, the flow patterns behavior are qualitatively and quantitatively studied by means of water volume fraction contours and superficial velocity calculations. Next, pressure drop and holdup are assessed though the pipeline. Finally, the numerical calculations are compared with experimental data from literature.

4.1 Flow patterns behavior

4.1.1 Dispersed bubble flow

A good numerical convergence and representation of the fluid dynamic associated with dispersed bubble flow was reached by using the homogenous approach with the particle model (particles diameter: 0.01mm). This flow pattern could be easily identified as it is shown in the fig. 1. The water volume fraction contour shows the dispersed gas phase as small bubbles into the continuous liquid phase.

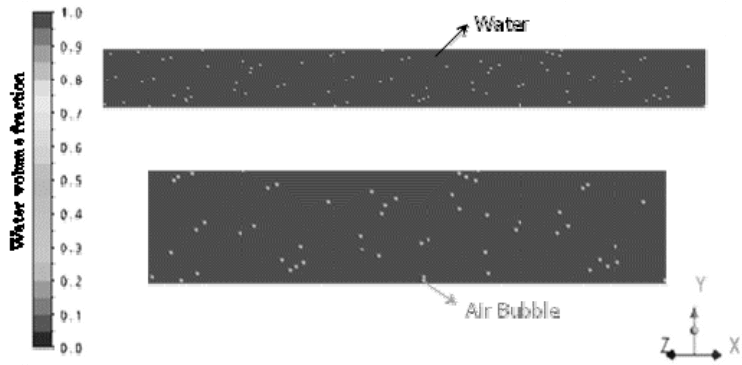

Figure 1: Dispersed bubble flow pattern throughout the pipe.

4.1.2 Stratified flow

This flow pattern was successfully reproduced with an inhomogeneous multiphase modeling, using the free surface model. In fig. 2, the liquid and gas velocities were plotted through the pipe. The figure presents a mixed flow at the inlet, and due to the buoyancy effect the phases are separated flowing through the pipe. The water flows at the bottom of the pipe and the air on the top. This stratified smooth flow takes place under relatively low flows of gas and liquid.

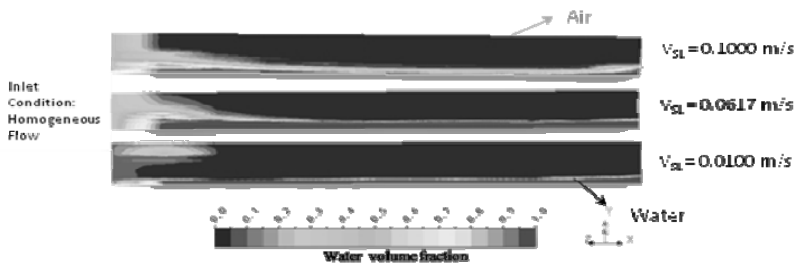

Figure 2: Stratified smooth flow pattern throughout the pipe.

Figure 3 depicts the liquid and gas velocities. It is possible to see that the gas phase moves faster than the liquid one.

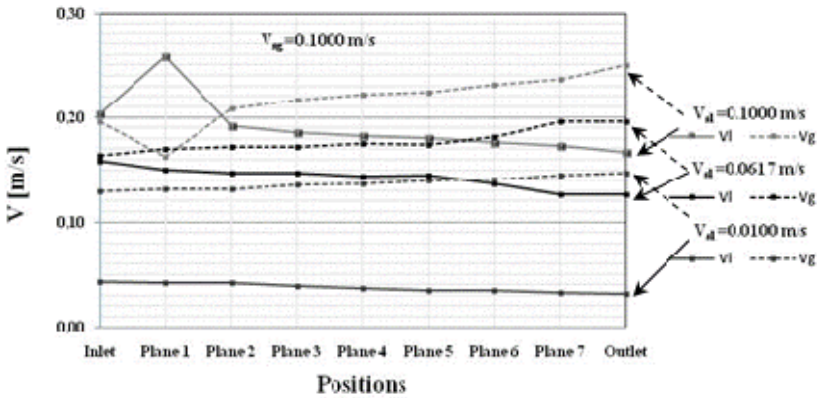

Figure 3: Velocities of the phases in stratified smooth flow pattern for V_{SG}=0.10 m/s.

4.1.3 Slug flow

With regard to the slug flow pattern, in spite of the fact that a sinusoidal perturbation in the free surface model was set and a good numerical convergence was reached during the calculation, the slug flow configuration could not be reproduced. Even though the beginning of the flow stratification was observed, the slug flow was not completed; this could be attributed to the short pipe length which might not have been long enough to establish the stratification of the flow and to the slug development. These observations are in accordance with that Vallée *et al.* [10] reported with regard to the pipe length needed for slug generation, which can have an important influence on the evolution of the flow regime along the pipe.

4.2 Pressure drop and holdup

4.2.1 Dispersed bubble flow

In the figures 4 and 5 are shown the comparisons between obtained pressure drop for a V_{SG}=0.1m/s and obtained pressure drop for a V_{SG}=1m/s, for several gas bubble diameter. As it was expected, the total pressure drop increases with increasing the superficial velocities of the liquid and gas phases. This is consistent with the fact of modeling the disperse bubble flow as a homogeneous flow with average physical properties. The relation between such parameters is directly proportional, so the greater the mixture velocity, the greater is the pressure obtained [3].

In addition, Figures 6 and 7 confirm the homogeneous flow condition in view of the fact that non slippage is observed between the liquid and the gas

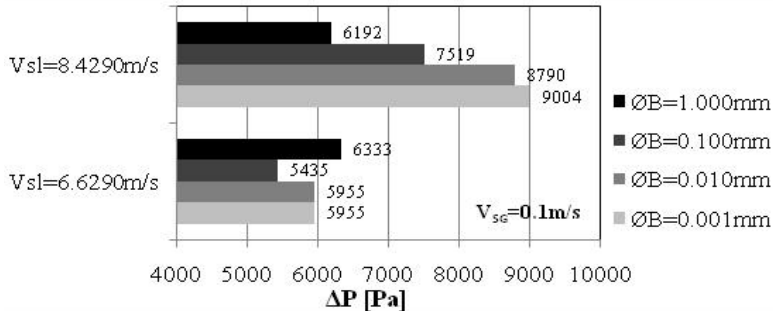

Figure 4: Total pressure drop in dispersed bubble for several bubble diameters and V_{SG}=0.10 m/s.

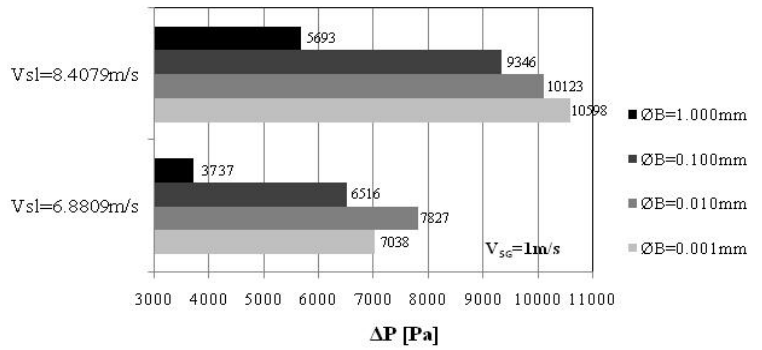

Figure 5: Total pressure drop in dispersed bubble for several bubble diameters and V_{SG}=1 m/s.

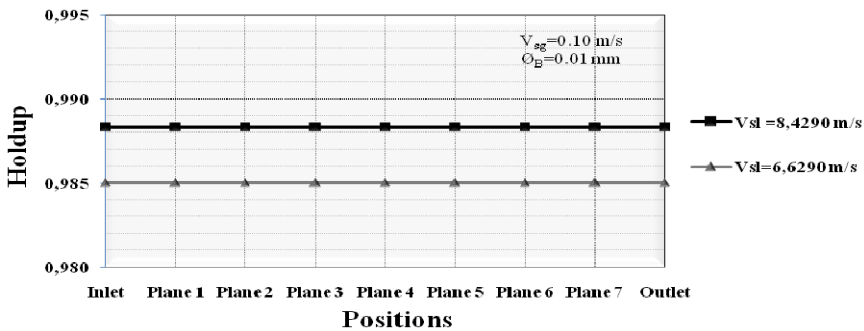

Figure 6: Holdup in dispersed bubble through the pipe for V_{SG}=0.10 m/s.

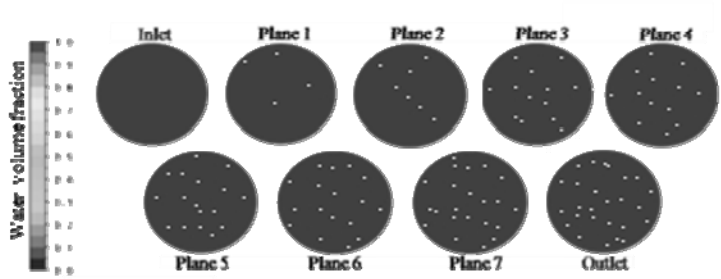

Figure 7: Holdup throughout each plane of the pipe for V_{SG}=0.10 m/s and V_{SL}=8.42m/s.

velocities. The gas bubbles are carried out by the liquid phase at the same velocity resulting in zero slippage. As it was expected, the holdup for each established superficial velocity remains constant.

4.2.2 Stratified smooth flow

The total pressure drop for a stratified flow is shown in the fig. 8. The increase of the superficial velocities of the phases leads to a significant pressure drop in the pipe; this occurs as a fluid dynamic response to the decrease of the total pressure at the outlet caused by the velocity increase, meaning greater pressure losses throughout the pipeline.

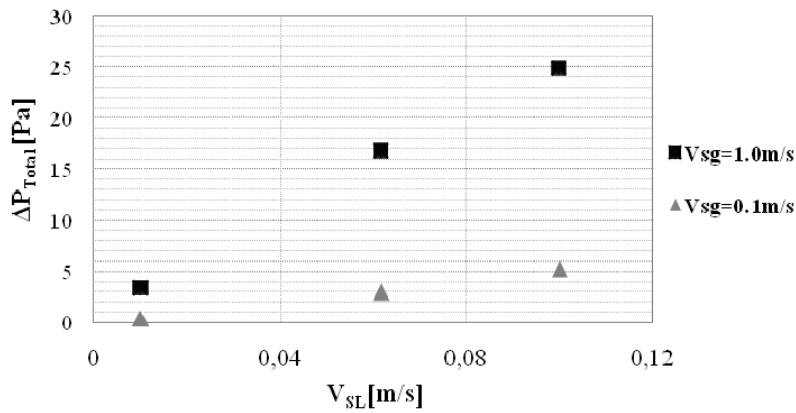

Figure 8: Total pressure drop in stratified smooth through the pipeline.

Fig. 9 shows the holdup along the pipe for several water superficial velocity values, keeping the air superficial velocity constant at 0.1m/s. As it was expected, greater holdup was obtained as liquid superficial velocity was increased. This is consistent with the mass conservation consideration. As a result, an increase of the amount of the liquid results in an increase of the liquid area and a decrease of the gas area, simultaneously. This is reflected with a larger

liquid accumulation in the bottom of the pipeline. Furthermore, fig. 10 shows how the slippage takes place between the two phases.

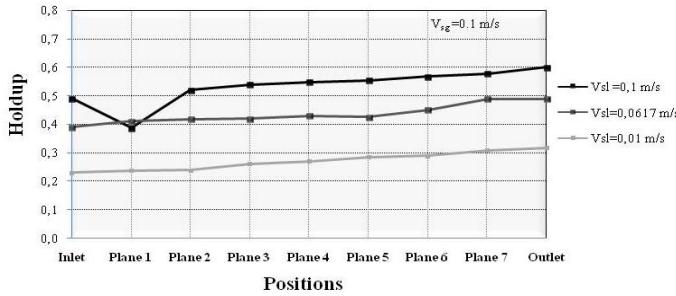

Figure 9: Holdup throughout each plane of the pipe for V_{SG}=0.10 m/s in stratified smooth.

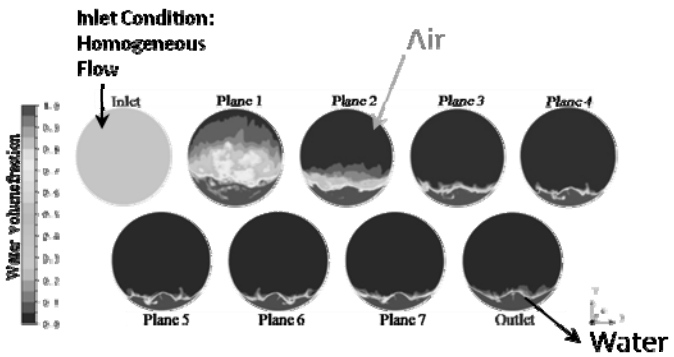

Figure 10: Holdup throughout each plane of the pipe for V_{SG}=0.10 m/s and V_{SL}=0.0617m/s, in stratified smooth.

4.3 Comparison with experimental data from literature

4.3.1 Dispersed bubble flow

With regard to the total pressure drop, in the figure 11it can be seen that for 0.01mm and 0.001mm bubble diameters, the obtained percentage deviations were smaller than 10%. The particle size that reproduces better the dispersed bubble behavior is 0.01mm (according to all the obtained results previously), which can be observed on the mentioned figure. This result was obtained for a V_{SG}=1m/s as well.

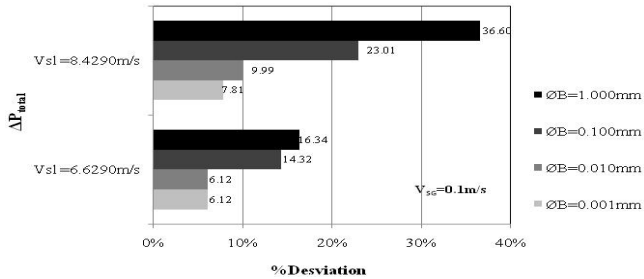

Figure 11: %Desviation of ΔP_{total} in dispersed bubble for V_{SG}=0.10 m/s.

In addition, with regard to holdup values, the error percentages are lower than 0.2% for all the particle sizes evaluated under different superficial velocity conditions (fig. 12). The outstanding results show consistency with the experimental data.

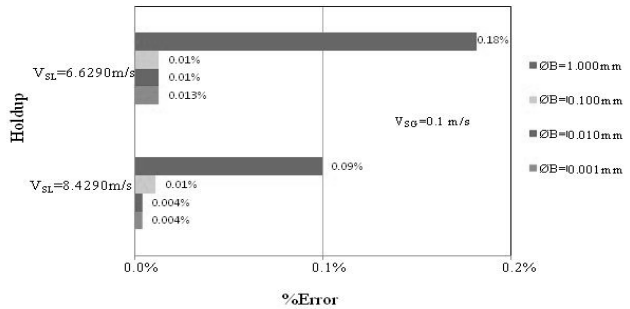

Figure 12: %Error of the holdup in dispersed bubble for V_{SG}=0.10 m/s.

4.3.2 Stratified smooth flow

In fig. 13, a comparison of the results of pressure drop obtained by CFD calculation with those calculated according to the Lockhart and Martinelli model, it was found that error percentages fluctuated between 0.98% and 7.09%, which shows a good accuracy.

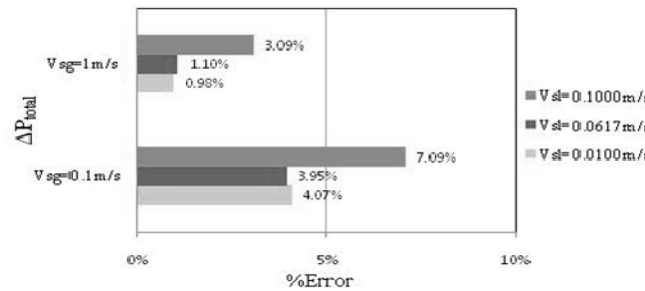

Figure 13: %Error of ΔP_{total} in stratified smooth for different V_{sl}.

Furthermore, figure 14 shows greater percentage of errors in the obtained holdup (between 2.55% and 20.24%). Nevertheless, the results are considered acceptable.

In summary, the set of simulation models have been addressed to reproduce flow patterns for several operation conditions. The results could be considered satisfactory for each flow pattern, since the errors were lower than 20% in relation which those reported in literature [3]. Thus, the numerical approach is widely useful in problems resolution with two-phase flow in horizontal pipe.

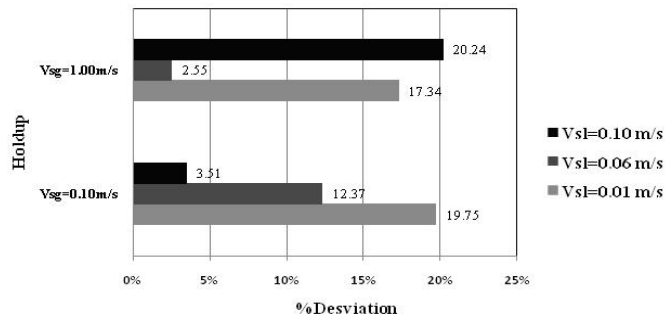

Figure 14: %Error of holdup in stratified smooth for different V_{sl}.

5 Conclusions

1. Two-phase air water flow behavior was evaluated in a horizontal pipe, ϕ=2in, by means of 3D CFD calculations.
2. Dispersed bubble flow pattern was reproduced accurately.
3. The dispersed bubble flow behaved homogenous. This result was obtained by using a homogenous modeling with the particle model, 0.01mm bubble diameter. For this diameter, the greater the mixture velocity, the greater was the obtained total pressure drop. The liquid holdup is remained constant, for each assessed air superficial velocity.
4. The inhomogeneous approach with free surface model reproduced in an expected way the stratified flow. As the water superficial velocity was increased, keeping constant V_{SG}, greater losses in the flow and greater accumulation of liquid in the bottom of the pipeline were reported.
5. Even though the slug flow existence was verified by using the literature models. It was found with CFD simulations that the pipe length used was insufficient to reproduce this flow pattern.
6. The CFD is suitably applicable in the behavior reproduction of the dispersed bubble and stratified smooth flow, obtaining reliable results with a deviation rate smaller than 20%.

6 Nomenclature

V_{SL}: Liquid superficial velocities [m/s]
V_{SG}: Gas superficial velocities [m/s]
ϕ_B: Bubble diameter [mm]
ΔP_{TOTAL}: Pressure total drop [Pa]
Holdup: Liquid holdup

References

[1] Aziz K.and Petalas N., A mechanistic model for multiphase flow in pipes. *SPE* 9839. 1998.
[2] Wongwises, S., Khankaew, W. and Vetchsupakun, W., Prediction of liquid holdup in horizontal stratified two-phase flow. *J. Sc. Tech*.,Vol. 3, pp. 48-59, 1998.
[3] Shoham, O., Mechanistic modeling of gas-liquid: two-phase flow in pipes. *SPE* 97816. 2006.
[4] Taitel, Y. and Dukler, A., A model for predicting flow regime transitions in horizontal and near horizontal gas liquid flow. *AIChE Journal*, Vol. 22, pp. 47-55, 1976.
[5] Vásquez, F. Evaluation of a Biphasic Fluid Behavior Air-Water in a Horizontal Pipe through numeric tools of Computational Fluids Dynamics (CFD). Engineering thesis. *University of Oriente.* 2009.
[6] Beggs, H. and Brill, J., A study of two phase flow in pipes. *J. Pet. Tech*. Vol. 25, pp 607-617. 1973.
[7] Wallis, G.B., One-Dimensional Two-Phase Flow, McGraw-Hill Book Co.: New York. 1969.
[8] Lockhart, R. and Martinelli, R., Proposed correlation of data for isothermal two-phase, two-component flow in pipes. *Chemical Engineering Science*. Vol. 45, pp 39-48. 1949.
[9] Dukler, A. and Hubbard, G., A model for gas-liquid slug flow in horizontal and near horizontal tubes. *Chemical Engineering Fundamentals.* 1975.
[10] Vallée, C., Höhne, T. and Sühnel., Experiments and CFD simulation of stratified horizontal two-phase flow. International topical, project number 150 1265. 2005.

Isenthalpic oscillations with quadratic damping in saturated two-phase fluids

J. V. Madison
Ebara International Corporation, Sparks, Nevada, USA

Abstract

Saturated two-phase fluid flows are often subject to pressure induced oscillations. Due to compressibility the vapour bubbles act as a spring with an asymmetric non-linear characteristic. The volume of the vapour bubbles increases or decreases differently if the pressure fluctuations are compressing or expanding; consequently, compressing pressure fluctuations in a two-phase pipe flow cause less displacement in the direction of the pipe flow than expanding pressure fluctuations. The displacement depends on the ratio of liquid to vapour, the ratio of pressure fluctuations over average pressure, on the exciting frequency of the pressure fluctuations and the damping factor.

In addition, pressure fluctuations in saturated vapour bubbles cause condensation and evaporation within the bubbles and change periodically the liquid to vapour ratio and influence the dynamic parameters for the oscillation. The oscillations conform to an isenthalpic process at constant enthalpy with no heat transfer and no exchange of work. Due to friction forces the oscillations are subjected to quadratic fluid damping.

The paper describes the governing non-linear equation for quadratically damped oscillations in saturated two-phase fluids with condensation and evaporation, and presents steady state approximate solutions for free and for pressure induced oscillations. Resonance criteria and stability are discussed.

Keywords: two-phase flow, isenthalpic oscillations, quadratic fluid damping, saturated fluid, condensation, evaporation, steady state solutions.

1 Introduction

A saturated two-phase fluid is a mixture of liquid and vapour. The volumetric ratio R between the vapour and the liquid portion is defined as

WIT Transactions on Engineering Sciences, Vol 74, © 2012 WIT Press
www.witpress.com, ISSN 1743-3533 (on-line)
doi:10.2495/AFM120351

$$R = \frac{V_v}{V_v + V_L} \tag{1}$$

where R=0 for pure liquid and R=1.0 for pure vapour. In standard books for Thermodynamics [1], the ratio R is called the quality of the fluid with the symbol x instead of R. V_V is the vapour volume and V_L is the liquid volume. With very good accuracy, the liquid portion can be assumed to be incompressible when compared to the compressible vapour portion. The vapour portion follows approximately the ideal gas equation of state with the vapour volume V_V inversely proportional to the pressure p at constant temperatures. Pressure changes Δp and volumetric changes are related by (2)

$$\frac{p+\Delta p}{p} = \frac{V_V}{V_V + \Delta V_V} \tag{2}$$

Eqn (2) may also be written in the form:

$$\Delta p = -p \frac{\Delta V_V}{V_V + \Delta V_V}. \tag{3}$$

Within a controlled volume of a two-phase fluid defined as the sum of V_V and V_L equals one. The volumetric vapour content is equal to

$$V_v = R \tag{4}$$

The amount of condensing and evaporating fluid depends on the pressure change, and with r as the rate of change the momentary vapour portion V_V as a function of the pressure is

$$V_v = R + r \cdot \Delta p\,. \tag{5}$$

Fig. 1 shows the asymmetric oscillations in a two-phase pipe flow. For a given absolute pressure difference Δp the absolute displacement $\Delta X(t)$ is smaller for compression than for expansion.

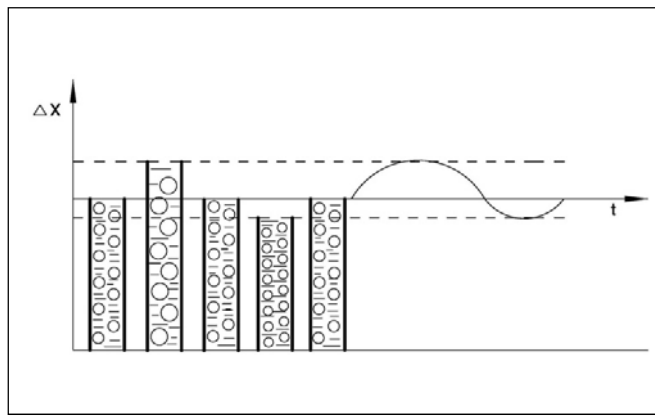

Figure 1: Asymmetric displacement of vapour bubbles for expansion and compression.

Fig. 2 demonstrates the condensation and evaporation within the vapour bubble for isenthalpic compression and expansion for saturated two-phase fluids, if the slope of the curves (R=constant) is positive [1]. The slope is positive towards the liquid side of the saturation dome. A pressure increase causes a partial condensation, and a pressure decrease causes a partial evaporation of the vapour bubble.

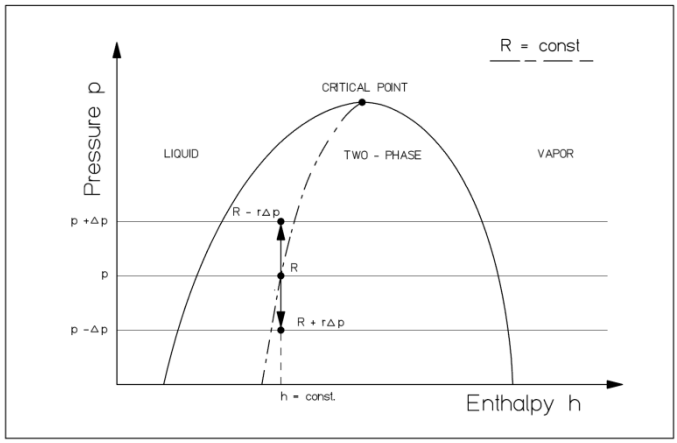

Figure 2: Isenthalpic oscillations with condensation for increasing pressure.

Fig. 3 demonstrates the condensation and evaporation for a negative slope of the *R*=constant curves. The slope is negative towards the vapour side of the saturation dome, and a pressure increase causes a partial evaporation, and a pressure decrease causes a partial condensation of the vapour bubble.

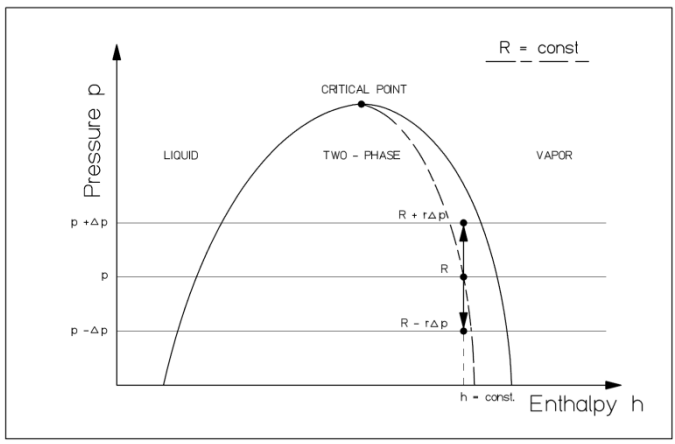

Figure 3: Isenthalpic oscillations with evaporation for increasing pressure.

Any evaporation makes the spring characteristic of the oscillating system softer and the mass smaller, and any condensation makes the spring characteristic stiffer and the mass larger. These changes of the system characteristics during a periodic oscillation result in complicated non-linear periodic oscillations.

2 Free isenthalpic oscillations in saturated fluids

Pressure changes Δp act as a force in the axial direction X of the pipe. The compressible vapour volume and the mass of the liquid volume form an oscillating system. The vapour volume acts as an asymmetric spring and generates axial forces non-linear to the displacement X as a function of time t.

$$\Delta p \approx -X \approx -\Delta V_V \tag{6}$$

The density of the vapour is negligibly small compared to the density ρ of the liquid, and the oscillating mass m within the controlled volume $V_V + V_L = 1$ depends only on the volume V_L of the liquid.

$$m = \rho V_L = \rho(1 - V_V) = \rho(1 - R + r\Delta p) = \rho(1 - R - r\,X) \tag{7}$$

Eqn (8) is a non-linear differential equation that models the free oscillation in saturated fluids with condensation and evaporation:

$$\rho\big(1 - R - r\,X(t)\big)\frac{d^2X(t)}{dt^2} + p\,\frac{X(t)}{R + r\,X(t) + X(t)} = 0. \tag{8}$$

For very small displacements, $X(t)$, the oscillating system can be considered as a linear harmonic oscillator,

$$\rho(1 - R)\frac{d^2X(t)}{dt^2} + p\,\frac{X(t)}{R} = 0. \tag{9}$$

with the natural frequency,

$$f_N = \sqrt{\frac{p}{\rho R(1-R)}}. \tag{10}$$

and

$$\frac{d^2X(t)}{dt^2} + f_N^2\,X(t) = 0. \tag{11}$$

The non-linear differential equation can be written now in term of the natural frequency and transforms into:

$$\big(1 - R - r\,X(t)\big)\frac{d^2X(t)}{dt^2} + f_N^2\,\frac{X(t)}{R + (1+r)X(t)} = 0. \tag{12}$$

Steady state approximate solutions for free isenthalpic oscillations are included in the solutions for the pressure induced oscillations.

3 Forced pressure induced oscillations in saturated fluids with quadratic damping

In the case of forced oscillations with harmonic excitation the non-linear differential equations transforms into:

$$\left(1 - R - r\,X(t)\right)\frac{d^2X(t)}{dt^2} + f_N^2\,\frac{R(1-R)X(t)}{R+(1+r)X(t)}\,,= Gf^2\cos(ft+\varphi) \qquad (13)$$

The exciting force Gf^2 depends on the exciting amplitude *G* and the square of the exciting frequency *f*. Friction forces generated by fluids are opposed to the velocity vector and proportional to the square of the displacement velocity multiplied by the damping factor D. In damped oscillations there is a phase angle φ between the harmonic excitation and the periodic oscillation.

The quadratic fluid damping force Q_D caused by the fluid friction is described with

$$Q_D = -D\,\frac{dX(t)}{dt}\left|\frac{dX(t)}{dt}\right| \qquad (14)$$

In the case of a forced oscillation with harmonic excitation and quadratic fluid damping the following non-linear differential equation describes the pressure-induced isenthalpic oscillations in saturated two-phase fluids

$$\left(1 - R - r\,X(t)\right)\frac{d^2X(t)}{dt^2} + f_N^2\,\frac{R(1-R)X(t)}{R+(1+r)X(t)}\,,= Gf^2\cos(ft+\varphi) - D\,\frac{dX(t)}{dt}\left|\frac{dX(t)}{dt}\right|. \qquad (15)$$

This highly non-linear differential equation cannot be solved by analytical methods and numerical or approximation methods have to be applied. The method described by A. Kimmel [3] using Fourier coefficients for the periodic error is applied to generate an approximate analytical solution for the steady state case.

If *X(t)* is an approximate solution, then *E(t)* is the function of the error for this approximate solution *X(t)*:

$$E(t) = \left(1 - R - r\,X(t)\right)\frac{d^2X(t)}{dt^2} + D\,\frac{dX(t)}{dt}\left|\frac{dX(t)}{dt}\right|\,,+ f_N^2\,\frac{R(1-R)X(t)}{R+(1+r)X(t)} - f^2\cos(ft+\varphi). \qquad (16)$$

The periodic functions of the error *E(t)* can be expanded in a Fourier series and the Fourier coefficients a_k and b_k of the periodic error are determined by (17) and (18).

$$a_k = \int_0^{2\pi} E(t)\cos(kft)\,d(ft)\,. \qquad (17)$$

$$b_k = \int_0^{2\pi} E(t)\sin(kft)\,d(ft)\,. \qquad (18)$$

By setting certain a_k and b_k equal to zero, the error for the *k-th* term of the Fourier series *E(t)* becomes zero. The approximate solution *X(t)* is then correct for the *k-th* term of the function *E(t).*

4 Approximate solution

For the given differential equation with forced oscillation through harmonic excitation $Gf^2\cos(ft+\varphi)$ the approximate solution *X(t)* corresponds to the same exciting frequency f but with a different amplitude A and with a phase angle φ between excitation and approximate solution.

$$X(t) = S + A\cos(ft)\,. \tag{19}$$

This is part of the Fourier series with $\frac{1}{2}a_0=S$ and $a_1=A$ and all other Fourier coefficients are equal to zero. By substituting *X(t)* into the differential equation the Fourier coefficients a_0 and a_1 of the error, *E(t)* can be determined by integration:

$$\begin{aligned} &-f^2\,(\mathrm{G}\cos(ft+\varphi) + A\cos(ft)\,(1-R-r(S+A\cos(ft)))),\\ &\quad +Df^2A\,sin(ft)|A\,sin(ft)| + f_N^2\,\tfrac{R(1-R)(S+A\cos(ft))}{R+(1+r)(S+A\cos(ft))}\,. \end{aligned} \tag{20}$$

Integration of (20) leads to the functions (21) and (22) for a_0 and a_1 respectively, and for b_1 to the function (23).

$$a_0 = a_0(A,S,f,\varphi,f_N,R,r,D,G) = 0\,. \tag{21}$$
$$a_1 = a_1(A,S,f,\varphi,f_N,R,r,D,G) = 0\,. \tag{22}$$
$$b_1 = b_1(A,S,f,\varphi,f_N,R,r,D,G) = 0\,. \tag{23}$$

Setting all three functions (21), (22) and (23) equal to zero produces the approximate solutions for A, S and φ as a function of the exciting frequency f, the exciting force *G* and the damping factor D determined by the vapour to liquid ratio *R* and the condensation and evaporation parameter *r*. The coefficient *S* can be determined from $a_0 = 0$ with (21).

$$S = -\frac{R}{1+r} + \sqrt{A^2 + \frac{4(1-R)^2\,\mathrm{R}^4}{(1+r)^2(A^2f_S^2r(1+r)+2(1-R)R)^2}}\,. \tag{24}$$

The scaled frequency f_S is the ratio of exciting frequency f over natural frequency f_N.

$$f_S^2 = f^2/f_N^2\,. \tag{25}$$

Eliminating φ using functions a_1 and b_1 generates the implicit function (26) for *A*, *S* and f_S.

$$\left(A(-1+R+rS) + \frac{2(1-R)R^2(R+S+rS-\sqrt{(R+S+r\,S)^2-A^2(1+r)^2}\,)}{A\,f_S^2(1+r)^2\sqrt{(R+S+r\,S)^2-A^2(1+r)^2}}\right)^2 + \left(\frac{8A^2D}{3\pi}\right)^2 = G^2. \tag{26}$$

Substituting eqn (24) into eqn (26) the solution for A and f_S is found as an implicit function.

Solutions of the functions a_0 , a_1 and b_1 are the stable steady state solutions for isenthalpic oscillations with condensation and evaporation in saturated two-phase fluids with quadratic damping.

The phase angle φ between the harmonic excitation and the periodic oscillation depends on *A*, *D* and *G*.

$$\varphi = \arcsin\left(\frac{8DA|A|}{3\pi G}\right). \tag{27}$$

The range of the phase angle is $0 \le \varphi \le \pi$ for

$$-3\pi G \le 8DA|A| \le 3\pi G\,. \tag{28}$$

5 Approximate solution examples

Steady state oscillations with quadratic damping in saturated two-phase fluid exist only with forced excitation.

A typical forced oscillation spectrum with G = 0.5 and R = 0.5 with a positive quality change rate of r = 0.1 and damping factors of D = 0, D = 0.25, D = 0.5 and D = 2.0 are shown in Fig. 4.

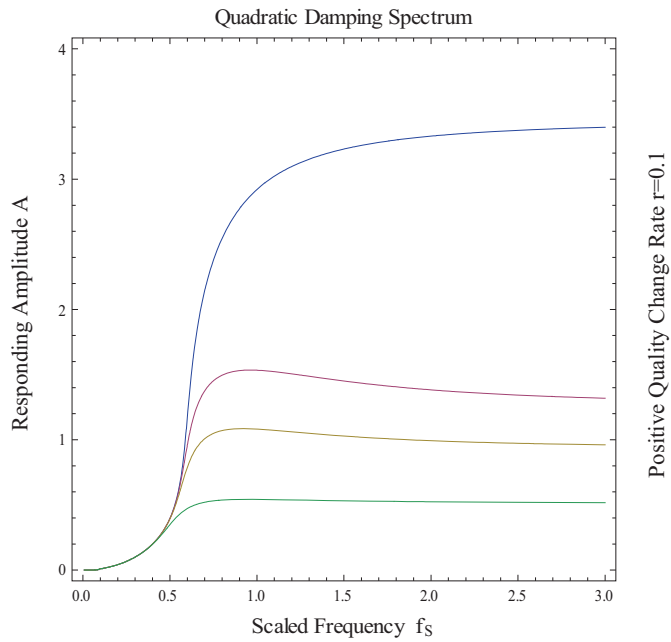

Figure 4: Forced oscillations with quadratic damping and positive quality change rate.

Fig. 5 shows the oscillation spectrum for the same parameters G, R, and D as in Fig. 4, but for a negative quality change rate of r = - 0.1.

Fig. 6 demonstrates the oscillation spectrum for the same parameters G, R, and D as in Fig. 4 and 5, but for a constant quality value with the quality change rate of r = 0.

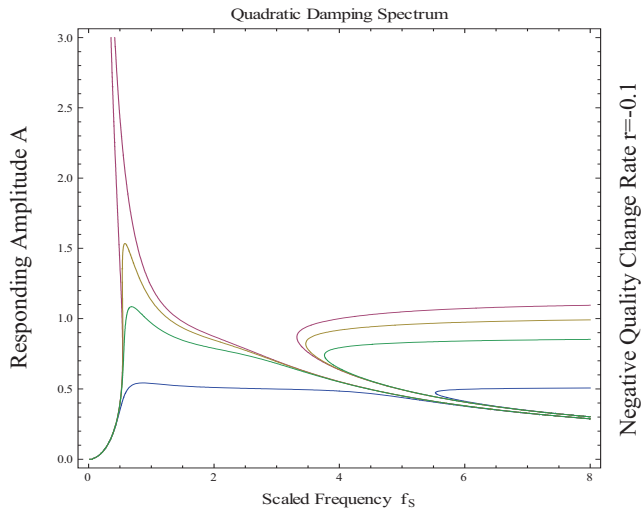

Figure 5: Forced oscillations with quadratic damping and negative quality change rate.

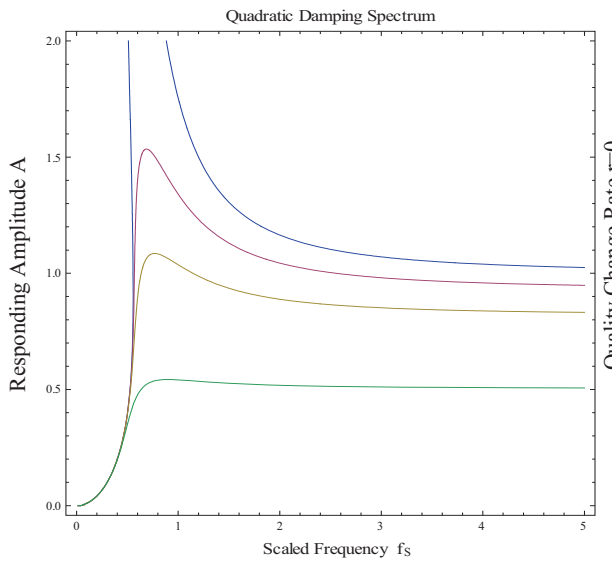

Figure 6: Forced oscillations with quadratic damping and constant quality value.

6 Experimental application example

Eqn (27) defines the phase angle between the harmonic excitation and the responding oscillation. By solving the equation for the damping factor D, eqn (27) transforms into eqn (29) with D as a function of φ, *A*, and *G*.

$$D = \left|\frac{3\pi G}{8\,A^2}\,\sin(\varphi)\right| \quad . \tag{29}$$

The exciting amplitude G, the responding amplitude A and the phase angle φ can be measured during the isenthalpic oscillations. With these three values, the quadratic damping factor D can be calculated and experimentally determined. In general it is difficult to determine the damping factor in steady state oscillations. Using eqn (29) and the measured listed parameters the quadratic damping factor D can be found.

7 Conclusion

Pressure induced isenthalpic oscillations with condensation and evaporation in saturated two-phase fluids have stable solutions for the whole range of the saturated fluid within the saturation dome. The solution pattern is more complicated close to the vapour side of the saturation dome at negative slopes of the constant quality curve. There are no instabilities for free or forced oscillations. The effect of quadratic fluid damping reduces the responding amplitudes significantly.

References

[1] Yunus A. Cengel, Michael A. Boles, “Thermodynamics: An Engineering Approach,” 3rd Edition, McGraw-Hill, 1998.
[2] Tse, Francis S. et al. “Mechanical Vibrations”, Allyn and Bacon Inc., Boston, MA 02210, 1978, ISBN 0-205-05940-6.
[3] Andrew Kimmel, “Pressure induced non-linear oscillations in two-phase LNG pipe flow,” AIChE Spring National Meeting 2006, Orlando FL, April 23-27, 2006.
[4] Joel V. Madison et al. ”Pressure Induced Isenthalpic Oscillations with Condensation and Evaporation in Saturated Two-Phase Fluids” ICFM 2010 International Conference on Fluid Mechanics, September 28-30, 2010, Amsterdam, NL, Proceedings ISSN 1307-6892.
[5] Wolfram Mathematica 7, http://www.wolfram.com.

This page intentionally left blank

Study of the application of Acoustic Emission technology for on-line monitoring of bubble phenomena and flow patterns in two-phase gas-liquid flow

S. Husin[1], A. Addali[2] & D. Mba[2]
[1]*Universiti Kuala Lumpur Malaysian Spanish Institute, Malaysia*
[2]*Cranfield University, School of Engineering, UK*

Abstract

An investigation into single bubble dynamics detection in a liquid-filled column, and monitoring and measurement of gas void fraction in a horizontal pipe using AE technology has been performed. A correlation between Acoustic Emission (AE) and Gas Void Fractions in two-phase gas-liquid flow in a horizontal pipe has been established from this work. The results demonstrate the feasibility of employing AE technology as an on-line monitoring tool for bubble dynamics and flow patterns in two-phase gas-liquid flow in pipes.
Keywords: Acoustic Emission (AE), gas bubble, two-phase flow.

1 Introduction

Acoustic Emission (AE) technology is very practical as a passive and intrusive tool for the monitoring of material processes and for the testing, detection, and characterization of any present defect or particular event. AE describes the process associated with the emission and propagation of strain waves, resulting from localized modifications of materials [1]. If there is a transient release of energy within a solid/medium, it is dissipated in the form of elastic waves which can be detected on the surface by transducers. This process is known as Acoustic Emission (AE) [2]. The frequency of the elastic wave is usually beyond the human hearing threshold (25 kHz). The sensitivity of the AE transducer which is made of piezoelectric material can detect sound beyond the human range of hearing, i.e. 25 kHz-1MkHz is regarded as the backbone of AE technology.


WIT Transactions on Engineering Sciences, Vol 74, © 2012 WIT Press
www.witpress.com, ISSN 1743-3533 (on-line)
doi:10.2495/AFM120361

The application of AE technology as a monitoring tool in two phase gas-liquid flow in pipeline is relatively new. It is gaining attention because the advantages of the AE technology over the other measuring techniques has been realised. It offers significantly reduced installation time as it can be fitted non-intrusively to the pipe; in addition, the cost of the AE technology is considerably less than existing systems. An active-observing benefit from the on-line monitoring technique offered by AE technology provides information of current process conditions such as flow patterns and velocity in a pipe.

Recently, AE technology's application as a measurement and monitoring tools for the two-phase gas-liquid system has been explored. Yen and Lu [3] employed the AE technique, combined with artificial neural network technology in their experiment to determine and observe the flow patterns (bubbly, slug, churn and annular flow) of the two-phase flow in a vertical column bed. In a very recent study, 2009, the AE technology was employed in the monitoring of slugs and in the measurement of their characteristics – gas void fraction [4]. It is concluded therefore that the GVF can be determined by measurement of the AE. However, its applications in multi-phase and two-phase gas-liquid systems are relatively few and still in their infancy stage. The opportunity for on-line monitoring in two-phase flow with AE offers industry a complementary technology. A passive AE technology offers an alternative to the intrusive ultrasonic methods.

2 Background work of bubble detection

The concept of sound propagation interference which contributed by surface discontinuities in solid material particularly metal, has been used in detecting surface defects such as cracking and pitting. Such defects are known as mechanical sources in moving parts/elements such as gears, bearings etc. In addition, in a fluid system the AE could be attenuated/excited by sources such as bubble activities including bubble formation, coalescence, break-up and collapse/burst [5–7]. The other sources of AE generation in liquid flow are flow turbulence, flow past restrictions, liquid flashing and recirculation/turbulence [5, 8–10]. Those sources caused a change of pressure wave or sound pressure in liquid. The establishment of AE from bubble activities in two phase gas-liquid flow is interesting and has motivated this technique to be used for correlation with gas void fraction in pipeline.

Phenomena in two-phase flow are quite complex and knowledge of two phase gas-liquid flow and measuring techniques as related to key parameters (e.g. phase velocities) and bubble activities such as bubble inception, coalesce, break-up and collapse in liquid are not sufficient so far. In addition, two phase gas–liquid flow plays an important role in industrial applications; hence, it seems a strong reason for two-phase flow to be investigated [11].

Kloeppel [12] relates the sound generated from bubble collapse with liquid wave where noted that the sonic energy is converted into mechanical energy, causing shock waves and motion in the surrounding liquid. In another reference, Ross [13] noted that the pressure pulse emitted by collapsing bubbles is of

sufficient amplitude to produce shock waves. De-Bosset *et al*. [14] used a pressure sensor to record the pressure change from bubble activities and the results confirmed the association of pressure peaks with the shockwaves emitted at cavity inception and collapse. It has been observed by many researchers that the pulse started just as the bubble separates/pinches off from the nozzle [15–18]. Beside bubble inception and collapse events, bubble break-up and coalescence are also sources of sound in liquid [5, 15, 19, 20].

Liquid stream in a pipeline is complicated with inter-phases induced due to turbulence flow. Turbulence flow caused rupture of liquid where cavities were thus generated [21]. This type of cavity is known as cavitation bubble. Turbulence flow also caused bubbles' coalescence which contributed to a greater size. The bigger the size of bubble, the higher bubble potential energy contained [14, 22–24]. The generated bubble/cavity as a result of the turbulence flow in a pipe is commonly categorized as transient cavity and generally exists for less than one cycle before collapsing violently [25]. Rebounds from a relatively bigger size would probably be detected by transducers. Multiple bubbles collapse/burst or rebound: the sound produced would increase whilst the frequency remained the same. A single bubble activity generates an AE transient signal in the waveform. Multiple bubbles' activities (from bubbles cloud or higher bubble population); inception, coalescence, break-up and burst resulted in a mixed signal type of waveform.

There are four types of flow regimes has been characterized in two-phase flow in a horizontal pipe; stratified, wavy, bubble, slug, and annular flow. The flow patterns are dependent on the phase flow rates, see figure 1 [26].

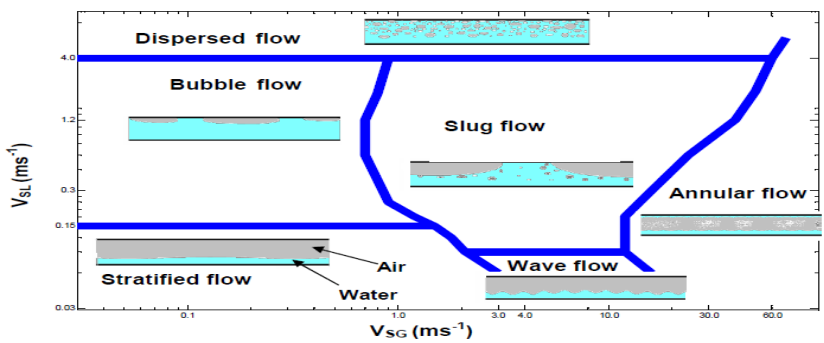

Figure 1: Horizontal flow regimes map [26].

Briefly, it can be explained that the gradual increase in liquid velocity (VSL) will result in converting the wavy flow to what is described as slug flow. In this flow pattern large waves of liquid form a slug that can fill the whole cross-section of the pipe leading to the blocking of the downstream gases, see figure 1 and 9. In the case of slug flow in the pipeline, the elongated bubble induces greater interfaces where the concentration of bubbles at its nose and tail would collapse/burst at the free surface of a film region, see figure 9. This phenomenon is one the reasons why at the presence of slug flow, the AE generated is higher.

The contribution of bubbles, particularly at the region of nose and tail of liquid slug body, can be illustrated as below and well explained in reference [4].

Evidence has been provided by many researchers that the acoustic pressure waves are detected in the initial shape distortion of bubble formation phase when a bubble detaches from the nozzle and in the subsequent collapse phase. Pressure impulses depend on the bubble energy where it is estimated only ~10 to 15% of the bubble energy contributed to the generation of pressure impulses [27]. High pressures arise from the bubble activities (formation and collapse) which cause compression to liquid and become an important factor in the motion near the end of collapse when eventually the pressure pulse radiated from the bubble collapse centre will take the form of a shockwave [28]. Shockwave then propagates with a direct function of the pressure at any given point: the higher the pressure, the greater the velocity of sound [29]. This shock wave propagation can be detected by underwater sensor pressures such as hydrophone, microphones and AE transducers.

Based on the evidence from a background survey and previous work at Cranfield University, it is determined that the AE technology is feasible for detecting gas bubble activities; formation, coalescence and collapse. Furthermore, it is strongly believed that pressure pulses associated with the bubble formation, coalescence in the liquid and burst at free surface are potential sources for AE. This gives an indication that correlates with gas phase/Gas Void Fraction (GVF) measurement in a horizontal pipe.

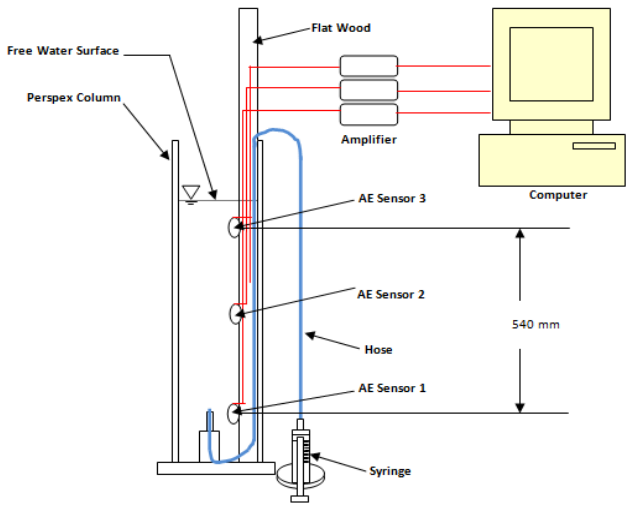

Figure 2: Schematic diagram of the experiment for AE single bubble detection.

3 Detection of a single bubble formation and burst

The apparatus employed for AE detection of a single bubble is shown in figure 6. The rig consists of a column filled with water and salt-water for comparison on

the effect of liquid viscosity on the emission of bubble activities. A single bubble in the column was produced with a syringe. Sensor-1 was positioned at the bottom near to the nozzle; sensor-3 was positioned near to the water free surface; sensor-2 was positioned in mid-way of bubble travelling. The transducers had an operating frequency of 100-750 kHz and a pre-amplification at 60 dB was applied. The sampling rate for acquisition of AE waveforms was 2 MHz. Threshold level 24 dB was set above the electronic background noise of the acquisition system.

4 Experimental results

A waveform associated with a single bubble inception is shown in figure 3 (top). A corresponding time-frequency plot was generated by the AGU-Vallen software tool, see figure 3 (bottom) which showed the intensity of frequency over the time of the signal captured during bubble inception.

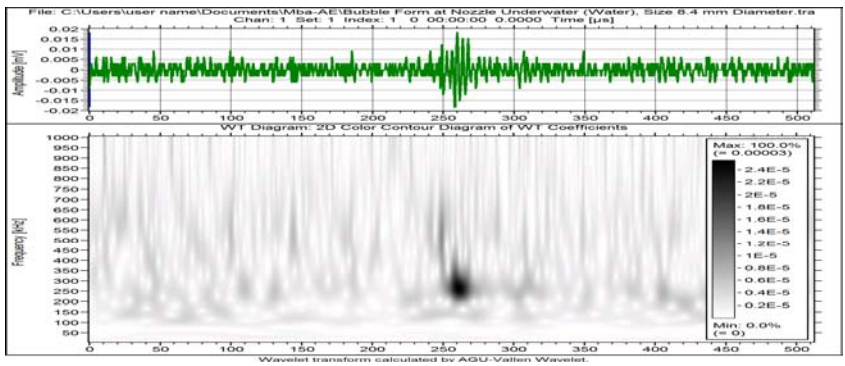

Figure 3: AE from a single bubble inception (nozzle size 8.4 mm in water (1 cP)).

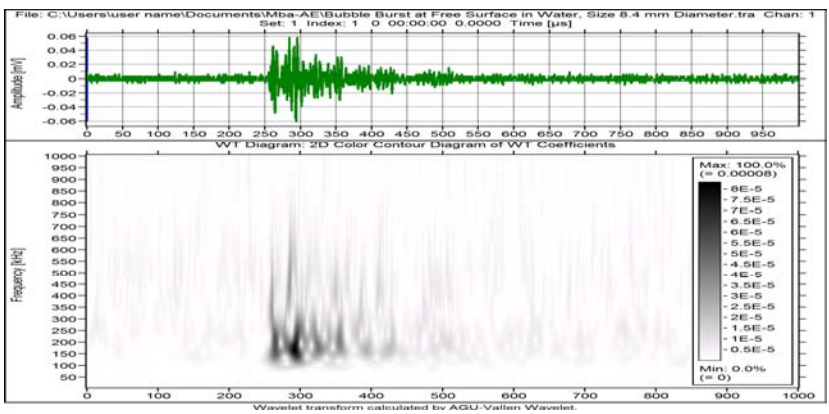

Figure 4: AE from a single bubble burst from nozzle size 8.4 mm in water (1 cP).

The waveform and wavelet plot from the data acquired from bubble burst at the free surface is presented in figure 4. Both figures 3 and 4 show that the bubble inception or burst has high frequencies of up to 750 kHz at the start of the AE event.

The findings demonstrated that AE technology is very sensitive where it can differentiate the emission from bubble activity with difference test parameters. The magnitude of AE energy from bubble burst was dependent on liquid properties; surface tension and viscosity, as well as the bubble size, see figure 5.

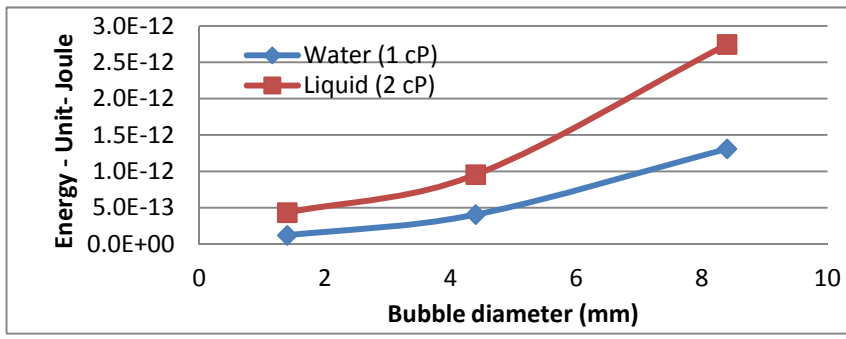

Figure 5: Average of energy from a single bubble burst as a function of bubble size and viscosity.

5 Monitoring gas void fraction in horizontal pipe with AE

Having showed that AE has been successfully detected from a single bubble activity (inception and burst), the application of this technique (AE technology) has been explored to assess whether AE could be correlated to Gas Void Fraction (GVF). In this experiment, three important parameters have been used that commonly used to describe two-phase flow: Gas Void Fraction, Superficial Liquid Velocity and Superficial Gas Velocity. Briefly, GVF is defined as the ratio of the volumetric of the gas to the total volumetric flow-rate. In two-phase flow Superficial Liquid Velocity (VSL) is defined as the volumetric flow rate of liquid phase divided by the cross-sectional area of the pipe. Superficial Gas Velocity (VSG) is defined as the volumetric flow rate of gas phase divided by the cross-sectional area of the pipe [30].

Liquid superficial velocity (VSL) ranging from 0.3 m/s to 1.0 m/s at increments of 0.1 m/s, and the gas superficial velocity (VSG) ranged from 0.8 m/s to 9.4 m/s at increments of 0.2 m/s have been employed in this experiment. For a reference/comparison measurement, conductivity rings which are commonly used for GVF measuring devices were installed in the experimental apparatus for gas void fraction (GVF) measurements (see fig 6 and 7). Correlation of AE energy with the value obtained from conductivity rings then has been performed.

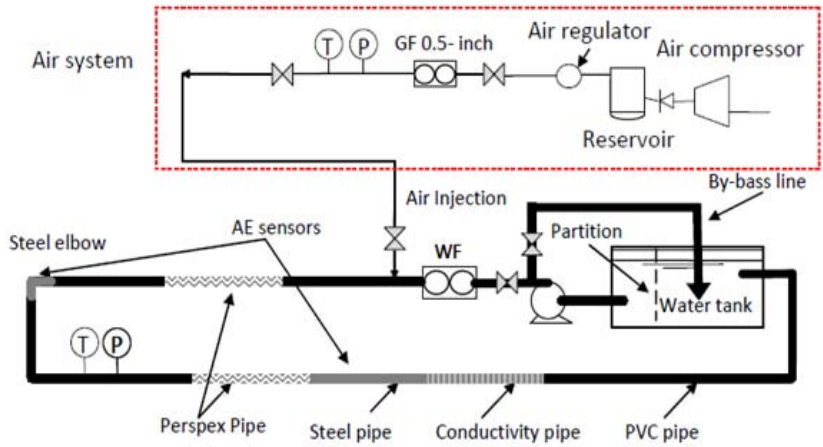

Figure 6: Experimental setup for two-phase GVF monitoring and measurement.

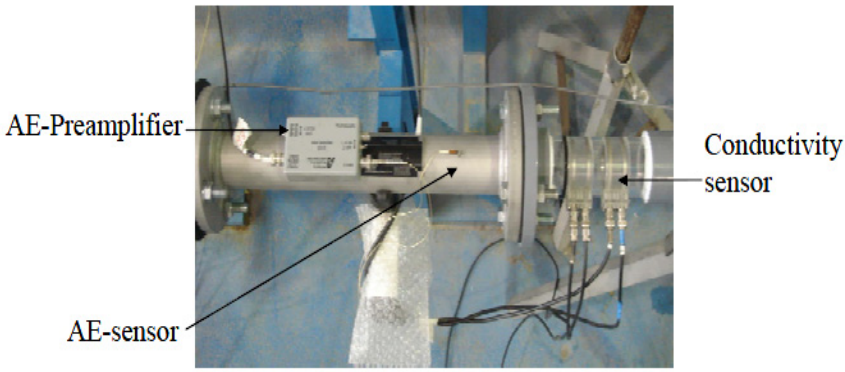

Figure 7: Test section: AE sensor, preamplifier and conductivity sensor.

Prior to the test; calibration work on the conductivity rings had been performed. The gas-liquid phase fractions were achieved by injecting known liquid volumes using an air compressor.

6 Experimental results and discussion

The results show that AE absolute energy steadily increased with the increase of VSG at all VSL velocities, see figure 8. The AE obtained could be associated with the flow pattern which was introduced by VSG. The results show evidence that the main contribution for increasing AE energy was VSG. In other words, the AE excitement was contributed by bubbles' activities.

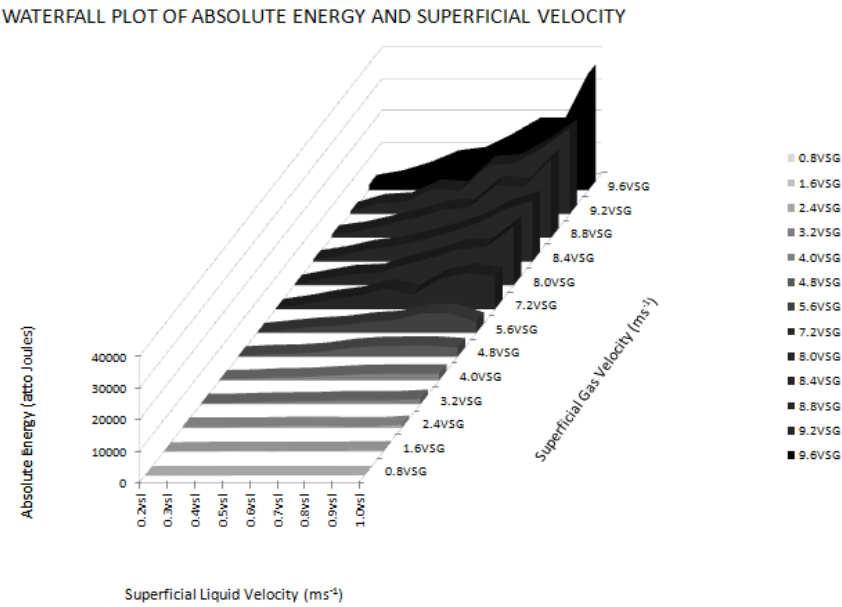

Figure 8: AE absolute energy level measured at various VSL and VSG.

AE phenomenon of slug flow in a horizontal pipe could be correlated with the slug head and tail respectively, see figure 9. A time-frequency plot (figure 9) of an AE waveform associated with the slug showed frequencies of up to 500 kHz at the earliest part of the AE slug wave. This high frequency was contributed by bubble activities as shown in figures 3 and 4 for single bubble inception and burst respectively.

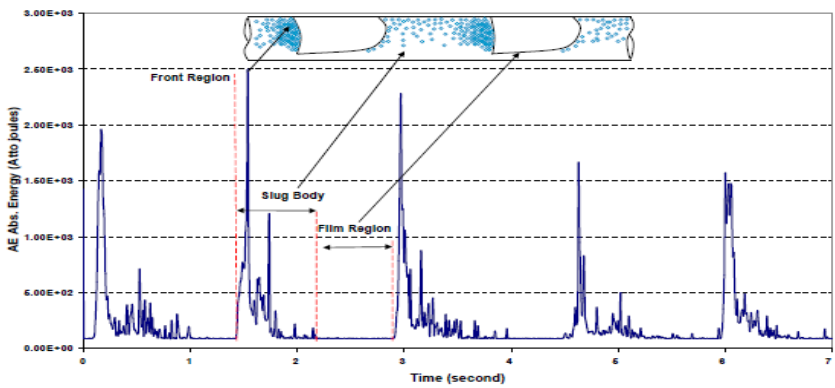

Figure 9: Typical AE Signal from fully developed slug flow.

The results of WT of AE signal obtained from one of slug flow condition in horizontal pipe, which present both contour map and 3D-plot are shown in figures 10 and 11. Since the AE events are of short duration (tens of μs) and of relatively high frequency, the 3D plots of the WT show very sharp peaks at high frequencies at about 40– 50 μs. The contour maps (fig 10), shows the AE events appear in the form of a very closed space ‘‘island’’ shaped contours at average frequency around 400 kHz. Each AE signal appears as a distinctive peak “mountain” in the 3D representation. This implies that the high-energy AE signals, which have high amplitude and long duration, are composed of several closely spaced individual events. The wavelet as presented in figures 10 and 11 just showing an example of the characteristics of AE on slug flow.

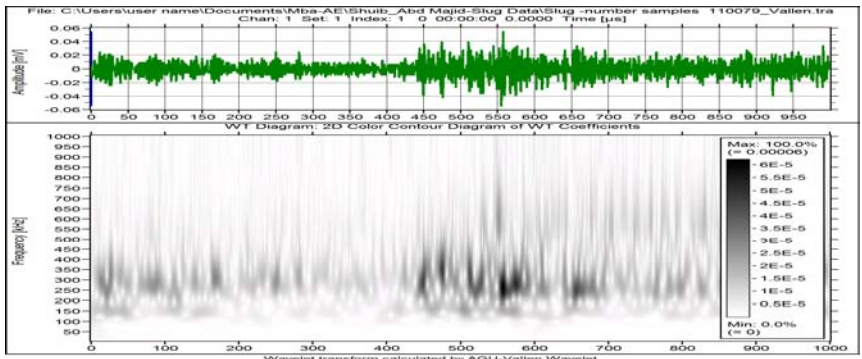

Figure 10: Example; time-frequency contour map of slug flow in horizontal pipe.

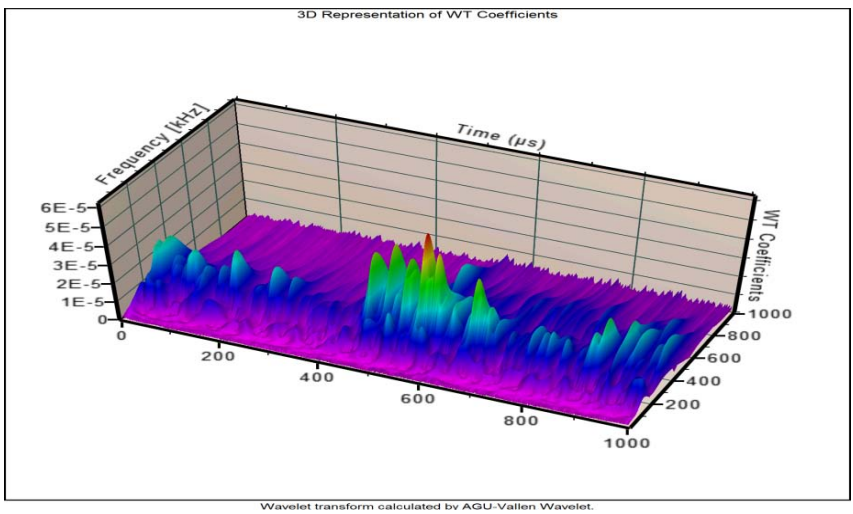

Figure 11: 3-D plot of wavelet transform (WT) of AE signal in fig 10.

Figure 12 presents the measured GVF, calculated GVF and absolute energy level of AE signal acquired at varying V_{SG} and a fixed V_{SL} of 2.0 ms-1. Results showed that any increase in GVF resulted in an increase in AE absolute energy. This manifests a correlation between AE (AE Technology) and the calculated and measured GVF (Conductivity rings).

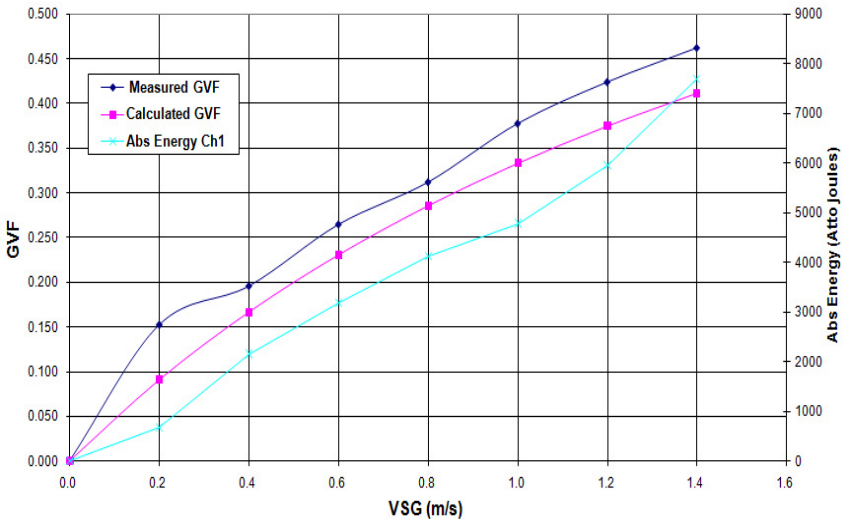

Figure 12: Correlation; GVF and AE abs energy levels at VSL=2.0 m/s for Ch1.

7 Conclusions

The sensitivity of an AE sensor has been demonstrated in this experiment to capture the emission from single bubble activities; inception and burst/collapse. The result showed the AE level associated with bubble activity increases as a function of bubble size and liquid viscosity. These findings confirmed the source of AE activities in two phase flow which comes from bubble dynamics; therefore it is evident that it provides a basis for assessing the applicability of AE to monitoring gas content in multi-phase flow. AE technology has the potential to be developed as a tool for flow pattern identification and monitoring in two phase flow in pipes.

References

[1] Yoon, D.J., Weiss, W.J. and Shah, S.P., Assessing damage in corroded reinforced concrete using acoustic emission. Journal of Engineering Mechanics, 273, March 2000.

[2] Serrano, E.P and Fabio, M.A., Application of the wavelet transform to Acoustic Emission Signals Processing. IEEE Transaction on Signal Processing. Vol. 44, No. 5, May 1996.
[3] Yen, G., and Lu, H., Acoustic Emission Data Assisted Process Monitoring, ISA Transactions 41, 273-282, 2002.
[4] Al-lababidi, S., Addali, A., Yeung, H., Mba, D. and Khan, K., Gas void fraction measurement in two-phase gas/liquid slug flow using acoustic emission technology. J. Vib. and Acoustics, ASME, vol. 131, 6, 064501, 2009.
[5] Strasberg, M., 1956, Gas Bubbles as Source of Sound in Liquids. The Journal of the Acoustical Society of America, 28, 1, 1956.
[6] Leighton, T.G, The Acoustic Bubble. Academic Press, London, 1994.
[7] Mba, D. and Rao, R. B.K.N., Development of Acoustic Emission Technology for Condition Monitoring and Diagnosis of Rotating Machines; Bearings, Pumps, Gearboxes, Engines and Rotating Structures. The Shock and Vibration Digest, Vol. 38(1), pp. 3-16, 2006.
[8] Derakhshan, O., Houghton, J.R., Jones, R.K. and March, P.A., Cavitation Monitoring of Hydroturbines with RMS Acoustic Emission Measurements. World Meeting on Acoustic Emission, March 1989, p305-315, 1989.
[9] Brennen, C.E., Cavitation and Bubble Dynamics. Oxford University Press, New York, 1995.
[10] Neill, G.D., Reuben, R.L. and Sandford, P.M., Detection of Incipient cavitation in Pumps Using Acoustic Emission. Journal of Process Mechanical Engineering, ImechE, 211(4), pp. 267-277, 1997.
[11] Kuwahara, T., and Yamaguchi, H., Void fraction measurement of gas-liquid two-phase flow using magnetic fluid. Journal of Thermophysics and Heat Transfer, Vol. 21, No. 1, pp. 173, 2007.
[12] Kloeppel, James E., Scientists measure energy dissipation in a single cavitating bubble. Physical Sciences Editor, (217) pp. 244-1073, 2002. Online. http://www.news.uiuc.edu/ii/02/0801/0724bubbleenergy_P.html 10/11/2002
[13] Ross, D. Mechanic of underwater noise (Chapter 7). *Topic in Cavitation*, pp. 202-242. Pergamon Press, 1976.
[14] De-Bosset, A., Obreschkow, D., Kobel, P., Dorsaz, M. and Farhat, N., 2007. Direct effects of gravity on cavitation bubble collapse. 58 International Astronautical Congress 2007, pp. 1-5, 2007.
[15] Longuet-Higgins, M.S., Bryan R. Kerman and Knud Lunde, The Release of Air Bubble from an Underwater Nozzle. J. Fluid Mech, Vol. 230, pp. 365-390, 1991.
[16] Leighton, T.G., Fagan, F.K. and Field, J.E., Acoustic and Photographic Studies of Injected Bubbles. Eur. J. Phys. 12, pp. 77-85, 1991.
[17] Manasseh, R., Bui, A., Sandercock, J. and Ooi, A., Sound emission processes on bubble detachment. Proc. 14th Australian Fluid Mechanics Conf, Adelaide, South Australia, 9-14th Dec 2001, Vol. 1, pp. 857-860, 2001.

[18] Deane, G.B., and H. Czerski, H., A mechanism stimulating sound production from air bubbles released from a nozzle. J. Acoust. Soc. Am (JASA Express Letters), pp. 126-132, 2008.
[19] Manasseh, R., Riboux, G. and Risso, F., Sound generation on bubble coalescence following detachment. Int. J. Multiphase Flow, pp. 938-949, 2008.
[20] Manasseh, R., Riboux, G., Bui, A. and Risso, F., Sound emission on bubble coalescence: imaging, acoustic and numerical experiments. 16th Australasian Fluid Mechanics Conference, Gold Coast, Australia 2nd-7th December 2007.
[21] Lauterborn, W. and Ohl, C.D., Cavitation Bubble Dynamic. Ultrasonics Sonochemistry, 4, pp. 65-75, 1997.
[22] Blake, J.R and Gibson, D.C., Growth and collapse of a vapour cavity near a free surface. J. Fluid Mech, vol. 111, pp. 123-140, 1981.
[23] Buogo S. and Canneli, G.B., Implosion of an underwater spark-generated bubble and acoustic energy evaluation using the Rayleigh model. Acoustical Society of America, 111(6), pp. 2594-2600, 2002.
[24] Obreschkow, D., Kobel, P., Dordaz, N., De Bosset, A., Nicollier, C. and Farhat, M., Cavitation dynamics inside liquid drops in microgravity. Physical review Letters, 97, pp. 1-4, 2006.
[25] Neppiras, E.A., Acoustic Cavitation. Physics Report (Review Section of Physical Letters) 61, No. 3, pp. 159-251, 1980.
[26] Mandhane, J.M., Gregory, G.A., and Aziz, K., A flow pattern map for gas-liquid flow in horizontal pipes. International Journal of Multiphase Flow 1(1974), p 537-553, 1974.
[27] Shangguan, H., Casperson, L.W and Prahl, S.A. Pressure impulse during microsecond laser ablation. Applied Optics, Vol.36, No. 34, pp. 9034-9041, 1997.
[28] Benjamin, T.B., and Ellis, A.T., The collapse of cavitation bubbles and the pressure thereby produced against solid boundaries. Phil. Trans. R. Soc. Lon. 260, no. 1110, pp. 221-240, 1966.
[29] Isseline, J.C., Alloncle, A.P. and Autric, M., On laser induced single bubble near a solid boundary: Contribution to the understanding of erosion phenomena. Journal of Applied Physics, vol. 84, no 10, 1988.
[30] Clayton T. Crowe, Multiphase Flow Handbook, Taylor and Francis, ISBN-10: 0849312809, 2005.

Acoustic frequency for bubble size correlation using acoustic emissions

S. Husin[1], A. Addali[2] & D. Mba[2]
[1]*Universiti Kuala Lumpur Malaysian Spanish Institute, Malaysia*
[2]*Cranfield University, School of Engineering, UK*

Abstract

In this study, a correlation between acoustic frequency and the bubble size of a single bubble burst at the free surface has been demonstrated. Bubble burst was used as it is an acoustically noisy process, independent parameter and potential source of AE in a liquid medium. An AE transducer was used to record sound as the bubble bursts at the free surface. The acoustic data were then processed to extract the bursting frequency associated with the bubble size. The frequency of the acoustic bursting has been shown to be related to the size of the bubble. The effects of liquid viscosity on acoustically determined bubble size has also been demonstrated.
Keywords: Acoustic Emission (AE), gas bubble, gas bubble burst, frequency spectra.

1 Introduction

Bubble burst characteristics-acoustic frequency can be used as a basis for interpreting bubble properties, particularly bubble size. Sound pressure detection from a single bubble burst at free surface is an important parameter for estimating bubble and liquid properties where the process is independent from external forces. Bubble bursting by its nature at a free surface is deemed useful for empirical parameter which is more accurate and detectable with an AE transducer. However, study of the acoustic frequency of a single bubble burst at free surface using AE technology is never attempted for bubble properties' determination, particularly for bubble sizing. This proposed technique is passive, can be employed either intrusively or non-invasively and is a rapid measurement technique. Furthermore, the robust acoustic transducer is more practical in

WIT Transactions on Engineering Sciences, Vol 74, © 2012 WIT Press
www.witpress.com, ISSN 1743-3533 (on-line)
doi:10.2495/AFM120371

hostile industrial or environmental flows where more delicate and complicated instruments are impractical [1].

The other bubble properties such as bubble natural oscillation frequency, rising velocity and shape have been used for interpreting bubble and liquid characteristics in bubble columns [2, 3]. However, the method with these bubble properties is very complicated in terms of apparatus and calculation. For instance, Sinha [3] has developed a pattern of apparatus and methods for measuring properties of bubbles that can be used for liquid properties/characteristics' determination. These liquid properties are density and surface tension. The apparatus he used was a cylindrical transducer and Doppler probe as the invasive and active method. A non-invasive method has also been developed where a ring piezometer transducer/cavitation transducer was attached externally to the container wall. A syringe was used for injecting air into the liquid bulk which is placed vertically at the container bottom. He used bubble properties (oscillation frequency [4], terminal velocity [5] and oscillation of shape mode [6] to calculate liquid density and surface tension.

Boyd and Varley [7] commented that other techniques such photography and conductivity probes used to measure bubble properties such as gas hold-up and size would not be suitable for application in industries; this is due to the limitation of the visualisation and the intrusive techniques to liquids involved which can foul the probes. On the other hand, AE monitoring is relatively non-invasive and is a rapid measurement technique. In their investigation of acoustic emission measurement of low velocity plunging jets to monitor bubble size, they found that larger bubbles resulted from increasing the height which showed a shift to lower frequency in the spectra.

Leighton *et al.* [8] employed a Gabor transform time-frequency signal analysis technique to determine bubble size in their investigation of bubble entrainment and bubble cloud generation under a waterfall, and a plunging jet. Computing the Gabor expansion of a signal is one form of time-frequency analysis. A time-frequency representation via the Gabor coefficients was used to identify the bubble signatures. They used a hydrophone (Bruel & Kjaer 8104) with flat frequency response from 20 Hz to 22 kHz. They found that peaks occurred at 2 kHz and 700 Hz, which correspond to bubbles of approximately 3 mm and 9 mm in diameter respectively oscillating at its natural frequency. Their findings noted that the bigger bubble size showed a lower frequency in the spectra.

Jin and Kim [2] found that the mean frequency of the pressure spectrum decreases with the increase of bubble size. They also correlated dynamic minimum pressure with the radius of curvature and the maximum pressure to the vertical bubble length. In other words, the pressure spectrum is correlated with the bubble properties; particularly bubble size (radius curvature). The pressure variation is a function of bubble properties; size, shape, rising velocity and wake properties, and therefore the bubble characteristics can be determined from the Fourier transform [2]. In addition, the energy dissipation rate which was determined from the pressure spectrum was found to increase with the growth of the bubble radius. In their investigation on bubble properties and spectral

analysis of a single bubble in water, it was found that large bubbles have low peak frequency in the pressure spectrum. Their findings agree with those of Boyd and Varley [7]

2 Experimental apparatus

This experiment employed two apparatus. The first apparatus was a square column filled with water. The second apparatus was a cylinder column filled with water (1 Cp) and salt-water (2 Cp) to show the effect of liquid viscosity on the emission of bubble burst.

2.1 Apparatus 1

The apparatus (1) used for AE detection in this investigation are shown in figures 1 (schematic diagram), 2 and 3. A bubble rig was filled with water. A manifold

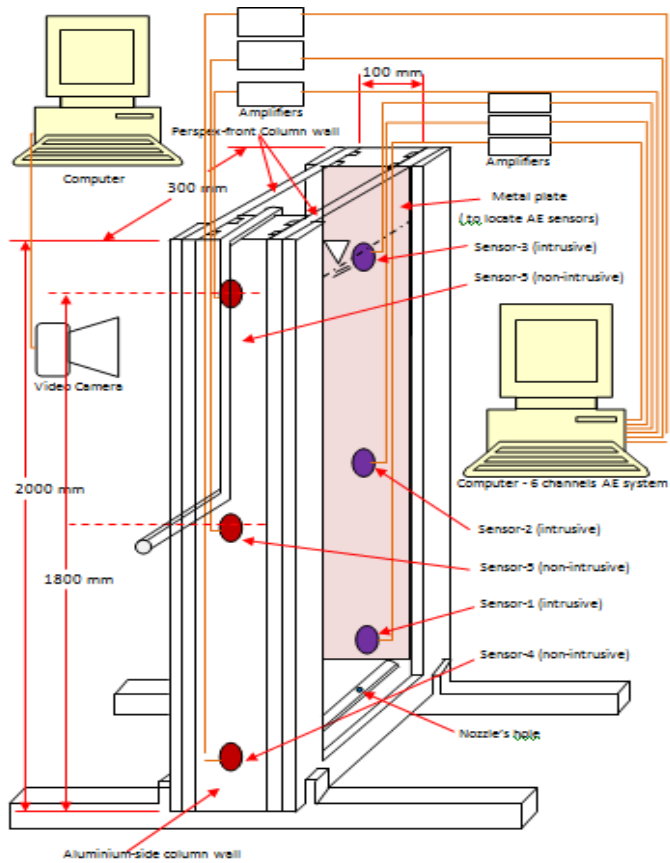

Figure 1: Schematic diagram of apparatus 1.

pipe consists of a vertical nozzle fixed to the bottom of bubble rig, see figure 2. Air has been supplied to the manifold by a compressed cylinder. A single bubble was released from the nozzle when the valve was gently opened. Four sizes of nozzle were used in this investigation; 1.4, 2.8, 5.6 and 8.4 mm internal hole-diameter. It was assumed that the bubble created using these nozzles is equivalent to the nozzles' internal hole-diameter.

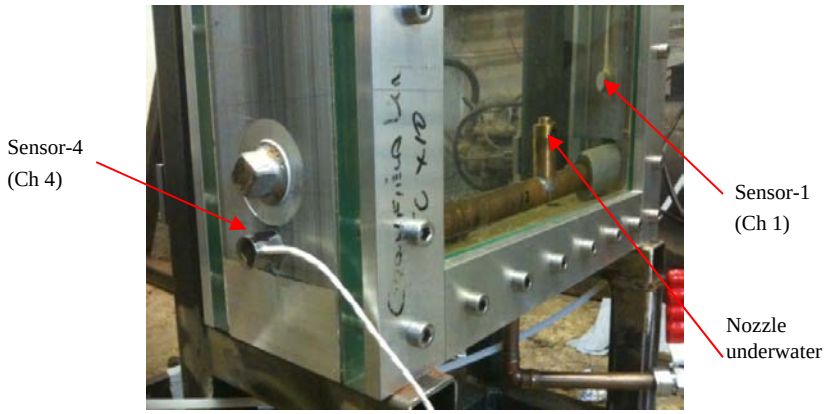

Figure 2: Bubble formation mechanism at the bottom of bubble rig.

Sensors 3 and 4 were mounted onto the column intrusively and non-intrusively to detect bubble burst emissions, see figure 3. Broadband AE transducers (Physical Acoustic Corporation type Wideband Differential, WD) with an operating frequency range of 100-750 kHz and a pre-amplification at 40 dB was applied. The sampling rate for acquisition of AE waveforms was set at 2 MHz.

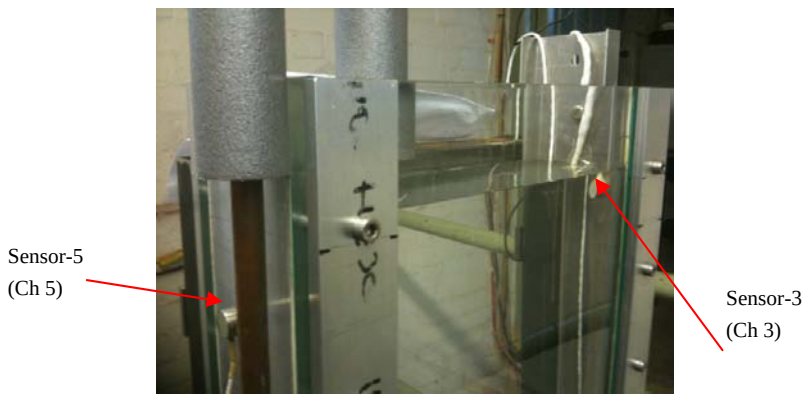

Figure 3: AE sensors mounted at the top (free surface) of bubble rig to detect the emission of bubble burst.

2.2 Apparatus 2

The schematic diagram of apparatus (2) employed for AE measurements is shown in figures 4. The rig consists of a bed column filled with a fluid. An AE sensor was placed just beneath the free surface of the fluid to detect the emission of bubble burst at free surface. The column was made of Perspex pipe and was 150 mm in diameter with a height of 1500 mm. The transducers had an operating frequency of 100-750 kHz and a pre-amplification at 60 dB was applied. The sampling rate for acquisition of AE waveforms was set at 2 MHz. A single bubble was created with a syringe as gas (air) was forced through different sized nozzles (diameters of 1.4, 4.4 and 8.4 mm) placed at the bottom of the water column. Two fluid conditions were investigated; plain water with a viscosity of 1 cP and a fluid with a salt solution and a viscosity of 2 cP.

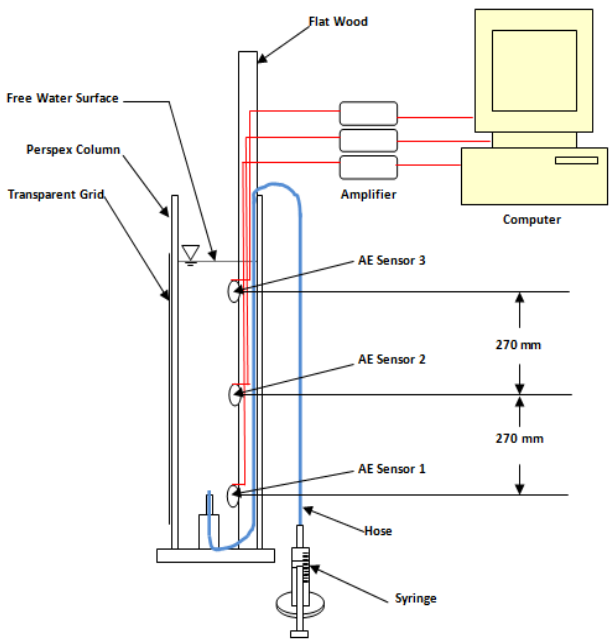

Figure 4: Schematic diagram of apparatus 2.

3 Experimental results

3.1 Test 1(from apparatus 1)

Table 1 shows an example of a signal detected using the AE sensor. The waveform shows a transient upon the bubble burst event and it decays in a very short time (~10 μs), see Table 1. The transient at the waveform plots clearly show that AE amplitude rises with the increase in bubble size.

Table 1: AE from a single bubble burst as a function of bubble size.

Nozzle Size 1.4 mm	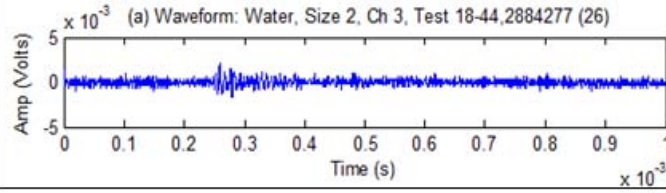
Nozzle Size 2.8 mm	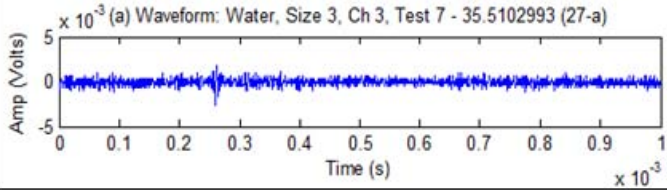
Nozzle Size 5.6 mm	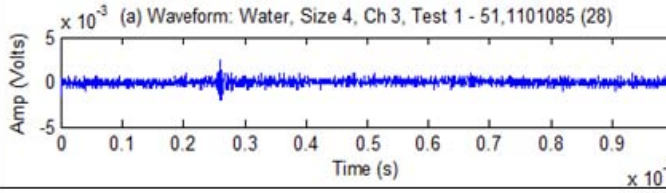
Nozzle Size 8.4 mm	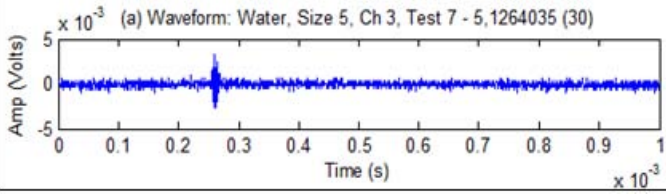

A Fourier analysis highlighted frequency characteristics for all sizes (see Table 2 presenting the average of FFT). The averaged frequency spectra (from 10 samples) of all AE events associated with differing bubble sizes showed an increase in size amplitude across the broad frequency range. Peak amplitude started at ~120 KHz for all sizes. Higher peak amplitude was observed with the bigger nozzle/bubble size. It was found that the peak amplitude at 120 kHz grew with the increasing bubble size. Peak amplitude at 120 kHz for respective sizes 1.4, 2.8, 5.6 and 8.4 mm were 0.5×10^{-5}, 0.6×10^{-5}, 0.7×10^{-5} and 1.5×10^{-5} Volts. Table 3 presents the summary of peak amplitude comparison at a frequency of 120 kHz for all bubble/nozzle sizes.

Table 2: Frequency spectra of data acquired by sensor-3 as a function of bubble size.

	Spectral Analysis of bubble burst
Nozzle 1.4 mm	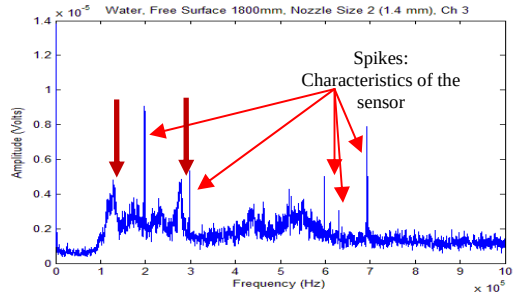
Nozzle 2.8 mm	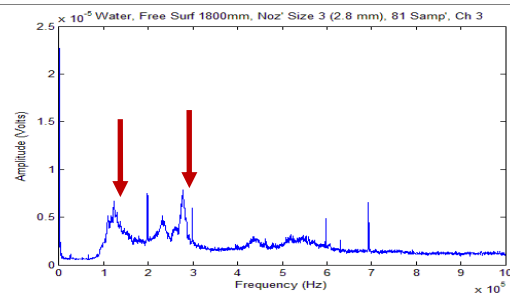
Nozzle 5.6 mm	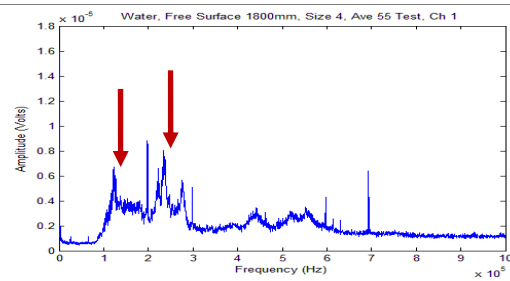
Nozzle 8.4 mm	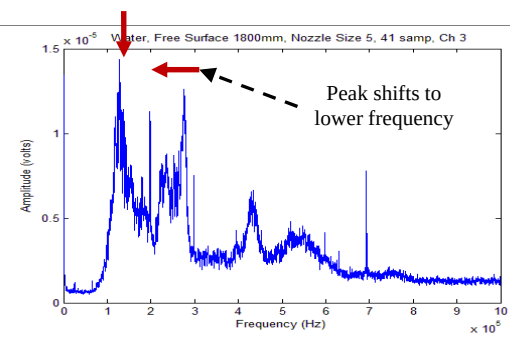

Table 3: Comparison of peak amplitude at frequency 120 KHz for all sizes.

	Size 1.4 mm	Size 2.8 mm	Size 5.6 mm	Size 8.4 mm
Peak amplitude at 120 kHz	0.5×10^{-5} Volts	0.6×10^{-5} Volts	0.7×10^{-5} Volts	1.5×10^{-5} Volts

The FFT plot in Table 2 shows that the peak amplitude occurs at the same frequency. This indicates that peak amplitude can be used as a parameter for correlation with bubble size at burst event at free surface. A very close inspection of peak amplitude value at frequency 120 kHz for the size of bubble burst that generated from nozzle sizes 1.4, 2.8 and 5.6 mm implies that there is not much difference in size generated from those nozzle sizes. However, peak amplitude from the frequency spectrum of nozzle size 8.4 mm shows an obvious difference value which indicates a big difference of bubble size generated, compared with the previous three bubbles.

Another indicator can be seen in the FFT plot which can be used to indicate that the bubble size is the shift of frequency corresponding to the size of bubble. For nozzle sizes 1.4 and 2.8 mm it is noted that the peak occurs at 280 kHz. The peak shifts to 240 kHz for size 5.6 mm. For the bigger size 8.4 mm, the peak more obviously shifts to the left at the lower frequency (120 kHz). This agrees with the results obtained by previous researchers (Jin and Kim [2]; Pandit *et al*. (1992); Leighton *et al.* [8]; Boyd and Varley [7]) where large bubbles have a low peak frequency in the pressure spectrum.

Some spikes in the FFT plot can be seen in all plots for every bubble size (Table 2) which actually result from the characteristics of the AE sensor used. The spikes exist at the same frequency. There are 5 spikes identified, as shown by the arrows in Table 2.

3.2 Test 2 (from apparatus 2: Effect of liquid viscosity on bubble burst emission

The results from test 2 (see Table 4) generally show the same trend as the results from test 1 (see Table 2) where the bigger the size, the higher the amplitude in pressure spectra. Also, it is noted that a shift in the peak in the bubble pulse range to a lower frequency as nozzle size increases, suggests that the bubble size increases correspondingly and this concurs with visual observations of larger bubbles being formed at bigger nozzle sizes.

Table 4: Average frequency spectra of bubble bursts at free surface.

Nozzle Diameter (mm)	Frequency Spectra in Water	Frequency Spectra in Salt Water
Size 1.4	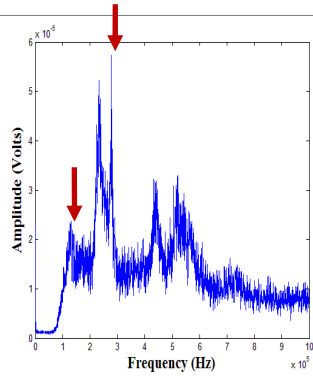	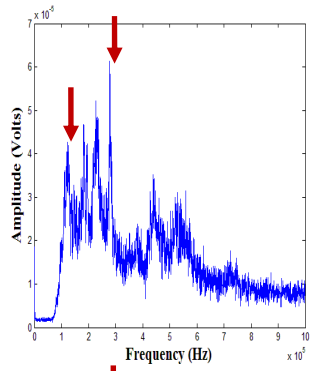
Size 4.4	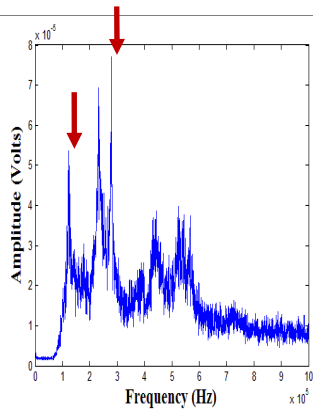	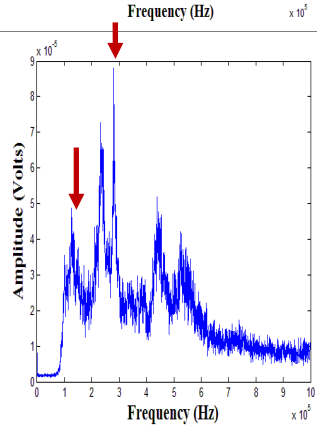
Size 8.4	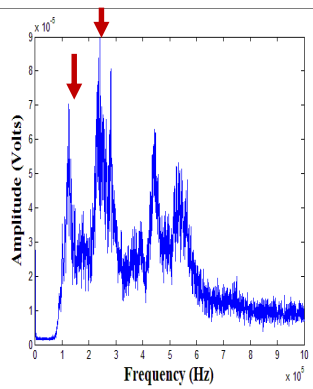	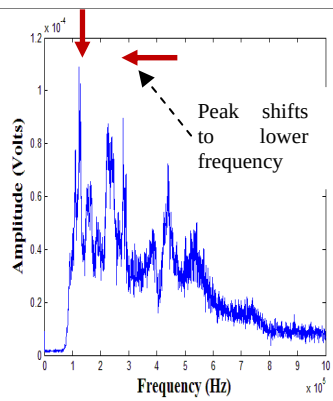

Table 5 shows the comparison of peak amplitude at frequency 120 kHz and 280 kHz for both liquid conditions; water and salt-water. It is noted that peak amplitude at a higher viscosity (salt-water, 2 Cp) is higher than lower viscosity (water, 1 Cp). For nozzle sizes 1.4 and 4.4 mm, peak occurs at the same frequency, 280 kHz. However, for nozzle size 8.4, it is found to shift to the left to a lower frequency; in water peak frequency shifts to 220 KHz, while in salt-water it shifts to 120 KHz.

Table 5: Comparison of peak amplitude at frequency 120 KHz for all sizes in water and salt-water.

	Size 1.4 mm	Size 4.4 mm	Size 8.4 mm
Peak amplitude at 120 kHz in Water	2.5×10^{-5} Volts	5.5×10^{-5}Volts	7.0×10^{-5} Volts
Peak amplitude at 280 kHz in Water	5.8×10^{-5} Volts	7.8×10^{-5}Volts	9.0×10^{-5} Volts
Peak amplitude at 120 kHz in Salt-Water	4.3×10^{-5} Volts	4.8×10^{-5}Volts	11.0×10^{-5} Volts
Peak amplitude at 280 kHz in Salt-Water	6.2×10^{-5} Volts	9.0×10^{-5}Volts	9.0×10^{-5} Volts

4 Conclusions

Increasing the size of bubble burst at free surface has been observed with a shift to lower frequency in the spectra. This experiment demonstrated that the size of bubble burst at free surface was inversely proportional to frequency.

The acoustic frequency was related to the bubble size, and liquid viscosity on acoustically determined bubble size has been demonstrated. This gives an indication that bubble size can be determined from the calibrated peak amplitude and frequency of a single bubble burst at the frequency spectra. However, this is not an easy task and really needs a lot of correlation tasks before becoming well established as we know that a spectral analysis would be biased unless a correction is introduced [1]. Correlations include bubble properties, liquid properties and the distance of the source (bubble burst location) to the AE sensor.

References

[1] Manasseh, R., and Chanson, H., Void-Fraction and Acoustic Characteristics of Gas Bubbles Entrained by a Circular Plunging Jet. In: 4th International Conference on Multiphase Flow, ICMF'01, New Orleans, USA, pp. 1-12, 2001.
[2] Jin, G.T. and Kim S.D., Bubble properties and pressure fluctuations of a single bubble in water. Journal of Chemical Engineering of Japan, Vol 23, No 5, pp. 523-529, 1990.
[3] Sinha, N.N., Characterization of Liquids Using Gas Bubbles. United States Patent No: US 7,010,962 B2. Mar. 14, 2006.
[4] Minnaert, M., On Musical Air-Bubbles and the Sounds of Running Water. Philosophical Mag. 16, pp. 235-248, 1993.
[5] Kellerman, H., Juttner, K. and Kreysa, G., Dynamic Modelling of Gas-Hold-up Electrolyte Systems. Journal of App Electrochemistry, 28, pp. 311-319, 1998.
[6] Strasberg, M., Gas Bubbles as Source of Sound in Liquids. The Journal of the Acoustical Society of America, 28, 1, pp. 20-26, 1956.
[7] Boyd, J.W.R and Varley, J.., Acoustic Emission Measurement of Low Velocity Plunging Jets to Monitor Bubble Size. Chemical Engineering Journal, 97, pp. 11-25, 2004.
[8] Leighton, T.G., White, P.R., and Schneider, M.F. The detection and dimension of bubble entrainment and comminution. J. Acoust. Soc. Am. 103 (4), pp. 1825–1835. 1998.

This page intentionally left blank

A microfluidic study of oil-water separation kinetics

T. Krebs[1,2], C. P. G. H. Schroen[2] & R. M. Boom[2]
[1]*Institute for Sustainable Process Technology, The Netherlands*
[2]*Wageningen University, Food Process Engineering Group, The Netherlands*

Abstract

We present the results of experiments studying droplet coalescence in a dense layer of emulsion droplets using microfluidic circuits. The microfluidic structure allows direct observation of shear-induced collisions and coalescence events between oil droplets dispersed in water. A mineral oil was chosen as the dispersed phase and a 9 wt% NaCl aqueous solution as the continuous phase. We determine the coalescence rate as a function of the droplet velocity and droplet concentration from image sequences measured with a high-speed camera. A trajectory analysis of colliding droplet pairs allows evaluation of the film drainage profile and coalescence time t_c. From the coalescence times obtained for ten thousands of droplet pairs we calculate the coalescence time distributions for each set of experimental parameters, which are the mean droplet approach velocity $\langle v_0 \rangle$ and the mean dispersed phase fraction $\langle \phi \rangle$. We discuss the potential of the procedure for the prediction of emulsion stability in industrial applications.
Keywords: emulsion, microfluidic, coalescence, kinetics, image analysis, droplet, film drainage, petroleum.

1 Introduction

The control of emulsion stability is an important issue in many industrial applications. Our motivation is rooted in the field of crude-oil/water separation which is a key processing step in oil production. In this application, a common way to separate the liquid mixture is by using mechanical devices [1], like gravity settlers, centrifugal separators such as hydrocyclones or in-line swirl elements [2]. A criterion for the successful operation of these separators is

WIT Transactions on Engineering Sciences, Vol 74, © 2012 WIT Press
www.witpress.com, ISSN 1743-3533 (on-line)
doi:10.2495/AFM120381

that the demulsification time of the oil/water mixture must be smaller than the residence time of the fluids in the separator. To recover pure oil and water phases, coalescence between emulsion droplets needs to take place; this coalescence time will depend on the nature of the flow as well as the presence of emulsifying agents. To assess the feasibility of a device to separate a crude-oil/water mixture, the kinetic parameters governing coalescence must be known. This becomes especially important in view of Enhanced Oil Recovery methods that use surfactants, which may lead to the formation of stable emulsions. As the separation typically is performed on the oil rig, a fast and robust method to assess crude-oil/water emulsion stability using lab-scale experiments would be useful, which may aid in separator design for a given produced fluid.

A large number of theoretical and experimental studies on droplet coalescence have been performed until now. Generally, the physical processes determining coalescence are well understood [3,4], but difficult to model, as the solution of the involved equations, such as the Navier-Stokes equations to describe the drainage of continuous phase between the droplets, is only possible numerically [5]. The presence of surfactants causes additional complications due to the introduction of colloidal forces [6] and modification of the interfacial rheology [7]. For these reasons, simplified models are often used [8, 9], which provide the necessary accuracy to reliably predict coalescence only for chemically simple systems, and if the droplet deformation during film drainage is not significant.

Extensive experimental studies on coalescence between isolated droplet pairs colliding in simple shear flow have been performed. The influence of collision geometry [10], viscosity ratio of the liquids [11] and the flow field [12] on the droplet trajectories and coalescence probability was studied. As these methods typically use light microscopy to study droplet interactions, density-matched liquids are employed to avoid movement of droplets out of the focal plane due to buoyancy. In doing this, the choice of liquids is limited to very specific model systems. An experimental route to study coalescence in dilute emulsions is to optically measure the evolution of the droplet size distribution of a sheared emulsion in a rheometer. Both *ex*-situ [13] and *in*-situ [14] droplet size measurements have been reported. In the work of Korobko *et al.* [14], a mean coalescence probability was evaluated from the temporal evolution of the droplet size distribution.

The rate r_{ij} of coalescence between droplets of volume V_i and V_j can be expressed as [15]:

$$r_{ij} = \Theta_{ij} p_{ij} = \Theta_{ij} e^{-\langle t_{ij} \rangle / \langle \tau_{ij} \rangle} \tag{1}$$

In eq. (1), Θ_{ij} and p_{ij} are the collision frequency and coalescence probability; $\langle t_{ij} \rangle$ and $\langle \tau_{ij} \rangle$ are the mean coalescence time and the mean contact time between the two droplets for a given flow and fluid properties. Θ_{ij} can be calculated from $\Theta_{ij} = n_i n_j \sigma_{ij} \Delta v_{ij}$, where n_i and n_j are the concentrations of the droplets, σ_{ij} is the collision cross section, and Δv_{ij} is a characteristic velocity difference between the droplets. From an application point of view, it would be ideal being able to directly measure r_{ij} for a given experimental condition, or to measure $\Theta_{ij}, \langle t_{ij} \rangle$ and $\langle \tau_{ij} \rangle$

independently. Further, the set of r_{ij} measured for a given flow condition and fluid properties may be used as an input parameter in the coalescence rate equations of population balance equation (PBE) models [16]. The PBE are used in multiphase Computational Fluid Dynamics methods to describe the evolution of droplet size distributions in fluid-liquid flows [17].

In this article, we present the results of a microfluidic analysis on droplet coalescence in a dense two-dimensional oil-in-water emulsion without added surfactant. We monitor the interactions in an ensemble of droplets in a collision chamber. We perform a detailed evaluation of the droplet interactions in the microchannel and analyze the trajectories of colliding droplets which allows to calculate the coalescence rates for different flow conditions. Further, we obtain the individual coalescence times for droplet pairs as a function of the initial film drainage velocity of the droplets. From this data, we are able to calculate coalescence time distributions for each set of experimental parameters. We will discuss the potential of the method as a predictive tool for crude-oil/water demulsification kinetics.

2 Experimental section

2.1 Chemicals

The physical properties of the mineral oil at 293 K are density $\rho = 869$ kg m^{-3} and viscosity $\eta = 20.1$ mPa s. The aqueous phase was a 9 wt. % solution of NaCl in water (at 293 K: $\rho = 1063$ kg m^{-3}, $\eta = 1.18$ mPa s). Purified water obtained from a Millipore Milli-Q system (ZMQS 50001) and sodium chloride (ACS reagent, $\geq$ 99%, Sigma Aldrich) were used to prepare the solution. All liquids were degassed before use. The interfacial tension of the oil/brine interface at 293 K was measured to be 11 mN m^{-1}.

2.2 Microfluidic experiments

Custom-designed microfluidic circuits were purchased from Micronit B.V., The Netherlands. The microchips are made from glass and have a rectangular cross-section. Figure 1 displays the layout of the chip. All channels have a depth of 45 μm. The width of the channels is 100 μm, except for the channel in the center of the chip, where the droplets collide. This collision channel has a width of 500 μm and a length of 5 mm. The chip contains four inlet and two outlet sections. For droplet creation T-junctions are used, where the continuous (flow rate q_c) and dispersed phase channels (q_d) intersect. By controlling the flow rate ratio q_c/q_d, the droplet volume and frequency can be controlled for a given T-junction geometry [18, 19]. After formation, the droplets then enter a wider channel, where they undergo collisions and coalesce. In this collision channel the droplets are not spherical, but take on a flattened, disk-like shape. The effective hydraulic diameter d_h of a droplet is given by $d_h = 4A/P$, where A and P are the cross sectional area and the perimeter of the droplet. For a disk-shaped droplet, we obtain

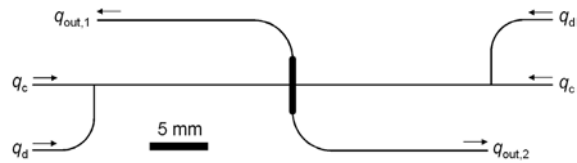

Figure 1: Layout of the microfluidic chips used for the experiments. q_d and q_c denote the inlet sections of the continuous and dispersed phases; $q_{out,1}$ and $q_{out,2}$ denote the outlet sections for the liquids. The channels have a uniform depth of 45 μm, the width of all channels is 100 μm, except for the wider channel in the center of the chip. The width of this channel is 0.5 mm, and the length 5 mm.

$d_h = 4h(d_d - (1-\pi/4)h)/(\pi h + 2(d_d - h))$, where d_d is the diameter of the disk-like droplet and h the channel height. For the flow conditions used in this work, we obtained 70 μm $< d_d <$110 μm, corresponding to 55 μm $< d_h <$ 64 μm.

Before each experiment, the microfluidic chips underwent a cleaning procedure to ensure the hydrophilicity of the channels. First, the channels were filled with an alkaline cleaning solution (Decon 90, Decon Laboratories Ltd.), sonicated for 15 minutes, and afterwards flushed with water. The chips were then blown dry and baked out in an oven for 3 h at 600 °C. Finally, the chips were subjected to an oxygen plasma for 10 minutes (Zepto B Plasma Cleaner, Diener Electronic GmbH).

The microfluidic chips are mounted on a chip holder (4515 Nanoport, Micronit B.V., The Netherlands). The inlet sections of the chips are connected to silica capillary tubing (Grace Altech, inner diameter 150 μm). The liquids are dosed using syringe pumps (NE 1000, New Era Pump Systems, Inc.). The flow rates of dispersed phase q_d at the two different inlets of the dispersed phase were always kept equal, as were the flow rates of continuous phase q_c. This was done to assure identical droplet volumes and formation rates obtained from both T-junctions. The two outlet sections have the same hydraulic resistance. To change the flow rate ratio $q_{out,1}/q_{out,2}$ of the outlet sections, and thus the flow rate ratio in the upper and lower part of the collision channel, capillary tubings of different length (inner diameter 50 μm) were attached to the outlet sections.

The droplet interactions in the collision channel are monitored using a microscope (Axiovert 200 MAT, Carl Zeiss GmbH, 2.5× magnification) and a camera (HS4, IDT Inc.). The frame rate of the recorded movies was 10000 s^{-1}. Sequences of images were recorded from one half-section of the collision channel, thereby sampling an area of 0.5×2 mm^2. Experimental parameters were the continuous and dispersed phase flow rates, q_c and q_d, as well as the outlet flow rates $q_{out,1}$ and $q_{out,2}$. By varying these parameters, the mean drop velocity in the collision chamber v_d and the dispersed volume fraction ϕ can be controlled independently from each other. For each experimental condition, movies with a length of 2 s were recorded (Motion Studio Software, IDT Inc.). The range of

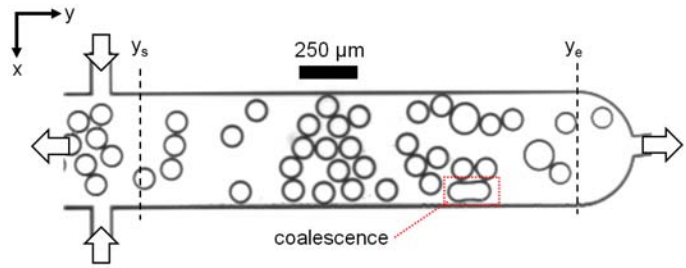

Figure 2: Snapshot of the collision channel. Monodisperse oil droplets ($d_d = 97$ μm in this example) dispersed in the aqueous phase enter the chamber from two inlets, where they collide and coalesce. The total fluid flow rate in the collision channel is 60 μl min^{-1}. y_s and y_e denote the start and end y-coordinate for the evaluation of coalescence events in the chamber. The red dotted rectangle encloses a droplet that was formed through coalescence between the displayed and the previous frame.

experimental parameters was $0.21 < q_d/q_c < 0.71$, 2 μl min^{-1} $< q_t <$ 300μl min^{-1} and 70 μm $< d_d <$ 110 μm. q_t denotes the total fluid flow rate, $q_t = q_c + q_d$.

3 Results and discussion

Figure 2 displays a snapshot of the collision channel during an experiment as an example. Monodisperse oil droplets with $d_d \approx 97$ μm enter the channel from two inlets and then move into the wider channel were they undergo collisions. The flow rate q_{out} in each section of the collision channel in this example is $q_{out} \approx 60$ μl min^{-1}. The flow rate ratio is $q_d/q_c \approx 0.15$, but the dispersed phase fraction ϕ in the collision channel is $\phi \approx 0.29$. This difference is caused by the fact that the disk-shaped droplets in the collision channel will experience a larger drag due to contact with the wall and will thus move significantly slower than the continuous phase. Due to this effect, there will be a holdup of droplets in the collision channel.

The mean droplet size increases as the droplets move downstream in the collision channel. This growth in droplet size is caused by coalescence between colliding droplets, which will lead to droplet sizes in the channel ranging from the original volume of a droplet V_1 entering the chamber, to a droplet volume of $V_i = iV_1$, where $i-1$ indicates the number of coalescence events that led to the formation of the droplet. The collisions are caused by differences in droplet velocity, which originate from local differences in hydraulic resistance caused by the presence of neighboring drops, and from the velocity profile that exists in laminar channel flow.

3.1 Evaluation of the coalescence rate

Counting the number of coalescence events permits to calculate the coalescence rate r_{ij}. We define r_{ij} for a combination of droplets of volume V_i and V_j as

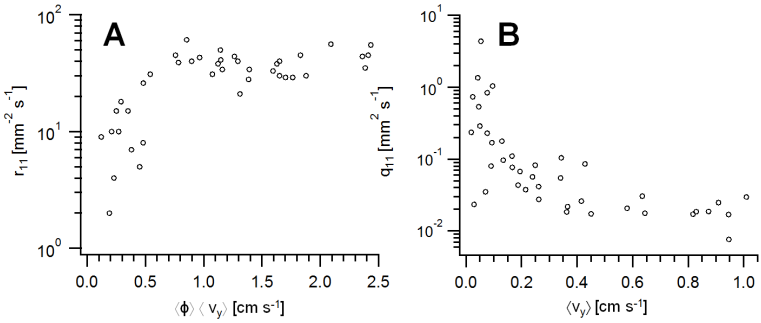

Figure 3: Coalescence rate r_{11} of the oil/brine system for droplets of relative volume $V_i/V_1 = 1$, as a function of the mean dispersed phase flux $\langle\phi\rangle\langle v_y\rangle$ (shown in panel A). $\langle\phi\rangle$ denotes the mean dispersed phase volume fraction and $\langle v_y\rangle$ the mean y-component of the droplet velocity in the collision channel. Panel B displays the specific coalescence rate q_{11} of the oil/brine system as a function of the mean y-component of the droplet velocity $\langle v_y\rangle$ in the collision channel. The mean hydraulic diameter of the droplets entering the collision channel was $d = (58 \pm 4.7)\ \mu$m.

$r_{ij} = n_{c,ij}/A_c t_{exp}$, where $n_{c,ij}$ is the number of coalescence events between droplets i and j, A_c is the area of the collision channel, and t_{exp} the experiment time. The procedure to determine r_{ij} from the image sequences is described elsewhere [20]. Only coalescence events occurring between the y-coordinates y_s and y_e were counted (see Figure 2).

r_{11} is shown in Figure 3A as a function of the mean dispersed phase flux $\langle\phi\rangle\langle v_y\rangle$ in the collision channel. $\langle\phi\rangle$ denotes the mean dispersed phase volume fraction and $\langle v_y\rangle$ the mean y-component of the droplet velocity in the collision channel. The mean hydraulic diameter of the droplets was $(58 \pm 4.7)\ \mu$m. The scatter of the data points is significant, this is caused by the relatively small number of droplets passing through the chamber in 2 s, which ranged from 200–5000, depending on the flow rate. The r_{ij} for $i \geq 1$ and $j > 1$ are not shown. r_{12} was on average approximately one order of magnitude smaller than r_{11} and all other r_{ij} were on average zero.

The measured dependence $r_{11}(\langle\phi\rangle\langle v_y\rangle)$ can be qualitatively explained from equation (1). The mean shear rate $\langle\dot{\gamma}\rangle$ in the microchannel is related to v_y by $\langle\dot{\gamma}\rangle \propto v_y$ [21]. In simple shear, the collision frequency will depend on $\langle\dot{\gamma}\rangle$ as $\Theta_{ij} \propto \dot{\gamma}$ and the coalescence probability $ln(p_{ij}) \propto \dot{\gamma}^{-n}$. Korobko *et al.* found $n = 1.5 \pm 1$ from experiments on coalescence in simple shear flow [14]. The flow in the microfluidic channel is not simple shear flow due to the large dispersed phase fractions, but qualitatively we would expect a similar scaling of the parameters in equation 1 in our system. Depending on the value of n, r_{ij} may increase monotonously or pass through a maximum in a given range of $\dot{\gamma}$.

To account for the effect of droplet concentrations on the coalescence rate, we calculate the specific coalescence rate $q_{11} = r_{11}/\langle n_1\rangle^2$. $\langle n_1\rangle$ is the mean

concentration of droplets with volume V_1 in the collision channel. q_{11} is formally equivalent to a second-order rate constant. Figure 3B displays q_{11} as a function of the mean y-component of droplet velocity $\langle v_y \rangle$ in the collision channel. From eq. (1), the decrease of q_{ij} with v_y indicates a decrease of the coalescence probability p_{ij} with increasing v_y, as Θ_{ij} will increase with increasing $\langle v_y \rangle$.

3.2 Evaluation of the film drainage profiles and coalescence times

If experimental data for q_{ij} is not available, then eq. (1) can, in principle, be used to predict q_{ij}. For turbulent flow and laminar shear flow, analytical relations for the collision frequency Θ_{ij} and contact time τ_{ij} can be derived if the characteristic velocity variation Δv between droplets in the flow is known. For the turbulent flow this property is related to the rate of energy dissipation ε through $\Delta v \propto \varepsilon^{1/3}$ [22]. For laminar shear flow the shear rate $\dot{\gamma}$ will determine the magnitude of Δv, $\dot{\gamma} \propto \Delta v$ [15, 22]. For the coalescence time t_c no general analytical equation can be derived, except for certain idealized situations, which are typically not encountered in applications. Hence, a possible experimental measurement of $t_c(\Delta v)$ can also be useful for coalescence modeling. We argue that the $t_c(\Delta v)$, which we measure, can also be used to describe coalescence in other flow conditions. On a microscopic scale the approach velocity and force will determine the timescale of coalescence, rather than the mechanism which is bringing the droplets together in the flow. In this section, we will derive $t_c(\Delta v)$ from the recorded trajectories of coalescing droplets in the microchannels.

Evaluation of the trajectories of colliding droplets permits to calculate the coalescence time t_c, which we define as the time it takes the droplets to approach each other from a given initial distance h_0 to a critical thickness h_c at which coalescence takes place, i.e. $t_c = \int_{h_0}^{h_c} dh/v_f$. In the equation, $v_f = -dh/dt$ denotes the velocity of drainage of the continuous phase film between the two droplets. Due to the limited spatial resolution of the microscope that was used in the experiments we cannot resolve the film drainage process until h_c is reached, as $h_c < 100$ nm [23]. We can, however, identify a coalescence event. The occurrence of coalescence indicates that $h \leq h_c$ between two recorded frames, thus permitting to calculate $t_c \approx (F(h_0) - F(h_c))/f$, whereas F indicates the frames with the relevant film thicknesses and f indicates the frame rate of the camera.

The inset in Figure 4 schematically displays the geometry of a pair of colliding droplets k and l. The film thickness can be calculated from $h \approx ((x_k - x_l)^2 + (y_k - y_l)^2 - (r_k + r_l))^{1/2}$. In doing this, a spherical shape of the droplets is assumed. The validity of this assumption was checked by evaluation of the circularity parameter $c = 4\pi A/P^2$. For circular objects, $c = 1$. It was found that for $\sim 90\%$ of all analyzed droplets c was > 0.95, which indicated circular or almost circular shape of the droplets. Droplets for which $c < 0.95$ were discarded from the analysis.

As long as the droplets are still visibly separated, the drag force on a droplet will be balanced by the force exerted by the flow. Thus, we can calculate a relative initial approach or film thinning velocity of the droplets along the line connecting

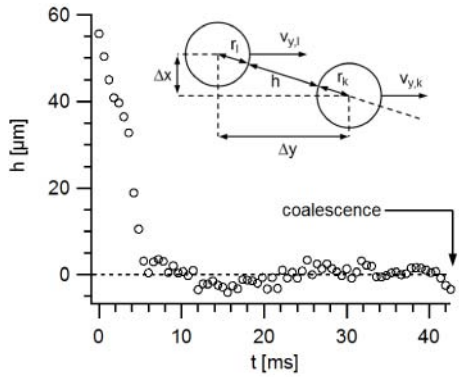

Figure 4: Film drainage profile $h(t)$ of two colliding droplets k and l. The droplets approach each other, spend time in close contact and then coalesce. The end of the curve at $t = 42.4$ ms marks the time when coalescence takes place. The initial film thickness ($h_0 = d_h/8 \approx 7\ \mu$m in this example) is reached after 4.4 ms, thus a coalescence time $t_c = 38$ ms is obtained. The mean initial approach velocity v_0, which was evaluated in the interval 0–4.4 ms, is ≈ 9.4 mm s^{-1} in this example. The inset shows the collision geometry. $\Delta x = x_k - x_l$ and $\Delta y = y_k - y_l$ signify the difference of the x- and y- coordinates of the centers of mass of the droplets, respectively. r_l and r_k are the droplet radii, h is the thickness of the film of continuous phase between the droplets. $v_{y,k}$ and $v_{y,l}$ are the velocity components of the droplets parallel to the downstream channel direction.

their center of mass $v_0 = -dh/dt$. From all the videos recorded for different flow conditions and dispersed phase fractions, the coalescence time of colliding droplets was evaluated. Only droplet pairs for which the initial separation distance was $\geq 30\ \mu$m were considered, in order to obtain enough data points to calculate v_0. v_0 was calculated for each droplet pair as a mean value $\langle \Delta h/\Delta t \rangle$ in the interval $h_0 < h < 30\ \mu$m, whereas $h_0 = d_h/8$, which is an estimate for the film thickness at which the film drainage rate becomes smaller than the shear-induced velocity bringing the droplets together [7]. The coalescence time was then calculated using the same definition of h_0 for the initial film thickness.

From all recorded videos, a total of $\sim$ 10000 film drainage profiles fulfilled the aforementioned criteria for evaluation. To each data point also a hydraulic droplet diameter d_h and a dispersed phase volume fraction ϕ are assigned. Visual inspection of the data set indicated that there was a distribution of coalescence times for a given v_0. These coalescence time distributions may depend on ϕ and d_h in addition to the dependence on v_0. As the range of d_h was relatively small (55–64 μm), the dependence $t_c(d_h)$ was not investigated. To evaluate the dependence $t_c(\phi)$ we sort the data into 5 bins of different ranges of ϕ with equal amounts of data points. For the dependence $t_c(v_0)$ for a given $\langle \phi \rangle_i$, we further sort a given set of data points of bin i into 5 bins of ascending v_0 and calculate the

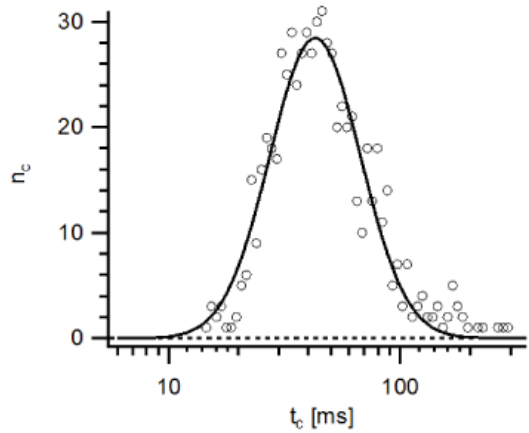

Figure 5: Distribution of coalescence times $n_c(t_c)$ for $\langle\phi\rangle$ = 0.61 ± 0.087 and $\langle v_0\rangle = (5.8 \pm 1.1)$ mm s^{-1}. The mean hydraulic diameter of the colliding droplets was (54 ± 4.7) μm. The solid line is a log normal distribution which was fitted to the data points. The expected value E_{t_c} of this data set is 53 ms.

distribution of coalescence times for each bin. The upper and lower boundaries of the v_0 bins were chosen in a way to obtain the same geometric mean $\langle v_0\rangle_j$ for different $\langle\phi\rangle_i$, to allow a better comparison of the results. Figure 5 displays the distribution of coalescence events $n_c(t_c)$ for the bin with $\langle\phi\rangle_i = 0.61 \pm 0.087$ and $\langle v_0\rangle = 5.8 \pm 1.1$ mm s^{-1} as an example. It was found that all $n_c(t_c)$ distributions calculated in this way could be well described by log normal distributions:

$$n_c(t_c) \propto \frac{1}{\sqrt{2\pi}t_c\sigma} e^{-\frac{(lnt_c-\mu)^2}{2\sigma^2}} \tag{2}$$

The expected value E_{t_c} and standard deviation σ_{t_c} of the distribution can be calculated from the parameters μ and σ, $E_{t_c} = e^{\mu+0.5\sigma^2}$ and $\sigma_{t_c} = E_{t_c}\sqrt{e^{\sigma^2}-1}$. From all the distributions obtained for the different $\langle\phi\rangle_i$ and $\langle v_0\rangle_j$ bins, we evaluate E_{t_c} and σ_{t_c}. E_{t_c} is shown in Figure 6 as a function of $\langle v_0\rangle$ for the different $\langle\phi\rangle_i$. It can be seen that E_{t_c} decreases weakly with increasing $\langle v_0\rangle$. From power law fits to the data series, we obtain $E_{t_c} = (31.7 \pm 2.8) \times 10^{-3}\langle v_0\rangle^{-0.097\pm0.012}$. Hydrodynamical theory predicts $t_c \propto \dot{\gamma}^{-0.5}$ in the limit of $Ca = \eta_c d_h \dot{\gamma}/\sigma \to 0$ [12], and an increase of the exponent −0.5 to a maximum value of 0.5 for $Ca \to \infty$ [7]. We can calculate a local shear rate of colliding droplets for our experiments from $\dot{\gamma}_{kl} = (v_{y,l} - v_{y,k})/(|\, x_l - x_k\,|)$ (see Figure 4). From plotting E_{t_c} vs. $\langle\dot{\gamma}_{kl}\rangle$ we obtain $E_{t_c} = (37.6 \pm 2.7) \times 10^{-2}\langle\dot{\gamma}_{kl}\rangle^{-0.067\pm0.009}$ from a power law fit to the data points. The range of 10^{-3} m s$^{-1} < v_0 < 10^{-1}$ m s^{-1} corresponds approximately to a range of shear rates 1 s$^{-1} < \dot{\gamma}_{kl} < 1000$ s^{-1}. The exponent of -0.067 found by us for our experimental system thus lies within the range of theoretically possible values.

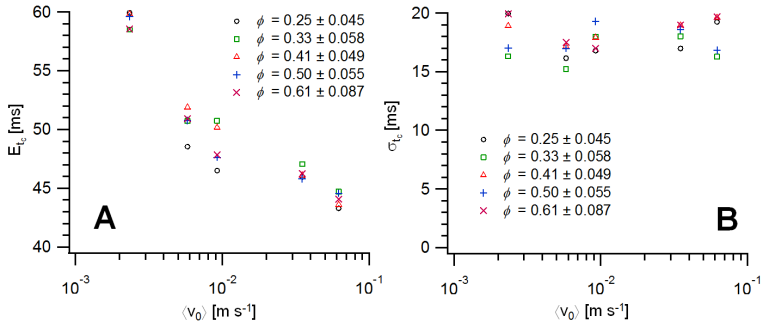

Figure 6: Expected values E_{t_c} (panel A) and standard deviations σ_{t_c} (panel B) of the coalescence time distributions as a function of the mean initial approach velocity $\langle v_0 \rangle$ for different mean dispersed phase fractions $\langle \phi \rangle_i$.

There is no trend of t_c for the different $\langle \phi \rangle_i$ for a given $\langle v_0 \rangle$, which indicates that the presence or absence of neighboring droplets does not modify the average coalescence time. Panel B of Figure 6 displays σ_{t_c} as a function of $\langle v_0 \rangle$ for the different $\langle \phi \rangle_i$. Neither a clear trend of σ_{t_c} as a function of $\langle v_0 \rangle$ and $\langle \phi \rangle_i$ can be observed. Thus we can conclude that the presence of neighboring droplets also does not lead to a broadening of the coalescence time distributions.

Even though we do not know why the coalescence time distribution can be described by a log-normal distribution, we think that the major reason for the existence of a rather wide distribution is that the droplets are moving in an external flow field. During the collision, the leading droplet will induce a wake which will effect the drag force acting on the trailing droplet [24]. Depending on the magnitude of the absolute velocities of the droplets and the collision angle, the wake effect can cause a net attraction or repulsion of the droplets [25]. The magnitude of the effect increases with decreasing h. Further, as the droplets are subjected to shear flow, droplet deformation during the collision can be expected to be asymmetrical. These factors will influence the timescale of film drainage and magnitude of droplet deformation. Additionally, the critical film thickness itself in a quiescent emulsion has a probability distribution, which contributes to the observed coalescence time distribution [3, 8].

4 Conclusions and outlook

We have presented a method to evaluate the demulsification kinetics of liquid-liquid mixtures. The coalescence rate in a hexadecane-in-water emulsion without added surfactant was measured, which is a parameter that has been difficult to obtain directly until now. Due to the simplicity of the experimental setup and the evaluation procedure, the method provides an easy-to-use diagnostic tool for the assessment of the stability of flowing dispersions. As the flow rates can be adjusted quickly, a complete set of coalescence parameters can be obtained as a function of the experimental variables d, ϕ and q_t within a few hours.

In the current design, the method is best suited for the investigation of oil-in-water emulsions. For crude-oil-production, the breakup of water-in-oil emulsions is equally important. When using glass chips, the channels can be made temporarily hydrophobic in a simple manner by adsorption of alkylsilanes on the glass surface for the duration of an experiment [26], to enable the formation of water droplets. Alternatively, the microstructures can be made from hydrophobic materials [27].

The measured coalescence times are smaller than the residence times of the droplets in the collision channels, which in our experiments ranged from 0.1 to 2 seconds, depending on the fluid flow rate. If the viscosity of the continuous phase is increased, or surfactant is present in the system, then the coalescence time will be increased [8]. For these systems, the length of the collision channel can be increased to increase the residence time of the droplets.

The range of accessible hydraulic diameters is currently limited due to the droplet being squeezed into a disk-like shape in the collision channel. This issue may be solved by producing microstructures with a non-uniform depth, where the height of the collision channel will be several times larger than the height of the T-junction. This will allow the droplet to take on a spherical shape, thus increasing its hydraulic diameter.

Acknowledgement

This work is carried out as part of a project of the Institute for Sustainable Process Technology: development of an Ω^2R separator focusing on oil/water separation (project number OG 00-04).

References

[1] Lyons, W., *Standard Handbook of Petroleum and Natural Gas Engineering*. Elsevier, 2nd edition, 2004.
[2] Slot, J., Van Campen, L., Hoeijmakers, H. & Mudde, R., Separation of oil droplets in swirling water flow. *7th International Conference on Multiphase Flow - ICMF 2010 Proceedings*, p. 11.4.2, 2010.
[3] Walstra, P., *Physical Chemistry of Foods*. Marcel Dekker, 1st edition, 2003.
[4] Sjöblom, J., (ed.) *Encyclopedic Handbook of Emulsion Technology*. Marcel Dekker, 1st edition, 2001.
[5] Hartland, S., Yang, B. & Jeelani, S., Dimple formation in the thin film beneath a drop or bubble approaching a plane surface. *Chem Eng Sci*, **49(9)**, pp. 1313–1322, 1994.
[6] Danov, K., Petsev, D. & Denkov, D., Pair interaction energy between deformable drops and bubbles. *J Chem Phys*, **99(9)**, pp. 7179–7189, 1993.
[7] Chesters, A. & Bazhlekov, I., Effect of insoluble surfactants on drainage and rupture of a film between drops interacting under a constant force. *J Colloid Interf Sci*, **230**, pp. 229–243, 2000.
[8] Ivanov, I., Danov, K. & Kralchevsky, P., Flocculation and coalescence of micron-size emulsion droplets. *Colloid Surface A*, **152**, pp. 161–182, 1999.

[9] Rommel, W., Meon, W. & Blass, E., Hydrodynamic modeling of droplet coalescence at liquid-liquid interfaces. *Separ Sci Technol*, **27(2)**, pp. 129–159, 1992.
[10] Guido, S. & Simeone, M., Binary collision of drops in simple shear flow bycomputer-assisted video optical microscopy. *J Fluid Mech*, **357**, pp. 1–20, 1998.
[11] Baldessari, F. & Leal, G., Effect of overall drop deformation on flow-induced coalescence at low capillary numbers. *Phys Fluids*, **18**, pp. 013602 1–20, 2006.
[12] Yang, H., Park, C., Hu, Y. & Leal, L., The coalescence of two equal-sized drops in a two-dimensional linear flow. *Physics of Fluids*, **13**, pp. 1087–1106, 2001.
[13] Nandi, A., Mehra, A. & Khakhar, D., Coalescence in a surfactant-less emulsion under simple shear flow. *AIChE J*, **52(3)**, pp. 885–894, 2006.
[14] Korobko, A., Van Den Ende, D., Agterof, W. & Mellema, J., Coalescence in semiconcentrated emulsions in simple shear flow. *J Chem Phys*, **123**, pp. 204908 1–11, 2005.
[15] Prince, M. & Blanch, H., Bubble coalescence and break-up in air-sparged bubble columns. *AIChe J*, **36**, pp. 1485–1499, 1990.
[16] Schütz, S., Gorbach, G. & Piesche, M., Modeling fluid behavior and droplet interactions during liquid-liquid separation in hydrocyclones. *Chem Eng Sci*, **64**, pp. 3935–3952, 2009.
[17] Ansys cfx user manual. http://www1.ansys.com/customer/content/documentation/120/cfx/xthry.pdf.
[18] Christopher, G. & Anna, S., Microfluidic methods for generating continuous droplet streams. *J Phys D Appl Phys*, **40**, pp. R319–R336, 2007.
[19] Garstecki, P., Fuerstman, M., Stone, H. & Whitesides, G., Formation of droplets and bubbles in a microfluidic t-junction - scaling and mechanism of break-up. *Lab Chip*, **6**, pp. 437–446, 2006.
[20] Krebs, T., Schroen, C. & Boom, R., to be submitted for publication.
[21] Bruus, H., *Theoretical Microfluidics*. Oxford University Press, 1st edition, 2008.
[22] Chesters, A., The modelling of coalescence processes in fluid-liquid dispersions: A review of current understanding. *Trans IChemE*, **69A**, pp. 259–270, 1991.
[23] Birdi, K., *Handbook of Surface and Colloid Chemistry*. CRC Press, 2nd edition, 2003.
[24] Happel, J. & Brenner, H., *Low Reynolds Number Hydrodynamics: With Special Applications to Particulate Media*. Prentice-Hall, 1st edition, 1965.
[25] Hallez, Y. & Legendre, D., Interaction between two spherical bubbles rising in a viscous liquid. *Journal of Fluid Mechanics*, **673**, pp. 406–431, 2011.
[26] Butt, H., Graf, K. & Kappl, M., *Physics and Chemistry of Interfaces*. Wiley VCH, 1st edition, 2003.
[27] Xia, Y. & Whitesides, G., Soft lithography. *Annual Reviews in Material Science*, **28**, pp. 153–184, 1998.

Section 7
Heat and mass transfer

This page intentionally left blank

The role of natural convection and density variations in the solidification process of water in an annular enclosure

E. M. Alawadhi & R. I. Bourisli
Mechanical Engineering Department, Kuwait University, Kuwait

Abstract

Unsteady natural convection flow during the solidification process of water in the annulus is numerically modeled using the finite element method. The annulus inner surface temperature is kept at a temperature lower than the solidification temperature. Ice is formed at the inner surface while natural convection flow is induced in the liquid portion. The goal of this study is to evaluate the effect of natural convection and variations in the density of water on the solidification process. The water density peak near the solidification temperature creates a unique flow structure. High resolution capturing of the solid/liquid moving boundary and the details of the flow structure and temperature contours are presented.
Keywords: natural convection, solidification, density variation, annulus enclosure.

1 Introduction

Phase change heat transfer has been extensively studied experimentally and theoretically in literature during the past two decades. Phase change has a wide range of utility in scientific and engineering applications. These applications include, for example, solar energy storage units, industrial refrigeration, crystal growth, welding and casting. During melting process, the effective specific heat of a substance is increased by more than 100 times, storing a large amount of energy. On the other hand, during solidification process, the specific heat is decreased to release a large amount of energy. Phase-change materials (PCM's) are substances that are used to store/release thermal energy by utilizing this effective specific heat


WIT Transactions on Engineering Sciences, Vol 74, © 2012 WIT Press
www.witpress.com, ISSN 1743-3533 (on-line)
doi:10.2495/AFM120391

variation. Small but influential variations in density often accompany this process and can have detrimental impact on the solidification process.

Common PCM's include waxes, many types of salts, as well as water. Wax PCM's are extensively employed in electronic devices as a method of thermal management [1], and in thermal control units [2]. In electronic cooling, PCM's are used to absorb heat from high thermal dissipating components during operating times, and then, release the stored energy during OFF times [3]. In thermal storage systems, especially in solar storage units, water is commonly used to store energy during high-energy demand periods [4]. Understanding phase change heat transfer mechanism in an enclosure is essential to predict the thermal performance of a PCM thermal unit.

Modeling the melting and solidification processes within a fixed enclosure has been of special interest to engineers. Modeling such processes can be intricate because of the need to deal with conduction in the solid portion, and conduction plus convection in the liquid portion. The phenomena are strongly coupled and the modeling results are extremely sensitive to the set up as well as the physics of the problem. Giangi *et al.* [5] performed numerical and experimental studies on natural convection flow during solidification of water in a rectangular enclosure with constant temperature boundary conditions. PCM melting in a rectangular enclosure by heating the bottom side was also studied by Gong and Mujumdar [6]. The resulting complex flow patterns were consistent with experimental results. Phase change heat transfer for a pure metal in a rectangular enclosure was studies by Mbaye and Bilgen [7]. Their results indicated that the Nusselt number passed through the maximum when the enclosure aspect ratio is unity. A rectangular composite cell filled with PCM and water was studied by Ho and Chu [8], and the effect of an ON/OFF pulsing of boundary heat load was analyzed. El Omari *et al.* [9] also studied the impact of the shape of the enclosure on the PCM solidification process, and found that non-slender shapes provide little control over the process.

More importantly, and more relevant to the subject of this work, Pal and Joshi [10] investigated the effect of natural convection on PCM melting rate in a honeycomb enclosure. When the PCM in the system is relatively small, or the PCM is placed in a metal matrix, natural convection flow in the liquid portion is often neglected, the rationale being that conduction dominates in the overall domain. While this approximation is widely used in phase change simulations [11–13], it could produce significant error. This also related to the variation in the density of the material as it changes temperature and phase. Kuznetsov and Sheremet [14] numerically studied the influence of Rayleigh number on fluid motion and heat (and mass) transfer in enclosures. They related these quantities specifically to the dimensional time and outlined regions of variations in the general behavior of flow as a result of phase change.

In this research, solidification process of pure water in an annulus enclosure is investigated. The annulus enclosure represents a practical geometry for thermal storage pipes [15]. Water is commonly used in thermal storage units, because of its availability, non-toxicity, non-flammability, and chemical stability. In addition, its

latent heat of fusion is relatively high compared to other PCM's. Initially, the water temperature in the annulus is higher than solidification temperature. At a certain instant, the boundary temperature at the inner surface is decreased to temperature lower than the solidification temperature. Ice is formed at the inner surface, and density gradients in the liquid portion induce natural convection flow. The main objective of this paper is to evaluate the significance of the natural convection effect on the solidification time.

2 Problem formulation

A schematic diagram of the model that was used for numerical simulations is shown in figure 1. As shown, it consists of a two-dimensional annulus enclosure of outer radius r_o and inner radius r_i, with $r_o = 2r_i$. The enclosure is initially at a temperature $T_{ini} = 38°\text{C}$, well-higher than water's solidification temperature, $T_s = 0°\text{C}$. At a certain instant $t = 0$, the annulus inner wall temperature is dropped to $T_w = -2°\text{C}$, which is lower than the water solidification temperature. The peak-density temperature of water is denoted by $T_p = 4°\text{C}$.

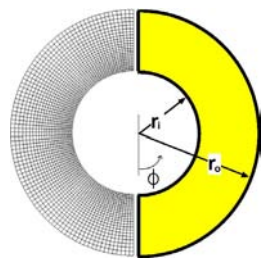

Figure 1: Problem schematics and mesh of annular enclosure.

2.1 Governing equations

Phase change simulations were done using apparent capacity paradigm. The apparent capacity is the sum of the sensible and latent heats, as follows

$$\overline{C}_p = C_p + \frac{\partial L}{\partial T} \tag{1}$$

where C_p is the specific heat, and $\partial L/\partial T$ is the released latent heat. The apparent capacity can be approximated if the phase change transient temperature is finite, as follows:

$$\overline{C}_p = C_p + \frac{\Delta L}{\Delta T} \tag{2}$$

The value of $\partial L/\partial T$ is equal to zero in the liquid and solid phases.

The governing equations are nondimensionalized using the following parameters: Rayleigh number Ra, Prandtl number Pr, Stefan number St, and Fourier number Fo; they are defined, respectively, as,

$$Ra = \frac{g\beta\Delta T\, r_o^3}{\nu\alpha}, \qquad Pr = \frac{\nu}{\alpha}, \qquad Ste = \frac{C_p\Delta T}{L}, \qquad Fo = \frac{\alpha t}{r_o^2}$$

Based on these dimensionless groups, the non-dimensional forms of the continuity, x-momentum, y-momentum, and energy equations are obtained as follows,

$$\frac{\partial u^\star}{\partial x^\star} = 0 \tag{3}$$

$$\frac{\partial u^\star}{\partial Fo} + u^\star\frac{\partial u^\star}{\partial x^\star} + v^\star\frac{\partial u^\star}{\partial y^\star} = -\frac{\partial p^\star}{\partial x^\star} + Pr(\theta)\left[\frac{\partial^2 u^\star}{\partial x^{\star\,2}} + \frac{\partial^2 u^\star}{\partial y^{\star\,2}}\right] \tag{4}$$

$$\frac{\partial v^\star}{\partial Fo} + u^\star\frac{\partial v^\star}{\partial x^\star} + v^\star\frac{\partial v^\star}{\partial y^\star} = -\frac{\partial p^\star}{\partial v^\star} + Pr(\theta)\left[\frac{\partial^2 v^\star}{\partial x^{\star\,2}} + \frac{\partial^2 v^\star}{\partial y^{\star\,2}}\right] + Ra\,Pr\,\theta \tag{5}$$

$$\Phi(Ste,\theta)\frac{\partial\theta}{\partial Fo} + u^\star\frac{\partial\theta}{\partial x^\star} + v^\star\frac{\partial\theta}{\partial y^\star} = \frac{\partial^2\theta}{\partial x^{\star\,2}} + \frac{\partial^2\theta}{\partial y^{\star\,2}} \tag{6}$$

where

$$\Phi(Ste,\theta) = \begin{cases} 1, & \theta \le \theta_s \\ 1/Ste, & \theta_s < \theta < \theta_s + \Delta\theta \\ 1, & \theta \ge \theta_s + \Delta\theta \end{cases} \tag{7}$$

Star-superscripted symbols signify dimensionless quantities where the following were used in the nondimensionalization,

$$x^\star = \frac{x}{r_o}, \quad y^\star = \frac{y}{r_o}, \quad u^\star = \frac{u}{\alpha/r_o}, \quad v^\star = \frac{v}{\alpha/r_o},$$
$$p^\star = \frac{p}{\rho\alpha^2/r_o^2}, \quad \theta = \frac{T - T_w}{|T_s - T_w|}$$

Finally, initial and boundary conditions are written in dimensional forms, using the dimensionless time τ, as,

$$\tau = 0: \qquad u^\star = v^\star = 0 \qquad \text{and} \qquad \theta = \theta_0 = 20 \tag{8}$$

$$\tau > 0,\ r = r_i: \qquad u^\star = v^\star = 0 \qquad \text{and} \qquad \theta = \theta_w = 0 \tag{9}$$

$$\tau > 0,\ r = r_o: \qquad u^\star = v^\star = 0 \qquad \text{and} \qquad \frac{\partial\theta}{\partial n} = 0 \tag{10}$$

2.2 Finite element model

The finite element model is used to solve simultaneously the set of coupled governing equations for this viscous flow. A four-node quadrilateral element is used to discretize the computational domain, as shown in figure 1. The finite element model consists of 2,250 elements and 2,366 nodes. The computational domain is reduced by half after taking advantage of symmetry in the problem.

Kuehn and Goldstein [16] conducted an experimental study of natural convection without phase change in a cylindrical annulus. The present code was validated by simulating natural convection in an annulus for the conditions presented by Kuehn and Goldstein. The inner and outer radii of the annulus are 0.0463m and 0.0178 m, respectively. The working fluid is air. The inner and outer

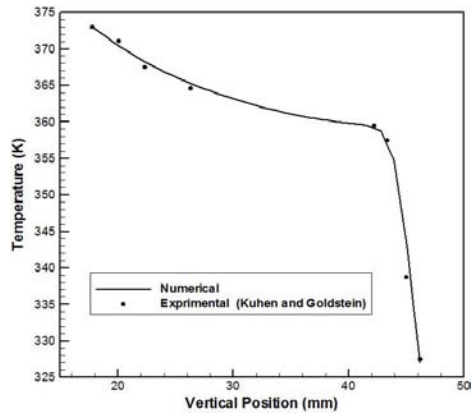

(a)

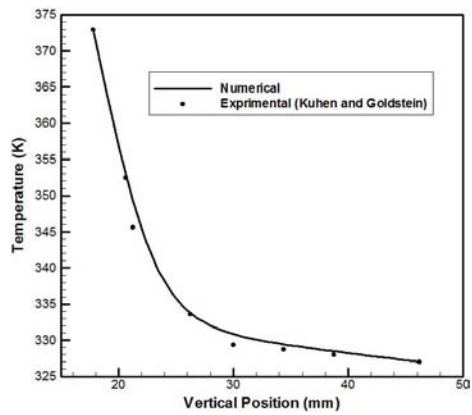

(b)

Figure 2: Comparison of temperature along the top symmetry line for natural convection flow in an annulus.

cylinder walls are set to temperatures of 373 and 327K, respectively. The Rayleigh number is 4.95×10^4. The temperature profiles long the top symmetry line of the numerical results and the experimental data are shown in figure 2. As shown, the agreement between the numerical and experimental results is excellent.

3 Results and discussion

Water is selected as the PCM for its common use in thermal storage pipes. Its thermo-physical properties are listed in table 1. Water exhibits a negative volume expansion coefficient at a temperature below 4°C and a positive volume expansion above 4°C. This phenomenon creates a unique flow structure during water solidification. The effect of free convection flow in the liquid portion during the solidification process is examined in the following sections.

Table 1: Thermo-physical properties of water [5].

Specific heat (C_p)	4.202 kJ/kg-K
Thermal conductivity (k)	0.56 W/m-K (liquid) 2.26 W/m-K (solid)
Dynamic viscosity	1.53×10^{-3} Pa-s
Latent heat (L)	335 kJ/kg-K
Density (ρ)	$999.84 + 0.067326T - 0.008944T^2$ $+8.87 \times 10^{-5}T^3 - 6.62 \times 10^{-7}T^4$

3.1 Flow field and temperature contours

Figures 3 show the velocity streamlines of the flow field alongside the resulting temperature contours at four time steps: $\tau = 0.05$, 0.1, 0.15 and 0.25, for $Ra = 10^7$. Each curve in the plot on the right-hand-side of these figures represents a streamline, while each curve on the left-hand-side represents an isotherm. Initially, water is in liquid phase ($\theta_0 = 20$). At $\tau > 0$, the inner wall temperature is dropped to a temperature lower than the water solidification temperature ($\theta_w = 0$).

Figure 3(a) shows how one recirculating cell is formed and the temperature of water is higher than its peak-density temperature of $\theta_p = 3$. Cold water adjacent to the inner cylinder is continually replaced by warm water coming from the outer cylinder. The water stream is cooled as it flows naturally close to the inner cylinder to leave the inner to outer cylinder. Therefore, the temperature differences between the inner cylinder and the water is maximum at the upper region, and minimum at the lower region. The variations of the temperature difference explain the observed wide temperature gradient at the upper region of the annulus. Up to this time

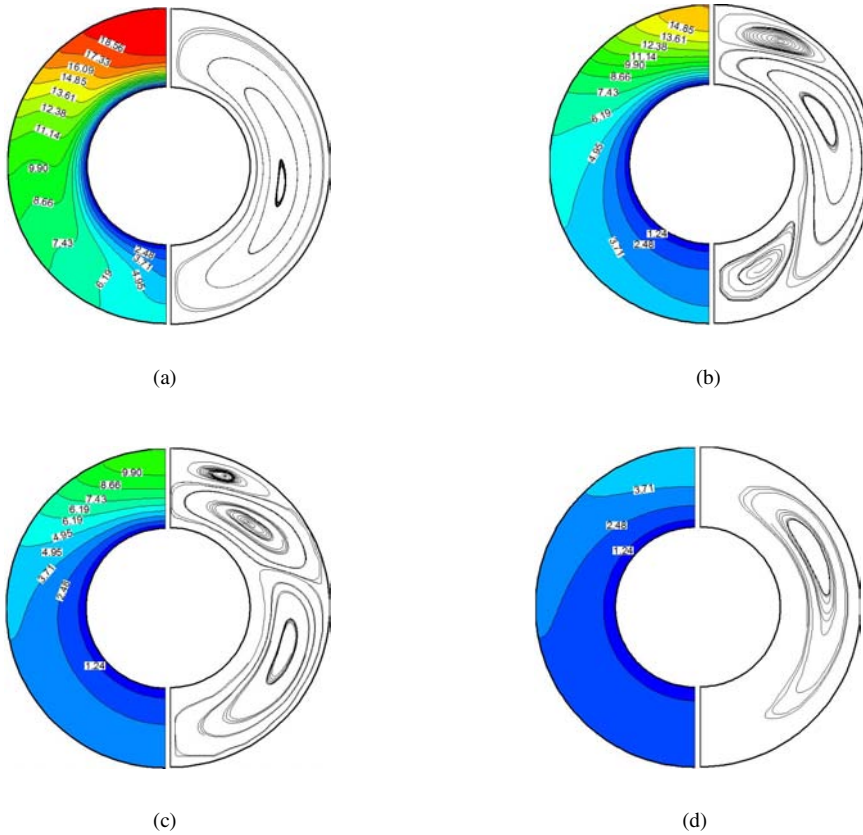

Figure 3: Flow field streamlines and temperature contour of the solidification process for $Ra = 10^7$ at (a) $\tau = 0.05$, (b) $\tau = 0.1$, (c) $\tau = 0.15$, (d) $\tau = 0.25$.

($\tau = 0.05$), one recirculating cell exists in the annulus. As time progresses, two additional recirculating cells are formed, as shown in figure 3(b), one at the top and another at the bottom of the original recirculating cell. Furthermore, while the original cell recirculates in the counter clockwise direction, the two newly formed cells have clockwise directions. Water temperature decreases as it flows close to the inner cylinder, and reaches the peak-density temperature. When water temperature becomes less than (θ_p), water density decreases to create a clockwise flow cell, and therefore, the direction of flow is reversed from counterclockwise to clockwise, creating a small cell below the original cell. The direction of original cell is still counterclockwise, because the temperature of the cell is higher than the peak-density temperature. These results are consistent with those of de Souza and Vielmo [17] who studied ice formation and melting processes in tubes for HVAC applications.

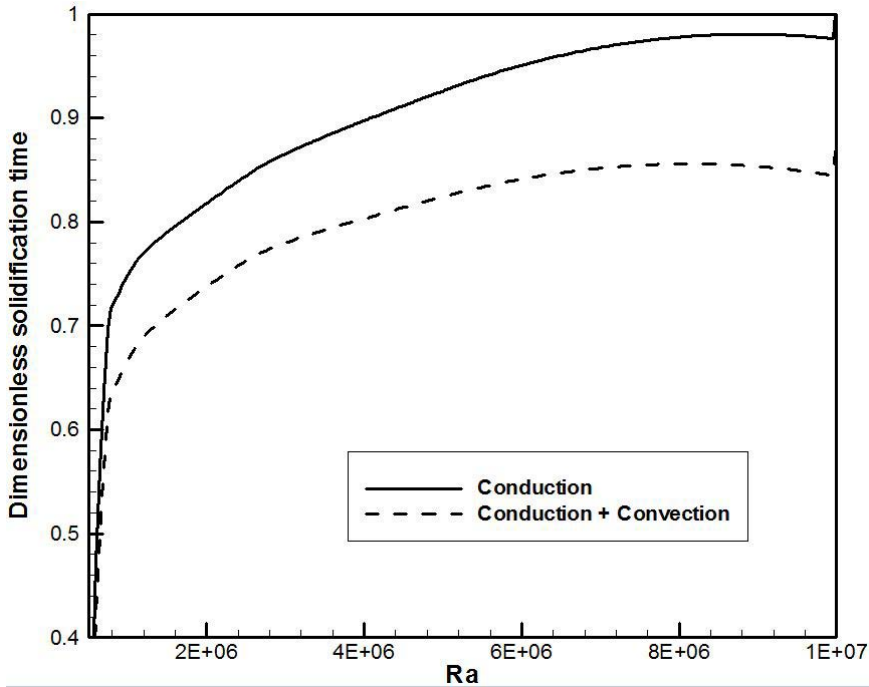

Figure 4: Effect of Rayleigh number on the water solidification time, for conduction and conduction-plus-convection modes of heat transfer, for $Ra = 10^7$.

3.2 Effect of natural convection flow

Figure 4 shows the solidification time for the conduction and conduction-plus-convection modes of heat transfer with $Ra = 10^6$ to 10^7. For $10^6 < Ra < 1.25 \times 10^6$, the solidification times for conduction and conduction-plus-convection are almost the same, showing a negligible effect of the convection as a heat transfer mechanism. Hence, eliminating the natural convection flow during phase change simulation is an acceptable approximation for this range of Ra. For $Ra \geq 1.25 \times 10^6$, figure 4 indicates that the effect of natural convection becomes significant. With $Ra = 10^7$, the natural convection decreases the solidification time by 13.3%.

Figures 5 show the average heat flux at the inner cylinder for conduction and conduction-plus-convection for $Ra = 10^6$ and 110^7. For $Ra = 10^6$, figure 5(a) indicates that the heat flux differences between the conduction and conduction plus convection is negligible. The strength of the natural flow is so weak that it does not decrease the thermal resistance in the annulus. On the other hand, when the Ra is increase to 10^7, figure 5(b) indicates that the effect of natural convection is only initially insignificant ($\tau < 0.15$) (note the negligible difference between the two

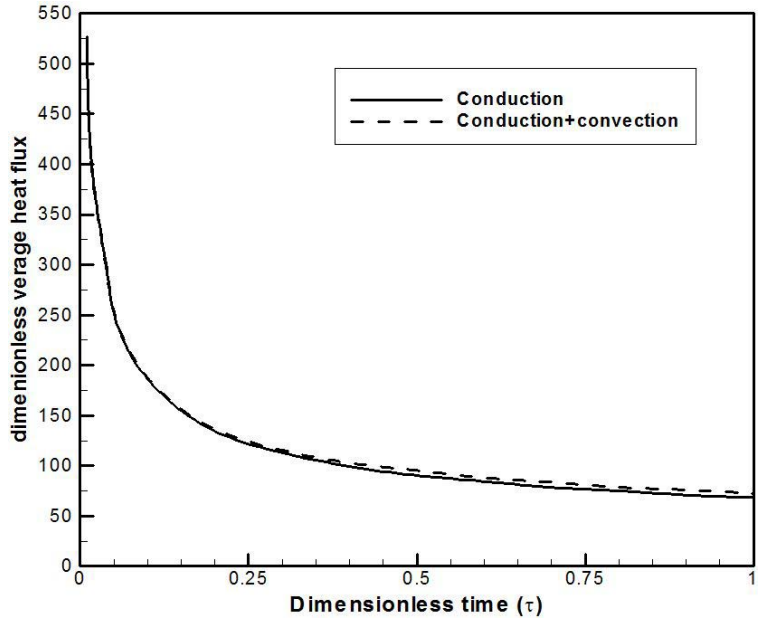

(a)

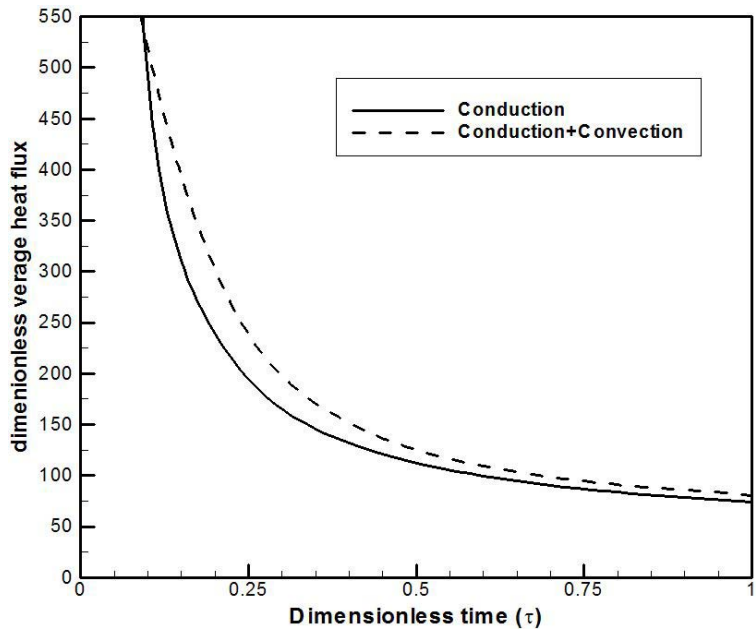

(b)

Figure 5: Variation of average heat flux at the inner cylinder with time, for (a) $Ra = 10^6$ and (b) $Ra = 10^7$

cases.) During the period $0.15 < \tau < 0.6$, however, the natural convection flow increases the heat transfer into the annulus by decreasing the thermal resistance in the annulus. Natural convention flow improves heat flow in the annulus by transporting warm water from the outer boundary to the freezing interface. For $\tau > 0.6$, the heat flux of the two cases is close again, indicating that the natural convection flow is slowing down and flow temperature becomes close to freezing temperature.

4 Conclusions

The main objective of this paper was to evaluate the effect of natural convection flow during water solidification process. Natural convection is commonly neglected in phase change simulations, even if the Rayleigh number is high. The results indicate that the effect of natural convention flow is significant for a wide range of Rayleigh numbers, and this significance is increased as the Rayleigh number is increased. Specifically, when the Rayleigh number is less than 1.25×10^6, the convection mode of heat transfer is an insignificant factor with regards to the solidification rate. For Rayleigh numbers higher than 1.25×10^6, natural convection flow plays an important role in reducing thermal resistance in the domain, enhancing heat transfer, and increasing the solidification rate. Therefore, neglecting natural convection flow can produce significant errors in numerical simulations.

References

[1] Ravi Kandasamy, Xiang-Qi Wang, and Arun S. Mujumdar. Transient cooling of electronics using phase change material (PCM)-based heat sinks. *Applied Thermal Engineering*, 28(8-9):1047–1057, 2008.

[2] D. P. Covin, J. C. Mulligan, and Y. G. Bryant. Enhanced heat transport in environmental systems using microencapsulated phase change materials. In *22nd International Conference on Environmental Systems*, 1992.

[3] R. C. Estes. The effect of thermal capacitance and phase change on outside plant electronic enclosure. *IEEE Transactions on Components, Hybrids, and Manufacturing Technology*, 5:843–849, 1992.

[4] R. Velraj, R. V. Seeniraj, B. Hafner, C. Faber, and K. Schwarzer. Heat transfer enhancement in a latent heat storage system. *Solar Energy*, 65:171–180, 1999.

[5] Marilena Giangi, Fulvio Stella, and Tomasz A. Kowalewski. Phase change problems with free convection: fixed grid numerical simulation. *Computing and visualizeation in science*, 2:123–130, 1999.

[6] Zhen-Xiang Gong and Aron Mujumdar. A finite element method for convection-dominated melting and solidification problem. *International Journal of Numerical Methods for Heat & Fluid Flow*, 8:393–408, 1998.

[7] M. Mbaye and E. Bilgen. Phase change process by natural convection-diffusion in rectangular enclosures. *Heat and Mass Transfer*, 37:35–42, 2001.
[8] C. Ho and C. Chu. On cooling behavior of vertical planes in a phase change/water composite enclosure under pulsing heat load. *International Journal of Heat and Mass Transfer*, 34:509–514, 1999.
[9] Kamal El Omari, Tarik Kousksou, and Yves Le Guer. Impact of shape of container on natural convection and melting inside enclosures used for passive cooling of electronic devices. *Applied Thermal Engineering*, 31(14-15):3022–3035, 2011.
[10] D. Pal and Y. Joshi. Thermal management of an avionics model using solid-liquid phase change materials. *Journal of Thermophysics and Heat Transfer*, 256:12–17, 1998.
[11] T. J. Lu. Thermal management of high power electronics with phase change cooling. *International Journal of Heat and Mass Transfer*, 43:2245–2256, 2000.
[12] Y. Cao and A. Faghri. Performance characteristics of a thermal energy storage module: a transient pcm/forced convection conjugate analysis. *International Journal of Heat and Mass Transfer*, 34:93–101, 1991.
[13] M. Lacroix. Study of the heat transfer behavior of a latent heat thermal energy storage unit with a finned tube. *International Journal of Heat and Mass Transfer*, 36:2083–2092, 1993.
[14] Geniy V. Kuznetsov and Mikhail A. Sheremet Applying computer-based simulation to energy auditing: A case study. *International Journal of Thermal Sciences*, 50(10):1878–1886, 2011.
[15] K. A. R. Ismail and M. M. Goncalves. Thermal performance of a pcm storage unit. *Energy Conversion & Management*, 49:115–138, 1999.
[16] T. H. Kuehn and R. J. Goldstein. An experimental study of natural convection heat transfer in concentric and eccentric horizontal cylindrical annuli. *Journal of Heat Transfer, Transactions of the ASME*, 100:635–640, 1978.
[17] S. I. S. de Souza and H. A. Vielmo. Numerical analysis of water melting and solidification in the interior of tubes. *Journal of the Brazilian Society of Mechanical Sciences and Engineering*, XXVII(2):119–131, 2005.

This page intentionally left blank

Bénard convection with rotation and a periodic temperature distribution

S. J. D. D'Alessio & K. A. Ogden
Department of Applied Mathematics, University of Waterloo, Canada

Abstract

This study investigates the effects of a sinusoidally varying temperature distribution and rotation on free convection between two rigid plates. The domain is assumed to be much larger in the horizontal direction than in the vertical direction, which naturally introduces a small parameter. An approximate analytical solution for the steady-state flow is derived by expanding the flow variables in the small parameter. The steady-state solution was also determined numerically using the commercial CFD software package CFX. A comparison of the results shows that the form of the steady-state flow pattern is indeed captured by the approximate analytical solution. Unsteady numerical calculations are also carried out for various sets of parameters to determine when the flow destabilizes, how the modulated temperature boundary condition and rotation affect the critical Rayleigh number, and also to illustrate the flow pattern that develops when the flow becomes unstable.
Keywords: Bénard convection, rotation, sinusoidally varying boundary condition, shallow flow, analytical, numerical.

1 Introduction

The problem of free convection within a long, rotating rectangular domain driven by a sinusoidally varying bottom temperature is studied. This problem is an extension of traditional Bénard convection to account for both rotation and a periodic temperature distribution along the bottom plate. Numerous studies have been devoted to Bénard convection. One previous related study is the work by Pascal and D'Alessio [1], which addresses the stability of the flow with rotation and a quadratic equation of state. Schmitz and Zimmerman [2] studied the effects of a spatially varying temperature condition together with wavy boundaries, but

WIT Transactions on Engineering Sciences, Vol 74, © 2012 WIT Press
www.witpress.com, ISSN 1743-3533 (on-line)
doi:10.2495/AFM120401

without rotation. They also simplified their governing equations by assuming a very large Prandtl number. The current work, on the other hand, takes advantage of the thinness of the fluid layer to simplify the governing equations. Other related work includes that of Malashetty and Swamy [3], who consider the effects of rotation and a temperature boundary condition which varies with time, and that of Basak *et al.* [4], who study the flow resulting from a spatially varying temperature boundary condition in a square cavity without rotation.

One goal of this research is to compare the steady and unsteady flows to that of traditional Bénard convection (henceforth referred to as the basic case) so as to assess the combined impact of rotation and a periodic temperature condition on the stability of the flow. Another objective is to contrast the approximate analytical steady-state solution with a fully numerical solution obtained from a commercial CFD software package.

2 Governing equations

The two-dimensional flow is confined to a thin rectangular domain shown in figure 1. The domain is allowed to rotate about the z-axis and the flow is assumed to be uniform in the x-direction.

The governing equations are given by

$$\vec{\nabla} \cdot \vec{v} = 0 \,, \tag{1}$$

$$\frac{\partial \vec{v}}{\partial t} + \left(\vec{v} \cdot \vec{\nabla}\right) \vec{v} + f\hat{k} \times \vec{v} = \frac{-1}{\rho_0}\vec{\nabla} p - \frac{\rho}{\rho_0} g\hat{k} + \nu \nabla^2 \vec{v} \,, \tag{2}$$

$$\frac{\partial T}{\partial t} + \left(\vec{v} \cdot \vec{\nabla}\right) T = \kappa \nabla^2 T \,, \tag{3}$$

where $\vec{v} = (u, v, w)$ is the velocity, T is the temperature, $\vec{\Omega} = (f/2)\hat{k}$ is the rate of rotation, $\vec{g} = -g\hat{k}$ is the acceleration due to gravity, and the density, ρ, is taken

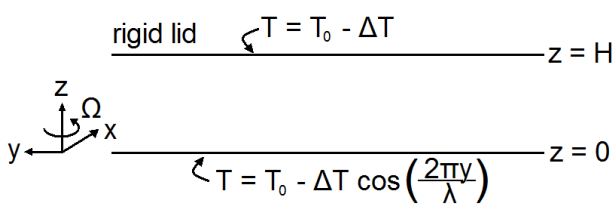

Figure 1: The coordinate system and flow configuration.

to vary with temperature according to

$$\rho = \rho_0 \left(1 - \alpha \left[T - T_0\right]\right) \ , \tag{4}$$

with α denoting the thermal expansion coefficient and ρ_0, T_0 representing reference values for density and temperature. The remaining fluid properties ν, κ refer to the kinematic viscosity and thermal diffusivity, respectively.

Since the flow is assumed to be uniform in the x-direction, the continuity equation permits a stream function, ψ, to be defined such that

$$v = \frac{\partial \psi}{\partial z} \ \text{ and } \ w = -\frac{\partial \psi}{\partial y} \ . \tag{5}$$

The system of equations (1)-(5) can be expressed in terms of the stream function and the x-component of vorticity, ζ, as follows

$$\zeta = -\left(\frac{\partial^2 \psi}{\partial y^2} + \frac{\partial^2 \psi}{\partial z^2}\right) \ , \tag{6}$$

$$\frac{\partial \zeta}{\partial t} + \frac{\partial}{\partial y}\left(-\frac{\partial \psi}{\partial z}\frac{\partial^2 \psi}{\partial y^2} + \frac{\partial \psi}{\partial y}\frac{\partial^2 \psi}{\partial y \partial z}\right) - \frac{\partial}{\partial z}\left(\frac{\partial \psi}{\partial z}\frac{\partial^2 \psi}{\partial y \partial z} - \frac{\partial \psi}{\partial y}\frac{\partial^2 \psi}{\partial z^2}\right) - f\frac{\partial u}{\partial z} = \alpha g \frac{\partial T}{\partial y} + \nu\left(\frac{\partial^2 \zeta}{\partial y^2} + \frac{\partial^2 \zeta}{\partial z^2}\right) \ , \tag{7}$$

$$\frac{\partial u}{\partial t} + \frac{\partial \psi}{\partial z}\frac{\partial u}{\partial y} - \frac{\partial \psi}{\partial y}\frac{\partial u}{\partial z} - f\frac{\partial \psi}{\partial z} = \nu\left(\frac{\partial^2 u}{\partial y^2} + \frac{\partial^2 u}{\partial z^2}\right) \ , \tag{8}$$

$$\frac{\partial T}{\partial t} + \frac{\partial \psi}{\partial z}\frac{\partial T}{\partial y} - \frac{\partial \psi}{\partial y}\frac{\partial T}{\partial z} = \kappa\left(\frac{\partial^2 T}{\partial y^2} + \frac{\partial^2 T}{\partial z^2}\right) \ . \tag{9}$$

These equations are to be solved in the rectangular region spanning one wavelength in the y-direction subject to the no-slip and prescribed temperature conditions given by

$$u = v = w = 0 \ \text{ at } \ z = 0, H \ \text{ and } \ y = 0, \lambda \ , \tag{10}$$

$$T = T_0 - \Delta T \cos\left(2\pi \frac{y}{\lambda}\right) \text{ at } z = 0 \ , \ \ T = T_0 - \Delta T \text{ at } z = H \ , \ y = 0, \lambda. \tag{11}$$

The corresponding boundary conditions for ψ become

$$\psi = \frac{\partial \psi}{\partial z} = 0 \ \text{ at } z = 0, H \ \text{ and } \psi = \frac{\partial \psi}{\partial y} = 0 \ \text{ at } \ y = 0, \lambda \ . \tag{12}$$

It is noted that the vorticity lacks conditions. This can be resolved by utilizing the over-specified conditions for ψ and applying Green's Second Identity

$$\int_V \left(\phi \nabla^2 \chi - \chi \nabla^2 \phi\right) dV = \int_S \left(\phi \frac{\partial \chi}{\partial n} - \chi \frac{\partial \phi}{\partial n}\right) dS \ , \tag{13}$$

where ϕ and χ denote arbitrary differentiable functions, $\frac{\partial}{\partial n}$ is the normal derivative, and S is the surface enclosing the volume V. Choosing ϕ to satisfy

$\nabla^2\phi = 0$ and letting $\chi \equiv \psi$, then $\nabla^2\chi = \nabla^2\psi = -\zeta$. Also, applying the boundary conditions $\frac{\partial\psi}{\partial n} = \psi = 0$ on S, the above leads to integral constraints for the vorticity given by

$$\int_0^H \int_0^\lambda \phi_n \zeta dy dz = 0 \,, \tag{14}$$

where

$$\phi_n(y,z) = e^{\pm 2n\pi z} \left\{ \begin{array}{c} \sin(2n\pi y) \\ \cos(2n\pi y) \end{array} \right\} \text{ for } n = 1, 2, 3, \cdots \,. \tag{15}$$

2.1 Non-dimensionalization

The governing equations and associated conditions are non-dimensionalized using the following scaling

$$t \to \frac{H^2}{\kappa} t \,,\; y \to \lambda y \,,\; z \to Hz \,,\; \psi \to \kappa\psi \,,\; \zeta \to \frac{\kappa}{H^2}\zeta \,,$$
$$T \to (T_0 - \Delta T) + \Delta T T \,,\; u \to \frac{\kappa}{H} u \,. \tag{16}$$

This introduces the non-dimensional parameters

$$Ra = \frac{\alpha g H^3 \Delta T}{\nu\kappa} \,,\; Ro = \frac{\kappa}{Hf\lambda} \,,\; Pr = \frac{\nu}{\kappa} \,,\; \delta = \frac{H}{\lambda} \,. \tag{17}$$

Cast in dimensionless form, the equations now become

$$\frac{\partial\zeta}{\partial t} - \delta\frac{\partial}{\partial z}\left(\frac{\partial\psi}{\partial z}\frac{\partial^2\psi}{\partial y\partial z} - \frac{\partial\psi}{\partial y}\frac{\partial^2\psi}{\partial z^2}\right) + \delta^3\frac{\partial}{\partial y}\left(-\frac{\partial\psi}{\partial z}\frac{\partial^2\psi}{\partial y^2} + \frac{\partial\psi}{\partial y}\frac{\partial^2\psi}{\partial y\partial z}\right)$$
$$- \frac{\delta}{Ro}\frac{\partial u}{\partial z} = \delta PrRa\frac{\partial T}{\partial y} + Pr\left(\delta^2\frac{\partial^2\zeta}{\partial y^2} + \frac{\partial^2\zeta}{\partial z^2}\right) \,, \tag{18}$$

$$\zeta = -\left(\delta^2\frac{\partial^2\psi}{\partial y^2} + \frac{\partial^2\psi}{\partial z^2}\right) \,, \tag{19}$$

$$\frac{\partial u}{\partial t} + \delta\left(\frac{\partial\psi}{\partial z}\frac{\partial u}{\partial y} - \frac{\partial\psi}{\partial y}\frac{\partial u}{\partial z}\right) - \frac{\delta}{Ro}\frac{\partial\psi}{\partial z} = Pr\left(\delta^2\frac{\partial^2 u}{\partial y^2} + \frac{\partial^2 u}{\partial z^2}\right) \,, \tag{20}$$

$$\frac{\partial T}{\partial t} + \delta\left(\frac{\partial\psi}{\partial z}\frac{\partial T}{\partial y} - \frac{\partial\psi}{\partial y}\frac{\partial T}{\partial z}\right) = \delta^2\frac{\partial^2 T}{\partial y^2} + \frac{\partial^2 T}{\partial z^2} \,, \tag{21}$$

while the boundary conditions are

$$u = \psi = \frac{\partial\psi}{\partial z} = 0 \text{ at } z = 0, 1 \text{ and } u = \psi = \frac{\partial\psi}{\partial y} = 0 \text{ at } y = 0, 1 \,, \tag{22}$$

$$T = 1 - \cos(2\pi y) \text{ at } z = 0 \text{ and } T = 0 \text{ at } z = 1, y = 0, 1 \,, \tag{23}$$

and the integral constraints become

$$\int_0^1 \int_0^1 \phi_n \zeta dy dz = 0 \ , \tag{24}$$

where

$$\phi_n(y,z) = e^{\pm 2n\pi\delta z} \left\{ \begin{array}{c} \sin(2n\pi y) \\ \cos(2n\pi y) \end{array} \right\} \ \text{for} \ \ n = 1, 2, 3, \cdots \ . \tag{25}$$

3 Steady and unsteady solutions

The steady-state solution corresponding to the problem considered in this investigation is more complicated than that pertaining to the basic case due to the presence of a horizontal temperature gradient. Two methods are used to determine the steady-state solution. The first is an approximate analytical solution found by expanding the flow variables in a series in the small parameter δ, while the second is a numerical solution obtained using a commercial CFD software package.

3.1 Approximate analytical solution

For small δ, an approximate analytical solution can be constructed by expanding the flow variables in the following series

$$\begin{aligned} \psi &= \psi_0 + \delta\psi_1 + \cdots \ , \\ \zeta &= \zeta_0 + \delta\zeta_1 + \cdots \ , \\ u &= u_0 + \delta u_1 + \cdots \ , \\ T &= T_0 + \delta T_1 + \cdots \ . \end{aligned} \tag{26}$$

With the understanding that the Rossby (Ro) and Prandtl (Pr) numbers are $O(1)$, and the Rayleigh (Ra) number is $O(1/\delta)$, the leading-order unsteady problem becomes

$$\frac{\partial T_0}{\partial t} = \frac{\partial^2 T_0}{\partial z^2} \ , \tag{27}$$

$$\frac{\partial \zeta_0}{\partial t} = Pr\frac{\partial^2 \zeta_0}{\partial z^2} + Pr\delta Ra\frac{\partial T_0}{\partial y} \ , \tag{28}$$

$$\frac{\partial^2 \psi_0}{\partial z^2} = -\zeta_0 \ , \tag{29}$$

$$\frac{\partial u_0}{\partial t} = Pr\frac{\partial^2 u_0}{\partial z^2} \ , \tag{30}$$

subject to

$$u_0 = \psi_0 = \frac{\partial \psi_0}{\partial z} = 0 \ \ \text{at} \ \ z = 0, 1 \ , \tag{31}$$

$$T_0 = 1 - \cos(2\pi y) \text{ at } z = 0 \text{ and } T_0 = 0 \text{ at } z = 1 , \tag{32}$$

the integral constraint

$$\int_0^1 \zeta_0 dz = 0 , \tag{33}$$

and the initial conditions

$$\zeta_0 = \psi_0 = u_0 = 0 . \tag{34}$$

Taking the initial temperature to be the steady-state solution given by

$$T_0 = (1 - z)(1 - \cos(2\pi y)) , \tag{35}$$

it follows that the temperature remains constant for all time. It is also easily deduced that $u_0 = 0$. Thus, rotation does not affect the solution at leading order.

A straight-forward calculation yields the solution

$$\begin{aligned}\zeta_0(y, z, t) = &- \pi\delta Ra \left(z^2 - \frac{z^3}{3} - \frac{7z}{10} + \frac{1}{10}\right) \sin(2\pi y) \\ &+ \sum_{n=1}^{\infty} a_n e^{-n^2\pi^2 Prt} \cos(n\pi z) ,\end{aligned} \tag{36}$$

$$\begin{aligned}\psi_0(y, z, t) = &\pi\delta Ra \left(\frac{z^4}{12} - \frac{z^5}{60} - \frac{7z^3}{60} + \frac{z^2}{20}\right) \sin(2\pi y) \\ &- \sum_{n=1}^{\infty} \frac{a_n}{n^2\pi^2} e^{-n^2\pi^2 Prt} (1 - \cos(n\pi z)) ,\end{aligned} \tag{37}$$

where

$$a_n = 2\pi\delta Ra \sin(2\pi y) \int_0^1 \left(z^2 - \frac{z^3}{3} - \frac{7z}{10} + \frac{1}{10}\right) \cos(n\pi z) dz , \tag{38}$$

for $n = 1, 2, 3, \cdots$. It is worth noting that it is impossible for ψ_0 to satisfy all the boundary conditions; although the condition $\psi_0 = 0$ at $z = 1$ is not exactly satisfied, all the other ones are.

As $t \to \infty$, the following leading-order steady-state solution emerges

$$\zeta_s = -\pi\delta Ra \left(z^2 - \frac{z^3}{3} - \frac{7z}{10} + \frac{1}{10}\right) \sin(2\pi y) , \tag{39}$$

$$\psi_s = \pi\delta Ra \left(\frac{z^4}{12} - \frac{z^5}{60} - \frac{7z^3}{60} + \frac{z^2}{20}\right) \sin(2\pi y) . \tag{40}$$

The steady-state solution reveals a non-zero background flow, which results from the horizontal temperature gradient; recall that for the basic case the background flow is stationary. Dimensionalized plots showing the leading-order

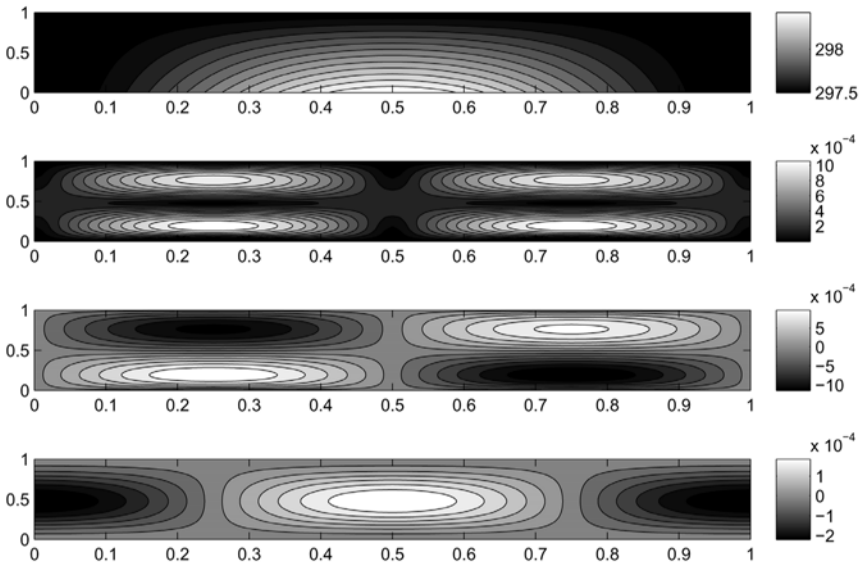

Figure 2: Leading-order solution for: T_0 (top) in K, speed ($|\vec{v}_0|$) (second from top), v_0 (second from bottom), and w_0 (bottom), in m/s.

steady-state solution are shown in figure 2, and indicate that two circulation cells develop. The simulations correspond to air at 298 K in a domain having a length of 20 cm and a height of 2 cm. The temperature difference is $\Delta T = 0.5$ K. The values of the non-dimensional parameters are $Ra = 388.7$, $Pr = 0.7046$, and $Ro = 0.0548$.

3.2 Steady-state numerical simulations

The steady-state solution is calculated numerically using the CFD software package CFX which solves the full Navier-Stokes and energy equations for arbitrary values of the non-dimensional parameters. In these simulations periodicity conditions are applied at the left and right boundaries of the domain. Results for two steady-state simulations will be discussed. The first corresponds to the basic case, while the second illustrates the effects of a sinusoidally varying bottom temperature and rotation. The parameter values are the same as those used in figure 2 for the analytical solution (i.e. $Ra = 388.7$, $Pr = 0.7046$ and $Ro = 0.0548$). Plotted in figure 3 are the temperature distributions for the two cases. It should be noted that the range of temperatures is smaller for the basic case because the bottom temperature for this case is taken to be the average value of the second case. Plots of the magnitude of the velocity ($|\vec{v}|$) for each case are shown in figure 4. It should be noted that while the velocity is not exactly zero for the basic case, it is two orders of magnitude smaller than that in the second case. Contour

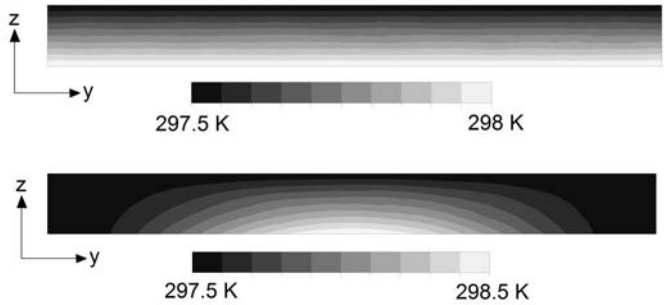

Figure 3: Steady-state temperature distribution for: basic case (top), and sinusoidal bottom temperature with rotation (bottom).

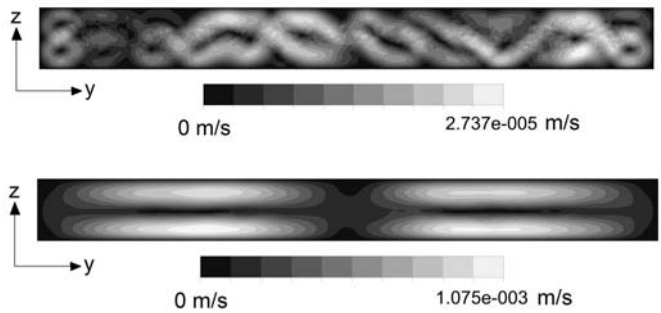

Figure 4: Steady-state plots of $|\vec{v}|$ for: basic case (top), and sinusoidal bottom temperature with rotation (bottom).

plots of the v and w velocity components for the case having a sinusoidally varying bottom temperature and rotation are displayed in figure 5. The v and w velocity components illustrate the circulation resulting from the horizontal temperature gradient. Comparing figure 2 with figures 3–5, it is clear that the leading-order analytical solution is in good agreement with the fully numerical solution, both in the qualitative flow pattern and also in the magnitude of temperature and velocities.

4 Unsteady numerical simulations and flow stability

The flow pattern that develops for unstable cases was also numerically investigated using CFX. As before, the basic case is also presented for comparison purposes. Shown in figure 6 is the basic case for an unstable case having $\Delta T = 4\,\mathrm{K}$, $Ra = 3109$ and $Pr = 0.7046$.

Figure 6 clearly shows that 5 pairs of counter-rotating cells develop. Since the length of the domain is ten times its height, each cell forms a square. Figure 7

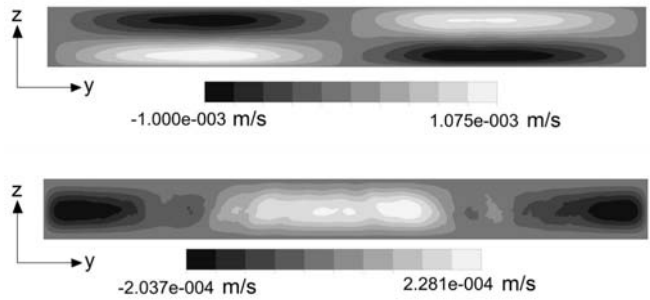

Figure 5: Steady-state velocity contour plots for the case with a sinusoidal bottom temperature and rotation: v velocity component (top), w velocity component (bottom).

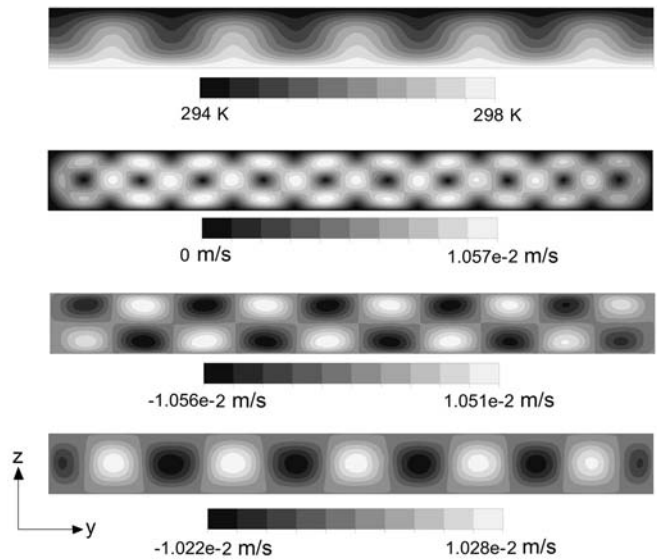

Figure 6: Unsteady case with a constant bottom temperature and no rotation: temperature (top), speed ($|\vec{v}|$) (second from top), v (second from bottom), and w (bottom).

shows the corresponding case with a sinusoidal bottom temperature and rotation ($Ro = 0.0548$). The flow patterns are noticeably different from those shown in figures 3–5. Here, the flow destabilizes and breaks up into a greater number of cells; the number of cells was found to depend on ΔT. Velocity plots are presented in figure 8 for both cases and for various temperature differences, and hence

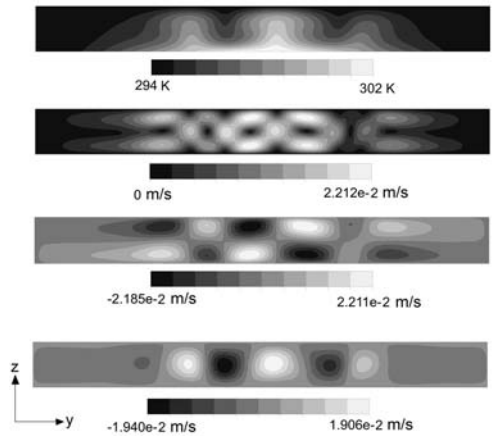

Figure 7: Unsteady case with a sinusoidally varying bottom temperature and rotation: temperature (top), speed ($|\vec{v}|$) (second from top), v (second from bottom), and w (bottom).

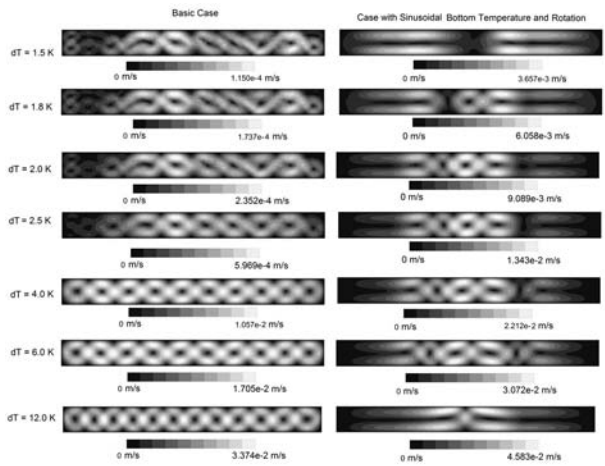

Figure 8: Speed ($|\vec{v}|$) plots for the basic case and for bottom temperature variation with rotation, for increasing Rayleigh numbers ($Pr = 0.7046$ and $Ro = 0.0548$ for the case with rotation).

Rayleigh numbers. The results suggest that for the case with bottom temperature variation, the flow becomes unstable for ΔT between 1.5 K and 1.8 K, while for the basic case this occurs for ΔT between 2.5 K and 4.0 K. Since Pascal and D'Alessio [1] showed that rotation stabilizes Bénard convection, this indicates that the impact of bottom temperature variation significantly influences the stability

of the flow. An interesting feature occurs when $\Delta T = 12$ K for the case with variable bottom temperature. The apparent trend is that increasing ΔT increases the number of cells that develop in an unstable flow; however, once the temperature difference is sufficiently large, the flow pattern resembles that of a stable flow with two cells, despite the fact that the circulation is intensified.

5 Summary

The combined effect of a sinusoidal bottom temperature and rotation on the background flow and on the stability of free convective flow was investigated. Contrary to Bénard convection, a non-zero background flow ensues. This background flow was determined analytically by taking advantage of the relative thinness of the fluid layer, and performing an expansion in terms of the thinness parameter. The background flow was also determined numerically using a commercial CFD software package. The leading-order analytical solution was found to be in good agreement with the numerical solution for stable cases. The impact on the stability of the flow was then investigated through numerical simulations. Although rotation has previously been found to stabilize the flow, variations in the bottom temperature was found to dominate and destabilize the flow when compared to Bénard convection. Lastly, interesting features emerging from unstable numerical simulations were also presented and discussed.

References

[1] Pascal, J.P. & D'Alessio, S.J.D., The effects of density extremum and rotation on the onset of thermal instability, *International Journal of Numerical Methods for Heat & Fluid Flow* **13**, pp. 266–285, 2003.
[2] Schmitz, R & Zimmerman, W., Spatially periodic modulated Rayleigh-Bénard convection, *Physical Review E* **53**, pp. 5993–6011, 1996.
[3] Malashetty, M.S., & Swamy, M., Effect of thermal modulation on the onset of convection in a rotating fluid layer, *International Journal of Heat and Mass Transfer* **51**, pp. 2814–2823, 2008.
[4] Basak, T., Roy, S. & Balakrishnan, A.R., Effects of thermal boundary conditions on natural convection flows within a square cavity, *International Journal of Heat and Mass Transfer* **49**, pp. 4525–4535, 2006.

This page intentionally left blank

Research on the heat transfer law of gas-liquid two-phase flow in a deepwater wellbore

B. J. Sun, Y. H. Gao, Y. Q. Ma, Z. Y. Wang & H. Li
College of Petroleum Engineering, China University of Petroleum (Huadong), China

Abstract

According to the features of low temperature and Type III boundary conditions during deepwater oil and gas exploitation, an experimental system was designed and built to simulate the heat transfer of deepwater oil and gas. A large number of laboratory experiments were carried out and the relational expressions of the heat transfer as well as the influence of the gas-liquid discharge on the heat transfer of each gas-liquid two-phase flow patterns under the deepwater and low-temperature Type III boundary conditions were obtained. The results show that the expression in the laminar flow obtained in this paper is largely different from the relational expression of the heat transfer at ordinary temperatures under the simple boundary conditions. The two expressions are in substantial agreement in the turbulent flow. The liquid discharge is the principal factor which influences the heat transfer in the bubbly flow, slug flow and annular flow while the gas-liquid two-phase flow has little influence on the heat transfer in the churn flow.
Keywords: deepwater, gas-liquid two-phase flow, transfer, experiment.

1 Introduction

In process of the deepwater oil development, the low-temperature characteristic (2-6ºC) of the seawater can bring about low temperature in a portion of the wellbore. In addition, if it is gas-liquid two-phase flow in the wellbore, the temperature field will be more complex. According to the published documents, the temperature range of current experimental research of the non-boiling cooling heat transfer of the gas-liquid two-phase flow is generally at ordinary temperatures (above 20ºC) (e.g. Taitel and Barnea [1]) or low temperature (80K-85K with the medium of liquid nitrogen) [2, 3]. There is no experimental

WIT Transactions on Engineering Sciences, Vol 74, © 2012 WIT Press
www.witpress.com, ISSN 1743-3533 (on-line)
doi:10.2495/AFM120411

research result reported for the circumstances of deepwater and low temperature (0-6ºC). However, the characteristic of liquid within this temperature range is largely different from that of the normal temperature. It has some unique parameter. In this paper, the heat transfer laws of the fluid in the pipe in cold circumstance and the heat transfer laws of the gas-liquid two-phase flow in the pipe are studied. It lays the foundation for the design of the technological parameters of the offshore deepwater oil and gas exploitation.

2 Experimental system

2.1 Experiment equipment and process

Fig. 1 shows the sketch of equipment and operation flow diagram of the imitating system that simulates the cooling heat transfer of the gas-liquid two-phase flow in the deepwater wellbore. The main wellbore consists of two parts, the inner tube for the hot fluid and the annulus for the cold fluid. The sizes are as follows: length × outer diameter of inner tube × outer diameter of outer tube × outer diameter of insulating sheath = 12000 × 60 × 100 × 200mm; outer diameter of annulus: Φ108 × 5mm, inner diameter of annulus: Φ60 × 5mm. The working temperature is between 5-65℃. Wherein, the inner tube refers to the pipe such as a riser or a drill rod contacting with the seawater. The fluid in the annulus between the inner tube and the outer tube imitates the deepwater circumstance. In the experiment, the hot liquid (20-65ºC) is injected from the bottom of the inner tube. The hot liquid can be gas-liquid two-phase flow that has been fully mixed before entering the heat transfer section. The cold liquid is injected

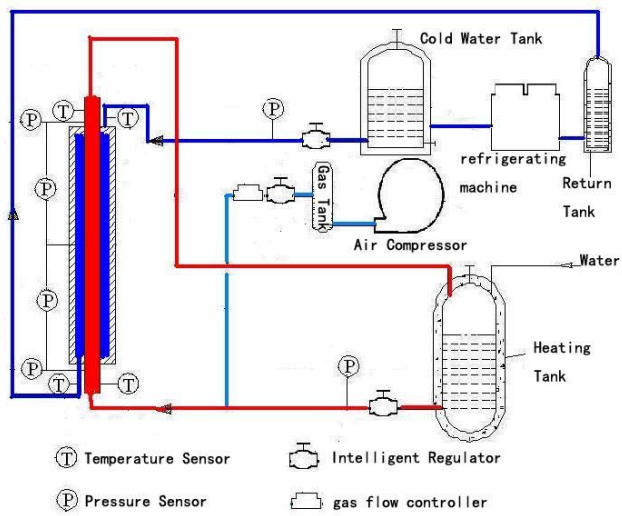

Figure 1: Experiment equipment.

from the top of the annulus with adjustable flow. Thus a simulating process of the cryogenic cooling heat transfer of the wellbore flow in the deepwater circumstance forms.

The return tank is equipped with an insulating sheath and an electrically heated temperature control system to heat the water in the return tank and carry out the thermostatic control. The temperature is controllable between the ordinary temperatures to 60ºC with control precision of ±0.5%. The maximum flow is 12m^3/h with control precision of 1%.

The cold water is provided by the chiller. The cold water at different temperatures is obtained by adjusting the thermostat of the chiller. The compressor shuts down when the temperature reaches the set value. The temperature is controllable between 2ºC to 6ºC with precision of ±0.5ºC. The maximum flow is 10m^3/h with control precision of 1%.

The injected air is generated by the compressor, buffered in the gas tank and dried in the condenser. The injected gas discharge is adjusted automatically in the gas discharge control system to keep constant. Injected gas discharge: controllable input between 1-8Nm^3/min with flow measurement accuracy of 1%

To reduce energy loss, the return tank, the refrigerating tank, and the experiment pipes are all packed in heat shield and thus the complete experiment measurement system can be regarded as an isolated process, which accords with the energy conservation law. In addition, the data in this experiment is collected when the flow and heat transfer become stable.

2.2 Experimental data acquisition and processing

2.2.1 Data acquisition of differential pressure

As it is multiphase flow in the inner tube and it is sealed within the annular space in the system, the flow pattern is hard to identify through the fluctuation of void fraction. So the method of differential pressure fluctuation is adopted for the identification of this flow pattern. The PCI2013 data acquisition card driver is adopted in the data acquisition system. The set ratings of the basic parameters are as follows: The acquisition frequency is 5 kHz and the resolving power is 12bit; 2 analog input channels are provided.

The principles of the hardware structure of the data acquisition system are shown in Fig. 2. The differential pressure parameters are converted into standard current signals of 4~20mA by the sensor. Then the multi-channel signal converter converts the different kinds of current signals that the sensors output into voltage signals. Then the voltage signals are sent to the 16 A/D converters. The A/D Converter converts the input analog voltage into binary digital signals, which are sent to the computer through the data bus of the computer. The data acquisition and processing software of the differential pressure fluctuation is built with Lab VIEW. The data is output to the file and the analytical processing of it is carried out by the software.

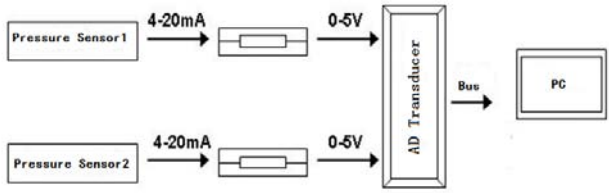

Figure 2: Schematic diagram of the differential pressure acquisition system.

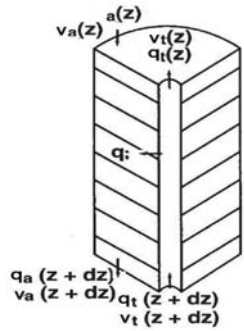

Figure 3: Heat transfer model of experimental equipment.

2.2.2 Experimental data processing

The heat transfer model is built based on the experimental pipes, as shown in Fig. 3. Then the energy equation of vertical annulus (e.g. Gao *et al.* [5]). is obtained:

$$H_a(z+dz) - H_a(z) + \frac{1}{2} w_a {v_a}^2(z+dz) - \frac{1}{2} w_a {v_a}^2(z) + q_i = 0 \tag{1}$$

Derived equation:

$$\frac{dH_a}{dz} + w_a \cdot \frac{v_a dv_a}{dz} + \frac{dq_i}{dz} = 0 \tag{2}$$

$H_a(z+dz)$ is the enthalpy of the fluid that enters the element in unit time, J/s;

$H_a(z)$ is the enthalpy of the fluid that outflows the element in unit time, J/s;

q_i is the energy that is transferred from the inside of the tube to the element of the annulus in unit time, J/s;

v_a is the speed of the fluid, m/s; w_a is the mass flow of the fluid in the annulus, kg/s;

The energy that is transferred from the inner tube to the element of the annulus in unit time:

$$q_{ta} = \frac{w_a C_a}{B}(T_t - T_a)dz \tag{3}$$

T_a and T_t are the temperatures in the annulus and the tube, ℃; C_a is the specific heat of the fluid, J/kg℃;

The intermediate parameter

$$B = \frac{w_a c_a}{2\pi r_{ti} U_t}$$

U_t is the heat transfer coefficient of the annulus fluid and the drill rod, W/(m^2°C) (e.g. Jakob [6]):

$$U_t = \left[\frac{1}{h_t} + \frac{r_{ti} \ln(r_{t0}/r_{ti})}{k_t} + \frac{r_{ti}}{r_{to}} \frac{1}{h_a} \right]^{-1} \tag{4}$$

k_t is the coefficient of heat conductivity of the tube, W/(m^2°C); r_{ti} and r_{to} are the inner radius and the outer radius of the tube, m;
h_t and h_a are the convective heat transfer coefficients of the fluid in the tube and the annulus, W/(m^2°C).

Additionally, because the flow is stable and the compressibility of the fluid can be ignored, the following equation can be obtained:

$$\frac{dT_a}{dz} = \frac{1}{B}(T_a - T_t) \tag{5}$$

The differential equation of the energy of the inner tube can be obtained in the same way:

$$\frac{dT_t}{dz} = \frac{w_a}{w_t B}(T_a - T_t) \tag{6}$$

w_t is the mass flow of the fluid, kg/s;

The following equation can be obtained by solving the differential equation of the energy of the annulus and the inner tube simultaneously:

$$\frac{d^2 T_a}{dz^2} + \frac{1}{B}\left(\frac{w_a}{w_t} - 1 \right) \frac{dT_a}{dz} = 0 \tag{7}$$

Boundary conditions: while z=0, $T_t=T_{t1}$ and $T_a=T_{a1}$; while z=L, $T_t=T_{t2}$; the experimental result value of the overall heat transfer coefficient is obtained:

$$U_t = w_a c_{pa} \ln\left(\frac{T_{t2} - T_{a1} + (T_{t1} - T_{a1})/(1-W)}{W(T_{t1} - T_{a1})/(1-W)} \right) \Big/ \left[(1-W) 2\pi r_{ti} L \right] \tag{8}$$

wherein $W = w_a / w_t = v_a A_a / (v_t A_t)$, then the expression of the experimental value of heat transfer coefficient in the tube:

$$\frac{1}{h_t} = \frac{(1 - u_a A_a/(u_t A_t)) 2\pi r_{ti} L}{\rho_l A_a u_a c_{pa} \ln\left\{ \dfrac{T_{t2} - T_{a1} + (T_{t1} - T_{a1})/[1 - u_a A_a/(u_t A_t)]}{u_a A_a/(u_t A_t) \cdot (T_{t1} - T_{a1})/[1 - u_a A_a/(u_t A_t)]} \right\}} - \frac{r_{ti}}{k_t} \ln\left(\frac{r_{t0}}{r_{ti}} \right) - \frac{r_{ti}}{r_{to}} \frac{1}{h_a} \tag{9}$$

wherein v_t is the speed of the fluid in the inner tube, m/s; A_a and A_t are the areas of the annulus and the inner tube, m^2.

3 Cryogenic cooling heat transfer laws in the wellbore

Although the heat transfer calculation methods of the flow patterns are different, the expression for the calculation of the single-phase flow or its revised type is used for all the flow patterns. Thus the heat transfer of the single phase is the basis for the heat transfer calculation of each two-phase flow pattern. Currently, as for the research on the fluid heat transfer at low temperatures (0-6℃) in deepwater, there is still no document reported. Additionally, the seawater belongs to Type III boundary condition that is more complicated than the fluid in the wellbore and it is unrealistic to deduce the heat transfer expression purely in theory. So in this paper, the heat transfer laws of the fluid in the wellbore that simulates the cryogenic deepwater circumstance are studied by experiment.

As the three processes of the convection heat transfer between the fluid in the annulus and the outer layer of the inner tube, the heat conduction of the tube wall and the convection heat transfer between fluid in the tube and the inner tube wall are included in the heat transfer and the three processes are interrelated, it cannot be directly solved. In this paper, the trial and error procedure are adopted to obtain the convection heat-transfer coefficient. Then the parameters in the equation are determined according to the criterion equation $Nu = C\,\mathrm{Re}^{n}\,\mathrm{Pr}^{m}$. Wherein, *C*, *n* and *m* are the undetermined coefficient and index in line with their definitions. Set CPr^{m} equal to A and take the logarithm of both sides of the equation above. Then equation (10) is obtained:

$$\lg Nu = \lg A + n \lg \mathrm{Re} \tag{10}$$

Because the *Nu* and *Re* in different flow patterns measured in the experiment are in a straight line on the coordinate axes of *lgRe* and *lgNu*, thus A and n can be determined.

The experiment is carried out under the condition of cooling heat transfer. According to the conventional criterion relational expression of heat transfer, 1/3 is selected for the exponent of *Pr* in the laminar flow and the transition flow and 0.3 is selected in the turbulent flow because *Pr* is the function of the natural characteristic of the fluid and it is independent of the flow speed. Based on the experimental data, we obtain the relationship between *Re* and *Nu*, as shown in Fig. 4. On the whole *lgNu* and *lgRe* are linear. Especially they are entirely consistent with the criterion equation in the laminar flow and the turbulent flow. But the laws in the transition flow are very complicated. So many researchers suggest that the transition flow should be evaded for the research of heat transfer. In view of the actual engineering requirements, the above-mentioned criterion definition is still adopted because the scope of the transition flow is narrow and too complicated expression will be too difficult for the calculation. The relational expression of *Nu* in the tube is obtained through regression:

$$\begin{aligned} Nu &= 0.001873\,\mathrm{Re}^{1.02}\,\mathrm{Pr}^{1/3} && \mathrm{Re}<2000 \\ Nu &= 0.10219\,\mathrm{Re}^{0.6384}\,\mathrm{Pr}^{1/3} && 2000<\mathrm{Re}<10000 \\ Nu &= 0.02694\,\mathrm{Re}^{0.7922}\,\mathrm{Pr}^{0.3} && \mathrm{Re}>10000 \end{aligned} \tag{11}$$

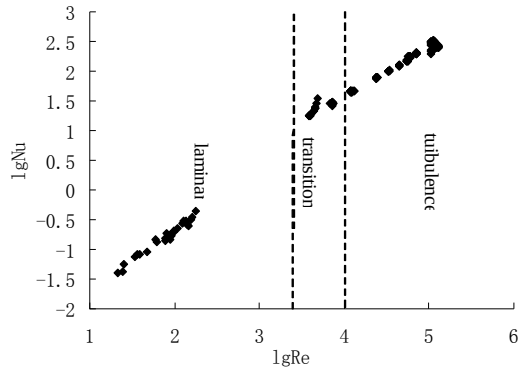

Figure 4: Relationship of Nu and Re in tuibulence flow.

According to the relational expression of the heat transfer in each flow pattern, the exponent of the Reynolds number decreases and the strength of the heat transfer increases from the laminar flow to the turbulent flow. That is because the temperature distribution of the turbulent flow core is flat except the adherent lower layer of the laminar flow, according to the heat transfer boundary layer theory. The main thermal resistance is in the lower layer of the laminar flow, which is extremely thin. So the temperature gradient is extremely great (e.g. Yang and Wenquan [7]). From the perspective of energy, the flow speed in the laminar flow is relatively low and thus the interaction among the particles of the fluid is very small. The flow becomes very disordered with vortex and fluctuation when it reaches the turbulent flow. Then the interaction among the particles of the fluid becomes strong. The internal energy increases because of the converted internal energy from partial kinetic energy. And then the change of the temperature gradient is more obvious and the heat transfer is more intense.

4 Influence factors of cryogenic cooling heat transfer in each flow pattern

4.1 Bubbly flow

The bubbly flow is the simplest and most basic flow pattern in the gas-liquid two-phase flow. Its characteristic is that the gas phase is distributed in the continuous liquid phase in the form of small discrete bubbles with the feature of stable and uniform flow. Because of limited experimental conditions, the gas discharge Qg has to be limited above 8m3/hr and the liquid discharge also must be within 11m^3/hr. A series of experiments are carried out for the research on the influence of the liquid discharge on the convective heat-transfer coefficient in the tube (h,W/(m2ºC)) and the results are shown in Fig. 5.

The numerical relational expression of the heat transfer coefficient and the liquid discharge is obtained with the gas discharge of 8m^3/hr through regression:

$$h = 91.093Q_l + 740 \tag{12}$$

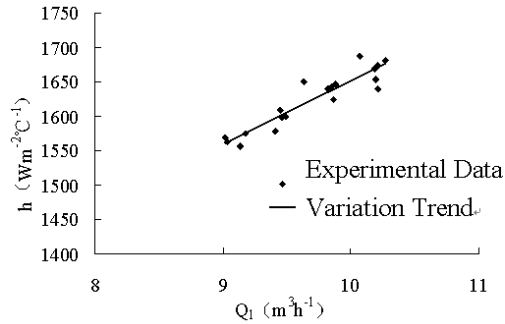

Figure 5: Influence of liquid discharge on heat transfer.

The results of the experiment show that the convective heat-transfer coefficient in the tube rises in a straight line along with the increase of the liquid discharge. That is because the liquid phase is the main part in this kind of pseudo-single-phase flow such as the bubbly flow and the proportion of the liquid in the annulus increases along with the liquid discharge. From the formula of the heat transfer $h = Nu\lambda/d$, we can see that the heat transfer coefficient *h*, *Nu*, and the coefficient of heat conductivity of the fluid λ are related with the tube diameter *d*. However, in the bubbly flow, the liquid discharge is greater than the gas discharge. Then according to the expression of *Nu*, the relevant parameters of the two phases of gas and liquid, and the much larger heat conductivity of the liquid phase than the gas phase, the conclusion is drawn that the heat transfer is mainly influenced by the liquid phase. The Reynolds number *Re* and the heat transfer coefficient increases along with liquid phase discharge.

4.2 Slug flow

As the gas content rises, some big bubbles accumulated by some smaller bubbles appear in the center of the tube at intervals. The big bubble is called Taylor bubble. The differential pressure decreases obviously while a big Taylor bubble passes. The slug flow is also a kind of basic flow pattern. However, because of the obvious feature of subsections of the slug flow, both the void fraction distribution and the differential pressure distribution have large fluctuations. It has characteristic of great flow fluctuation and alternation of gas and liquid. a large amount of experiments are carried out for the research on the influence of the liquid discharge and the gas discharge on the convective heat-transfer coefficient. The experimental results are shown in Fig. 6 and Fig. 7. Through regression the numerical relational expressions of the heat transfer coefficient with the discharge are obtained when the liquid discharges are 14m^3/h, 15m^3/h and 30m^3/h and the gas discharges are 5.44 m^3/h, 6.14 m^3/h and 7.89 m^3/h. Wherein, the heat transfer coefficient is an average value in a long time period when the flow and the heat transfer are stable.

$$h_{l1} = 2352.4Q_{l1} - 5431.6,$$
$$h_{l2} = 2250.9Q_{l2} - 5906.4, \quad (13)$$
$$h_{l3} = 1298.8Q_{l3} - 3886.3$$

$$h_{g1} = 2.0625Q_{g1} + 1780.5$$
$$h_{g2} = 11.961Q_{g2} + 1681.6, \quad (14)$$
$$h_{g3} = 18.552Q_{g3} + 1651.8.$$

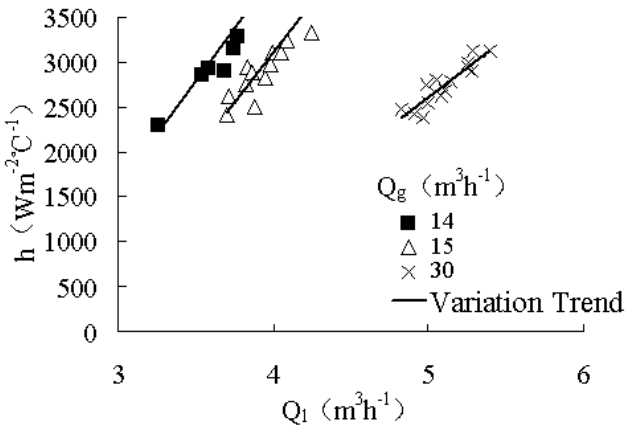

Figure 6: Influence of liquid discharge on heat transfer.

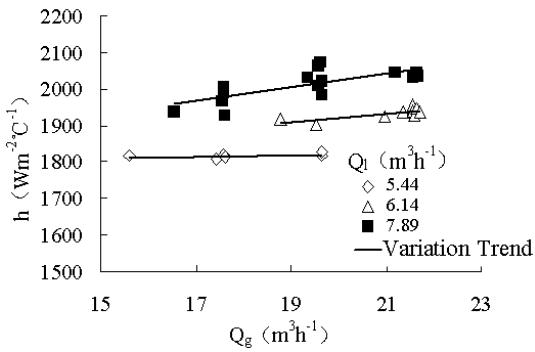

Figure 7: Influence of gas discharge on heat transfer.

From the relational expression, it can be seen that both the heat transfer coefficient-liquid discharge and the heat transfer coefficient-gas discharge are linear. As the liquid discharge rises, the convective heat-transfer coefficient in the tube rises rapidly. However, the change of the convective heat-transfer coefficient is very small as the gas discharge rises. On the other hand, when the gas discharge is larger, the influence of the liquid discharge on the convective heat-transfer coefficient decreases. And when the liquid discharge is larger, the influence of the gas discharge on the convective heat-transfer coefficient increases. In the slug flow, the liquid discharge is still the main influence factor. That is because the heat transfer coefficient, *Nu*, and the heat conductivity of the fluid are related with the tube diameter. In the slug flow, the liquid discharge and the gas discharge are still of the same order of magnitude and the difference is not very large. Then according to the expression of *Nu*, the relevant parameters of the two phases of gas and liquid, and the much larger heat conductivity of the liquid phase than the gas phase, the conclusion is that the heat transfer is mainly influenced by the liquid phase. The *Re* number and the heat transfer coefficient increases along with liquid phase discharge.

4.3 Churn flow

If the void fraction is greater than the scope of the slug flow, the Taylor bubble bursts and the flow changes to churn flow. The appearance of big vortexes and bubbles cause violent jarring to the flow. The shape and size of the gas become irregular. The gas and liquid intrudes each other and they are highly decentralized in the area away from the wall. At this time, a highly disordered state emerges. It has the characteristic of a high degree of disorder and violent jarring. A large amount of experiments are carried out for the research on the influence of the liquid discharge and the gas discharge on the convective heat-transfer coefficient of the churn flow. The experimental results are shown in Fig. 8 and Fig. 9. Through regression the numerical relational expression of the heat transfer coefficient and the liquid discharge and the gas discharge is obtained with the gas discharge of 46m^3/hr and the liquid discharge of 2.5m^3/hr.

$$h = -8.7564Q_l + 2047 \tag{15}$$

$$h = 0.2777Q_g + 2006.6 \tag{16}$$

From the relational expression, it can be seen that the change of the liquid discharge and the gas discharge has little influence on the heat transfer coefficient in the tube. That is because the gas constitutes the most part in the churn flow while what influences the heat transfer most is the liquid area near the wall. The core entrainment rate of the gas increases as the liquid discharge increases (e.g. Azzopardi and Wren [8]). Therefore, even if the change of the liquid discharge is great, its influence on the heat transfer coefficient is still small. In addition, during the research, the speed of the gas is basically over 5m/s. So the entraining liquid discharge in the gas also does not change

(e.g. Azzopardi and Wren [8]) according to the formula of the entrainment rate of the gas. So the liquid area near the wall is stable. Even if the gas discharge increases, the heat transfer coefficient is basically stable.

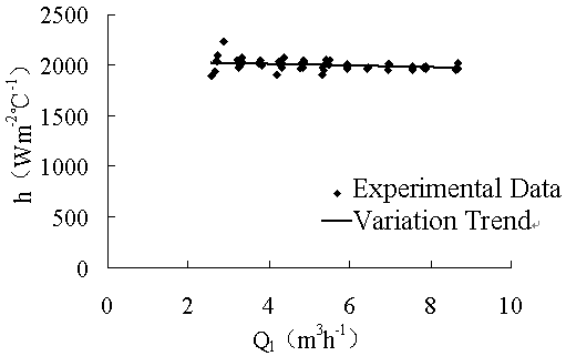

Figure 8: Influence of liquid discharge on heat transfer.

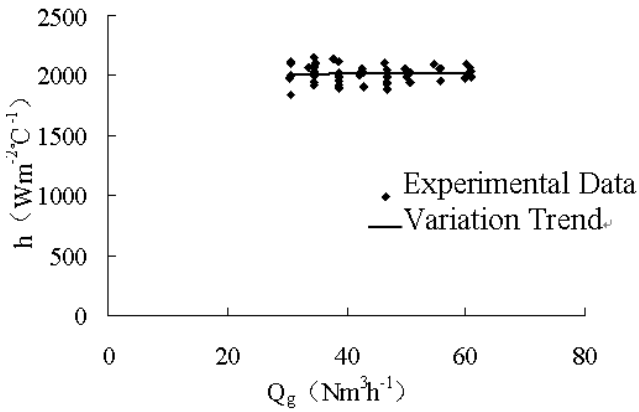

Figure 9: Influence of gas discharge on heat transfer.

4.4 Annular flow

When the void fraction reaches a certain value, the liquid proportion in the cross section reduces further. For the speed of the gas increases further, its entrainment function becomes more and more obvious. Then the liquid film forms in the area near the wall and the mist flow core formed by the entraining liquid in the gas forms in the center of the tube, which is called annular flow. In the annular flow, the mist flow core and the liquid film near the wall are in a relatively stable state because the amount of the liquid that the mist flow core can entrain is balanced. Then both the gas phase and the liquid phase near the wall are continuous phases. The liquid in the mist core is discontinuous phase. It has the characteristic of stable flow. A series of experiments are carried out for the

research on the influence of the liquid discharge and the gas discharge on the convective heat-transfer coefficient in the tube. The experimental results are shown in Fig. 10 and Fig. 11.

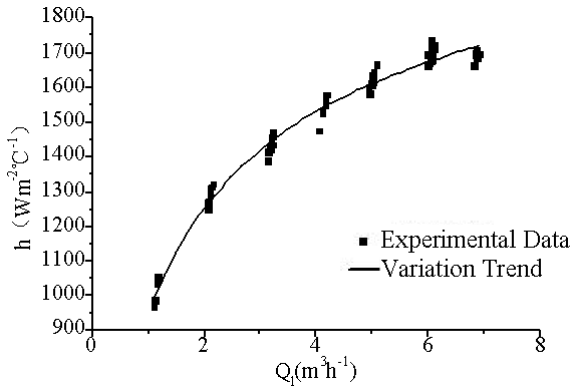

Figure 10: Influence of liquid discharge on heat transfer.

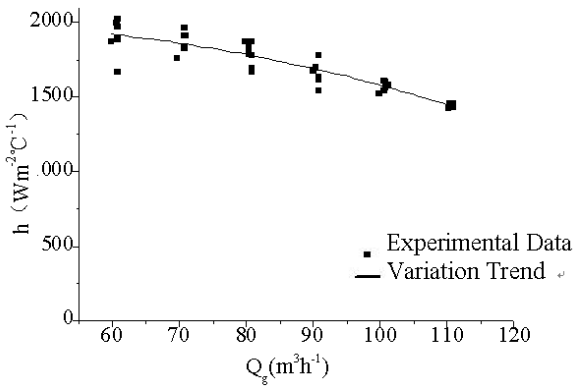

Figure 11: Influence of gas discharge on heat transfer.

The numerical relational expression of the heat transfer coefficient and the discharge is obtained with the gas discharge of 170m^3/hr and the liquid discharge of 0.707m^3/hr through regression:

$$h = 2467.78347 - \frac{3358.81169}{1+\left(\frac{Q_l}{0.7161}\right)^{0.55174}} \tag{17}$$

$$h = 2044.77436 - 0.00285Q_g^{2.6064} \tag{18}$$

The convective heat-transfer coefficient increases with non-linearity as the liquid discharge while it decreases with non-linearity as the gas discharge. That is because the density and relevant thermal parameters of the gas and the liquid differ by two orders of magnitude, although the amount of the liquid is small, when the change of the liquid discharge is larger, it still has obvious influence on the heat transfer. On the other hand, what influences the convective heat transfer mostly in the annular flow is the liquid film area near the wall. The liquid entrainment rate of the mist flow core is only related with the apparent speed of the gas. If the gas discharge increases, the entrainment rate increases with non-linearity. The discharge in the liquid film is bound to reduce when the entrainment amount increases. Then it brings about the reduction of the convective heat-transfer coefficient in the tube.

4.5 Influence of average void fraction

To understand the influence of the gas discharge and the liquid discharge on heat transfer more fully, the parameter average void fraction is selected in this paper. Its definition:

$$\alpha_s = \frac{v_{sg}}{v_{sg} + v_{sl}} = \frac{Q_g}{Q_g + Q_l} \tag{19}$$

The heat transfer experiments with different liquid discharge and gas discharge are carried out, as shown in Fig. 12.

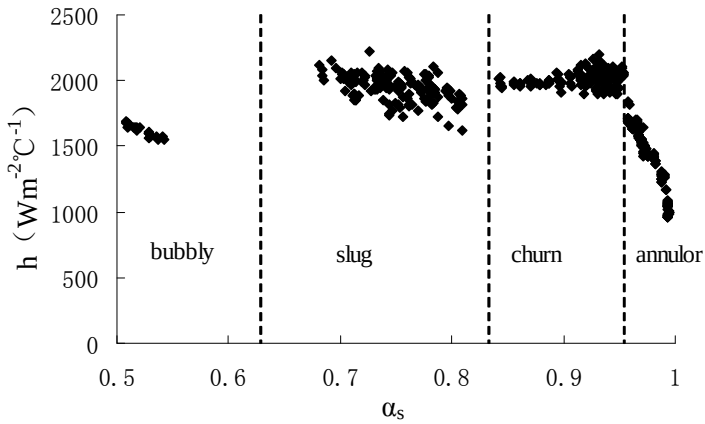

Figure 12: Influence of average void fraction on heat transfer.

On the whole, when the average void fraction increases, the heat transfer coefficient increases first and then decreases. However, the change trend of each specific flow pattern differs. The numerical expression of the heat transfer coefficient and the average void fraction is obtained under the experimental condition through regression:

$$h = 3518.8 - 3637.6\alpha_s \tag{20}$$

$$h = -19716\alpha_s + 20682 \tag{21}$$

$$h = -1419.3\alpha_s + 3013.9 \tag{22}$$

$$h = 442.93\alpha_s + 1604.8 \tag{23}$$

The convective heat-transfer coefficient in the tube decreases as the average void fraction increases in the scope of the bubbly flow and the slug flow. The convective heat-transfer coefficient changes little in the scope of the churn flow. The convective heat-transfer coefficient decreases rapidly in the scope of the annular flow. That is because the bubbly flow is similar to the single phase flow. The proportion of the gas in the section of the tube increases as the average void fraction increases. The difference of the *Nu* number of the gas and the liquid is not great in the bubbly flow and the heat conductivity of the liquid phase is much larger than the gas phase. So the heat transfer coefficient is bound to decrease as the proportion of the liquid phase. In the slug flow, the void fraction changes little in the section of Taylor bubbles when the average void fraction increases. However, in the liquid slug section, the proportion of the gas in the section of the tube increases when the average void fraction increases and the thermal property of the air is much worse than the water. So for the two reasons the overall heat transfer coefficient decreases. In the churn flow and the annular flow, the changes of the heat transfer coefficients under the two conditions have been expounded above.

5 Conclusion

(1) In the paper, several heat transfer experiments are designed with the consideration of the heat transfer characteristics of each flow pattern and the characteristics of the cooling heat transfer based on the current research. The experimental system and the data processing methods are introduced in the paper.
(2) The relational expression for the calculation of the heat transfer in the turbulent flow under the deepwater cryogenic condition is basically consistent with that at normal temperature. However, the difference of the relational expression in the laminar flow is great.
(3) The liquid phase discharge is the main factor that influences the heat transfer in the bubbly flow, slug flow and the annular flow.
(4) The changes of the liquid discharge and the gas discharge have little influence on the heat transfer in the churn flow. Although the amount of the entraining liquid in the mist flow core will increase relatively when the liquid discharge increases, the mist flow core has little influence on the heat transfer. The net upwardly change of the liquid near the wall is the most important factor on the heat transfer in the churn flow.

Acknowledgements

This work is supported by the Major Program of National Natural Science Foundation of China (No.51034007), the National Science and Technology Major Project of China (No.2011ZX05026-001-02), the National Natural Science Foundation of China (No.50874116, No.51104172 and No.51004113), the Natural Science Foundation of Shandong Provence of China (No.ZR2010EL101 and No.ZR2009FQ005) and the Fundamental Research Funds for the Central Universities, China.

References

[1] Taitel Y, Barnea D, Two phase slug flow. Adv Heat Transfer, 20, pp. 3-132, 1990.
[2] Zheng zheng quan, Transient Simulation and Experiment Investigation of Cryogenic Two Phase Flow. Cryogenics and Superconductivity, 27(4), pp. 21-26, 1999.
[3] Liu Jinghua, Temperature Measurement in Void Test of Low Temperature Two-Phase Flow. Cryogenics, 86, pp. 12-14, 1995.
[4] Fan Shangchun, Zhou Haomin, Signal and Measurement Technology. Beijing: Press of Beijing University of Aeronautics and Astronautics, 2003.
[5] Gao Yonghai, Sun Baojiang, Wang Zhiyuan, Calculation and Analysis of Wellbore Temperature Field in Deepwater Drilling. Journal of the University of Petroleum, China (Edition of Natural Science).
[6] Jakob M, Heat transfer. New York: John Wiley and Sons Inc, 2, pp. 211-260, 1957.
[7] Yang Shiming, Tao Wenquan, Heat Transfe. Beijing: Higher Education Press, pp. 104-108, 1998.
[8] B.J.Azzopardi, E.Wren, What is Entrainment in Vertical Two-phase Churn Flow. International Jounal of Multiphase Flow, 30, pp. 89-103, 2004.
[9] A.R.Hasan, C.S.Kabir, A Simple Model for Annular Two-Phase Flow in Wellbores. SPE Annual Technical Conference and Exhibition, Dallas, pp. 9-12, 2005.
[10] Zhang Zixion, Dong Zengnan, Viscous Fluid Flow. Beijing: Tsinghua University Press, pp. 351-387, 1998.

This page intentionally left blank

On the exact solution of incompressible viscous flows with variable viscosity

A. Fatsis[1], J. Statharas[2], A. Panoutsopoulou[3] & N. Vlachakis[1]
[1]*Technological University of Chalkis, Department of Mechanical Engineering, Greece*
[2]*Technological University of Chalkis, Department of Aeronautical Engineering, Greece*
[3]*Hellenic Defence Systems, Greece*

Abstract

Flows of variable viscosity fluids have many industrial applications in fluid mechanics and in engineering such as pump flows for highly viscous fluids. Carrying out a literature survey, it was found that in most cases the fluid viscosity is mainly temperature dependent. Numerical investigation of such flows involves the solution of the Navier-Stokes equations with an extra difficulty arising from the fact that the viscosity is not constant over the flow field. This article presents an analytical solution to the Navier-Stokes equations for the case of laminar flows in rotating systems with variable viscosity fluids. The equations are written in a cylindrical relative frame of reference rotating with a constant angular velocity. In the following, appropriate reference quantities are chosen to provide the non-dimensional form of the partial differential equations. The proposed solution that satisfies the continuity, the momentum and the energy equation, is expressed in terms of the Bessel function of the first kind and of exponential functions. Carrying out algebraic manipulations, it is proven that the proposed solution satisfies all the governing equations. Plots of the velocity, pressure and temperature distributions show the influence of the radius and of the axial coordinate to the flow field.
Keywords: variable viscosity, exact solution, Navier-Stokes, incompressible flow, laminar flow, Bessel functions.

WIT Transactions on Engineering Sciences, Vol 74, © 2012 WIT Press
www.witpress.com, ISSN 1743-3533 (on-line)
doi:10.2495/AFM120421

1 Introduction

Exact solutions of the Navier-Stokes equations are very important not only because they are solutions of certain fundamental flows but also because they serve as accuracy checks for experimental, numerical, empirical and asymptotic methods An excellent review summarizing the basic steady and unsteady flows providing their exact solutions is presented by Drazin and Riley [1].

These are exact solution methods, treating non-Newtonian fluids, such as polymer solutions, special soap solutions, blood, paints, certain oils and greases, for which a different model has to be used to account for the non-Newtonian behavior. Such a model based on the theory of Oldroyd [2], is described by Fetecau [3].

The exact solutions of the Navier-Stokes equations when the viscosity is variable are rare, however the literature in which the viscosity is variable is dependent upon the space, time, temperature, pressure etc. Martin [4] used for the first time an elegant method in the study of the Navier-Stokes equations for an incompressible fluid of variable viscosity. Martin reduced the order of the governing equations from second order to first order by introducing the vorticity function and the generalized energy function.

Naeem and Nadeem [5] generalized Martin's approach to study the steady-state, plane, variable viscosity, solving the incompressible Navier-Stokes equations. They transformed the equations to a new system with viscosity, vorticity, speed and energy function. The transformation matrices included the unknown functions and helped determine some exact solutions for vortex, radial and parallel flows.

Naeem [6] presented recently a class of exact solutions of the equations governing the steady plane flows of incompressible fluid of variable viscosity for an originally specified vorticity distribution.

The effects of linearly varying viscosity and thermal conductivity on steady free convective flow of a viscous incompressible fluid along an isothermal vertical plate in the presence of heat sink were investigated by Mahanti and Gaur [7]. The governing equations of continuity, momentum and energy are transformed into coupled and non-linear ordinary differential equations using similarity transformation and then solved using Runge-Kutta fourth order method.

Variable viscosity Couette flow was investigated by Makinde and Maserumule [8] by solving analytically the Navier-Stokes equations using a perturbation method coupled with a Hermite-Padė approximation technique to obtain the velocity and temperature distributions.

This article presents a method providing analytical solutions to the incompressible Navier-Stokes equations. The equations are written in cylindrical coordinates suited for applications in rotating machinery flows. It is proven that the analytical solutions obtained satisfy the partial differential equations.

2 Governing equations

Considering that the model aims to describe the motion of a Newtonian fluid, the Navier-Stokes equations are the governing equations of the problem [9]. It was chosen to express the equations in cylindrical coordinates because it is more convenient for axisymmetric bodies or rotating systems. Moreover since many applications of rotating systems concern fluid rotating machinery such as compressors, turbines or pumps, the relative frame of reference is preferred. Adopting the relative cylindrical frame of reference, (r,θ,z), the $z-$axis coincides to the axis of rotation, the $r-$axis is directed radially outwards and the $\theta-$axis is in the peripheral direction and it is rotating with a constant rotational speed with the rotor. In this case the relative velocity is linked to the absolute velocity and the rotation speed of the relative system of coordinates:

$$\vec{V} = \vec{W} + \vec{U} = \vec{W} + \left(\vec{\omega} \times \vec{r}\right) \tag{1}$$

where $\vec{V} = v_r \cdot \vec{i}_r + v_\theta \cdot \vec{i}_\theta + v_z \cdot \vec{i}_z$ is the absolute velocity vector, $\vec{W} = u_r \cdot \vec{i}_r + u_\theta \cdot \vec{i}_\theta + u_z \cdot \vec{i}_z$ is the relative velocity vector and $\vec{U} = \left(\vec{\omega} \times \vec{r}\right) \cdot \vec{i}_\theta$ is the rotating speed of the relative system of coordinates.

The following equation was chosen to express the viscosity in terms of temperature, as proposed by Schilling *et al*. [10]:

$$\mu = \mu_0 \cdot \left(1 - \beta \cdot T\right) \tag{2}$$

where β is the thermal expansion of the fluid.

The system of the 3-D Navier-Stokes equations for incompressible flow in cylindrical coordinates can be non-dimensionalised by using the following parameters:

$$\left.\begin{aligned} u^* = \frac{u_r}{\omega \cdot R}, v^* = \frac{u_\theta}{\omega \cdot R}, w^* = \frac{u_z}{\omega \cdot R}, R^* = \frac{r}{R}, z^* = \frac{z}{R}, H^* = \frac{\mu}{\mu_0} \\ P^* = \frac{P}{\rho \cdot \left(R \cdot \omega\right)^2}, T^* = \frac{c_p \cdot T}{\left(R \cdot \omega\right)^2}, \mathrm{Re} = \frac{\rho \cdot R \cdot \omega^2}{\mu_0}, Ec = \frac{\beta \cdot \left(R \cdot \omega\right)^2}{c_p} \end{aligned}\right\} \tag{3}$$

where R is a characteristic radius of the geometry in consideration, *Re* and *Ec* are the non-dimensional Reynolds and Eckert numbers based on the rotational speed and the radius of the rotor, [9].

Thus, the continuity equation can be written:

$$\frac{\partial u^*}{\partial R^*} + \frac{u^*}{R^*} + \frac{\partial w^*}{\partial z^*} = 0 \tag{4}$$

Using the above non-dimensional parameters, the *r*-momentum equation can be written:

$$u^* \cdot \frac{\partial u^*}{\partial R^*} + w^* \cdot \frac{\partial u^*}{\partial z^*} - \frac{v^{*2}}{R^*} = -\frac{\partial P^*}{\partial R^*} + \frac{H^*}{\mathrm{Re}} \cdot \left(\frac{\partial^2 u^*}{\partial R^{*2}} + \frac{1}{R^*} \cdot \frac{\partial u^*}{\partial R^*} - \frac{u^*}{R^*} + \frac{\partial^2 u^*}{\partial z^{*2}} \right) +$$
$$R^* + 2v^* + \frac{1}{\mathrm{Re}} \cdot \frac{\partial H^*}{\partial z^*} \cdot \frac{\partial u^*}{\partial z^*} + \frac{1}{\mathrm{Re}} \cdot \frac{\partial H^*}{\partial z^*} \cdot \frac{\partial w^*}{\partial R^*} + \frac{2}{\mathrm{Re}} \cdot \frac{\partial H^*}{\partial R^*} \cdot \frac{\partial u^*}{\partial R^*} \tag{5}$$

The non-dimensional form of the θ-momentum equation is:

$$u^* \cdot \frac{\partial v^*}{\partial R^*} + w^* \cdot \frac{\partial v^*}{\partial z^*} + \frac{u^* \cdot v^*}{R^*} =$$
$$-2 \cdot v^* + \frac{H^*}{\mathrm{Re}} \left[\frac{\partial}{\partial R^*} \left(\frac{\partial v^*}{\partial R^*} \right) + \frac{1}{R^*} \cdot \frac{\partial v^*}{\partial R^*} - \frac{v^*}{R^{*2}} + \frac{\partial}{\partial z^*} \left(\frac{\partial v^*}{\partial z^*} \right) \right] +$$
$$+ \frac{1}{\mathrm{Re}} \cdot \frac{\partial \mathrm{H}^*}{\partial z^*} \cdot \frac{\partial v^*}{\partial z^*} + \frac{1}{\mathrm{Re}} \cdot \frac{\partial \mathrm{H}^*}{\partial R^*} \cdot \left(\frac{\partial v^*}{\partial R^*} - \frac{v^*}{R^*} \right) \tag{6}$$

The non-dimensional form of the *z*-momentum equation is:

$$u^* \cdot \frac{\partial w^*}{\partial R^*} + w^* \cdot \frac{\partial w^*}{\partial z^*} = -\frac{\partial P^*}{\partial z^*} + \frac{H^*}{\mathrm{Re}} \cdot \left(\frac{\partial^2 w^*}{\partial R^{*2}} + \frac{1}{R^*} \cdot \frac{\partial w^*}{\partial R^*} + \frac{\partial^2 w^*}{\partial z^{*2}} \right) +$$
$$\frac{1}{\mathrm{Re}} \cdot \frac{\partial H^*}{\partial R^*} \cdot \left(\frac{\partial u^*}{\partial z^*} + \frac{\partial w^*}{\partial R^*} \right) + \frac{2}{\mathrm{Re}} \cdot \frac{\partial H^*}{\partial z^*} \cdot \frac{\partial w^*}{\partial z^*} \tag{7}$$

Using the above non-dimensional parameters, the energy equation is becoming:

$$\frac{\partial^2 T^*}{\partial R^{*2}} + \frac{1}{R^*} \cdot \frac{\partial T^*}{\partial R^*} + \frac{\partial^2 T^*}{\partial z^{*2}} = 0 \tag{8}$$

3 Solution of the equations

Resolving the system of eqns (4) to (8), it was found that the axial velocity w^*, the radial velocity u^*, the tangential velocity v^* can be expressed in terms of the functions:

$$w^* = J_0(rb) \cdot e^{b \cdot z^*} \tag{9}$$

$$u^* = -J_1(rb) \cdot e^{b \cdot z^*} \tag{10}$$

$$v^* = -r \tag{11}$$

where $J_0(rb)$ and $J_1(rb)$ are the Bessel functions of the first kind and $b = 2{,}4056405$ defined in details in [11].

Pressure P^*, temperature T^* and viscosity H^* can be expressed in terms of the functions:

$$P^* = \frac{\xi}{2} \cdot \left[J_0^2(rb) + J_1^2(rb) \right] \cdot e^{2 \cdot b \cdot z^*} \tag{12}$$

$$\xi = \frac{2 \cdot b}{\mathrm{Re}} - 1 \tag{13}$$

$$T^* = A + B \cdot J_0(rb) e^{bz} \tag{14}$$

$$H^* = J_0(b \cdot r) \cdot e^{b \cdot z} \tag{15}$$

where the constants $A = \frac{1}{Ec}, \quad B = -\frac{1}{Ec}$

The above solutions (eqns 9 to 15) are implemented to the system of the non-dimensional partial differential equations (4) to (8). The governing equations are satisfied, as shown below:

3.1 Continuity equation

Substituting the solutions for u^*, w^*, v^* the continuity equation yields:

$$\frac{\partial\left(J_1 \cdot e^{-b \cdot z^*} e^{k \cdot t} + \frac{B}{R^*} \right)}{\partial R^*} + \frac{J_1 \cdot e^{-b \cdot z^*} e^{k \cdot t} + \frac{B}{R^*}}{R^*} + \frac{\partial\left(J_0 \cdot e^{-b \cdot z^*} e^{k \cdot t} + A \cdot (1 - R^{*2}) \right)}{\partial z^*} =$$

$$\frac{J_1(b \cdot R^*) \cdot e^{-b \cdot z^*} e^{k \cdot t}}{R^*} + \frac{B}{R^{*2}} + \left(b \cdot J_0(b \cdot R^*) - \frac{J_1(b \cdot R^*)}{R^*} \right) \cdot e^{-b \cdot z^*} e^{k \cdot t} +$$

$$\left(-\frac{B}{R^{*2}} \right) + (-b) \cdot J_0(b \cdot R^*) \cdot e^{-b \cdot z^*} e^{k \cdot t} = 0$$

meaning that the continuity equation is satisfied.

3.2 R-momentum equation

Introducing the expressions for the flow velocities u^*, v^*, w^*, in the *r*-momentum equation, one can see that these expressions satisfy the equation.

The left hand side of the equation is:

$$\frac{\partial u^*}{\partial R^*}+w^*\cdot\frac{\partial u^*}{\partial z^*}-\frac{v^{*2}}{R^*}=b\cdot\left(e^{b\cdot z^*}\right)^2\cdot J_0\left(b\cdot R^*\right)\cdot J_1\left(b\cdot R^*\right)-$$

$$\frac{\left(e^{b\cdot z^*}\right)^2\cdot\left(J_1\left(b\cdot R^*\right)\right)^2}{R^*}--b\cdot\left(e^{b\cdot z^*}\right)^2\cdot J_0\left(b\cdot R^*\right)\cdot J_1\left(b\cdot R^*\right)=-\frac{e^{2\cdot b\cdot z^*}\cdot\left(J_1\left(b\cdot R^*\right)\right)^2}{R^*}-R^*$$

The right hand-side terms of the equation are:

The term $\frac{\partial P^*}{\partial R^*}$ is becoming:

$$-\frac{\partial P^*}{\partial R^*}=\frac{\left(\frac{2b}{\mathrm{Re}}-1\right)\cdot e^{2\cdot b\cdot z^*}}{2}\cdot\frac{\partial}{\partial R^*}\left[J_1^2\left(b\cdot R^*\right)+J_0^2\left(b\cdot R^*\right)\right]$$

$$=\frac{2\cdot b\cdot e^{2\cdot b\cdot z^*}J_1^2\left(b\cdot R^*\right)}{\mathrm{Re}\cdot R^*}-\frac{e^{2\cdot b\cdot z^*}J_1^2\left(b\cdot R^*\right)}{R^*}$$

The terms:

$$\frac{H^*}{\mathrm{Re}}\cdot\left(\frac{\partial^2 u^*}{\partial R^{*2}}+\frac{1}{R^*}\cdot\frac{\partial u^*}{\partial R^*}-\frac{u^*}{R^*}+\frac{\partial^2 u^*}{\partial z^{*2}}\right)=$$

$$=\frac{H^*}{\mathrm{Re}}\cdot\left[b^2\cdot e^{b\cdot z^*}\cdot J_1\left(b\cdot R^*\right)+\frac{b\cdot e^{b\cdot z^*}\cdot J_0\left(b\cdot R^*\right)}{R^*}-\frac{2\cdot e^{b\cdot z^*}J_1\left(b\cdot R^*\right)}{\left(R^*\right)^2}-\right.$$

$$\left.-\frac{b\cdot e^{b\cdot z^*}\cdot J_0\left(b\cdot R^*\right)}{R^*}+\frac{2\cdot e^{b\cdot z^*}J_1\left(b\cdot R^*\right)}{\left(R^*\right)^2}-b^2\cdot e^{b\cdot z^*}\cdot J_1\left(b\cdot R^*\right)\right]=0$$

The terms:

$$R^*+2v^*+\frac{1}{\mathrm{Re}}\cdot\frac{\partial H^*}{\partial z}\cdot\frac{\partial u^*}{\partial z}+\frac{1}{\mathrm{Re}}\cdot\frac{\partial H^*}{\partial z}\cdot\frac{\partial w^*}{\partial R^*}+\frac{2}{\mathrm{Re}}\cdot\frac{\partial H^*}{\partial R^*}\cdot\frac{\partial u^*}{\partial R^*}=$$

$$=-R^*-\frac{2b^2\cdot e^{2b\cdot z^*}\cdot J_0(b\cdot R^*)\cdot J_1(b\cdot R^*)}{\mathrm{Re}}+$$

$$\frac{2}{\mathrm{Re}}\cdot\left(2b^2\cdot e^{2b\cdot z^*}\cdot J_0(b\cdot R^*)\cdot J_1(b\cdot R^*)-\frac{2b\cdot e^{2b\cdot z^*}\cdot J_1^2(b\cdot R^*)}{R^*}\right)=$$

$$=-R^*-\frac{2b\cdot e^{2b\cdot z^*}\cdot J_1^2(b\cdot R^*)}{\mathrm{Re}\cdot R^*}\equiv\frac{\partial P^*}{\partial R^*}$$

Thus, we see that the *r*-momentum equation satisfies the proposed solution.

3.3 Θ-momentum equation

Introducing the expressions for the flow velocities u^*, v^*, w^*, in the θ-momentum equation, one can see that these expressions satisfy the equation.

The left hand side of the equation is:

$$u^* \cdot \frac{\partial v^*}{\partial R^*} + w^* \cdot \frac{\partial v^*}{\partial z^*} + \frac{u^* \cdot v^*}{R^*} = \left(-J_1(b \cdot R^*) \cdot e^{b \cdot z^*}\right) \cdot \frac{\partial(-R^*)}{\partial R^*} +$$

$$\left(J_0(b \cdot R^*) \cdot e^{b \cdot z^*}\right) \cdot \frac{\partial(-R^*)}{\partial z^*} + \frac{\left(-J_1(b \cdot R^*) \cdot e^{b \cdot z^*}\right) \cdot (-R^*)}{R^*} =$$

$$-J_1(b \cdot R^*) \cdot e^{b \cdot z^*} + J_1(b \cdot R^*) \cdot e^{b \cdot z^*} = 0$$

The right-hand side of the θ-momentum equation is:

The term

$$\frac{1}{\mathrm{Re}} \cdot \frac{\partial \mathrm{H}^*}{\partial z^*} \cdot \frac{\partial v^*}{\partial z^*} = \frac{1}{\mathrm{Re}} \cdot \left(b \cdot J_0(b \cdot R^*) \cdot e^{b \cdot z^*}\right) \cdot \frac{\partial(-R^*)}{\partial z^*} =$$

$$\frac{1}{\mathrm{Re}} \cdot \left(b \cdot J_0(b \cdot R^*) \cdot e^{b \cdot z^*}\right) \cdot 0 = 0$$

The term

$$\frac{1}{\mathrm{Re}} \cdot \frac{\partial \mathrm{H}^*}{\partial R^*} \cdot \left(\frac{\partial v^*}{\partial R^*} - \frac{v^*}{R^*}\right) =$$

$$\frac{1}{\mathrm{Re}} \cdot \left(-b \cdot J_1(b \cdot R^*) \cdot e^{b \cdot z^*}\right) \cdot \left[\frac{\partial(-R^*)}{\partial R^*} - \frac{(-R^*)}{R^*}\right] = 0$$

The term

$$\frac{\omega^2 \cdot L \cdot H}{\mathrm{Re}} \left[\frac{\partial}{\partial R^*}\left(\frac{\partial v^*}{\partial R^*}\right) + \frac{1}{R^*} \cdot \frac{\partial v^*}{\partial R^*} - \frac{v^*}{R^{*2}} + \frac{\partial}{\partial z^*}\left(\frac{\partial v^*}{\partial z^*}\right)\right] =$$

$$\frac{J_0(b \cdot R^*) \cdot e^{b \cdot z^*}}{\mathrm{Re}} \cdot \left[\frac{\partial}{\partial R^*}(-1) + \frac{1}{R^*} \cdot (-1) + \frac{R^*}{R^{*2}} + 0\right] =$$

$$\frac{J_0(b \cdot R^*) \cdot e^{b \cdot z^*}}{\mathrm{Re}} \cdot \left(-\frac{1}{R^*} + \frac{1}{R^*}\right) = 0$$

Hence the proposed solution satisfies the θ-momentum equation.

3.4 Z-momentum equation

Introducing the expressions for the flow velocities u^*, v^*, w^*, in the z -momentum equation, one can see that these expressions satisfy the equation.

The left hand side of the equation is:

$$u^* \cdot \frac{\partial w^*}{\partial R^*} + w^* \cdot \frac{\partial w^*}{\partial z^*} =$$

$$= \left(-J_1\left(b \cdot R^*\right) \cdot e^{b \cdot z^*}\right) \cdot \left(-b \cdot e^{b \cdot z^*} \cdot J_1\left(b \cdot R^*\right)\right) + \left(J_0\left(b \cdot R^*\right) \cdot e^{b \cdot z^*}\right) \cdot$$

$$\frac{\partial\left(J_0\left(b \cdot R^*\right) \cdot e^{b \cdot z^*}\right)}{\partial z^*} = b \cdot e^{2 \cdot b \cdot z^*} \cdot \left[J_1^2\left(b \cdot R^*\right) + J_0^2\left(b \cdot R^*\right)\right]$$

The term $-\frac{\partial P^*}{\partial z^*}$ can be written:

$$-\frac{\partial P^*}{\partial z^*} = -\frac{\partial\left[\frac{\xi}{2} \cdot \left(J_1^2\left(b \cdot R^*\right) + J_0^2\left(b \cdot R^*\right)\right)\right]}{\partial z^*} =$$

$$-\frac{\xi}{2} \cdot \left[J_1^2\left(b \cdot R^*\right) + J_0^2\left(b \cdot R^*\right)\right] \cdot \frac{\partial\left(e^{2 \cdot b \cdot z^*}\right)}{\partial z^*} =$$

$$-\xi \cdot \left[J_1^2\left(b \cdot R^*\right) + J_0^2\left(b \cdot R^*\right)\right] \cdot b \cdot e^{2 \cdot b \cdot z^*} =$$

$$b \cdot e^{2 \cdot b \cdot z^*} \cdot \left(\frac{2 \cdot b}{\mathrm{Re}} - 1\right) \cdot \left[J_1^2\left(b \cdot R^*\right) + J_0^2\left(b \cdot R^*\right)\right]$$

The term

$$\frac{H^*}{\mathrm{Re}} \cdot \left(\frac{\partial^2 w^*}{\partial R^{*2}} + \frac{1}{R^*} \cdot \frac{\partial w^*}{\partial R^*} + \frac{\partial^2 w^*}{\partial z^{*2}}\right) =$$

$$\frac{J_0\left(b \cdot R^*\right) \cdot e^{b \cdot z^*}}{\mathrm{Re}} \cdot \left[\begin{array}{l} -b^2 \cdot e^{b \cdot z^*} \cdot J_0\left(b \cdot R^*\right) + b \cdot e^{b \cdot z^*} \cdot \frac{J_1\left(b \cdot R^*\right)}{R^*} - \\ b \cdot e^{b \cdot z^*} \cdot \frac{J_1\left(b \cdot R^*\right)}{R^*} + b^2 \cdot e^{b \cdot z^*} \cdot J_0\left(b \cdot R^*\right) \end{array}\right] = 0$$

The term

$$\frac{1}{\mathrm{Re}}\cdot\frac{\partial H^*}{\partial R^*}\cdot\left(\frac{\partial u^*}{\partial z^*}+\frac{\partial w^*}{\partial R^*}\right)=\frac{2\cdot b^2\cdot e^{2\cdot b\cdot z^*}\cdot J_1^2\left(b\cdot R^*\right)}{\mathrm{Re}}$$

The term

$$\frac{2}{\mathrm{Re}}\cdot\frac{\partial H^*}{\partial z^*}\cdot\frac{\partial w^*}{\partial z^*}=\frac{2}{\mathrm{Re}}\cdot\left[\left(b\cdot e^{b\cdot z^*}\cdot J_0\left(b\cdot R^*\right)\right)\cdot\left(b\cdot e^{b\cdot z^*}\cdot J_0\left(b\cdot R^*\right)\right)\right]=\frac{2\cdot b^2\cdot e^{2\cdot b\cdot z^*}\cdot J_0^2\left(b\cdot R^*\right)}{\mathrm{Re}}$$

Substituting the above expressions to the non-dimensional form of the z-momentum equation, we obtain:

$$b\cdot e^{2\cdot b\cdot z^*}\cdot\left[J_1^2\left(b\cdot R^*\right)+J_0^2\left(b\cdot R^*\right)\right]=$$

$$-b\cdot e^{2\cdot b\cdot z^*}\cdot\left(\frac{2\cdot b}{\mathrm{Re}}-1\right)\cdot\left[J_1^2\left(b\cdot R^*\right)+J_0^2\left(b\cdot R^*\right)\right]+$$

$$\frac{2\cdot b^2\cdot e^{2\cdot b\cdot z^*}\cdot J_1^2\left(b\cdot R^*\right)}{\mathrm{Re}}+\frac{2\cdot b^2\cdot e^{2\cdot b\cdot z^*}\cdot J_0^2\left(b\cdot R^*\right)}{\mathrm{Re}}$$

which equals the left hand side, meaning that proposed solution for the temperature satisfies the z-momentum equation.

3.5 Energy equation

$$\frac{\partial^2 T^*}{\partial R^{*2}}+\frac{1}{R^*}\cdot\frac{\partial T^*}{\partial R^*}+\frac{\partial^2 T^*}{\partial z^{*2}}=0$$

The term

$$\frac{\partial T^*}{\partial R^*}=\frac{\partial\left(A+B\cdot J_o\left(b\cdot R^*\right)\cdot e^{b\cdot z^*}\right)}{\partial R^*}=-B\cdot b\cdot e^{b\cdot z^*}\cdot J_1\left(b\cdot R^*\right)$$

The term

$$\frac{\partial T^*}{\partial z^*}=\frac{\partial\left(A+B\cdot J_o\left(b\cdot R^*\right)\cdot e^{b\cdot z^*}\right)}{\partial z^*}=B\cdot b\cdot e^{b\cdot z^*}\cdot J_0\left(b\cdot R^*\right)$$

The derivative

$$\frac{\partial\left(-B\cdot b\cdot e^{b\cdot z^*}\cdot J_1\left(b\cdot R^*\right)\right)}{\partial R^*}=$$

$$-b^2\cdot B\cdot e^{b\cdot z^*}\cdot J_0\left(b\cdot R^*\right)+\frac{B\cdot b\cdot e^{b\cdot z^*}\cdot J_1\left(b\cdot R^*\right)}{R^*}$$

The derivative

$$\frac{\partial\left(B\cdot b\cdot e^{b\cdot z^*}\cdot J_0\left(b\cdot R^*\right)\right)}{\partial z^*}=b^2\cdot B\cdot e^{b\cdot z^*}\cdot J_0\left(b\cdot R^*\right)$$

Thus the energy equation is:

$$-b^2\cdot B\cdot e^{b\cdot z^*}\cdot J_0\left(b\cdot R^*\right)+\frac{B\cdot b\cdot e^{b\cdot z^*}\cdot J_1\left(b\cdot R^*\right)}{R^*}-\frac{B\cdot b\cdot e^{b\cdot z^*}\cdot J_1\left(b\cdot R^*\right)}{R^*}$$

$$+b^2\cdot B\cdot e^{b\cdot z^*}\cdot J_0\left(b\cdot R^*\right)=0$$

which means that the proposed solution for the temperature satisfies the energy equation.

The distributions of axial and radial velocity components in terms of the non-dimensional radius R^* for different axial positions z^*, are shown in figure 1. One can see that the axial velocity distribution (figure 1a) respects the condition that its value is zero at $R^*=1$ for all axial positions z^*. Similarly, the radial velocity distribution (figure 1b) respects the condition that for all axial positions z^* its values is zero at $R^*=0$.

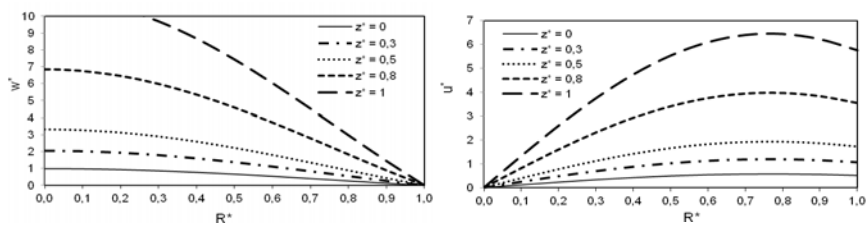

(a) (b)

Figure 1: (a) Axial and (b) radial velocity distribution in terms of R*.

The temperature and the pressure distributions in terms of the non-dimensional radius R^* for different axial positions, are shown in figure 2. From the temperature distribution, it can be seen that at the outer radial boundary corresponding at $R^*=1$ all the curves converge to the same value of temperature.

The fact that from figure 2a we can observe variations of temperature in terms of the radius and in terms of axial coordinate, reveals a three-dimensional field of the distribution.

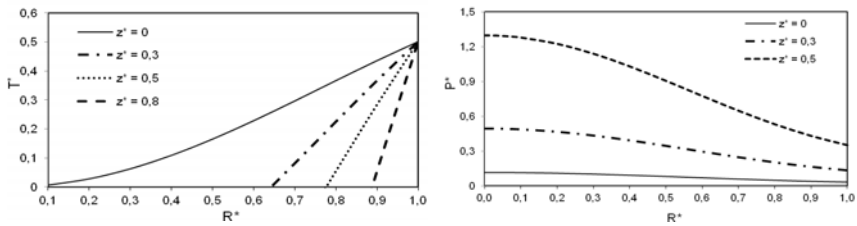

(a) (b)

Figure 2: (a) Temperature and (b) pressure distribution in terms of R*.

Similar observations occur for the case of the pressure field. The pressure variations at the inlet corresponding at $z^*=0$ are negligible, whereas the variations are more intense as the axial distance z^* increases.

4 Conclusions

In this article, an original work has presented an exact solution of the Navier-Stokes equations in cylindrical coordinates for incompressible, laminar, axisymmetric, viscous flows with constant and variable viscosity. The fluid viscosity was assumed to be a function of temperature, as literature survey indicated for flows in rotating machinery [10]. It was proven that the solution field consisting of the Bessel functions of the first kind and of exponential functions satisfies the continuity equation, the equations of motion and the energy equation. It was shown that the present method based on Bessel functions can be used to provide reference solutions for numerical and empirical methods for flow field predictions in rotating systems involving fluids of variable viscosity.

References

[1] Drazin P.G. and Riley N., The Navier-Stokes equations: a classification of flows and exact solutions, *London Mathematical Society Lecture Note Series*, Cambridge University Press, 2007.
[2] Oldroyd J.G., On the formulation of rheological equations of state, *Proc. R. Soc. London A200*, pp. 523–541, 1950.
[3] Fetecau C., Analytical solutions for non-Newtonian fluid flows in pipe-like domains, *Int. J. of Non-linear Mechanics*, 39, pp. 225-231, 2004.
[4] Martin M.H., The flow of a viscous fluid, *Arch. Rat. Mech. Anal. 41*, pp. 266-286, 1971.

[5] Naeem R.K. and Nadeem S.A., Study of plane steady flows of an incompressible fluid of variable viscosity using Martins method, *International Journal of Applied Mechanics and Engineering*, 1(3), pp. 397-433, 1996.
[6] Naeem R.K., A class of exact solutions of the Navier-Stokes equations for incompressible fluid of variable viscosity for defined vorticity distribution, *International Journal of Applied Mathematics and Mechanics* 7(4), pp. 97-118, 2011.
[7] Mahanti N.C. and Gaur P., Effects of Varying Viscosity and Thermal Conductivity on Steady Free Convective Flow and Heat Transfer along an Isothermal Vertical Plate in the Presence of Heat Sink, *Journal of Applied Fluid Mechanics*, 2(1), pp. 23-28, 2009.
[8] Makinde O.D. and Maserumule R.L., Thermal criticality and entropy analysis for a variable viscosity Couette flow, *Psys. Scr.*, 78, pp. 1-6, 2008.
[9] Bird R.B., Stewart W.E. Lightfoot E.N., *Transport Phenomena*, 2nd edition, John Wiley and Sons, Inc., 2002.
[10] Schilling R., Siegle H. and Stoffel B, Strömung und Verluste in drei wichigen Elementen radialer Kreiselpumpen. Eine Literaturübersicht, Universität Karlsruhe (TH), Nr. 16, 1974.
[11] Kreuszig, E., *Advanced Engineering Mathematics*, 11th edition, John Wiley and Sons Inc., pp. 187-191, 2011.

Hybrid synthetic jet actuator with a novel fluidic diode

J. Kordík & Z. Trávníček
Institute of Thermomechanics AS CR, Prague, Czech Republic

Abstract

The paper deals with a new design of the hybrid synthetic jet actuator (HSJ), which is based on a novel fluidic diode. The fluidic diode was tested by a static experiment and its diodicity was evaluated. The same experiment was performed for a second fluidic diode whose planar geometry was taken from the literature and the resultant diodicities were compared. Higher diodicities were achieved with the new design of the diode.

The velocity resonance curves were measured at the nozzle output for two variants of the HSJ with a short or with a long nozzle. After that the volumetric efficiencies of the HSJ were evaluated as functions of the frequency. The highest efficiency (over 80%) was achieved at the second resonant frequency of the actuator with the long nozzle.
Keywords: synthetic jet, hybrid synthetic jet, rectification effect.

1 Introduction

Hybrid synthetic jets, which were first introduced in [1–4], combine the usual synthetic jet and valveless pump principles. The valveless pump [5–10] is a pumping device consisting of a chamber equipped with a moving piston or diaphragm, the chamber is connected to a fluidic diode and a nozzle. The orientation of the fluidic diode is adjusted so that its forward direction is oriented toward the inside of the chamber. Once the diaphragm oscillates, a nonzero net mass flow is created in the nozzle (rectification effect). Unlike the valveless pump, the nozzle of the hybrid synthetic jet actuator (HSJA) issues into ambience where the hybrid synthetic jet (HSJ) is formed.

The experimental investigation offers many unexplored possibilities, as hybrid synthetic jets represent a new research topic, with only a few papers dedicated


WIT Transactions on Engineering Sciences, Vol 74, © 2012 WIT Press
www.witpress.com, ISSN 1743-3533 (on-line)
doi:10.2495/AFM120431

to their study [1–4, 11–15]. The motivation of the present work is based on improvements in the rectification effect of a hybrid synthetic actuator, which is desirable particularly for the augmentation of convective heat transfer of the jet. To quantify this flow rectification, the volumetric efficiency of the actuator is defined.

2 Hybrid synthetic jet principles

Figure 1 shows two basic working modes of the valveless pump on which the hybrid synthetic jet actuators (HSJAs) are based. In the first mode, the supply mode, the piston (or diaphragm) of the valveless pump moves left, and a fluid is sucked in. A conical duct element, which was chosen as the fluidic diode here, has a low hydraulic resistance during the inward flow (forward direction), and at the end of the supply cycle, a fluid volume V_{SD} is supplied into the chamber through it. The fluid volume sucked into the chamber through the nozzle is denoted V_{SN}.

In the pump mode, the fluid is extruded through the fluidic diode, which possesses a higher hydraulic resistance during the outward flow (reverse direction). This causes the fluid volume V_{PD} passed during the pump cycle through the diode to be smaller than the V_{SD}, and the volume pumped through the nozzle V_{PN} is larger than the sucked volume in the supply mode V_{SN}. Periodic cycling of the pump and supply modes results in a nonzero net flow in both elements, the diode and nozzle. A measure of the pumping efficiency is the ratio defined in [5] (volumetric efficiency):

$$\varepsilon_V = \frac{V_{PN} - V_{SN}}{V_{SD} + V_{SN}}. \tag{1}$$

Compared with the valveless pump, the nozzle of the HSJA is terminated, and the flow issues into ambience creating flow structure similar to the synthetic jet. The flow structure is called a hybrid synthetic jet (HSJ) and was studied, for example, in [3, 4]. The paper [4] also introduces another definition of the volumetric efficiency

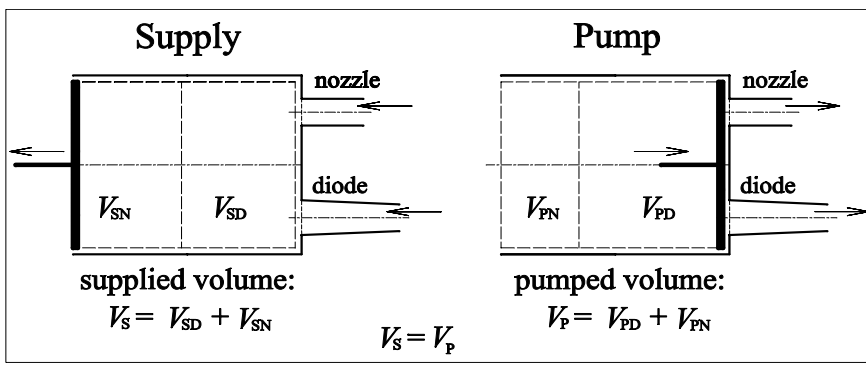

Figure 1: A sketch of the valveless pump (or the HSJA).

for the hybrid synthetic jet:

$$\varepsilon_{\mathrm{N}} = \frac{V_{\mathrm{PN}} - V_{\mathrm{SN}}}{V_{\mathrm{PN}} + V_{\mathrm{SN}}}. \tag{2}$$

This is a more user-friendly definition because the ε_{N} is based on HSJ measurement only, without (extremely complicated) measurement of a fluid flux through the diode. This definition was also used as a criterion for comparing hybrid synthetic jet actuators (HSJAs) in [14–16]. The efficiency ε_{N} is also used for the investigated HSJA in this work. A criterion for the fluidic diode efficiency can be expressed as the ratio of the pressure loss coefficient in the reverse direction ξ_o and the pressure loss coefficient in the forward direction ξ_i. This is called the diodicity (denotation: Di) [17–20]:

$$Di = \frac{\xi_o}{\xi_i}. \tag{3}$$

3 Experimental setup and data processing

3.1 The design of the hybrid synthetic jet actuator

The actuator based on the loudspeaker TVM ARN-165-01/4 is comprised of two fluidic diodes D1 and D2 (see Fig. 2) and is projected such that the diodicity of the both fluidic diodes can be tested by static measurement (see the section 4.1). Concurrently, after an easy adaptation of the HSJA, the hybrid synthetic jet can be investigated at the nozzle output. Two nozzles N1 and N2, which differ by length (30 mm and 150 mm respectively), are prepared in the actuator. The hybrid synthetic jet based on the fluidic diode D1 is studied separately for each nozzle, this means that the remaining nozzle will be always sealed during the experiments. The fluidic diode D1 was selected by a static experiment as the one with the higher diodicity (see the section 4.1, Fig. 3). The new design for the diode D1 was developed, and the planar geometry of diode D2 was taken from the paper [20]. According to this paper, the diode is expected to have a high diodicity (around $Di \approx 1.6$). The experimental conditions, selected dimensions, and properties of the HSJA are summarized in Table 1.

3.2 Data acquisition and hardware setup

The experiments aimed at evaluating the volumetric efficiencies ε_{N} of HSJAs were performed using velocity measurement in the actuator nozzle. The velocities were measured by the hot-wire probe 55P16 placed 1 mm inward from the nozzle exiting area along the nozzle axis. The hot-wire signal from the anemometer MiniCTA 54T30 DANTEC was sampled in the data acquisition device NI-PCI 6023E. The sampling frequency was set to 10 kHz, and the number of samples was 65536. The hot-wire probe was calibrated in the velocity range 0.2–50 m/s after each two hours of continuous operation. The maximal relative uncertainty of single velocity sample was 17%, usual value of the relative uncertainty was under 5%

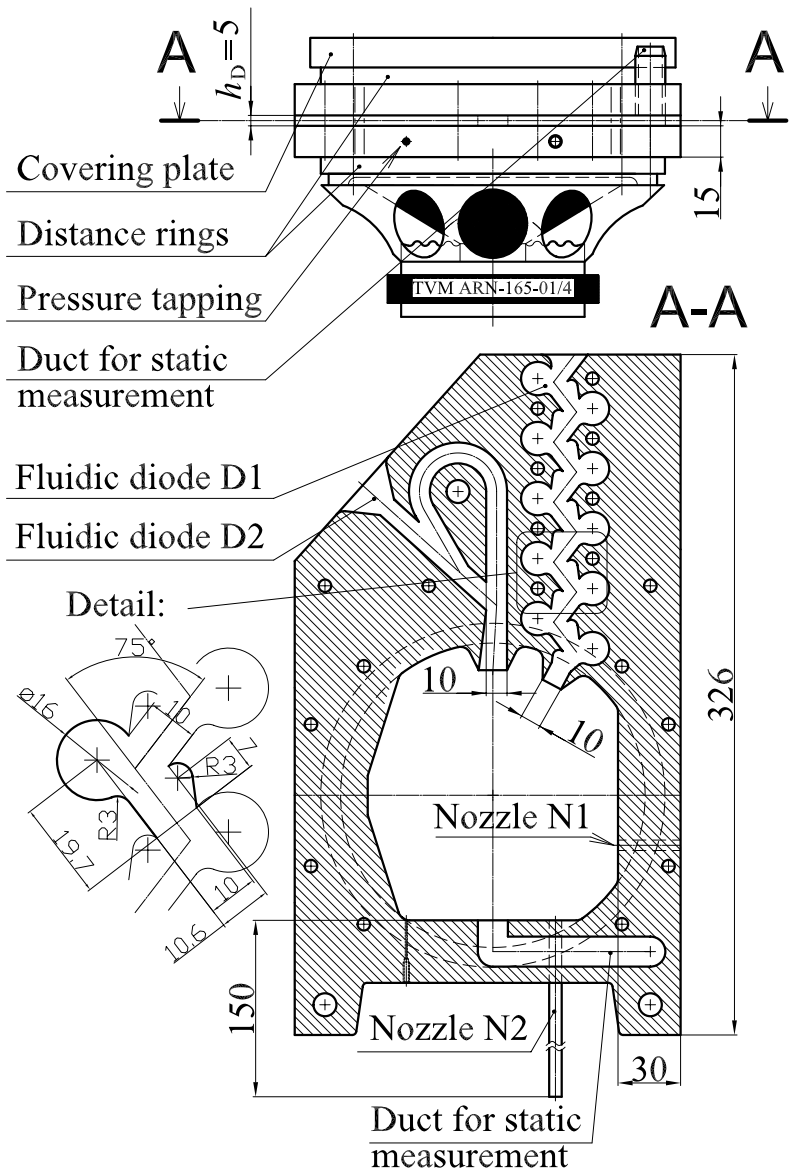

Figure 2: The present hybrid synthetic jet actuator.

for velocities in range 2–50 m/s. A more detailed description of the anemometer settings, probe calibration method, and uncertainty evaluation can be found in [21].

During the velocity measurement the loudspeaker of the actuator was supplied by a harmonic electrical current whose effective value 0.8A was kept constant and the frequency of the current was a variable parameter.

Table 1: The parameters of the experiment.

	Unit	Value/formula
Dimensions:		
$D_0 = 2R_0$	(mm)	131 (diaphragm diameter)
$D_2 = 2R_2$	(mm)	5 (nozzle diameter)
h_{D}	(mm)	5 (diode height)
w_{D}	(mm)	10 (diode width)
L_2	(mm)	30 or 150 (lengths of nozzles N1 or N2)
Fluid properties:		
r	(J/(kg·K))	287 (specific gas constant)
κ	(1)	1.4 (specific heat ratio)
p_{b}	(Pa)	98900 (barometric pressure)
T	(K)	292.15 (air temperature)
ρ	(kg/m^3)	$\frac{p_{\mathrm{b}}}{rT} = 1.18$ (air density)
ν	(m^2/s)	$1.55 \cdot 10^{-5}$ (kinematic viscosity)
Electric supply:		
I_{eff}	(A)	0.8 (effective value of current supply)
P (power)	(W)	≈ 2.7 at $f = 20$Hz (effective value of power supply)

3.3 Hot-wire data reduction

The volumetric efficiencies ε_{N} of the HSJAs were evaluated from the phase-averaged velocity waveforms with help of additional SJ measurements. The SJ was achieved by sealing off the fluidic diodes ducts of the HSJA, and its velocity waveforms were measured at the same input current, location, and frequencies as the HSJ. The following corrective factor g_{SJ} was evaluated from the SJ phase-averaged velocities $U(t)$:

$$g_{\mathrm{SJ}} = \frac{\int_0^{T_{\mathrm{E}}} U(t)\mathrm{d}t}{\int_{T_{\mathrm{E}}}^{T} |U(t)|\,\mathrm{d}t} \Leftrightarrow \int_0^{T_{\mathrm{E}}} U(t)\mathrm{d}t - g_{\mathrm{SJ}} \int_{T_{\mathrm{E}}}^{T} |U(t)|\,\mathrm{d}t = 0, \tag{4}$$

where T_{E} is the extrusion stroke duration time and T is the period. The correction factor g_{SJ} forces the fulfillment of the continuity equation, which is applied to the centerline velocity measured in the nozzle output. The factor evaluation method is based on the behavior of the SJ/HSJ, which creates slug velocity profiles during the extrusion stroke, and the velocity measured by the hot-wire technique at the nozzle output is in accordance with the cross-sectional averaged velocity. Thus, we obtain a good result for the extruded volume by the integration of the velocity $U(t)$ from 0 to T_{E}, and no correction is necessary.

During the suction stroke, the flow is sucked from a large area behind the nozzle, and the streamlines converge into the nozzle. This outcome causes the

velocities measured at the nozzle output to not correspond to the cross-sectional averaged velocity and to meet the continuity equation, they must be corrected. The correction factor g_{SJ} modifies the volume $S_2 \int_{T_\mathrm{E}}^{T} |U(t)|\,\mathrm{d}t$ so that it is equal to the extruded volume, which is known quite precisely from the integration of $S_2 U(t)$ from 0 to T_E (S_2 is the nozzle cross-sectional area).

The factor g_{SJ} obtained from the SJ data is then also applied to the HSJ phase-averaged velocity , which are acquired under the same conditions and from which the volumetric efficiency is evaluated:

$$\varepsilon_\mathrm{N} = \frac{\int_0^{T_\mathrm{E}} U(t)\mathrm{d}t - g_{\mathrm{SJ}} \int_{T_\mathrm{E}}^{T} |U(t)|\,\mathrm{d}t}{\int_0^{T_\mathrm{E}} U(t)\mathrm{d}t + g_{\mathrm{SJ}} \int_{T_\mathrm{E}}^{T} |U(t)|\,\mathrm{d}t}. \tag{5}$$

4 Experimental results

4.1 Experimental evaluation of diodicities

The static experiments for the fluidic diodes were performed within the HSJA from Fig. 2. The loss coefficients were measured in the forward and reverse directions for the diodes D1 and D2 at 13 different mass flows in the range 3–30 $\mathrm{l_n}$/min. The mass flows were measured by a precise digital thermal mass flow meter Bronkhorst EL-FLOW F-201A-50k-AAD-33-V equipped with a particle filter M-422-19-00-V. To evaluate a volume flow from the measured mass flow, the flow temperature and barometric pressure were measured.

In order to evaluate loss coefficients, pressure drop along a diode was measured by the digital manometer Greisinger GMH 3156. Pressure taps were located at the ends of the diode in places where the flow velocity was negligible compared with the flow velocity inside the diode. To measure the pressure drops in forward directions, additional flanges with pressure taps were mounted at the exits of the diodes. The flanges were equipped with hose connections for the volume flow supply and comprise a suitable enlarged cross-sectional area for the static pressure measurement.

During the measurement of the pressure drop in the reverse flow direction, the volume flow was supplied by a duct particularly designed for this purpose in the HSJA (see Fig. 2 duct for static measurement). Another arrangement of the HSJA was used for this experiment; the loudspeaker was removed and substituted by a solid plate with a rubber gasket, and the nozzles and remaining fluidic diode were hermetically sealed. The loss coefficients were evaluated using the measured pressure and volume flow Q as:

$$\begin{aligned} \xi_i &= \tfrac{2\Delta p_{\mathrm{d}i} S_3^2}{\rho Q^2}, \\ \xi_o &= \tfrac{2\Delta p_{\mathrm{d}o} S_3^2}{\rho Q^2}, \end{aligned} \tag{6}$$

where $\Delta p_{\mathrm{d}i}$, $\Delta p_{\mathrm{d}o}$ are pressure drops in the forward and reverse directions, respectively and S_3 is the diode cross-sectional area. The loss coefficients

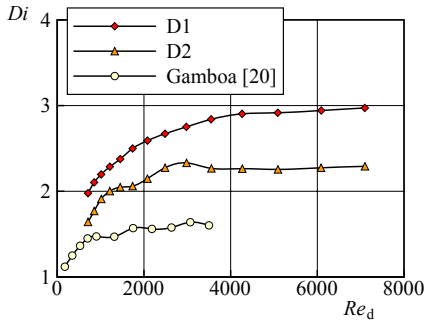

Figure 3: The measured diodicities.

evaluated from the experiments using Eq. (6) were not constant with varying Reynolds number Re_{d}. The Reynolds number was computed as $Re_{\mathrm{d}} = \frac{Q}{h_{\mathrm{D}}\nu}$ (where h_{D} is the diode duct height, this dimension was the same for both diodes $h_{\mathrm{D}} = 5$ mm – see Fig. 2).

The diodicities were evaluated as functions of the Reynolds number Re_{d} using Eq. (3) and are shown in Fig. 3. All of the measured diodicities increased with the Reynolds number, and the highest values of the diodicity were achieved with the diode D1. For this reason, the fluidic diode D1 is used in unsteady hybrid synthetic jets experiments.

The maximal diodicity of the diode D2 was about 2.3 at $Re_{\mathrm{d}} = 3000$, this diodicity is even higher than the diodicity of the diode from [20] having the same planar geometry. The strong deviation can be caused by a non-similarity in an aspect ratio of both channels. The aspect ratio of the present diode channel is 0.5, whereas for the other diode is 2.5.

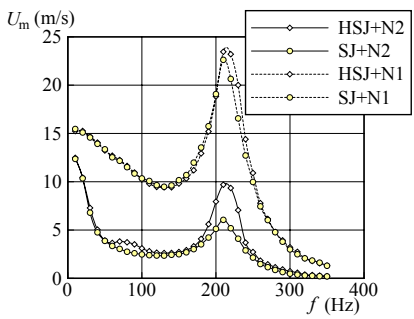

Figure 4: Velocity resonance curves for SJs and HSJs.

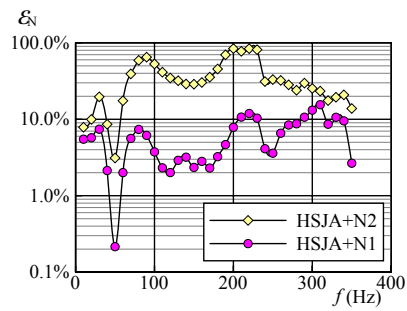

Figure 5: The measured efficiencies of both HSJA variants.

4.2 Velocity resonance curves

Figure 4 compares the velocity resonance curves acquired for the HSJA and SJA measured at constant effective value of electrical current $I_{\text{eff}} = 0.8\text{A}$ (for other power details see Table 1). The velocity resonance curves are evaluated here as dependencies of the centerline time-mean velocity $U_{\text{m}} = \frac{1}{T_{\text{E}}} \int_0^{T_{\text{E}}} U(t)\text{d}t$ on the driving current frequency. The curves were measured with the nozzle N1 and N2; for nozzle N1, the experimental results for HSJ and SJ show nearly the same velocity amplitudes. The curves, however, slightly diverge behind the second velocity resonance (210 Hz), where the HSJ has higher velocity amplitudes, and beyond that merge again (at 260 Hz).

A much larger difference between the HSJ and SJ is noticeable for the experiment with the nozzle N2. The velocity amplitude differences can be found in the range of 50 to 120 Hz and especially in the vicinity of the second velocity resonance (170–270 Hz). The largest difference is at 220 Hz, where the velocity amplitude of HSJ is nearly 1.8 times higher than the SJ amplitude.

4.3 Volumetric efficiency ε_{N}

In Fig. 5 we can see the comparisons of the volumetric efficiencies ε_{N} for HSJA with nozzle N1, or nozzle N2. The curves in Fig. 5 reach local maxima around 80–90 Hz. Other local maxima of ε_{N} can be found for both variants of HSJA close the second velocity resonance (around 220 Hz); for the HSJA with nozzle N2, the volumetric efficiency ε_{N} exceeds even the value of 80% at this point.

4.4 Velocity waveforms

The phase-averaged velocity waveforms of SJA and HSJA are depicted in Figs. 6, 7, and 8 at frequencies where the local maxima of volumetric efficiencies ε_{N} were found.

The effect of enlargement of the extrusion duration time described in [4], combined with positive velocity amplitude enhancement, is noticeable in Fig. 6, where the waveforms of the SJ and HSJ with the nozzle N1 are compared. However, much higher volumetric efficiencies were achieved for the configuration using nozzle N2; see Figs. 7, 8, where enlargement of the extrusion stroke duration time, the enhancement of the positive velocity amplitude, and the decrease of the negative velocity amplitude are apparent.

5 Conclusion

Two fluidic diodes were studied in this paper. The planar geometry of the first one was taken from the literature [20] and the second diode was newly developed. Functionalities of the fluidic diodes were verified by a static experiment, and their diodicities were determined. The diodicity of the first diode showed to be

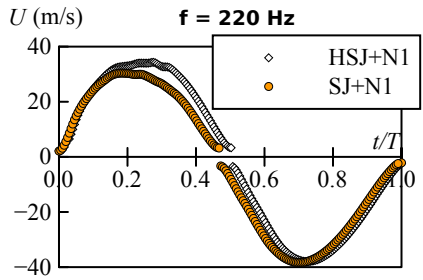

Figure 6: The velocity waveform for HSJA with short nozzle N1.

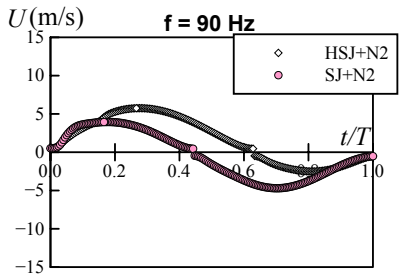

Figure 7: The velocity waveform for HSJA with long nozzle N2 acquired at 90 Hz.

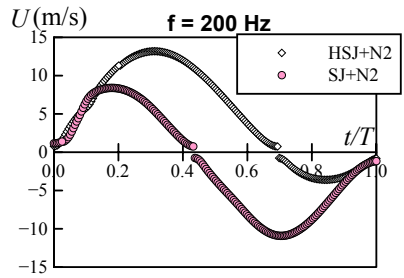

Figure 8: The velocity waveform for HSJA with long nozzle N2 acquired at 200 Hz.

approximately 2.3 and the diodicity of the novel diode was about 3.0 (both at the Reynolds number 6000).

The novel diode was used in the HSJA, which was tested in two variants – with a short nozzle and with a long nozzle. To quantify the quality of the HSJA the volumetric efficiency ε_N (defined in Eq. (2)) was measured. The volumetric efficiency was tested for both variants of the HSJA in the frequency range from 10 to 300 Hz. A very high volumetric efficiency ε_N was achieved for the case with a longer nozzle at the second velocity resonance; the value of the efficiency exceeded 80%.

Acknowledgement

We gratefully acknowledge the financial support of the GAČR P101/12/P556 and GA AV ČR (IAA200760801).

References

[1] Trávníček, Z., Fedorchenko, A. & Wang, A.B., An enhancement of synthetic jets by means of an integrated valveless pump. *Proceedings of the Tenth Asian Congress of Fluid Mechanics (ACFMX)*, ed. J.J. Wijetunge, Peradeniya, pp. 535–540, 2004.

[2] Trávníček, Z., Fedorchenko, A. & Wang, A.B., Enhancement of synthetic jets by means of an integrated valve-less pump Part I. Design of the actuator. *Sensors and Actuators A: Physical*, **120(1)**, pp. 232–240, 2005.

[3] Trávníček, Z. & Vít, T., Hybrid synthetic jet intended for enhanced jet impingement heat/mass transfer. *13th International Heat Transfer Conference IHTC-13*, Sydney, p. 12, 2006.

[4] Trávníček, Z., Vít, T. & Tesař, V., Hybrid synthetic jets as the nonzero-net-mass-flux synthetic jets. *Physics of Fluids*, **18(8)**, pp. 081701–1–081701–4, 2006.

[5] Stemme, E. & Stemme, G., A valveless diffuser/nozzle-based fluid pump. *Sensors and Actuators A: Physical*, **39(2)**, pp. 159–167, 1993.

[6] Gerlach, T. & Wurmus, H., Working principle and performance of the dynamic micropump. *Sensors and Actuators A: Physical*, **50(1-2)**, pp. 135–140, 1995.

[7] Olsson, A., Stemme, G. & Stemme, E., Diffuser-element design investigation for valve-less pumps. *Sensors and Actuators A: Physical*, **57(2)**, pp. 137–143, 1996.

[8] Gerlach, T., Microdiffusers as dynamic passive valves for micropump applications. *Sensors and Actuators A: Physical*, **69(2)**, pp. 181–191, 1998.

[9] Olsson, A., Larsson, O., Holn, J., Lundbladh, L., Ohman, O. & Stemme, G., Valve-less diffuser micropumps fabricated using thermoplastic replication. *Sensors and Actuators A: Physical*, **64(1)**, pp. 63–68, 1998.

[10] Morris, C.J. & Forster, F.K., Optimization of a circular piezoelectric bimorph for a micropump driver. *Journal of Micromechanic and Microengineering*, **10(3)**, pp. 459–465, 2000.

[11] Tesař, V., Hung, C. & Zimmerman, W., No-moving-part hybrid-synthetic jet actuator. *Sensors and Actuators A: Physical*, **125(2)**, pp. 159–169, 2006.

[12] Tesař, V., Trávníček, Z., Kordík, J. & Randa, Z., Experimental investigation of a fluidic actuator generating hybrid-synthetic jets. *Sensors and Actuators A: Physical*, **138(1)**, pp. 213–220, 2007.

[13] Tesař, V., Configurations of fluidic actuators for generating hybrid-synthetic jets. *Sensors and Actuators A: Physical*, **138(2)**, pp. 394–403, 2007.

[14] Trávníček, Z., Tesař, V. & Kordík, J., Performance of synthetic jet actuators based on hybrid and double-acting principles. *Journal of Visualization*, **11(3)**, pp. 221–229, 2008.

[15] Hsu, S.S., Kordík, J., Trávníček, Z. & Wang, A.B., The performance of hexagonally arranged hybrid synthetic jets. *The 7th Pacific Symposium on Flow Visualization and Image Processing*, Kaohsiung, p. 6, 2009.

[16] Trávníček, Z., Tesař, V. & Kordík, J., Double-acting hybrid synthetic jets with trigonally and hexagonally arranged nozzles. *9th International Conference on Fluid Control, Measurements, and Visualization (FLUCOME-9)*, Tallahassee, p. 10, 2007.
[17] Yastrebova, E.V., Fluidic diodes (review). *Automatika i Telemechanika*, **3**, pp. 101–106, 1971.
[18] Bradel, R.L., *The diodicity mechanism of Tesla-type no-moving-parts valves*. PhD. thesis, University of Washington, Washington, 2000.
[19] Forster, F.K. & Williams, B.E., Parametric design of fixed-geometry microvalves-the tesser valve. *ASME International Mechanical Engineering Congress & Exposition, IMECE2002*, IMECE2002-33628: New Orleans, p. 7, 2002.
[20] Gamboa, A.R., Morris, C.J. & Forster, F.K., Improvements in fixed-valve micropump performance through shape optimization of valves. *Transactions of the ASME – Journal of Fluids Engineering*, **127(2)**, pp. 339–346, 2005.
[21] Kordík, J., *Theoretical and experimental analysis of synthetic and hybrid synthetic jet actuators*. PhD. thesis, Czech Technical University, Prague, 2011.

This page intentionally left blank

Section 8
Hydrodynamics

This page intentionally left blank

Superquadratic fluidic restrictors and their applications

V. Tesař
Institute of Thermomechanics ASCR v.v.i., Prague, Czech Republic

Abstract

In a little-known type of flow restrictors the resistance to flow is due to centrifugal force acting on the fluid rotating in a shallow cylindrical chamber into which it enters tangentially. The advantage over other restrictor types is high achievable pressure drop in relation to quite large flowpath cross-sections. The super-quadraticity – which is steeper than the quadratic rise of the pressure drop with increasing flow rate – is an interesting and yet almost unknown property of these restrictors. This paper presents examples of the effect and its applications.
Keywords: flow restrictors, vortex devices, rotating flow, fluidics.

1 Introduction

In view of the general requirements of efficiency it may seem contradictory to common sense to develop and use hydraulic and pneumatic devices having no other purpose than to dissipate the energy of fluid that passes through them. Yet such devices, hydraulic or pneumatic restrictors (general term: fluidic restrictors) are not only useful but actually very important. Their typical application is limiting the discharge of fluid accumulated in a pressure vessel after its sudden opening. Another use is suppression of fluid flow pulsation. Related case is damping mechanical motion converted by a piston transducer into the fluid flow. Yet another use is "gagging" of the inlets into several parallel flowpaths to secure uniform flow distribution into them. There are also numerous applications in sensors: a well-known example is the evaluation of flow rate by measuring the pressure drop across a restrictor.

Presented in Fig. 1 are three different operating principles used for these tasks, named according to the ideal value of the exponent n of their characteristic – the dependence of pressure drop ΔP on volume flow rate

$$\Delta P \sim \dot{V}^n \tag{1}$$

WIT Transactions on Engineering Sciences, Vol 74, © 2012 WIT Press
www.witpress.com, ISSN 1743-3533 (on-line)
doi:10.2495/AFM120441

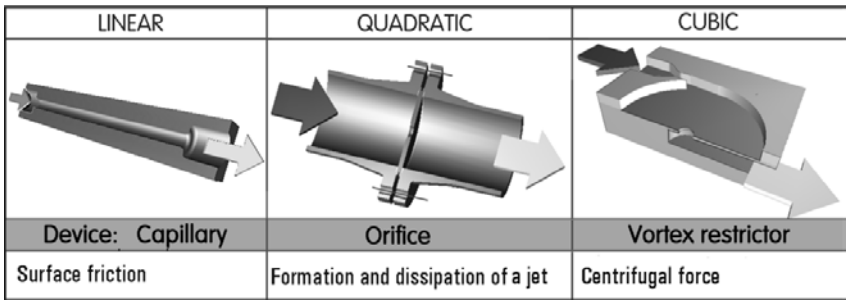

Figure 1: Three basic types of flow restrictors. It is not easy to get characteristics perfectly linear or perfectly quadratic in the well-known capillary or orifice devices, respectively, and equally difficult to achieve is the perfectly cubic behaviour in the less known vortex restrictors.

It is advisable to replace eq. (1) by the dependence between conserved quantities: specific energy drop and mass flow rate

$$\Delta e \sim \dot{M}^{n} \tag{2}$$

Eq. (1) remains nevertheless a convenient choice (because it uses directly measurable quantities) if it is acceptable to neglect compressibility and also the difference in the kinetic energy in the inlet and outlet.

The *linear* characteristic (ideal exponent n =1) of the laminar *capillary*-type restrictors (Fig. 1) is sometimes considered desirable, mainly because the conditions in – and dynamics of – circuits composed of linearly behaving devices are amenable to analytical solutions. Usually, however, the linearity is imperfect, marred by inevitable additional non-linear components of resistance, such as the one caused by the flow development in the capillary entrance or by the formation of a jet in the exit (and the jet energy dissipated further downstream). The condition of laminarity requires small inner diameter d of the capillary, prone to clogging by dirt or by objects carried with the fluid. An also unpleasant property is the ease with which the characteristic varies due to accretion, precipitation, or temperature dependence of viscosity ν. The dissipation is characterised by Euler number

$$\mathrm{Eu} = \frac{\pi^2 d^4 \Delta e}{8\dot{V}^2} \tag{3}$$

For a capillary of length l, Euler number for fully developed flow is

$$\mathrm{Eu} = \frac{64}{\mathrm{Re}}\frac{l}{d} \tag{4}$$

It is usually desirable to have Re as high as is compatible with the laminarity requirement (let us say Re ~ 1000, higher values may lead to sensitivity to disturbances). Manufacturing very long capillaries, longer than about l/d ~ 20, may be difficult. As a result, typical Euler numbers are Eu ~ 1.3.

Less sensitive to the obliteration, temperature changes, and blockage by foreign objects are the *orifice* type restrictors, called *quadratic* in Fig. 1 although their actual value of the exponent n in eq. (2) is usually less than the ideal $n = 2$ due to the inescapable presence of wall friction, negligible only at very high Re, usually above Re ≈ 10 000 (cf. Tesař [1]). Total dissipation of the energy drop Δe converted into the kinetic energy of the jet issuing from the orifice would result in Eu = 1. In real flows, typical values (depending on the orifice shape) of Euler number are around Eu ≈ 1.4 – i.e. of the same magnitude as for the linear restrictors.

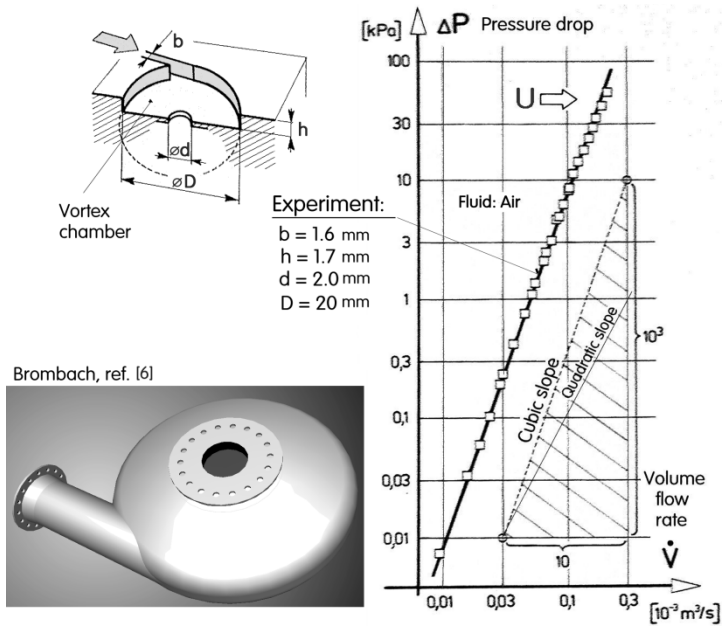

Figure 2: (Top left) Simple vortex-type flow restrictor with single inlet. Fluid enters tangentially the vortex chamber where it rotates at increasing rate as it progresses towards the central exit, opposed by centrifugal effects. (Right) Typical steady-state characteristic of vortex-type restrictor – note the cubic slope in logarithmic co-ordinates. (Bottom left) Clever manufacturing of the largest vortex restrictors: two standard pressure vessel heads welded together. Resultant geometry is not very favourable: chamber height increasing towards the exit tends to slow down rather than promote the rotation.

2 Vortex-type restrictors

This less known class of restrictors was invented by Thoma in 1928 [2] as one of the earliest purely fluidic (no-moving-part) devices, and later was developed in particular by Zobel [3]. While both in linear and quadratic devices the flow

restriction is achieved by dissipating fluid energy *e*, in the vortex restrictors is used an effect actually opposing the flow in the vortex chamber (Fig. 2(top left)). It is the centrifugal force acting against the fluid motion towards the central exit if the fluid in the chamber rotates – which is easily arranged by the tangential orientation of the entrance. It is easy to achieve Euler number values as high as Eu ~ 50 – even values near to Eu ~ 150 are not unheard of. Rotation speed increases as fluid progresses towards the exit as the moment of momentum conservation requires the speed to be inversely proportional to the decreasing radius. Friction effects (mainly in boundary layers formed on the chamber floor and ceiling), however, break the momentum conservation. The friction may dominate at low Reynolds numbers so that for obtaining effective flow restriction, Re should be reasonably high (details: Figs. 5(left) and 11(right)), otherwise the rotation stops (as demonstrated by visualisation in related vortex mixers, Tesař and Low [5]) and the characteristic reduces to a quadratic one. The almost two orders of magnitude higher pressure drop for a given flowpath size makes them the choice for flows having to cope with occasional presence of

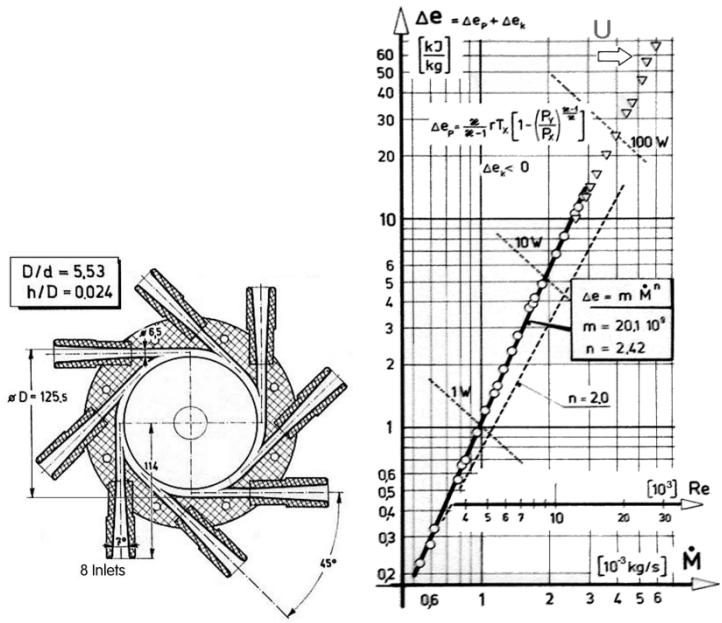

Figure 3: (Left) More tangential inlets ensure symmetry of the vortical flow and thus increase the generated fluidic resistance. Details of this design are in ref. Tesař [4]. (Right) Characteristic – dependence of specific energy on mass flow rate, here in logarithmic co-ordinates – of the design shown in the figure on the left. With its large size, it was possible to reach without compressibility effects a quite high Re and yet there is (as in Fig. 2(right)) the decreased-slope region U at high flow rates.

foreign objects (Brombach *et al.* [6]). Those used in rainwater retention basins, Brombach [7] – an example is shown in Fig. 3(bottom left) – can resist high pressure drops while the physical dimension of their smallest cross sections are large enough to be not blocked even by objects as large as dead small animals, not infrequently carried with the rainwater.

Not only typical values of Eu in vortex type restrictors are very high – they were found to increase with increasing flow rate, which is the very opposite to the typical decrease of Eu with increasing Re in most other fluidic devices.

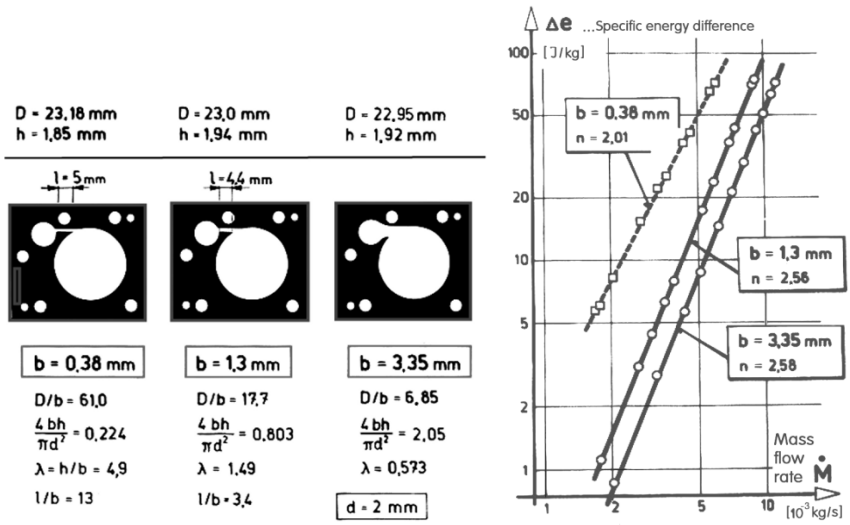

Figure 4: (Left) Experimental tests of influence of the tangential inlet width *b*. Right) Characteristics obtained with the three plates shown in the figure on the left demonstrate the negligible effect of the width b on superquadraticity – unless the inlet is extremely wide, apparently leading to too slow rotation in the chamber.

3 Superquadratic behaviour

This increase of Eu with increasing Re is the *superquadratic* behaviour (Tesař [8], Brombach [9]), originally found in experiments with the small, shallow-chamber, single-inlet restrictor shown in Fig. 2(top left). The exponent *n* (eq. (1)) had the cubic law value $n = 3$ across several decimal orders of the pressure drop (Fig. 2(right)). This was and still remains rather surprising, in view of the otherwise almost ubiquitous quadratic behaviour in fluidics. Those few (extremely rare) other examples of superquadratic behaviour were known so far only in a narrow Reynolds number range, since they are usually associated with transition between two regimes - and therefore tend to be unstable.

Later, the phenomenon was again found to be present (though mostly unnoticed) in many devices of the vortex type, irrespective of the size or the number of inlets (Fig. 3). In many cases, e.g. in the domed shapes like that in

Fig. 2(right), the exponent may be only slightly above $n \sim 2$. The data presented in Figs. 4, 5 and 10(left) were collected in (unproductive) search for an exponent n higher than the cubic law value $n = 3$. The experiments involved systematic variations of the three geometric parameters *b/D*, *h/D*, and *d/D* in a design according to Fig. 2(top left). While *b/D* is seen in Fig. 4 to have a negligible influence – as has also the number of inlets, Fig. 3 (as long as this does not make the entrance velocity too slow, as is the case $b = 0.38$ mm in Fig. 4(left)) – the variations of *h/D*, and *d/D* did lead to changes in the exponent *n* (Figs. 5(right), 10(left)), but with the conclusion that the value $n = 3$ is actually the achievable maximum that was chosen fortuitously in the initial experiment.

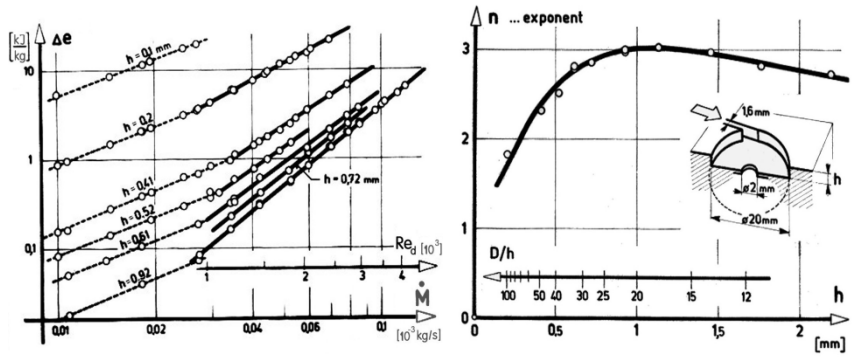

Figure 5: (Left) Characteristics obtained in testing the influence of the chamber height *h*. Loss of superquadraticity is found at very low Re where friction stops the rotation. (Right) Cubic behaviour (*n*=3) was the limit found near $h \sim 20\ D$.

4 Significance for possible applications

Potential uses of the rapid build-up of pressure with increasing flow rate in superquadratic devices are numerous and often quite interesting, though not widely known. The more rapid rise of the pressure across the vortex chamber with increasing flow rate shown in Fig. 6 makes possible more precise flow rate measurement (or relaxed demands on the manometer), Tesař [11]. Another particularly sensitive flow rate measurement method with the vortex restrictor was described by Tesař in [12]. Another use is the gagging of the entrances into parallel evaporator tubes, Tesař [13], to counter the instability associated with the segment of negative slope (Fig. 7(left)). The advantage gained by the cubic characteristic is reduction of the overall pressure (and therefore the input power) required for driving the fluid through the system. In [14] Tesař describes the advantages offered by superquadratic flow restrictors in shock absorbers.

Useful applications were also found for the series connection of the vortex restrictor V with standard orifice-type quadratic restrictor R, as shown in Figs. 7(right) and 8(left). The experimental results presented in Fig. 8(right) demonstrate that the ratio of their pressure drops varies in the perfectly linear manner with the flow rate passing through both devices. Obviously, the

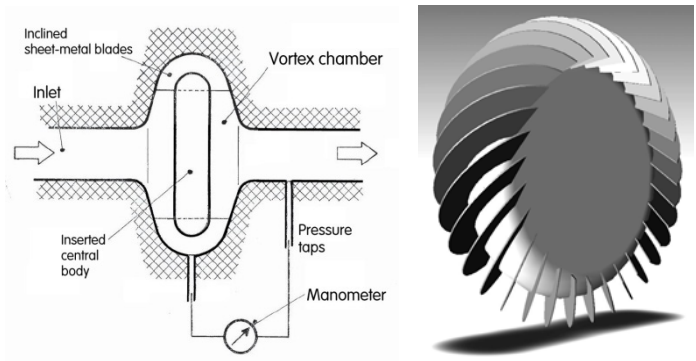

Figure 6: (Left) Flowmeter with vortical flow generated by inclined vanes inserted into slits of the central body circumference. Superquadraticity increases the measured pressure drop. (Right) The central body with simple plane vanes (they may be bent to evade separation on the leading edges).

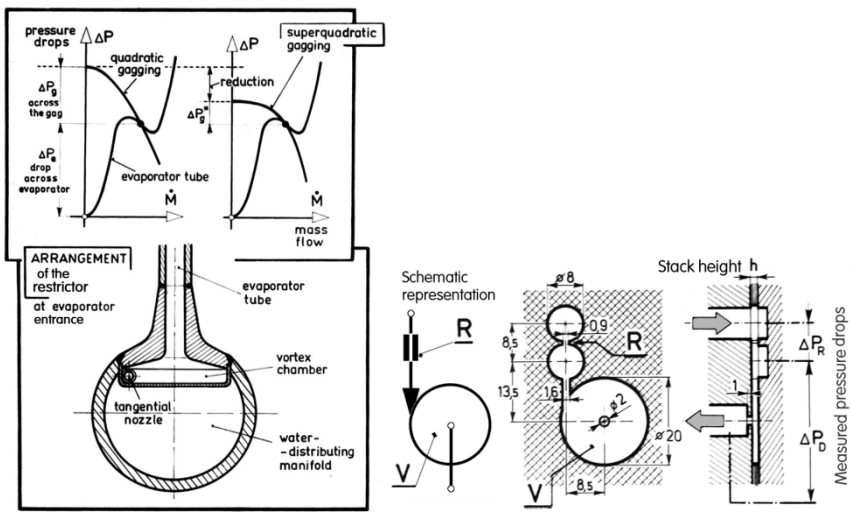

Figure 7: (Left) Inlets into the evaporator tubes. Instability due to negative slope in a part of evaporator characteristics is eliminated by gagging, superquadraticity reduces the pressure delivered by the supply pump. (Right) Series-connected quadratic restrictor R and the vortex restrictor V as they were used in the tests (dimensions in millimetres).

deviations from the ideal $n = 3$ of the vortex valve V and from $n = 2$ of the orifice R cancel mutually so that the slope of the ratio is constant over at least a decimal order of flow rate magnitude. Tesař [15] describes the use of this linearity in a sensor employing the property of resistance ratios in a Wheatstone bridge.

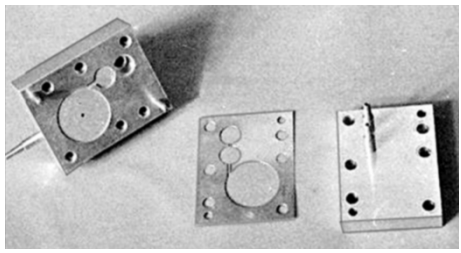

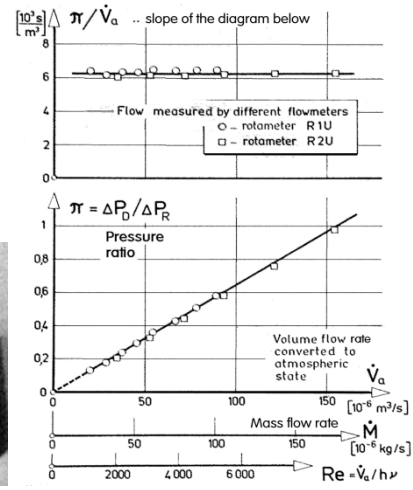

Figure 8: (Left) Photograph of laboratory model containing the two different restrictors according to Fig. 7(left). They were made in a stack of thin foils so that it was possible to change the height h by varying the number of foils in the stack. (Right) Experimental results obtained with the pair of restrictors in series shown in Fig. 7(left). Ratio of the pressure drop ΔP_D across the vortex-type restrictor V to ΔP_R across the orifice-type restrictor R varies in strictly linear manner with the flow rate passing through the two devices as if their characteristics were purely cubic and purely quadratic, respectively. Apparently, deviations from the ideal power laws cancel themselves in evaluation of the ratio.

Perhaps even more useful is the other connection – the parallel one – of the pair of restrictors V and R, as shown schematically in Fig. 9(right). The different properties cause a change in the ratio of the two output flows if the pressure increases. The outputs may be connected to the inputs of a fluidic jet-deflection amplifier, which then reacts by generating an amplified output signal indicating (with proper sign) the deviation from a desirable condition (zero difference set by adjusting the orifice restrictor). The layout may be actually simpler than suggested by the schematic representation since the role of the orifice resistor R may be fulfilled by any component already present in the system (due to the usual quadratic hydrodynamic characteristics). The advantage of this method of sensing the deviations from a desired flow rate (or pressure) is the robustness (operation, e.g., at a high temperature), low cost (just a shallow cylindrical cavity is all that is necessary) and no need for bringing electricity to the sensor.

Described in Tesař [16] is the extremely simple, no-moving-part regulator used to keep a constant total regulated flow. This bifurcates into the parallel-connected R and V restrictors, as shown in Fig. 9(right). The difference in the flow rates, Fig. 9(left), is used in the vortex amplifier valve [17, 18] – the third component of the regulator, besides the resistors V and R. The tangential inlet

flow into the vortex amplifier, passing through the quadratic-behaving nozzle e, increases with increasing total flow more rapidly than the radial inflow so that the total flow is turned down. Without a feedback, the control effect is only approximate, but the advantage is the extreme simplicity (with consequent low cost) and robustness. A similar pressure regulator may be built on the same principle, with just interchanged radial and tangential inlets into the vortex valve. This was described as a part of a fuel flow control device in Tesař [19].

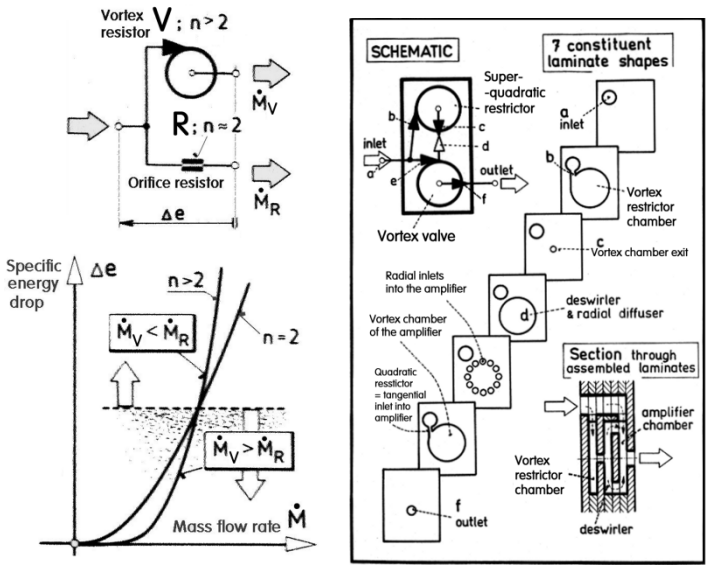

Figure 9: (Left) Schematic representation of orifice-type R and the vortex-type V restrictors in parallel and (below) their intersecting characteristics. Above the intersection more fluid passes through the quadratic restrictor. Below that point the fluid prefers flowing through the vortex device. (Right) The principle described in the figure on the left applied to control of a vortex amplifier valve keeping (in an open-loop control) a constant total flow passing through the set of 7 plates in which the circular holes form the flow regulator.

5 Transition into the rotation-less regime K

In the early stages of the search for high values of the exponent *n* (before the experience has shown the cubic case is the extreme, Figs. 5(left) and 10(right)) it was believed that high *n* may be obtained by extremely vigorous rotation in the vortex chamber produced by extreme ratios of vortex chamber diameter *D* to the exit diameter *d*. The model made for these tests is shown in Fig. 10(right). The disillusion learned is apparent in the results presented in Fig. 11: the large shallow chamber only resulted in dominance of friction, which limits the

superquadratic behaviour to the range of Reynolds number above the transition at Ⓣ. Tests with increasing *d/D* did not result in the high exponent but just in a removal of progressively higher Reynolds numbers from the useful operating region.

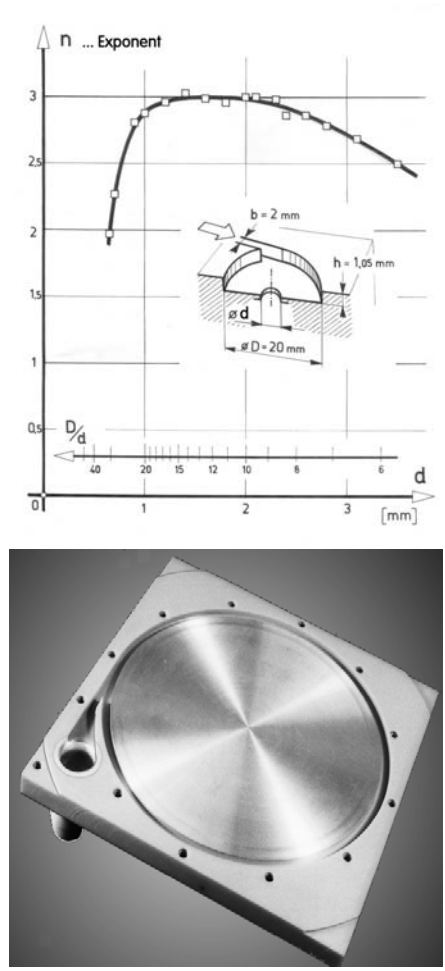

Figure 10: (Left) Dependence of the exponent *n* on the exit diameter *d* of the basic restrictor as shown in Fig. 2(top left). (Right) Restrictor model design made for experiments with large ratio of vortex chamber diameter *D* to exit diameter *d*. The exit is not visible in this photograph as it is in the top (removed) part of the body. The groove on the periphery of the vortex chamber was intended to improve the flow symmetry.

6 Upper limit: regime U

Closer investigations of vortex restrictor characteristics have revealed that the cubic or near-cubic region, despite the wide range of Reynolds numbers in which it was found, is not only limited by the transition at Ⓣ at small flow rates but has also a limit at high flow rates. An onset of deviation U from the behaviour was already found at the upper end of the range of experimental conditions in the earliest tests as shown in Fig. 2(right). This effect is not very prominent – in fact, the behaviour remains superquadratic. The deviation was initially thought to be a mere experimental imperfection, but plotting in terms of Eu (Fig. 12(left)) has shown it to be a systematic phenomenon. Because it was found always at very high pressure drops ΔP, necessary to force the large flow through the small models (e.g., Fig. 2(right)), an explanation was later sought in compressibility. Only after the effect was investigated in detail by numerical flowfield computations

(Fig. 12(right)) and by evaluation of circulation Γ (by a method analogous to the one used in Tesař and Low [5]) this upper-limit transition was explained to be the consequence of the vortex breakdown.

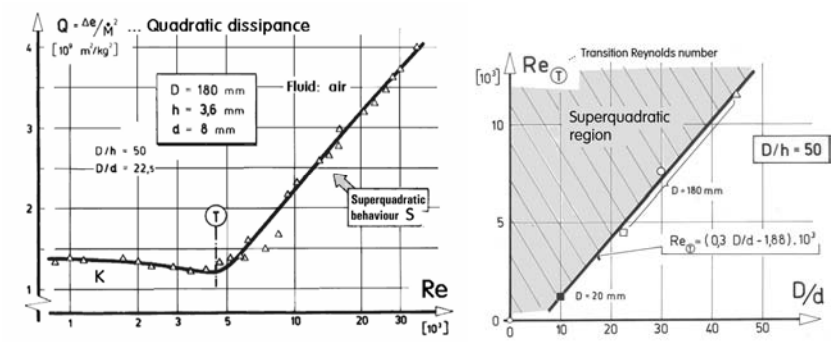

Figure 11: (Left) An example of results obtained with the model shown in Fig. 10(right). The superquadratic behaviour was found only above the transition at Ⓣ – below which there is the more or less quadratic regime K. (Right) Instead of resulting in extremely high values of the exponent *n* as originally expected, the very small diameters *d* of the exit resulted in large Reynolds number of the transition.

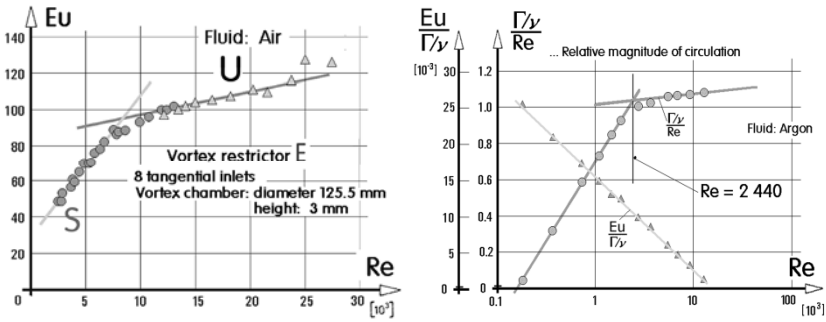

Figure 12: (Left) Dependence of Euler number Eu on Re evaluated for the design from Fig. 3(left) shows clearly the transition into the U flow regime characterized by less steep Eu growth with increasing Re. (Right) Circulation Γ in the vortex chamber exit (argon was used to simulate uranium hexafluoride, less pleasant to work with) shows transition into the U flow regime. The change ceases to become discernible when the circulation is non-dimensionalised with respect to Euler number.

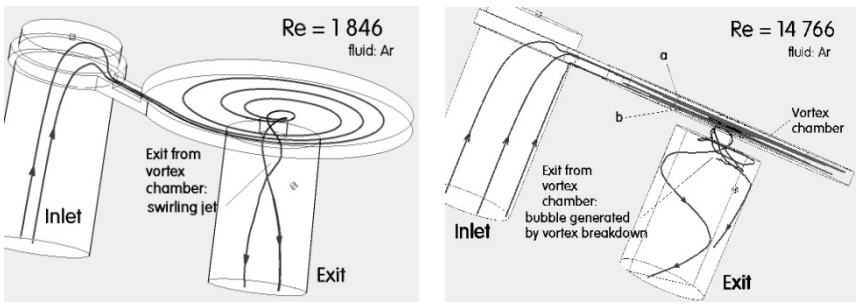

Figure 13: (Left) Computed pathlines for the basic superquadratic flow regime: fluid leaves the vortex chamber exit as a narrow swirling jet.(Right) Pathlines for very high Re flow regime U. There is a vortex breakdown bubble immediately downstream from the exit. Also interesting is the separation of the arbitrarily chosen pathlines into the upper a and lower b flow through the chamber, indicative of the fluid passing through the boundary layers.

7 Conclusions

Vortex type restrictors and their interesting properties are not as much known and used as they deserve. The paper focuses one of their properties: the superquadratic behaviour, which offers a number of particularly useful application possibilities.

Acknowledgements

Gratefully acknowledged is the support by the research plan AV0Z20760514, by grants TA02020795 from TAČR as well as P101/11/J019 donated by GAČR.

References

[1] Tesař V., *Characterisation of subsonic axisymmetric nozzles*, Chemical Engineering Research and Design, Vol. 86, Issue 11, p. 1253, 2008.
[2] Thoma D., *Fluid lines*, U. S. Patent No. 1,839,616, 1928.
[3] Zobel R., *Experiments on a hydraulic reversing elbow*, UKAEA Risley Transl. into English, No. 439, Mitteilungen des Hydr. Inst., Munich, Germany, Vol. (Bd.) 8, p. 1, 1936.
[4] Tesař V.: F*luidics: the answer to problems of handling hazardous fluids* , Proc. of 4th Int. Conf. SAFE IV, p. 465, Antwerp. 2011.
[5] Tesař V., Low Y.Y., *Study of shallow-chamber vortex mixers for micro-chemical applications*, Proc. of 9th Internat. Symp. on Flow Visualization, Edinburgh, paper No. 445, 2000.
[6] Brombach H. *et al.* Energieabbau mit Wirbeldrosseln in einer Waschwasser-rohrleitung eines Kalksteibruches, 3R International, Heft 5, p. 330, 1989.
[7] Brombach H., *Flood protection by vortex valves*, Journal of Dynamic Systems, Measurement, and Control, ASME, Vol. 3, p. 338, 1981.
[8] Tesař V., *Superquadratic behaviour of vortex diodes*, Proc. of IFAC Symp. 'Pneumatic and Hydraulic Components.' Warsaw, Poland, p. 79, 1980.
[9] Brombach H., Diskusionsbeitrag zum Aufsatz G. Koplitz-Weissgerber: Berechnungsverfahren für kreisformige Wirbeldrosseln, in German, Wasserwirtschaft Bd. 71, Nr. 7+8, p. 218, 1981.
[10] Kotowski A., Wójtowicz P., *Analysis of hydraulic parameters of cylindrical vortex regulators*, Environment Protection Engng., Vol. 34, p. 43, 2008
[11] Tesař V., *Apparatus for measurement of fluid flow*, Czechoslovak Patent No. 195802, filed 31st Aug. 1977.
[12] Tesař V., *Connection of a jet-type flow sensor*, Czechoslovak Patent No. 195116, filed 20th Sept. 1977.
[13] Tesař V., Gagging of the inlet of liquid into evaporator tubes of a steam generator, Czechoslovak Patent No. 192856, 1st Sept. 1977.
[14] Tesař V., Setup for damping fluid flow and of mechanical motion converted into fluid flow, Czechoslovak Patent No. 212574, filed 30th Nov. 1979.
[15] Tesař V., *Ways of evaluating fluid flow and means for performing it*, Czechoslovak Patent No. 202 201, filed 1st Sept. 1977.
[16] Tesař V., *Fluid flow regulator*, Czechoslovak Patent No. 186043, filed 20th Oct. 1976.
[17] Wormley D.N., *An analytical model for incompressible flow in short vortex chambers*, Trans. of ASME, Journ. of Basic Engineering, p. 264, 1969.
[18] Tesař V., *Pressure-driven microfluidics*, Artech House Publ., USA, 2007.
[19] Tesař V., *Ways and means for generating a small controllable liquid flow*, Czechoslovak Patent No. 186614, filed 28th Dec. 1976.

This page intentionally left blank

Numerical analysis of the circulation variability in the Zadar channel area (east Adriatic)

G. Lončar[1], G. Beg Paklar[2] & V. Andročec[1]
[1]*Faculty of Civil Engineering, Water Research Department, University of Zagreb, Croatia*
[2]*Institute of Oceanography and Fisheries, Split, Croatia*

Abstract

Three numerical hydrodynamic models, ROMS, POM and MIKE 3 FM, were used to simulate circulation variability in the middle Adriatic coastal area. ROMS and POM models were used to perform a year-long simulation of the Adriatic circulation with the spatial resolution of approximately 2 km. Temperature, salinity and sea level fields, obtained by the ROMS model, were used for the initial and boundary conditions in the MIKE 3 FM local domain covering the channel area off Zadar. A similar area was covered with the POM local domain nested within the shelf and Adriatic-scale POM models using three-dimensional velocity, temperature and salinity fields, as well as two-dimensional sea level fields from coarser resolution grids. Current fields obtained by both modelling systems are in agreement with the ADCP measurements performed in the area of the local models. During winter northwestward currents dominate in the surface layer, while in the lower layers of the channel topographically controlled gyres can be observed. Both measurements and numerical simulations indicate current reversal to southeastern direction in the coastal area off Zadar during summer.
Keywords: hydrodynamic models, ROMS, POM, MIKE 3 FM, wind-induced currents, tidal currents, ADCP measurements, Adriatic Sea, Zadar.

1 Introduction

Croatian coast of the Adriatic Sea has complicated coastline and bathymetry with more than 1200 islands, innumerable channels, bays and inlets. Such complex geometry severely influences the coastal circulation mainly driven by

WIT Transactions on Engineering Sciences, Vol 74, © 2012 WIT Press
www.witpress.com, ISSN 1743-3533 (on-line)
doi:10.2495/AFM120451

meteorological and hydrological forcings. Although occasionally in some parts of the eastern coastal strip tidal currents and buoyancy-driven circulation can be important, in general these current components tend to be secondary in comparison with wind-induced motions [1].

Physical processes in the middle Adriatic coastal area were studied within several national and international projects. The Zadar and Pašman channel area was investigated during early nineties due to the planned implementation of the public sewage system. Temperature, salinity and current measurements were made during two campaigns, the first one in June/July and the second one during August/September 2004, focused on the near coastal area. Although the main goal of Vilibić and Orlić [2] investigation were surface seiches and internal Kelvin waves in the Zadar and Pašman channel, they also calculated and discussed tidal, wind-induced and residual circulation. Tidal dynamics in the wider Zadar area is particularly interesting because of its close position to the Adriatic semidiurnal amphydromic point [3]. Wind-driven currents in the channel are predominantly baroclinic during summer and two-layer response was clearly observed during strong sirocco episode. Similar result describing wind influence on the currents was obtained by Leder *et al*. [4]. Residual currents were oppositely directed during two campaigns, and the reversal was related to the meteorological activity. The interesting feature of the residual dynamics was cyclonic and anticyclonic gyres, controlled by topography. Three-dimensional model [5] developed for the area off Zadar agreed with measurements and moreover indicated that vertically averaged currents at the basin mouth formed an anticyclonic gyre during a bora episode and a cyclonic gyre when sirocco wind blows.

Measurements in the open sea area off Zadar and Pašman channel were performed within international project 'East Adriatic Coastal Experiment' (EACE). Two maxima detected in the East Adriatic Current, the first one during winter and the second one during spring, were related to the water and heat air-sea fluxes, respectively [6]. Wind-induced currents were barotropic during winter and baroclinic during spring due to different stratification and stability conditions.

This paper gives insight into the numerical modelling of the circulation in the channel area off Zadar (Fig. 1) made within 'The Adriatic Sea monitoring program' during 2007 and 2008 [7]. Since the objective of the Program was the development of an efficient monitoring system and supporting models for the Adriatic coastal waters, besides modelling, Program also comprised extensive oceanographic measurements within the Croatian territorial waters. Two modelling systems were developed during the Program: the first one consisted of the Regional Ocean Modeling System (ROMS) [8, 9] and MIKE 3 FM [10] models, while the other one was made of nested Princeton Ocean Model (POM) [11] models. In the following second section of the paper the basic characteristics of both modelling systems will be described. The third section presents the results of the modelling and their comparison with measurements, while final fourth section brings brief discussion and conclusions.

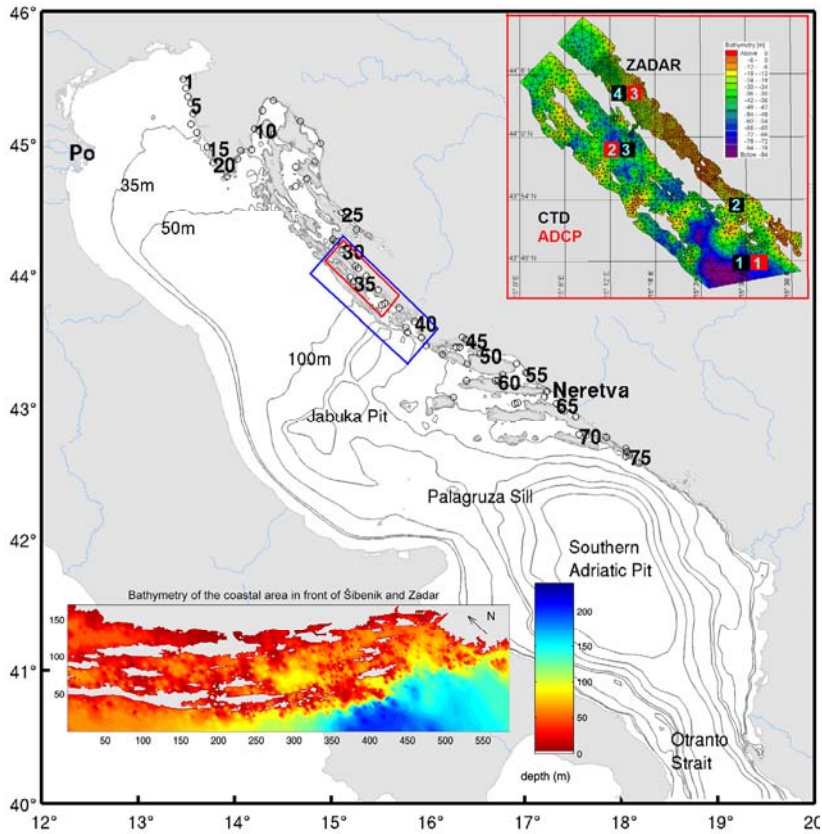

Figure 1: Spatial domain of the Adriatic-scale POM and ROMS models with MIKE 3 FM and POM local spatial domain. Monitoring sites are denoted with circles.

2 Numerical models implementation

Circulation variability in the middle Adriatic coastal area was reproduced with two nested modelling systems. The first one was made of the Adriatic-scale ROMS model and MIKE 3 FM applied for the local domain off Zadar. The second modelling system was made of three nested POM-based models: the Adriatic-scale model, shelf model and local POM model. POM and ROMS models are finite difference, terrain-following, primitive equation models. On the other hand, MIKE 3 FM is a finite volume model with sigma vertical component. In the application for the channel area off Zadar MIKE 3 FM uses unstructured horizontal grid with resolution ranging from 2 km at the outer part of the domain up to 150 m close to the coast.

As a first step in the modelling, the Adriatic Sea dynamics has been simulated with two three-dimensional nonlinear sigma models: POM and ROMS for the

period between November 2007 and October 2008. Both models had almost the same setup which allowed for a reliable comparison between their results. In a year-long simulation numerical models were forced with atmospheric, river and tidal forcing. Atmospheric forcing for the ocean models was calculated from the output fields of the meteorological mesoscale model ALADIN [12] having 8 km horizontal resolution and 3 hour resolution in time using standard bulk formulation. The ALADIN model has been used for operational purposes at the Meteorological and Hydrological Service of Croatia and, in particular, it has been applied for studying the mesoscale environment in which severe winds in the Adriatic region occur [13, 14]. Used (Croatian version) of the operational ALADIN is run on a domain which covers the Adriatic region together with the surrounding orography of the Alps, the Dinaric Alps and the Apennines [15]. Influence of 48 Adriatic rivers in the ROMS and POM domains has been defined through the climatological data according to Raichich [16] with the exception of Po and Neretva Rivers where hourly averaged measured values of discharges and temperatures were utilized. Tidal function was applied on the southern open boundaries of both models at the Otranto Straight for denivelation and transport using seven harmonic constituents – M2, S2, N2, K1, O1 and P1, while radiation condition was applied for the three-dimensional current field. Both Adriatic-scale models had horizontal resolution of approximately 2 km while along vertical 22 and 30 sigma layers were defined for POM and ROMS, respectively (Table 1). POM and ROMS models used also the same initial conditions. Both models were initialized with mean summer fields of temperature and salinity on standard oceanographic levels from Dartmouth Adriatic Data Base (DADB) [17].

Table 1: Implemented numerical models and numerical simulations.

Model	Period	Horizontal resolution	Vertical resolution
Adriatic-scale POM	15 October 2007 – 15 October 2008	2.5 km	22 sigma layers
Middle Adriatic-shelf POM	17 February – 13 March 2008	1 km	16 sigma layers
	17 July – 16 August 2008		
Local POM	17 February – 13 March 2008	200 m	16 sigma layers
	17 July – 16 August 2008		
Adriatic-scale ROMS	15 October 2007 – 15 October 2008	2 km	30 sigma layers
MIKE 3 FM	17 February – 13 March 2008	150 – 2000 m	20 sigma layers
	17 July – 16 August 2008		

The results obtained from Adriatic-scale models were used to define open boundary conditions for the fine resolution models embedded along the eastern coast using one-way offline nesting procedure. Temperature, salinity and surface elevations calculated with ROMS model were extracted, interpolated and implemented on the open boundaries of the MIKE 3 FM model. On the other

hand, open boundary conditions of the local POM model are defined through direct nesting with inclusion of all hydrodynamic fields: temperature, salinity, current velocity and surface elevation using procedure described by Zavatareli and Pinardi [18]. Initial conditions for the local models were defined according to the corresponding Adriatic model results. Atmospheric and river forcings in the fine resolution models were defined in the manner described for Adriatic models. Simulations covered the periods 17/2/08-13/3/08 and 17/7/0-16/8/08 by both of the local models. The spatial resolutions used in MIKE 3 FM and POM shelf and local models together with simulation periods are shown in Table 1.

During the modelling periods oceanographic parameters were measured within territorial water of the Republic of Croatia. Oceanographic sites were divided into groups in accordance with measured parameters: current meter sites and CTD sites (Fig. 1). Measurements undertaken on CTD verticals were used for calibration and validation of ROMS and POM Adriatic models, while currents measured at ADCP sites were used for the comparison with local models results.

3 Modelling results and comparison with measurements

Surface mean monthly current fields obtained by the POM model show significant resemblance with the corresponding fields from ROMS. Although considerable variability can be observed in the modelled current fields, they also indicate some common features in accordance with well-known characteristics of the Adriatic-scale circulation. General circulation is cyclonic with several imbedded, mostly cyclonic gyres. Two cyclonic gyres are around the main pits – South Adriatic and Jabuka Pit, and one can be observed in the northernmost part of the Adriatic. Current fields in the winter period resemble bora induced current fields [19], indicating bora wind as an important driving mechanism for the Adriatic general circulation. Current intensities during summer decreased and numerous small-scale eddies appeared. South Adriatic cyclonic gyre is present in all monthly current fields but with variable intensities. Cyclonic gyre above the South Adriatic Pit is a well-known characteristic of the Adriatic circulation and it is supposed to be topographically controlled by the South Adriatic Pit and Palagruža Sill. The main difference between POM and ROMS monthly averaged fields is manifested through the current intensity, mainly in jet currents. They are attached to the outer boundary of the Croatian outer islands, as well as through the intensity of the cyclonic South Adriatic gyre.

Calibration of ROMS and POM Adriatic models is referenced to the results of the CTD measurements at the positions of the oceanographic stations 1-75 (Fig. 1). Comparison of the modelling results with measurements during winter simulation period at the oceanographic stations 1–4 (Zadar area, Fig. 1) is presented in Fig. 2. Generally, deviations of the POM model results from the temperatures measured in March 2008 are less than 1°C and both modelled and measured temperature profiles shows vertical homogeneity typical for the winter season. Maximal model deviations from the salinity measurements are 1 psu in the surface layer of all stations, while modelled and measured salinities are in

better accordance in the bottom layer. Modelled temperature and salinity profiles for the summer period show stronger departures from the measured values if compared to the winter profiles, with lower agreement in the vertical structure and higher absolute differences. Simulated values of both temperatures and salinities are in agreement with their realistic values for summer in the coastal Adriatic area, but stronger homogeneity in the model results is suggesting too strong vertical mixing in the POM model. Generally, better agreement between modelled and measured thermohaline properties is obtained in the northern Adriatic in comparison to the middle and southern coastal areas. High correlation between measured and modelled temperature and salinity profiles is obtained also with ROMS model, particularly in simulations with more realistic initial and open boundary files from operational model [20].

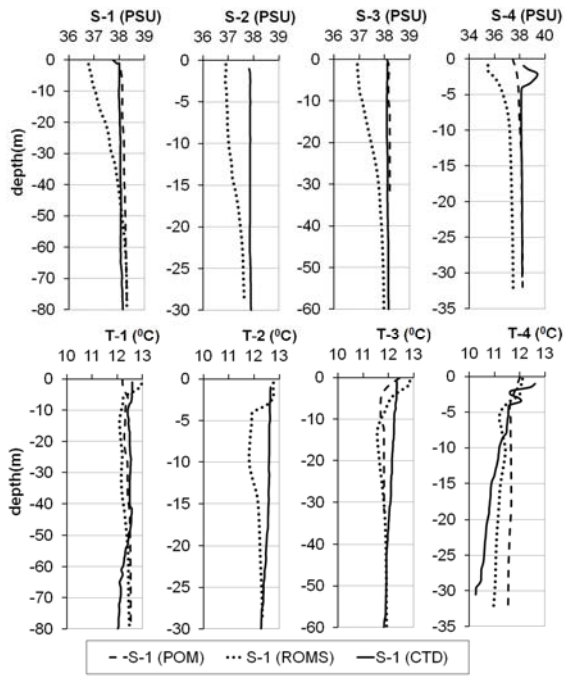

Figure 2: Comparison of measured (CTD) and model (ROMS, POM) verticals for T, S (13 March 2008).

Both local models reproduced almost homogeneous northwestern flow in the surface layer during winter (Figs. 3 and 4). Current intensities in the lower layers are reduced and in the outer part of the POM domain flow is northwestward while in the channel topographically-controlled gyres are present. Similar structures cannot be seen in the MIKE 3 FM results. Modelled current vectors agree well with measured monthly means directed toward northwest [7]. Modelled and measured current components indicate the importance of the tidal signal in the

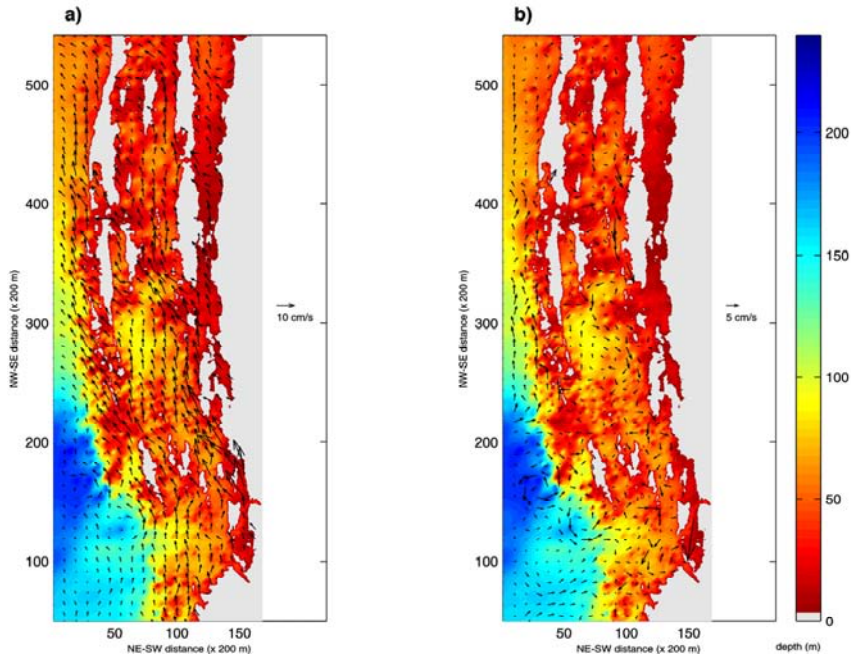

Figure 3: Current fields in the Zadar-Šibenik area at 8 (a) and 26 m (b) during winter obtained by local POM model.

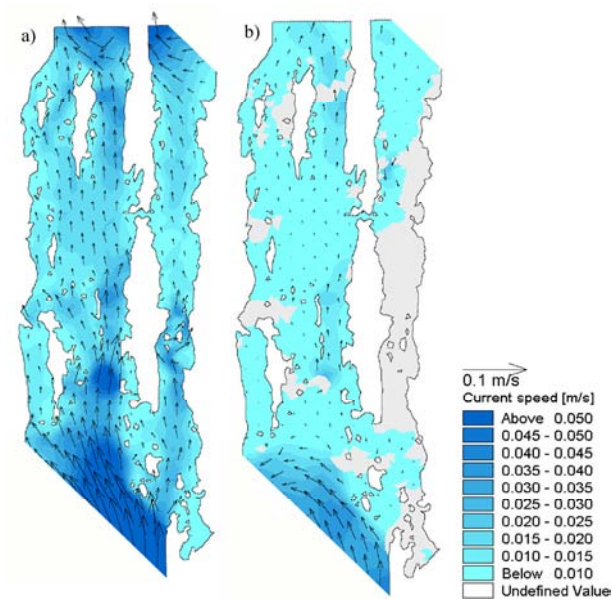

Figure 4: Current fields in the Zadar-Šibenik area at 8 (a) and 26 m (b) during winter obtained by MIKE 3 FM model.

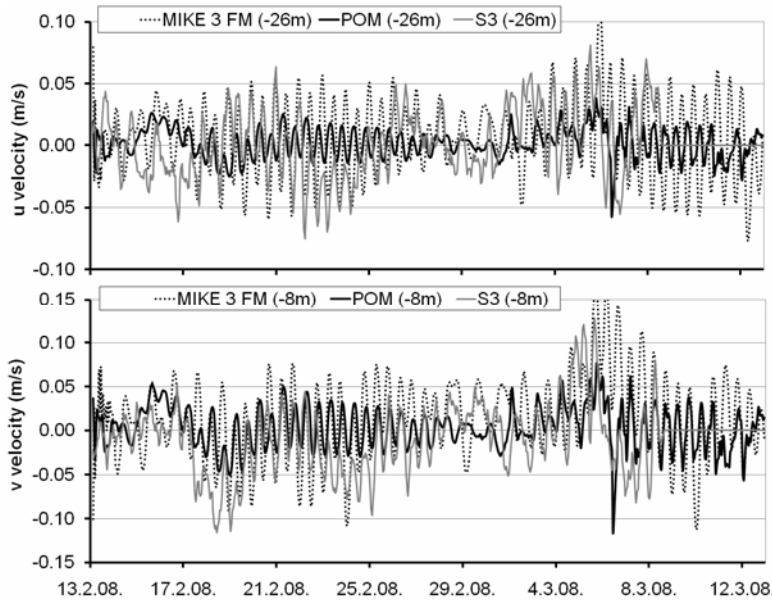

Figure 5: Comparison of the measured and modelled hourly averaged current velocity components at the ADCP site S3 at the depth of 8 m.

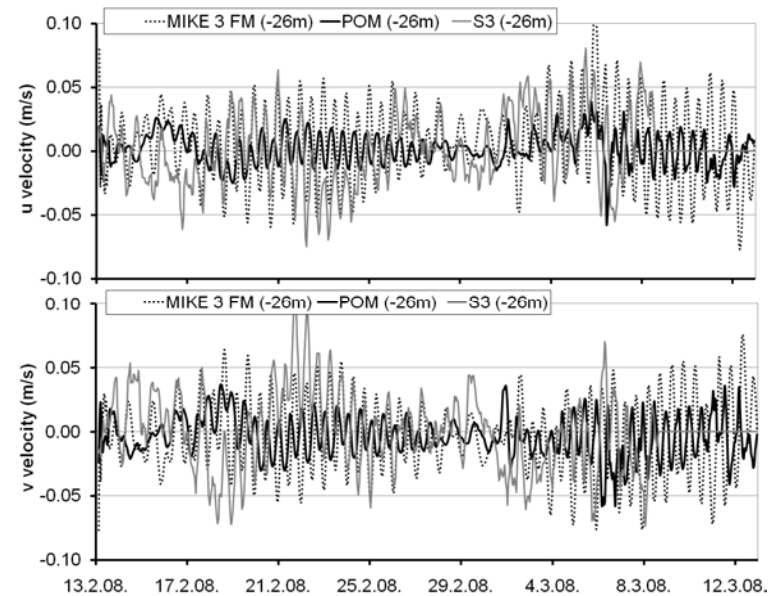

Figure 6: Comparison of the measured and modelled hourly averaged current velocity components at the ADCP site S3 at the depth of 26 m.

studied channel area during winter (Figs. 5 and 6). POM modelled current component time series show well reproduced bora influence at ADCP station 3. Bora started on 5 March and induced downwind current in the surface layer.

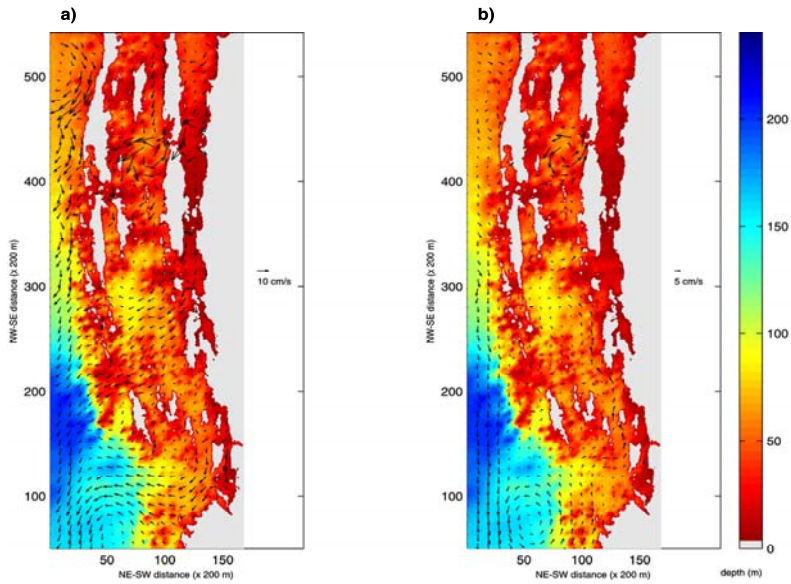

Figure 7: Current fields in the Zadar-Šibenik area at 8 (a) and 26 m (b) during summer obtained by local POM model.

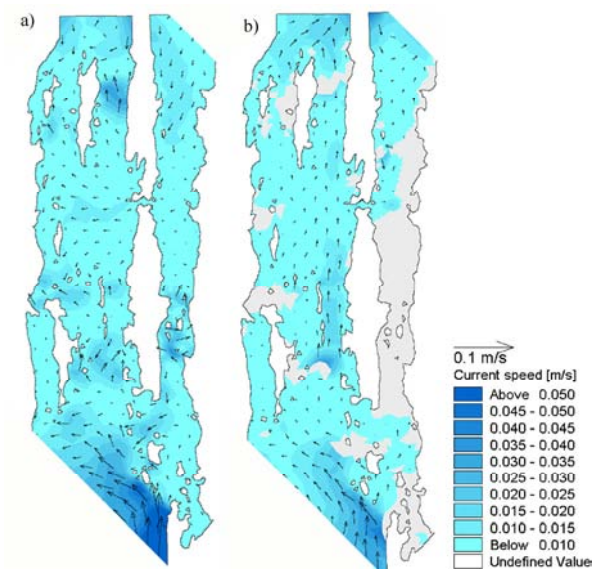

Figure 8: Current fields in the Zadar-Šibenik area at 8 (a) and 26 m (b) during summer obtained by MIKE 3 FM model.

Dominant southeastern flow can be observed in the outer part of the POM model domain during summer simulation period. MIKE 3 FM reproduced southeastern flow in front of the mainland. Occurrence of the southeastern flow in the modelled fields is in agreement with measurements. Mean monthly current vector obtained at ADCP station 2 is also of southeastern direction during August 2008 and it is related to the intensive winds from northeast and northwest. As well as during winter, tidal signal is important component of the current field and it is well reproduced by both models.

4 Conclusions

Sea temperature, salinity and current fields in the eastern Adriatic coastal region are resolved through implementation of numerical models ROMS, POM and MIKE 3 FM. ROMS and POM were used for the hydrodynamic analysis on the whole Adriatic area with the spatial resolution of approximately 2 km. The results of that analysis were used to generate the initial and boundary conditions for nested local domains covering the part of the middle Adriatic channel system in the vicinity of the city of Zadar.

In the scope of the work presented in this article, ROMS and POM models applied on the Adriatic scale both had the same setup. The comparison of results revealed that both models could successfully reproduce basic characteristics of the Adriatic circulation: global cyclonal flow with series of smaller, mostly cyclonal vortexes. Furthermore, current fields modelled by ROMS and POM indicate major similarity on a monthly scale, though in some areas differences appear. Main difference between POM and ROMS monthly averaged current field is manifested through the current velocity intensities, mainly in jet currents that are attached to the outer boundary of the Croatian outer islands, as well as through the intensities of the cyclonic South Adriatic gyre. Since unfortunately current measurements in the open sea area were not performed during periods of the simulations, modelled circulations could not be verified and it was impossible to say which model gave better results on the Adriatic scale. Evaluation of the Adriatic models was made with CTD measurements. Modelled temperature and salinity profiles are of acceptable accuracy with errors increasing from north to south Adriatic and during heating season.

Validation of the local models POM and MIKE 3 FM with results of the ADCP measurements indicate acceptable agreement for both modelling systems. During winter season modelled currents in the outer part of the POM domain are northwestward along the whole water column. In the channel area surface currents are also northwesteward during winter simulation period, while topographically controlled gyres can be observed in the lower layers of the POM model results. Both measurements and numerical simulations indicate current reversal to southeastern direction in the coastal area off Zadar during summer. Moreover, current measurements and model results point to the dominance of the tidal signal off Zadar during both winter and summer.

Increased accuracy of both nested modelling systems could be attained by using higher resolution of the atmospheric forcing, implementation of the

realistic river discharges instead of the used climatological values and by solving the open boundary conditions with nesting of the Adriatic scale models with one of the operational Mediterranean systems.

References

[1] Orlić, M., Croatian coastal waters. In *Physical Oceanography of the Adriatic Sea: Past, Present and Future*, ed. Cushman-Roisin, B., Gačić, M., Poulain, P.M. and Artegiani, A., Kluwer Academic Publishers: Dordrecht, Boston, London, pp. 189-214, 2001.

[2] Vilibić, I. and Orlić, M., Surface Seiches and Internal Kelvin Waves Observed Off Zadar (East Adriatic). *Estuarine, Coastal and Shelf Science*, **48,** pp. 124-136, 1999.

[3] Polli, S., Le propagazione delle mare nell' Adriatico. *Atti del IX Convegno dell'Associazione Geofisica Italiana, Rome*, pp. 1-11, 1960.

[4] Leder, N., Beg Paklar, G., Gržetić, Z., Smirčić, A. and Vilibić, I., Wind-driven currents in the channel area: An example of the channels zadarski kanal and pašmanski kanal (East Adriatic area). *Rapport du 35e Congrès de la CIESMM*, **35(1)**, pp. 166-167, 1998.

[5] Bone, M., Development of a non-linear levels model and its application to bora-driven circulation on the Adriatic shelf. *Estuarine, Coastal and Shelf Science*, **37**, pp. 475-496, 1993.

[6] Orlić, M., Dadić, V., Grbec, B., Leder, N., Marki, A., Matić, F., Mihanović, H., Beg Paklar, G., Pasarić, M., Pasarić, Z. and Vilibić, I., Wintertime buoyancy forcing, changing seawater properties and two different circulation systems produced in the Adriatic. *Journal of Geophysical Research*, **112(C3)**, C03S07, doi: 10.1029/2005JC003271, 2007.

[7] Andročec, V., Beg Paklar, G., Dadić, V., Djakovac, T., Grbec, B., Janeković, I., Krstulović, N., Kušpilić, G., Leder, N., Lončar, G., Marasović, I., Precali, R. and Šolić, M., The Adriatic Sea Monitoring Program - *Final Report, MZOPUG, Zagreb*, pp. 623, 2009.

[8] Schepethin, A. and McWilliams, J., The Regional Ocean Modeling System (ROMS): A split explicit, free-surface, topography-following coordinates ocean model. *Ocean Modelling*, **9**, pp. 347-404, 2005.

[9] Wilkin, J.L., Arango, H.G., Haidvogel, D.B., Lichtenwalner, C.S., S.C. Glenn, S.C., and Hedstrom, K.S., A regional ocean modeling system for the long term ecosystem observatory. *Journal of Geophysical Research*, **110(6)**, pp. 1-13, 2005.

[10] DHI, Mike 3 flow model: hydrodynamic module – scientific documentation, DHI Software 2007, Denmark, 2007.

[11] Blumberg, A.F., and Mellor, G.L., A description of three-dimensional coastal ocean circulation model. In: *Three Dimensional Coastal Ocean Models*, ed. Heaps, N.S., Coastal and Estuarine Science 4, American Geophysical union, Washington, D.C., pp. 1-16, 1987.

[12] Cordoneanu, E., and Geleyn, J.F., Application to local circulation above the Carpathian-Black Sea area of a NWP-type meso-scale mode. *Contributions to Atmospheric Physics*, **71**, pp. 191-212, 1998.
[13] Brzović, N., Factors affecting the Adriatic cyclone and associated windstorms, *Contributions to Atmospheric Physics*, **72**, pp. 51-65, 1999.
[14] Brzović, N., and Strelec-Mahović, N., Cyclonic activity and severe jugo in the Adriatic, *Physics and Chemistry of the Earth (B)*, **24**, pp. 653-657, 1999.
[15] Ivatek-Šahdan, S., and Tudor, M., Use of high-resolution dynamical adaptation in operational suite and research impact studies, *Meteorologische Zeitschrift*, **13**, pp. 99-108, 2004.
[16] Raicich, F., Note on the Flow Rates of the Adriatic Rivers, *IST-CNR Technical Report, RF 02/94*, pp. 1-6, 1994.
[17] Galos, C., Seasonal circulation in the Adriatic Sea, M.S. thesis, Dartmouth Coll., Hanover, N.H., pp 127, 2000.
[18] Zavatarelli, M., and Pinardi, N., The Adriatic Sea modeling system: A nested approach. *Annales Geophysicae*, **21**, pp. 345-364, 2003.
[19] Beg Paklar, G., Isakov, V., Koračin, D., Kourafalou, V. and Orlić, M., A case study of bora-driven flow and density changes on the Adriatic shelf (January 1987), *Continental Shelf Research*, **21**, pp. 1751-1783, 2001.
[20] Janeković, I., Dutour Sikirić, M., Tomažić, I., and Kuzmić, M.: Hindcasting the Adriatic Sea surface temperature and salinity: A recent modeling experience, *Geofizika*, **27**, pp. 85–100, 2010.

Vortices in micro/nano channel flows

Z.-H. Silber-Li[1], X. Zheng[1], G.-P. Kong[1] & T. H. Moulden[2]
[1]*Chinese Academy of Sciences, China*
[2]*The University of Tennessee Space Institute, USA*

Abstract

The paper describes a series of experiments that study the formation of three-dimensional vortices in micro/nano channel flows subject to an applied electric field. The discussion is supported by a theoretical discussion of the vorticity generation process in such flows.
Keywords: micro/nano flows, vorticity, electric fields.

"……
Under Maple Bridge the boat is moored
For my long journey will resume at dawn"
Chang Chi (8^{th} century).

1 Introduction

A good reason exists as to why electro-osmosis flows are coming into common use at the micro/nano scale. For small diameter fluidic devices the flow rate, Q, is given as $Q = \pi D^4 P/(128\mu L)$ and the Reynolds number low. Hence for pressure driven flows operating a fixed flow rate, the pressure required varies as D^{-4} and becomes very large as $D \to 0$. On the other hand, for electro-osmotic driven flows, there is only a D^{-2} proportionality.

For electro-osmotic flows in simple channels, the flow is uniform outside a thin, viscous, charge layer that exists near the channel walls. This, of course, is no longer true if the channel contains large area changes when flow separation could occur. The study of Takhistov *et al.* [1] demonstrated, both theoretically and experimentally, that electrolyte depletion occurs at the junction between a wide ($400\mu m$) diameter and a small ($80\mu m$) diameter channel. Vortical flow was also observed in that flow and, it was suggested, changes to the local zeta potential gave


WIT Transactions on Engineering Sciences, Vol 74, © 2012 WIT Press
www.witpress.com, ISSN 1743-3533 (on-line)
doi:10.2495/AFM120461

rise to the vortex motion. Park *et al.* [2] provided a small disturbance analysis of the electro-osmotic flow in a bottleneck geometry and found that both vortical flow and an EOF profile distortion occurred in the constriction. These authors postulated that the presence of eddies was partly geometric, the flow passing into a narrow constriction, and partly due to a redistribution of ions. Kim *et al.* [3] first observed vortices located at the corners of a micro/nano channel using 500nm fluorescent particles and drew attention to the importance of concentration polarization initiated near the nano-channel. They located two pairs of vortices near the sidewalls of the micro-channel which were due, it was suggested, to the non-equilibrium electro-osmotic flow. Huang and Yang [4] visualized the recirculating flow field using $2\mu m$ latex particles and simulated the vortices inside the channel during their study of the depletion and enrichment process in a micro/nano-channel. Hybrid micro/nano channels have also been constructed from two separate micro-channels separated by a porous membrane. For example, Jin *et al.* [5] simulated the flow field in this kind device and noticed electro-osmotic flow of the second kind. These authors suggested that the net space charge in the depletion region gave rise to non-linear electrokinetic transport (the second kind electro-osmotic flow) and hence to vortical motion.

Two distinct flow mechanisms are at work in these devices:

1) the electro-osmotic generation of vorticity as described in section 2

2) discrete vortical flow development

Some vortex flows (such as those produced in sudden enlargement of a channel where wall vorticity has been generated) are the same in electro-osmotic flows as in familiar fluid dynamic flows; but with the presence of additional vorticity from the electric field (as in equation (6) below). The underlying fluid dynamics cannot be ignored. For example, the usual viscous vorticity creation mechanism is still present and need not be discussed herein. Note that Moffatt [6] computed corner eddies in low Reynolds number flow.

Micro/nano channel devices have potential application in many important practical situations. Hence the operational properties, and the physics associated with that operation, must be understood. In particular, does any vortical motion found in such flows enhance, or detract from, the intended operation of the device? The objective in the present paper is to observe the vortices in a three-dimensional hybrid micro/nanochannel using fluorescent particles of $200nm$ diameter and to establish the theoretical structure required to explore the electro-osmotic vorticity creation mechanism. This requires a study of both the Navier Stokes and Nernst-Planck equations.

2 Theoretical background

It is assumed for the theoretical structure discussed below that the fluid could be treated as a continuum. Thus, the smallest length scale associated with the experiment described in section 3 was that of the pores, of the order of $50nm$, in the nano-porous membrane. For the fluids of interest in the experiments reported below (conducted at room temperature) there were approximately 10^{10} molecules

per $(\mu m)^3$ for both DI water and the buffer solution. This implied a pore-Knudsen number of $K_n \approx 0.04$.

2.1 Some theorems

Given this finding, it is appropriate to adopt the Navier Stokes equations as a model of the fluid motion inside a micro/nano scale device. Since the fluid velocities are very low with respect to the sound speed, it is also appropriate to assume that the fluid density is a constant. With these assumptions, the field equations for the fluid motion are given as:

$$\frac{\partial v_i}{\partial x_i} = 0; \qquad \frac{\partial v_i}{\partial t} + v_j \frac{\partial v_i}{\partial x_j} + \frac{\partial P}{\partial x_i} + \nu \frac{\partial^2 v_i}{\partial x_j \partial x_j} + f_i \qquad (1a, b)$$

In equation (1b), $P(\mathbf{x}, t)$ denotes the fluid pressure normalized by the fluid density and $\mathbf{v}(\mathbf{x}, t)$ represents the fluid velocity. ν is the, assumed constant, kinematic viscosity of the fluid. $\mathbf{f}(\mathbf{x}, t)$ represents a body force which in the present application will be Lorentz (see equation 2a).

Gurtin [7] gave a simple uniqueness theorem in the form:

> **Result:** *Let* $(\mathbf{v}_1, P_1)$ *and* $(\mathbf{v}_2, P_2)$ *be two solutions of the equations (1a,b) (with the same boundary conditions and an independent body force). Then:* $\mathbf{v}_1 = \mathbf{v}_2$; $P_1 = P_2 + Q(t)$; *such that the quantity* $Q = Q(t)$ *is an arbitrary function of time.* ∎

and is valid provided that the regularity required by the proof holds. This regularity concerns the existence of a finite velocity gradient tensor $\mathbf{L}$; that is $\|\mathbf{L}\| \equiv \|\partial \mathbf{v}/\partial \mathbf{x}\| < \infty$. The result of Gurtin [7] shows that while the velocity field is specified uniquely by the field equations, the pressure field need not be unique. This independence of the pressure level has been known experimentally since the work of Dubuat (a fact noted by Stokes [8]).

While the above result of Gurtin [7] is of importance for many applications, it is not appropriate in the present circumstances since the Lorentz body force, is *dependent upon the flow variables*. Specifically:

$$\mathbf{f} = \rho_e \mathbf{E} \quad \text{with} \quad \rho_e = F \sum (z^\alpha c^\alpha) \qquad (2a,b)$$

Here ρ_e denotes the charge density (with F the Faraday constant and z^α the valence of charge c^α) and $\mathbf{E}$ is the electric field. Now the charges, c^α are coupled with the fluid velocity, $\mathbf{v}(\mathbf{x}, t)$ in equations (1a,b), via the Nernst–Planck flux and the charge conservation equation:

$$\frac{\partial c^\alpha}{\partial t} + \frac{\partial J_i(\alpha)}{\partial x_i} = 0 \quad \text{with} \quad J_i(\alpha) = -D \frac{\partial c^\alpha}{\partial x_i} + v_i\, c^\alpha - \mu_{ep}\, z^\alpha F\, c^\alpha \frac{\partial \Psi}{\partial x_i} \qquad (3)$$

which completes the specification of the fluid motion.

It is assumed that there are no magnetic fields, either applied or induced, acting on the fluid so that the Maxwell equations state that:

$$\nabla^2(\Psi) = -\rho_e/\epsilon \tag{4}$$

for the permittivity ϵ and electric potential, Ψ, defined such that the electric field $\mathbf{E}$ is given by $\mathbf{E} = -\boldsymbol{\nabla}(\Psi)$. The Poisson equation (4) shows, directly, that if the charge density ρ_e is uniquely defined then the potential Ψ is unique and so is the electric field $\mathbf{E}$. Uniqueness of the Poisson equation is discussed in Stakgold [9]. Vorticity generation by this process is discussed in more detail in Silber–Li *et al.* [10]. How this vorticity is wrapped into a discrete vortex depends upon the geometry of the device and cannot be established from the present equations in isolation.

The above system of equations can now be stated in the standard form:

$$\begin{aligned}
\frac{\partial v_i}{\partial t} + v_j\frac{\partial v_i}{\partial x_j} + \frac{\partial P}{\partial x_i} &= \nu\frac{\partial^2 v_i}{\partial x_j \partial x_j} + \rho_e\, E_i \\
\frac{\partial v_i}{\partial x_i} &= 0 \qquad\qquad (5a,b,c,d) \\
\frac{\partial \rho_e}{\partial t} + v_i\frac{\partial \rho_e}{\partial x_i} &= D\frac{\partial \rho_e}{\partial x_i \partial x_i} - \mu_{ep}\, F\, z^1\left[\frac{\partial \rho_e}{\partial x_i}E_i + \rho_e\frac{\partial E_i}{\partial x_i}\right] \\
\frac{\partial E_i}{\partial x_i} &= \frac{\rho_e}{\epsilon}
\end{aligned}$$

if it is assumed that there are the same number of positive and negative ions. Here D denotes the diffusivity and μ_{ep} the mobility. Both are assumed to be constant in the following deliberations. The electric field provides directionality in equation (5a).

A result of fundamental physics can be noted from direct inspection:

Lemma I: *The system of equations (5a,b,c,d) is not covariant under time reversal. Neither is it covariant under electric field reversal.* ∎

The first part of the lemma, lack of time reversibility, just recognizes that the processes involved are not *"ideal"* and some increase in entropy must take place as the flow field develops. The second part of the Lemma is more interesting and suggests, in the context of the experimental results to be discussed below, that reversal of the electric field cannot *"unwind"* the vorticity after it has started to develop.

With the assumptions made above, a simple estimate suggests that:

Lemma II: *Let* $(\mathbf{v}_1, P_1, \rho_e^1, \mathbf{E}_1)$ *and* $(\mathbf{v}_2, P_2, \rho_e^2, \mathbf{E}_2)$ *be two solutions of the equations (5a,b,c,d) (with the same boundary conditions). Then:*

$$\mathbf{v}_1 = \mathbf{v}_2; \qquad P_1 = P_2 + Q(t); \qquad \mathbf{E}_1 = \mathbf{E}_2; \qquad \rho_e^1 = \rho_e^2$$

such that the quantity $Q = Q(t)$ *is an arbitrary function of time. The physical constants of the fluid are assumed the same for both flows.* ∎

and the experimentally observed repeatability of the physics of micro/nano scale flows would be contained in the flow model discussed above.

2.2 Vorticity and pressure

Let attention pass to the consideration of vorticity dynamics in micro/nano scale flows driven by a Lorentz force. The *curl* operator applied to equation (1b), with the Lorentz body force, gives the vorticity evolution equation:

$$\frac{d\zeta_i}{dt} = \frac{\partial v_i}{\partial x_j}\zeta_j + \nu\nabla^2\zeta_i - F\,\epsilon_{ijk}\left[\sum z^\alpha \frac{\partial c^\alpha}{\partial x_j}\right]\frac{\partial \Psi}{\partial x_k} \tag{6}$$

which differs from the classical form in fluid dynamics due to the specific nature of the Lorentz body force. Now it is clear that vorticity is generated by the cross product of the concentration gradient with the electric field gradient. Form an equation for the global norm, $|\boldsymbol{\zeta}|_g^2 = \int_D \langle \boldsymbol{\zeta}, \boldsymbol{\zeta} \rangle \, dV$, of the vorticity vector as an integral over the entire device using equation (6). As discussed in Silber–Li *et al.* [11] the vorticity in the device establishes a global norm which evolves as:

$$\frac{\partial}{\partial t}|\boldsymbol{\zeta}|_g^2 + \nu L_\zeta^2 |\boldsymbol{\zeta}|_g^2 \leq 2\|\mathbf{L}\|_g |\boldsymbol{\zeta}|_g^2 + \frac{1}{\nu L_\zeta^2}|\mathbf{g}|_g^2$$

which couples to the velocity field via the velocity gradient $\mathbf{L} = \boldsymbol{\nabla}(\mathbf{v})$: the magnitude of the velocity global norm influences the rate of increase on global vorticity. More important is the influence of the vector $\mathbf{g} = curl(\mathbf{f})$ which, for the present application, is bounded in norm by:

$$|\mathbf{g}|_g^2 \leq 2|\mathbf{E}|_g^2 \, |\boldsymbol{\nabla}(\rho_e)|_g^2$$

to give an upper bound on the electro-osmotic vorticity generation process.

For reference note that the *divergence* operation applied to equation (1b) generates a Poisson equation for the fluid pressure which has the form:

$$\nabla^2 P = \frac{1}{\rho}\left[\frac{\partial \rho_e}{\partial x_i}E_i + \rho_e \frac{\partial E_i}{\partial x_i}\right] - \frac{\partial v_j}{\partial x_i}\frac{\partial v_i}{\partial x_j} \tag{7}$$

Both the hydrodynamics and the electric field establish the pressure.

While the concepts leading to equations (6) and (7) are quite standard in classical fluid mechanics, their implications for micro/nano scale flows is less well recognized. Equation (6) only shows how vorticity $\boldsymbol{\zeta} = curl(\mathbf{v})$ is generated: it gives no indication of how this vorticity evolves into the discrete vortex structures observed experimentally. As noted in the Introduction, there are several factors involved in this process which are related to the geometry of the device. At the same time, the present study is not concerned with wall generated vorticity and possible flow separation.

As noted before, the non-linear term in the linear momentum equation is often neglected in these low velocity micro/nano scale flows. If that is done in equation (6) it follows that the $curl(\mathbf{f})$ term is collinear with the vorticity vector. In this

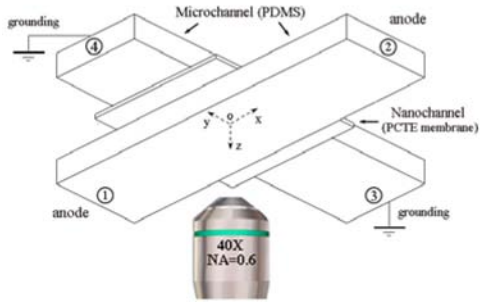

Figure 1: The micro/nano device used in the experiments. Not to scale.

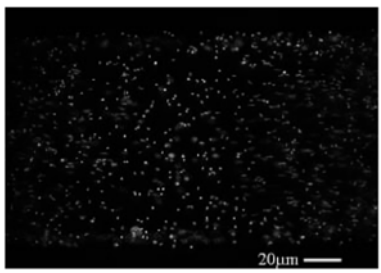

Figure 2a ($t^* = 0.25$)

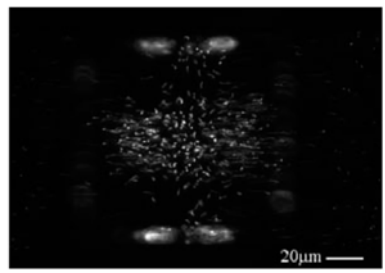

Figure 2b ($t^* = 0.65$)

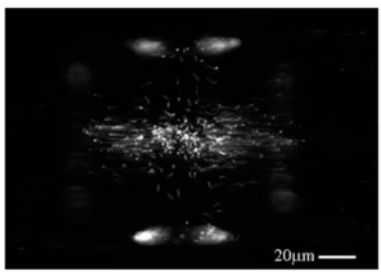

Figure 2c ($t^* = 0.98$)

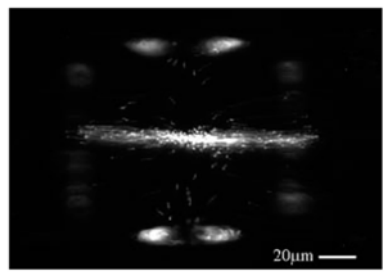

Figure 2d ($t^* = 1.28$)

Figure 2: Vortex evolution.

case equation (6) specifies the direction of the vorticity field. This directionality of the vorticity field then implies the initial direction of the evolving vortex. The experiments discussed below study the significance of equation (6) for vorticity generation in a specific micro/nano scale flow (see Figure 1 for the device in question and Figure 2 for the emergence of discrete vortices from that vorticity).

3 The experimental method

The experimental study discussed herein formed part of a research program on micro/nano scale fluid mechanics that has been carried out at the Laboratory for Non-Linear Mechanics (LNM) in the Chinese Academy of Science, Beijing, China. In the course of that experimental program it was observed that vortices were generated inside a micro/nano scale device (that shown in Figure 1) as the flow field developed under the action of an applied electric field. All the experiments reported herein relate to a visual study of the flow field in that same device. Preliminary results have been reported in Silber–Li *et al.* [12] and Yu and Silber–Li [13].

The theoretical study outlined in section 2 above suggests how vorticity can be generated in micro/nano scale flow devices due to the applied electric field interacting with the distribution of ions. The interpretation of the flow field development discussed herein will ignore the viscous flow boundary layers that develop on the walls of the device since the rotational sense of such wall vorticity is not consistent with the observed vortex structures. While the overall flow development is crucially dependent upon the device geometry, only one geometry, that shown in Figure 1, was tested. Flows in other devices, adopting different geometries, have been reported upon in the literature and have found different vortex configurations.

The interest herein concerns the coalescence of the generated vorticity into discrete vortex structures. This process is examined experimentally since a study of the field equations (equations 5a,b,c,d above), in isolation from the boundary conditions, cannot provide much information about this vortex development process. Indeed, a numerical solution of the full set of equations is required for that.

3.1 Experimental setup

As noted above, the experimental work reported herein was carried out at the LNM, and the chip adopted for the experiments that was shown in Figure 1 above. In order to allow visualization of the flow field the device was mounted upon an inverted fluorescence microscope (type Olympus IX–71 fitted with a $40 \times /0.6$ lens). The flow field images were recorded by an EMCCD camera (type Andor 885). The electrical potential was obtained from a DC power supply (Zolix Instruments Co., Ltd, Model DYY–$12C$) whose output was stable to $\pm 0.03\%/h$. The voltage range was 0 to $1100V$.

3.2 The micro-chip

The hybrid micro/nano-channels used in the experimental study (see Figure 1) were constructed from two polydimethyl-siloxane (PDMS) micro-channels connected together across a polycarbonate nano-porous membrane (PCTE). The micro-channels were $100\mu m \pm 0.1\mu m$ in width, $20\mu m \pm 0.1\mu m$ in depth and

$9mm \pm 0.02mm$ in length. The two channels were mounted orthogonally across the membrane as shown in Figure 1. The nano-pores of the PCTE membrane were distributed randomly and had a nominal diameter of $50nm$, with a porosity of less than 1.57%. The membrane thickness was $8\mu m$ with a measured error of $\pm 0.8\mu m$. The random nature of the porosity demands that the vortex structures observed in the experiment are not directly related to the membrane pore geometry.

3.3 The working fluid and tracer particles

The buffer solution concentration adopted in the experiment was $10mM$ Borax at $pH9.2$. The fluorescent particles used to visualize the motion were of $200nm$ diameter with a negative surface charge. The particle density, $1.05g/cm^3$, was close to that of water and any buoyancy effects were very small. These tracer particles were excited by a mercury lamp light source and made visible with a filter wavelength of $616nm$. The particles were diluted into DI water to a relative volume concentration of 5×10^{-5} and then diluted into the Borax solution with a 1:2 volume ratio.

3.4 Experimental processes

The experiment started with the bottom channel of the micro/nano-channel device being filled with the buffer solution containing the fluorescence particles. The upper channel was filled with the pure borax buffer solution. Platinum electrodes were inserted into the reservoirs of the micro-channel to provide the electrical potential across the PCTE membrane. A DC voltage of $2V$, was applied to the reservoirs of the bottom channel while those of the upper channel were grounded (Figure 1). This voltage was too low to induce electrolysis. A detailed discussion of the concentration profile development was reported in Yu and Silber–Li [13]. It is the passage of this concentration profile through the channel that provides the concentration gradient, $\boldsymbol{\nabla}(c^{\alpha})$, that featured in equation (6) for vorticity generation.

The focal plane of the EMCCD camera was adjusted to view, from vertically below, flow in the lower micro-channel. The focal plane was located $15\mu m$ below the bottom surface of the nano-porous membrane. The maximum image size was $(200 \times 200) \pm 0.26mm$. A sequence of images were recorded with an exposure time of $\Delta t_p = 100ms$ and an interval time of $\Delta t = 130ms$. Images from the experiments showing the evolution of the vortical structures are shown in Figure 2 and will be discussed below.

4 Results from the experiment

The initial stages of vortex formation in the device shown in Figure 1 can be observed by flow visualization techniques and the results of such an experiment are shown in Figure 2 using the tracer particles as discussed above. For the flows

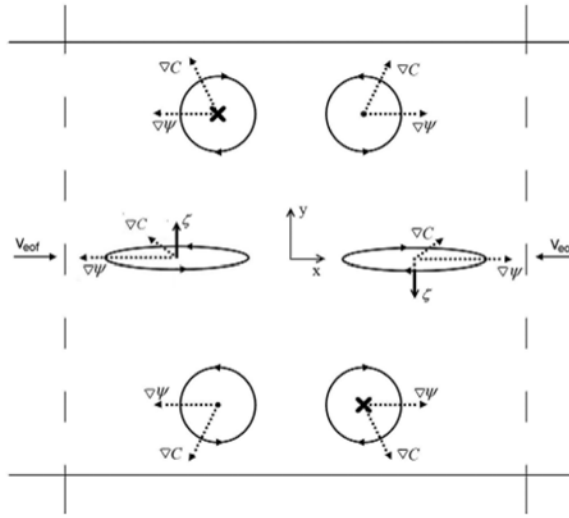

Figure 3: Schematic showing the direction of the eddies relative to the two local gradients, $\boldsymbol{\nabla}(c^{\alpha})$, and, $\boldsymbol{\nabla}(\Psi)$ in the junction region of the hybrid macro/nano channel. In this figure, "**x**" represents a clockwise rotating vortex (with rotation along the $-z$ axis). At the same time the symbol "$\cdot$" represents count-clockwise rotating vortices (rotation is along the z axis).

considered herein there is no wall vorticity included as the vortices develop in the flow field and not adjacent to solid boundaries.

4.1 Evolution of the vortices

At the start of the experiment, the fluorescence particles in the bottom micro-channel were at rest as discussed above in section 3. Motion of the particles was, however, observed after the electric field was applied across the channel. It is meaningful to discuss the flow evolution in a non-dimensional time scale, t^*, where: $t^* = v_{eof}t/\ell$. Here, ℓ is the depth of the micro-channel and $v_{eof} = \epsilon\,\zeta_w E/\mu$ denotes the Smoluchowski velocity. Also t denotes the physical time, measured in seconds, from the instant when the electric field was applied. For the present application the wall zeta potential had the value $\zeta_w = -30mV$. The electric field was $E \approx 2V/cm$ while the value for the dialectric constant was $\epsilon = 7 \times 10^{-10}c^2/Nm^2$. The fluid viscosity was taken to be $\mu = 10^{-3}Pa.s$. Figure 2a shows the state at time $t^* = 0.25$ ($t = 1.25s$). At $t^* = 0.65$ ($t = 3.25s$) three dominant pairs of vortices began to emerge from the cloud of particles (Figure 2b). Two pairs of small vortices are located near the upper and bottom side walls. These vortices were seen to rotate in opposite direction. A pair of vortices (the principle vortices) was found to be located in the (horizontal), $x \sim y$, plane in

4a: lower–right vortex (2V; $\Delta t_p = 20ms$; $\Delta t = 30ms$ with $T = 22\Delta t$)

4b: center–left vortex (5V; $\Delta t_p = 20ms$; $\Delta t = 40ms$ with $T = 6\Delta t$)

Figure 4: Traces for two of the vortices.

the lower micro-channel $15\mu m$ from the membrane. At time $t^* = 0.98$ ($t = 4.9s$) the particles in the principle vortices are migrating towards the central plane of the micro-channel as shown in Figure 2c. The last figure, Figure 2d, shows the location of the vortices at $t^* = 1.28$ ($t = 6.4s$). At this time all the particles in the principle vortices are located on the central plane. Figure 3 summarizes the final vortex locations and their sense of rotation.

4.2 Rotation directions of the vortices

To illustrate the vortex rotation more clearly, the motion was observed with fewer particles than used for Figure 2. Figure 4 presents a pair of vortex images and their sketch maps. The vortex in Figure 4a is located at the bottom-right hand corner on Figure 3. The photograph in Figure 4a was obtained by overlapping 22 images with the tracer particle captured at a time $T = 22\Delta t$. The numbers in the picture indicate the time order of the tracer particle as it moved within the vortical flow. For locations $2,\ 5,\ 10$ the particle was within the vortex boundary. Then for location $10,\ 20$ the particle departs from the vortex and migrates towards the center of the micro-channel. This vortex rotated clockwise and the axis of rotation was essentially along the $-z$ axis. The dotted-line on the figure indicates the wall of the micro-channel. Similarly for the vortex in the lower-left (on Figure 3), the

vortex rotated counter-clockwise and the axis of rotation was along the +z axis. The sense of rotation of the upper left and upper right vortices is as shown on Figure 3. For the principle vortices resided in the center of the junction region, it was observed that the tracer particles of vortex in the center-left moved round the vortex as indicated by the numbers on the tracer particles (Figure 4b). However, the rotation axis of this vortex is along $+y$ axis. Symmetrically for the vortex in the center-right, its rotation axis is along $-y$ axis. The vortex system is symmetric about the y–z plane.

4.3 Velocity field in the vortices

The tracer particle velocities were computed from the images in Figure 4. For the vortex in Figure 4a, the trace moved $2.5\mu m$ during the time interval Δt_p so that its velocity was $125\mu m/s$. This data implies a Strouhal number $S_t = 0.021$ for the center vortex and a Reynolds number (based upon v_{eof}) of $R_e = 0.0013$. Hence $R_e/S_t \approx 0.062$. The creeping flow condition, $R_e/S_t \ll 1$, is not well satisfied. From Figure 4b, the velocity in the center left vortex was about $270-500\mu m/s$. As it is noted in section 4.1, the Smoluchowski velocity v_{eof} is $13\mu m/s$ in $5V$. The electro-phoresis velocity of the fluorescent particle was $22\mu m/s$ ($v_{ep} = \epsilon\zeta_p E/\mu$, here, $\zeta_p = -50mV$ denotes the zeta potential of the particle surface). Since the direction of v_{eof} and v_{ep} are opposite, the net velocity of particle movement is only $10\mu m/s$. Hence the tracer velocity gives the line speed of the vortices.

5 Discussion of the results

The present section discusses the distribution of both the electric field gradient, $\boldsymbol{\nabla}(\Psi)$, and the ion concentration gradient, $\boldsymbol{\nabla}(c^{\alpha})$, in order to identify the sense of vortex rotation shown in Figure 3 and to compare with the experimental data in Figures 3 and 4.

5.1 Distribution of $\boldsymbol{\nabla}(\boldsymbol{\Psi})$

The electric field strength, $\mathbf{E} = -\boldsymbol{\nabla}(\Psi)$, with potential Ψ was introduced in section 2 above. This potential Ψ includes two parts: that due to the applied electric field and the EDL potential ζ_w. For the buffer solution used in the present experiments, the EDL thickness was approximately $10nm$ and the corresponding potential $\zeta_w \approx 30mV$. Hence the influence of ζ_w on the potential Ψ for the bulk flow in the micro-channel can be neglected. According to Figure 1, the applied voltage is positive in the lower micro-channel and negative in the upper micro-channel. Hence the direction of the gradient, $\boldsymbol{\nabla}(\Psi)$, was from the upper to the lower micro-channel (the electric potential is increasing). This implies that in the lower micro-channel the potential gradient, $\boldsymbol{\nabla}(\Psi)$, increased from the center (that is in the junction region) to both ends 1 and 2 (see Figure 1).

5.2 Distribution of $\nabla(c^{\alpha})$

The applied electric field produces enrichment in the upper micro-channel and depletion in the lower channel. From previous experimental results (see Yu and Silber–Li [13]), the depletion zone in the lower micro-channel will develop from the junction region and pass along the micro-channel towards the reservoirs. Therefore, the gradient, $\nabla(c^{\alpha})$, is directed along the normal to the depletion zone profile and toward the higher concentration.

5.3 Vortices with $\nabla(c^{\alpha})$ and $\nabla(\Psi)$

The vortices rotate about the span of the vector $\nabla(c^{\alpha}) \times \nabla(\Psi)$. Now consider each vortex shown in Figure 3. For the upper-left vortex as noted in Figure 3a, $\nabla(\Psi)$ and $\nabla(c^{\alpha})$ are in the x–y plane while $\nabla(\Psi)$ is along the $-x$ axis and $\nabla(c^{\alpha})$ is along the normal direction of the depletion zone. While the front of the depletion zone moves away from the center of the micro-channel, it does so most rapidly in the region near the nano-porous membrane. That is, the normal to the front is, locally, not along the $-x$ axis but rather between the $-x$ and the y directions (see Figure 3). Therefore, rotation of upper-left vortex is along the $-z$ axis. Similarly, the rotation of upper-right vortex is along the axis z. By means of a similar analysis, the rotation of the lower-left vortex is along axis z and the rotation of lower-right vortex is along axis $-z$. For the principle vortices at center-left, the $\nabla(\Psi)$ and $\nabla(c^{\alpha})$ are both in the x–z plane, with $\nabla(\Psi)$ along the $-x$ axis and $\nabla(c^{\alpha})$ along the normal direction to the depletion zone. Therefore, rotation of the center-left vortex is along the y axis. Similarly, the rotation of the center-right vortex was along the $-y$ axis.

6 Conclusions

Vortices in a three-dimensional hybrid micro/nano channel, subjected to an applied electric field, have been visualized. In addition, an analysis of the vorticity origin, based on the Navier Stokes and Nernst–Planck equations, was undertaken. The main points from the study are as follows:

(1) Three pairs of vortices were found from the experimental images. The rotations of the vortices near the sidewalls are orthogonal to the principle vortices in center channel. This differs from the situation in two-dimensional channels where the axes of rotation of the vortices are parallel. The velocities of the vortices was also calculated. The results show that the line velocities are much larger than the electro-osmotic flow velocity, and the directions of the velocity near the wall were the same as v_{eof}, but in the channel center, the velocity was opposite to this.

(2) The theoretical analysis has indicated that vorticity in the micro-channel resulted from the cross product of the concentration gradient and the electric field gradient. It was found that the experimentally observed vortices were consistent with this finding.

The flow visualization experiments reported herein illuminated the complexity of the flow field resulting from the applied electric field interacting with charged ions in the buffer solution. There is a need for further work.

Acknowledgements

The authors wish to thank the following organizations for financial support: Knowledge Innovation Project of The Chinese Academy of Sciences (KJCX2-YW-H18) and the Natural Science Foundation of China (10872203).

References

[1] Takhistov, P.; Duginova, K. and Chang, H. C: *Electrokinetic Mixing Vortices due to Electrolyte Depletion at Micro-channel Junctions.* J. Colloid and Interface Sci., vol. 263, pp 133–143, 2003.

[2] Park, S. Y; Russo, C. J; Banton, D. and Stone, H. A: *Eddies in a Bottleneck: An Arbitrary Debye Length Theory for Capillary Electro-osmosis.* J. Colloid and Interface Sci., vol. 297, pp 832–839, 2006.

[3] Kim, S-J.; Wang, Y-C.; Lee, J-H.; Jang, H. and Han, J: *Concentration Polarization and Nonlinear Electro-kinetic Flow Near a Nonfluidic Channel.* Phys. Rev. Lett., 99:044501, 2007.

[4] Huang, K-D and Yang R-J: *Formation of Ionic Depletion/enrichment zones in a Hybrid Micro/nanochannel.* Microfluid Nanofluid, vol. 5, pp 631–638, 2008.

[5] Jin, X.; Joseph, S.; Bohn, P. W. and Aluru, N. R: *Induced Electrokinetic Transport in Micro-Nanofluidic interconnect.* Langmuir, vol. 23, pp 13209–13222, 2007.

[6] Moffatt, H. K: *Viscous and Resistive Eddies near a Sharp Corner.* JFM, vol. 18, 1964.

[7] Gurtin, M. E: *Introduction to Continuum Mechanics.* Academic Press, New York, 1981.

[8] Stokes, G. G: *On the Theories of the Internal Friction of Fluids in Motion and of the Equilibrium and Motion of Elastic Solids.* Trans. Camb. Phil. Soc. vol. 8, pp 287–319, 1845.

[9] Stakgold, I: *Boundary Value Problems of Mathematical Physics.* Macmillan, 1967.

[10] Silber–Li, Z-H, Kong, G-P, Zheng, X, Yu, Q and Moulden, T. H: "Vorticity and Pressure Fields in Micro/Nano Channel Flows". In preparation.

[11] Silber–Li, ZH; Kong, GP; Yu,Q and Moulden, T. H: *Observation of Vorticity generation in Micro/nano-channel Flows Subject to an Electric Field.* Proc. 11th Asian Symp. Visualization, Japan, 2011.

[12] Silber–Li, ZH; Yu, Q and Kong, GP: *The Experiments about Ionic Exclusion–Enrichment Effects in a Hybrid Micro/Nano-channel.* Proc. 2nd Euro. Conf. on Microfluidics, France, 2010.

[13] Yu, Q and Silber–Li, ZH: *Measurement of the Ion-depletion Zone Evolution in a Micro/Nano-channel* MicroFluid–Nanofluid, vol. 11, pp 623–631, 2011.

This page intentionally left blank

A turbulence closure based on the maximum entropy method

R. W. Derksen
Department of Mechanical and Manufacturing Engineering, University of Manitoba, Winnipeg, Canada

Abstract

The fundamental problem of turbulence is that of closing the infinite sequence of equations that result from the application of Reynolds averaging to the governing relations for momentum, heat and mass transfer. These equations model the moments of the turbulent probability density, PDF, such as the first, second, third, and higher order moments, each equation depending on higher order moments. The ability to relate the set of moments of order n to moments of n+1 would permit closure to a finite system of equations as we could truncate the sequence of equations. The concept of the Shannon entropy allows us to model the degree of uncertainty of a PDF. The Shannon entropy is related to the concept of thermodynamic entropy. The maximum entropy method determines the PDF that maximizes the entropy subject to a number of constraints. The most usual method is to use a finite number of lower order moments. A maximum entropy PDF is often used to approximate the shape of a PDF as the solution has desirable features such as being positive definite. The maximum entropy method is of great value as an approximation method in general. An examination of the behavior of the moments generate from a maximum entropy for a single degree of freedom fit to real, turbulent PDFs for velocity, skin-friction, and temperature fluctuations have been carried out to examine the methods ability predictive capability. In this examination experimentally determined data sets that contained data for all moments up to the sixth order were compiled from the literature. The maximum entropy method was applied using the first four moments. The fifth and sixth moments computed from the maximum entropy approximations were compared and found to compare very favorably with those measured. The presentation will start with a review of the maximum entropy method for a finite number of moments and a discussion of the computational

WIT Transactions on Engineering Sciences, Vol 74, © 2012 WIT Press
www.witpress.com, ISSN 1743-3533 (on-line)
doi:10.2495/AFM120471

issues that arise. This will be followed by a review of the experimental data used, and a comparison of the maximum entropy moments with the experimental data. The presentation will conclude with a presentation of the solution to the maximum entropy method for up to four degrees of freedom.
Keywords: turbulence closure, maximum entropy, turbulence modelling, turbulent PDF.

1 Introduction

The fundamental problem of turbulence is that of closing the infinite sequence of equations that result from the application of Reynolds averaging to the governing relations for momentum, heat and mass transfer. These equations model the moments of the turbulent probability density, PDF, such as the first, second, third, and higher order moments, each equation depending on higher order moments. The ability to relate the set of moments of order n to moments of $n+1$ would permit closure to a finite system of equations as we could truncate the sequence of equations.

The maximum entropy method is of great value as an approximation method in general. An examination of the behaviour of the moments generated from a maximum entropy fit to real, turbulent PDFs for velocity, skin-friction, and temperature fluctuations have been carried out to examine the methods ability predictive capability. In this examination experimentally determined data sets that contained data for all moments up to the sixth order were compiled from the literature. The maximum entropy method was applied using the first four moments. The fifth and sixth moments computed from the maximum entropy approximations were compared and found to compare very favourably with those measured.

The presentation will start with a review of the single degree of freedom maximum entropy method for a finite number of moments and a discussion of the computational issues that arise. This will be followed by a review of the experimental data used, and a comparison of the maximum entropy moments with the experimental data. We will conclude with the development of a four degree of freedom maximum entropy solution.

2 The Shannon entropy of a probability density function

The concept of the Shannon entropy allows us to model the degree of uncertainty of a PDF for a random variable U, expressed as $p = p(U)$, through an integral given by

$$s = -\int_{-\infty}^{\infty} p(U) \ln p(U)\, dU.$$

The concept of the Shannon entropy also applies where the PDF has finite support allowing us to consider integrals with finite limits. The Shannon entropy

is related to the concept of thermodynamic entropy as developed by Boltzmann, see Atkins [1].

The maximum entropy method determines the PDF that maximizes the entropy subject to a number of constraints. The most usual method is to use a finite number of lower order moments. A maximum entropy PDF is often used to approximate the shape of a PDF as the solution has desirable features such as being positive definite.

3 The maximum entropy method for one degree of freedom

The maximum entropy approximation to $p(U)$ yields the maximum entropy subject to a set of constraints on the PDF. The range of possible constraints is limitless in general; however we will examine the case where the first *n* central moments have given values.

We will note that an implied constraint always applies to any PDF, that is

$$\int_{-\infty}^{\infty} p(U)\,dU = 1.$$

We also observe that the mean value of *U* is

$$\overline{U} = \int_{-\infty}^{\infty} Up(U)\,dU$$

which is not equal to zero in general. The central moments are obtained by subtracting the mean value to give a new set of continuous random variable given by $u = U - \overline{U}$. This yields the following formula for the i^{th} moment

$$\mu_i = \int_{-\infty}^{\infty} u^i p(u)\,du.$$

Here we note that the previous discussion indicates that $\mu_0 = 1$ and $\mu_1 = 0$ as basic minimum constraints for any PDF.

We will examine the case which constrains the moments up to the 4^{th} order, with the additional requirement that *u* has bounded support between $-a$ and a. The entropy of the PDF is now given by

$$s = -\int_a^b p \ln p\,du.$$

The determination of the PDF that maximizes this integral requires us to turn to the calculus of variation. The PDF that yields the extreme value of the entropy requires us to solve Euler's equation

$$\frac{\partial \Phi}{\partial y} = 0,$$

where $\Phi = -p\ln p + \lambda_0' C_0 + \lambda_1 C_1 + \lambda_2 C_2 + \lambda_3 C_3 + \lambda_3 C_3$ where the λ are constants. Hence the equation for p is obtained from

$$\frac{\partial \Phi}{\partial p} = -\ln(p) + 1 + \lambda_0' + \lambda_1 u + \lambda_2 u^2 + \lambda_3 u^3 + \lambda_4 u^4 = 0.$$

The general form of p is thus given by

$$\begin{aligned} p &= \exp\left(1 + \lambda_0 + \lambda_1 u + \lambda_1 u^2 + \lambda_3 u^3 + \lambda_4 u^4\right) \\ &= \exp\left(\lambda_0 + \lambda_1 u + \lambda_1 u^2 + \lambda_3 u^3 + \lambda_4 u^4\right) \\ &= \exp\left(F(u)\right), \end{aligned}$$

where $\lambda_0 = 1 + \lambda_0'$.

4 Solving for the coefficients

Analytical determination of the coefficients for the maximum entropy approximation to the PDF requires us to obtain closed form integrals of the moments. Many of these integrals are known to be unknown, so analytical solution is not possible. Hence we must resort to a numerical scheme to solve for the coefficients. The method that was used was based on Newton's method. A linear approximation of any of the moments can be written as follows for incremental changes in the coefficients

$$\mu_i - \hat{\mu}_i = \frac{\partial \hat{\mu}}{\partial \lambda_0} d\lambda_0 + \frac{\partial \hat{\mu}}{\partial \lambda_1} d\lambda_1 + \frac{\partial \hat{\mu}}{\partial \lambda_2} d\lambda_2 + \frac{\partial \hat{\mu}}{\partial \lambda_3} d\lambda_3 + \frac{\partial \hat{\mu}}{\partial \lambda_4} d\lambda_4.$$

The hat indicates that the moments are for an initial, guessed set of coefficients $\hat{\lambda}_i$. Examination of the partial derivatives shows that they have a particularly simple form,

$$\frac{\partial \hat{\mu}_i}{\partial \lambda_j} = \int_a^b x^i \left(x^j \exp\left(F(x)\right)\right) dx = \hat{\mu}_{i+j}.$$

Hence we obtain the following system of linear equations given by

$$\begin{bmatrix} \hat{\mu}_0 & \hat{\mu}_1 & \hat{\mu}_2 & \hat{\mu}_3 & \hat{\mu}_4 \\ \hat{\mu}_1 & \hat{\mu}_2 & \hat{\mu}_3 & \hat{\mu}_4 & \hat{\mu}_5 \\ \hat{\mu}_2 & \hat{\mu}_3 & \hat{\mu}_4 & \hat{\mu}_5 & \hat{\mu}_6 \\ \hat{\mu}_3 & \hat{\mu}_4 & \hat{\mu}_5 & \hat{\mu}_6 & \hat{\mu}_7 \\ \hat{\mu}_4 & \hat{\mu}_5 & \hat{\mu}_6 & \hat{\mu}_7 & \hat{\mu}_8 \end{bmatrix} \begin{bmatrix} d\lambda_0 \\ d\lambda_1 \\ d\lambda_2 \\ d\lambda_3 \\ d\lambda_4 \end{bmatrix} = \begin{bmatrix} 1 - \hat{\mu}_0 \\ \mu_1 - \hat{\mu}_1 \\ \mu_2 - \hat{\mu}_2 \\ \mu_3 - \hat{\mu}_3 \\ \mu_4 - \hat{\mu}_4 \end{bmatrix}.$$

The initial values of the λ_j's are estimated or guessed and the values of the $\hat{\mu}$'s are numerically computed. Then the values of the $d\lambda_j$ are computed from this equation, finally they are added to the guessed values and the process is

repeated if need be. This iterative procedure can be stopped when either the coefficients of the polynomial converge to within some preset precision or the estimated moments are accurate to within some preset value.

In the numerical scheme that is reported, the iteration were repeated if the magnitude of the $d\lambda$ vector divided by the magnitude of the λ vector was less than 10^{-4}. Computing the coefficients to a greater accuracy was not examined. A similar scheme for terminating the iterations can be based on the computed moments.

This presentation of the numerical method to solve for the maximum entropy problem minimizes some of the numerical problems that have been encountered. First the initial values of the coefficients must be chosen with some care for large order systems. The starting guesses that were examined were to make all of the coefficients equal to zero, but this caused the initial matrix to be a Hilbert matrix. Unfortunately, Hilbert matrices have the well documented property of being ill conditioned. Hence, for a large order approximation, order say 10 or more, we might not be able to even start the iteration process. If the order of the system is smaller we can however always use an initial guess that the coefficients are zero. Notice that setting the initial values of the coefficients to zero is equivalent to guessing that the PDF is uniform on the interval $[a,b]$.

The second difficulty that was encountered is that of computing the moments. For a distribution that is very smoothly distributed across the interval, virtually any numerical integration scheme will work. The computed moments will be accurate with relatively little work. However, if the distribution is very spiky, approaching that of a delta function, the integration will require either an inordinate number of intervals or some sort of adaptive method. Simpson's method with 1000 subintervals was selected to compute the moments for the results given here. It is quite clear that some distributions will tax the accuracy of this kind of integration scheme to the point of making the iterations unstable.

The final difficulty that was encountered is that of solving the system of equations. For smooth distributions, it has been observed that the system of equations is relatively well conditioned, and that the system can be solved using Gauss-Jordan elimination. For very spiky distributions, the system of equations is not well conditioned, and the iterative procedure is then unstable. Singular value decomposition must be used to deal with this ill-condition of the matrix. The singular value decomposition algorithm that was used for this work is that given by Press *et al.* [2]. The values of the terms of the diagonal matrix were set to zero if they were less that P times the maximum value of the diagonal. By experiment, it was found that $P=10^{-12}$ was the minimum value of this factor that would allow the iterations to proceed stably for all cases that were examined. If P was chosen too large, a solution could be obtained but it would be very misleading. Results of a numerical experiment for values of P that ranged from 10^{-6} to 10^{-12} clearly showed the effect of P being too large.

As a concluding remark on the numerics of the maximum entropy approximation it should be clearly stated that the method does work and it appears to work quite well. However, there are some difficulties that must be carefully addressed in any algorithm that is going to be used to obtain the

coefficients of the polynomial. To repeat, they are the numerical integration of the moments, selection of the initial values of the coefficients and ill-condition of the generated system of equations. However, these problems can be satisfactorily resolved if they are directly addressed.

As a note on the computational efficiency of this scheme we should state that most of the computer time was spent performing the integrations. If the scheme is to be made more efficient, we would have to find computationally more efficient means of performing the integrations. Solving the system of equations, updating the coefficients and testing for convergence generally took less than evaluating even one of the moments. The number of iterations that must be performed is strongly dependent upon the initial guess of the coefficients and the final shape of the PDF. For very narrow distributions close to zero, the scheme required in the order of 50 iterations to converge. It can be hypothesized that better starting values could reduce the iteration count significantly. However, there is no *a priori* means of determining the initial guess. If one of the moments is tracked as the iterations proceed it will appear that the process converges, diverges and then converges again. This is due to all of the moments being fit so the behavior of one moment may appear oscillatory.

5 The maximum entropy for four degrees of freedom

Assume that $p(U,V,W,\Psi)$ is the probability density function describing the turbulent flow as a function of the velocity components (*U*, *V*, and *W*) and the pressure, Ψ. Then the statistical entropy for this PDF is given by

$$s = -\int_{-\infty}^{\infty}\int_{-\infty}^{\infty}\int_{-\infty}^{\infty}\int_{-\infty}^{\infty} p(U,V,W,\Psi)\ln p(U,V,W,\Psi)\,dUdVdWd\Psi.$$

For a given set of conditions, $p(U,V,W,\Psi)$ is the function that maximizes *s*. Based on physical considerations we would expect that $p \to 0$ when any of the variables go to $\pm\infty$.

The basic requirement for a PDF is that

$$\int_{-\infty}^{\infty}\int_{-\infty}^{\infty}\int_{-\infty}^{\infty}\int_{-\infty}^{\infty} p(U,V,W,\Psi)\,dUdVdWd\Psi = 1.$$

We will employ $(N+1)^4$ constraints on the statistical moments about the mean, given by

$$C_{i,j,k,l} = \int_{-\infty}^{\infty}\int_{-\infty}^{\infty}\int_{-\infty}^{\infty}\int_{-\infty}^{\infty} u^i v^j w^k \psi^l\, p(u,v,w,\psi)\,dudvdwd\psi$$

where the lower case indicates the fluctuation from the mean, and the *i*, *j*, *k*, and *l* are any integers from 0 through *N* inclusive.

The known solution to this problem (Weinstock [3]) is obtained by forming the function

$$f^* = -p \ln p - \sum_{i=01}^{N}\sum_{j=0}^{N}\sum_{k=0}^{N}\sum_{l=0}^{N} u^i v^j w^k \psi^l \lambda_{ijkl}\, p$$

and solving for

$$\frac{\partial f^*}{\partial p} = 0.$$

This yields

$$\frac{\partial f^*}{\partial p} = -\ln p - 1 - \sum_{i=0}^{N}\sum_{j=0}^{N}\sum_{k=0}^{N}\sum_{l=0}^{N} u^i v^j w^k \psi^l \lambda_{ijkl} = 0$$

Thus p is given by

$$\ln p = 1 - \sum_{i=0}^{N}\sum_{j=0}^{N}\sum_{k=0}^{N}\sum_{l=0}^{N} u^i v^j w^k \psi^l \lambda_{ijkl}.$$

Hence the maximum entropy PDF for the stated constraints is given by

$$p = \exp\left(1 - \sum_{i=0}^{N}\sum_{j=1}^{N}\sum_{k=0}^{N}\sum_{l=0}^{N} u^i v^j w^k \psi^l \lambda_{ijkl}\right).$$

The constants, λ_{ijkl} are set so the final PDF has the same moments as given by the constraints.

6 Experimental data

Experimental data for one-dimensional moments of turbulent flows of order 5 or higher are very difficult to find and tend to come from work published in the 1970's. The sources of experimental data used for this work come from the following sources. Antonia and Sreenivasan [4] presented moments up to 8th order of the axial and cross-stream velocities and temperature for a turbulent heated jet. Py and Duhamel [5] presented moments up to the 5th order moment for the partial derivative of the velocity at the wall as a function of Reynolds number for a two-dimensional channel. The moments up to the 6th order of the fluctuating wall shear stress for an eight degree conical were reported by Derksen [6].

6.1 Comparison to the maximum entropy approximation

The maximum entropy approximation was applied to the experimental data using the measured moments up to and including the fourth as constraints. In all cases, the final predicted movements up to and including the fourth matched to better than four decimal places, confirming that the approximation was correct.

Table 1: The maximum entropy and measured fifth order moments.

Source	Meas.	Comp.	Source	Meas.	Comp.
Antonia, u, $\eta = 0.00$	-1.52	-1.34	Py, τ_w, Re=1935	120	117
Antonia, u, $\eta = 0.67$	0.17	0.22	Py, τ_w, Re=2300	27.9	27.7
Antonia, u, $\eta = 0.89$	2.28	2.36	Py, τ_w, Re=2615	5.76	4.42
Antonia, u, $\eta = 1.19$	8.54	9.37	Py, τ_w, Re=3500	4.98	4.50
Antonia, u, $\eta = 1.48$	39.3	55.2	Py, τ_w, Re=5000	4.37	4.20
Antonia, u, $\eta = 1.63$	24.5	39.5	Py, τ_w, Re=7200	4.44	4.04
Antonia, v, $\eta = 0.00$	-0.53	-0.96	Py, τ_w, Re=9950	4.25	3.90
Antonia, v, $\eta = 0.67$	1.24	1.53	Py, τ_w, Re=15000	4.17	3.84
Antonia, v, $\eta = 0.89$	3.45	4.22	Derksen, τ_w, x=4.62	9.80	9.10
Antonia, v, $\eta = 1.19$	9.52	13.0	Derksen, τ_w, x=15.59	5.22	4.98
Antonia, v, $\eta = 1.48$	37.7	51.2	Derksen, τ_w, x=19.58	3.30	2.97
Antonia, v, $\eta = 1.63$	74.6	112	Derksen, τ_w, x=23.57	3.94	3.53
Antonia, θ, $\eta = 0.00$	-3.35	-3.84	Derksen, τ_w, x=31.55	4.69	4.23
Antonia, θ, $\eta = 0.67$	-1.09	-1.51	Derksen, τ_w, x=39.53	4.40	3.86
Antonia, θ, $\eta = 0.89$	0.79	0.31	Derksen, τ_w, x=50.71	9.43	8.96
Antonia, θ, $\eta = 1.19$	3.80	3.11	Derksen, τ_w, x=55.69	9.55	8.69
Antonia, θ, $\eta = 1.48$	20.3	18.1	Derksen, τ_w, x=69.46	7.13	6.75
Antonia, θ, $\eta = 1.63$	70.9	64.9	Derksen, τ_w, pipe	1.97	1.87
Py, τ_w, e=1700	12.3	0.21			

The resulting fifth and sixth order moments from the maximum entropy approximation are compared to the measured moments in Table 1 for the fifth order moments and Table 2 for the sixth order moments. General agreement between the measured and computed fifth order moments is observed with two exceptions. These exceptions are: (1) The agreement is poor at the outer edge of the heated jet, $\eta = 1.48$ and 1.63, This may be due to the flow being highly intermittent in this zone. (2) The Py data at the lowest Reynolds numbers, 1700 and 1935, also does not agree well, however the agreement is much better as the Reynolds number increase. So this may be due to the flow not being fully turbulent.

Table 2: The maximum entropy and measured sixth order moments.

Source	Meas.	Comp.	Source	Meas.	Comp.
Antonia, $u,\ \eta = 0.00$	15.7	15.1	Antonia, $\theta,\ \eta = 0.89$	7.28	7.30
Antonia, $u,\ \eta = 0.67$	12.6	11.9	Antonia, $\theta,\ \eta = 1.19$	10.0	8.07
Antonia, $u,\ \eta = 0.89$	14.2	12.6	Antonia, $\theta,\ \eta = 1.48$	72.0	55.0
Antonia, $u,\ \eta = 1.19$	32.0	31.6	Antonia, $\theta,\ \eta = 1.63$	358	282
Antonia, $u,\ \eta = 1.48$	234	369	Derksen, τ_w, x=4.62	41.1	36.0
Antonia, $u,\ \eta = 1.63$	508	878	Derksen, τ_w, x=15.59	22.7	21.8
Antonia, $v,\ \eta = 0.00$	17.6	21.6	Derksen, τ_w, x=19.58	18.0	17.5
Antonia, $v,\ \eta = 0.67$	14.3	13.7	Derksen, τ_w, x=23.57	18.6	17.2
Antonia, $v,\ \eta = 0.89$	19.7	20.3	Derksen, τ_w, x=31.55	20.1	18.3
Antonia, $v,\ \eta = 1.19$	44.4	59.0	Derksen, τ_w, x=39.53	18.4	16.5
Antonia, $v,\ \eta = 1.48$	223	319	Derksen, τ_w, x=50.71	39.7	36.4
Antonia, $v,\ \eta = 1.63$	594	1000	Derksen, τ_w, x=55.69	39.0	33.0
Antonia, $\theta,\ \eta = 0.00$	18.7	21.0	Derksen, τ_w, x=69.46	27.6	25.7
Antonia, $\theta,\ \eta = 0.67$	9.46	10.1	Derksen, τ_w, pipe	14.3	14.0

The results for the sixth moment mirror those for the fifth moment, however it should be noted that no data for the sixth moment was available from the Py data.

These results indicate that the maximum entropy approximation predictions of the fifth and sixth order moments are in general agreement to those obtained from measurement where the flow is fully turbulent. This is an interesting observation but further experimental studies would need to be done to confirm that turbulence generated PDFs are maximum entropy PDFs that constrain moments to the fourth order.

One factor that needs careful consideration in further studies is that of the uncertainty in measuring the higher order moments. This mandates the use of very large samples, in the order of 100,000 to 1,000,000 samples, to ensure that the rare events can be observed.

7 Conclusions

The results presented here present a compelling case for assuming that the PDF from a turbulent process results in a maximum entropy approximation that constrains moments up to the fourth order. However, it is recognized that more study needs to be done to confirm the validity of this statement.

References

[1] P.W. Atkins, *The 2nd Law, Energy, Chaos, and Form*, Scientific American Library, New York, 1994.

[2] W.H. Press, B.P. Flannery, S.A. Teukolsky and W.T. Vetterling, *Numerical Recipes: The Art of Scientific Computing*, Cambridge University Press, Cambridge, 1986, pg 52-64.

[3] R. Weinstock, *Calculus of Variations with Applications to Physics and Engineering*, Dover, New York, 1974, pg. 134.

[4] R.A. Antonia and K.R. Sreenivasan, *Statistical Properties of Velocity and Temperature Fluctuations in a Turbulent heated Jet*, University of Newcastle Report, T.N.F.M. (1976).

[5] B. Py, and P. Duhamel, Mesure des Distributions Statistiques du Gradient Parietal de Vitesse Longitudinale en Canal Bidimensional, *C.R. Acad. Sc. Paris* 275 (1972) 373-376.

[6] R.W. Derksen, An Experimental Investigation of the Fluctuating Wall Shear Stresses in an Eight Degree Conical Diffuser, Ph.D. thesis, University of Manitoba, Winnipeg, MB, Canada, 1985.

Section 9
Applications in biology

This page intentionally left blank

Use of heart blood flow analysis in clinical practice

A. K. Macpherson[1], S. Neti[1], M. Averbach[2], P. A. Macpherson[3] & C. Chutakositkanon[4]
[1]*Institute of Biomedical Engineering and Mathematical Biology, Lehigh University, USA*
[2]*Division of Cardiology, St Luke's Hospital, USA*
[3]*Department of Applied Technology, Rogers State University, USA*
[4]*Department of Mechanical Engineering, Mahidol University, Thailand*

Abstract

Often in the treatment of patients echocardiograms are performed to analyse cardiac function. As part of the calculation the shear and normal stress on the endocardial surface of the left ventricle can be calculated. This was undertaken for five elderly women patients undergoing stress testing. It was found that when the stress was plotted as a function of strain rate the expected variation would be a linear increase in stress. In some patients there was initially a sharp increase in stress with strain rate then an abrupt change in the stress at the apex or at the mitral valve annulus. With further increase in strain rate the rate of increase in stress decreased. This would suggest that there was some defect in the wall structure. The variation of ventricular volume with strain rate can be obtained. In this case the volume should decrease initially and as the strain rate increases the volume change becomes less. In two of the five patients the expected initial rise in stress did not occur. This suggests a lack of strength of the ventricle. As expected these were not the same patients where the abrupt increase in stress occurred. Such information may be helpful to a clinician in reaching a diagnosis.
Keywords: cardiography, blood flow, echocardiograms, patient diagnosis, stress test, dobutamine.

WIT Transactions on Engineering Sciences, Vol 74, © 2012 WIT Press
www.witpress.com, ISSN 1743-3533 (on-line)
doi:10.2495/AFM120481

1 Introduction

Physicians obtain a graphical outline of the heart's movement using high-frequency sound waves, called ultrasound. The result is called an echocardiogram (known as an echo). This test also provides pictures of the heart's valves and chambers. When combined with Doppler ultrasound and colour Doppler, pictures of the blood flow across the heart's valves can be obtained as shown in figure 1.

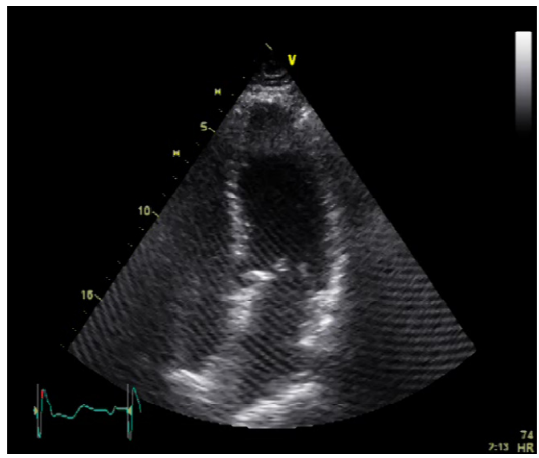

Figure 1: Echocardiogram that could be machine read.

It is possible to undertake the calculation of blood flow to include the whole of the left ventricle using the rate of change of the myocardium and the septum walls [1]. This additional information would be useful for physicians in making a diagnosis of a patient's condition. If the quality of the echo is very good, such as those produced by the equipment manufacturers, then automating the reading of the position of the heart walls can be undertaken. However the quality of many echos is such that it is difficult to discern the edge of the heart, figure 2.

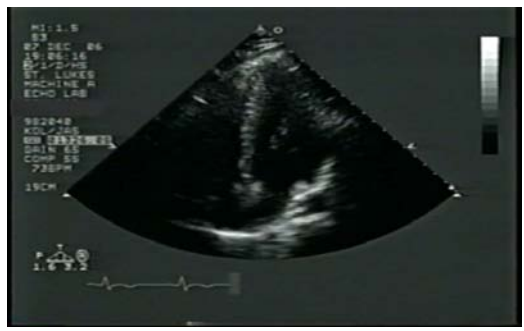

Figure 2: Echocardiogram which could not be machine read.

Thus a problem arises in implementing this on a wide scale as it would be necessary to automate the reading of the position of the heart walls. As the equipment improves in ease of use this should not present a problem.

2 Method of calculation

The general method of calculation used here has been described previously [3, 4]. The method is based on [5] and known as the immersed boundary method. The modification made in the method is that instead of specifying the boundary force the shape of the ventricle as a function of time is taken from the echocardiograms. The immersed boundary method has been reviewed in [6]. In the solution the blood flow into the left atrium is simulated by a source distributed throughout the atrium. In order to conserve mass sinks are distribute around the periphery of the integration domain. The change in shape is obtained from the echocardiograms and used as boundary conditions for the flow. The source strength has to match the change in volume of the ventricle. The valves have to be modelled as thicker than in reality as Lagranian integration must go around both sides of the valve. The Navier-Stokes equations are then solved with a predictor corrector scheme [4].

The Navier Stokes equations defined on an x-y Cartesian co-ordinate system for an incompressible fluid are

$$\rho\left(\frac{\partial \hat{u}}{\partial t} + \hat{u} \bullet \nabla \hat{u}\right) + \nabla p = \mu \nabla^2 \hat{u} + \hat{F} \tag{1}$$

$$\nabla \hat{u} = 0 \tag{2}$$

where $\hat{u}$ is the velocity vector, ρ is the density, t is the time, p is the pressure and the viscosity is μ.

The boundary force $\hat{F}$ arising from the heart muscles is

$$\hat{F}(\hat{x},t) = \int_0^L \hat{f}(s,t)\delta\left(\hat{x} - \hat{X}(s,t)\right)ds \tag{3}$$

Here $\hat{f}$ is the force on the boundary element at the point s defined on a Lagrangian system where $\hat{x}$ is defined on the Cartesian system and $\hat{X}^n$ is the *nth* point on the Lagrangian system

The flow velocities and pressures can be used to calculate the stresses on the surface of the heart walls. These forces can then be used to examine the microscopic interaction with the cells in the heart wall (endocardium).

The first step in the solution involves obtaining the shape of the ventricle at various times. This is often difficult as echocardiogram images are sometimes indistinct. Following a method often used by echocardiographers only five images in a cardiac cycle were selected. One image when the valves were closed, a second image when the valves were fully open, a third just before the atrium starts to contract, one at the end of the ventricle filling (diastole) stage and a

final one as the aortic valve opens. A linear variation was assumed between each image, time frame. It was assumed that the motion of the wall would be normal to the surface. As described below the times required for valve opening and atrium contraction can be obtained from Doppler measurements of the velocity through the mitral valve and the shape was obtained from the echocardiogram contained many irregularities. The echocardiogram tracing was obtained as a digital image. If the source was allowed to start while the valves were closed then the program would fail due to excessive pressure. Similarly the wall could not be allowed to start moving until the source started. Thus an initial short period was required without source or wall motion to allow the valves to start opening (these events are independent of fluid motion are dependent on cardiac electrical signals).

The second step required the simulation of the atrium. The atrium changes shape during the diastole stage and thus changes the pressure. However the use of a source in place of the correct inflow pattern to the atrium was an artifice which made the actual atrium shape unimportant. The atrium shape was fixed at near hemispherical shape with valves in the closed and early open positions. After some time the atrium contracts for a period before the mitral valve closed... The shape was expanded and contracted as required for the different sized mitral valves. The source strength was increased slowly as the valves opened in accordance with the increase in volume of the ventricle.

Once the calculation of the flow velocities and pressures were completed the stresses at the walls were calculated. This was undertaken following [7] and [8] as the gradient of the velocity near the wall. As the shear stress is continuous at the wall interface this will be equal to the shear force on the ventricle wall. In accordance with the aim of the research, evaluation of wall stresses, the boundary layer had to be modelled properly... Two points were chosen as close to the wall as possible along a line normal to the surface. A finite difference method was used to obtain the derivative of the velocity along this line. Similarly the velocity normal to the wall was calculated along the same line. As only pressure gradients are used in the calculations, an arbitrary constant was added to the pressure to make it relative to atmospheric pressure.

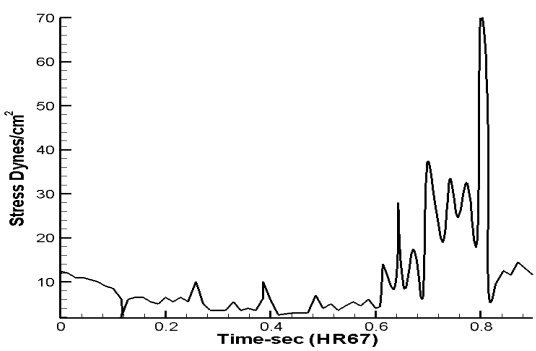

Figure 3: Time variation of shear stress.

3 Results

The results are presented as the variation of time averaged stress with heart rate.

In viewing the results it should be remembered that all five patients were elderly women.

Consider patient 1. From figure 5 it can be seen there is a peak in the shear stress around 90 BPM. This could be due to the apex not relaxing sufficiently as the heart rate increases. This is later, figure 4, reflected in the normal stress around the mitral valve at a higher heart rate. Thus at a later time the mitral valve could develop problems.

Patient 2. Both the shear and normal stresses figures 6 and 7, suggest that this patient appears to be the most normal of the five patients without any sharp changes in stress.

Patient 3. From figures 8 and 9 this patient bears some similarity to patient 1 where there is a peak in the shear stress at the apex and an increase in the normal stress at a slightly higher heart rate. As in patient 1 the peak occurs around 90 BPM. However both the shear and normal stresses increase around the mitral valve with increased heart rate.

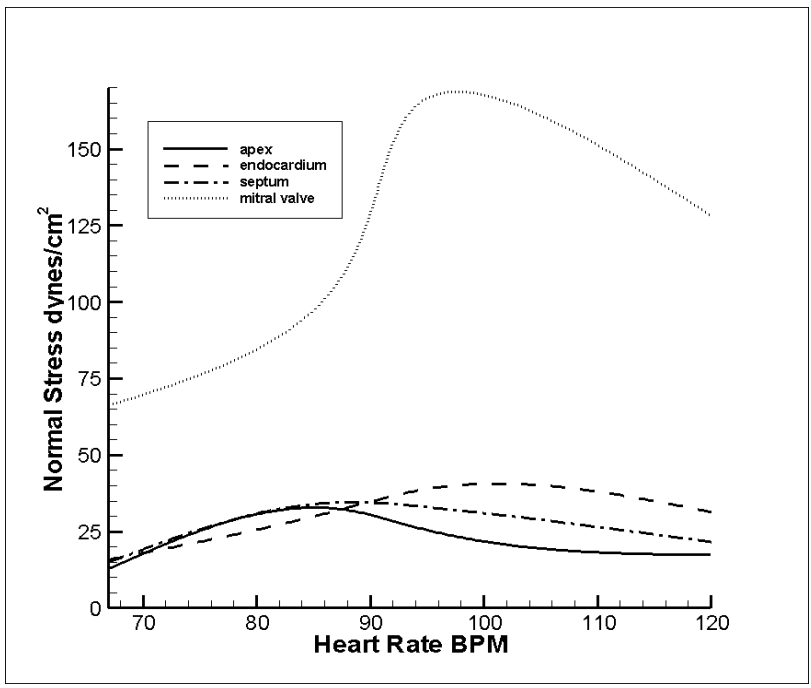

Figure 4: Patient 1 average normal stress over one cycle at various heart rates.

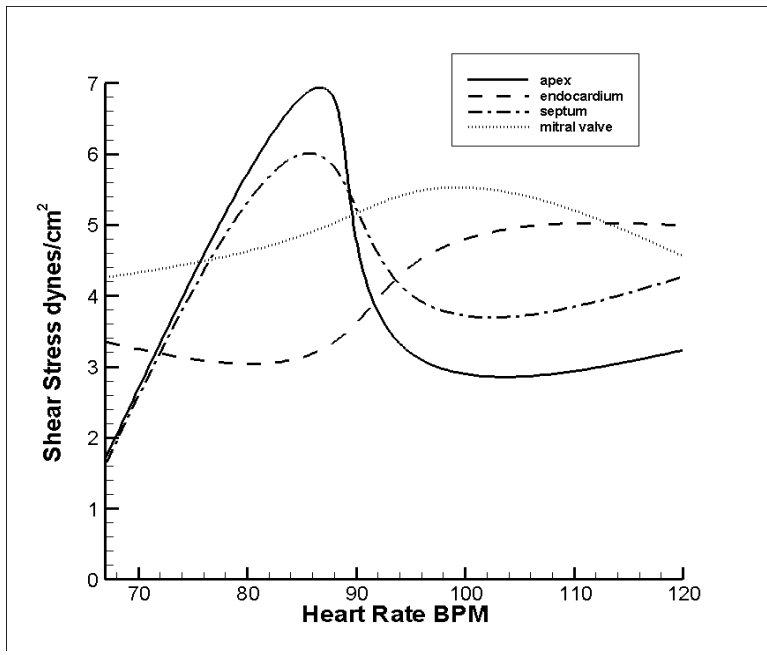

Figure 5: Patient 1 average shear stress over one cycle at various heart rates.

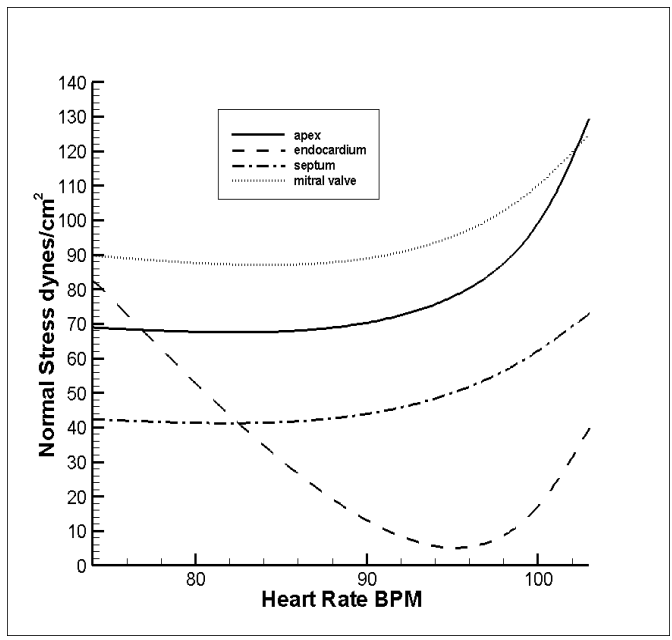

Figure 6: Patient 2 average normal stress over one cycle.

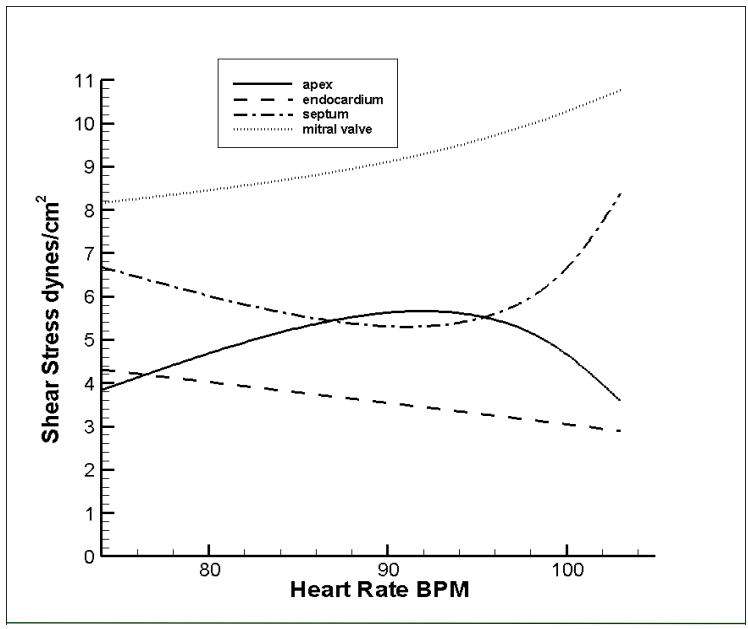

Figure 7: Patient 2 average shear stress over one cycle.

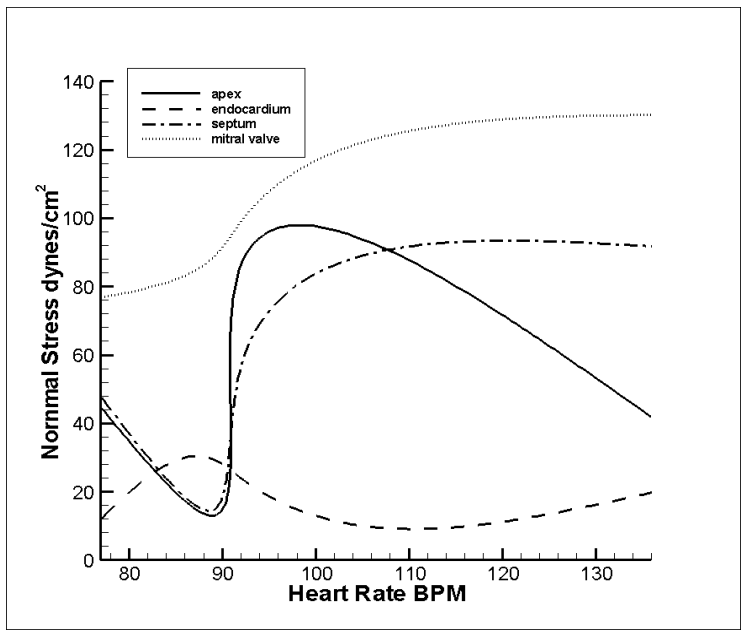

Figure 8: Patient 3 average normal stress over one cycle.

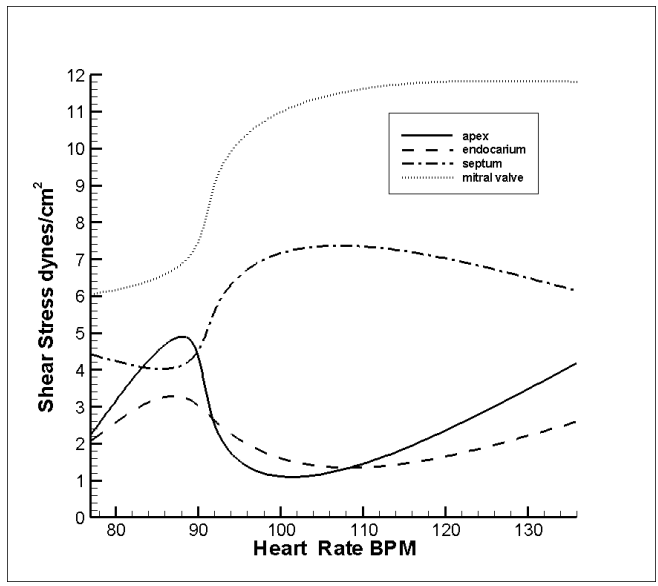

Figure 9: Patient 3 average shear stress over one cycle.

Patient 4. With this patient there is an increase in normal stress around the mitral valve at 95 BPM, figure 11 and a subsequent increase in shear stress figure 10 at the apex occurred at 115 BPM. There are subsequent increases in the shear stress around the mitral valve.

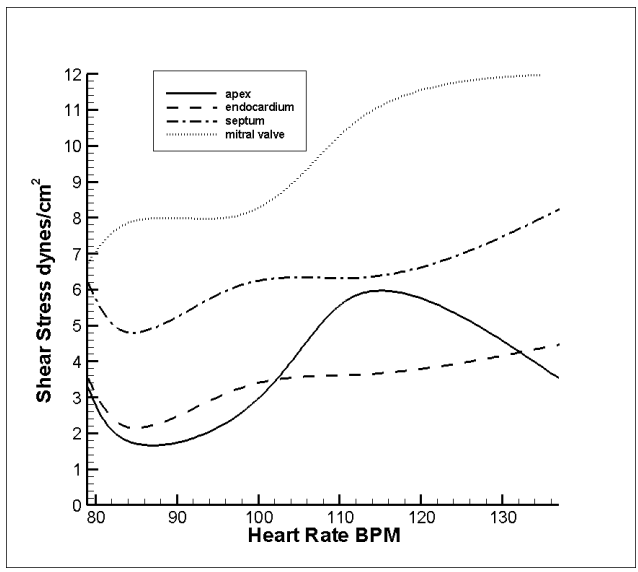

Figure 10: Patient 4 average normal stress over one cycle.

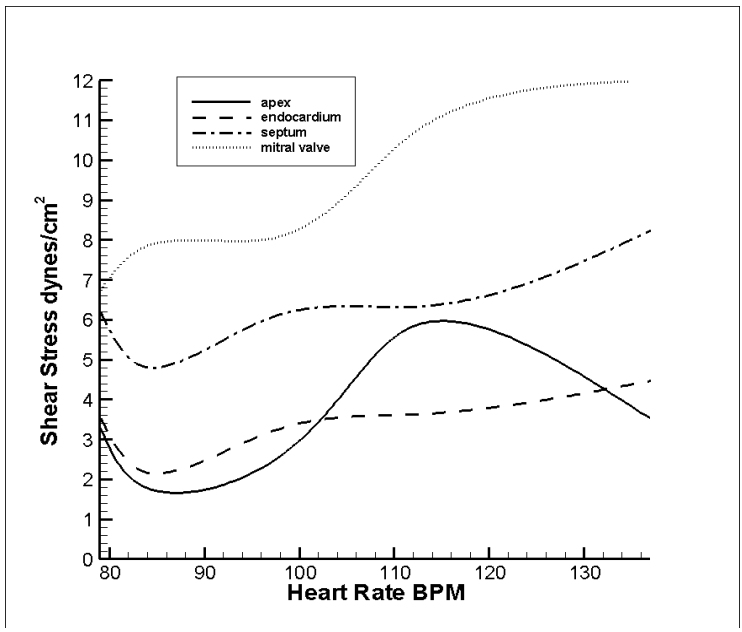

Figure 11: Patient 4 average shear stress over one cycle.

Patient 5. There was a steady increase in stress with BPM figures 12 and 3... Thus it may be possible that this patient would require treatment to lower the stress before such problems as ischemia occurred.

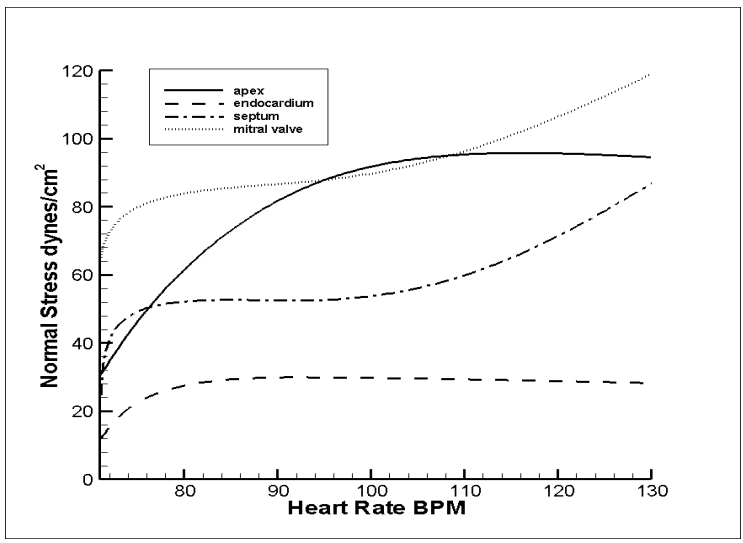

Figure 12: Patient 5 average normal stress over one cycle.

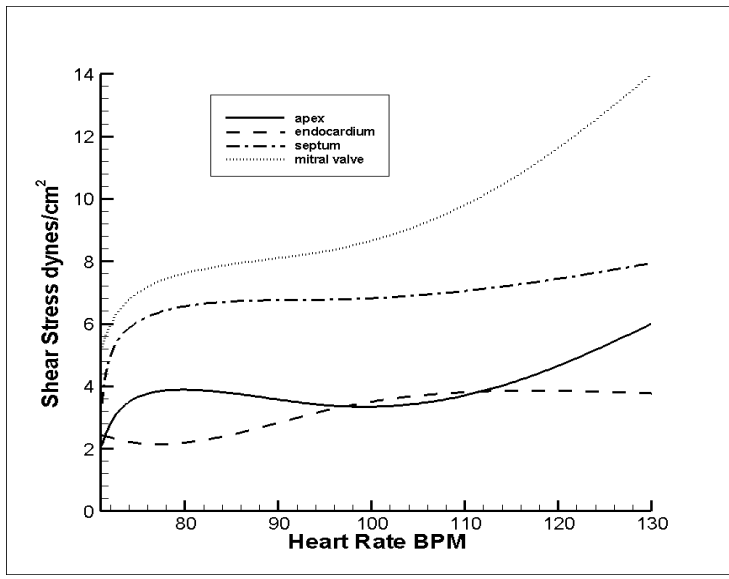

Figure 13: Patient 5 average shear stress over one cycle ventricle with time.

4 Conclusions and future work

It has been demonstrated that additional potentially useful information could be developed from an analysis of the blood flow in the left ventricle. The main problem involved before clinical trials could be undertaken is the automation of the reading of echocardiograms produced in clinician's offices. It would not be possible to recruit busy clinicians for such a study if their intervention was required. This is one of our foremost objectives to use artificial intelligence methods to estimate the ventricle position. It is intended to expand the data base as more data becomes available.

References

[1] Macpherson, A. K., Neti, S., Mannisi, J., Mavromoustakos T and Macpherson P.A. "Temporal analysis of left ventricular shape and volume" Cardiovascular Disease Prevention VI, 2003.

[2] Macpherson, A. K., and Neti S, "The effect of Angiotensin II on heart blood flow and hypertension", *Advances Fluid Mechanics IV, eds M. Rahman, R.Verhoeven, C.A. Brebbla, WIT press*, Southampton, 1-12, 2002.

[3] Macpherson, A. K., Neti, S., Macpherson, P.A., Houser, S.R., Hari M and Marzillier J. Mechanical Stress and Hypertrophy, *Modelling in Medicine and Biology VI*, eds M. Ursino, Ca, C.A. Brebbia, G. Pontrelli, E. Magasso, *WIT press*, Southampton, 171-179, 2005.

[4] Peskin, C.S. “Numerical Analysis of Blood Flow in the Heart”, *Journal of Computational Physics*, 25, 1977, 220-252.
[5] Mittal, R, Iaccarino, G “Immersed Boundary Methods” *Annu. Rev. Fluid Mech.* 2005 37:239-61.
[6] Macpherson A.K., Neti, S., Averbach, M. and Macpherson, P.A. “Calculation of stress and the absorption of Angiotensin in the left ventricle based on two dimensional echocardiograms and MRIs” Modelling in Medicine and Biology VI. ed C.A.,WIT press, Southampton,2007,25-32.
[7] Macpherson, A.K., Neti, S., Chutakositkanon, C., Averbach, M and Macpherson, P.A. “*The variation of dobutamine induced heart stress with heart rate”* Modelling in Biomedicine and Biology VIII, ed C.A,WIT press, Southampton, 2009,17-26.

This page intentionally left blank

Application of statistical methods in human airway flow analysis

F. Lizal[1], M. Fusek[2], J. Jedelsky[1] & M. Jicha[1]
[1]*Energy Institute, Faculty of Mechanical Engineering, Brno University of Technology, Czech Republic*
[2]*Institute of Mathematics, Faculty of Mechanical Engineering, Brno University of Technology, Czech Republic*

Abstract

Understanding of the air flow in human airways is the cornerstone for targeted delivery of a medication to the lungs. Direct in-vivo measurement in lungs is complicated; therefore in-vitro measurements in human lung models are frequently performed employing optical measurement methods. Irregularly sampled data acquired by Phase Doppler Anemometry in various locations of a model of human lungs for different breathing conditions were statistically processed to facilitate comparison and influence of diverse factors on the lung airflow. Tests based on signs of differences, Kendall's rank correlation coefficient test and Spearman's rank correlation coefficient test were used to detect a linear trend between the samples, while a median test of randomness and a turning point test were used to detect differences of a periodical nature. The presented statistical tools allow detection of inter-cycle variability in velocity course as well as evaluation of the influence of breathing pattern change or gradual flow development in an airway. Application of the above mentioned methods on our data confirmed the essential influence of lung geometry on flow profiles and revealed remarkable flow behaviour in the main bronchi. Usability of the statistical tools is not limited to measurements in human lung models, but can be extended to any flow measurements, for comparison of irregularly and regularly sampled data and also for comparison of numerical simulations with experiments.
Keywords: flow analysis, human airways, lung flow, statistical analysis, airflow measurement.

WIT Transactions on Engineering Sciences, Vol 74, © 2012 WIT Press
www.witpress.com, ISSN 1743-3533 (on-line)
doi:10.2495/AFM120491

1 Introduction

Targeted delivery of aerosolized medication to human lungs is of growing interest, since respiratory as well as systemic diseases can be treated using inhaled pharmaceuticals. Inhalation route represents a less harmful and a less painful way of drug administration when compared with the intravenous and oral methods, respectively. The necessary precondition to achieve minimal side-effects of medication is to deliver the right amount of drug to the right location. Failing to achieve this goal leads to increased load of organism which may result into wastage of often very expensive medication (Kleinstreuer *et al.* [1]).

Deposition area of inhaled aerosol depends on many factors, such as breathing pattern, lung capacity, geometry of airways, size and shape of particles, their initial velocity and others. Measurement of influence of these parameters on aerosol deposition *in vivo* is complicated due to restricted access and variability of geometry related to physiological factors; therefore *in vitro* experiments are frequently performed on models of human airways with various degree of simplification [2–4]. Also numerical modelling has been often used to simulate the flow and fate of inhaled particles [5–7].

In vitro measurement of flow velocity in different parts of airways can be performed using optical measuring methods, such as Particle Image Velocimetry (PIV) or Phase Doppler Anemometry (PDA). Application of PIV is limited by optical distortions on the model/fluid boundaries arising from different refractive index of air and material of the model. This problem could be avoided by using liquid with identical refractive index as the material of model walls as a carrier medium for tracing particles [8, 9]. However, for measurements with aerosol PDA is the only possibility. In addition to particle velocity PDA measures the size of particles and consequently can serve for investigation of clustering of particles or velocity spectra analysis, for it provides time-resolved velocity record. The disadvantage of the PDA is only point-wise measurement, hence other methods have to be used for identification of the general flow behaviour and identification of eddies and wakes.

Comparison of PDA results acquired for different input conditions such as various breathing patterns or various sizes of particles is often a complex issue, but can be solved by assessment of experienced researcher; nevertheless, the result is always influenced by a subjective perspective. Statistical methods presented in this paper allow unbiased evaluation of such data sets.

2 Methods

Realistic human airway model was used for PDA measurements of velocity and size of aerosol particles in 16 cross-sections. Breathing was simulated using computer controlled mechanism moving piston in a cylinder with sinusoidal shape of the piston velocity. Measured velocities were then processed to allow comparison of various breathing regimes and velocities in different measuring location employing statistical tests of randomness.

2.1 Measurement setup

The airway model was fabricated from optically transparent thin walled silicone as described in Lizal *et al.* [10]. The model incorporates airways down from pharynx up to fourth bifurcation level, and has asymmetrical branching and realistic curved tubes, fig. 1. In this paper only seven cross-sections (marked A – G in fig. 1) were included and 5 points in each cross-section were used for comparison. Nomenclature of measuring points is as follows: the first character represents cross-section, the second stands for measuring point (F – front, B – back, R – right, L – left, no letter – point in the axis), please note that due to different orientation of the tube axis in left and right bronchi and trachea, position R is in the left bronchus on the lower side of the tube, while in the right bronchus position R is on the upper side of the tube. The third entry of the code is the distance of the point from the tube axis.

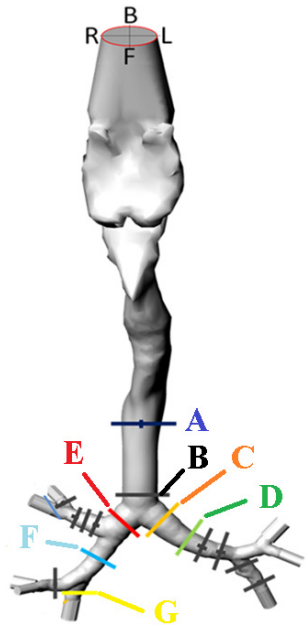

Figure 1: Model of human airways with measuring cross-sections.

The measuring setup (fig. 2) consists of Condensation Monodisperse Aerosol Generator (4) (CMAG, TSI 3475, TSI Inc.) producing liquid 3 μm particles from di-2-ethyl-hexyl sebacate (DEHS); Process Aerosol Monitor (PAM, TSI 3375, TSI Inc.) for on-line measurement of size and concentration of aerosol particles, mixing chamber (3), where aerosol is mixed with air from breathing mechanism (5) driven by motor (6) and controlled by computer to simulate three breathing patterns (resting conditions with tidal volume V_t = 0.5 liter and period T = 4 s,

deep breathing with V_t = 1 liter and T = 4 s and light activity with V_t = 1.5 liter and T = 3 s); realistic model of human lungs (1) and PDA transmitting and receiving optics (7). Aerosol is led to an elastic bag (2) which collects particles for the inhalation phase.

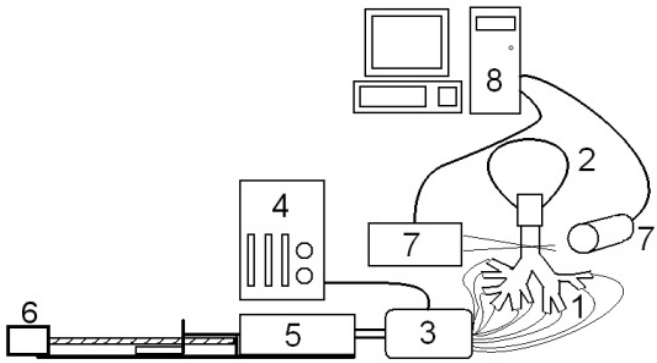

Figure 2: Diagram of the measurement setup.

PDA system (Dantec Dynamics, Skovlunde, Denmark) was adjusted for time-resolved measurement of axial velocity component and for complementary measurement of the particle size (for details see Jedelsky *et al*. [11]).

2.2 Data processing

The irregularly sampled data acquired by Phase Doppler Anemometry describe the breathing cycle in various locations of a model for different breathing patterns. Therefore, the data files contain various numbers of non-equidistantly distributed measurements. Novel software CIRDA [12] was created for processing of this kind of data. The software is suitable for comparison of large irregularly sampled data files.

To reduce the size of data files and to overcome the difficulty of irregularly sampled data, smoothing techniques were used, that is the kernel regression with local linear kernel estimator

$$f_h(x) = \frac{1}{n}\sum_{i=1}^{n} \frac{[s_2(x) - (x_i - x)s_1(x)]K_h(x_i - x)y_i}{s_2(x)s_0(x) - [s_1(x)]^2}. \quad (1)$$

where

$$s_r(x) = \frac{1}{n}\sum_{i=1}^{n} (x_i - x)^r K_h\,(x_i - x). \quad (2)$$

and Gaussian kernel

$$K_h(u) = \frac{1}{h\sqrt{2\pi}} e^{-\frac{u^2}{2h^2}}. \quad (3)$$

In our case, when a rather regular structure of data is observed, the use of some simple rule for the optimal bandwidth selection is sufficient. Thus the bandwidth is of the form (see Bowman and Azzalini [13])

$$h_x = \left(\frac{4}{3n}\right)^{\frac{1}{5}} \frac{\text{median}(|x_i - \tilde{x}|)}{0.6745}, \quad (4)$$

where $\tilde{x}$ represents the sample median. In order to cover the variability of the data in the direction of both x- and y-axis, the bandwidth is selected as

$$h = \sqrt{h_x h_y}. \quad (5)$$

The local linear estimator was chosen because of its favourable asymptotic properties and boundary behaviour (see e.g. Wand and Jones [14]).

A pair of irregularly sampled data files was processed by the above mentioned regression techniques, which results in regression curves with regularly sampled values. These regression curves were subtracted from each other and normalized by the square root of the sum of variances of the particular data files. This technique gave rise to a set of velocity values scattered around a constant. For cases where different breathing patterns were observed (e.g., normal breathing vs. light activity), particular regression curves were scaled to one of the breathing modes.

To decide whether two velocity profiles are similar or whether they differ, it is necessary to find out whether the subtracted velocity values are randomly scattered around a constant or whether there is a systematic component. Tests of randomness, as described below, were used to elucidate the velocity profiles

2.3 Tests of randomness

Tests of randomness (Cipra [15]) are often used for identification of a random, or systematic component (linear or periodic) in the series. The hypotheses simply are H_0: $x_i \sim$ *i.i.d.* (independent and identically distributed) and H_1: *otherwise*.

2.3.1 Test based on signs of differences

The test based on signs of first differences in the series $x_1,\ldots,x_n$ can be carried out by counting the plus and minus signs in the differences. The test is based on the number k of positive differences $x_{i+1} - x_i$, $i = 1,\ldots,n-1$, in the series.

Let's define a random variable V_i as

$$V_i = 1 \text{ for } x_{i+1} > x_i, \quad (6)$$

$$V_i = 0 \text{ for } x_{i+1} < x_i.$$

It can be shown, that the number of positive differences k has the expected value

$$E(k) = \frac{n-1}{2}. \tag{7}$$

and variance

$$Var(k) = \frac{n+1}{12}. \tag{8}$$

Variable k has the asymptotic normal distribution, thus for a sufficiently large sample size n the hypothesis H_0 is rejected on significance level α if

$$\frac{|k-(n-1)/2|}{\sqrt{(n+1)/12}} \geq u(\alpha/2). \tag{9}$$

where $u(\alpha/2)$ is a quantile of standard normal distribution N(0,1).

2.3.2 Kendall's rank correlation coefficient test

Let v be the number of pairs x_i and x_j, that $x_i < x_j$ for $i < j$. Kendall's rank correlation coefficient

$$\tau = \frac{4v}{n(n-1)} - 1. \tag{10}$$

has the asymptotic normal distribution with zero mean and variance

$$Var(\tau) = \frac{2(2n+5)}{9n(n-1)}. \tag{11}$$

The hypothesis H_0 is rejected on the significance level α if

$$\frac{|\tau|}{\sqrt{\frac{2(2n+5)}{9n(n-1)}}} \geq u(\alpha/2). \tag{12}$$

2.3.3 Spearman's rank correlation coefficient test

Let $q_1,\ldots,q_n$ be the ranked observations in the series $x_1,\ldots,x_n$. Ordinal ranking is used, thus all items receive distinct ordinal numbers, including items that compare equal. For example, if $x_1 = 10$, $x_2 = 1$, $x_3 = 5$, $x_4 = 1$, then $q_1 = 4$, $q_2 = 1$, $q_3 = 3$, $q_4 = 2$. Spearman's rank correlation coefficient ρ

$$\rho = 1 - \frac{6}{n(n^2-1)} \sum_{i=1}^{n} (i - q_i)^2 \ . \tag{13}$$

has the asymptotic normal distribution and the hypothesis H_0 is rejected on the significance level α if

$$|\rho| \sqrt{n-1} \geq u(\alpha/2) \ . \tag{14}$$

2.3.4 Turning point test

This test is based on the number of turning points (peaks and troughs) in the series $x_1,\ldots,x_n$. The upper turning point x_i is the local maximum $x_{i-1} < x_i > x_{i+1}$ and the lower turning point x_i is the local minimum $x_{i-1} > x_i < x_{i+1}$, $i = 2,\ldots,n-1$. Let p be the number of upper and lower turning points in the series. It can be shown that

$$E(p) = \frac{2(n-2)}{3} \ , \tag{15}$$

$$Var(p) = \frac{16n - 29}{90} \ . \tag{16}$$

Variable p has the asymptotic normal distribution and the hypothesis H_0 is rejected on the significance level α if

$$\frac{|p - 2(n-2)/3|}{\sqrt{(16n-29)/90}} \geq u(\alpha/2) \ . \tag{17}$$

2.3.5 Median test of randomness

This test is based on the sample median $\tilde{x}$ of the series $x_1,\ldots,x_n$. Each observation is compared with the median of the series and assigned "+" to those samples larger than the median and "–" to the samples less than the median. Assume that the ordered series has n samples, n_1 of "+", n_2 of "–", n_3 of observations equal to median and $n = n_1 + n_2 + n_3$. If $n_1 \neq n_2$, then one observation equal to median is assigned to "+" or "–" in order to fulfill $n_1 = n_2$. The numbers of runs of to "+" and "–" are denoted r_1, r_2 and then total number of runs is $r = r_1 + r_2$.

The hypothesis H_0 is rejected on the significance level α if

$$\frac{|r - (n_1 + 1)|}{\sqrt{n_1(n_1-1)/(2n_1-1)}} \geq u(\alpha/2) \ . \tag{18}$$

The test based on signs of differences, Kendall's rank correlation coefficient test and Spearman's rank correlation coefficient test are recommended (Cipra [15])

for linear trend detection in a given series. On the contrary, if there is a possibility of presence of periodic component in the data, the turning point test and median test of randomness are recommended.

3 Results and discussion

The first step of the data analysis using statistical tests implemented in software CIRDA involved tuning in of the kernel size for the regression of data. In general, the larger the kernel size, the stronger the suppression of the small fluctuations and vice versa. There is no rule for determination of the kernel size, because the size always depends on the character of the flow and phenomena, which is to be studied. Therefore in our case seven sizes of kernel were tested in the range 0.1 to 10 times the basic kernel size on three test cases. The first case were 2 cycles from one measurement, where no significant difference was expected; the second case was comparison of flow in tracheal cross-sections A and B, where major differences were expected; and the third case was comparison of cross-sections E and G, where completely different flow characteristics are present. The best agreement of the software results with expected values was achieved using kernel with 0.5 size of the basic kernel size. This size was used for comparison of all data files.

The sample results are presented in fig. 3. In the upper part are presented compared data sets. Both graphs include eight overlapped cycles plotted on a

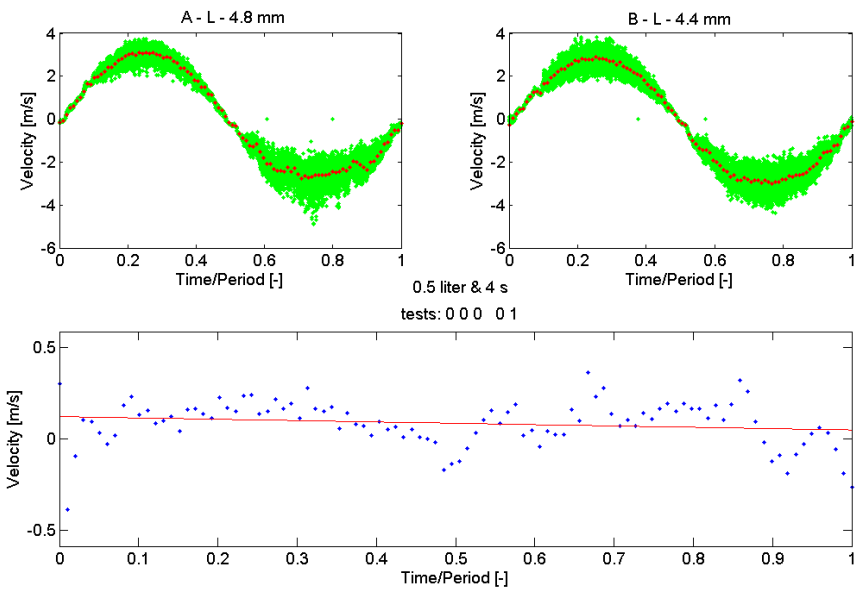

Figure 3: Comparison of measurement in points L above the left principal bronchus in trachea cross-section A (on the top left) and B (on the top right); subtracted velocities with linear regression (bottom).

dimensionless horizontal axis and regression of the cycle. Original sinusoidal course of the velocity induced by breathing mechanism is influenced by passage of the air through larynx and following airways during inhalation and by mixing of air from daughter branches during exhalation. Passage of a vortex through the measuring volume appears in the PDA velocity record as a wavelet (successive drop and increase or reverse) in the velocity course. The bottom part of fig. 3 contains calculated difference of velocities.

Table 1: Comparison of breathing patterns.

		0.5 liter & 4s vs. 1liter & 4s	1liter & 4s vs. 1.5 liter & 3s	0.5liter & 4s vs. 1.5 liter & 3s
A	0 mm	0 1 1 0 1	0 1 1 0 1	0 1 1 1 1
	R 4.4 mm	0 1 1 0 1	0 1 1 0 1	0 0 0 1 1
	L 4.4 mm	0 1 1 0 1	0 1 1 0 1	0 1 1 0 1
	F 4.4 mm	0 1 1 1 1	0 1 1 0 1	0 1 1 1 1
	B 4.4 mm	1 1 1 0 1	1 1 1 0 1	0 1 1 1 1
B	0 mm	0 0 0 0 1	0 1 1 0 1	0 1 1 0 1
	R 4.8 mm	0 1 1 0 1	0 1 1 0 1	1 0 0 1 1
	L 4.8 mm	0 0 0 0 1	0 1 1 0 1	0 1 1 1 1
	F 4.8 mm	0 1 1 0 1	0 1 1 0 1	0 1 1 0 1
	B 4.8 mm	0 1 1 0 1	1 0 0 1 1	0 1 1 1 1
C	0 mm	0 0 0 1 1	0 0 0 0 1	0 0 0 1 1
	R 3 mm	0 0 0 0 1	0 0 0 0 1	NED
	L 3 mm	0 0 0 0 1	0 0 0 0 1	0 1 1 0 1
	F 3 mm	0 0 0 1 1	0 1 1 1 1	0 0 0 0 1
	B 3 mm	0 1 1 0 1	1 0 0 0 1	1 1 1 1 1
D	0 mm	0 1 1 0 1	0 1 1 0 1	0 0 0 0 1
	L 2.3 mm	0 0 1 1 1	1 0 0 0 1	0 1 1 1 1
	R 2.3 mm	0 0 0 0 1	0 1 1 0 1	0 0 0 0 1
	F 2.3 mm	0 1 1 1 1	0 1 1 1 1	0 1 1 0 1
	B 2.3 mm	0 1 1 0 1	0 1 1 1 1	0 1 1 1 1
E	0 mm	1 1 1 0 1	0 1 1 0 1	0 1 1 1 1
	R 3.5 mm	0 0 0 0 1	0 1 1 1 1	0 0 0 1 1
	L 3.5 mm	0 0 0 0 1	NED	NED
	F 3.5 mm	0 0 0 1 1	0 1 1 1 1	1 1 1 1 1
	B 3.5 mm	0 1 1 1 0	NED	1 1 1 1 0
F	0 mm	0 0 0 1 1	0 1 1 1 1	0 1 1 1 1
	R 2 mm	NED	0 1 1 0 1	0 1 1 0 1
	L 2 mm	0 0 0 0 1	0 1 1 0 1	0 1 1 0 1
	F 2 mm	0 1 1 1 1	0 1 1 1 1	0 1 1 0 1
	B 2 mm	0 1 1 1 1	0 1 1 1 1	0 1 1 1 1
G	0 mm	0 1 1 1 1	0 1 1 1 1	0 1 1 1 1

NED (not enough data) – due to complicated conditions in some measuring points was not possible to acquire sufficient number of data points for relevant statistical analysis

The result of statistical analysis consists of five digits, which correspond to the outcome of the signs of differences, Kendall's, Spearman's, turning point and median test respectively. The first three digits answer the supposition about the existence of a linear trend and the last two represent the result of search for existence of periodical trend in the data. Number 0 stands for failure to reject the null hypothesis, that the two data sets are independent and identically distributed on the significance level $\alpha = 0.05$; number 1 stands for rejection of the null hypothesis.

All data files were primarily tested for inter-cycle variability. Every data record contains five to eight subsequent cycles; second and last but one cycle were used for testing. All data records except those with not enough data (NED) gave the same result – failure to reject the null hypothesis from all tests. Interpretation is that the flow behaviour is repeated every cycle with sufficient accuracy. Therefore all cycles from one data record were condensed into one dimensionless cycle (overlapped) and the following comparisons were performed on the dimensionless cycle.

Comparison of the influence of three breathing patterns mentioned in section 2.1 is presented in table 1. It is apparent that the change in flow is more reflected in middle of trachea (cross-section A) than in following airways, where the effect of geometry is essential.

The least influenced cross-section by the breathing pattern change is cross-section C, possibly because of the length of the left principal bronchus which helps to create similar flow patterns especially during the expiration phase. The results also proved that the most sensitive test is the median test, reflecting response to changes of periodical nature; on the contrary the test based on signs of differences, reflecting changes of linear nature, is the least sensitive to breathing pattern change.

Comparison of velocity behavior in corresponding points in different cross-sections of the model is presented in table 2. Points for comparison were selected on a basis of supposition where the specific particle flowing out from the one cross-section would enter the second cross-section assuming laminar flow.

The flow in right bronchus is significantly different from the flow in trachea. The test based on signs of differences is insensitive to the different flow, whereas median test gives rejection of the null hypotheses in all cases. Some similarity can be expected in cross-sections of the same branch and surprisingly in cross-sections B and C; however this claim is supported only by turning point test.

4 Conclusions

Presented statistical tools allow unbiased comparison of different data sets. Application of the tests on velocity data measured by PDA in realistic model of human airways proved essential influence of the lung geometry on the flow. Our results showed that the velocity profile in the left lung preserves basic shape for resting conditions breathing regime. For the more rapid breathing, the flow

Table 2: Comparison of flow in different locations. Column headers denote compared cross-sections, row labels denote measuring points: O - tube axis, R – right, L – left, F – front, B – back (see fig. 1).

		A-B	B-E	B-C	E-F	C-D
0.5 liter & 4s	O	0 1 1 0 1	0 1 1 1 1	0 1 1 1 1	0 1 1 1 1	0 1 1 1 1
	R	0 1 1 1 1	0 1 1 1 1	0 1 1 0 1	0 1 1 1 1	0 1 1 0 1
	L	0 0 0 0 1	0 1 1 1 1	0 1 1 1 1	0 1 1 1 1	0 1 1 1 1
	F	0 1 1 1 1	0 1 1 1 1	0 1 1 0 1	0 1 1 1 1	0 1 1 0 1
	B	0 1 1 1 1	0 1 1 1 1	0 1 1 1 1	0 1 1 1 1	0 1 1 1 1
1 liter & 4s	O	0 1 1 0 1	0 1 1 1 1	0 1 1 1 1	0 1 1 1 1	0 1 1 1 1
	R	0 1 1 1 1	0 1 1 1 1	0 1 1 1 1	0 1 1 1 1	0 1 1 0 1
	L	0 1 1 0 1	0 1 1 1 1	0 1 1 1 1	0 1 1 1 1	0 1 1 1 1
	F	0 1 1 1 1	0 1 1 1 1	0 1 1 0 1	0 1 1 1 1	0 1 1 1 1
	B	0 1 1 1 1	0 1 1 1 1	0 1 1 1 1	0 1 1 1 1	0 1 1 0 1
1.5 liter & 3 s	O	0 1 1 1 1	0 1 1 1 1	0 1 1 1 1	0 1 1 1 1	0 1 1 1 1
	R	0 1 1 1 1	0 1 1 1 1	0 1 1 1 1	0 1 1 1 1	NED
	L	1 1 1 1 1	NED	0 1 1 1 1	NED	0 1 1 1 1
	F	0 1 1 1 1	NED	0 1 1 1 1	0 1 1 1 1	0 1 1 1 1
	B	0 1 1 1 1	0 1 1 1 1	0 1 1 1 1	0 1 1 1 1	0 1 1 1 1

NED (not enough data) – due to complicated conditions in some measuring points was not possible to acquire sufficient number of data points for relevant statistical analysis

changes quickly during the passage through the airways, and statistical tests found significant differences in almost all measuring points. The statistical tests are also useful for detection of inter-cycle variability in velocity course. It should be noted that the most difficult part of the process is the interpretation of the results. In the first step of the statistical analysis the kernel size should be adjusted. Different choices of the size give different results due to suppression or amplification of small fluctuations. However, each setting provides specific information which can be useful for specific purpose. Usability of the statistical tools is not limited for measurements in human lungs models, but can be extended to any flow measurements, for comparison of irregularly and regularly sampled data and also for comparison of numerical simulations with experiments.

Acknowledgements

The authors are grateful to Mark Omara (Center for Air Resources Engineering and Science at Clarkson University) for reviewing this manuscript. This work was supported by the Czech Grant Agency under the grant GA P105/11/1339, by COST Action 0806 project OC10052 and by project ME 09030 of the program KONTAKT supported by the Czech Ministry of Education, Youth and Sports.

References

[1] Kleinstreuer, C., Zhang, Z., Li, Z., Roberts, W. L. and Rojas, C., A new methodology for targeting drug-aerosols in the human respiratory system. *International Journal of Heat and Mass Transfer*. **51(23-24)**, pp. 5578-5589, 2008.

[2] Gurman, J. L., Lippmann, M. and Schlesinger, R. B., Particle deposition in replicate casts of the human upper tracheobronchial tree under constant and cyclic inspiratory flow. 1. Experimental. *Aerosol Science and Technology*. **3(3)**, pp. 245-252, 1984.

[3] Kim, C. S. and Fisher, D. M., Deposition characteristics of aerosol particles in sequentially bifurcating airway models. *Aerosol Science and Technology*. **31(2-3)**, pp. 198-220, 1999.

[4] Zhou, Y. and Cheng, Y. S., Particle deposition in a cast of human tracheobronchial airways. *Aerosol Science and Technology*. **39(6)**, pp. 492-500, 2005.

[5] Katz, I. M., Davis, B. M. and Martonen, T. B. A numerical study of particle motion within the human larynx and trachea. *Journal of Aerosol Science*. **30(2)**, pp. 173-183, 1999.

[6] Isaacs, K. K., Schlesinger, R. B. and Martonen, T. B., Three-dimensional computational fluid dynamics simulations of particle deposition in the tracheobronchial tree. *Journal of Aerosol Medicine-Deposition Clearance and Effects in the Lung*. **19(3)**, pp. 344-352, 2006.

[7] Lin, C. L., Tawhai, M. H., McLennan, G. and Hoffman, E. A., Characteristics of the turbulent laryngeal jet and its effect on airflow in the human intra-thoracic airways. *Respiratory Physiology & Neurobiology*. **157(2-3)**, pp. 295-309, 2007.

[8] Adler, K. and Brucker, C., Dynamic flow in a realistic model of the upper human lung airways. *Experiments in Fluids*. **43(2-3)** , pp. 411-423, 2007.

[9] Hopkins, L. M., Kelly, J. T., Wexler, A. S. and Prasad, A. K., Particle image velocimetry measurements in complex geometries. *Experiments in Fluids*. **29(1)**, pp. 91-95, 2000.

[10] Lizal, F., Elcner, J., Hopke, P. K., Jedelsky, J. and Jicha, M., Development of a realistic human airway model. *Proceedings of the Institution of Mechanical Engineers Part H-Journal of Engineering in Medicine*. **226(H3)**, pp. 197-207, 2012.

[11] Jedelsky, J., Lizal, F. and Jicha, M., Some aspects of particle motion under cyclic flow in realistic human airway model. *Proceedings of the 21st ISTP*, Kaohsiung, Taiwan, 2010.

[12] Fusek, M., *CIRDA 1.0 (software for Comparison of IRregularly sampled DAta)*, Brno University of Technology, Brno, 2011, www.sw.howto.cz/CIRDA/

[13] Bowman, A. W. and Azzalini, A., *Applied smoothing techniques for data analysis : the kernel approach with S-Plus illustrations*, Clarendon Press; Oxford University Press, Oxford, New York, 1997.

[14] Wand, M. P. and Jones, M. C., *Kernel smoothing*, 1st ed Chapman and Hall, London; New York, 1995.
[15] Cipra, T., Analýza časových řad s aplikacemi v ekonomii, SNTL, Praha, 1986.

This page intentionally left blank

Author Index

Dam-break Problems, Solutions and Case Studies

Edited by: ***D. DE WRACHIEN*** *and* ***S. MAMBRETTI****, Politecnico di Milano, Italy*

This book provides an up-to-date review on dam-break problems, along with the main theoretical background and the practical aspects involved in dam failures, design of flood defence structures, prevention measures and the environmental, social, economic and forensic aspects related to the topic. Moreover, an exhaustive range of laboratory tests and modelling techniques is explored for dealing effectively with shock waves and other disasters caused by dam failures.

Disaster management refers to programs and strategies designed to prevent, mitigate, prepare for, respond to and recover from the effects of these phenomena. To manage and minimise these risks, it is necessary to identify hazards and vulnerability by means of a deep knowledge of the causes that lead to dam failures, and to understand the flow propagation process.

Knowledge and advanced scientific tools play a role of paramount importance in coping with flooding and other dam-break problems along with capacity-building in the context of political and administrative frameworks. All these aspects are featured in the book, which is a comprehensive treatise that covers the most theoretical and advanced aspects of structural and hydraulic engineering, together with the hazard assessment and mitigation measures and the social, economic and forensic aspects related to the subject.

ISBN: 978-1-84564-142-9 eISBN: 978-1-84564-384-3
Published 2009 / 368pp / £140.00

Computational Methods in Multiphase Flow VI

Edited by: ***A.A. MAMMOLI****, University of New Mexico, USA and* ***C.A. BREBBIA****, Wessex Institute of Technology, UK*

Multiphase flows, which can involve compressible or incompressible linear or nonlinear fluids, are found in all areas of technology, at all length scales and flow regimes. In spite of their ubiquitousness, multiphase flows continue to be one of the most challenging areas of computational mechanics and experimental methods, with numerous problems remaining unsolved to date.

Multiphase flow problems are so complex that advanced computational and experimental methods are often required to solve the equations that describe them. The many challenges include modelling nonlinear fluids, modelling and tracking interfaces, dealing with multiple length scales, characterising phase structures, and treating drop breakup and coalescence. Models must be validated, which requires the use of expensive and difficult experimental techniques.

This book presents contributions on the latest research in these techniques, presented at the sixth in a biennial series of conferences on the subject that began in 2001. Featured topics include: Multiphase Flow Simulation; Turbulent Flow; Bubble and Drop Dynamics; Heat Transfer; Incline Flows; Energy Applications; Flow in Porous Media.

WIT Transactions on Engineering Sciences, Vol 70
ISBN: 978-1-84564-518-2 eISBN: 978-1-84564-519-9
Published 2011 / 344pp / £148.00

Monitoring, Simulation, Prevention and Remediation of Dense and Debris Flows IV

Edited by: ***D. DE WRACHIEN****, Politecnico di Milano, Italy;* ***C.A. BREBBIA****, Wessex Institute of Technology, UK and* ***S. MAMBRETTI****, Politecnico di Milano, Italy*

Containing papers presented at the fourth and latest in a series of biennial International Conferences dealing with the Monitoring, Simulation, Prevention and Remediation of Dense and Debris Flow, this book addresses the need for a better understanding of the ever more frequent phenomena known as debris flows.

Due to the increased occurrence of debris and hyper-concentrated flows and the impact they have on both the environment and human life, these extreme events and the related processes have been attracting increased attention from research groups and land planning and management professionals. A full understanding of these phenomena will lead to an integrated risk management approach that can include measures to prevent a hazard turning into a disaster.

The papers presented at the conference deal with: Debris Flow Modelling; Debris Flow Triggering; Risk Assessment; Hazard Mitigation; Sediment Transport and Debris Flow Monitoring and Analysis; Landslide Phenomena; Debris Flow Rheology; Active and Passive Disaster Management; Vulnerability Studies; Structural and Non-structural Controls; Field Tests. The book will be useful to engineers, scientists and managers from laboratories, industry, government and academia who deal with risk management, natural disasters, and the phenomenon itself.

WIT Transactions on Engineering Sciences, Vol 73
ISBN: 978-1-84564-586-1 eISBN: 978-1-84564-587-8
Published 2012 / 264pp / £114.00

This page intentionally left blank